ISSN 0288-4534
CODEN: KONAE7

KONA

POWDER AND PARTICLE

No. 19 (2001)
Published by Hosokawa Powder Technology Foundation

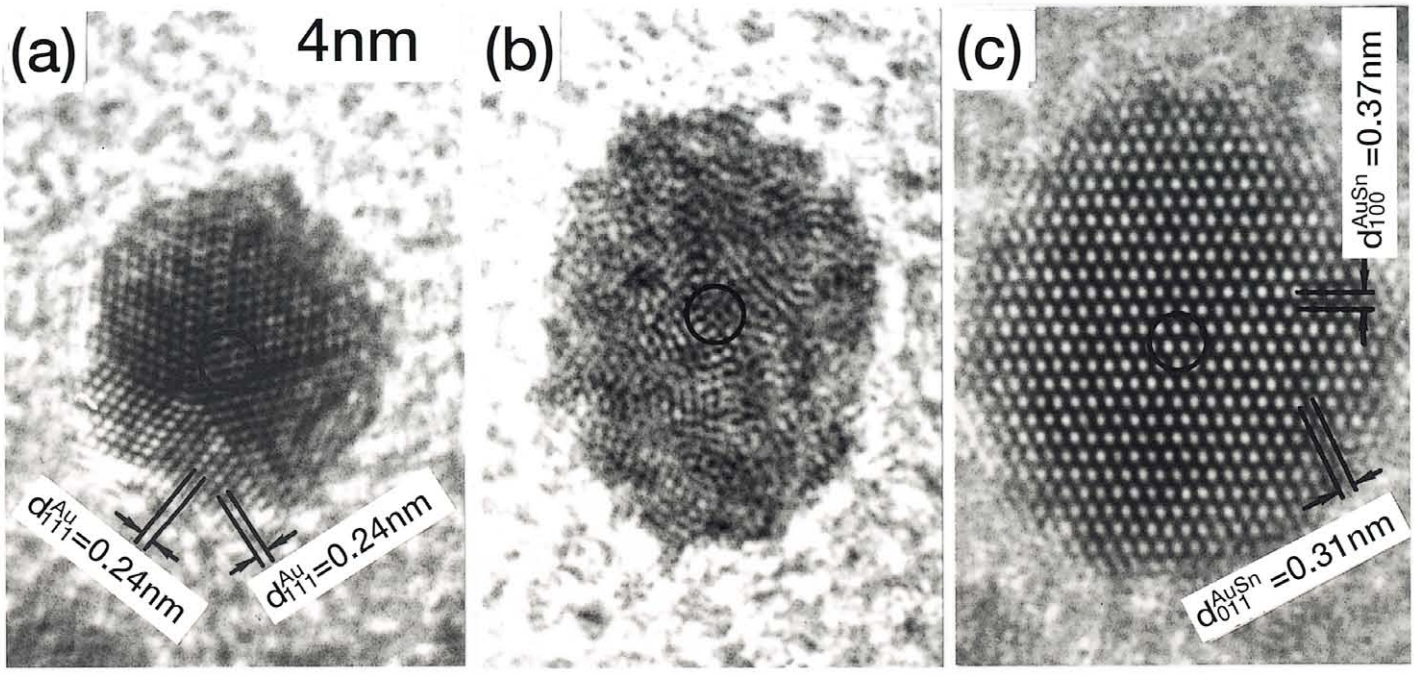

Alloy phase formation in nanometer-sized isolated particles

KONA

POWDER AND PARTICLE

KONA is a refereed scientific journal that publishes articles on powder and particle sciences and technology. KONA has been published annually since 1983 by the Hosokawa Powder Technology Foundation in Japan. KONA is distributed to researchers, members of the scientific community, universities and research libraries throughout the world.

About the Cover of Journal "KONA"

The Chinese character "粉" is pronounced "KONA" in Japanese, and means "Powder". The hand written "粉" is after the late Mr. Eiichi Hosokawa, founder of the Hosokawa Micron Corporation.

Hosokawa Micron Corporation and its R&D Center

■ **Publication Office**

Hosokawa Powder Technology Foundation (Japan) in Hosokawa Micron Corporation
No. 9, 1-chome, Shoudai Tajika, Hirakata-shi, Osaka 573 Japan

■ **Notes**

○ Hosokawa Powder Technology Foundation has entrusted the editorial duty to the editorial board organized by the Council of Powder Technology, Japan.

(Complimentary Copy)

Printed in Japan

The Letter from the Editor

Yasuo Kousaka
Editor-in-Chief

The Fourth World Congress on Particle Technology (4WCPT) will be held in Sydney from July 21st to 26th, 2002. In advance of the 4WCPT, the First Asian Particle Technology Symposium (APT 2000) was successfully held in Bangkok, Thailand, from December 13th to 15th, 2000. This meeting was partially supported by the Hosokawa Powder Technology Foundation. The number of participants totaled 297 from 20 separate countries from around the globe. In attendance were participants from 14 countries from the Asia/Oceania region (Australia, China, Indonesia, India, Japan, Malaysia, Mongolia, Philippines, Russia, Singapore, South Korea, Taiwan, Thailand and Vietnam) and participants from 6 countries from other regions of the world (France, Mexico, Netherlands, Sweden, UK and USA). APT will usually be held every 2 years. However, since the 4WCPT will be held in the Asia/Oceania region in 2002, the Second APT will be held in 2003, at Penang, Malaysia. I believe that this kind of regional symposium will strongly contribute to the promotion of particle science and technology in the future.

The Fine Powder Processing 2001, an International Conference on Formation, Characterization, Classification, and Processing of Micron and Smaller Powders, organized by the NSF Particulate Materials Center and Hosokawa Micron Powder Systems was held at Penn State Conference Center Hotel, in State College, Pennsylvania from October 1st to 3rd, 2001. On September 11th just prior to the international conference, the terrible terrorism incidents took place in USA and the number of participants was suddenly reduced down to about 100, almost half of the first conference held two years before in the same place. Despite the difficult situation, active discussions occurred in a wide range of powder processing and functional particle topics including nanopowders, pharmaceutical compounds, particle characterization, chemical processing methods and properties of powder-processed materials. Professor Brian Kaye, a significant contributor to the science and technology of particles and a long time Kona Board member, was awarded the "Lifetime Achievement Award" at the meeting for his contributions to fine powder processing by the NSF Particulate Materials Center. I would like to express my deep sense of condolence to the victims of the incidents in New York City and Washington D.C. and heartily wish a peaceful world for human beings and powder technology.

Anyway, I hope that the forthcoming Fourth WCPT will be fruitful and successful, and that we will have an opportunity to exchange ideas and opinions among the editors about the brilliant future developments of the KONA journal.

Yasuo Kousaka

KONA

GENERAL INFORMATION

HISTORY OF THE JOURNAL

KONA journal has been published by the Council of Powder Technology, Japan. (CPT), from No.1 to No.12 issues, under the sponsorships of Hosokawa Micron Corporation (No.1 to No.9) and Hosokawa Powder Technology Foundation (No.10 to No.12).

The CPT has been established in 1969 as a non-profit organization to enhance the activities of research and development on powder science and technology in Japan under the sponsorship of Hosokawa Micron Corporation. In 1983, the CPT has decided to issue an international journal named "KONA", which publishes the excellent articles appeared in Japanese journals concerning powder science and technology, after translated into English, throughout the world. After the seventh volume issued in 1989, the CPT has changed its policy to internationalize the "KONA" from the 8th issue (1990) and on by incorporating the monographs originally written in English from the authors throughout the world. Immediately, the present editorial board including Asian, Americas' and European Blocks has been organized.

From the 13th issue and on, the Hosokawa Powder Technology Foundation has taken over the role of KONA publisher from the CPT and the Foundation has entrusted the editorial duty to the present KONA editorial board organized by the CPT without requesting any shift in our present editorial policies. This switching of publisher has been simply and only to make the aim and scope of the Foundation definite. Essentially no change has been observed in continuously editing and publishing this journal except in the designation on a part of the journal cover.

AIMS AND SCOPE OF THE JOURNAL

KONA Journal is to publish the papers in a broad field of powder science and technology, ranging from fundamental principles to practical applications. The papers discussing technological experiences and critical reviews of existing knowledge in specialized areas will be welcome.

These papers will be published only when they are judged, by the Editor, to be suitable for the progress of powder science and technology, and are approved by any of the three Editorial Committees. The paper submitted to the Editorial Secretariat should not have been previously published except the translated papers which would be selected by the Editorial Committees.

CATEGORY OF PAPERS

- Invited papers
  Original research and review papers invited by the KONA Editorial Committees.
- Contributed papers
  Original research and review papers submitted to the KONA Editorial Committees, and refereed by the Editors.
- Translated papers
  Papers translated into English, which were previously published in other languages, selected by the KONA Editorial Committees with the permission of the authors and / or the copyright holder.

SUBMISSON OF PAPERS

Papers should be sent to each KONA Editorial Secretariat.

- Asia / Oceania Editorial Secretariat
  T. Kawamura
  Hosokawa Micron Corporation Micromeritics Laboratory 1-9, Shoudai Tajika, Hirakata 573 JAPAN
- Europe / Africa Editorial Secretariat
  Dr. P. van der Wel or Mrs. P. Krubeck
  Hosokawa MikroPul GmbH
  Welserstr. 9-11, 51149 Köln
  Postfach 900749, 51117 Köln
  GERMANY
- Americas Editorial Secretariat
  Dr.I. Pikus or D.A. Scort
  Hosokawa Micron International Inc.
  10 Chatham Road, Summit, NJ 07901 USA

PUBLICATION SCHEDULE

KONA is published once a year.

SUBSCRIPTION

KONA is distributed free of charge to senior researchers at universities and laboratories as well as to institutions and libraries in the field throughout the world. The publisher is always glad to consider the addition of names of those who wish to obtain this journal regularly to the mailing list. Distribution of KONA is made by each Secretariat.

INSTRUCTIONS TO AUTHORS

(1) Manuscript format

- Two copies should be submitted to the Editorial Secretariat, in double-spaces typing on pages of uniform size.
- Authorship is to give author's names, and the mailing address where the work has been carried out on the title page.
- Abstract of 100-180 words should be given at the beginning of the paper.
- Nomenclature should appear at the end of each paper. Symbols and units are listed in alphabetical order with their definitions and dimensions in SI units.
- Literature references should be numbered and listed together at the end of paper, not in footnotes. Alphabetical order is accepted. Please give information as in the following examples:
  1) Carslaw, H.C. and J.C. Jaeger: "Conduction of Heat in Solids", 2nd ed., Clarendon Press, Oxford, England (1960).
  2) Howell, P.A.: US Patent, 3,334,603 (1963).
  3) Rushton, J.H., S.Nagata and D.L. Engle: AlChEJ., 10. 294 (1964).
  4) Seborg, D.E.: Ph.D. Dissertation, Princeton Univ., N.J., U.S.A. (1969).
- Original figures with each single copy should be submitted, on separate sheets. Authors' names and figure numbers are marked in the corner.
- Figure numbers and captions are listed on a separate sheet.
- Place of figure insertion is to be indicated in the margin of the manuscript.
- Tables should be typed on separated sheets.
- Submit an IBM-readable floppy disk ($3_{1/2}$) with your unformatted text file in ASCII code. If you use either WORD or WORD PERFECT—as word processing system, please add the formatted text file.

(2) Reprints

- The authors shall receive 50 free reprints. Additional reprints will be furnished when ordered with return of galley proofs.

(3) Publication policy

- All papers submitted for publication become immediately the property of the CPT and remain so unless withdrawn by the author prior to acceptance for publication or unless released by the Editor. Papers are not to be reproduced or published in any form without the written permission of the CPT.

KONA Powder and Particle No. 19 (2001)

Contents

Explanation of the Cover Photograph

Alloy phase formation in nanometer-sized isolated particles

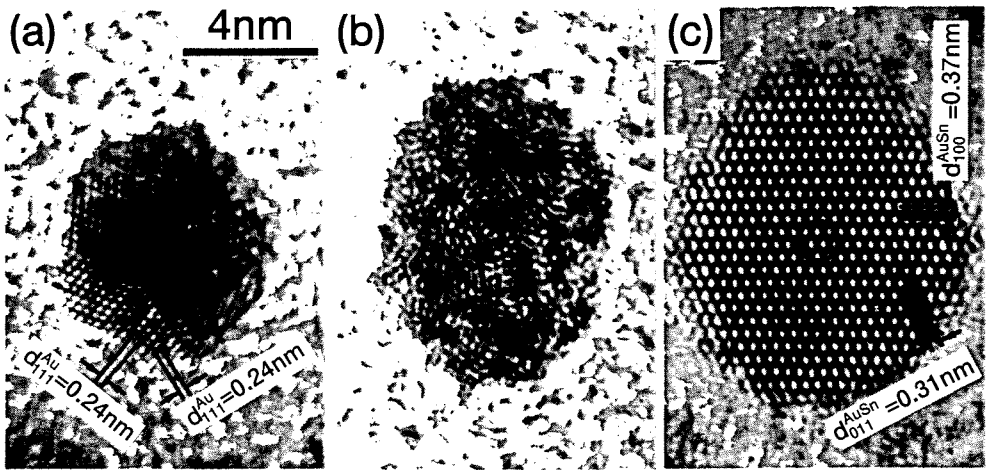

Recent remarkable progress in transmission electron microscopy (TEM) enables us to study not only the structure but also the chemical composition of nm-sized target materials, and with the use of the technique it now becomes possible to examine the phase stability of isolated nm-sized alloy particles as a function of temperature (T), composition (C), and size (d) of the system. This situation would open a wide, unexplored research field on the structure stability of nm-sized condensed matter in two- (or multi-) component systems.

Based upon this premise, the effect of particle size on the phase stability in nanometer-sized Au-Sn alloy particles has been studied by TEM, over a composition range from pure Au to Au-50at%Sn. Observations indicate when the size of particles is larger than about 10 nm an essentially similar phase equilibrium is obtained both in particles and bulk materials. However, when the size of particles becomes smaller than about 8 nm, alloy phase formation which is quite different from that in bulk materials appears. Namely, when tin atoms are vapor-deposited onto a nm-sized gold particle, rapid dissolution of tin atoms into the gold particle takes place and as a result the gold particle changes into a solid-solution particle, a topologically-disordered amorphous-like alloy particle and an AuSn compound particle, with increasing amount of tin atoms deposited. Details are shown in Figures (a) to (c).

Figure (a) shows a high-resolution image (HRI) of an Au-18at%Sn alloy particle. The diameter of the particle is approximately 5 nm. In Fig. (a), there appear lattice fringes with a spacing of 0.24 nm. The spacing is very close to the (111) lattice spacing of fcc Au-18at%Sn solid solution. This fact suggests that the particle is an Au-Sn solid solution and that the solid solubility of tin in nm-sized gold particles amounts to at least 18 at%Sn, which is much higher than that in bulk gold (i.e. ~3 at%Sn at room temperature). Figure (b) shows an HRI taken from Au-32at%Sn alloy particle. The diameter of the particle is approximately 6 nm. The particle exhibits a contrast similar to the salt and pepper contrast characteristic of topologically-disordered materials, suggesting that a topologically-disordered, amorphous-like phase is produced in the 6 nm-sized alloy particle. Such an amorphous-like phase, which is never present in the equilibrium bulk phase diagram, appears over a composition range from 32 to 40 at%Sn. Figure (c) shows an HRI of an approximately 8 nm-sized AuSn compound particle. The compound particle is single crystalline. The 0.31 nm- and 0.37 nm-spaced fringes in the image are the (011) and (100) lattice fringes of AuSn, respectively. EDS spectra taken from the region encircled in the figure indicate that the tin concentration of the particle is 46 at%Sn (which is by ~4 at% lower than the stoichiometric composition of AuSn). From this result, it is evident that remarkable enhancement of solubility has been induced in AuSn compound particles, as compared with that in the corresponding bulk AuSn which is a line compound.

Mechanochemical Technology: Application to Material Synthesis and to the Separation and Processing of Recyclable Materials from Wastes[†]

Qiwu Zhang, Junya Kano and Fumio Saito
*Institute of Multidisciplinary Research for Advanced Materials, Tohoku University**

1. Introduction

In mechanochemistry, an academic discipline with a long history, mechanical energy is used to drive chemical reactions, and the mechanisms of the resulting reactions, the changes in the characteristics of reaction products, and other phenomena are conceived from a materials science perspective in order to elucidate reaction phenomena. Its advantage is that instead of using heat to cause reactions, it changes the characteristics of substances by breaking bonds mechanically. For this reason the substances produced have a basically random structure while at the same time retaining their crystallinity, and therefore, in not a few cases they have characteristics differing considerably from those of perfectly crystalline substances. In other words, milling, ultrasound, and other mechanical energy sources engender stress that changes the state of the bonds in substances, and thus their physico-chemical properties. Because of this, substances exhibit chemical interactions with other substances (gases, liquids, solids) in their midst, and acquire characteristics different from those of the original substances. Changes induced have very unsteady states, and vary widely depending on the magnitude and extent of the stress acting on a substance, the length of time it affects the substance, and the time of release from that effect. In any event, the stress action process brings about frictional heat and other effects, but does not involve any active application of heat. Energy levels in mechanochemical processes are said to exceed thermochemical levels, [1] and many unusual phenomena have been reported. [2] In mechanical alloying, which is mechanochemistry applied to metals, unstable (active) intermediate substances are formed from mixing and diffusion achieved by the repeated deformation and folding of different types of metals, giving way to solid-state reactions that form alloys. This change differs from the route followed in heating and fusion methods. [3] Disrupting the ordered crystal structure of a substance by milling and activating it is known as mechanical activation, and reactions with nearby substances in that process are called mechanochemical reactions. In either case, physical manipulation can be achieved easily when performing subsequent chemical manipulation such as dissolution, or when heating. For example, recrystallization and pyrolysis can be achieved at low temperatures, and there are many other advantages. Milling and ultrasound exposure are simple and easy operations, but the phenomena they engender are chemical reactions that occur on the molecular and atomic levels.

As noted above, mechanochemistry research has a long history of work on both inorganic and organic substances. Recently people have undertaken to apply mechanochemistry in areas such as functional material synthesis, waste treatment, resource recycling, and global environmental conservation. And while mechanochemistry cannot do everything, it is comparatively simple to activate substances and create substances with random structures using milling, ultrasound exposure, and other processes, making it sometimes possible to express specific properties and accomplish solid-state synthesis that cannot be achieved by other methods. This suggests that mechanochemistry could in some cases make a contribution to separating substances, recycling, environmental conservation, and other areas.

The authors present some of their efforts on resource processing, functional material synthesis, new ways to recycle resources, and environmental conservation using mechanochemical phenomena, mechanical activation, and mechanochemical reactions brought about primarily with dry milling.

2. Milling Processes and Mechanochemical Phenomena

Fig. 1 shows the milling-induced change over time

* 2-1-1 Katahira, Aoba-ku, Sendai 980-8577, Japan
† Accepted: May 7, 2001

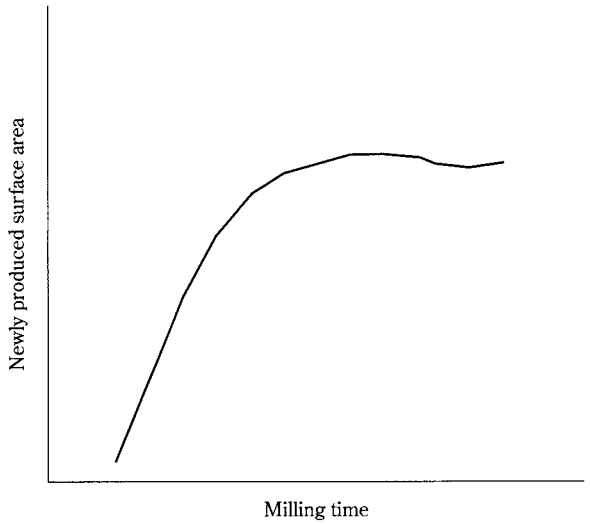

Fig. 1 Milling-induced change over time in the surface area of a solid

in the surface area of a solid. In the initial milling phase, surface area increases with the passage of time, but the rate of increase gradually lessens and then declines after reaching a critical point. This surface area change during the milling process signifies the breaking of bonds on the new surfaces, and the increased numbers of surface atoms and molecules that have lost their joints. Disruption of the state of their bonds extends from the surface layer to the bulk, and the powdered solid is activated (by mechanical activation) and assumes a random structure. The above-mentioned decline in surface area due to long milling indicates agglomeration by fine particles caused by this mechanical activation. When activation heightens, agglomeration becomes dominant, and the milled substance interacts other substances in its midst (such as by adsorption of moisture and gases in the air). As a result, fine particle surfaces stabilize because their chemical potentials fall. In one form of this stabilization, milling of a single kind of solid may bring about polymorphic phase transition (mechanochemical (MC) phase transition). During MC phase transition one can observe crystal lattice strain, and the formation of amorphous phases, intermediate crystalline phases, and others. While the mechanism differs depending on the substance, the pressure, heat, and other forces that arise in the milling process bring about the accumulation of mechanical energy in the crystal lattice, and transition is promoted when that store of energy attains a level exceeding the activation energy of crystallization and transition. In not a few cases the effects of atmosphere contribute significantly to MC phase transition. For example, in the phase transition from calcite to aragonite by dry milling, the presence of even slight moisture in the atmosphere cannot be ignored. [4]

3. Solid-Phase Synthesis Without Heat

Sometimes composite compounds can be directly synthesized by wet or dry milling different kinds of substances together. In many instances a condition is that change in the free energy of formation be negative. In dry milling, the uniform mixing of different powders and the formation of mechanically activated powders proceed at the same time, and reactions occur due to the self-liberation of mechanical energy that has accumulated over the tolerance level.

Metals that readily undergo plastic deformation will become alloys when mutual diffusion occurs by mechanical alloying. **Fig. 2** is the x-ray diffraction (XRD) patterns for the substance formed when mixing Mg and Ni and dry milling them in an Ar atmosphere. The pattern shows that without applying heat it is possible to synthesize the hydrogen storage alloy Mg_2Ni with dry milling. As the model illustrated in **Fig. 3** shows, this process forms alloys through the mutual deformation (due to ductility) and repeated folding of different metal substances.

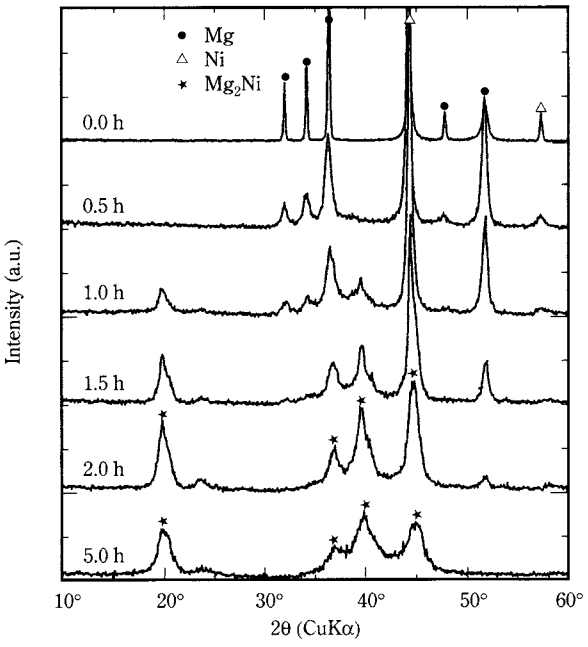

Fig. 2 XRD patterns of the mixture of Mg and Ni milled for different periods of time

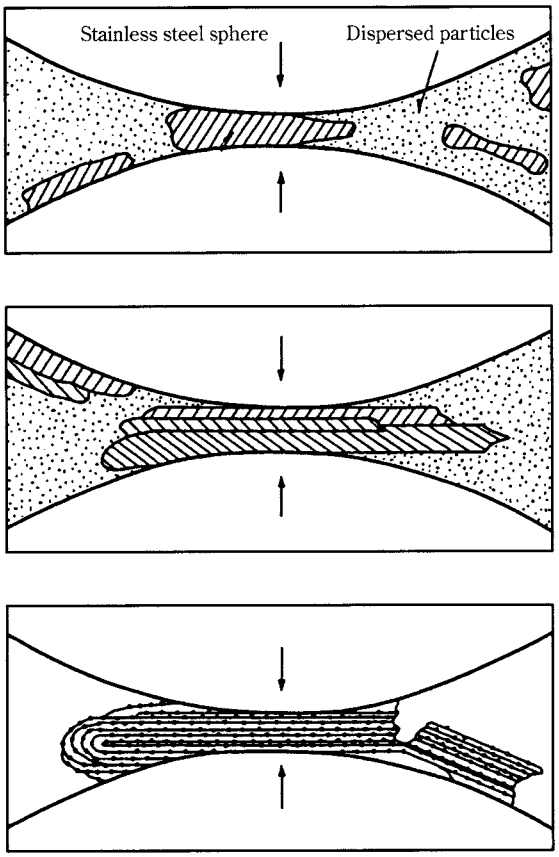

Fig. 3 Effect of kneading in mechanical alloying

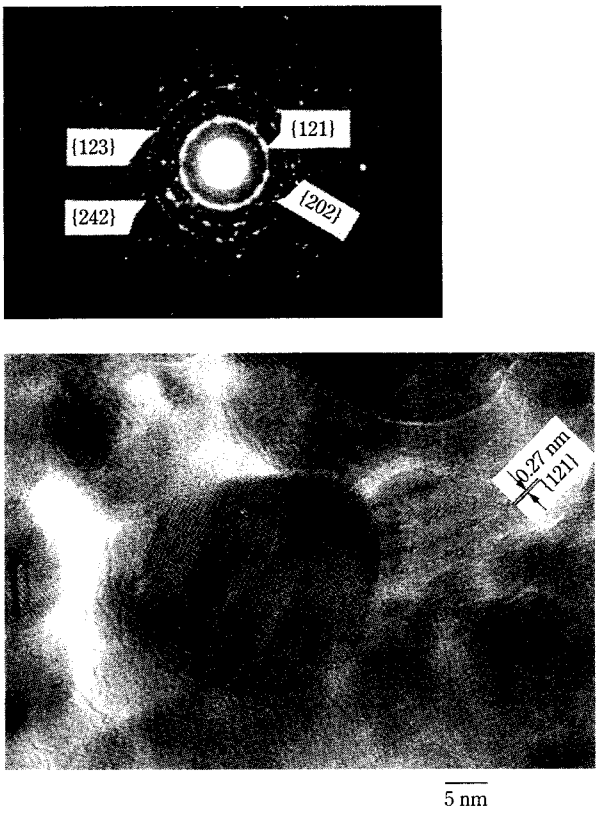

Fig. 4 An HR-TEM micrograph of the mixture ($CaO+Tio_2$) ground for 5 h (Photomicrograph of substance (CaO with TiO_2) taken with a high-resolution transmission electron microscope after 5 h of milling)

When processing brittle materials the phenomenon is likely analogous, but it is hard to elucidate the mechanism of the phenomenon in detail owing to the difficulty of visualizing the alloying process as in the case of metals. But because there is little resultant plastic deformation, it seems likely that the materials undergo a solid-state reaction by turning into fine particles that mutually diffuse on the micro level as they enlarge their interfacial areas. For example, when CaO and TiO_2 (rutile and anatase) were milled for a short time, small $CaTiO_3$ crystals formed after the passage of adequate milling time, even though crystallization was insufficient. [5] When processing time was lengthened, crystal nuclei grew and good crystallization resulted. **Fig. 4** is a photomicrograph taken with a high-resolution transmission electron microscope after 5 h of milling when crystal nuclei had grown to a certain extent. Crystal particles are 20 to 30 nm large, and one can clearly distinguish particle boundaries and the spaces between lattice planes.

In wet milling as well, MC reactions will occur if the right conditions exist. For example, in the presence of water it is possible to directly synthesize a number of calcium silicate hydrates from silica and slaked lime. [6, 7] Although one can only speculate about the reaction mechanism, the possible explanation is that the localized high-pressure state of a high-concentration solid slurry squeezed between media resembles the conditions for hydrothermal treatment. [8]

4. Material Synthesis that Combines Heating

In ceramics processing it is known that if materials are mechanically activated by milling, and then molded and sintered while maintaining activation, the sintering temperature that yields a single phase is far lower than when milling is not involved. With kaolinite, for instance, the crystal structure is easily changed by milling it alone, and XRD produces a broad pattern that is amorphous. Normally the temperature at which kaolinite dehydrates by heating is about 800 K, but if its structure is first changed by milling, that temperature is low, and depends on the extent of milling. This means that kaolinite is easily broken down (made amorphous) by milling. It is known that aluminum hydroxides ($Al(OH)_3$)) like

gibbsite also exhibit the same kind of changes. Therefore if kaolinite and gibbsite are mixed to assume the composition of mullite ($3Al_2O_3 \cdot 2SiO_2$), milled to change the crystal structure, and then heated, a mullite single phase will be obtained at a temperature that is far lower than that needed when milling is not used. [9] It is likely that in the milling process the composition becomes progressively more uniform on the micro scale as the kaolinite-gibbsite interaction brings about conversion into fine particles and the change of the crystal structure, thereby forming a mullite single phase at low temperature due to the interaction. Similar examples are seen in other kinds of ceramics processing. However, although activation by milling advantageously promotes sintering, reactions sometimes proceed quickly in heating processes because materials are activated, thus making optimum milling control necessary to obtain sintered products of fine texture.

5. Natural Resource Processing and Molecular Design

Milling is capable of mineral processing and molecular design of various kinds. As a representative example, we shall discuss the process in which the dry milling of gypsum dihydrate ($CaSO_4 2H_2O$) and quick lime forms a powder containing hemihydrate gypsum, i.e., plaster. The powder formed by milling hardens when water is added because hemihydrate gypsum has formed. Because gypsum dihydrate is comparatively stable, usually a temperature of about 400 K is required to make plaster by heating, and milling in air cannot easily make gypsum dihydrate into hemihydrate gypsum. But when milling gypsum dihydrate after mixing with quick lime, as above, some of the gypsum's water of crystallization (clustered water) is expended in digesting the quick lime, bringing about the following molecular design reaction and yielding hemihydrate gypsum and slaked lime.

$$2CaSO_4 2H_2O + 3CaO = 2CaSO_4 0.5H_2O + 3Ca(OH)_2 \quad (1)$$

This quick lime-induced movement of clustered water in minerals is seen in other clay minerals as well. Here too is an example of how the simple operation of milling is capable of the molecular design of minerals on the micro scale.

Mechanochemical reactions can be used to change the valuable substances in minerals into an easy-to-extract form and recover them. For instance, to make and refine $SrCO_3$ from celestite (which is mainly $SrSO_4$), the current process entails transforming celestite into a sulfide by heating with coal, and then carbonating it. But according to Zhang, et al.: [10]

(1) Perform dry mechanochemical processing of celestite and solid NaOH to form $Sr(OH)_2$.

$$SrSO_4 + 2NaOH = Sr(OH)_2 + Na_2SO_4 \quad (2)$$

(2) Expose reaction product to air so $Sr(OH)_2$ becomes $SrCO_3$.

$$Sr(OH)_2 + CO_2 = SrCO_3 + H_2O \quad (3)$$

(3) Recover $SrCO_3$ that is not water soluble (whose solubility is extremely low) by washing to remove the soluble substance (Na_2SO_4) from the reaction product (refining).

The carbonation process (step 2) is necessary because reverse reaction back to $SrSO_4$ occurs when washing the product of step 1 directly. In this process, therefore, both dry mechanochemical processing and carbonation have a major effect on the final $SrCO_3$ yield. The same mechanochemical processing using no heat, i.e., milling, carbonation, and washing, can be applied to make and refine $BaCO_3$ from barite (which is mainly $BaSO_4$), but care is needed in choosing the solvent used in the washing (extraction) stage, and one must keep the concept of solubility product in mind. [11] This process is also effective when making hydroxides from magnesite ($MgCO_3$), dolomite ($CaMg(CO_3)_2$), and other carbonate ores, and when obtaining and separating soluble tungsten from scheelite ($CaWO_4$) and other tungstate ores. In these processes, however, the overall process can be simplified because step 2 above is unnecessary. [12, 13] This process is especially effective for reaction systems that cannot occur in the liquid phase.

6. Recycling Municipal Wastes and Recovering Recyclable Materials

(1) Disordering the Crystal Structure

(a) Recovery of rare earths from discarded fluorescent tubes [14]

Three-wavelength fluorescent tubes contain rare earths (Y, Eu, La, Ce, and Tb), and methods need to be developed to recover the rare earths from the many tubes that are discarded. The authors developed a method that combines dry MC processing and extraction with a weak acid to leach the aforementioned rare earths from waste fluorescent material

without applying heat. **Fig. 5** shows the XRD patterns for the products obtained by dry milling fluorescent material (three-wavelength type) with a planetary mill (Fritsch, Pulverisette-7). The fluorescent material comprises the blue phosphor $BaMgAl_{10}O_{17}:Eu^{2+}$ (BAT), the two green phosphors $LaPO_4:Ce^{3+}$, Tb^{3+} (LAP) and $CeMgAl_{11}O_{19}:Tb^{3+}$ (MAT), and the red phosphor $Y_2O_3:Eu^{3+}$ (YOX). Overall, diffraction peak intensity decreases as milling proceeds, and the peak for YOX especially decreases. **Fig. 6** shows the relationship between the yield (or leaching percentage) and milling time for each rare earth leached in 1 N hydrochloric acid. Despite the differences between rare earths in their leaching rates, yields are 80% or more when milling time is long. In research until now, rare earths have only been extractable from fluorescent material at 400 K and concentrated strong acids, but they can be extracted easily with preprocessing by milling because milling the phosphor fluorescent material makes the crystal structure of the rare earth compounds into disordered systems. Rare earth leaching rates can be calculated from E_N, the specific collision kinetic energy of the ball media obtained from a ball mill simulation based on the particle element method (collision kinetic energy divided by sample weight; in this example only the normal component). By seeking E_N from any desired mill operation conditions in a simulation, one can predict rare

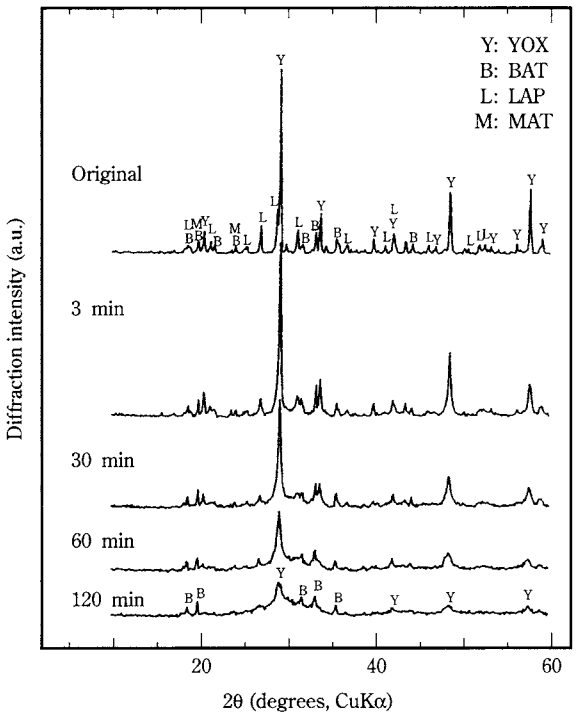

Fig. 5 XRD patterns of dry-milled fluorescent material

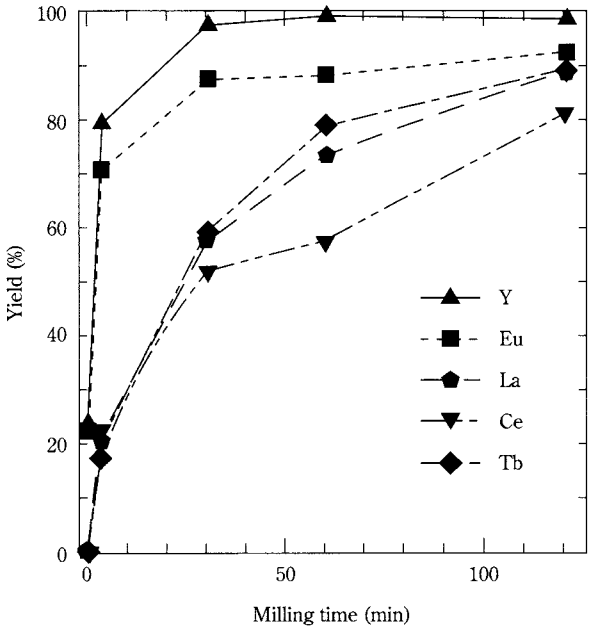

Fig. 6 Relationship between yield of extracted rare earths and milling time

earth leaching percentages under those conditions, making it possible to determine optimum milling conditions and to enlarge mill size. [15] A method for recovering rare metals from acid solutions in which they are dissolved has also been perfected.

(b) Other examples

There are a number of other examples of recyclable material recovery from municipal wastes through crystal structure change. Some of them are: recovery of Co and Li from lithium secondary battery positive electrode scrap and [16] recovery of In from ITO scrap. [17] For lack of space here, readers are encouraged to see the citations for details.

(2) Examples of Using Mechanochemical Reactions

(a) Vanadium recovery from EP dust [18]

The heavy oil combustion soot emitted by oil-fired thermal power plants contains much ammonium sulfate. Known as EP dust, its main constituents include about 62% ammonium sulfate and 28% carbon, and it also contains a small amount, about 1.5%, of vanadium. Due to the need for a way to efficiently recover the vanadium, the authors developed a method that can extract vanadium with water through the use of dry MC processing. **Fig. 7** plots the relationship between V yield and milling time when leaching soluble V compounds with distilled water after dry milling EP dust with a planetary ball mill, a vibration ball mill,

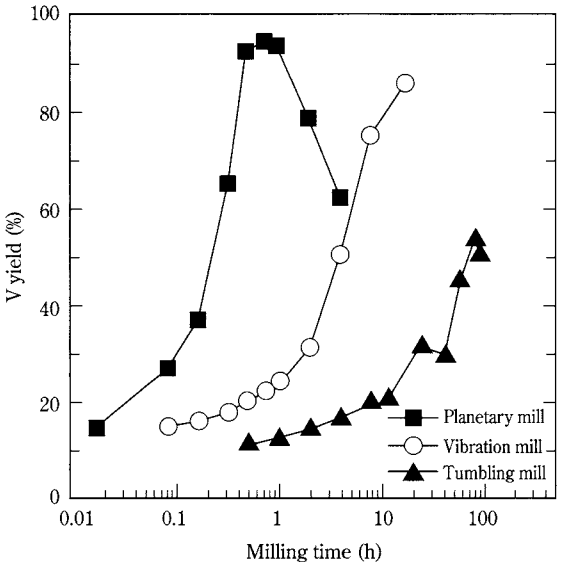

Fig. 7 Change in yield of water-soluble vanadium compounds from EP dust with milling time

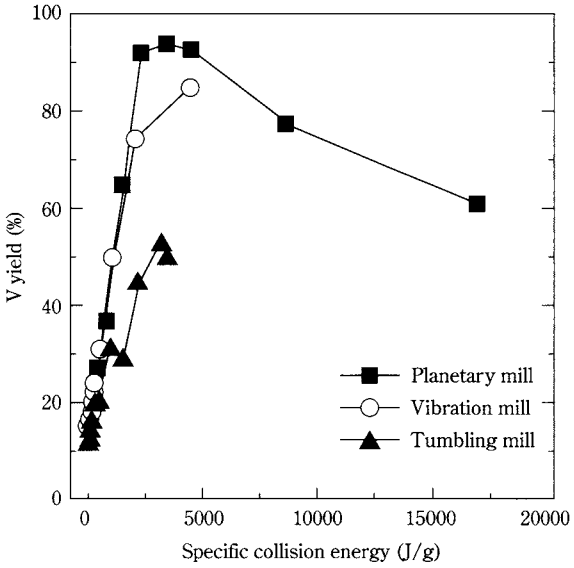

Fig. 8 Relationship between water-soluble vanadium compound yield in **Fig. 7** and specific collision energy of media according to simulation

and a tumbling ball mill. The V yield was over 90% after about 45 min of milling with the planetary mill, but decreased with further milling. Although there were differences in the milling time needed to obtain the same leaching percentage with the vibration and tumbling mills, the trends were the same. Soluble V compounds form through MC reactions between the V_2O_5 and ammonium sulfate in the EP dust, but wet processing offers no hope of raising the V yield. This is perhaps because in wet milling it is hard to apply enough mechanical energy to the EP dust, and because mechanical activation of solid surfaces is soon mitigated in a liquid phase. **Fig. 8** [19] presents the results obtained when converting the milling time on the horizontal axis of **Fig. 7** using the ball media specific collision energy obtained with the particle element method simulation (calculated from the resultant force of both the normal and shearing components). Although the curves for the three different mills were far apart in **Fig. 7**, here they nearly come together. This suggests that MC reactions are governed by the kinetic energy of the ball media, and shows that simulation-generated information is effective, for example, in predicting MC reaction yield, and in determining optimum operating conditions or the operating conditions for enlarged mills.

(b) Dechlorination of polyvinyl chloride (PVC) [20]

Because of its excellent chemical characteristics, low manufacturing cost, and other reasons, PVC is produced in large quantities and is used in a broad range of fields from industry, agriculture, pharmaceuticals, and other industrial applications to everyday goods. Discarded PVC is disposed by incineration or landfilling, but the former gives rise to concerns about dioxins, and the latter involves the difficulty of securing landfill space. And there are many other problems. The authors developed a process to dechlorinate PVC without heating by combining MC treatment with washing and filtration. In the MC stage, CaO or other dechlorination agents are added. The agent is determined by taking into account factors including reactivity with PVC, economy, ease of handling, and separation from the milled product. **Fig. 9** shows the XRD patterns obtained when using CaO as the dechlorination agent, preparing an equimolar mixture with PVC, and MC processing. From this figure one can see that the longer the processing time, the more CaOHCl was formed. This is a radical reaction. **Fig. 10** shows the relationship between the PVC dechlorination percentage and MC processing time for an equimolar mixture of CaO with PVC, and when CaO is mixed two-fold and four-fold in excess. The mixtures were MC processed, then washed and filtered, and chlorides separated from the product. The greater the amount of CaO, the larger (better) the dechlorination percentage and the faster the reaction rate. The chlorides formed by this reaction can be removed by washing, and the residue is a mixture of partly dechlorinated polymers and unreacted sub-

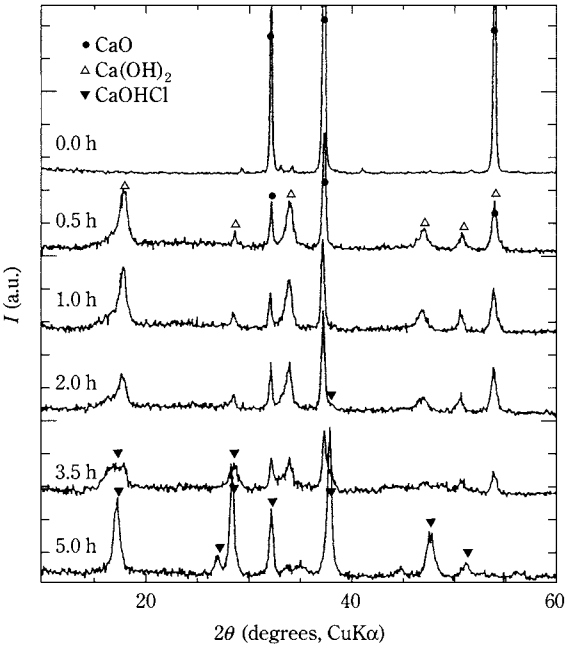

Fig. 9 XRD patterns of MC-processed CaO-PVC mixture

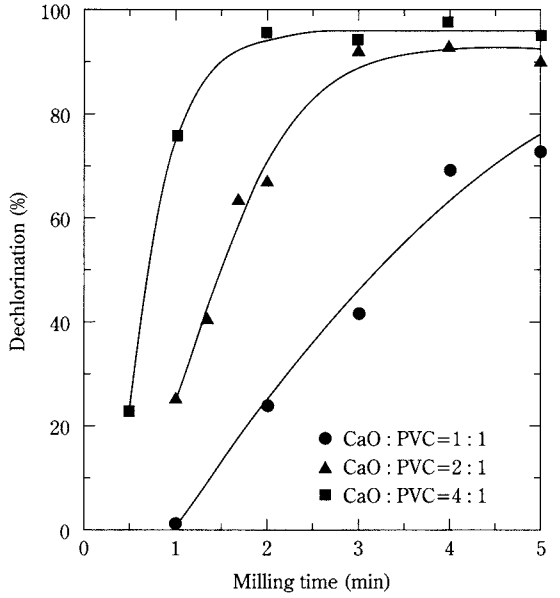

Fig. 10 Relationship between PVC dechlorination percentage and milling time

stances. To achieve 100% dechlorination it is essential to add the dechlorination agent to excess and perform MC processing to an appropriate degree. In addition to CaO, many other inorganic compounds, steel slag, and the like can be used as dechlorination agents. The dechlorination percentage can be estimated from the ball collision energy determined by a ball mill simulation.

(c) Other examples

There are other examples of organic waste processing using solid-state reactions, some of which are the defluorination of PTFE, PVDF, and other substances. For lack of space here, readers are encouraged to see the citations [21, 22] for details.

7. Making a Contribution to Environmental Conservation

(a) Detoxification of PCBs (liquid) without heating [23]

PCBs have characteristics such as excellent electrical insulation, flame retardancy, and chemical stability, but they are highly toxic because they accumulate in the body. Their use is now prohibited, but there is still no effective disposal method, and they are stored along with contaminated oils in large quantities under strict conditions. Proposed PCB disposal methods include heating and chemical processing, but these are not necessarily adequate due to cost, safety, and other reasons. By contrast, there are expectations for mechanochemical methods because operational procedures are easy due to the lack of heating, and because they are safe. **Fig. 11** shows the relationship between milling time and PCB breakdown (dechlorination) when milling a mixture of PCB and CaO. ESR analysis indicates that radicals form, and that they survive for the quite long time of several months.

(b) Detoxification of dioxin-contaminated soil [24]

Dioxins are hazardous substances found in incinerator ash and other places. Social concern is quickly rising over their dispersion into the soil and other parts of the environment. Methods of detoxifying dioxin-contaminated soil include the GeoMelt™ and catalytic methods, but just as with PCB disposal,

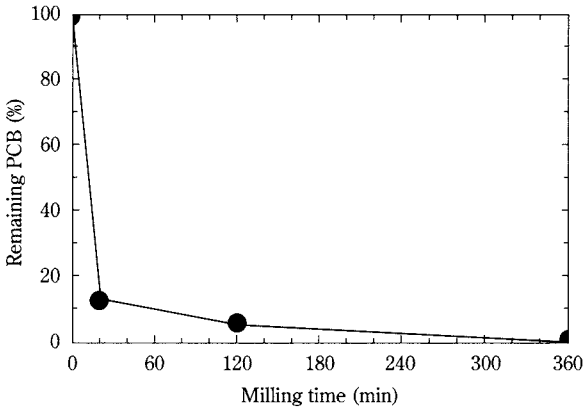

Fig. 11 Relationship between milling time and remaining PCB

these methods involve problems of safety and economy, and have not been practicalized. For that reason there are increasing expectations for mechanochemical methods. The authors' group has performed detoxification tests on contaminated soil, and some of the results appear in **Fig. 12**, which indicates that it is possible for mechanochemical processing to reduce dioxin toxicity to zero (i.e., not detectable).

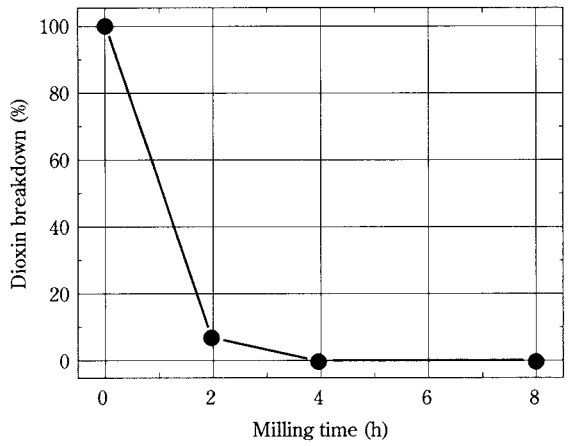

Fig. 12 Dioxin breakdown percentage according to milling time

8. Conclusion

This paper has discussed results and methods pertaining to one use for mechanochemical technology involving the mechanical activation manifested by dry milling and the synthesis of materials using mechanochemical reactions, followed by the recovery of recyclable materials by extraction with solvents, thereby confirming the technology's effectiveness in resource recycling and environmental conservation. At the MC processing stage, mechanical activation and the driving force behind reactions are unsteady, and we lack a detailed understanding of the changes and reaction mechanism at that stage. Products are influenced by atmosphere, operating conditions, and other factors during processing, and work still remains to be done in this area. In the synthesis of materials it is necessary to avoid the problem of abrasion dust from the mill mixing into the product, but this avoidance is to an extent possible. This contamination problem can be ignored when processing wastes, and in fact contaminants sometimes effectively act as a milling assistant. MC processing can to an extent process large volumes, which has been considered difficult until now, and in some cases it has become practical. It will be necessary to show some actual examples (material or process development) of MC processing as a means for synthesizing materials, processing wastes, and recycling resources, and one good way of doing this is combining MC processing with subsequent chemical processing (such as heating, dissolving, or leaching). Important to facilitating practicalization will be not only demonstrating the method's effectiveness on a variety of wastes, but also taking factors such as the economy of processes into account. While anticipating even greater future contributions by mechanochemistry to material synthesis, resource recycling, and environmental conservation, we intend to actively move ahead with seminal and pacesetting basic and practical research that will lead to the technologies of the future.

Citations

1) K. Tkacova. Proc. 1st INCOME, **1**, (1993) 9-17.
2) Senmei, T. *Progress in Chemical Engineering*, **19**, 160-172, ed. Society of Chemical Engineering (Maki Shoten) 1985 (in Japanese).
3) Watanabe, R., et al. *Journal of the Japan Society of Metallurgy*, **27**, (1988) 799-828 (in Japanese).
4) Shinohara, A. H., et al. *Advanced Powder Technology*, **4** (1993) 311.
5) Mi, G., et al. *Powder Technology*, **97** (1998) 178-182.
6) Mi, G., et al. *Powder Technology*, **93** (1997) 77-81.
7) Mi, G., et al. *Inorg. Materials*, **4** (1997) 591-595.
8) Kosova, N. *Solid State Ionics*, **101-103** (1997) 53-58.
9) Ryu, H., et al. *Shigen-to-Sozai*, **108** (1992) 221-226.
10) Zhang, Q., et al. *Chem. Eng. Journal*, **66** (1997) 79-82.
11) Zhang, Q., et al. *J. Chem. Eng. Japan*, **30** (1997) 724-727.
12) Zhang, Q., et al. *Shigen-to-Sozai*, **113** (1997) 175-178.
13) Zhang, Q., et al. *Inorg. Materials*, **4** (1997) 586-590.
14) Zhang, Q., et al. *Shigen-to-Sozai*, **114** (1998) 253-257.
15) Kano, J., et al. *J. Chem. Eng. Japan*, **31** (1998) 1014-1015.
16) Lee, J., et al. *Shigen-to-Sozai*, **116** (2000) 919-922.
17) Zhang, Q., et al. *Shigen-to-Sozai*, **115** (1999) 185-188.
18) Filio, J. M., et al. *J. Chem. Eng. Japan*, **27** (1994) 492-497.
19) Kano, J., et al. *J. Chem. Eng. Japan*, **31** (1998) 1014-1015.
20) Zhang, Q., et al. *J. Soc. Powder Techno. Japan*, **36** (1999) 468-473.
21) Zhang, Q., et al. *J. Applied Polymer Sci.*, **81** (2001) 2249-2252.
22) Zhang, Q., et al. *Chem. Lett.*, 2001, 148-149.
23) Zhang, Q., et al. *Environmental Science and Technology*, in press (2001).
24) Kano, J., et al. *J. Chem. Eng. Japan*, to be submitted.

Author's short biography

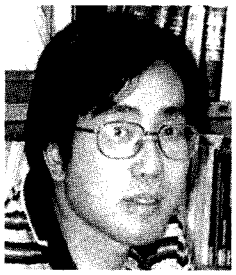

Qiwu Zhang

Qiwu Zhang received the degrees of BS and MSc in Mineral Processing from Wuhan University of Technology, China in 1984 and 1987, respectively. He has worked at Zhengzhou Institute of Multipurpose Utilization of Mineral Resources, China from 1987 to 1992. He joined Prof. Saito's group in 1992 and took his Ph.D. degree at Tohoku University, Japan under the supervision of Prof. F. Saito in 1997. He has started to work as a Research Associate at Institute for Advanced Materials Processing (IAMP), Tohoku University since 1997 to the present time, although the Institute has grown to be created a new one named Institute of Multidisciplinary Research for Advanced Materials (IMRAM), which became the biggest Institute in Tohoku University in April of 2001. He has been assigned to research work on mechanochemistry of different kinds of materials, aiming its engineering applications.

Junya Kano

Junya KANO received the degrees of BS in Chemical Engineering and MSc in Industrial Chemistry at Doshisha University in 1990 and 1992, respectively, and received his Ph.D. from the same university in 1997 in the area of Chemical Engineering. His main research work on his Ph.D course was computational simulation based on the DEM, in connection with monitoring and visualization of the flow of particles in different types of powder storage bins, tanks and a like. He has started to work with Prof. F. Saito as a Research Associate at IAMP (now, IMRAM (2001-)), Tohoku University since 1995. One of his research works focuses on development of computational simulation technique enabling to simulate particles flow in powder handling devices such as mills, hoppers and tanks. The second of his works is aimed on the optimum design of powder handling devices by a theoretical approach based on the simulation work. The final part of his works covers powder processing, looking at energy and environmental conservation. This brings him to estimate powder behavior and mechanochemical phenomena by harmonizing his simulation works with the experimental ones, leading to establishment of scaling-up law for the devices.

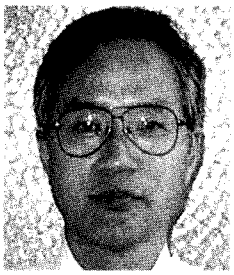

Fumio Saito

Fumio Saito received the degrees of BS and MSc in Chemical Engineering from Yamagata University, Japan in 1970 and 1972, respectively. He got his Ph.D. in Mining and Minerals Engineering at Tohoku University, Japan in 1982. He had moved his working place at Yokohama National University, Japan, and worked for about 8-years as a lecturer and an Associate professor. During his stay at Yokohama, he got a chance to collaborate with Prof. A.W. Nienow at the University of Birmingham, UK as a research fellow supported by British Council for more than one year. After his back to Japan, he was promoted as a full-time professor at Institute of Mineral Dressing and Metallurgy (now, IMRAM), Tohoku University in 1993. He has been working as a Visiting Professor at Ecole des Mines d'Albi-Carmaux, France supported by French Government since April to December, 2001. His main interests cover mechanochemical engineering for human life, molecular design by grinding, nano-technology in comminution and nano-structural control by an arc-plasma method.

Development of Smart Drug Delivery Systems that Learn from Nature†

Kakuji Tojo
Kyushu Institute of Technology College of Computer Science and Systems Engineering
*Ph.D., Professor, DDS Research Lab**

Since nitroglycerine transdermal patches were introduced on the United States market in 1982 for the treatment of angina pectoris, controlled release (CR) systems have come into wide use throughout the world to treat a broad variety of diseases. The system design is in the form of pills, capsules, transdermal patches, implanted drug delivery systems, intravitreal inserts, subcutaneous implants, and injectables. These preparations take the forms of particles endowed with controlled release (CR) functions, films formed after evenly mixing drug powders into polymer bases, or implantable rods that are made by the advanced processing of particles.

When transdermal therapeutic systems started to use clinically about 20 years ago, the purpose of CR technologies was the constant-rate, long-term release of active agents. In other words, a major objective of CR technologies was to develop dosage forms which, with one dose, release active agents at a constant rate effective over a long time period. There were two major underlying reasons. First, the optimum tissue concentration and release characteristics of drug molecules were not fully understood for treating diseases, and second, owing to the large individual differences in pharmacokinetics (ADME: absorption, distribution, metabolism, and elimination) within the body, the accurate control of concentrations in blood and tissue did not make sense. Of course even today, although long-term constant-release systems are effective in gaining patient compliance and treating many diseases, timed drug release systems are increasingly necessary. Attention is focused especially on time-dependent release rate CR technologies that can address the time dependence of the state of a disease and undesired side effects, prevent drug tolerance, and set dose intermissions.

The active agents in pharmaceuticals are bioinformation molecules that control bodily functions by acting as signal or false-signal molecules. Generally these are produced in the body and are released for the maximum effect and without waste. Recently research has started to learn about not only drugs (bioinformation molecules) like these, but also how plants and insects economically and effectively use their bioinformation molecules. Knowledge turned up in this research is then used in CR technologies. This science is called biomimicry, and considered as a valuable new scientific field in the 21st, or biotech, century. [1]

For example, the chemical reactions, and the processes of release and movement of informational molecules within organisms, are the most efficient functions achieved by organisms through the long course of evolution. Biomimicry, or the imitation of these biological functions, will likely play an essential role in developing sustainable CR technologies.

However, it is certainly not easy to correctly understand the ingenious functions of organisms and exactly mimic them. Hence at this stage of research the main purpose of biomimicry would be to develop novel CR and drug delivery systems with the inspiration gained in the course of learning from nature. [2]

For that reason this paper explores controlled release processes for bioinformation molecules as related to CR technologies and the biomimicry concept. I examine biomimicry in CR technologies in relation to three items: (1) mimicking elements, (2) mimicking mechanisms, and (3) utilizing mechanisms. Mimicking elements means controlling bioinformation by using the active agents produced when necessary in the body, which has been the mainstream of pharmaceutical research and development to date. Mimicking mechanisms means understanding the mechanisms that use bioinformation molecules, and using them in CR technologies, thus making them similar to what nature does. Utilizing mechanisms, on the other hand, means using biological functions as is to develop highly economical CR technologies.

* Iizuka City, Fukuoka 820-8502, Japan
Phone 0948-29-7816; Fax 29-7801
E-mail: tojo@bse.kyutech.ac.jp
† Accepted: June 1, 2001

1. Mimicking Elements: Bioinformation Molecules

The molecules that organisms generally release for alarming or communication, or that they use to transmit information internally, are here defined as bioinformation molecules. Researchers have come to focus on using these bioinformation molecules, and on putting them to work in pharmaceuticals, pesticides, and other products after chemically modifying them into more potent molecules. Some examples are the insect pheromones used to control insect pests, synthetic progestins used as a contraceptive, steroid hormones such as estrogen, and peptide hormones of which insulin is representative. Devices that release these bioinformation molecules at a constant rate over a long period are the CR systems that have generally been developed to date. [3]

For example, pheromone CR systems have already been commercialized as eco-friendly insect pest control systems in forms that include films, hollow fibers, and microcapsules. [4] Meanwhile, researchers have developed a subcutaneous injection which includes LHRH in microcapsules of the biodegradable polymer PLGA. This therapeutic system is effectively used to treat prostate cancer and endometriosis. [5] Estradiol transdermal patches are used clinically to treat menopausal disorders and osteoporosis. [6] These CR devices are roughly divided into matrix and reservoir types. In both, however, the release process is governed by the diffusion of drug molecules in the polymers. In matrix-type pheromone CR devices, for instance, pheromone molecules evenly dispersed in the film undergo a prolonged release that is driven by the concentration gradient. Cumulative release amount Q for this type is proportional to the square root of time. Likewise in hollow fiber devices, Q is proportional to the square root of time if diffusion in the hollow tubes is rate-determined. Reservoir-type CR systems, by contrast, keep the release rate constant with a release rate control membrane, and resulting Q proportional to time. However, the difference between the release characteristics of the matrix and reservoir types has little effect on actual treatment systems and insect pest control systems. [7] This is because the matrix-type release characteristics can be approximated as the initial burst and the subsequent constant-rate release. In fact, matrix systems have the advantages of no concerns about bursting release due to device destruction, and the easiness to adjust application area to fit the therapeutic efficacy.

Sustained CR systems described above are examples of biomimicry that use bioinformation molecules as mimicking elements. However, long-term release of bioinformation molecules is quite wasteful, and less efficient and economical, compared to its release processes occurring within organisms. Recent research has revealed that insect pheromones, peptide hormones (such as insulin), and other substances are not released at constant rates within organisms. [8] For example, insulin releases for controling blood glucose concentration come in pulses, starting and stopping in approximate 14-minute cycles even if the blood glucose level continually increases. [8] When the relationship between drug concentration and therapeutic efficacy follows a sigmoid profile, it is more efficient to deliver the drug at high concentrations by starting and stopping in cycles than to continually release it at low concentrations. Further, by delivering insulin in short cycles, it is possible even at the same concentration in the bloodstream to tell when it is rising or falling, thereby curbing excess insulin releases on the downswing and preventing hypoglycemia-induced coma. As this shows, it is generally more economical for organisms to release bioinformation molecules in pulses, and this suggests that in order to imitate such "elements" and use them in CR and drug delivery technologies we must properly learn about their release mechanisms as well.

2. Using External Energy for CR Time Control

Many of the DDS and CR systems currently in clinical use are designed, as shown in **Fig. 1**, to release the active substances according to a preprogrammed release pattern. [9] Accordingly, their design does not allow them to respond to environmental changes or

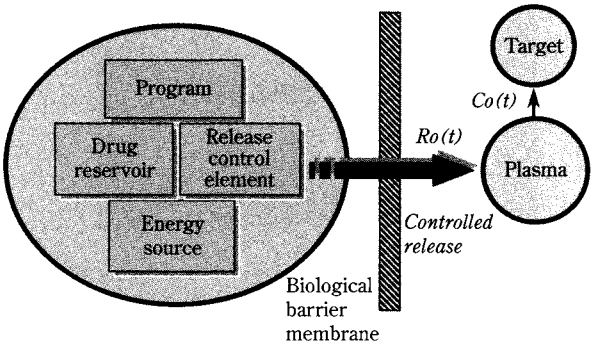

Fig. 1 Conventional drug delivery system. The rate of drug delivery is usually programmed to achieve a constant release rate for an extended period of time.

changes over time in the body's internal dynamics. In the treatment of pain, for instance, a DDS that can respond to sudden pain would have to time-control the release of the drug molecules in accordance with the pain. With such a DDS, time control would be possible by adding external energy to the energy source in **Fig. 1**. Ultrasound and electric fields are effective as this added energy. An in vitro membrane penetration experimental apparatus as shown in **Fig. 2** was used to investigate the effect of ultrasound exposure on LDPE membrane penetration by a drug (benzoic acid). **Fig. 3** shows the time course of the cumulative penetration when applying ultrasound for 10 min at three different frequencies. At 100 kHz penetration was hardly enhanced by ultrasound at all, but at 28 kHz and 45 kHz the penetration rate during exposure was, respectively, 3.5-fold and 5.5-fold more than the non-exposure intervals. It is interesting to see that when the ultrasound was switched off, the penetration rate instantly dropped to the same rate as the control. [10] In a membrane penetration experiment with continuous exposure the diffusion coefficient was determined from the time lag. We found that enhancement of penetration by ultrasound was mainly due to a rise in the drug diffusion coefficient, while the effects of temperature increase, solubility (distribution improvement), or other phenomena can be almost negligible.

Ultrasound exposure can also be used for the timed release of drugs from drug delivery systems implanted subcutaneously. Takasaki et al. developed an implantable biodegradable system with indomethacin dispersed in small polylactic acid rods 1 mm in diameter and 3 mm long, and succeeded in enhancing timed release with exposure to 1 MHz ultrasound. [11]

Researchers in various fields are also working on iontophoresis, which enhances penetration, by using electric fields for the cutaneous absorption of water-soluble drugs and large molecules. Akagi et al. used a vertical in vitro diffusion cell (**Fig. 4**) to elaborate the effect of an electric field on the penetration rate through hairless mouse skin. They determined the relationship of penetration enhancement to the intensity of electric field and the duration of current application (**Fig. 5**). CR systems using external energy such as ultrasound and electric field, constitute a new

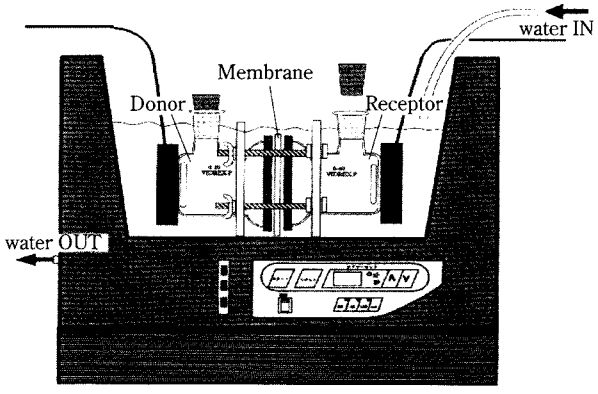

Fig. 2 Experimental setup for measuring the effect of ultrasound on the membrane permeation of drugs. The side-by-side diffusion cell system is placed in the ultrasonic water bath washer.
Model drug: benzoic acid; donor concentration: saturated concentration; effective volume: 68 ml; effective area: 12.5 cm^2; membrane; LDPE (50 μm in thickness); temperature: 37°C.

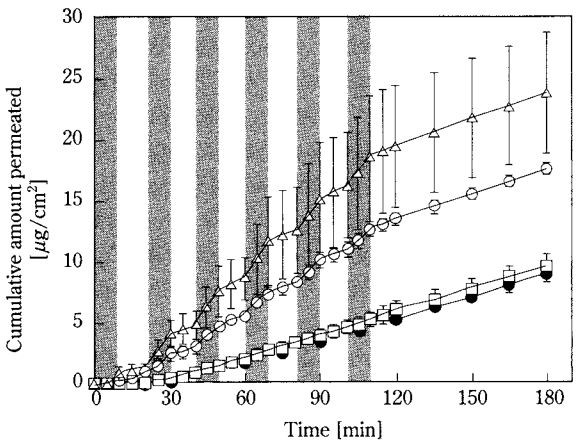

Fig. 3 Time course of cumulative amount of benzoic acid penetrated across an LDPE film.
Ultrasound was applied for 10-minute intervals at 0, 20, 40, 60, 80, and 100 minutes (shaded areas). Key: (●) control (no ultrasound), (□) 100 kHz, (○) 28 kHz, (△) 45 kHz.

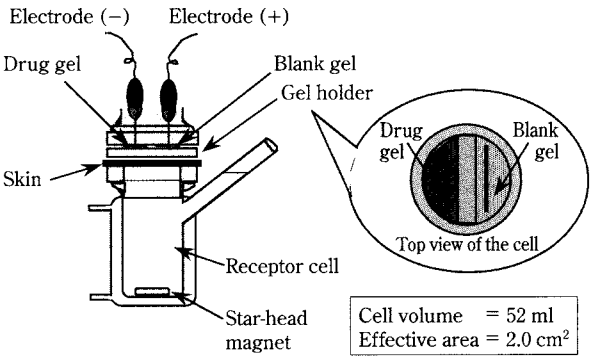

Fig. 4 Experimental setup for in vitro skin penetration by iontophoresis. The skin specimen was prepared from abdominal hairless mouse skin.

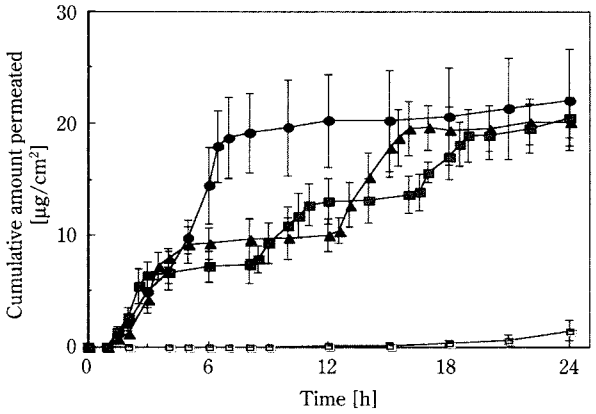

Fig. 5 Effect of the electric field application mode on the skin penetration over time of dexamethasone sodium m-sulfobenzoate (DMSB, mw=599). Key: (●) 0-6 h: on, 6-24 h: off, (▲) 0-3, 12-15 h: on, 3-12, 15-24 h: off, (■) 0-2, 8-10, 16-18 h: on, 2-8, 10-16, 18-24 h: off. (❑) control (passive diffusion)

Fig. 6 The ultimate controlled release system. Bombardier beetle (courtesy of Mr. S. Kuribayashi).

technological field that integrates information technology and biotechnology. This new area of research will likely be important as biomimetic drug delivery and CR systems in a broad array of medical treatments and insect pest control.

3. Mimicking Mechanisms

The bombardier beetle, a 1 cm-odd long insect that is seen in fallen leaves, under stones, and other places, has a marvelous defense against enemies. Eisner [13] notes that the beetle has two chambers in its abdomen. One stores hydrogen peroxide and hydroquinone, while the other is a reaction chamber enclosed by the enzyme catalase. When the beetle detects an enemy, it immediately sends the two chemical substances from the storage chamber to the reaction chamber, where it uses the enzyme to bring about an instantaneous exothermic oxidation reaction. The tissue surrounding the reaction chamber is not harmed by the heat because it is chitinous. In this way the insect fires rapid pulses of the toxic substance benzoquinone as hot as 100°C at targets without harming itself (**Fig. 6**). It is a living microbiochemical reactor system controlled exquisitely.

We have learned from the bombardier beetle's defense mechanism in developing a new multi-layer, timed-release transdermal drug delivery system [14] that replaces the bombardier beetle's abdominal chemical storage layer and reaction chamber with polymer reaction membranes, and has a impermeable separation membrane between the other membranes (**Fig. 7**). This separation membrane is removed just before use. In conventional design, an absorption-enhancing chemical is added to the adhesive layer of the transdermal therapeutic system. Depending on the properties and concentration of the substance, it sometimes impairs the stability of the drug during the storage period. With this device design, however, long-term stability is maintained because the drug molecules and enhancer come into contact just before use. Setting the drug absorption time lag with the lower drug storage layer (membrane B) makes it possible to develop new transdermal therapeutic systems that can control intermission periods for drug absorption or that take chronopharmacology into account. If an appropriate time lag can be set in transdermal absorption with the time lag control membrane while also lowering stratum corneum resistance to diffusion with the penetration enhancer dispersed in the adhe-

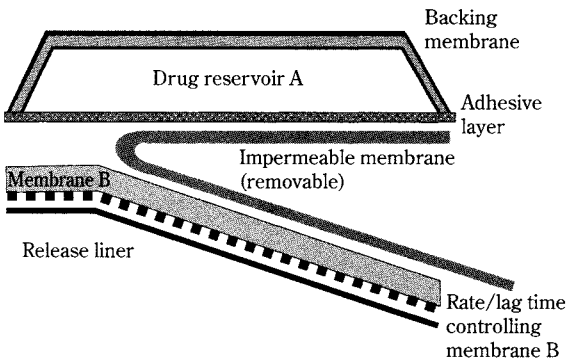

Fig. 7 Patient-activated temporal transdermal drug delivery system.

sive layer, and thus maintaining the effective absorption rate, then it would be possible to set the intermission period by repeated once-a-day application of the system. For example, in ethylene vinyl acetate copolymer membranes, the diffusion coefficient of the drug is constant because it is independent of the vinyl acetate content; solubility alone increases with vinyl acetate content. We have taken advantage of this property and confirmed with laboratory animals that the new system can set the time lag at about 8 h without lowering the steady-state penetration rate (**Fig. 8**). [14]

Transdermal therapeutic systems like this can be applied not only to setting intermission periods for transdermal treatments in which drug tolerance is a problem, but also in new time-control transdermal therapeutic systems which take circadian rhythms into account and avoid medication at unnecessary times (such as nicotine absorption during sleep with the nicotine patches that help people quit smoking). Another possibility is time-control systems that prevent drug transport to the bloodstream during sleep, and begin maintaining the effective concentration in the blood just before getting up in the morning. Users would accomplish this by merely changing their patch once daily just before retiring.

Further, research on the recently developed iontophoresis technology, which uses an electric field to time-control the cutaneous absorption of drugs, has shown for example that it is possible to deliver effective agents to the bloodstream in pulses or in any time-dependent manner by turning an electric field on and off, and that bioinformation molecules in the skin can be extracted by reversing electrode polarity.

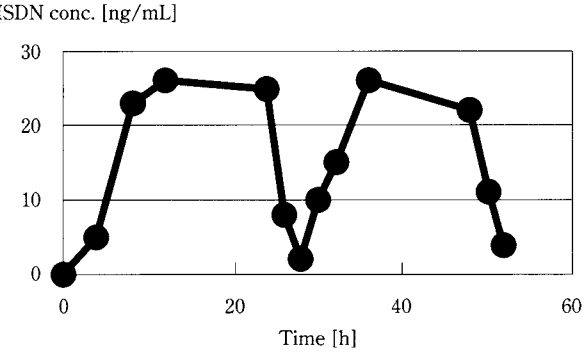

Fig. 8 The plasma concentration profile of time-lag transdermal delivery of isosorbide dinitrate using the patient-activated TTS system illustrated in **Fig. 7**.
Rat in vivo data (n=4): The device was replaced at 24 h and removed at 48 h.

Optimizing new drug delivery technologies like these might in the near future bring about novel therapeutic systems with feedback functions as illustrated in **Fig. 9**.

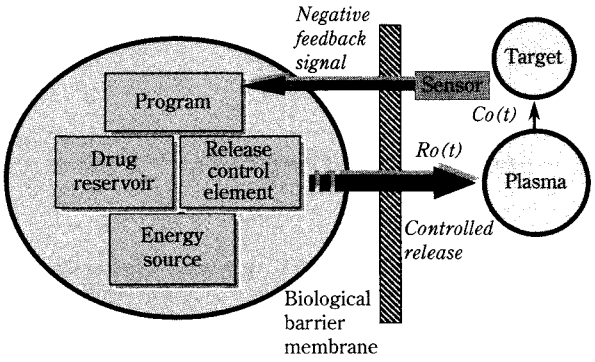

Fig. 9 Advanced drug delivery system with negative feedback control loop. Feedback signal may be the concentration of bioinformation molecules extracted from the body.

4. Utilizing Mechanisms

Australia's mountain ash is the world's largest tree, sometimes attaining a height of 100 m. Its leaves are believed to transpire as much as 1,000 L of water per day. [15] To keep its leaves from withering, the tree constantly brings water up from its roots, sends it via the trunk to the branches, and from there to the leaves. This is truly an amazing feat of nature, because the tree carries this on without producing any noise or vibration. One time I had the idea that it might be possible to use such economical natural mechanisms to efficiently deliver nutrients and insecticides or other active agents to an entire tree, and I decided to develop a "pesticide patch" that would deliver pesticides to the tips of a plant's leaves by absorbing them through stems (**Fig. 10**). [16] Literature survey indicates that less than 1% of generally used pesticide sprays are actually delivered to target insects. [7] Nearly all the applied pesticide instead contaminates not only the plants, but also the air, water, and soil. When pesticides are applied as granules by spreading them on the soil, they are washed away by rain, and soil contamination is unavoidable. This led to the idea of a transdermal absorption system for pesticide, or pesticide patch, that is applied to the bottom of a plant stem, where the pesticide is absorbed and then delivered through vessels to the entire plant. The pesticide's active agent imidacloprid and additives (penetration enhancers) are well dis-

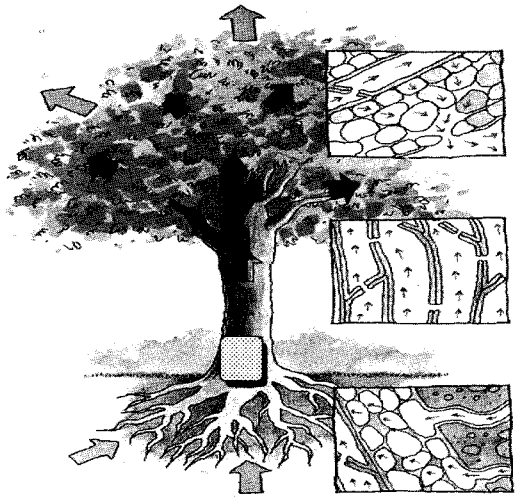

Fig. 10 Concept of biomimetic pesticide delivery through plant stems.

persed into an adhesive polymer base, and then made into a thin-film preparation using the doctor blade method (**Fig. 11**). The two small-scale, automatic manufacturing devices shown in **Fig. 16**, using the solvent and hot-melt methods, have been developed to make preparations for field and clinical trials. This patch was applied to the in vitro pesticide stem penetration apparatus shown in **Fig. 12** to measure the imidacloprid stem absorption rate. Penetration enhancers were l-menthol and d-limonene, for each of which we developed a high- and low-absorption pesticide patch. **Fig. 13** plots the effects of different l-menthol concentrations on the enhancement of imidacloprid stem penetration on eggplant.

We also applied this pesticide patch to the stems of model plants: tomato, eggplant, and chrysanthemum plants about 5 cm above ground level. Insecticidal efficacy was measured by putting 10 aphids each on the tops and undersides of leaves, and counting them each day (**Fig. 14**). **Fig. 15** compares the results from several devices. With the preparation containing no pesticide the number of aphids clearly increased day by day. This contrasted with the insecticidal characteristics of the pesticide-loaded preparations, with the high-absorption type (containing l-methanol) being fast-acting, and the low-absorption type (containing d-limonene) being time-lag. Although no figure is included here, measuring the insecticidal effect of the high-absorption preparation on aphids infesting chrysanthemum plants showed that all aphids died within three days. No harm to the plants was discerned.

We also found that using pesticide patches allowed a reduction of pesticide application amount of between 1/20th and 1/10th the amount applied in granular form. [17] Because the insecticidal agent is stored in the polymer base, its effectiveness is not influenced by rain, wind, or other weather conditions. Further, there is no environmental contamination because the pesticide is not lost to the soil or air. It is possible to develop totally new delayed-release pesticide delivery systems that allow time control of the insecticidal effect by controlling the absorption rate, thereby promising to raise the users' quality of life.

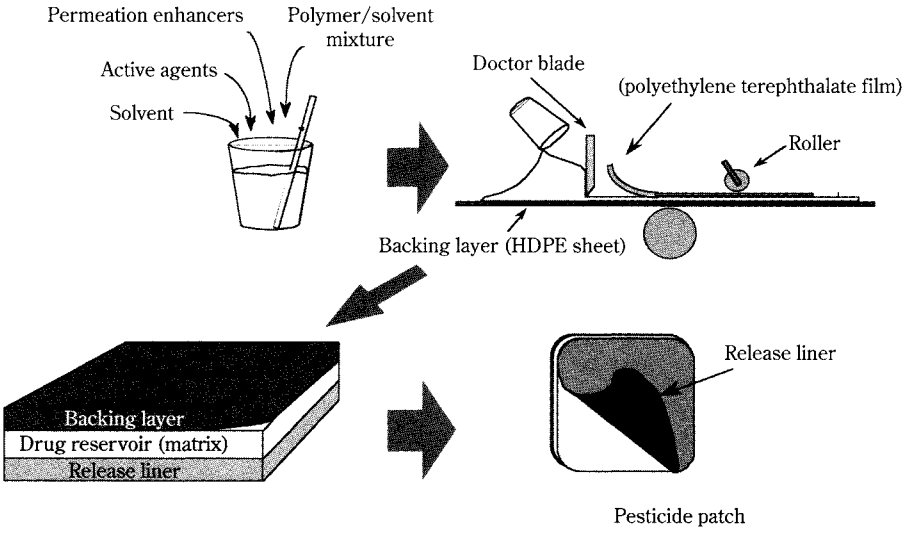

Fig. 11 Laboratory process for manufacturing pesticide patches.

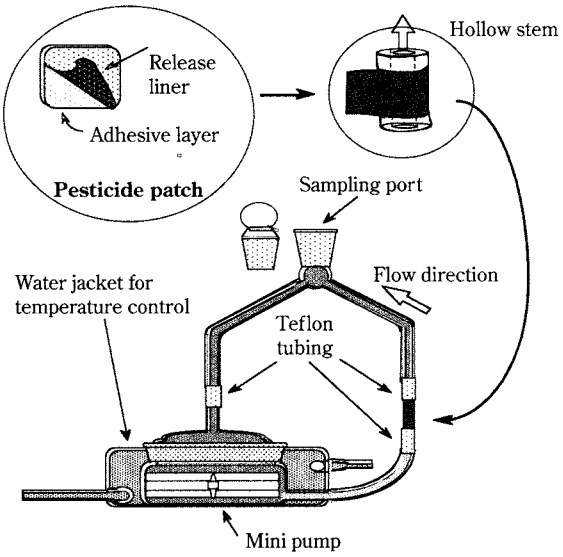

Fig. 12 In vitro system for measuring the pesticide penetration rate through plant stems. The adhesive pesticide delivery system is applied to the surface of the hollow stem.

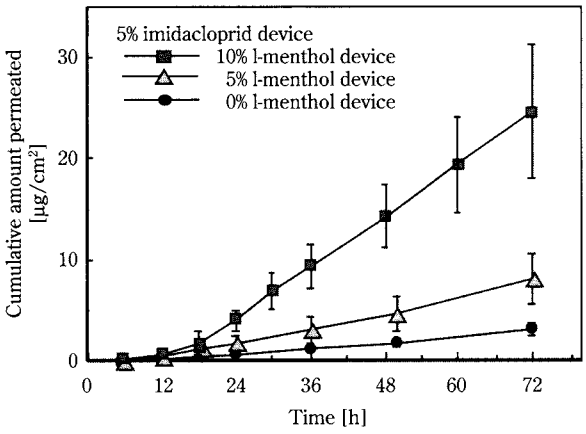

Fig. 13 Effect of l-menthol, a penetration enhancer, on the stem penetration of imidacloprid.
Model plant: eggplant (*Solanum melongena* L. cv. Senryo No. 2, eight weeks after germination)

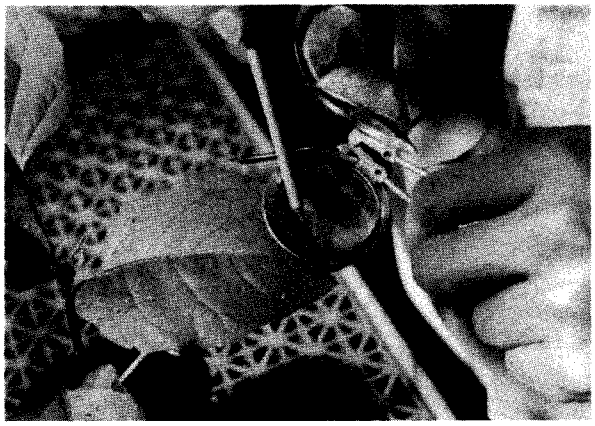

Fig. 14 Total number of aphids, both adults and newly born nymphs, was counted every 24 hours. The temperature (25°C), humidity (60%), and light-dark cycle (12 h/12 h) were controlled in a computer-controlled weather chamber.

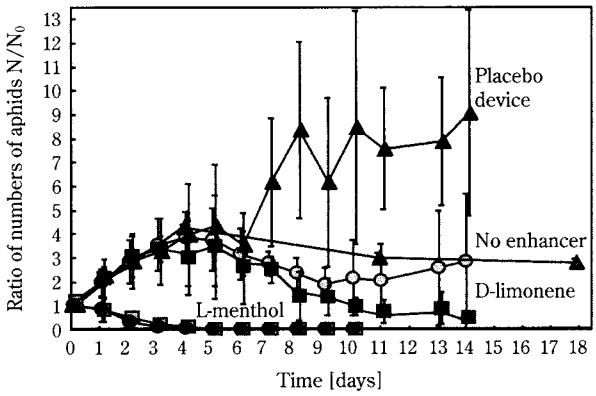

Fig. 15 Time variation in the ratio numbers of aphids surviving the acrylic adhesive delivery of imidacloprid through the stem of eggplant. Ten aphids were initally placed on both sides of each leaf (No=10).

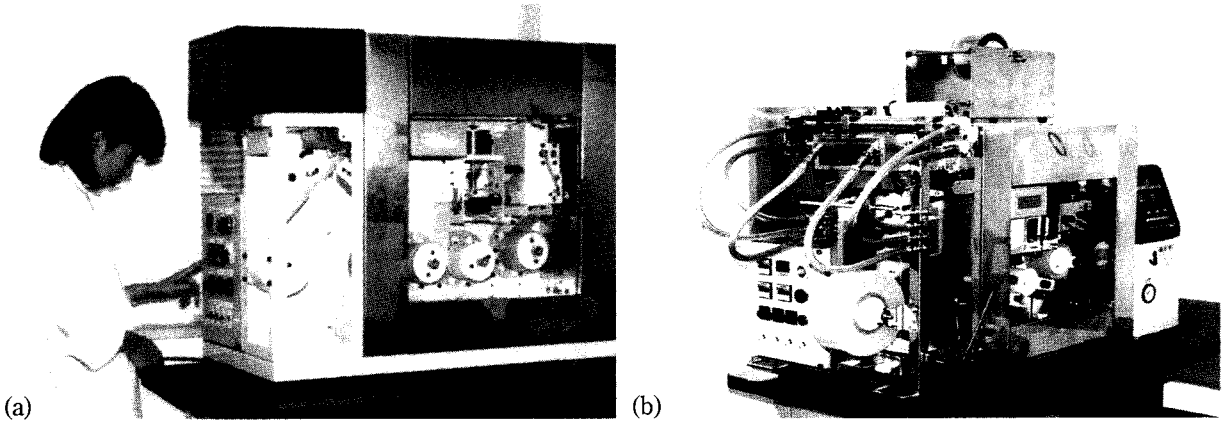

Fig. 16 Laboratory-scale equipment for manufacturing transdermal drug delivery devices. (a) Solvent method, (b) hot-melt method.

Conclusion

This paper has shown how biomimicry, or learning from nature, plays an important role in developing novel drug delivery systems that can time-control release and delivery rates. Further, examples were used to explain in general the three approaches for developing the DDS's that learn from nature: (1) mimicking elements, (2) mimicking mechanisms, and (3) utilizing mechanisms. The time-controlled release of bioinformation molecules is an efficient and economical process acquired by organisms over the long course of evolution, and organisms take ingenious advantage of both their internal and external environmental conditions, which change from moment to moment. When we learn from living functions and develop new DDS, we must keep in mind not only the functions of individual organisms, but also the roles of organisms as systems and the "natural systems" that comprise organisms and their surrounding environments. Living creatures make smart use of natural systems to achieve their efficient and economical release and delivery systems for bioinformation molecule. Accordingly, only when we study biomimicry by taking natural systems into account can we minimize the risk inherent in mimicking only certain facets of intricate natural functions.

References

1) Benyus, J. M. *Biomimicry*, William Morrow & Company, N.Y. USA (1997).
2) Tojo, K. "Biomimetic Drug Delivery Systems," *Chemistry Today*, No. 338, 28-34 (1999).
3) Tojo, K. *Drug Delivery Systems*, Biocom Systems Inc., Fukuoka, Japan (2001).
4) Tojo, K. "Pesticide Delivery without Environmental Pollution," *Chemistry Today*, No. 136, 22-29 (1982).
5) Okada, H. Proc. Int. Symp. Control. Rel. Bioactive Mater., 16, 12ff. (1989).
6) Nozaki, M. "Recent Advances in Hormone Replacement Therapy," Special Invited Lecture, 8th CIRD Symposium on Transdermal Drug Delivery, Iizuka, January 26-27 (2001).
7) Tojo, K. "Controlled Drug Delivery: Matrix Type vs. Reservoir Type," *Therapeutics & Engineering*, 12, 689-691 (2000).
8) Matthews, D. R. "Physiological Implication of Pulsatile Hormone Secretion, in Temporal Control of Drug Delivery," *Ann. New York Acad. Sci.* 618, 28-37 (1991).
9) Heilmann, K. *Therapeutic systems*, Georg Thieme Pub. Stuttgart (1978).
10) Yoshida, H. and K. Tojo. "Effect of Ultrasound on Membrane Transport of Drugs." In preparation.
11) Takasaki, H. and K. Tojo. "Effect of Ultrasound on Drug Release from Biodegradable Polymer Implant." In preparation.
12) Akagi, K., H. Ono, K. Muraoka, A. Yamashita and K. Tojo. "Timed Control of Percutaneous Absorption by Iontophoresis," *Therapeutics & Engineering*, 11, 622-625 (1999).
13) Dean, J. and T. Eisner. "Defensive spray of the bombardier beetle," Science, 248, 1219 (1990).
14) Tojo, K. "Controlled Release/Removal Technology," *KagakuKougaku* (Chemical Engineering), 64, 88-89 (2000).
15) Attenborough, D. *The Private Life of Plants*, YAMA-KEI Pub., Tokyo (1998).
16) Tojo, K. et al. Pesticide Patch, Jap. Patent 8-242695 (1996).
17) Tojo, K., N. Hatae, K. Nakawawa and A. Yoshida. "Adhesive Systems for Pesticide Delivery Through Plant Stems," *Pestic. Sci.* 49, 35-39 (1997).

Author's short biography

Kakuji Tojo

Dr. Kakuji Tojo is a professor of Biosystems Engineering at Kyushu Institute of Technology and is the Director of the DDS Laboratories at the Center of Iizuka Research and Development (CIRD). He graduated in Chemical Engineering from University of Osaka Prefecture (1969). He was a postdoctoral researcher at Kansas State University and later joined Rutgers University College of Pharmacy where he had been an Assistant Professor and tenured Associate Professor. He accepted a professorship at National Kyushu Institute of Technology in 1990, and served as the Regent Professor, 1995 to 98. His research interests include transdermal drug delivery, ophthalmic drug delivery and biomimicry in controlled release technology. He had served as a member of the Board of Governors, Controlled Release Society, 1991 to 1994. He is an editor or editorial board member of international journals including European Journal of Pharmaceutics and Biopharmaceutics, Archives of Pharmacal Research (Korea) and Journal of Chemical Engineering of Japan.

Laser Induced Plasma Spectroscopy for the Characterization of Aerosols and Particulates[†]

Benjamin W. Smith, David W. Hahn*, Emily Gibb, Igor Gornushkin and James D. Winefordner**
Departments of Chemistry and Mechanical Engineering
Engineering Research Center for Particle Science and Technology

Abstract

Laser induced plasma spectroscopy is beginning to find useful applications in the real time in situ detection of particulates and aerosols suspended in gases. Although the technique is almost 40 years old, it has become increasingly practical for this application during the last decade due to the development of more reliable lasers and optical detection systems, an improved understanding of the physical processes involved, and new data collection and analysis strategies. There is a pressing need for such detection techniques for industrial process and atmospheric monitoring. In this review, we examine literature concerned with the process of optical breakdown by focused lasers in gases, the role of particles in this process, and the characterization of particles using laser induced plasmas.

Introduction

Laser induced plasma spectroscopy (LIPS) or laser induced breakdown spectroscopy (LIBS) continues to receive wide attention for rapid, *in situ* chemical analysis of many different kinds of samples. (In this review, we use the acronyms interchangeably.) When a pulsed, high power laser is focused on any gas, liquid or solid, a bright, luminous plasma results, accompanied by a sharp acoustic shock wave. In simplistic terms, LIPS uses the emission spectrum of this plasma to obtain chemical composition information about the vaporized material. The vaporized sample is almost completely dissociated into free atoms and ions leading to a spectrum which is rich in elemental atomic and ionic lines. The technique, which dates to the early 1960's,[1] has enjoyed a revival during the last decade due to the development of array detectors and ever more reliable and rugged pulsed laser systems. It has found many applications in the direct, *in situ* analysis of solid,[2,3] and gaseous materials.[4] Telgheder and Khvostikov have reviewed most of the methods which are used to determine metal contaminants in gases.[5] In this review, we examine the specific application of LIPS to the chemical characterization of liquid and solid particles suspended in gases.

Laser induced plasma formation in gases has been the subject of continuous study ever since the first demonstration of optical breakdown by Maker *et al.*,[6] Meyerand and Haught[7] and Damon and Romlinson[8]. The process is quite complex and sensitive to many experimental parameters such as laser intensity, wavelength and pulse characteristics, and gas composition and pressure. Subtle differences in laser temporal and spatial character are important and therefore, only fair agreement among different experimental measurements of breakdown thresholds has been possible. By 1965, Wright,[9] Browne[10] and others had formulated the essentials of the breakdown mechanism and by the mid-1970's the basic features of laser breakdown in gases were well understood. Two excellent reviews from that period[11,12] and the book by Raizer[13] summarize the mechanism of plasma formation and development. Here, we will restrict our discussion primarily to breakdown in air by lasers with ≈10 ns pulse durations, which are most commonly used for spectrochemical analysis.

The process of laser plasma formation in gases is commonly considered in three phases, the initial ionization and breakdown, the continued interaction of

* University of Florida, Gainesville, FL 32611
**Corresponding Author
† Accepted: August 17, 2001

the developing plasma with the remainder of the laser pulse, and, finally the propagation of the shock wave with the accompanying plasma decay.[9] The initiation of plasma formation requires the presence of seed electrons. In rare instances, the natural background level of charge pairs, due to cosmic rays and radioactivity, may suffice, although the probability of such a charge pair being present in the small focal volume of a 10 ns laser pulse is extremely low.[14] It is far more probable that the seed electron will be produced through multiphoton ionization of either O_2 or N_2 by the pulsed laser. For breakdown in air, this is an 8 or 10-photon process at 1064 nm (for O_2 and N_2, respectively) and approaches a 2-photon process in the UV. The threshold for breakdown, which can be defined as the minimum irradiance necessary to cause the formation of a visible spark, is therefore expected to be wavelength dependent, requiring less irradiance to cause breakdown at shorter wavelengths. A rough estimate of the spatially uniform and temporally constant photon flux, F_{TH}, (photons/s-cm^2) needed to cause breakdown in a gas *via* multiphoton ionization has been given by Grey Morgan:[8]

$$F_{TH} \approx \frac{\nu}{\sigma}\left(\frac{\delta k!}{\tau \nu}\right)^{1/k}$$

where ν is the laser frequency, σ is the cross-section for absorption of a single photon, δ is the ionization fraction needed for breakdown to occur, k is the number of photon absorptions required to reach ionization, and τ is the laser pulse duration. This assumes that the lifetime of each virtual state is $1/\nu$, photon arrival follows a Poisson distribution and $F_{TH}\ \sigma/\nu << 1$. For the fundamental output of a Nd:YAG laser (1064 nm) in air, $k \approx 10$, $\tau \approx 10^{-8}$ s, $\sigma \approx 10^{-16}$ cm^2, and $<\nu \approx 2.8 \times 10^{14}$ s^{-1}. If we take $\delta \approx 10^{-3}$, the breakdown threshold is $\approx 1.4 \times 10^{30}$ photons/s cm^2, or about 300 GW/cm^2. For a UV laser (266 nm), $\nu = 1.13 \times 10^{15}$ s^{-1}, $k \approx 3$ and the calculated breakdown threshold is ≈ 7 GW/cm^2. These values are in reasonable agreement with experimental observations. In fact, experimental measurements vary widely because of the uncontrolled yet important influence of particles, which typically lower the threshold for breakdown by about 100 times.[15] The presence of particles in the breakdown region causes the observed breakdown threshold to be dependent upon the size of the laser focus, there being a higher probability that the laser will encounter a random particle with increasing focus spot diameter. In clean air, reported breakdown thresholds for 10 ns pulse duration 1064 nm lasers range from 90−1600 GW/cm^2. At 266 nm, literature values range from 30−380 GW/cm^2. At wavelengths much longer than the fundamental of the Nd:YAG laser (e.g., the CO_2 laser at 10.6 μm), the photon energy, and thus the probability of multiphoton ionization, is so small that other sources of seed electrons are invariably required.[16]

Once breakdown is initiated, the plasma rapidly develops through an avalanche process caused by increasing inverse bremsstrahlung absorption (free-free absorption), i.e., the absorption of a photon by a free electron with collisional energy transfer to a gas molecule. When the electrons gain enough energy from this process, the gas is ionized and the electron concentration increases exponentially. The increased absorption of laser energy rapidly increases the temperature of the developing plasma and by the time the laser pulse terminates, an energetic, dense, highly ionized, rapidly expanding plasma has been formed. The development and decay of this plasma can be followed spectroscopically. The emission spectrum at early times is predominately a continuum which gradually evolves into a conventional spectrum of atomic and ionic lines and molecular bands. **Figure 1** shows a time resolved spectrum of a laser plasma formed in atmospheric pressure laboratory air by a focused 1064 nm Nd:YAG laser with an irradiance of 175 GW/cm^2. The spectrum has been well-studied and is dominated by molecular bands due to N_2 and N_2^+ and by the ionic lines of N^+, N^{++}, O^+ and O^{++}.[17, 18] The luminous plasma ball expands as it cools, emitting detectable radiation for tens to hundreds of microseconds. The emitted radiation is subsequently collected, dispersed spectrally and recorded using a suitable

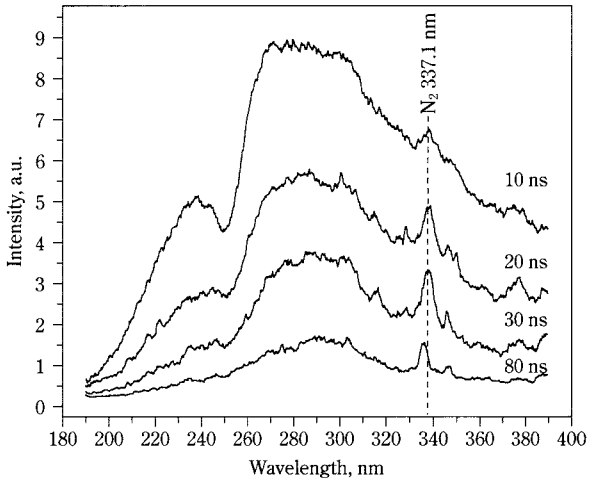

Fig. 1 Typical time-resolved laser induced plasma spectra in air at four delay times.

detector, commonly a charge-coupled device (CCD) or photodiode array. A typical LIPS schematic is shown in **Figure 2**, in which the primary focusing lens also collects the plasma emission. Fiber optic coupling of the plasma emission to the spectrometer is useful for many industrial and field applications. Typical measured values for the plasma temperature, at the peak of radiant intensity, range from 10,000–20,000 K and the plasma typically expands to a volume of several cubic mm. Villermaux *et al.* made a careful study of the spectroscopic and chemical behavior of plasmas formed by a Nd:YAG laser in various gases (N_2, CO_2, O_2, Ar, H_2 and He) from 100–760 torr.[19] They were able to isolate three effects relating to the plasma emission: the bremsstrahlung, atomic and molecular spectral lines and a late peak during the supersonic shock wave in the direction of the laser. They did not observe any multiphoton absorption or macroscopic chemical reactions below the breakdown threshold. In a more recent study, Simeonsson and Miziolek reported on the spectroscopy of plasmas formed in air, CO and CO_2 using lasers at 193, 266, 355, 532 and 1064 nm.[20] They measured breakdown thresholds which ranged from 7.3 GW/cm^2 at 193 nm in CO to 300 GW/cm^2 at 355 nm in CO. In air, the threshold was lowest at 193 nm (9.7 GW/cm^2), highest at 355 nm (270 GW/cm^2) and declined to 200 GW/cm^2 at 1064 nm. They also reported time-resolved plasma electron densities (2×10^{17}–2×10^{18} cm^{-3}), ionization temperatures (16,000–23,000 K) and excitation temperatures (11,000–22,000 K) for the various gas/wavelength combinations.

The physics of the laser breakdown process is greatly changed if particles happen to be present in the focal region.[21] Absorption of the laser light can now take place on the particle surface. Haught and

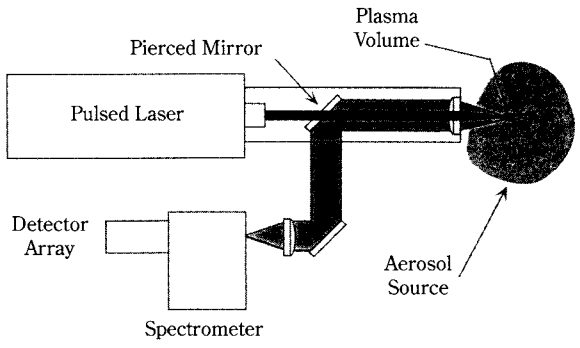

Fig. 2 Schematic diagram of a typical LIPS experiment for studying particles in a gas stream.

Polk,[22] in 1966, made one of the first observations of a laser induced plasma on a single particle. Using 10–20 μm diameter electrostatically levitated lithium hydride (LiH) particles and a ruby laser, they measured the total charge produced and demonstrated that the plasma was completely ionized, producing about 8.5×10^{14} charge pairs from about 10^{14} molecules of LiH. They also showed that the charge density was essentially isotropic about the laser beam focal point. Throughout the 1970's, there was great interest in the interaction of intense laser beams with particles, especially because of the important role which aerosols play in determining the transport of laser radiation through the atmosphere and because of nuclear fusion research. If a particle is present in the focal volume of the laser during breakdown, it will be vaporized and contribute to the developing plasma. Moreover, the threshold for breakdown will be greatly reduced due to local heating on the particle surface, thermoelectric emission and resonance effects. For transparent aerosols, there are additional effects due to localized focusing of the laser beam by the particle.[23] The relative importance of the various possible mechanisms involved in breakdown with particles depends on the particle size, refractive index and absorption at the laser wavelength. Reported breakdown thresholds for various particles (e.g., water, bromoform, pyridine, glycerol, carbon, NaCl, ethanol, methanol, CCl_4, ethylbromide, clay, aluminum, alumina, germanium, oleic acid, diesel fuel) of ≈10–150 μm diameter for laser wavelengths from 0.266–10.6 μm, range from 0.04–4 GW/cm^2 for lasers in the 10 ns pulse duration regime.[24, 25, 26] Usually, larger particles tend to cause lower breakdown thresholds. However, other factors, such as refractive index, play important roles, making it difficult to generalize. Several studies have been reported showing that the breakdown threshold is independent of particle size.[27, 28] Aqueous aerosols do not reduce the breakdown threshold as much as solid aerosols. For long wavelength lasers (e.g., the CO_2 laser at 10.6 μm), breakdown is only possible in the presence of a particle, the photon energy being far too low to produce any seed electrons from multiphoton ionization.[15, 29] Smith has developed a theoretical model for calculating the breakdown threshold on particles and solid surfaces which provided good agreement with measurements over a wide range of pulse durations, wavelengths and particle sizes.[30]

From the viewpoint of using laser induced plasmas for characterization of particles and aerosols, the important considerations are that plasmas are rela-

tively easy to produce in particle-laden gases (with a variety of laser systems) and any particle smaller than about 10−20 μm will be completely vaporized and incorporated into the plasma. Vaporization and subsequent excitation by the laser induced plasma forms the basis for chemical characterization of particles by emission spectroscopy.

Applications to Particle Characterization

The application of LIPS for chemical characterization of aerosols probably originated about 1978 with the suggestion by Belyaev *et al.* that such a technique would be ideal for remote, real time analysis.[31] About the same time, Gavrilov and co-workers[32] took the unique approach of using a CO_2 laser with a special pulse shape such that the initial, brief portion of the pulse was above the breakdown threshold and the long tail of the pulse well below it. This produced efficient breakdown and particle vaporization while allowing the subsequent plasma to be formed with the optimum temperature for good signal/noise ratio in the emission spectrum. Loree and Radziemski reported on time-integrated and time-resolved LIBS detection of various particles in gas streams in a pair of papers published in 1981.[33, 34] In the first paper,[32] using time-integrated measurements and a Nd:YAG laser (1064 nm, 10−100 MW/cm^2), they detected Na and K in a coal gasifier output, Be in air and P, S and Cl from various volatile organic compounds. In the companion paper,[33] they added time resolution using a gated optical multichannel analyzer or a gated photomultiplier tube. Here, they detected P (253 nm) and Cl (837.5 nm) in air with estimated limits of detection of 15 ppm and 60 ppm (w/w), respectively. Most of the essential aspects of the technique were presented by Radziemski *et al.* in 1983 in a study of the detection of Be particles in air.[35, 36] They measured temperature and electron densities in the air plasma and concluded that the plasma is in approximate local thermodynamic equilibrium at times longer than about 1 μs. Using the unresolved Be II doublet at 313.1 nm, they obtained a limit of detection of 0.7 μg/m^3 for Be in air (0.6 ng Be/g air). In field measurements at two coal gasifiers, they detected spectral features due to Na, K, H, O, O^+, C, C^+, C^{2+}, Ca, Ca^+, Si, Mg, CN, N_2, CO, O_2 and S, demonstrating the potential for practical real-time particle monitoring. They also reported limits of detection for Na, P, As and Hg of 0.006, 1.2, 0.5 and 0.5 μg/g air, respectively. In a related work, Cremers and Radziemski also studied the detection of Cl and F in air using both vapor and particle sample introduction.[37] They reported limits of detection for Cl and F of 8 and 38 ppm (w/w), respectively.

In 1984, Leslie, *et al.* used a D_2−F_2 laser with a 1 μs pulse width at 3.58−4.78 μm to study plasma formation in maritime liquid and solid aerosols.[38] For pure aqueous aerosols and aerosols containing NaCl, SiO_2 and Al_2O_3, they observed a breakdown threshold which decreased from about 8×10^8 W/cm^2 for 1 μm radius particles to 8×10^7 W/cm^2 for particles larger than about 10 μm. They also noted the characteristic propagation of the breakdown plasma in the direction of the incident laser beam, and demonstrated good agreement between their observations and a theoretical model.

Srchontaki and Crouch, in 1988, developed a single droplet sample introduction system for LIBS.[39] They vaporized single droplets ranging from about 100−160 μm in diameter and found that the spectral line intensity decreased slightly with increasing droplet size. They reported good linearity (about 3 decades) for Li, Na, Mg, Ca, Mn and Al with detection limits ranging from 0.3−7 ppm. Radziemski *et al.* used a similar approach to study dry aerosols of Cd, Pb and Zn.[40] Using an irradiance of $\approx 10^{10}$ W/cm^2 from a Nd:YAG laser (1064 nm), they reported limits of detection of 0.02, 0.2 and 0.24 μg/g (of air) for these three elements with linear ranges of about two orders of magnitude. They suspected that the upper limit of linear response was determined by the inability of the laser to completely vaporize particles larger than about 10 μm, although no direct experimental evidence was reported. After these initial studies, applications of LIBS to particle characterization have been primarily directed at *in-situ*, real-time detection in industrial processes (e.g., relatively dense particle concentration systems). Although the potential exists for real-time atmospheric monitoring (e.g., very dilute particle concentrations, see Sneddon's review[41] and Harith *et al.*[42]), this remains a research direction awaiting exploration.

The application of LIBS to industrial process monitoring is extremely attractive because there are very few techniques which can provide such real time, *in situ* measurements of elemental concentrations. The usual approach, collecting samples on filters followed by dissolution and elemental analysis in the laboratory, is time consuming and sacrifices all information regarding relationships between particle size and composition. One option, to preserve this information, is to use LIBS for rapid quantitative analysis of particulates collected on filters. Arnold and Cremers[43] have reported on the determination of thalium on fil-

ters in less than 1 minute with a limit of detection of 40 ng/cm^2. While not a real-time measurement, this approach significantly shortens the analysis time for samples collected in this way. Panne *et al.* have used an automated approach where a continuous filter belt conveys the collected particulate to a portable LIBS instrument (Nd:YAG, 1064 nm, 30 mJ/pulse) for near on-line analysis in a municipal waste incinerator.[44] They reported limits of detection ranging from 10–500 ng/cm^2 for Cd, Ni, As, Co, Mn, Sb, Cr, Tl, Sn, V, Cu and Pb. For their sampling system, these corresponded to 0.03–1.3 μg/m^3 in the stack gas. The first application of LIBS to a combustion environment for real-time, *in situ* measurements appeared in 1989 when Ottesen *et al.* reported on a hybrid technique which also provided information on particle size and velocity.[45] They used two continuous wave lasers (He-Ne at 633 nm and Ar-ion at 488 nm) for light scattering and velocimetry measurements simultaneously with a frequency-doubled Nd:YAG (100 mJ, 532 nm) for LIPS. They demonstrated simultaneous, semi-quantitative detection of Si, C, Fe, Al, Ca, Ti, Mg, Ba, Li, Mn and Sr in 30–75 μm diameter coal particles fed into a combustion reactor system. Measurements of bulk concentrations as well as on a particle by particle basis were presented. In a related work, Ottesen *et al.* demonstrated semi-quantitative determination of Mg, Ca, Al, Si, Fe and Ti in individual coal particles and made a particle-by-particle comparison with SEM[46]. There have been several studies of LIPS using bulk measurements in aqueous aerosols. Winefordner *et al.*, examined the use of an ArF laser (193 nm) for LIPS in dense aerosols.[47] They reported bulk concentration limits of detection ranging from 0.3–20 ppm for Li, Na, K, Mg, Ca, Mn, Sr, Al, Ga and In using a simple pneumatic nebulization system probed by the focused laser. Alexander and Poulain made a thorough study of LIBS on a salt water aerosol using a KrF laser (248 nm) delivering about 50 GW/cm^2.[48] They compared performance with mono- and polydisperse aerosols and reported on the spatial and temporal behavior of Na and H spectral lines. Using the ratio of the Na 589 nm emission to the H 656 nm emission as the analytical measure, they also obtained calibration curves as a function of particle size (23–90 μm) showing a somewhat higher sensitivity for larger particles. They reported a limit of detection of about 160 ppm for Na. Schechter has applied LIBS (Nd:YAG, 1064 nm) to the determination of Fe, Ca, Zn and Pb in particulate streams from a steel processing facility.[49] A unique software was used to manipulate the spectra on a single shot basis, allowing the rejection of spectra which were irregular or had poor S/N. Typically about 75% of the recorded spectra were discarded. A detection limit of about 1% was reported for Zn. Peng and coworkers at Sandia National Laboratories made the first really thorough study involving continuous emissions monitoring in an industrial environment.[50] They reported on the use of a LIBS instrument (Nd:YAG, 532 nm, 300 mJ/pulse) for the detection of 11 metals (Sb, As, Be, Cd, Ar, Co, Pb, Hg, Mn, Ni and Se) in stack gas emissions. They calibrated the system with a pneumatic nebulizer which produced 3×10^5 particles/cm^3 and of 0.3–15 μm diameter and demonstrated good accuracy in field measurements on a thermal waste treatment plant. Their limits of detection ranged from 0.1 μg/m^3 for Be to 250 μg/m^3 for Pb. Yalcin *et al.*, made a specific study of the influence of ambient and experimental conditions (variations in the background gas, the presence of particles, humidity and laser power) on the performance of LIPS for toxic metal monitoring.[51] Their system used a Nd:YAG laser at 532 nm and test aerosols were produced with a pneumatic nebulizer and desolvation system. They measured plasma temperatures and electron number densities as a function of the parameters listed above and concluded that none of these factors had any significant influence.

In the first demonstration of LIBS in a harsh, turbulent, highly luminous combustion system, Yueh *et al.* used a Nd:YAG laser (532 nm, 100 mJ/pulse, 130 GW/cm^2) to monitor Ca, Fe, Al, Ti an Sr in a large magnetohydrodynamic coal-fired flow facility.[52] They did not report limits of detection but only demonstrated the ability to detect these species in an operating combustion system. In a continuation of this work, another successful field demonstration involving measurements on the exhaust gas stream from a plasma torch waste treatment facility was reported by Singh *et al.*.[53] They used a similar Nd:YAG laser system (532 nm) and calibrated with nebulized aerosols. Using 50 s measurement times (500 laser shots), they reported limits of detection for As, Be, Co, Cr, Zn, Cd, Hg, Sb, Sn, Mn, Ni, Pb and Fe ranging from 1–680 μg/m^3 and obtained good correlation in field tests with reference methods (EPA Method 5 with a multiple metals sampling train). **Figure 3** shows a typical spectrum containing numerous elemental lines.

Hahn *et al.* used a conditional data analysis approach to obtain particle size and composition using LIBS (Nd:YAG, 1064 nm, 300 mJ) in dilute sample streams.[54] In measurements on a 220 kW natural-gas-fired pyrolytic waste processing unit burning municipal solid waste, they successfully measured Cr, Mn

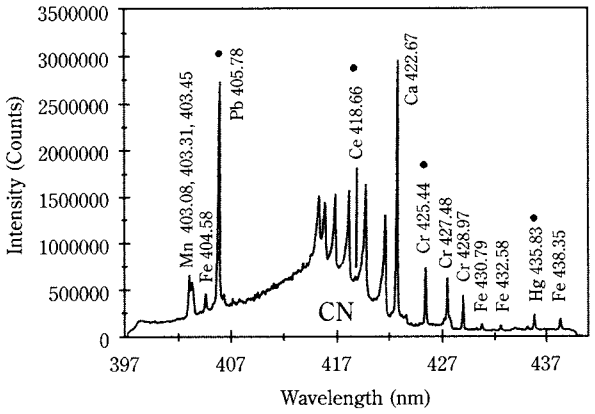

Fig. 3 Typical LIPS spectrum in an industrial effluent, taken from Ref. 50, p. 250, with permission.

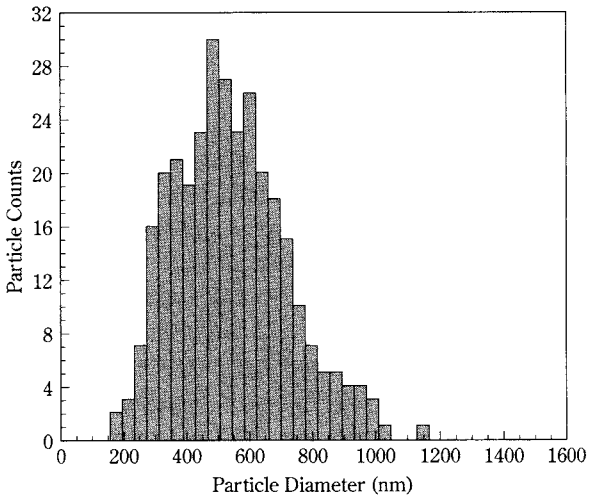

Fig. 4 A LIPS-based sized distribution for chromium particles.

and Fe in the exhaust gases and found good agreement with EPA Method 29. Their results demonstrated significant advantages of conditional data analysis of individual spectra compared to time-averaged data collection. In this approach, individual emission spectra were only retained if they contained emission features other than those found in the background gas. By taking into account the frequency with which these spectra occur, one obtains a calibration relationship with a greatly improved limit of detection. In an extension of this work, Hahn, extracted particle size information of individual particles using a calibration procedure based on known monodisperse polymer particles containing magnetite.[55] He also demonstrated the detection and sizing of individual magnesium-containing particles with an average diameter of about 300 nm in ambient air. Hahn and Lunden further explored single-particle analysis in a number of laboratory aerosol streams containing Cr, Mg, and Ca particles.[56] **Figure 4** shows a LIPS-based size distribution recorded for chromium particles at an overall mass concentration of 21 ng/g (ppb, mass basis).

Lemieux *et al.* reported the results of a major DOE/EPA sponsored field test of multimetal continuous emission monitoring technologies which took place in 1997 and included LIBS instrumentation.[57] Tests were carried out in the EPA rotary kiln incinerator simulator using seven monitoring systems, two commercial and five prototypes. Elements included in the tests included As, Be, Cr, Cd, Pb and Hg ranging from 20−182 μg/m^3. None of the systems evaluated were able to monitor all 6 test elements with the required relative accuracy of 20%. The LIBS instruments yielded accuracies ranging from 19−367% and a spectral interference problem for Cd and As lines was reported. Panne *et al.* have developed a LIPS system (Nd:YAG, 1064 nm, 200 mJ/pulse) optimized for the detection of Cr and evaluated it for rapid monitoring of optical emission from particulates at an electroplating facility.[58] Using nebulized solutions for calibration, they obtained a linear response from particle densities between 14 μg/m^3 and 5000 μg/m^3. Good correlation was obtained against a reference method and continuous emission monitoring was demonstrated.

Concluding Remarks

Laser-induced plasma spectroscopy has reached the point in development where it will begin to find routine applications in industrial process monitoring. It has already been demonstrated that reliable detection of many elements of interest are readily detectable in the necessary concentration ranges. Rugged systems have been designed and proven in field tests. Recent work has established the ability of this technique for the quantitative analysis of individual aerosol particles. Further work is needed to find a reliable means for calibration in order to improve the accuracy. The use of this technique for continuous monitoring of dilute atmospheric aerosols (such as in routine atmospheric pollution monitoring) has yet to be developed but nevertheless appears promising in light of recent work with industrial emissions.

Acknowledgements

This work was supported by the Engineering Research Center (ERC) for Particle Science and Technology at the University of Florida, the National

Science Foundation grant No. EEC-94-02989 and the Industrial Partners of the ERC.

References Cited

1) Brech, F.: "Optical microemission stimulated by a ruby maser," *Appl. Spectrosc.*, **16**, 59 (1962).
2) Rusak, D. A., Castle, B. C., Smith, B. W. and Winefordner, J. D.: "Fundamentals and applications of laser-induced breakdown spectroscopy," *Crit. Rev. Anal. Chem.*, **27**, 257-290 (1997).
3) *Laser-Induced Plasmas and Applications*, Ed. L. J. Radziemski and D. A. Cremers, Marcel Dekker, Inc., New York (1989).
4) Martin, M. Z., Cheng, M-D and Martin, R. C.: "Aerosol measurement by laser-induced plasma technique: A Review," *Aerosol Sci. Tech.*, **31**, 409-421 (1999).
5) Telgheder, U. and Khvoltikov, V. A.: "Collection and determination of metal contaminants in gases," *J. Anal. Atom. Spectrom.*, **12**, 1-6 (1997).
6) Maker, P. D., Terhune, R. W. and Savage, C. M.: "Optical third harmonic generation in various solids and liquids," Proc. 3rd Int. Conf. On Quantum Electronics, ed. P. Grivet and N. Bloembergen (New York: Columbia University Press), pp. 1559-1565 (1963).
7) Meyerand, R. G. and Haught, A. F.: "Gas breakdown at optical frequencies," *Phys. Rev. Lett.*, **11**, 401-403 (1963).
8) Damon, E. K. and Tomlinson, R. G.: "Observation of ionization of gases by a ruby laser," *Appl. Opt.*, **2**, 546-547 (1963).
9) Wright, J. K. Wright: "Theory of the electrical breakdown of gases by intense pulses of light," *Proc. Phys. Soc.*, **84**, 41-46 (1964).
10) Browne, P. F.: "Mechanism of gas breakdown by lasers," *Proc. Phys. Soc.*, **86** 1323-1332 (1965).
11) Smith, D. C. and Meyerand, Jr., R. G.: "Laser Radiation Induced Gas Breakdown," in *Principles of Laser Plasmas*, Ed. G. Bekefi, Wiley-Interscience, New York, 1976.
12) Grey Morgan, C.: "Laser-induced breakdown of gases," *Rep. Prog. Phys.*, **38**, 621-665 (1975).
13) Raizer, Yu. P.: *Laser-induced discharge phenomena*, Consultants Bureau, New York, 1977.
14) Tozer, B. A.: "Theory of the ionization of gases by laser beams," *Phys. Rev.*, **137**, 1665-1667 (1965).
15) Lencioni, D. E. and Pettingill, L. C.: "The dynamics of air breakdown initiated by a particle in a laser beam," *J. Appl. Phys.*, **48**, 1848-1851 (1977).
16) Caressa, J-P, Autric, M., Dufresne, D. and Bournot, Ph.: "Experimental study of CO_2-laser-induced air breakdown over long distances," *J. Appl. Phys.*, **50**, 6822-6825 (1979).
17) Armstrong, R. A., Lucht, R. A. and Rawlins, W. T.: "Spectroscopic investigation of laser-initiated low-pressure plasmas in atmospheric gases," *Appl. Opt.*, **22**, 1573-1577 (1983).
18) Nordstrom, R. J.: "Study of laser-induced plasma emission spectra of N_2, O_2, and ambient air in the region 350 nm to 950 nm," *Appl. Spectrosc.*, **49**, 1490-1499 (1995).
19) De Montgolfier, Ph., Dumont, P., Mille, Y. and Villermaux, J.: "Laser-induced gas breakdown: spectroscopic and chemical studies," *J. Phys. Chem.*, **76**, 31-37 (1972).
20) Simeonsson, J. B. and Miziolek, A. W.: "Spectroscopic studies of laser-produced plasmas formed in CO and CO_2 using 193, 266, 355, 532 and 1064 nm laser radiation," *Appl. Phys. B*, **59**, 1-9 (1994).
21) Lushnikov, A. A. and Negin, A. E.: "Aerosols in strong laser beams," *J. Aerosol Sci.*, **24**, 707-735 (1993).
22) Haught, A. F. and Polk, D. H.: "High-temperature plasmas produced by laser beam irradiation of single solid particles," *Phys. Fluids*, **9**, 2047-2056 (1966).
23) Hsieh, W. F., Eickmans, J. H. and Chang, R. K.: "Internal and external laser-induced avalanche breakdown of single droplets in an argon atmosphere," *J. Opt. Soc. Amer. B*, **4**, 1816-1820 (1987).
24) Pinnick, R. G., Biswas, A., Armstrong, R. L., Gerard Jennings, S., Pendleton, J. D. and Fernadez, G.: "Micron-sized droplets irradiated with a pulsed CO_2 laser: measurement of explosion and breakdown thresholds," *Appl. Opt.*, **29**, 918-925 (1990).
25) Pinnick, R. G., Biswas, A., Pendleton, J. D. and Armstrong, R. L.: "Aerosol-induced laser breakdown thresholds: effect of resonant particles," *Appl. Opt.*, **31**, 311-318 (1992).
26) Chylek, P., Jazembski, M. A., Chou, N. Y. and Pinnick, R. G.: "Effect of size and material of liquid spherical particles on laser-induced breakdown," *Appl. Phys. Lett.*, **49**, 1475-1477 (1986).
27) Smith, D. C. and Brown, R. T.: "Aerosol-induced breakdown with CO_2 laser radiation," *J. Appl. Phys.*, **46** 1146-1154 (1975).
28) Mamonov, V. K.: "Air breakdown minimized by breakdown in aqueous aerosol drops acted upon by radiation with $\lambda = 1.06$ μm," *Second All-Union Conference on Propagation of Laser Radiation in a Disperse Medium. Summary of Proceedings, Part II*, pp. 249-251, English trans., Plenium Publishing Corp., New York (1984).
29) Bunkin, F. V. and Savranskii, V. V.: "Optical breakdown of gases induced by the thermal explosion of suspended macroscopic particles," *Sov. Phys. -JETP*, **38** 1091-1096 (1974).
30) Smith, D. C.: "Gas breakdown initiated by laser radiation interaction with aerosols and solid surfaces," *J. Appl. Phys.*, **48**, 2217-2225 (1977).
31) Belyaev, E. B., Godlevskii, A. P. and Kopytin, Yu. D.: "Laser-spectroscopy analysis of aerosols," *Quant. Elect.*, (Moscow), **5**, 2594-2601 (1978).
32) Gavrilov, V. M, Golub, S. L. and Skripkin, A. M.: "Optimal conditions for laser elemental analysis of aerosols," *Second All-Union Conference on Propagation of Laser Radiation in a Disperse Medium. Summary of Proceedings, Part II*, pp. 265-268, English trans., Plenium Publishing Corp., New York (1984).
33) Loree, T. R. and Radziemski, L. J.: "Laser-induced breakdown spectroscopy: Time-integrated applications," *Plasma Chem. Plasma Proc.*, **1**, 271-279 (1981).

34) Radziemski, L. J. and Loree, T. R.: "Laser-induced breakdown spectroscopy: Time-resolved spectrochemical applications," *Plasma Chem. Plasma Proc.*, **1**, 281-293 (1981).
35) Radziemski, L. J., Loree, T. R., Cremers, D. A. and Hoffman, N. M.: "Time-resolved laser-induced breakdown spectrometry of aerosols," *Anal. Chem.*, **55**, 1246-1252 (1983).
36) Radziemski, L. J., Cremers, D. A. and Loree, T. R.: "Detection of beryllium by laser-induced-breakdown spectroscopy," *Spectrochim. Acta*, **38B**, 349-355 (1983).
37) Cremers, D. A. and Radziemski, L. J.: "Detection of chlorine and fluorine in air by laser-induced breakdown spectroscopy," *Anal. Chem.*, **55**, 1252-1256 (1983).
38) Amimoto, S. T., Whittier, J. S., Ronkowski, F. G., Valenzuela, P. R., Harper, G. N., Hofland, Jr., R., Trusty, G. L., Cosden, T. H. and Leslie, D. H.: "DF-1aser pulse breakdown induced by maritime aerosols," *AIAA Journal*, **22**, 1108-1114 (1984).
39) Archontake, H. A. and Crouch, S. R.: "Evaluation of an isolated droplet sample introduction system for laser-induced breakdown spectroscopy," *Appl. Spectrosc.*, **42**, 741-746 (1988).
40) Essien, M., Radziemski, L. J. and Sneddon, J.: "Detection of cadmium, lead and zinc in aerosols by laser-induced breakdown spectrometry," *J. Anal. Atom. Spectrom.*, **3**, 985-988 (1988).
41) Sneddon, J.: "Direct and near real-time determination of metals in the atmosphere by atomic spectroscopic techniques," *Trends Anal. Chem.*, **7**, 222-226 (1988).
42) Casini, M., Harith, M. A., Palleschi, V., Salvetti, A., Singh, D. P. and Vaselli, M.: "Time-resolved LIBS experiment for quantitative determination of pollutant concentrations in air," *Laser Part. Beams*, **9**, 633-639 (1991).
43) Arnold, S. D. and Cremers, D. A.: "Rapid determination of metal particles on air sampling filters using laser-induced breakdown spectroscopy," *AIHA Journal*, **56**, 1180-1186 (1995).
44) Neuhauser, R. E., Panne, U. and Niessner, R.: "Laser-induced plasma spectroscopy (LIPS): a versatile tool for monitoring heavy metal aerosols," *Anal. Chim. Acta*, **392**, 47-54 (1999).
45) Ottesen, D. K., Wang, J. C. F. and Radziemski, L. J.: "Real-time laser spark spectroscopy of particulate in combustion environments," *Appl. Spectrosc.*, **43**, 967-976 (1989).
46) Ottesen, D. K., Baxter, L. L., Radziemski, L. J. and Burrows, J. F.: "Laser spark emission spectroscopy for in situ, real-time monitoring of pulverized coal particle composition," *Energy & Fuels*, **5**, 304-312 (1991).
47) Ng, K. C., Ayala, N. L., Simeonsson, J. B. and Winefordner, J. D.: "Laser-induced plasma atomic emission spectrometry in liquid aerosols," *Anal. Chim. Acta*, **269** 123-128 (1992).
48) Poulain, D. E. and Alexander, D. R.: "Influences on concentration measurements of liquid aerosols by laser-induced breakdown spectroscopy," *Appl. Spectrosc.*, **49**, 569-579 (1995).
49) Schechter, I.: "Direct aerosol analysis by time resolved laser plasma spectroscopy – improvement by single shot measurement," *Anal. Sci. Tech.*, **8**, 779-786 (1995).
50) Peng, L. W., Flower, W. L., Hencken, K. R., Johnsen, H. A., Renzi, R. F. and French, N. B.: "A laser-based technique for continuously monitoring metal emissins from thermal waste treatment units," *Proc. Cont. Qual.*, **7**, 39-49 (1995).
51) Yalcin, S., Crosley, D. R., Smith, G. P. and Faris, G. W.: "Spectroscopic characterization of laser-produced plasmas for in situ toxic metal monitoring," *Haz. Waste Haz. Mat.*, **13**, 51-61 (1996).
52) Zhang, H., Singh, J. P., Yueh, F-Y and Cook, R. L.: "Laser-induced breakdown spectra in a coal-fired MHD facility," *Appl. Spectrosc.*, **49**, 1617-1623 (1995).
53) Singh, J. P., Yueh, F-Y, Zhang, H. and Cook, R. L.: "Study of laser induced breakdown spectroscopy as a process monitor and control tool for hazardous waste remediation," *Proc. Cont. Qual.*, **10**, 247-258 (1997).
54) Hahn, D. W., Flower, W. L. and Hencken, K. R.: "Discrete particle detection and metal emissions monitoring using laser-induced breakdown spectroscoy," *Appl. Spectrosc.*, **51**, 1836-1844 (1997).
55) Hahn, D. W.: "Laser-induced breakdown spectroscopy for sizing and elemental analysis of discrete aerosol particles," *Appl. Phys. Lett.*, **72**, 2960-2962 (1998).
56) Haln, D. W. and Lunden, M. M.: "Detection and analysis of aerosol particles by laser-induced breakdown spectroscopy," *Aerosol Sci. Technol.*, **33**, 30-48 (2000).
57) Lemieux, P. M., Ryan, J. V., French, N. B., Haas, Jr., W. J., Priebe, S. J. and Burns, D. B.: "Results of the September 1997 DOE/EPA demonstration of multimetal continuous emission monitoring technologies, "*Waste Management*, **18**, 385-391 (1998).
58) Neuhauser, R. E., Panne, U., Niessner, R. and Wilbring, P.: "On-line monitoring of chromium aerosols in industrial exhaust streams by laser-induced plasma spectroscopy (LIPS)," *Fresenius J. Anal. Chem.*, **364**, 720-726 (1999).

Author's short biography

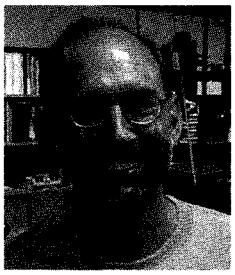

Benjamin W. Smith

Benjamin W. Smith received his PhD in analytical chemistry from the University of Florida in 1977. He is presently a Scientist in the Department of Chemistry, University of Florida. His research interests are in laser-based spectrochemical techniques.

David W. Hahn

David W. Hahn received his PhD in mechanical engineering from Louisiana State University in 1992. He was a researcher for the U.S. Food and Drug Administration and Sandia National Laboratories before joining the faculty of the Department of Mechanical Engineering at the University of Florida in 1998. His research interests are in the development and application of laser-based diagnostic techniques.

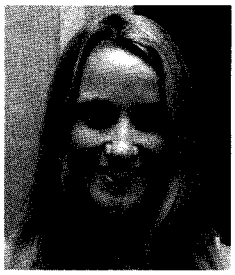

Emily Gibb

Emily Gibb is a graduate student in the Department of Chemistry, University of Florida. She received her BS in chemistry from the University of Richmond in 1999.

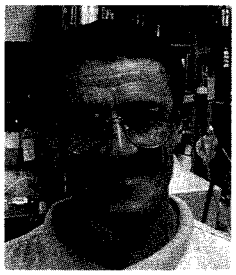

Igor Gornushkin

Igor Gornushkin received his PhD in Analytical Chemistry from the University of Florida in 1997. He is presently a postdoctoral scientist in the Department of Chemistry, University of Florida.

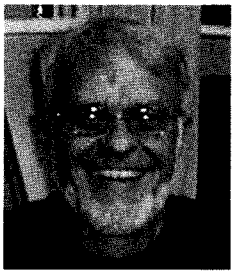

James D. Winefordner

James Winefordner is a Graduate Research Professor in the Department of Chemistry, University of Florida. He received his PhD in chemistry from the University of Illinois in 1959 and has been a member of the faculty at the University of Florida since that time. He has received, among many awards, the ACS Analytical Division Award in Chemical Instrumentation, the ACS Award in Analytical Chemistry, the Theophilus Redwood Lecture Award and the Royal Society of Chemistry Robert Boyle Medal. He has published over 840 papers in the field of analytical chemistry.

Powder Electrostatics: Theory, Techniques and Applications†

Joanne Peart, Ph.D.
*Aerosol Research Group, School of Pharmacy**

Abstract

Powder electrostatics remains an integral and challenging aspect of powder processing. During powder handling operations, such as particle size reduction, mixing and powder transfer processes, particles invariably develop electrostatic charge due to particle-particle and particle-surface interactions. Triboelectrification of powders is a complex phenomenon as most powders are organic crystals and behave as insulators under ambient conditions. However, it is generally accepted that charging occurs as a result of electron transfer between materials of different electrical properties. Factors influencing charging properties include particle size and shape, nature and work function of the contacting surface and the particulate material, area and frequency of contact, surface purity, and atmospheric conditions. Consequences of charge generation upon particle dynamics and powder behavior are often unpredictable. The standard method for measurement of electrostatic charge is the Faraday pail or well, with various application-specific modifications. Electrostatics, regarded by many as a nuisance and hazard, plays an important and ever emerging role in many industrial applications, including powder coating, xerography, and pharmaceutical processing.

1. Introduction

Electrostatics is an integral and challenging discipline in the field of powder technology. During common powder processing procedures, e.g. micronization, sieving, blending and powder transfer through hoppers, the relative movement of particles and collisions with surfaces provide ideal conditions for the development of electrostatic charge by triboelectrification [1]. Triboelectrification is an important surface phenomenon, and as such is sensitive to external parameters such as temperature, humidity and surface contamination [2]. Such environmental effects can cause powder-handling procedures to behave in a variable manner, giving rise to the unpredictable and frustrating reputation of electrostatics. Surface electrification also accounts for many of the nuisances and hazards of electrostatics – the relative forces of attraction and repulsion that exist between charged particles can cause adhesion of material to walls of the processing equipment and agglomeration of particles, resulting in the inefficient operation of equipment [3-5], as well as fire and explosion hazards [6-7].

Numerous industrial applications have evolved around electrostatic particle technology, with the emphasis being on careful control and manipulation of electrical charge. Xerography and powder coating are excellent examples of how controlled charging of individual particles can be utilized to the benefit of the industry [8-11]. Indeed, recent innovations have seen electrostatics utilized in novel tablet coating technology [12] and aerosol generation methods [13, 14].

2. Theoretical Considerations

2.1 Electrification of solids

Solid surfaces can acquire electric charge in many ways including triboelectrification, corona charging, spray charging, induction charging of sprayed liquids, ion and electron beam charging, photoelectric charging and charging by mechanical fracture of materials [15]. Triboelectrification will be the focus of this article.

Triboelectrification was first observed by Thales of Miletus around 600 BC, when rubbed amber was found to attract small particles of straw [16]. 'Tribo' literally means rubbing, but charge separation and accumulation can be achieved by contact alone. Contact electrification describes the primary mechanism

* Box 980533, Virginia Commonwealth University, Richmond, Virginia, 23298-0533, USA.
email: jpeart@vcu.edu
† Accepted: August 17, 2001

of charge generation, whereby an electrostatic charge is generated by the contact and separation of two dissimilar materials, resulting in oppositely charged surfaces. During powder handling procedures e.g. transport through a powder hopper, 'contact' charging between different materials is invariably accompanied by energetic friction, rubbing, sliding etc. It is very difficult to separate the phenomena of contact and frictional charging, and the term triboelectrification is used to describe the combined process [17]. Charge transfer between metal surfaces is reasonably well understood and can be explained in terms of electron transfer caused by the difference in work function between the materials. However, many powders are organic crystals, which behave as insulators under ambient conditions.

The simple model of electrification can be described by the example of metal-metal contact [15]. Electrons exist in the material within various energy levels up to the outermost or Fermi level (**Figure 1**). The work function (Φ) of a substance is defined as the difference in the energy state between the Fermi level and the vacuum energy level. On contact, electrons are transferred between the surfaces until the Fermi levels are equalized (**Figure 2**). The transfer of electrons from one surface to the other causes the generation of a contact potential, which is equal to the difference in work function ($\Phi_A - \Phi_B$) [15].

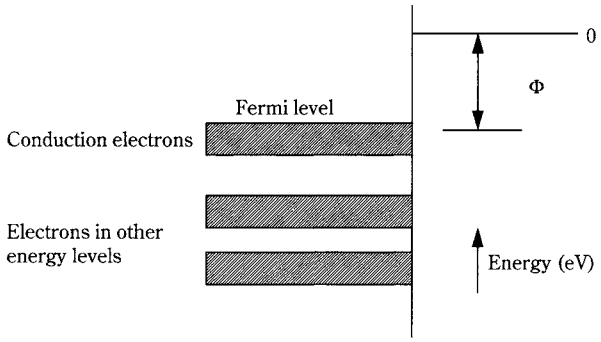

Fig. 1 Typical energy level diagram for a metal [15].

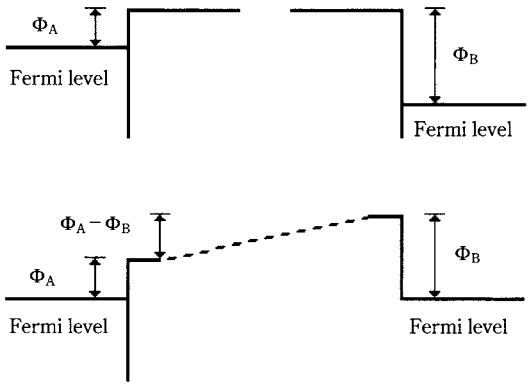

Fig. 2 Development of contact potential between materials A and B [15].

Although the metal-metal contact electrification model provides an excellent basis for charge transfer dynamics, triboelectrification of insulating materials is more complex. Polymer paint particles [11], and pharmaceutical powders [18] are inherently highly resistive (volume resistivities in excess of 10^{13} Ωm), and do not readily lend themselves to the accommodation of charge, or indeed charge exchange processes. It is generally believed that there are donor or acceptor sites at, or near, the insulator surface. Surface roughness of the insulator surface, together with contact pressure determine the true area of contact between the two materials. Finally, in the process of triboelectrification, there may be insufficient time for the charge transfer process to reach equilibrium, as a result of the frictional contact between the two surfaces [1].

On the basis of charging experiments, materials can be ranked in a Triboelectric Series, as illustrated in **Table 1** [Adapted from 19]. A triboelectric series is analogous to the electrochemical series; every material charges positive against materials below it in the table. While a triboelectric series can give an indication of the possible interaction between different surfaces, and facilitate charge exchange behavior, it is only specific to a set of experimental conditions.

Table 1 Typical triboelectric series of materials encountered during industrial processing. Adapted from [19]

Positive	Glass	Easily becomes (+) charged
	Calcite	
	Mica	
	Wool	
	Quartz	
	Nylon	
	Aluminum	
	Paper	
REFERENCE	Cotton	
	Wood	
	Amber	
	Stainless Steel	
	Hard Rubber	
	Copper/Nickel/Brass	
	Tin	
	Polyester	
	Polyurethane	
	Polyethylene	
	Polypropylene	
	PVC	
NEGATIVE	Teflon	Easily becomes (−) charged

2.2 Factors influencing Triboelectrification

Electrostatic charge generation in powders by the process of triboelectrification is a highly complex subject, and despite extensive research remains poorly understood. Many interrelated factors influence the mechanics of charge transfer and separation between dissimilar surfaces, including material properties (size, shape, surface roughness and purity, permitivity, frequency, duration and area of contact) and environmental conditions (temperature and relative humidity) [6, 16, 20-24]. Moreover, these conditions are in constant flux, and it is difficult to attribute an effect to any single parameter.

Clearly, charge transfer will be a function of the chemical nature of both the powder and the contact surface. Materials have varying capacity to act as electron donors or acceptors depending upon their chemical properties. Derjaguin [25] ranked some functional groups in a donor-acceptor series:

DONOR-NH_4>-OH>-OR>-COOR>-CH_3>-Ph>halogens>=CO>-CN **ACCEPTOR**

where each group in the series is an electron acceptor with respect to the preceeding group. Particle size has been reported to have a significant effect upon the work function of a material [20]. Computation of a theoretical expression demonstrated that the work function decreased as particle size increased [20]. For a specific material, this model predicted that the work function of a large particle would be lower than that of a smaller particle. Therefore, it would be predicted that electrons would transfer from larger to smaller particles, and larger particles would be expected to develop positive charges, and smaller particles negative charges. This phenomenon could account for the bipolar charging phenomenon, which is observed during powder handling operations. Cartwright reported that coarse polyethylene particles charged positively, and fines negatively, when investigated in a full-scale experimental silo system [6]. Furthermore, this observed bipolarity was also shown to be dependent upon relative humidity – at high levels of humidity, all particles, regardless of size, charged negatively. The theoretical model of the work function developed by Gallo and Lama also predicted a correlation between work function and particle permittivity [20]. Other workers have shown that contact charge exchange in polymers is influenced by the oxidative state of polymer materials [23]. Freshly prepared films of polyethylene exhibited low contact charge densities (≈10 $\mu C/m^2$), while exposure of the film to air led to a significant increase in contact charging (≈200 $\mu C/m^2$). In addition, high temperatures have been shown to reverse the natural tendency of polymers to accept electrons and charge negatively [16]. It is not surprising therefore when surfaces are rubbed and heat is generated that charging becomes much less predictable. Even during relatively simple contact experiments reproducible data can be difficult to produce, especially when contact is made repeatedly to different regions of a surface. Indeed, when a particular region of surface is repeatedly contacted the charge transfer is often dependent on the number of prior contacts, tending to decrease it to a saturation level. **Figure 3** illustrates this point well, by showing Specific Charge (or charge to mass ratio) developed

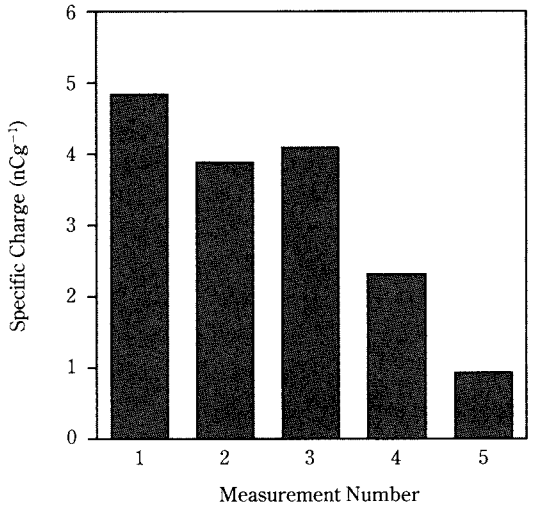

(a) salbutamol base

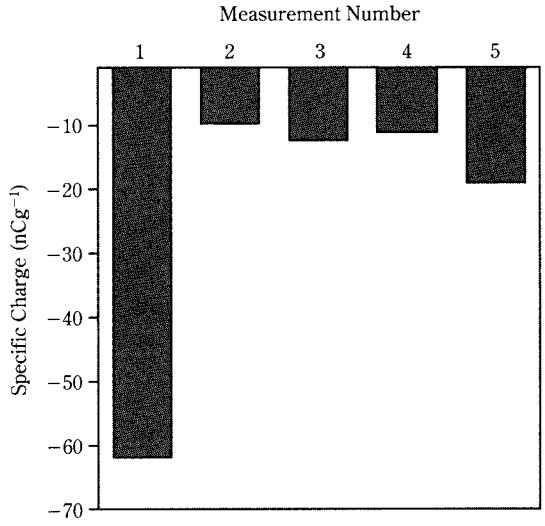

(b) Aerosil 200

Fig. 3 Successive charge measurements of (a) salbutamol base and (b) Aerosil 200 following contact with a PVC chute.

on (a) micronized salbutamol base and (b) Aerosil 200 particles following contact with a PVC chute, as a function of measurement number [26]. It is important to recognize that the material surface properties are constantly changing, as material can be transferred between the two surfaces. The simplest manifestation of this phenomenon is the adhesion of powder to processing equipment walls, resulting in particle-particle frictional contacts, and not particle-surface contact (**Figure 3**).

2.3 Properties of Charged Particles

Charge generation on the surface of particles influences particle dynamics and powder behavior. Surface charge distribution and, importantly, charge decay, are instrumental in our understanding of the practical consequences of electrostatic charge including particle deposition and adhesion to surfaces. Insulator surfaces are generally considered to accept charge at regions where imperfections and/or impurities are present. "Islands" of charge result, leading to a non-uniform surface charge density, as illustrated in **Figure 4**. It has been reported that charge can exist to depths of 1 μm in insulators [27].

When powders charge during handling, the charge transferred at the point of contact can redistribute itself over the particle surface, at a rate dependent upon both the particle resistivity (ρ) and particle permittivity (ε). Insulating powders ($\rho > 10^{13}$ Ωm [11, 18]) have a charge relaxation time of minutes to hours [28]. Therefore, charge redistribution can occur during typical industrial processing times. Literature in this area is limited, especially for powders used in the pharmaceutical industry. Carter *et al.* have recently reported charge decay properties in pharmaceutical powders (**Table 2**) [28]. The magnitude and sign of the charge on a powder compact following charging with a corona electrode was measured using a Faraday Well, as a function of time. Rapid charge decay was observed for PVC and lactose, while micronized salbutamol sulphate retained significant charge after 120 minutes.

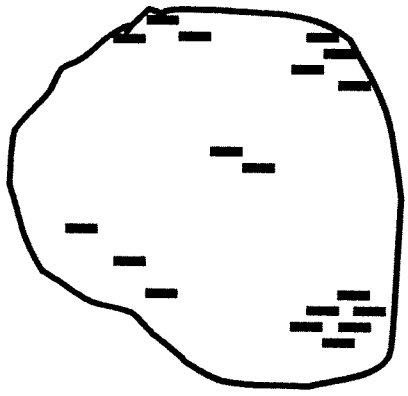

Fig. 4 Charge distribution on the surface of an isolated powder particle.

Table 2 Preliminary charge values measured by Faraday Well for salbutamol sulphate, lactose and PVC compacts before and after corona exposure. Mean (%CV) n=15. Adapted from [28]

	Mean Charge (nCg^{-1})			
Material	Immediately Before Corona Charging	Immediately After Corona Charging	After 30 Minutes	After 120 Minutes
Salbutamol	−0.27 (67)	−7.8 (25)	−4.1 (21)	−3.3 (26)
Lactose	0.00 (−)	−7.4 (34)	0.00 (−)	0.00 (−)
PVC	−1.06 (56)	−16.9 (14)	−2.7 (52)	−1.8 (17)

The existence of surface charge on a particle gives rise to an electrostatic field, which has a maximum intensity at the particle surface and decays inversely with the square of distance away from the surface. The maximum surface charge density that can be sustained at a particle surface depends on particle environment and size. Bailey [2] estimated typical surface charge density on spherical particles (50 μm diameter; density=1 g/cm^3) to be in the order of 1 $\mu C/m^2$; this corresponds to approximately 10^{13} electrons/m^2.

When a particle becomes charged, by triboelectrification, two types of interaction may contribute to the deposition and adhesion of the particle, namely electrical double layers and coulombic interactions. Electrical double layers are considered to result from the formation of a shell of oppositely charged electrical layers at the interface upon contact. Coulombic interactions result from the forces of interaction which arise between charged particles and uncharged surfaces.

An electronic theory of adhesion has been described by Derjaguin and Smilga [29]. In principle, the theory indicates that the formation of an electrical double layer, at the point of contact between two materials, is dependent upon the chemical nature of the substances involved, and their ability to act as either electron donors or acceptors. A donor-acceptor interaction results in positive and negative charges appearing on each surface. Consequently, the positive and negative surfaces interact. The contact potential

arising from the electron transfer between materials and thus the formation of the electrical double layer can be considered to be analogous to the structure of a parallel plate capacitor which possesses a certain electrical potential difference arising on contact between the two bodies. Thus the interactive force due to the contact potential can be derived on the same principles as the attractive force on the plates of a parallel plate capacitor [15, 25].

Therefore, the electrical force of interaction due to contact can be derived from:

$$F_e = \frac{2\pi q^2}{A} \qquad \text{Equation 1}$$

where F_e is the interactive force due to contact, q is the particle charge upon detachment, and A is the contact area between the particle and the carrier surface [30].

Coulombic interactions between solid materials arise when a charged particle induces an equal but opposite charge on an uncharged surface (**Figure 5**). The resultant adhesive force is expressed by:

$$F_{im} = \frac{Q^2}{I^2} \qquad \text{Equation 2}$$

where F_{im} is the coulombic image force, Q is the charge on the particle, and I is the distance between the centers of the charges. Equation 2 is a simplification of Coulomb's law. Coulomb's law states that the force between charges is proportional to the quantities of charge, and inversely proportional to the square of the separation distance [31]:

$$F = \frac{q_1 q_2}{4\pi\varepsilon_0 z^2} \qquad \text{Equation 3}$$

where q_1 and q_2 represent the quantity of charge, ε_0 is the permittivity of free space and z is the separation distance.

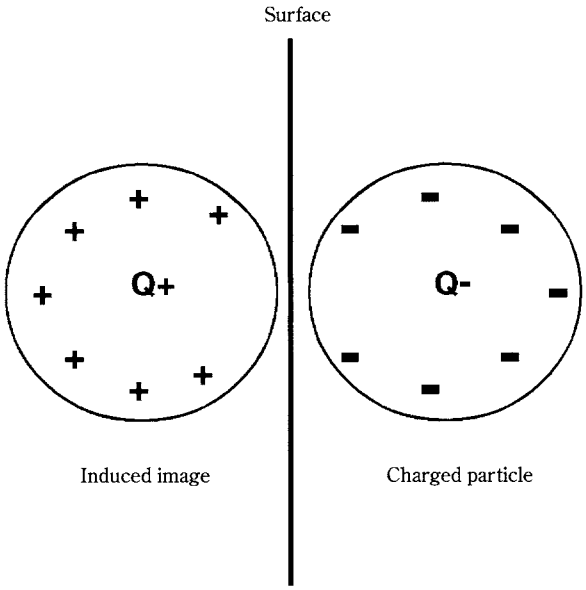

Fig. 5 Coulombic image interaction.

3. Measurement Techniques

3.1 Static Charge Measurement

The standard method for the measurement of electrostatic charge is the Faraday pail or well, coupled to a suitable monitoring circuit. A schematic representation of the Faraday well is illustrated in **Figure 6**.

The Faraday well is a conducting container, which is enclosed by an outer grounded well, to reduce interference from nearby electrostatic fields or charges. The inner well is connected to an electrometer, by a shielded co-axial cable, which measures charge by detecting the voltage built up across a known capacitance. When a charged object is introduced into the well, an equal and opposite charge flows from ground to electrically balance the charge residing in the well. This charge leaves behind an equal and opposite charge on the capacitor of the electrometer, which can be measured to give the charge inside the well. The insulation between the inner and outer wells must be extremely high to eliminate charge decay. Following the measurement of charge, the mass of powder in the inner well can be measured. Results are usually presented in terms of the charge to mass ratio, or specific charge, q/m, whereby the charge (q) is measured on a quantity of powder, which is then weighed (m).

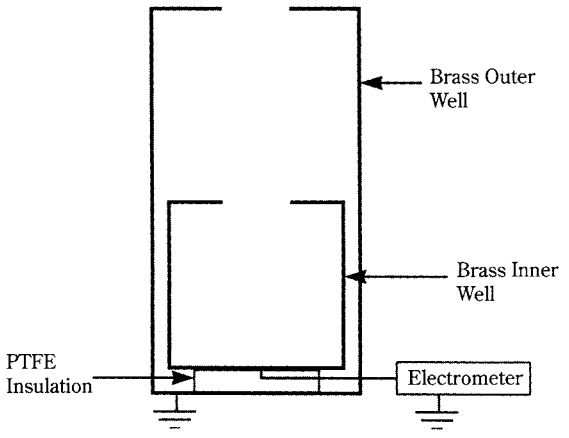

Fig. 6 Schematic diagram of the Faraday Well static charge detector.

The Faraday well has been used extensively to investigate the charging characteristics of powders following contact with materials encountered during routine handling operations [26, 28, 32-38]. However, the reproducibility of the system has been reported to be highly variable, with recorded variations of up to 50% in some determinations [32, 35]. In these experiments, [32, 35], uncontrolled quantities of powder were poured at an even rate, by hand, from glass, plastic and metal beakers, at ambient temperature and relative humidity. From the previous discussion relating to factors which influenced triboelectrification, humidity, together with the relative number of particle-particle and particle-surface collisions were considered to be significant parameters. Standardisation of these variables, achieved by simply conducting the experiments within a controlled environment, and using a vibrating powder chute, to control flow rate, were found to improve the reproducibility (relative standard deviations $< 20\%$) of electrostatic charge measurements [26, 36].

Interparticle electrostatic attraction between different powders can be quantified by measurement of static charges developed on materials, following contact with materials commonly encountered during processing [39]. In dry powder aerosol formulations for inhalation, micronized drug particles (e.g. salbutamol sulfate) are formulated with larger carrier particles (e.g. lactose), to facilitate powder processing. Following inhalation, the drug must be released from the larger carrier particles to favour deposition in the lung. **Table 3** summarizes the specific charge of salbutamol sulphate and lactose powders, following contact with a metal or plastic vibrating chute. Salbutamol sulphate particles were found to develop electropositive charges following contact with both metal and plastic surfaces, whereas lactose carrier material was shown to develop an electronegative charge following contact with a metal surface, and an electropositive charge following contact with a plastic surface, similiar to the polypropylene surface of an inhaler device [36, 39]. It would be predicted that blending and processing undertaken in metal vessels would ensure optimum drug homogeneity in the powder blend. Furthermore, the dry powder inhaler device should promote the separation of drug from carrier material.

Table 3 Specific charge of inhalation powders following contact with metal and plastic chutes. Mean (±S.D.) for n=5 measurements.

Material	Contact Surface	Polarity	Specific Charge (nCg^{-1})
Lactose	Plastic	+	3.87±0.48
	Metal	−	0.72±0.09
Salbutamol Sulphate	Plastic	+	7.14±1.07
	Metal	+	14.16±1.72

Importantly, it should be remembered that all aspects of powder handling prior to measurement will contribute to the powder charging characteristics including: storage (container type and relative humidity), powder transfer from bulk using powder hopper (industrial scale) or spatula (laboratory scale), blending operations etc. In order to obtain meaningful data, these factors should be considered, and consistent. Anecdotal reports from the pharmaceutical industry have attributed scale up issues to electrostatic phenomena. For example, excellent blending of powders in plastic containers can be achieved, at the laboratory scale, but unacceptable blend homogeneity has been attained when the process is transferred to the manufacturing plant, where stainless steel blending vessels are often utilized.

Modifications have been made to the basic Faraday well measurement system based upon the application under investigation, e.g. the assessment of the performance of electrostatic powder coating systems [10, 11, 40]. Electrostatic coating relies upon external corona charging of a dispersed powder cloud. However, this process is very inefficient, with only about 0.5% of all the available ions actually attaching to the particles [10]. The remaining 99.5% remains as free ions, which could enter the inner Faraday well, resulting in spurious charge measurements. To overcome this problem, the Faraday well can be completely redesigned and two flat plates, one vertical and one horizontal, in an L-shaped configuration replace the well [40]. Free-ions are trapped on a grid consisting of vertically strung, parallel wires. The wires are continuously washed with water so that any powder particles collected on the screen are removed, thus back ionization is eliminated [40].

A further limitation associated with the use of the standard Faraday well is related to the fact that it only measures the net charge on a powder sample and is incapable of differentiating bipolar powders, which are commonly encountered in electrostatic coating. Dynamic charge measurement techniques have been used to address this problem, e.g. the differential charge-to-mass apparatus for the determination of bipolar triboelectric characteristics of powders used in electrostatic coating systems [10, 11].

3.2 Dynamic Charge Measurement

Figure 7 illustrates a schematic diagram of the differential charge-to-mass apparatus. The system consists of an inner-measuring cup connected to an electrometer, and enclosed by a grounded shielding cup. Both ends of the Faraday cup are open, but can be covered by interchangeable end caps of different size meshes. The entire apparatus is vibrated, and reciprocating air blasts are directed into and through the inner cup. The test procedure begins with the very fine mesh ends in position, and then there is a gradual progression to the coarser sizes, with the result that a histogram of charge to mass ratio as a function of particle size can be constructed. The charge measured on the electrometer represents the charge of the powder remaining within the well, and thus the charge of the detached material will be of equal magnitude, but opposite polarity to that registered.

The differential charge-to-mass apparatus was based upon "blow-off" technology used originally in xerography to investigate the charging characteristics of toner particles [41-44]. "Blow-off" technology has also been extended to pharmaceutical systems to characterize charging properties of interactive mixtures [26, 36, 39, 45]. **Figure 8** illustrates the Airstream Faraday Cage, described by Kulvanich and Stewart [45]. The apparatus consists of a vertical Faraday cage sealed at each end with a mesh screen. An ordered powder blend is introduced into the cage, and dry compressed air blown through the cage at high velocity. Adhered drug particles are removed from the carrier particles inducing equal but opposite charges on the carrier and drug particles respectively. By suitable choice of screen size, drug particles are removed from the cage. However, carrier particles remain within the cage, and transfer their charge to the cage, which is registered by the electrometer [45].

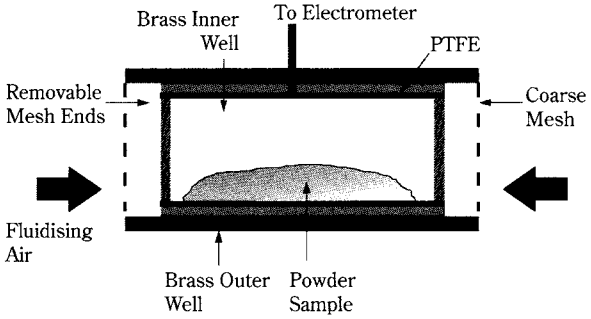

Fig. 7 Schematic diagram of the differential charge to mass test system [10].

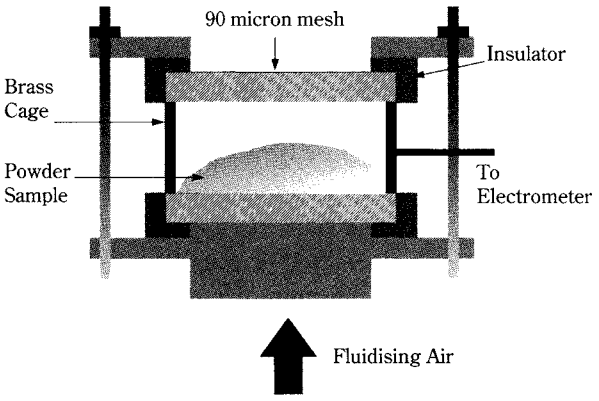

Fig. 8 Schematic diagram of the Airstream Faraday cage [45].

Schein and Cranch [42] reported that the electrostatic charge produced on the detachment of particles from carrier could be modified during charge measurement within the 'blow-off' cage. Detached particles would have to be removed from the cage without any contact with other surfaces, for a true detachment charge to be achieved. Contact with the cage wall, mesh or other carrier particles would cause charge exchange and produce spurious charge measurements. As a consequence, careful validation of "blow-off" techniques is critical.

Kulvanich and Stewart [45] proposed several mechanisms by which spurious, undesired charging associated with the airstream Faraday apparatus used for the measurement of electrostatic charge in pharmaceutical systems could occur, which would invalidate any charge measurements. These included interference from the surroundings, charge accumulation by the compressed air and charge accumulation through carrier interactions. In addition, Kulvanich and Stewart [45] investigated the effect of sample size, mesh size and cage lining on the charge developed upon detachment and reported no significant differences between the results observed. Cage wall interactions in the Airstream Faraday Cage are insignificant, because the cage presents as a vertically aligned shallow cylinder, with a diameter approximately ten times larger than the diameter of the compressed air jet. When the jet is directed centrally through the cage, the powder sample is fluidised in such a manner that the aerosolised cloud does not contact the cage wall. In contrast, the horizontal arrangement of the differential charge-to-mass test system (**Figure 7**) presents significant opportunities for particle-cage wall collisions, as described by Hughes [10].

Peart adopted these dynamic charge measurement

systems for the characterization of electrostatic properties of powder formulations for inhalation [26, 36, 39]. Surface charge developed when adhered salbutamol sulphate particles were detached from carrier lactose particles was investigated using both the Airstream Faraday Cage and the Differential Charge to Mass detector. **Figure 9** illustrates the electrostatic charge developed following salbutamol sulphate detachment from lactose carrier material at 60 l min^{-1}. Clearly, the magnitude of the detachment charge is significantly higher than that observed upon contact (**Table 3**), and of opposite polarity. Dynamic charge measurements provide an indication of the probable charging interactions between the particles when a powder is aerosolized, and is considered relevant to the performance of dry powder formulations. As an extension of this work, a novel method for the determination of charge on aerosolized particles, generated by powder inhalers, was developed [37]. A schematic diagram of the apparatus used to characterise the electrostatic properties of the fine particle fraction of an aerosol generated by a dry powder inhaler device is shown in **Figure 10**.

Briefly, the electrical currents induced by the collection of the fine particle fraction of the generated aerosol are measured as functions of time, following collection in an aerosol electrometer, connected to a chart recorder. The aerosol electrometer consists of an air filtration particle collector, which measures the total electrical current with an electrometer sensor. Charged aerosol particles enter the electrometer current sensor through a metal cover which shields the electrometer input from environmental electric fields.

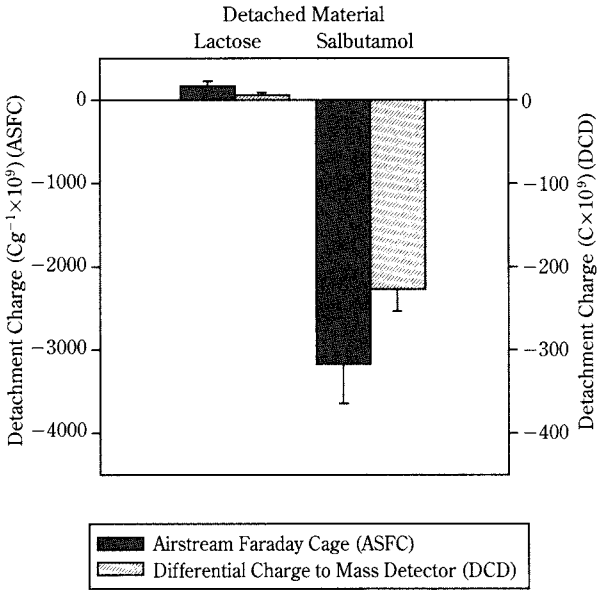

Fig. 9 Dynamic electrostatic charge measurements of salbutamol sulphate developed following detachment from lactose carrier material [39].

Within the electrometer current sensor, an absolute filter removes the charged particles from the airstream. The filter is mounted on a Teflon insulator within an enclosed metal housing, and is connected to the input of a solid state electrometer, which measures the electrical current due to the charged particles. The area under each individual aerosol current (pA) versus time (seconds) profile gives net aerosol charge in picocoulombs, and is defined as the fine particle dose charge. Using this technique, electrostatic properties on the potentially respirable aerosol

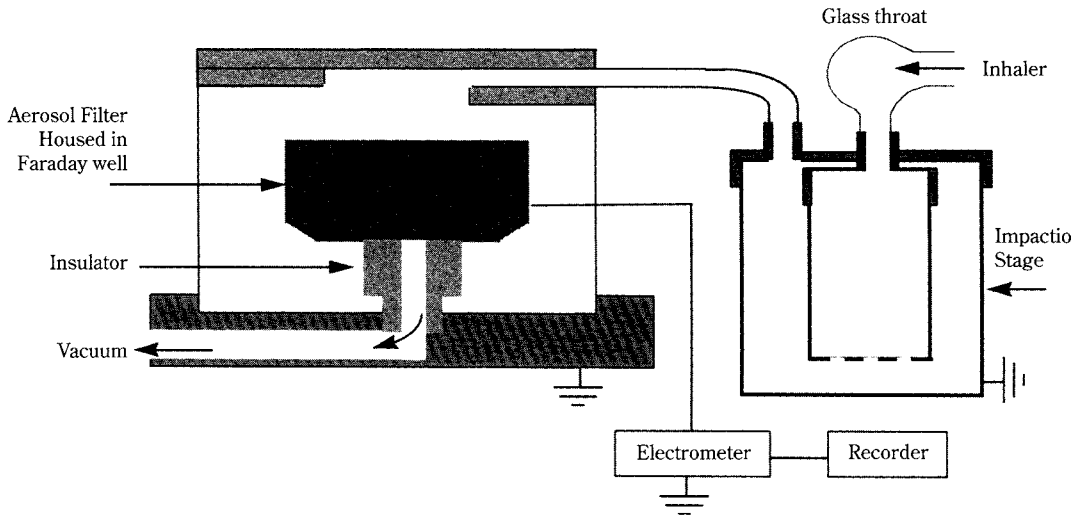

Fig. 10 Diagrammatic representation of aerosol sampling apparatus for the aerosol electrometer [37].

clouds generated by high efficiency dry powder inhalers (Turbohaler© and Dryhaler©) have been shown to be dependent upon the physical and chemical properties of the powder under investigation, as well as the construction and deaggregation mechanism of the inhaler (**Table 4**) [37].

Table 4 Average (n=10)[a] electrostatic characteristics[b] of micronized drugs in two prototype Dryhalers [37].

Micronized drug	Charge (pC/mg)		Charge per actuation (pC)
	Powder[c]	Retained[d]	<5 μm[e]
Terbutaline sulfate	−8.27 (3.63)	++	−171 (148)
Budesonide	−8.61 (4.91)	–	+138 (57.6)
Salbutamol sulphate	−0.96 (0.50)	++	+48.7 (122)
Salbutamol	−0.93 (0.75)	+++	−178 (48.1)
Beclomethasone dipropionate	−8.83 (5.55)	++	−184 (128)
Microtose	−0.90 (0.15)	–	+85.9 (114)

a 5 actuations from each of 2 prototype Dryhalers.
b Values in parentheses are sample standard deviations.
c Static charge on bulk powder.
d Sign and approximate magnitude of charge on powder remaining in aerosolization chamber after actuation 5.
e Measured Charge/Emitted Dose.

3.3 Powder Resistivity

Knowledge of the powder's resistivity (measure of the ability of a material to conduct electricity) is essential and critical with respect to powder charging behavior. Many of the materials used in powder coating processes are all inherently resistant (usually $\rho > 10^{13}$ Ωm) and are ideally suited for long-term charge retention and adhesion. Efficient charging of these materials is difficult. One of the simplest and widely used methods for the measurement of resistivity is the bulk resistivity cell technique. Briefly, the powder sample is poured into the resistivity cell and subjected to a steady dc potential (V), while the current (I) is measured. Powder resistance can be calculated from Ohm's Law R=V/I. Specific resistance or resistivity (ρ), is determined using the following equation:

$$\rho = \frac{VA}{Id} \qquad \text{Equation 4}$$

where A and d are the electrode area and separation distance respectively. Although the method is relatively simple, caution should be exercised with respect to measurement method and data interpretation. The cell itself should be made from an electrically insulating material, and should include a guard electrode, to eliminate conduction pathways that might occur through the cell wall. This ensures that any measurements are indeed powder, and not cell, resistivity. In addition, careful cell preparation is essential prior to measurement. Both the inside and outside surfaces of the cell should be thoroughly cleaned and de-greased to minimize surface conduction. Furthermore, because of polarization effects in the powder bed, it is important that the current is allowed to stabilize for 10 minutes prior to measurement [10, 11]. There are numerous commercially available instruments, which provide a direct readout of resistivity – however, the same precautions apply. Hughes [10] warned that although these instruments provide a measure of volume resistivity, it is more likely to represent the surface conduction characteristics of the powder sample. Any measured charge conduction will preferentially be over the surface of the test material, because most powders are inherently insulating.

For further information relating to instrumentation for electrostatic measurements, the reader is directed to a comprehensive review by Secker and Chubb [46].

4. Applications

Electrostatics although generally regarded as an unpredictable nuisance to the powder technologist, when controlled can be of immense value – from xerography [8, 9] and powder coating [10, 11] to improved powder processing in the pharmaceutical industry [47, 48].

4.1 Xerography

Xerography has revolutionized the modern office and represents the most common example of electrostatic deposition technology. A comprehensive review of xerography has previously been described [49], so only the basic principles will be reviewed. Essentially, a charge is applied to an insulating surface in the shape of the pattern to be copied. A charged image is applied to a rotating drum coated with a photoconducting material such as selenium. Photoconductors are electrically insulating materials, which display electrically conducting properties when exposed to light. Initially, the drum is charged to a uniform potential by a corona charging system. The drum is then exposed to light from the optical image, which is to be copied. When the photoconductor is illuminated, charge carriers are generated, and move in the

electric field so the surface potential is reduced approximately in proportion to the intensity of the illumination. The shadowed areas retain their charge producing the required electrostatic image. The latent image on the drum is developed by the application of a toner [8, 9, 16]. Toner particles are mixed with larger carrier particles of a different material. The small toner particles are charged by triboelectric or contact charging by the carrier particles and are held to the carrier surface by electrostatic forces. In the development process the toner particles are removed from the carrier, leaving the carrier with one sign and the toner particles oppositely charged. The toner particles are transferred to the photoconductor surface under the guiding influence of the electrostatic field of the latent image. Careful choice of both carrier and toner materials is necessary to ensure proper charging of the toner. The developed image is then transferred to the paper, which is then heated to fix the image.

4.2 Electrostatic Powder Coating

Electrostatic powder coating provides a means of applying a protective surface film to metallic substrates, and has been widely used within the automobile and electrical appliance industries. Individual paint particles are artificially charged, either by corona or tribo-charging and sprayed via high pressure atomizers. Any grounded substrate presented to the aerosol acquires an equal and opposite induced electrical charge. Opposites attract, hence the paint particles are attracted to the substrate. Comprehensive reviews of this subject have been described [10, 11, 50]. Recently, this technology has been extended to the coating of insulator substrates, in the form of pharmaceutical tablets [12, 18]. Because the substrate is an insulator, self-limiting deposition of powder on the tablet would be predicted to occur, as a consequence of the charged deposited layer repelling oncoming particles. However, powder coating of tablets was shown to feasible following conditioning of the tablet compacts, either by pre-storage at elevated humidities or powder coating in a high humidity environment [18]. Phoqus Pharmaceutical Technologies is developing drug loading (LeQradose) and coating (LeQracoat) technologies. Both processes involve a similar procedure. Tablets, positioned at the circumference of a wheel, are moved over a tray containing the drug/coating, which is electrostatically transferred to the tablet and then fused using an infrared heater. The tablet is then transferred to a second wheel so that the other side of the tablet can be coated.

A similar electrostatic deposition technology has been described by Delsys Pharmaceuticals [13, 51]. Accudep© is claimed to be a highly controlled process which deposits precise quantities of the active drug onto a variety of surfaces. Patterns of discrete charges of one polarity are applied to a film surface. The film is exposed to a cloud of oppositely charged drug particles. Very precise quantities of drug deposit on the film at each charge location. This technology claims to be suitable for a variety of dosage forms ranging immediate release wafers, transdermal delivery systems and dry powder inhaler dosing cartridges.

4.3 Pharmaceutical Processing

In pharmaceutical processing, electrostatic mixing has been used to facilitate ordered mixing, and minimise the segregation tendency of the resulting blends [32, 47, 48]. Staniforth and Rees [32, 47] have demonstrated that the stability of ordered mixes depended upon the electrostatic charges developed on the component materials during mixing. Excipient powders generally charged electronegatively when contacted with metal or glass surfaces, whereas many charged electropositvely when contacted with plastic surfaces [32]. Triboelectrification using a cyclone, or charging by ionisation using a high voltage corona discharge was used to increase the adhesive force between two particles. Increased electrostatic attraction between oppositely charged drug and excipient particles draws the particles closer together, and the resultant increase in surface forces, such as Coulomb, dipole and molecular forces, increases the stability of the drug-carrier agglomerates. Careful selection of the equipment construction material and processing conditions can enable the manipulation of the sign and magnitude of the electrostatic charge, and influence the adhesion characteristics.

5. Summary

Powder electrostatics regarded by many as a nuisance and hazard, plays an important and ever emerging role in many industrial applications, including xerography, powder coating, and pharmaceutical processing. Accurate assessment of powder charging is fundamental for process optimization and identification of potential processing problems. Most electrostatic measurements are straightforward provided certain precautions are taken, but meaningful data interpretation requires more skill.

Acknowledgements

JP would like to thank Professor John Staniforth and Brian Meakin (University of Bath, UK) and Dr. Peter Byron (Virginia Commonwealth University) for their encouragement and guidance throughout her research career in electrostatics.

Nomenclature

A	: Area of Contact	meters^2 [m^2]
F	: Force	newtons [N]
I	: Electrical current	amperes [A]
M	: Mass	kilograms [kg]
Q, q	: Charge	coulombs [C]
R	: Resistance	ohms [Ω]
t	: Time	seconds [s]
V	: Electric Potential Diffference	volts [V]
z	: Separation Distance	meters [m]
ρ	: Electrical resitivity	ohm meter [Ωm]
ε_0	: Permittivity of free space	farad/meter [F/m]
ε	: Permittivity	farad/meter [F/m]
π	: 3.1415...	
ϕ	: Work Function	volts [V]

References

1) Bailey, A.G: Powder Technology, 37, 71-85, (1984).
2) Bailey, A.G: Journal of Electrostatics, 30, 167-180, (1993).
3) Lachman, L. and S-L. Lin: Journal of Pharmaceutical Sciences, 57, 504-510, (1968).
4) Pavey, I: Pharmaceutical Technology Europe, 10, 24-28, (1998).
5) Eliasen, H., K. Gjelstrup, and T. Schaefer: International Journal of Pharmaceutics, 184, 85-96, (1999).
6) Cartwright, P., S. Singh, A.G. Bailey and L.J. Rose: IEEE Transactions on Industry Applications, 1A-21, 541-546, (1985).
7) Glor M: Electrostatic Hazards in Powder Handling. Research Studies Press Ltd.: Taunton, England (1988).
8) Winklemann, D: Journal of Electrostatics, 4, 193-213, (1977/1978).
9) Gundlach, R.W: Journal of Electrostatics, 24, 3-9, (1989).
10) Hughes, J.F: Journal of Electrostatics, 23, 3-23, (1989).
11) Hughes, J.F: Electrostatic Particle Charging: Industrial and Health Care Applications. Research Studies Press Ltd.: Taunton, England (1997).
12) Hogan, J., T. Page, L.A. Reeves and J.N. Staniforth: GB Patent 2,336,551 (1999).
13) Sun, S., B. Singh, C. Rivenburg, P. Datta and N. Desai: US Patent 5,857,456 (1999).
14) Fleming, S. A.L. Abrams and A.V. Gumaste: World Patent 9,964,095 (1999).
15) Hendricks, C.D: In: A.D. Moore (Ed.). Electrostatics and its applications. Wiley Interscience: New York, 57-85, (1973).
16) Cross, J.A: Electrostatics: principles, problems and applications. Adam Hilger: Bristol (1987).
17) Moore, A.D: Scientific American, 226, 47-58, (1972).
18) Grosvenor, M.P. and J.N. Staniforth: Pharmaceutical Research, 13, 1725-1729, (1996).
19) Johnson, M.A: Spray Technology & Marketing, 28-34, (1997).
20) Gallo, C.F. and W.L. Lama: Journal of Electrostatics, 2, 145-150, (1976).
21) Coste, J. and P. Pechery: 3rd International Congress on Static Electricity. Grenoble, 4a-4f, (1977).
22) Homewood, K.P: Journal of Electrostatics, 10, 299-304, (1981).
23) Hays, D.A: J. Chem. Phys., 61, 1455-1462, (1974).
24) Lowell, J: J. Phys. D., 17, 1859-1870, (1984).
25) Derjaguin, B.V., N.A. Krotova and V.P. Smilga: Adhesion of solids. Consultant Bureau: New York (1978).
26) Peart, J: Ph.D. Dissertation. University of Bath, UK (1996).
27) Hays, D: In: L-H. Lee (Ed.). Fundamentals of Adhesion. Plenum Publishing Corporation: New York, 249-278, (1991).
28) Carter, P.A., G. Rowley, E.J. Fletcher and V. Stylianopoulos: Drug Development and Industrial Pharmacy, 24, 1083-1088, (1998).
29) Derjaguin, B.V. and V.P. Smilga: Journal of Applied Physics, 38, 4609-4616, (1967).
30) Zimon, A.D: Adhesion of dust and powder. Consultants Bureau: New York (1982).
31) Page, L. and N.I. Adams: Principles of electricity. D. Van Nostrand Company Inc: New Jersey (1969).
32) Staniforth, J.N. and J.E. Rees: Journal of Pharmacy and Pharmacology, 34, 69-76, (1982).
33) Reis, G.E., J.N. Bierly and J.B. Schwartz (1984). American Journal of Pharmacy, Oct/Nov, 100-105, (1984).
34) Carter, P.A., G. Rowley, E.J. Fletcher and E.A. Hill: Drug Development and Industrial Pharmacy, 18, 1505-1526, (1992).
35) Lord, J.D: Ph.D. Dissertation. University of Bath, UK (1993).
36) Peart, J., J.N. Staniforth and B.J. Meakin: Institute of Physics Conference Series, 143, 271-274, (1995).
37) Byron, P.R., J. Peart and J.N. Staniforth: Pharmaceutical Research, 14, 698-705 (1997).
38) Bennett, F.S., P.A. Carter, G. Rowley and Y. Dandiker: Drug Development and Industrial Pharmacy, 25, 99-103, (1999).
39) Peart, J., J.N. Staniforth, P.R. Byron and B.J. Meakin: Proceedings of Respiratory Drug Delivery V (Phoenix, AZ), Interpharm Press: Buffalo Grove, IL, 85-94, (1996).
40) Moyle, B.D. and J.F. Hughes: IEEE Transactions on Industry Applications, IA-20, 1631-1635, (1984).
41) Donald, D.K. and P.K. Watson: Photographic Science and Engineering, 14, 36-41, (1970).

42) Schein, L.B. and J. Cranch: Journal of Applied Physics, 46, 5140-5149, (1975).
43) Lee, L-H. and J.E. Weser: Journal of Electrostatics, 6, 281-287, (1979).
44) Schein, L.B: Journal of Imaging Science and Technology, 37, 1-4, (1993).
45) Kulvanich, P. and P.J. Stewart: International Journal of Pharmaceutics, 36, 243-252, (1987).
46) Secker, P.E. and J.N. Chubb: Journal of Electrostatics, 16, 1-19, (1984).
47) Staniforth, J.N. and J.E. Rees: Powder Technology, 30, 255-256, (1981).
48) Tucker, C.L. and N.P. Suh: (1976). Polymer Science and Engineering, 16, 657-663, (1976).
49) Scharfe, M: Electrophotography, Principles and Optimization. Research Studies Press Ltd.: Taunton, England (1984).
50) Bailey, A.G: Journal of Electrostatics, 45, 85-120, (1998).
51) Chrai, S.S., B. Singh, M. Kopcha, R. Murari, S. Sun, N. Kumar, N. Desai, A. Levine, H. Rivenburg and G. Kagnanowicz: Pharmaceutical Technology, 106-110, (1998).

Author's short biography

Joanne Peart, Ph.D.

Joanne Peart is an Assistant Professor at Virginia Commonwealth University School of Pharmacy in Richmond, Virginia. She attained a degree in Pharmacy from the University of Bath in 1991, and is a registered pharmacist in Great Britain. Following a pre-registration year split between St Bartholomew's Hospital, London and Pharmaceutical Technology Department, Glaxo Group Research, Ware, Dr Peart received her PhD in Aerosol Pharmaceutics form the University of Bath in 1996. Her research was jointly supervised by Professor John Staniforth and Brian Meakin. The research involved the electrostatic characterisation of pharmaceutical dry powder formulations for inhalation. Dr. Peart currently works in the Aerosol Research Group at VCU, with Dr. Peter Byron, and continues to investigate the electrostatic properties of inhalation aerosols, including metered dose inhalers, dry powder inhalers and spacer devices.

Pharmaceutical Dry Powder Aerosol Delivery†

Nora Y.K. Chew and Hak-Kim Chan
*Faculty of Pharmacy, University of Sydney**

Abstract

The exigency for an inhalation system that does not contribute to ozone-depletion, but is suitable for the delivery of both small molecules and macromolecules, has led to the booming interest in powder aerosols delivery in the last decade. Successful delivery of drugs via powder aerosol depends on both the powder formulation and aerosol inhaler. This review focuses on the emerging technologies of these two determinants in optimising powder aerosol delivery.

1. Dry powder aerosols: the logical choice to deliver small and large molecules

Chlorofluorocarbon (CFC) propellant-driven metered-dose inhaler (pMDI) has been the dominant inhalation system in the 20th century. This 'lung-winning' dosage form has gained remarkable popularity due to its effectiveness, safety and convenience to patients. Although only low fractions (10 to 30 %) of the emitted dose can penetrate the deep lung (even with spacer devices) (1, 2), the number of prescriptions written by physicians for the CFC-pMDI still remained high.

During the last 10 – 15 years the prospective of the CFC-pMDIs has been radically changed due to the proven damage to the ozone layer by CFCs. While scientists are searching for alternatives to the CFC-pMDIs, the even greater compulsion for new methods is, in fact, the delivery of macromolecules to the lung.

The high cost, dosage requirement and payload versatility (i.e. flexibility to deliver a range of different doses) are some of the factors that are unique to the delivery of macromolecules compared with small molecular drugs. Some proteins and polypeptides for deep lung delivery may need milligram-level doses versus micrograms per dose for the most potent bronchodilators and steriods for the treatment of asthma. An aerosol system that exhibits payload versatility is especially important because macromolecular drugs vary widely in potency from a few micrograms to tens of milligrams per dose (3). Thus, the delivery of macromolecules to the lung must be precise and consistent at every inspiration.

Even though manufacturers have developed CFC-free propellant inhalers containing hydrofluoroalkane (such as HFA134a) to replace the CFC-pMDIs, direct switching between CFC- and HFA-containing formulations may not be plausible (4). The conventional nebuliser systems are rather inconvenient for patients to use on a daily basis. Powder aerosols, which do not consume propellants, are an ideal alternative. More importantly, powder aerosols exhibit the following advantages for the delivery of macromolecules:

- *A greater amount of drug can be contained in dry powders than in liquid forms*: Dry powder aerosols can carry more drug per unit volume than the CFC pMDIs and the nebulisers. The dosing frequency can therefore be reduced with a dry powder system for protein drugs that require higher doses, such as insulin or alpha-1 antitrypsin.
- *Minimised microbial growth*: Dry-powder formulations minimise the risk of microbial growth, to which liquids are more susceptible than solids.
- *Greater drug stability*: Drugs can be susceptible to biochemical and physical instability in organic solvents such as the CFC propellants (5, 6). Preparation of the actives as dry powders could be far more stable in the solid than in the liquid state (7) and has been shown to be a promising approach for delivering drugs to the respiratory tract (8, 9).

2. Dual to multiple challenges, from small molecules to macromolecules

Powders for inhalation delivery must be of particle size 0.5 – 5 μm and they must flow well during manu-

* Sydney 2006, New South Wales, Australia
Tel 612 9351 3054 Fax 612 9351 4391
Email: kimc@pharm.usyd.edu.au
† Accepted: August 17, 2001

facture, filling and emptying from the inhaler device. These small particles, however, are cohesive and adhesive, making them difficult to disperse and empty from the device. Coupled with these two opposing requirements, the delivery of therapeutic macromolecules by inhalation presents additional problems: the fragility of proteins imposes certain restrictions during manufacture and storage in order to maintain not only their dispersibility as an aerosol, but also their biochemical and physical stabilities.

In this article, we review the challenges confronted in the delivery of both small molecules and macromoelcules via inhalation powder aerosols. Specifically, this review focuses on the emerging technologies of both the powder formulation and inhaler devices that are used to optimise pulmonary drug delivery.

3. Cohesiveness of dry powders

Powder cohesiveness affects their flow and dispersion. It is dependent on the physicochemical properties, such as particle size, dielectric constant, morphology, moisture content and electrostatic charge. The three major cohesion forces between two particles are the universal van der Waals force, capillary force and electrostatic charge interaction (10, 11). The van der Waals force (F_{vdw}) arising between two identical spheres is given by (12):

$$F_{vdw} = A\,R/12\,H^2 \qquad \text{(equation 1)}$$

where A is the molecular interaction constant, R is the radius of the particles and H is the separation distance between the particles. Because the mass of the particle increases with the third power of the diameter, the force of attraction *per unit mass* of particles is inversely proportional to the square of the particle size (i.e. $F_{vdw}/\text{mass} \propto D^{-2}$, where D is the diameter of the particle) (12, 13). Thus finer particles are more cohesive and are more difficult to disperse.

The molecular interaction constant A is referred to as the Hamaker constant, A_H, based on the London-van der Waals theory (14). Thus, the molecular interaction of two particles, 1 and 2 is:

$$A_H = \pi^2\, q_1\, q_2\, \beta_{12} \qquad \text{(equation 2)}$$

where q_1 is the number of atoms per unit volume of particle 1, q_2 is the number of atoms per unit volume of particle 2, β_{12} is the London-van der Waals constant for the interaction between two atoms of the interacting particles, and is related to the polarisability of the atom (12). When A is derived from the dielectric properties of the interacting materials, it is referred to as the Lifshitz-van der Waals constant ($h\omega$), and the intermolecular interaction ($h\omega_{1,2}$) for two particles, 1 and 2, in vacuum is expressed as:

$$h\omega_{1,2} = h\int_0^{\infty} (\in_1(\iota\xi)-1)/(\in_1(\iota\xi)+1)\ (\in_2(\iota\xi)-1)/(\in_2(\iota\xi)+1)\,.\,d(\xi) \qquad \text{(equation 3)}$$

where $\in(\iota\xi)$ is the dielectric constant of the material, ι, and h is the Planck's constant. The Lifshitz-van der Waals interaction constant is related to the Hamaker constant via:

$$A_H = 3/4\,\pi h\omega \qquad \text{(equation 4)}$$

The interaction constant is hence strongly dependent on the physicochemical property of the interacting material.

When the separation distance in equation 1 vanishes (H approaches zero), Derjaguin proposed that the cohesion force, F_c becomes (12)

$$F_c = 2\,\pi\sigma R \qquad \text{(equation 5)}$$

where σ is the surface tension of the particles or of any adsorbed film present on the particles, and R is the particle radius. According to equation 1, the presence of an adsorbed moisture film would decrease the F_{vdw} by increasing the separation distance H. However, moisture can contribute to the capillary force through surface tension according to equation 5, as well as increasing the area of contact (15). In general, at high relative humidities ($\geq$65 %), capillary force due to condensation of liquid between the particles will dominate the interparticulate force (16).

Surface roughness and asperities will also contribute to the F_{vdw}. Depending on the nature of the roughness, the effective particle contact *per unit area* may either decrease or increase (17). It has also been suggested that R in equation 5 should be replaced by the size of surface asperities if their radii are larger than 0.1 μm (18).

When particles come into contact, plastic deformation (versus elastic deformation, which has negligible effect on particle cohesion (10)) at their contact points may occur depending on their relative hardness. This effect may increase the true area of contact and hence the cohesion force. Amorphous materials are generally more deformable, thus giving a stronger cohesion (18).

In a low relatively humidity environment, electrostatic forces will contribute to the cohesion of particles. The similar or different surface charges of particles, that lead to either repulsion or attraction of the particles, can be generated through either tribo-

electrification (frictional charging) and/or contact charging. The latter usually occurs when particles of different work functions are brought into contact (16). The force due to triboelectrification can be quantified by Coulomb's law (equation 6)

$$F_{triboelectric} = Q\,[1-H/(R^2+H^2)^{1/2}]/16\,\pi\varepsilon_o H^2 \quad \text{(equation 6)}$$

where Q are the charges on the particles in Coulomb, H is the separation distance between two particles, R is the particle radius and ε_o is the permittivity of a vacuum. Contact charging is usually applicable to particles of different compositions (16, 19). The work function of solid particles is defined as the energy required to remove an electron from the particle to infinity, and is related to the particle size and dielectric constant of the substance (20). The work function decreases with the particle size. Also, materials with higher dielectric constants are easier to ionise. Therefore, when two materials of different work functions come into contact, electrons will tend to transfer from the material with a higher work function to the material with a lower work function. This effect results in the formation of a contact potential between the two materials, giving rise to electrostatic charges. Humid environments will reduce the electrostatic interaction among particles by dissipating the charge.

4. Overcoming powder cohesion

4.1 Formulation: the traditional approach

Two traditional ways that have been used to optimise powder flow are (i) formation of a drug blends with coarse ('non-respirable') carrier particles (e.g. lactose), and (ii) formation of loose agglomerates from the primary drug particles.

Carrier particles should be physiologically inert and large in size (>50 μm). They are not intended to be delivered to the lung. The most commonly used carrier is lactose. Drugs blended with carriers are believed to adhere to the carrier to form an ordered mix (21). Because of the large carrier size, the powder flow is improved. Upon inhalation, the carrier should ideally be retained in the inhaler device or impacted on the patient's throat, whereas the drug should be released from the carrier and deposited in the lung. Therefore the interaction between the drug and the carrier should be strong enough to form an uniform ordered mix, but weak enough to be overcome by the patient's inspiratory flow to release the drug particles. This approach was first employed for the Spincap® used with the Spinhaler®.

Excipient carriers can also improve the availability of fine drug particles in the aerosol cloud. Depending on the nature of the active drug and the carrier, it is possible to generate desirable amount of fine drug particles with a minimal inspiratory effort (8, 22). Traditionally, the blend is a binary system, consisting of a drug and a coarse carrier. Recent studies have shown that the addition of fine carrier particles (<10 μm) (such as lactose or magnesium stearate) can further enhance the amount of drug particles in the aerosol cloud (23, 24). The fine carrier particles appear to reduce the drug-carrier interaction by occupying possible drug binding sites on the larger carrier particles. The formation of multiplets between fine carrier and drug may also occur in the presence of excess fine carrier, thereby hindering direct contact between the drug and the coarse carrier, and promoting drug particle detachment from the carrier surface during powder dispersion. Magnesium stearate at concentration as low as 0.1 % was found to be sufficient to increase the fine particles of salbutamol sulphate in the aerosol cloud (24).

Instead of being an external entity to the drug particles, excipient carrier may be co-spray dried with the active. This results in the excipient existing with the drug in the same particle. Chan and workers showed that the fine particle fraction of rhDNase in the aerosol was enhanced linearly with the amount of crystalline NaCl present as an excipient. Such an increase was correlated with the degree of crystallinity of the powder (8).

Formation of loose agglomerates for terbutaline sulphate and budesonide from drug particles (and excipients) to enhance the flow of powders has been employed with the proprietary product, Turbuhaler®. The aim is that these agglomerates should be robust enough to withstand filling and packing in the delivery device but at the same time they should readily be redispersed by the shear stress provided by the inhaler and the inspiratory energy of the patient. The size of these agglomerates, however, should not be too large, otherwise they could become trapped within the inhaler and would not be delivered to the lung (25).

Loose agglomerates can be formed by a variety of processes including low shear granulation, roller compaction or extrusion. The formation of such agglomerates often requires binding liquids that will not dissolve the powders and hence minimise crystalline bridges formation between particles upon drying. Commonly used liquids such as alkanols, however, can denature the actives e.g. proteins. Fluorocarbon

(FC) liquids, such as perfluorodecalin and perfluorooctyl bromide, have been found useful because they dissolve neither lipophilic nor hydrophilic compounds. FC has a low surface tension, which forms a relatively weak bond between the fine particles of the loose agglomerates, so that the agglomerates can be redispersed easily as an aerosol. The high vapour pressure of FC also renders it easy to remove from the agglomerate particles (25).

4.2 Formulation: the novel approach (See Section 5.1.4.)

4.3 Inhaler Device – new design, new technology

The dry-powder inhaler provides storage and protection to the medicament. More importantly, it aids the transfer of the powder from the device into the air stream and disperses the powder into fine particles for inhalation. It is known that the degree of dispersion of the powder depends not only on the powder cohesiveness, but also on the inhaler device and the energy input from the patient. Because different inhalers offer different resistances to air flow through the device, the inspiratory flow attained by a patient will, therefore, be dependent on the device used. Insufficient air flow through the inhaler will result in imprecise dosing to the patient and affect drug deposition. This behaviour is especially important with devices of high resistance (26 – 28). Some recent inventions, therefore, aim at improving the inhaler's dispersion efficiency by reducing the resistance of the device and the influence of patient's inspiration on powder dispersion.

4.3.1 Orbital®

Orbital® Inhalation System (BrinTech International, Nottingham, UK) is a low resistance unit-dose device, with the dose contained within a hollow disk, which is perforated by a series of small evenly spaced openings arranged around the outside edge (**Figure 1**) (29). During inhalation, the disk rotates following an 'orbital' path and the drug powder is released through the openings. The particles undergo rapid acceleration and de-aggregation as they are released under the influence of centrifugal force. The device has demonstrated aerosol performance comparable to the relatively high resistance Turbuhaler®.

4.3.2 Twisthaler®

The Twisthaler® (Schering-Plough, Kenilworth, NJ, USA) features specially designed nozzle geometry

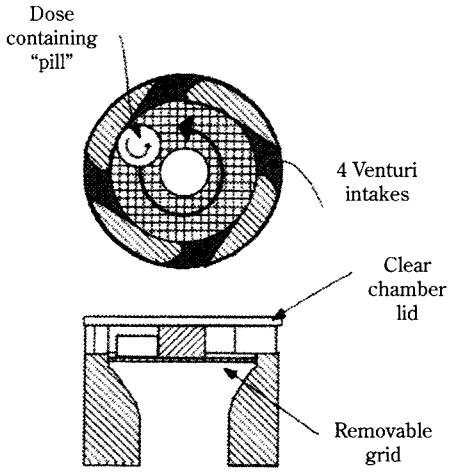

Fig. 1 Schematic diagram of the Orbital® Inhalation System. (Reprinted with permission. Serentec Press, Raleigh, NC. All rights reserved).

to optimise deagglomeration of powders, but at the same time minimises drug caught in the inhaler nozzle and mouthpiece (30). The design of the nozzle creates an airflow pattern which carries the small particles out of the device via the fluted chimney, while the larger particles or agglomerates will be spun into a centrifugal pattern which deagglomerates into fine particles for inhalation (**Figure 2**).

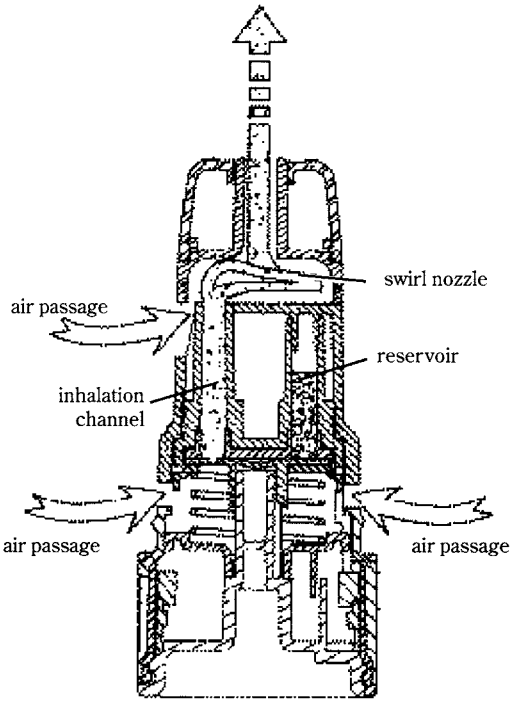

Fig. 2 Inhalation through the ASMANEX™ TWISTHALER™ DPI. (Reprinted with permission. Serentec Press, Raleigh, NC. All rights reserved).

4.3.3 Microdose Technology

The recently patented design (Microdose Technologies Inc., Monmonth Junction, NJ, USA) utilises electrostatic charging and ultrasonic vibration to facilitate suspension of powder in air (31). The device may include a user-actuable control to allow the user to choose the vibration frequencies and/or amplitudes for optimally suspending the drug in air.

4.3.4 Hovine FlowCaps®

Hovine FlowCaps® (Hovione SA, Loures, Portugal) dry powder inhaler features a tube which receives capsule(s) at one end (**Figure 3a**) (32, 33). The capsule is pierced by two blades (instead of the traditional needle piercing) giving rise to a narrow slit across each end of the capsule. As the patient inhales through the device, most of the air rushes into the inhaler tube inlets, whereas only little enters the capsules. This effect creates a pressure difference within the capsule causing very high turbulence for powder dispersion within the capsule before emptying from the device (**Figure 3b**).

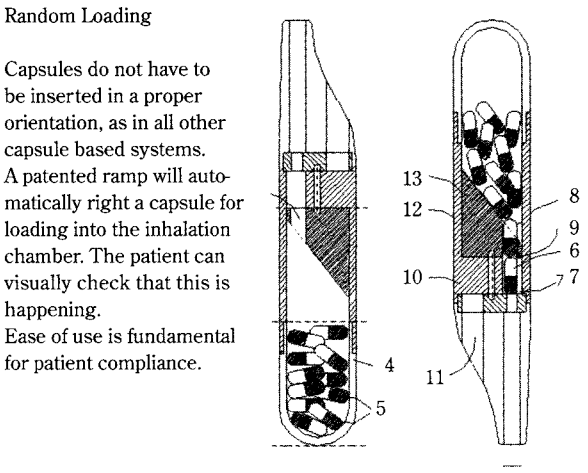

Fig. 3a Hovione SA FlowCaps® dry powder device. (Courtesy of Hovione Productos Farmaceuticos SA, Portugal).

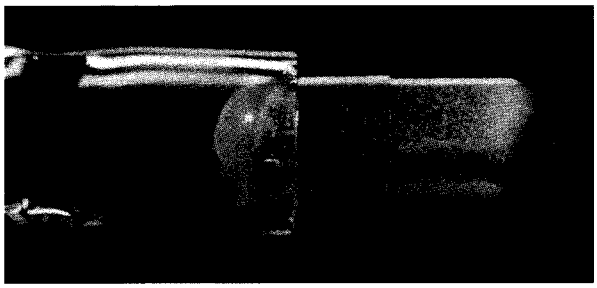

Fig. 3b Photograph showing the dispersion of powders within the capsule in a Hovione SA FlowCap® dry powder inhaler. (Courtesy of Hovione Productos Farmaceuticos SA, Portugal).

5. Stability and dispersibility of protein powders

The bioactivity of proteins is governed by their secondary and higher order structures. Therapeutic proteins prepared as dry powders have been found unstable when dried alone. Inclusion of certain excipients in the formulation prior to drying has significantly improved the stability of the dried products. The choice of excipients is dependent on the powder preparation methods (see below), the protein itself, the physicochemical properties of the excipient, and the subsequent storage conditions. Besides the amorphous glassy carbohydrates, other excipients, such as polymers (e.g. polyvinylpyrrolidone), proteins (e.g. human serum albumin) and amino acids or peptides (e.g. aspartame) have also been used to stabilise protein powders.

Based on the empirical observations, the protective effects imparted by the excipients can be explained by one or more of the following interrelated factors (34): (i) formation of an amorphous-glassy protein-excipient system; (ii) increase of the glass transition temperature of protein formulation; (iii) residual water content; (iv) water replacement via hydrogen bonding between the excipient and protein molecules; and (v) crystallinity of excipeint.

Solid exists as an amorphous glass which is characterised by the glass transition temperature (T_g) above which the glassy state softens to the rubbery state. In a glassy state, the mobility of protein molecules is much slower than those in the rubbery state; thus any reactions that may lead to protein degradation are almost impeded (35). From this behaviour, it seems logical and beneficial to render T_g well above the maximum temperature to which the dried product will be exposed during powder preparation and storage in order to preserve the structural integrity of protein and to minimise protein degradation. Crowe and coworkers found that large carbohydrates form a glass with a higher T_g than the small ones (36).

Water affects the stability of proteins by enhancing the mobility of the surface groups of the protein as demonstrated by solid-state NMR spectroscopy (37, 38). However, the effect of drying may remove water molecules that are hydrogen-bonded to the polar groups on the protein surface. This effect may alter the protein structure via the formation of intra- or interprotein hydrogen bonds (39). The function of the

excipient is to serve as a water substitute to preserve the native structure of the proteins as evidenced by FTIR spectroscopy (40, 41). Maintaining the protein/excipient combination in an amorphous state allows maximal hydrogen-bonding for protein stabilisation (39).

Crystalline excipients, such as mannitol, were found to reduce the stability of proteins (9, 42, 43). Excipients, such as glycine and sodium phosphate, appeared to inhibit the crystallisation of mannitol. Water facilitates crystallisation, resulting in the loss of amorphous glassy matrix for protein stabilisation (39). Since recrystallisation readily leads to interparticulate bridging as evidenced in the co-spray dried rhDNase powders (44) during storage at >40 % RH, the flowability and dispersability were adversely affected (45). Thus, a balance must be achieved between the choice of stabiliser to maintain/improve protein stability without compromising powder aerosol performance. Controlling the humidity of the environment during powder manufacturing and storage is also critical for the powder formulations.

5.1 Preparation of powders

5.1.1 Lyophilisation/milling

Lyophilisation is a freeze-drying process in which water is sublimed from the solution after it is frozen. A particular advantage of the process is that pharmaceuticals, which are relatively unstable in aqueous solution (e.g. proteins), can be dried without being subjected to elevated temperatures which may have an adverse effect on the product stability. However, lyophilised powders are often too large for inhalation. Jet milling may reduce the particle size, but a milling stabiliser (such as mannitol, sorbitol) is often required to reduce the shear, pressure and/or temperature degradation of the protein during milling. Significant loss of activity of interferon was found when sorbitol was not included in the formulation (46, 47). The adverse effect of the high energy from milling compromises the application of this technique.

5.1.2 Solvent precipitation

Precipitation of solids using organic anti-solvents often raises health concerns due to residual solvents. Non-solvents, such as supercritical carbon dioxide (SC CO_2), which exhibits remarkable solvent power for high molecular weight, low vapour pressure solids, is an ideal alternative. CO_2 is particularly attractive for operation due to its low critical temperature of 31.1°C. It is also non-toxic, inexpensive and readily available. This technique was found feasible to prepare anti-asthmatic drugs such as salmeterol xinafoate (48) and cromolyn sodium (49). Fine-tuning of this technique may result in particles of desirable size, shape and solid state properties for inhalation (50).

The majority of proteins are soluble in aqueous solutions. However, being non-polar and immiscible with water, SC CO_2 cannot be used as an anti-solvent to precipitate proteins from aqueous solutions. Methods, such as the use of a co-axial nozzle to enhance mixing of the water-based protein solution with SC CO_2, were able to overcome this hurdle (51). Alternatively, protein particles can be produced using a supercritical or near critical CO_2-assisted aerosolisation and bubble drying process (49).

5.1.3 Spray drying

Spray drying is a one step process, which involves converting the atomised liquid droplets into dry powders by hot air. Depending on the concentration of the feed solution, the spray temperature, cyclone efficiency and chemical nature of the feed, spray drying can yield powders of narrow particle size distribution suitable for inhalation (52).

Proteins, however, are susceptible to degradations due to the tremendous surface area of the atomised droplets. The relatively high drying temperatures and mechanical stress during atomisation may also adversely affect the integrity of the protein. Excipients are often co-spray dried with proteins for stabilisation. For example, thermal degradation of the protein, beta-galactosidase, is minimised in the presence of trehalose as excipient (53). Similarly, the presence of sucrose prevents the formation of a degradation product, oxyhemoglobin, during spray drying (54). The addition of surfactant polysorbate-20 in the liquid feed and/or divalent zinc ion significantly reduces the formation of insoluble aggregates of the recombinant human growth hormone (rhGH) (55). The formation of the zinc ion dimerised complexes with the protein and the occupancy of the surfactant at the air/liquid interface of the spray droplets have prevented protein unfolding and aggregation.

Spray drying of recombinant humanised monoclonal antibody, anti-IgE (rhMAbE25) containing trehalose or lactose had less than 1 % of aggregation following spraying drying (9). Formulation with trehalose, however, was found too cohesive and thus not suitable for aerosol delivery. Mannitol was less capable of stabilising rhMAbE25, with 1 − 3 % aggregates found following spray drying. Upon storage, the protein stability and aerosol performance were reduced

due to the recrystallisation of mannitol. Even though lactose improved the protein stability without compromising the aerosol performance, the antibody was subjected to glycation during storage. These results imply that each protein/sugar system requires individual characterisation to identify an optimal formulation for protein stability and powder aerosol performance.

5.1.4 'Tailored-made' particles from spray drying

Despite the challenges faced in preparing stable protein powders, spray drying still remains the most popular method of preparing inhalation dry powders. A number of therapeutic proteins have been effectively prepared by spray drying, as shown in **Table 1**.

5.1.4.1 Pulmosphere™

Spray drying has been applied to non-aqueous systems. Pulmosphere™ (Inhale Therapeutic Systems, San Carlos, CA, USA) particles are created by a proprietary spray-drying procedure in which the feed comprises two parts: an aqueous solution containing dissolved or dispersed active drug, and a fluorocarbon-in-water emulsion, stabilised by a monolayer of phospholipid (such as dipalmitoylphosphatidylcholine) (61). Pulmosphere™ particles have size between 2 and 4 μm, a hollow porous morphology and a bulk density of 0.05 – 0.2 g/cm^3 (**Figure 4**). Pulmosphere™ particles can be dispersed more readily than the traditional drug-carrier blend with lactose.

5.1.4.2 Technosphere™

Local and systemic inhalation therapies can often benefit from a relatively slow controlled release of the active drug (62). The invention of Technosphere™ (Pharmaceutical Discovery Corporation, Elmsford, NJ, USA) aims to provide particles with a controlled pulsed or sustained release profile. The process is based on the formation of diketopiperazine microparticles, which is targeted the specific cell types and is released only after reaching the targeted cells (63). Microcapsules prepared by spray drying contain the active drug suspended or dissolved in the polymer solution. This solution or suspension is then spray-dried to produce particles in which the drug is entrapped in the diketopiperzine matrix.

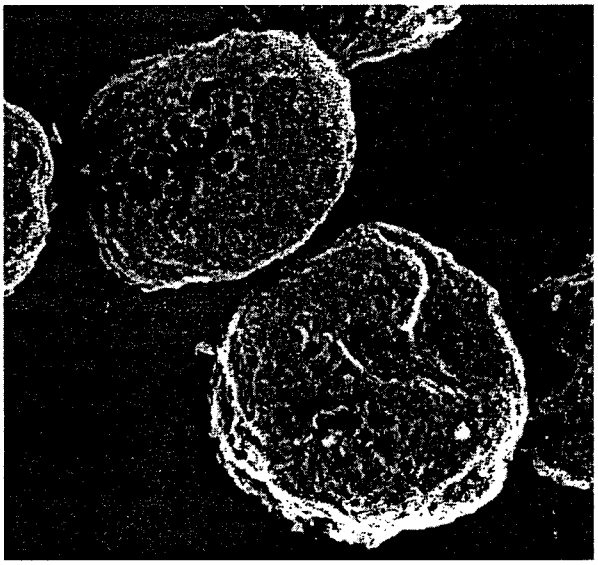

Fig. 4 Pulmosphere™. (Courtesy of Inhale Therapeutic Systems Inc. San Carlos, Carlifornia, USA).

5.1.4.3 AIR™ particles

AIR™ particles (Alkermes, Inc., Cambridge, MA, USA) also aim to release drugs in the airways in a controllable manner (64). The particles (**Figure 5**) are prepared by spray drying solutions containing a mixture of drug and biodegradable material (e.g. polyglycolic acid, polylactic acid or copolymers). AIR™ particles have a low tapped density of less than ~ 0.4 g/cm^3, with a irregular surface. Low density

Table 1 Some recent patents for preparing dry powders of macromolecules by spray drying

Proteins	Spray feed compositions	Ref.
pCMVβ (DNA plasmid)	PCMVβ in Tris/Mannitol/HAS solution.	56
Insulin	Insulin in citrate buffer (pH 6.7) containing mannitol or raffinose or neither.	57
IgA- and IgG- antibody	Antibody was dissolved in citrate buffer containing different excipients (sugar/polymer/protein).	58
Cystic fibrosis transmembrane conductance (CFTR) gene	CFTR gene, linked with a promotor, was dissolved in phosphate buffer saline solution containing lactose.	59
Interferon-β	Interferon-β was dissolved in a solution containing sodium chloride or mannitol and spray dried accordingly.	60

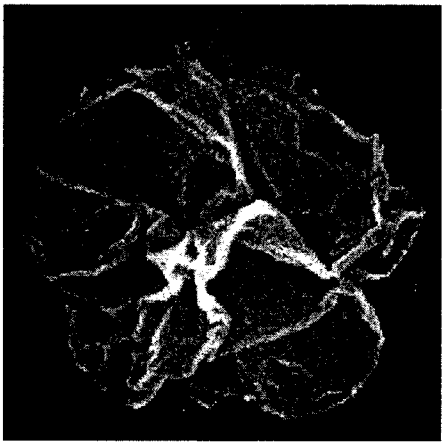

Fig. 5 AIR™ particle. (Courtesy of Alkermes, Inc. Cambridge, MA, USA).

particles are aerodynamically small and are ideal for deep lung delivery. The irregular surface of the particles may reduce cohesiveness of particles for powder dispersion. Furthermore, large particles could minimise phagocytic uptake, thereby providing the potential for controlled release of drugs into or via the lungs (65, 66). Addition of surfactants, such as L-alpha-phosphatidylcholine dipalmitoyl, to the formulation may also improve the dispersion of the AIR™ particles (67).

5.1.4.4 NanoCrystals™

NanoCrystals™ (Elan Pharmaceutical Technologies, King of Prussia, PA, USA) are small particles (less than 1000 nm in diameter) made entirely of crystalline drug, stabilised by adsorption of selected polymers (e.g. HPMC) onto their surfaces. The powders are first prepared by a wet-milling process to reduce the particle size to the nanometer range and are further processed by spray-drying to yield nearly spherical aggregates of the NanoCrystals™ within an aerodynamic particle size range suitable for pulmonary deposition.

The unique small size of NanoCrystals™ containing budesonide (mean diameter of 1.35 μm) leads to a nearly two-fold increase in the respirable fraction compared to the micronised particles of size 3.22 μm. The dose uniformity of budesonide is also better controlled with NanoCrystal™ budesonide delivery (RSD 8.5 – 11.4) than with the micronised powder (RSD 13.3 – 13.8) (68).

5.1.4.5 Wrinkled particles

Manipulations of the spraying conditions and protein formulations may produce particles of different shape and morphology (69, 70). *Non-porous solid* protein particles with wrinkled surfaces (**Figure 6**) have recently been prepared in our laboratory. The wrinkled particles gave a significant improvement in fine particle fraction over non-wrinkled spherical particles of bovine serum albumin (**Figure 7**) (71). A distinct advantage of these particles is that the inhaler choice and air flow becomes less critical for the dispersion of these particles as an aerosol.

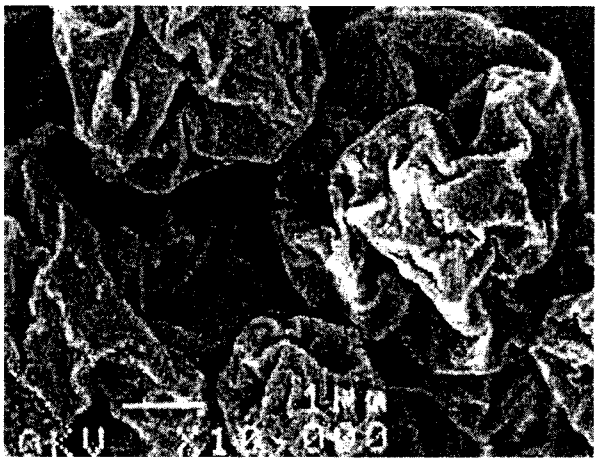

Fig. 6 Wrinkled bovine serum albumin particles, produced by spray-drying.

5.1.4.6 Spray freeze-dried particles

Spray freeze-drying involves spraying the feed solution into liquid nitrogen followed by lyophilisation. This process produces light and porous particles of rhDNase and anti-IgE with superior aerosol performance and high production yield (> 95 %) (72). However, the overall process is much more costly, time consuming and complex (requiring the additional use of liquid nitrogen and freeze-drying) compared with spray drying.

6. Summary

Recent developments in powder technology and inhaler devices have demonstrated the suitability of powder aerosols as alternatives to the propellant-driven inhaler. More importantly, dry powder systems have demonstrated success for the delivery of macromolecules. These drug delivery systems open new opportunities for powder technology scientists to play a key role in the emerging field of pharmaceutical powder aerosol delivery.

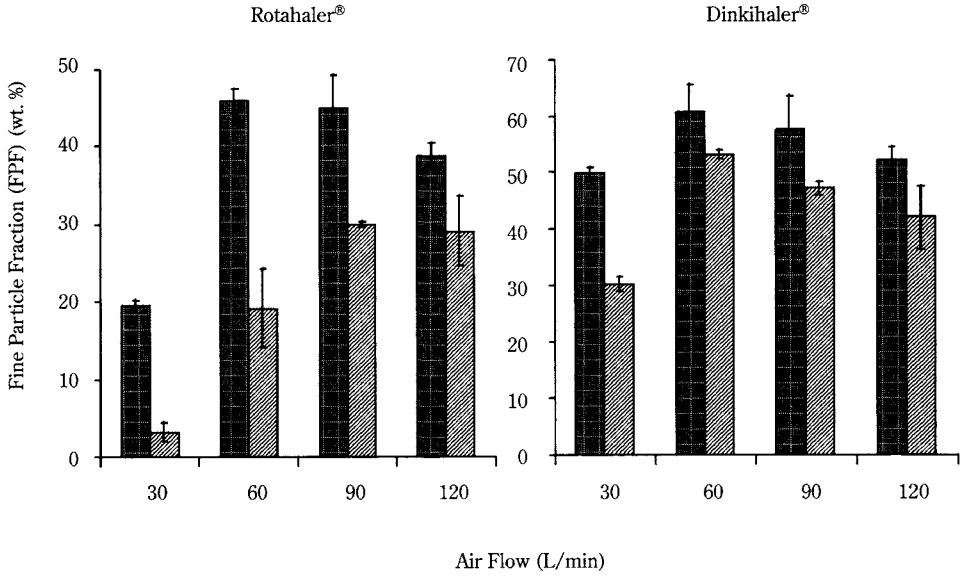

Fig. 7 Aerodynamic behaviour of wrinkled ■ versus spherical ▨ BSA particles at different air flows. (Reprinted with permission. Serentec Press, Raleigh, NC. All rights reserved).

Literature cited

1) Newman, S.P., A.R. Clark, N. Talaee and S.W. Clarke: Thorax, 44. 706-710 (1989).
2) Zar, H.J., E.G. Weinberg, H.J. Binns, F. Gallie and M.D. Mann: Arch. Dis. Child., 82. 495-498 (2000).
3) Patton, J.S.: CHEMTECH, December. 34-38 (1997).
4) Wilson, A., E. Sims, L. Orr and B. Lipworth: Lancet, 354. 1357-1358 (1999).
5) Brown, A.R. and J.A. Pickrell: J. Aerosol Med., 8. 43-58 (1995).
6) Tzou, T.Z., R.R. Pachuta, R.B. Coy and R.K. Schultz: J. Pharm. Sci., 86. 1352-1357 (1997).
7) LiCalsi, C., T. Christensen, J.V. Bennett, E. Phillips and C. Witham: Vaccine, 17. 1796-1803 (1999).
8) Chan, H.K., A. Clark, I. Gonda, M. Mumenthaler, C. Hsu: Pharm. Res., 14. 431-437 (1997).
9) Andya, J.D., Y.K. Maa, H.R. Constantino, P.A. Nguyen, N. Dosovich, T.D. Sweeny, C.C. Hsu and S.J. Shire: Pharm. Res., 16. 350-358 (1999).
10) Visser, J.: Part. Sci. Technol., 13: 169-196 (1995).
11) Hickey, A.J. and N.M. Concessio: Pharm. Technol., 18: 88, 90, 92, 94, 96, 98 (1994).
12) Zimon, A.D.: "Adhesion of dust and powder" Plenum Press, New York (1969) pp. 22-36.
13) Berbner S. and F. Loeffler: Powder Technol., 78. 273-280 (1994).
14) Visser, J.: Advan. Colloid Interface Sci., 3. 331-363 (1972).
15) Coelho, M.C. and N. Harnby: Powder Technol., 20. 210-205 (1978).
16) Visser, J.: Powder Technol., 58. 1-10 (1989).
17) Ranade, M.B.: Aerosol Sci. Tech., 7. 161-176 (1987).
18) Xie, H.-Y.: Powder Technol., 94. 99-108 (1997).
19) Berezin, A.: A. Electrification of solid materials in "Handbook of Electrostatic Processes" (eds. Chang J.-S., A.J. Kelly and J.M. Crowley) Marcel Dekker, New York (1995) pp. 25-49.
20) Gallo, C.F. and W.L. Lama: J. Electrost., 2. 145-150 (1976).
21) Hersey, J.A.: Powder Technol., 11. 41-44 (1975).
22) Zeng, X.M., G.P. Martin, S.-K. Tee, A.A. Ghoush and C. Marriott: Int. J. Pharm., 182. 133-144 (1999).
23) Lucas, P., K. Anderson, and J.N. Staniforth: Pharm. Res., 15. 562-569 (1998).
24) Musa R., P. Ventura and P. Chiesi: World IPO, 0053157 (2000)
25) Johnson, K.A., M.S. Gordon and S.W. Lyons: US Patent, 610327 (2000).
26) Clark, A.R. and A.M. Hollingworth: J. Aerosol Med., 6. 99-110 (1993).
27) Olsson, B. and L. Asking: J. Aerosol Med., 7. 201-204 (1994).
28) Srichana, T., G.P. Martin and C. Marriott: Eur. J. Pharm. Sci., 7. 73-80 (1998).
29) Barrowcliffe, J., B. Chawla, S. Carson, K. Owen and M. Walters: An assessment of in vitro performance for the Orbital® inhalation system in "Respiratory Drug Delivery VII" (eds. Dalby R.N., Byron P.R., Farr S.J., and J. Peart) Serentec Press, Raleigh, North Carolina (2000) Vol. 2, pp. 361-364.
30) Fan B.J., Yang T.T. and D. Kenyon: Application of computer modeling in the design and development of the new mometasone furoate dry powder inhaler (MF-DPI) nozzle in "Respiratory Drug Delivery VII" (eds. Dalby R.N., Byron P.R., Farr S.J. and J. Peart) Serentec Press,

Raleigh, North Carolina (2000) Vol. 2 pp. 491-493.
31) Abrams, A.L. and A.V. Gumaste: US Patent, 6026809 (2000).
32) Villax, P., R. Peres, W.R. Treneman, I.G. McDerment and M. Bunce: US Patent, 5673686 (1997).
33) Bunce M., J. Lamb, M. Greeves, I.G. McDerment and P. Villax: US Patent, 5881721 (1999).
34) H.-K. Chan. Excipients – Powders and Solid Dosage Forms in "Encyclopedia of Pharmaceutical Technology" Second edition. (eds. Swarbrick, J and J.C. Boylan), Marcel Dekker, New York (1998) pp. 121-136.
35) Frank, F.: Biotech., 12. 253-256 (1994).
36) Crowe, J.H., L.M. Crowe and J.F. Carpenter: Bio-Pharm., 6 (2). 40-43. (1993).
37) Yoshioka, S., Y. Aso and S. Kojima: Pharm. Res., 13. 926-930 (1996).
38) Separovic, F., Y.H. Lam, X. Ke and H.K. Chan: Pharm. Res., 15. 1816-1812. (1998).
39) Wang W.: Int. J. Pharm., 203. 1-60 (2000).
40) Allison, S.D., B. Chang, T.W. Randolph and J.F. Carpenter: Arch. Biochem. Biophys., 365. 289-298 (1999).
41) Carpenter, J.F. and J.H. Crowe: Biochemistry, 28. 3916-3922. (1989).
42) Costantino, H.R. J.D. Andya, P.-A. Nguyen, N. Dosovich, T.D. Sweeney, S.J. Shire, C.C. Hsu and Y.F. Maa: J. Pharm. Sci., 87. 1406-1411 (1998).
43) Izutsu K., S. Yoshioka, T. Terao: Pharm. Res., 10. 1232-1237. (1993).
44) Chan, H.-K. and Gonda I. J. Pharm. Sci., 87. 647-654 (1998).
45) Clark A.R., N. Dasovich, I. Gonda, H.-K. Chan: The balance between biochemical and physical stability for inhalation protein powders: rhDNase as an example in "Respiratory drug delivery V" (eds. Dalby R.N., P.R. Byron and S.J. Farr) Interpharm Press, Buffalo Grove, IL. (1996) pp. 167-174.
46) Platz, R.M., A. Ip and C.L. Whitham: US Patent, 5354562 (1994).
47) Platz, R.M., J. Utsumi, Y. Satoh and N. Naruse: World IPO 9116038A1 (1991).
48) Cooper, S.M.: World IPO 9955319 A1 (1999).
49) Sievers, R.E., S.P. Sellers, G.S. Clark, J.A. Villa, B. Mioskowski and J. Carpenter: Supercritical fluid carbon dioxide technologies for fine particle formation for pulmonary drug delivery in "Book of Abstracts, 219th ACS National Meeting, San Francisco, CA, 2000", American Chemical Society, Washington DC (2000) MED-173.
50) Beach, S., D. Latham, C. Sidgwick, H. Mazen and P. York: Org. Press Res. Dev., 3. 370-376, (1999).
51) Sloan, R. H.E. Hollowood, G.O. Humpreys, W. Ashraf and P. York: Proceedings of the 5th meeting of Supercritical fluid, Nice, France (1998).
52) Vidgren M.T., P.A. Vidgren and T.P. Paronen: Int. J. Pharm., 35. 139-144 (1987).
53) Broadhead, J., S.K. Edmond Rouan, I. Hau and C.T. Rhodes: J. Pharm. Pharmacol. 46. 458-467 (1994).
54) Labrude, P.M., M. Rasolomanana, C. Vigneron, C. Thirion and B. Chaillot: J. Pharm. Sci. 78. 223-229 (1989).
55) Maa, Y.-F., P.A. Nuygen, and S.W. Hsu: J. Pharm. Sci. 87. 152-159. (1998).
56) Eljamal, M., J.S. Patton, L. Foster and R.M. Platz: US Patent, 6136346 (2000).
57) Patton, J.S., L. Foster and R.M. Platz: US Patent, 5997848 (1999).
58) Platz, R.M., J.S. Patton, L.C. Foster and M. Eljamal: US Patent, 6019968 (2000).
59) Eljamal, M., J.S. Patton, L. Foster, R.M. Platz: US Patent, 5994314 (1999).
60) Platz, R.M., S. Kimura, Y. Satoh and L.C. Foster: US Patent, 6123936 (2000).
61) Tarara, T., J. Weers and L. Dellamary: Engineered powders for inhalation in "Respiratory Drug Delivery VII" (eds. Dalby R.N., P.R. Byron, S.J. Farr S.J. and J. Peart) Serentec Press, Raleigh, North Carolina (2000) Vol. 2 pp. 413-416.
62) Gonda, I.: Phyisco-chemical principles in aerosol delivery in "Topics in Pharmaceutical Sciences 1991" (ed. Crommelin, D.J.A. and K.K. Midha), Medpharm Sci. Publ., Stuttgart (1992) Ch. 7, pp. 95-115
63) Steiner, S.S., R. Feldstein, H. Lain, C.A. Rhodes and G.S. Shen: US Patent, 6071497 (2000).
64) Edwards, D.A., G. Caponetti, J.S. Hrkach, N. Lotan, J. Hanes, A.A. Ben-Jebria, R.S. Langer and S. Robert: US Patent, 5874064 (1999).
65) Rudt, S. and R.H. Muller: J. Control. Rel. 22. 263-271 (1992).
66) Kawaguchi, H., N. Koiwai, Y. Ohtsuka, M. Miyamoto, S. Sasakawa: Biomaterials. 7. 61-6 (1986).
67) Hanes, J., D.A. Edwards, C. Evora and R. Langer: US Patent, 5855913 (1999).
68) Ostrander, K.D., D.C. Hovey, D.A. Knapp and M. Parry-Billings. Potential delivery advantages of spray-dried NanoCrystals™ colloidal budesonide with the Clickhaler® in Respiratory Drug Delivery VII (ed. R.N. Dalby, P.R. Byron, S.J. Farr, J. Peart) Serentec Press, Raleigh, North Carolina. (2000) Vol. 2 pp. 227-229.
69) Maa, Y.F., H.R. Costantino, P.A. Nguyen and C.C. Hsu: Pharm Dev Technol. 2. 213-23 (1997).
70) Masters, K.: Spray drying handbook. John Wiley & Sons, New York (1976).
71) Chew N.Y.K. and H-K. Chan: Effect of particle size and surface morphology on the dispersion of albumen powders in "Respiratory Drug Delivery VII" (ed. Dably, R.N. P.R. Byron, S.J. Farr and J. Peart) Serentec Press, Raleigh, North Carolina. (2000) Vol. 2 pp. 619-622.
72) Maa, Y.F., P.A. Nguyen, T. Sweeney. S.J. Shire and C.C. Hsu: Pharm. Res., 16. 249-54 (1999).

Author's short biography

Nora Y.K. Chew

Dr Nora Chew obtained the Bachelor of Pharmacy degree in the Faculty of Pharmacy, University of Sydney in 1996. She has just been awarded a PhD degree from the same institution. Her research interest is on the formulation and characterisation of pharmaceutical powder aerosols.

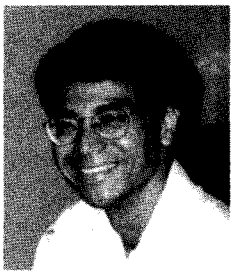

Hak-Kim Chan

Dr Hak-Kim Chan is a senior lecturer in the Faculty of Pharmacy, University of Sydney. He received a PhD from the same institution studying particle engineering with applications on pharmaceutical powder aerosols. He was a postdoctoral fellow in the Universities of Minnesota and Sydney in 1988-91. In 1992, Dr Chan joined the world leading biotechnology company, Genentech Inc. in USA, where he was a scientist working on aerosol formulations for proteins until his return to the University of Sydney in 1995. His expertise in pharmaceutical aerosol technology has been recognised internationally. He has been an invited keynote speaker in numerous conferences of scientific bodies, including the American Association of Pharmaceutical Scientists, the American Institute of Chemical Engineers, the Australasian Pharmaceutical Sciences Association, the Australia & New Zealand Society of Respiratory Sciences, and the International Society for Aerosol in Medicine (ISAM). Dr Chan has received the Sigma Drug Delivery Prize Australia in 1989, and the John A Brodie Medal from The Institute of Chemical Engineers Australia in 1999. Dr Chan has published extensively and is the holder of three US patents on protein aerosol formulation and delivery.

Recent Applications of Supercritical Fluid Technology to Pharmaceutical Powder Systems†

Rana T. Bustami[1], Hak-Kim Chan[1]*, Fariba Dehghani[2] and Neil R. Foster[2]**

[1] *Faculty of Pharmacy, The University of Sydney*

[2] *School of Chemical Engineering and Industrial Chemistry, University of New South Wales*

Abstract

The unique characteristics of supercritical fluids can be utilised to overcome the drawbacks associated with the conventional techniques for the generation of pharmaceutical powders. These characteristics include high diffusivity compared with those of liquids, relatively high solvent density and solvent power intermediate between those of gases and liquids. Such characteristics make it possible to use supercritical fluids either as solvents or antisolvents. The application of supercritical fluid technology to various pharmaceutical processes such as micronisation of a wide spectrum of pharmaceutical compounds, encapsulation and polymer impregnation, coprecipitation of pharmaceutical compounds and liposome formation, has been explored. The present review critically discusses the novel supercritical fluid techniques that are currently available and the applications of such techniques to pharmaceutical powder systems.

Introduction

Supercritical fluid technology includes a broad range of processes that utilise the properties of fluids at operating conditions above both the critical temperature and pressure of the solvent. The technology offers tremendous potential for the pharmaceutical and food industries, forest product industries, separations and chemical processing, and for the processing of polymers.

The use of supercritical fluids (SCF) is a relatively new approach in pharmaceutical research. The low critical temperature and pressure of SCFs such as carbon dioxide (CO_2) (Tc=31.1°C, Pc=72.9 atm) make them attractive for use in the processing of pharmaceuticals. Supercritical fluid technology provides viable alternatives to conventional methods of size reduction and has significant potential in the preparation of fine powders of thermally labile drugs. In particular, the technology offers a solvent-free process for the preparation of drug-loaded microspheres. Conventional techniques for microencapsulation of pharmaceuticals, such as double emulsion, utilise large amounts of organic solvents. Health concerns associated with solvent emissions from conventional pharmaceutical processes, difficulties associated with the removal of residual solvent from the product, and the drive for energy efficient and inexpensive processes have provided an incentive for increased focus on the development of novel clean technologies. Supercritical fluid processes are generally environmentally acceptable, and often require fewer processing steps than conventional methods.

Supercritical fluids can be used for recrystallisation as solvents as well as antisolvents. In the antisolvent mode, a SCF can be added to a solution, or vice-versa, to induce precipitation of the solid of interest. As with traditional solvents, solutions of supercritical fluids can also be used in spray-drying processes.

Certain limitations need to be addressed before the full potential of supercritical fluid technology can be realised. Among the challenges facing successful implementation of the technology is the lack of complete understanding of the fundamental principles involved and the costs associated with the specialised equipment required.

Supercritical fluid technology has been successfully

[1] NSW 2006, Australia

* Ph. No. +61 2 93513054 Fax No. +61 2 93514391
e-mail: kimc@pharm.usyd.edu.au

[2] NSW 2052, Australia

** Ph. No. +61 2 93854341 Fax No. +61 2 93855966
e-mail: n.foster@unsw.edu.au

† Accepted: August 17, 2001

employed at laboratory and pilot plant scales, and the pharmaceutical industry is beginning to exploit the technology commercially. This review covers recent applications of supercritical fluid technology for processing of pharmaceutical powder systems.

Fundamentals

Each compound possesses a critical temperature (T_C) and pressure (P_C) above which no liquid phase formation can be induced by further compression. A pressure-temperature phase diagram of a pure component is shown in **Figure 1**. The lines divide the P-T diagram into three regions: solid, gas, and liquid. The three phase boundary lines meet at the triple point at which all phases are in equilibrium. As the pressure and temperature increase, the critical point will eventually be reached. At this condition the gas and liquid have the same density, and exist as a single phase. The compressibility of a compound approaches infinity as the critical point is approached. In the vicinity of the critical region, the thermal-physical properties exhibit very high rates of change with respect to temperature and pressure. Along a near-critical isotherm (between T_C=1.0 and 1.2), the density and transport properties, such as viscosity and diffusivity, as well as other physical properties, such as dielectric constant

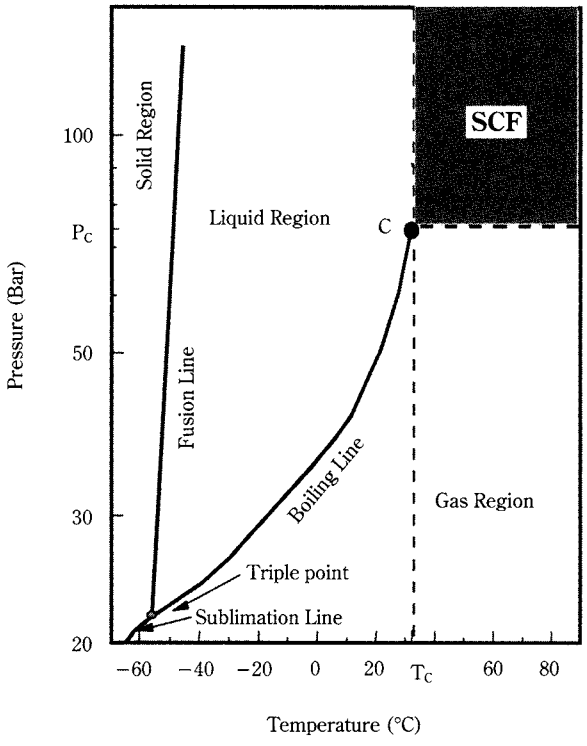

Fig. 1 Pressure – temperature diagram of carbon dioxide.

and solvent strength, can be varied continuously from gas-like to liquid-like with relatively small changes around the critical pressure (0.9-2.0 P_C). Supercritical fluids possess solvent density and solvent powers intermediate to those of liquids and gases. Solute solubilities in SCFs can be in the range of 3 to 12 orders of magnitude higher than those predicted by ideal gas behaviour. Supercritical fluids have solute molecular diffusivities much higher than liquids and viscosities intermediate to those of gases and liquids. Supercritical fluid properties can be easily controlled between liquid-like and gas-like extremes by changing the pressure.

The solvents that are commonly used as supercritical fluids are listed in **Table 1** [1]. Carbon dioxide is a commonly used supercritical fluid in pharmaceutical applications as it is nonflammable, inexpensive, has a moderate critical temperature (31.1°C) and is relatively non-toxic.

Table 1 Critical parameters for solvents that can be used as supercritical fluid [1].

Compound	T_b (°C)	T_C (°C)	P_C (bar)
Carbon dioxide	−78.5	31.1	72.9
Ammonia	−33.4	132.5	112.5
Ethane	−88.6	32.3	48.1
Ethylene	−102.7	9.2	49.7
Propane	−42.1	96.7	41.9
Nitrous oxide	−88.6	36.5	71.7
Pentane	36.1	196.6	33.3
Water	100.0	374.2	218.3
Dichlorodifluoromethane	−29.8	112	44.1
Chlorotrifluoromethane	−81.4	28.9	39.2

Supercritical Fluid Techniques in Powder Generation

The first observation of changes in particle size and morphology upon the expansion of supercritical solutions was made by Hannay and Hogarth [2], who characterised precipitated solids as snow in a gas and frost on glass. More than a century elapsed before Smith *et al.* (1986) [3] carried out the first investigations of rapid expansion of supercritical solutions, demonstrating the potential of this technique for particle formation, size reduction, and comminution of a wide variety of materials.

Supercritical fluids as solvents or antisolvents can be used for the generation of fine powders. The

process is called rapid expansion of supercritical solutions (RESS) when the SCF is a solvent and is used when the compound of interest is soluble in the supercritical fluid. The technology is known as the gas antisolvent (GAS) process, supercritical antisolvent (SAS) process, aerosol solvent extraction system (ASES) or solution-enhanced dispersion by supercritical fluids (SEDS) when the SCF is an antisolvent. These techniques are used when the compound has limited solubility in the SCF. Two other areas in which dense gases and SCFs are utilised for powder generation are supercritical fluid drug delivery (SFDD) and impregnation of polymers with pharmaceutical compounds.

Rapid Expansion of Supercritical Fluids

The rapid expansion of supercritical solutions is a novel method of particle formation, recrystallisation and particle size reduction, formation of thin films, microencapsulation, and powder mixing [4-6]. In this process, the solute is first dissolved in a supercritical fluid, which is then subjected to rapid expansion by passing through a nozzle at sonic speeds. During expansion, the density and solubilizing power of the supercritical fluid decreases dramatically, resulting in a high degree of solute supersaturation and subsequent precipitation of solute particles [7]. The combination of high supersaturation ratios and a rapid propagating mechanical perturbation is a distinguishing characteristic of the RESS process [8].

A schematic diagram of a typical RESS set up is shown in **Figure 2**. In general the RESS apparatus consists of two main units: the extraction or solubilization unit and the precipitation unit. In the extraction unit, the extraction vessel is packed with the solute and placed in a constant temperature environment. The supercritical fluid is then passed through a preheater and the vessel at a particular temperature and pressure. After equilibrium, the saturated solution is passed through an expansion device, such as a capillary nozzle [8, 9], laser drilled nozzle [5, 8, 9] or frit nozzle [10], which is located in the precipitation unit. The temperature-controlled nozzle is used to define the pre-expansion temperature. Heating of the nozzle and the connections between the extraction and the precipitation units is necessary to prevent condensation and phase changes and premature precipitation. The temperature is typically higher than the extraction temperature. During expansion or decompression, the density and solubilising power of the supercritical fluid decreases dramatically, resulting in a high degree of solute supersaturation and subsequent precipitation.

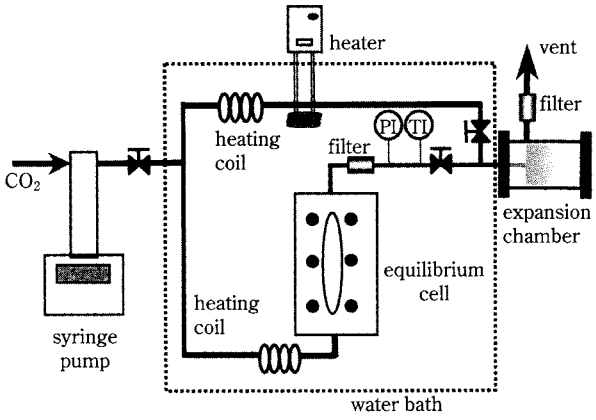

Fig. 2 A schematic diagram of rapid expansion of the supercritical solutions apparatus.

The major limitation of using RESS in pharmaceutical applications is that some pharmaceutical compounds including high molecular weight compounds, such as proteins and polymers, are insoluble in supercritical carbon dioxide at moderate conditions (<60°C and 300 bar). The low solubility necessitates either using large quantities of the supercritical fluid, or using polar co-solvents, which can complicate the phase behaviour of the system and may remain in the precipitated product. In addition, the scale-up of the process requires a comprehensive understanding of the underlying physical phenomena and the development of mathematical models to predict the characteristics of the product for a given set of operating conditions.

Supercritical Antisolvent Techniques

The low solubility of the pharmaceutical compounds in SCFs can be used to advantage by employing a dense gas (fluids close to the critical point) as anti-solvents. In the gas antisolvent techniques, the solute is soluble in the organic solvent, which in turn must be completely or partially miscible with the dense gas. There are two modes of performing gas antisolvent recrystallisation. The first mode, known simply as the GAS process, involves the gradual addition of anti-solvent to the organic solution containing the solute until precipitation occurs [11]. The second mode, known as the ASES, involves introducing the organic solution of the solute through a capillary nozzle into a flowing dense gas stream [12]. The recent high level of interest in antisolvent techniques stems from the fact that they are more flexible than conventional processes and are broadly applicable.

GAS

It is possible to induce rapid crystallisation by introducing the antisolvent gas into a solution containing dissolved solute. The dissolution of the dense gas in liquids is often accompanied by large volume expansion, and consequently a reduction in the solvent power of the liquid. Rapid addition of SCF results in a sudden reduction in the density of the liquid, a drastic rise in the supersaturation within the liquid mixture, and the subsequent formation of small and uniform particles. The process is a semi-batch and is known as gas antisolvent recrystallisation [11, 13]. A schematic diagram of a typical GAS set-up is presented in **Figure 3**. The standard GAS procedure begins by passing the antisolvent through a pre-heater into the precipitation chamber in which an organic solvent containing the solute has been charged. The homogeneity of the gas and the liquid during expansion is maintained by mechanical agitation, or by using a frit as a gas sparger. Once particle formation or crystallisation is complete, the antisolvent is delivered at a constant pressure to the vessel to wash the precipitate, and the system is then depressurised followed by powder collection.

Many of the experimental designs rely on the gas bubbling through the solution for mixing. This method of mixing has been proved to be as efficient as a magnetic stirrer for small volume crystallisation vessel [14]. In larger vessels, such as those exceeding one-litre, an efficient mixer is required to keep a uniform concentration in the expanded solution.

Process parameters that may influence particle formation in GAS precipitation include the rate of expansion of the solution, the physico-chemical properties of the solvent and antisolvent type [15, 16], the concentration of the solute [15, 17, 18], temperature [17, 18], and agitation and stirring [14].

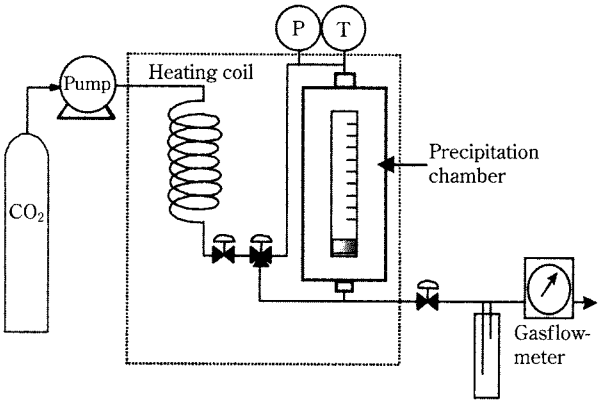

Fig. 3 A schematic diagram of the gas antisolvent apparatus.

ASES

In addition to the ASES, other terms for the continuous gas anti-solvent process have been reported in the literature. The various techniques are similar and include supercritical antisolvent (SAS), precipitation with compressed antisolvents (PCA), and the solution enhanced dispersion by supercritical fluids (SEDS).

In the ASES process, the solute can be precipitated by spraying the liquid solution into a dense gas or supercritical fluid. The process is continuous compared to the GAS process, the latter being a batch or semi-batch process. The basic experimental set-up is shown in **Figure 4**. The liquid containing the solute and the dense gas are fed continuously into the precipitation chamber. The liquid solution is aerosolized through a small orifice or capillary nozzle (i.d. 20-500 μm) and the droplets come in contact with the antisolvent. The antisolvent rapidly diffuses into the liquid solvent as the carrier liquid solvent diffuses into the antisolvent. The expanded solvent has a lower solvent strength than the pure solvent; thus the mixture becomes supersaturated resulting in the precipitation of the solute [12, 19]. After precipitation of the solute, the solid is filtered and washed from traces of solvent by the addition of antisolvent.

The basic experimental apparatus has been modified to tailor the process to specific applications. For micronisation applications, nozzles of different diameters and designs have been employed to control particle size and distribution, and agglomeration of precipitated products. Nozzles and orifice sizes employed in the studies to date have ranged from 20 μm to 500 μm. Ultrasonic [20], hi-energy [21], double [22, 23] and triple coaxial nozzle arrangements have been incorporated to further improve the quality of micro-

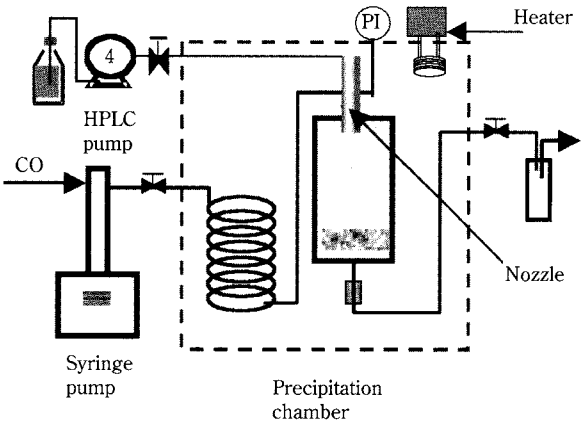

Fig. 4 A schematic diagram of the aerosol solvent extraction system apparatus.

nised jet breakup, reducing particle agglomeration, and controlling the extent of mixing and solute-solvent interaction at the point of precipitation [24-26].

The mechanism of precipitation in the ASES process is more complicated than for the GAS technique. In this process, mass transfer, the hydrodynamics and thermodynamics of the system influence the precipitation. It has been proposed that for precipitation under sub-critical conditions, the hydrodynamic effect is generally the dominant factor. Particles are generated by solvation of the SCF into the droplet and jet break up followed by extraction of the solvent from the droplet resulting in dry powder formation. Above the critical conditions, the organic solution is completely miscible in the antisolvent so particles are formed by nucleation and growth in the whole volume of the precipitation vessel [27].

Supercritical Fluid Drug Delivery (SFDD)

In this technique, the pulmonary drug delivery of fine aerosol particles of pharmaceutical compounds is made feasible by supercritical fluid technology [28, 29]. Fine aerosols of the desired substance are formed by mixing a supercritical fluid with the desired substance that is present in solution, suspension or dispersion. A gas borne dispersion of fine particles having an average diameter between 0.1 μm and 6.5 μm is formed after rapidly reducing the pressure of the mixture to the atmospheric pressure, which is then rapidly mixed with a large amount of air before being passed to the lung of a subject. A hand held device has been patented for the pulmonary delivery of fine aerosol particles through oral and nasal passages to humans [30, 31].

Impregnation of polymers with pharmaceutical compounds

Supercritical fluids may cause swelling of polymers. Pharmaceutical compounds can thus be impregnated with a solid polymer [32, 33]. The supercritical fluid swells the polymer at or near supercritical conditions and causes the impregnation of the active material into the polymer matrix, examples of which include polyethylene, polypropylene, ethylene-ethyl acrylate copolymer and ethylene vinyl acetate copolymer [32]. The approach can be used to develop novel controlled-release dosage forms to deposit thermolabile materials into polymers.

In a similar study of the impregnation of polymers with bioactive compounds, the loading of drugs on cross-linked polymer using supercritical fluids has been described [33]. The method involved contacting the SCF containing the solubilized drug with a cross-linked polymer, resulting in impregnation of the polymer with the drug after the removal of the SCF.

Applications of SCF in Pharmaceutical Powder Systems

1. Micronisation and Recrystallisation of Pharmaceutical Compounds

Fine particles of pharmaceuticals with a narrow particle size distribution are essential for the development of inhalation aerosols, injectable suspensions, controlled release dosage forms, and other specialised drug delivery systems. In addition, particle size is a critical parameter that determines the rate of dissolution of the drug in the biological fluids and hence has a significant effect on the bioavailability of the poorly water-soluble drugs for which the dissolution is the rate-limiting step in the absorption.

Micronisation and recrystallisation of pharmaceutical compounds using SCFs has many advantages over conventional techniques, such as minimum product contamination, reduced waste streams, enabling the processing of thermolabile, shock- and chemically-sensitive compounds, and the possibility of producing particles with narrow size distribution in a single step operation.

Numerous investigators have employed SCFs as alternative approaches to reduce the particle size of a broad spectrum of pharmaceutical compounds including small molecular weight compounds, peptides, proteins and polymers (**Table 2, 3**).

Rapid expansion of supercritical solutions has been utilised for the recrystallisation of pharmaceutical compounds. Some of the compounds that have been processed to date are listed in **Table 2**. In a recent study, ibuprofen, a poorly water-soluble anti-inflammatory agent, has been micronised by RESS to enhance its dissolution characteristics. A typical SEM of the RESS processed ibuprofen powder is shown in **Fig. (5d)** [34]. The study showed that the RESS processed powder exhibited higher powder dissolution rates compared with the conventionally crystallised and micronised ibuprofen powder. Interestingly, there was no significant difference in the disc intrinsic dissolution rate between the RESS processed and the conventionally crystallized and micronised powder, thus indicating that the higher powder dissolution rate is a result of particle size reduction of the crystals and not a change in crystallinity.

The RESS technique has also been used for the production of microspheres and microparticles of low

Table 2 Particle size reduction of pharmaceuticals using rapid expansion of supercritical fluids.

Materials	Solvent	Size and morphology	Reference
Phenacetin	CO_2-CHF_3		[35]
Lovastatin	CO_2 with 3% methanol	10-50 μm	[36]
Lovastatin	CO_2	40 μm needles	[37]
Salicylic acid	CO_2	needles, spheres	[38]
Salicylic acid	CO_2	needles, filament	[39]
Caffeine	CO_2	needles	[40]
Caffeine	CO_2	needles, filament	[39]
Griseofulvin	CHF_3	quasispherical particles, long needles	[41]
Naproxen	CO_2	microparticles (<15 μm), agglomerates (<200 μm)	[9]
Progesterone	CO_2	dentrite, prismatic structure	[7]
Theophyllin	CO_2	needles, branch, band	[39]
Aspirin		2-5 μm	[10]
Ibuprofen	CO_2	irregular crystals	[34]
Cyclosporine	CO_2	highly irregular in shape (3-50 μm)	[42]
L-PLA (M_W=5,500)	CO_2, CO_2+1wt% acetone, $CClF_3$	needles, regular shaped crystals, spherical and irregular particles, microparticles, dendrites	[5, 37]
PGA (M_W=6,000)	CO_2,	regular shaped particles (ovals, rectangles), needles of up to 40 μm	[5, 37]
L-PLA (M_W=2,000)	CO_2	microspheres (<75 μm), microparticles (2-15 μm)	[9]
PLA (M_W=10,000)	CO_2-$CHClF_2$, CO_2=40-80 wt%	micropaticles, microspheres, fibers	[8]
HYAFF-11	CO_2	microspheres (D<10 μm), aggregated particles	[17]

RESS: rapid expansion of supercritical fluids, CHF_3: fluoroform, PGA: poly(glycolic acid), $CHClF_2$: difluorochloromethane, L-PLA: poly(lactic acid), HYAFF11: hyaluronic acid ethyl ester.

molecular weight biodegradable polymers (**Table 2**). Microparticles and microspheres of polylactic acid (PLA) (M_W=5,500) in the size range of 4 to 25 μm were precipitated from CO_2 and a CO_2-acetone mixture [5]. Irregular-sized particles of PLA (M_W= 5,500) ranging from 10 to 20 μm were precipitated from CO_2 [5]. The precipitation of polyglycolic acid (PGA) (M_W=6,000) from CO_2 produced needle particles of 10-40 μm length and regular particles [5].

Gas antisolvent techniques have also been utilised for the crystallisation and micronisation of a broad spectrum of pharmaceutical compounds. Some of the compounds micronised by the various gas antisolvent techniques are listed in **Table 3**.

Small molecular weight pharmaceuticals have been successfully recrystallised and micronised using gas antisolvent techniques. Salmeterol xinafoate, a bronchodilator, was precipitated using the SEDS technique as micron-sized crystals with higher fine particle mass compared with the conventionally crystallised and micronised product [50]. Poorly water-soluble compounds have also been successfully micronised using the ASES technique [66, 67] (**Figure 5b, c, d**). Higher powder dissolution profiles were observed for the processed powders of mefenamic acid, phenytoin, griseofulvin compared with the conventionally crystallised and micronised powders. It is concluded that although the crystallisation process in the ASES technique is instantaneous, the crystallinity of the processed powders was favourably comparable with the conventionally recrystallised and micronised powders [57, 66, 67].

Gas antisolvent techniques have also been used for the production of micron-sized particles of proteins suitable for inhalation delivery, such as insulin [18, 45, 47], catalase [43, 46], trypsin and lysozyme [49, 68]. Catalase precipitated as 1 μm spherical and rectangular particles whereas insulin formed both agglomerated nanospheres and 1 μm thick needles 5 μm in length. Temperature, solute concentration and

Table 3 Particle size reduction of pharmaceuticals using the aerosol solvent extraction system technique.

Materials	Solvent	Size and morphology	Reference
Catalase, Insulin	DMSO	1 μm crystals and microspheres	[43] [44]
Catalase, Insulin	Ethanol	<2 μm crystals and microspheres	[45]
Insulin	DMSO, DMF	2.5 μm microspheres	[46, 47]
Methylprednisolone	THF, methanol/CH_2Cl_2	2.8 μm needles	[48]
Trypsin, Lysozyme, Insulin	DMSO	Microspheres	[49]
Salmeterol xinafoate	Acetone, Ethanol	Irregular needles and particles	[50]
Steroids	CH_2Cl_2	<5 μm microspheres	[51]
Sodium cromoglycate	Methanol	1 μm microspheres	[52]
Trypsin, Lysosyme Antibody Fv and Fab Plasmid DNA	Water and Ethanol	<2 μm irregular particles and micro-spheres	[53, 54]
Prednisolone acetate	Acetone	0.4-6.3 μm	[55]
Streptomycin		0.1-0.4 μm spheroidal	[56]
Lactose monohydrate	Water+Ethanol Water+Methanol	Platelet like crystals	[57]
Hydrocortisone Poly(DL-lactideglycolide) RG503H, HYAFF-7 Ibuprofen, Camptothecin	DMSO Ethyl acetate	Spherical Whiskers Hollow microspheres Flakes, resin	[21, 58]
Paracetamol, Lysozyme	Water+Ethanol	Acicular, microspheres	[23]
Sugars R-TEM betalactamase	Water+methanol Water+ethanol		[59, 60]
Paracetamol	Ethanol	Spheres, faceted crystals, needles. 3-300 μm	[61]
Griseofulvin Ampicillin Amoxicillin, Tetracycline	DMSO Ethanol CH_2Cl_2	Needles Flat crystals Spherical aggregates	[62, 63]
Paracetamol, Ascorbic acid	Ethanol	Crystals, small aggregates	[64]
rhIG	Water+Ethanol	ND	[65]
Griseofulvin	Acetone	5-30 μm platelet crystals	[66]
Mefenamic acid, Phenytoin	Acetone	5-50 μm needles, 5-30 μm plates	[67]
Lysozyme, Albumin rhDNase, and Insulin	Water	0.05-1 μm microspheres	[22]

ASES: aerosol solvent extraction system, DMSO: dimethylsulfoxide, DMF: dimethylformamide, THF: tetrahydrofuran, rhIG: recombinant human immunoglobulin, rhDNase: recombinat human deoxyribonuclease, ND: not determined.

the nature of the solvent had little effect on particle size. The biological activity of the insulin powder was also shown by in-vivo studies to be unchanged. Raman spectroscopy further confirmed the maintenance of the secondary structure of the protein [47].

Precipitation of solutes using gas antisolvent techniques relies on the solubility of the solute in an organic solvent that is miscible with the antisolvent. The difficulty of applying gas antisolvent techniques to the processing of proteins is that they involve exposure of the protein to organic solvents, the latter being potential denaturants and very poor solvents for most therapeutic macromolecules. The ASES has been modified to enable the spraying of aqueous protein solution simultaneously with an organic solvent into carbon dioxide [24] or directly into carbon dioxide, which has been modified with an organic solvent [22, 65].

Recombinant human immunoglobulin (rhIG) [65], lysozyme [22], albumin, recombinant human deoxyribonuclease (rhDNase), insulin [22], trypsin [53], a therapeutic peptide antibody Fv and Fab and plasmid DNA [54] have been precipitated from aqueous based solutions. Except for rhIG, which was not obtained as

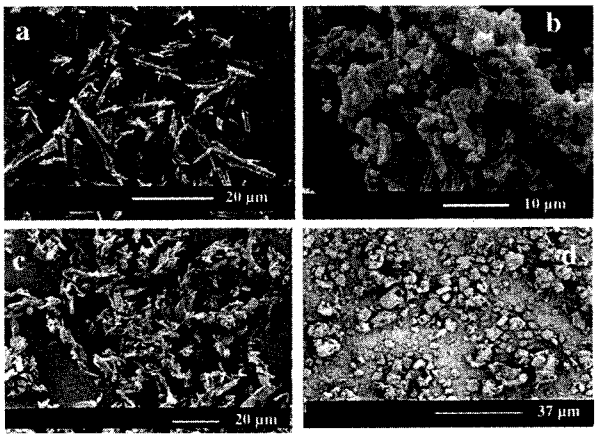

Fig. 5 SEM images of poorly water soluble compounds, mefenamic acid (a), phenytoin (b), griseofulvin (c) processed by ASES (66, 67), ibuprofen (d) by RESS (34).

a stable powder, all the proteins precipitated as micron-sized particles or agglomerated nano-spheres. The SEM images of the typical precipitate that is produced by the modified ASES are shown in **Figure 6**. Particle sizing of lysozyme by the impaction technique has shown a fine particle mass (<5 μm) of more than 60% for the processed powder [22]. Depending on the protein, the biochemical integrity of the proteins micronised using the modified ASES can be a problem. While lysozyme recovered almost complete biological activity after reconstitution in water, other proteins were denatured to various extents.

Application of the GAS antisolvent techniques was extended to the precipitation of bio-erodible polymers as encapsulating agents. Bio-erodible polymers include slow-degrading types of high molecular weight such as PLA [5, 17, 20, 26, 69-71], and polycaprolactone [70], as well as faster-degrading copolymers such as poly (lactide-co-glycolic acid) (PLGA) [72].

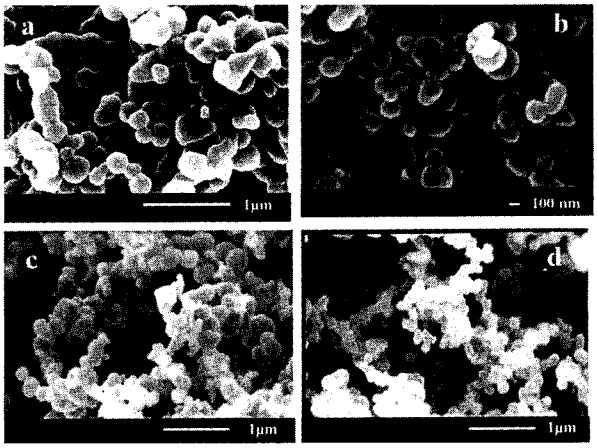

Fig. 6 SEM images of proteins, lysozyme (a), insulin (b), rhDNase (c), albumin (d), precipitated from aqueous solutions using ASES technique [22]. (Reprinted with permission Generation of micro-particles of proteins for aerosol delivery using high pressure modified carbon dioxide, Bustami et al, Pharm Res, 2000, Kluwer Academic/Plenum Publishers.)

Sub-micron to micron-sized particles of PLA were produced using near-critical or supercritical carbon dioxide as an antisolvent [20]. Other studies have consistently precipitated PLA in the form of discrete microspheres throughout a broad range of operating conditions and solution concentrations [17, 26, 69-71].

Attempts have been made to reduce the agglomeration of the precipitated particles of polymer [25]. A coaxial nozzle was utilised to modify the solution injection device through which polystyrene and PLA particles were precipitated from toluene and methylene chloride (CH_2CL_2), respectively [25]. A stabiliser, (poly(1,1-dihydroperfluorooctyl acrylate)), was added into the solutions to further reduce particle flocculation and agglomeration [25]. The addition of the stabiliser was found to significantly reduce flocculation.

2. Encapsulation and co-precipitation

In the development of special delivery systems like controlled release therapeutics, it is frequently desirable to disperse the material into very fine, uniform particles. Such particles may then be advantageously incorporated into controlled-release delivery vehicles such as polymeric microspheres or implantable devices, or delivered to the lung as aerosol.

Conventional methods to prepare drug-loaded microspheres include solvent evaporation, spray-drying, freeze-drying and double emulsion technique. Both drug and carrier are dissolved in an aqueous or non-aqueous solvent, which is then removed to results in polymer-coated drug particles. These methods are associated with difficulties with the complete removal of organic solvents from the end product, thermal degradation upon solvent removal by heating, low process yields, wide particle size distribution, and low drug loading.

Supercritical fluid technology is an alternative microencapsulation process, which is still in its early stages with many areas yet to be explored. The first application of the SCFs in the production of polymer-drug microspheres was described by Muller and Fischer using SC carbon dioxide as antisolvent in an ASES process [12]. Microspheres of 100 micron containing clonidine hydrochloride and PLA (17000) were produced from methylene chloride solution at 60°C and 100 bar. The *in-vitro* release studies have shown that 50% of the drug was released after 24 hours in phosphate buffer pH 7.5 at 37°C.

The potential of the ASES process for microencapsulation of pharmaceuticals has been demonstrated by several studies (**Table 4**). Studies have involved the simultaneous precipitation of neat core and coating solute solutions or the precipitation of pre-mixed solutions with different types of nozzles.

Various studies have shown that drug loading is a function of the solubility of the drug in the antisolvent and therefore is a function of the pressure or density of the system [72, 74, 78]. It was generally found that the higher the solubility of the drug, the lower the drug loading due to the enhancement in solubility and thus the extraction of the drug into the antisolvent phase. Drug loadings of nonpolar drugs, such as piroxicam in PLA particles, were relatively low and decreased significantly as the pressure was increased from 90 to 200 bar at 40°C [73]. Experiments with the more polar drugs, such as hyoscine-butylbromide achieved drug loadings of 19.5 wt %, which remained unchanged even at higher pressures due to the negligible change in solubility in the carbon dioxide antisolvent system [74].

Microencapsulation of ionic compounds, which are not soluble in an organic solvent suitable for ASES processing, was achieved after complexation with hydrophobic ion pairing in methylene chloride [78, 79]. Drug loading efficiencies of up to 37.4%, 24.7%, and 9.2% were achieved for rifampin, gentamycin and naltrexone, respectively. Similar approaches to encapsulate ionic compounds, such as α-chymotrypsin, imipramine, insulin, ribonuclease, cytochrome C, pentamidine and streptomycin have been reported [56].

The potential of the ASES process to encapsulate proteins has been investigated in few studies [76, 77, 82]. In an attempt to encapsulate lysozyme with L-PLA, or PLGA from a dichloromethane solution [82], a suspension of lysozyme in the polymer solution was injected into the carbon dioxide antisolvent existing as a vapour to partially solidify the droplets before they fell into a carbon dioxide liquid phase. The integrity of the polymer coating or the biological activity of the lysozyme was not investigated.

The effect of polymer crystallinity and thermal behaviour on the encapsulation of two model drugs, albumin and estriol, have been investigated [77]. The drug content and the release studies confirmed that the blocked copolymers b-poly-L-lactide-co-D,L-lactide-co-glycolide and poly-D,L-lactide-co-glycolide in the microparticles gave the same protein content, which was mainly on the surface or immediately below.

The feasibility of utilising RESS for encapsulation of

Table 4 Encapsulation of pharmaceutical compounds using the aerosol solvent extraction system technique.

Materials	Solvent	Size and morphology	Reference
Indomethacin with PLA Thymopentin with PLA Piroxicam with PLA Hyoscine butylbromide with PLA	Methylene chloride	<8 μm microsphere and fibre network	[73]
Hyoscine butylbromide with PLA	Methanol, Methylene chloride	1.7 μm microspheres	[74]
Naproxen with PLA (RESS process)	Acetone	<20 μm	[75]
Insulin with PLA Lysozyme with PLA Chymotrypsin with PLA	Trifluoroacetic acid Dimethylsulfoxide Methylene chloride	1 to 5 μm microsphere	[76]
Estriol with DL-lactide-co-glycolide 50:50 Albumin with DL-lactide-co-glycolide 50:50	2,2,2-Trifluoroethanol CH_2Cl_2	150 to 5 μm microspheres	[77]
Rifampin with PLA Naltrexone with PLA Gentamycin sulfate with PLA	Methylenechloride	0.2 to 1 microspheres	[78, 79] [80]
Hyaluronic acid benzylic ester (HYAFF-11) with two steroids or with a protein	Dimethylsulfoxide	>1 μm	[81]
Glass and sugar beads with hydrocortisone or RG503H	Dimethylsulfoxide Ethyl acetate	Coating of the beads with microspheres of the polymer	[58]
p-Hydroxybenzoic acid with PLA or poly(lactide-co-glycolide)	Methanol Acetone	Microsphere and fibre network	[26]
Lysozyme with PLA or PLGA	Methylenechloride	0.5 to 500 μm	[82]

ASES: aerosol solvent extraction system, PLA: poly(lactic aicd), HYAFF-11: hyaluronic acid ethyl ester, PLGA: poly(lactide-co-glycolic acid).

drugs in DL-PLA (M_W=10,000) has been demonstrated. Microparticles consisting of lovastatin crystals coated with DL-PLA polymer were formed by combining the extraction of drug and polymer into one stream prior to expansion [8]. Precipitates with high lovastatin concentration (>30%) showed a network morphology while those with low concentration showed microparticle and microsphere morphology. The particles consisted of drug needles coated with polymer.

In a similar study, the suitability of RESS as an encapsulation procedure was demonstrated by the co-precipitation of naproxen and L-PLA (M_W=2,000) [9]. The drug and polymer were pre-mixed and loaded in the same extraction vessel, a capillary nozzle was used as an expansion device. Composite particles containing microcrystalline naproxen particles at the core, with coated polymer on the surface, were observed.

Supercritical carbon dioxide was also employed in the inclusion of drug compounds in cyclodextrin molecules using the RESS technique. A piroxicam-β-cyclodextrin inclusion complex was prepared to enhance the dissolution characteristics of poorly water-soluble piroxicam [83].

3. Co-precipitation and Mixing of powders

Mixing of powders can be achieved by co-precipitation of the solutes of interest using SCF. The application of RESS was extended to the processing of a homogeneous mixture of powders in a single step process. Mixing of active ingredients and excipients was demonstrated using the RESS process [84]. The method involved solubilising and mixing the active ingredients and the excipients in the liquid carbon dioxide under a pressure sufficient to maintain carbon dioxide in liquid state (20°C and 700-900 psi). Depressurisation of the solution resulted in the co-precipitation of both the active ingredients and the excipients.

The co-precipitation of caffeine and β-carotene using two separated extraction vessels in a RESS process has been reported [85]. Under the same conditions, β-carotene precipitated as shorter needles compared to caffeine. The results also showed the ultimate mixing of both caffeine and carotene needles with no aggregation, and the precipitates were separated from each other. More caffeine precipitates were observed in the mixture due to the higher solubility of caffeine in CO_2 compared to that of β-carotene. The ratio of caffeine to β-carotene precipitates was approximately 16. It was concluded that the homogeneity of the mixture precipitated by RESS in this study could not be obtained by mechanical mixing.

The ASES process was also utilised in the production of powder mixtures of pharmaceutical compounds. Combinations of urea/chloramphenicol and ascorbic acid/paracetamol have been co-precipitated from ethanol at 40°C and 90 bar using the ASES process [86]. The quality of the products produced each time was not quantified, although problems with particle agglomeration and fractionation below 85 bar were identified for the co-precipitation of paracetamol with ascorbic acid.

4. Liposome Formation

Liposomes are microscopic vesicles in which an aqueous volume is entirely enclosed by a membrane normally composed of single or multiple phospholipid bilayers. Liposomes can entrap hydrophilic or lipophilic compounds so they are used as carriers or vesicles for the delivery of therapeutic compounds. Liposomes can be made with different features, which can enhance drug efficacy, reduce toxicity, and prolong the therapeutic effect. Because of their similarity to natural cells, liposomes have been reported to be ideal carriers for parenteral administration.

Conventional techniques of liposome formation include methods that involve the use of organic solvents or detergents, which often leave residues in the end product, or methods which involve the use of high pressure extrusion of the liposome through polycarbonate filters of controlled pore size. Furthermore, liposome sterility is accomplished by independently sterilizing the component parts by autoclave or filtration and then mixing in a sterile environment. This process is difficult, time consuming, and expensive. In addition, sterilization techniques may cause damage or alter the features of the multilayered liposomes.

Formation of liposomes containing drugs using supercritical technology is a new application that has been reported recently [87, 88]. Supercritical fluid methods and apparatus capable of forming liposomes that carry hydrophobic drugs, have been described [87]. One method of forming liposomes containing the drug is referred to as the decompression method. The method involves forming a solution or mixture of a phospholipid, a hydrophobic drug, an aqueous medium, and the supercritical or sub-critical carbon dioxide, which is then decompressed to form the liposomes. The other method is referred to as the injection method of forming liposomes. In contrast to the

decompression method, the injection method does not involve pressurisation of the aqueous phase. Instead, the solution or the mixture of the drug, a phospholipid and the supercritical or sub-critical CO_2, is injected through a tip or orifice into an aqueous phase. At the time of injection or afterwards, the solution or the mixture is decompressed to form the liposomes containing the drug.

Preparation of liposomes encapsulating water-soluble compounds using supercritical carbon dioxide has also been reported [88]. The encapsulation method involves dissolving the lipid components (1-palmityl-2-oleoyl phosphatidylcholine (PoPc) and cholesterol, 7:3 molar ratio) under pressure in supercritical carbon dioxide. The homogenous supercritical solution is expanded and simultaneously mixed with the aqueous phase containing the water-soluble compound to form liposomes encapsulating the compound. Liposomes with average diameter of 200 nm with an encapsulating efficiency of 20% could be reproducibly prepared. The amount of organic solvent used compared to conventional preparation methods could be considerably reduced.

Scale up

The experimental scale of the majority of the gas antisolvent studies has involved high-pressure precipitation vessels of about 50-100 mL in volume, with a sight gauge to enable visual observations during operation. The ASES process has been scaled up to a 50-L precipitation vessel that has been used in the generation of microparticles of PLA [71]. Recently the SEDS particle formation process has been scaled from a 50 mL laboratory vessel through a pilot plant of 1-10 L and to a small manufacturing plant. It was reported that the size and solid state properties of each scale of manufacture are comparable to the targeted mean sizes ranging from sub-micron to 20 μm [89]. A production plant for gas antisolvent crystallisation was scaled up to a 250 L crystalliser in which the drug solution is fed into the crystalliser via a nozzle system with a consumption of 2-3 kg antisolvent per kg of solid product [86].

Conclusions

Supercritical fluids provide a promising option for designing stable protein formulations. They also offer alternative means of processing some peptides and proteins without affecting the activity and integrity of the molecule. Supercritical fluid technology provides a processing option for size reduction and recrystallisation of pharmaceuticals in a single step operation. It also provides a solvent free alternative to traditional microencapsulation techniques. The research on protein encapsulation is still in its infancy. For coating operations, the solid content in coating solutions can be significantly increased by employing supercritical fluids.

Rapid expansion of supercritical fluids and supercritical antisolvent recrystallisation are techniques which are capable of generating micron-sized particles suitable for special delivery systems. Many factors have to be considered in the selection of the appropriate technique. Based on the need for reasonably high drug solubilities in SCFs to make RESS commercially viable, it appears that the antisolvent recrystallisation techniques may be more broadly applicable.

Despite recent advances in the development of SCF techniques, fundamental studies on phase behaviour and mass transfer information that are required to obtain a reliable picture of the process are lacking. Models validated on reliable sets of experimental data are also required to enable the scale-up to industrial scales. However, the process has already proved to be very effective in several fields. The achievements so far will be the driving force for further effort in scaling up this technology.

Acknowledgments

The financial support of the Australian Research Council (Ref. A89800901) is greatly acknowledged. The authors thank Dr. Terry Sweeney (Genentech Inc., USA) for the donation of rhDNase solution, Tony Romeo for technical support on the SEM, and Nora Chew for assistance in sizing on Malvern Mastersizer. Rana Bustami would like to acknowledge the provision by the Australian Government of a Postgraduate Research Award.

Nomenclature

ASES	: aerosol solvent extraction system
$CCLF_3$	: trifluorochloromethane
$CHCLF_2$	: difluorochloromethane
CH_2CL_2	: methylene chloride
CHF_3	: fluoroform
CO_2	: carbon dioxide
DMF	: dimethylformamide
DMSO	: dimethylsulfoxide
HYAFF-11	: hyaluronic acid ethyl ester

P_C : critical pressure
PCA : precipitation with compressed antisolvents
PGA : poly(glycolic acid)
PLA : poly(lactic acid)
PLGA : poly(lactide-co-glycolic acid)
RESS : rapid expansion of supercritical solution
rhDNase : recombinant human deoxyribonuclease
rhIG : recombinant human immunoglobulin
SAS : supercritical antisolvent
SCF : supercritical fluid
SEDS : solution-enhanced dispersion by supercritical fluids
SFDD : supercritical fluid drug delivery
SFT : supercritical fluid technology
T_b : boiling point temperature
T_C : critical temperature
THF : tetrahydrofuran.

References

1) McHugh M.A. and Krukonis V.J.: "Supercritical Fluid Extraction: Principles and Practice", 2nd ed., Butterwoth-Heinemann, Boston, (1994).
2) Hannay J.B., and Hogarth, J.: Proc. Royal Soc. London, 29. 324 (1879).
3) Smith, R.D.: US Patent 4,582,731 (1986).
4) Philips, E.M., Stella, V.J.: Int. J. Pharm., 94. 1 (1993).
5) Tom, J., Debenedetti, P.G.: Biotechnol Prog., 7. 403 (1991).
6) Tom J., Debenedetti, P.G.: J Aerosol Sci., 22, 555 (1991).
7) Alessi P, Cortesi, A., Kikic, I., Foster, N.R., Macnaughton, S.J., Colombo, I.: Ind. Eng. Chem. Res., 35. 4718 (1996).
8) Tom J.W, Debenedetti, P.G., Jerome, R.: J. Supercrit. Fluids, 7. 9 (1994).
9) Kim J.H., Paxton, T.E., Tomasko, D.L.: Biotechnol. Prog., 12. 650 (1996).
10) Domingo C, Berends, E.M., Van Rosmalen, G.M.: J. Supercrit. Fluids, 10. 39 (1997).
11) Yeo S.D., Debenedetti, P.G., Radosz, M., Schmidt, H.W: Macromolecules, 26. 6207 (1993).
12) Fischer W.M., Muller, B.W.: US patent 5,043,280 (1991).
13) Subramaniam B.R, Rajewski, R.A., Snavely, K.: J Pharm Sci., 86. 885 (1997).
14) Gallagher P.C, Coffey, M.P., Krukonis, V.J.: J. Supercrit. Fluids, 5. 130 (1992).
15) Thiering R.D., Dehghani, F., Dillow, A., Foster, N.R.: J. Chem. Technol. and Biotechnol, 75. 1 (1999).
16) Gallagher-Wetmore P.C., Coffey, M.P. Krukonis,V.: Respiratory Drug Delivery IV. 287 (1994).
17) Benedetti, L.B., Bertucco, A., Pallado, P.: Biotechnol. and Bioeng., 53. 232 (1997).
18) Yeo, S.L., Lim, G.B., Debenedetti, P.G., Bernstein, H.: Biotechnol and Bioeng., 4. 341 (1993).
19) Schmitt, W.J.: WO Patent 900037728A3 (1990).
20) Randolph, T.R., Randolph, A.D., Mebes, M., Yeung, S.: Biotechnol. Prog., 9. 429 (1993).
21) Subramaniam, B.R., Saim, S., Rajewski, A., Stella, V.: US Patent 5,874,029 (1999).
22) Bustami, R.T., Chan, H-K., Dehghani, F., Foster, N.R.: Pharm Res, 17. 1360 (2000).
23) Gilbert DP, Palakodaty, S. Sloan, R., York, P. Particle Engineering for Pharmaceutical Applications: The 5th International Symposium on Supercritical Fluids, Atlanta, Georgia, USA: 1 (2000).
24) Hanna, M., York, P.: WO Patent 9501221A1 (1995).
25) Mawson, S., Kanakia, S., Johnston, K.P.: J App Polym Sci., 64. 2105 (1997).
26) Sze Tu, L., Dehghani, F., Foster, N.R.: Powder Technol., in press.
27) Palakodaty, S., York, P.: Pharm. Res., 16. 976 (1999).
28) Hyberston B.M., Repine, J.E., Beehler, C.J., Rutledge, K.S., Lagalante, A.F., Sievers, R.E.: J Aerosol Med, 6. 275 (1993).
29) Sievers, R., Karst, U., Milewski, P.D. Sellers, S.P. Miles, B.A., Schaefer, J.D., Stoldt, C R. Xu, CY: Aerosol Sci Technol., 30. 3 (1999).
30) Sievers, R.E, Hyberston, B.M., Hansen, B.N.: US Patent 5,301,664 (1994).
31) Sievers, R.E, Hyberston, B.N.: US Patent 5,639,441 (1997).
32) Sand, M.L.: US Patent 4,678,684 (1987).
33) Carli F.: WO Patent, 99/25322 (1999).
34) Charoenchaitrakool, M., Dehghani, F., Foster, N.R., Chan, H.K.: Ind. Eng. Chem. Res., 39. 4794-4802 (2000).
35) Loth, H. and Hemgesberg, E.: Int J Pharm., 32. 265 (1986).
36) Larson, K.A. and King, M.L.: Biotechnol. Prog., 2. 73 (1986).
37) Tom, J.W. and Debenedetti, P.G.: Polym Prepr., 33. 104 (1992).
38) Reverchon, E., Donsi, G., Gorgoglione, D.: J Supercrit Fluids, 6. 241 (1993).
39) Subra, P. and Debenedetti, P.: Process Technol. Proc., 12. 49 (1996).
40) Ksibi, H., Subra, P., Garrabos, Y.: Adv Powder Technol., 6. 25 (1995).
41) Reverchon E, Della Porta G, Taddeo R: Ind Eng Chem Res., 34. 4087 (1995).
42) Young, T.J., Mawson, S., Johnston, K.P., Henriksen, I.B., Pace, G.W., Mishra, A.K.: Biotechnol. Prog., 16. 402 (2000).
43) Debenedetti, P.G., Tom, J.W., Yeo, S.D., Lim, G.B.: J Control Rel., 24. 27 (1993).
44) Debenedetti, P.G., Lim, G-B, Prud'homme, R.K.: US Patent 6,063,910 (2000).
45) Tom, J.W., Lim, G-B., Debenedetti, P.G., Prudhomme, R.K.: Supercritical Fluid Engineering Fundamentals and aplications, Kiran, E. and Brennecke, J.F. eds (1993).
46) Yeo, S-D, Lim, G-B, Debenedetti, P.G., Bernstein, H.: Biotechnol Bioeng., 41. 341 (1993).
47) Yeo, S-D, Debenedetti, P.G., Patro, S.Y., Przybycien,

T.M.: J Pharm Sci., 83. 1651 (1994).
48) Schmitt, W.J., Salada, M.C., Shook G.G., Speaker, S.M.: AICHE., 41. 2476 (1995).
49) Winters, M.A., Knutson, B.L, Debenedetti, P.G., et al.: J Pharm Sci., 85. 586 (1996).
50) York, P., Hanna, M.: WO Patent 6501324A1 (1995).
51) Steckel, H., Thies, J., Muller, B.W.: Int J Pharm., 152. 99 (1997).
52) Jaarmo, S., Rantakyla, M., Aaltonen, O., Particle Tailoring with Supercritical Fluids: Production of Amorphous Pharmaceutical Particles: Proceedings of the 4th International Symposium on Supercritical Fluids, Sendai, Japan, 263 (1998).
53) Sloan, R., Hollowood, H.E., Hupreys, G.O., Ashraf, W., York, P., Supercritical Fluid Processing: Preparation of Stable Protein Particle: Proceedings of the 5th meeting on Supercritical Fluids, France. 301 (1998).
54) Sloan, R., Tservistas, M., Hollowood, M.E., et al., Controlled Particle Formation of Biological Material Using Supercritical Fluids: Proceedings of the 6th Meeting on Supercritical Fluids, Nottingham, United Kingdom, 169 (1999).
55) Kulshreshtha, A.K., Smith, G.G., Anderson, S.D., Krukonis, V.J.: US Patent 5,803,966 (1998).
56) Manning, M.C., Randolph, T.W., Shefter, E., Falk, R.F.: US Patent 5,770,559 (1998).
57) Palakodaty, S., York, P., Pritchard, J.: Pharm Res., 15. 1835 (1998).
58) Subramaniam, B., Saim, S., Rajewski, R.A., Stella, V.: US Patent 5,833,891 (1998).
59) Hanna, M., York, P.: US Patent 5,851,453 (1998).
60) Hanna, M., York, P.: US Patent 6,063,138 (2000).
61) Shekunov, B.Y., Hanna, M., York, P.: J Cryst Growth, 198/199. 1345 (1999).
62) Reverchon, E., Porta, D.G.: Powder Technol., 106. 23-29 (1999).
63) Reverchon, E., Porta, D.G., Falivene, M.G.: J Supercrit Fluids, 17. 239 (2000).
64) Wubbolts, F.E., Bruinsma, O.S.L., Van Rosmalen, G.M.: J Cryst Growth, 198/199. 767 (1999).
65) Nesta, D.P., Elliott, J.S., Warr, J.P.: Biotechnol Bioeng. 67. 457 (2000).
66) Bustami R.T., Chan, H-K, Dehghani, F., Foster, N.R., Improvement of Griseofulvin Dissolution Characteristics using Supercritical Fluid Technology: The proceedings of the Australasian Pharmaceutical Scientists Association meeting, Newcastle, Australia. 34 (2000).
67) Bustami R.T., Jiang X., Chan H-K., Dehghani F., Foster N.R., Dissolution Characteristics of Poorly Water-Soluble Drugs Micronized by Supercritical Fluid Technology: The proceedings of the American Association of Pharmaceutical Scientists meeting, Indianapolis, USA (2000).
68) Winters, M.A., Debenedetti, P.G., Carey, C., Sparks, H.G., Sane, S.U., Przybycien, T.M.: Pharm Res., 14. 1370 (1997).
69) Ruchatz, F., Kleinebudde, P., Muller, B.W.: J Pharm Sci., 86. 101 (1997).
70) Bodmeier, R., Wang, H., Dixon, D.J., Mawson, S., Johnston, K.P.: Pharm Res., 12. 1211 (1995).
71) Thies, J.M. and Muller, B.W.: Eur J Pharm Biopharm., 45. 67-74 (1998).
72) Bleich, J., Muller, B.W., Wassmus, W.: Int J Pharm., 97. 111 (1993).
73) Bleich, J., Muller, B.W.: J Microencapsul., 13. 131 (1996).
74) Bleich, J., Kleinbudde, P., Muller, B.W.: Int J Pharm., 106. 77 (1994).
75) Chou Y-H and Tomasko D.L.: Proceedings of the 4th International Symposium on Supercritical Fluids, Sendai, Japan: 55 (1997).
76) Elvassore, N., Bertucco, A., Caliceti, P., Production of Protein-Polymer Micro-Capsules by Supercritical Anti-Solvent Techniques: Proceedings of the 5th International Symposium on Supercritical Fluids, Atlanta, USA. 1 (2000).
77) Engwicht, A., Girreser, U., Muller, B.W.: Int J Pharm., 185. 61 (1999).
78) Falk, R., Randolph, T.W., Meyer, J.D., Kelly, R.M., Manning, M.C.: J Control Rel., 44. 77 (1997).
79) Falk, R.F., Randolph, T.W.: Pharm Res., 15. 1233 (1998).
80) Meyer, J.D., Falk, R.F., Kelly, R.M., et al.: J Pharm Sci., 87. 1149 (1998).
81) Johnston K.P., Luna-Barcenas G., Dixon D., Mawson S., Polymeric Materials by Precipitation with a Compressed Fluid Anti-Solvent: Proceedings of the 3rd International Symposium on Supercritical Fluids, Strasbourg, France. 359 (1994).
82) Young, T.J., Johnston, K.P., Mishima, K., Tanaka, H.: J Pharm Sci., 88. 640 (1999).
83) Hees, T.V., Piel, G., Evrard, B., Otte, X., Thunus, L., Delattre, L.: Pharm Res., 16. 1864 (1999).
84) Lindsay, A.D., Omilinsky, B.A.: US Patent 5,169,433 (1992).
85) Ksibi, H., Subra, P.: Adv. Powder Technol., 7. 21 (1996).
86) Weber, A., Tschernjaew, J., Kummel, R., A Production Plant for Gas Antisolvent Crystallization: Proceedings of the 5th Meeting on Supercritical Fluids, Nice, France. 281 (1998).
87) Castor, T.P., Chu, L.: US Patent 5,776,486 (1998).
88) Frederiksen, L., Anton, K., Van Hoogevest, P., Keller, H.R., Leuenberger, H.: J Pharm Sci., 86. 921 (1997).
89) Walker, S.E., Palakodaty, S., Gilbert, D., Townend, G.M, York, P., Process Development Experience in Particle Formation With a Supercritical Fluid Plant: The proceedings of the American Association of Pharmaceutical Scientists meeting, Indianapolis, USA (2000).

Author's short biography

Rana T. Bustami

Rana Bustami received her B.S. in pharmacy from University of Jordan. Following her graduation, she joined the Arab Pharmaceutical Manufacturing Co. where she was involved in the development of stability indicating assays and then in the development of sustained release dosage forms for wide range of pharmaceuticals. She received her graduate diploma in science from the University of Sydney in 1997. Rana has recently submitted her PhD Thesis titled The Application of Supercritical Fluid Technology in the Micronisation of Pharmaceuticals.

Hak-Kim Chan

For photo & biography, please refer to the accompanying article to KONA "Pharmaceutical Dry Powder Aerosol Delivery" by Nora YK Chew & Hak-Kim Chan to be published in this volume (No.19, 2001)

Fariba Dehghani

Fariba Dehghani received her B.S. and M.S. in chemical engineering from the Shiraz University in Iran. For her Masters she worked on the "Evaluation of CORGC Equation of State for Prediction of Thermodynamic Properties of Polar and Nonpolar Compounds" under the direction of Prof. M. Moshfeghian. She received her PhD in chemical engineering from the University of New South Wales in 1996 under the supervision of Prof. Neil R. Foster concerned the "Extraction of Rare Earth Metals Using the Dense Gas Process". Following her graduation she continues research on application of dense gases for processing fine chemicals as a senior research scientist at the University of New South Wales. Her research involves sterilization, micronisation / crystallization of pharmaceutical compounds, study the solute-solvent interaction in supercritical fluids.

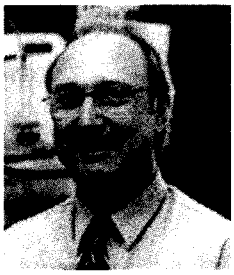

Neil R. Foster

Neil Foster received his B.S. and PhD in Chemical Technology from the University of New South Wales. His PhD research involved heterogeneous oxidation of aromatic organics. Following his graduation he completed a postdoctoral year at McMaster University, Canada, where he was involved in polymer reaction engineering. In 1979 he returned to Australia to take up an appointment with CSIRO where he was involved in the Fossil Fuels Liquefaction program which involved high temperature, high pressure reaction engineering. Neil returned to the University of New South Wales in 1986 and is currently Professor of Chemical Engineering and leads the UNSW Supercritical Fluids Research Group. The major focus of current work is the formulation of novel delivery systems for therapeutic drugs using dense gas technology. Neil has published more than 150 scientific and technical papers and is currently working closely with an industry partner, Eiffel Technologies Limited (a publicly listed Australian company) to develop and commercialise dense gas technology applications for processing of pharmaceuticals.

The Potential of Phase-Doppler Anemometry†

Klaus Bauckhage
*Stiftung Institut für Werkstofftechnik (IWT)**

Abstract

Phase-Doppler anemometry (PDA) is a well-established optical measuring technique for the non-intrusive and simultaneous determination of size and velocity of spherical particles in various engineering processes. The design of a phase-Doppler system includes simulations based on the Mie theory, which describe the scattering of a plane wave by a spherical particle. Although the greater number of particles in technical processes or in the natural environment are non-spherical, the real shape is neglected and the particles are assumed to be perfectly spherical, with smooth surfaces, and to consist of homogeneous materials. In practice, it was found that the size-response of a phase-Doppler system deviates from the theoretical prediction when these assumptions are not fulfilled. In this paper, optical arrangements and adaptations of theories of light scattering will be discussed which utilize these deviations to provide even more information on the nature of the particles being examined.

1. Introduction

The main field of successful PDA application has been established in the atomization of liquids in connection with heat and mass transfer processes. Research has focused mainly on spray analysis and droplet transport of pure liquids (e.g. water, fuels and organic liquids) in gaseous two-phase flows. Good progresses were made in this area not only in process automation, but also in high-precision on-line and in-line measurements [1 to 6]. This is not surprising, since in most of these cases, the real shape of, e.g. water droplets in air, is indeed perfectly spherical, and the particulate material is homogeneous, thus fulfilling the main assumptions of the *Mie* theory.

On the other hand, adaptations of the optical set-up have to be provided for measuring droplets of opaque (absorbing) fluids, of metal melts, or (instead of pure liquids) droplets which contain inclusions – so-called optical inhomogeneities. Problems may also occur due to the surface roughness of solid particles. Therefore, it is in many cases helpful to use light scattering simulations based on geometrical optics (GO) and the *Mie* theory for the design and arrangement, and finally for optimisation, of the optical set-up prior to taking measurements.

The assumption that PDA measurements from single particles may apply as absolute measures has to be given up when particle collectives such as sprays or powders need analysing, resulting in measured size distributions which often contain under-representations of the fine particle spectrum.

The purpose of this paper, after a short explanation of the standard PDA set-up and a brief discussion about the necessity of optimisation of PDA arrangements (against the background of small particles), is to outline the problems of inhomogeneous and deformed droplets and the rough surfaces of particles, because these give rise to a number of problems in spray analysis. Since the sizing errors of larger particles caused by the *Gaussian* beam effect of the intensity distribution of the laser beams are widely described and can be eliminated either by upgraded PDA arrangements or by special signal post-processing programs, this aspect needs no discussion here.

2. Standard PDA set-up

A PDA system in its most simple form is made up of two laser beams and two optical detectors. The schematic of such a standard PDA system is shown in **Fig. 1**. (Commercial PDA systems often employ a

* Bremen, Germany
† Accepted: September 17, 2001

third or a fourth detector to allow cross-validation of the individual results.) The two laser beams intersect and define the optical probe volume, which can be interpreted as consisting of parallel planes of alternating light intensity resulting from interference of the laser beams. Particles passing this intersection volume scatter the light of both incident laser beams. Interference between the scattered light leads to the detection of so called bursts by two optical receivers (PM1 and PM2). The main frequency $f_D=1/T$ of these bursts is a measure of the particle velocity component v_z, while a temporal delay between the signals ΔT (or phase-difference $\Delta\Phi$) can be related to particle diameter d by means of appropriate light scattering computations. As long as individual particles moving through the probe volume are spherical, homogeneous and clearly larger than the laser wavelength λ of the laser, the intensity of the scattered light is strong enough to be detected without any difficulty.

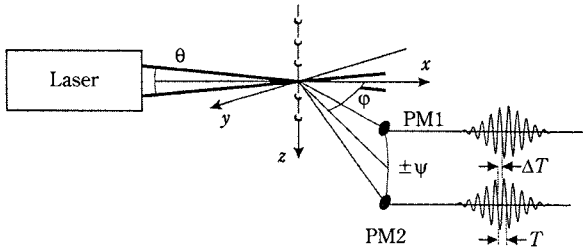

Fig. 1 Set-up of a standard phase-Doppler anemometer (with two optical receivers). Definition of beam-crossing angle θ, elevation angles ψ, and off-axis angle φ. The phase-difference is defined as $\Delta\Phi = 2\pi\Delta T/T$

Furthermore, for defining an optimal arrangement of the set-up, a careful analysis of the performance characteristics of the instrumentation system with respect to the measuring task is required. This holds true for the positions of the detectors (the off-axis angle φ, and the elevation angles ψ are the important parameters) and the beam configuration system (laser wavelength λ, power P, beam waist radius ω, and beam-crossing angle ϕ). These parameters should be chosen mainly according to the particulate material (i.e. the refractive index $m=n+k\,i$) and the individual size range of the particles. The relation between the measured phase-difference $\Delta\Phi$ and the particle diameter d is linear as given in Equation (1) in **Table 1**. The exact relation can be obtained in a closed form from geometrical optics for solely reflecting (Eq. 2) or refracting (Eq. 3) particles as given in **Table 1**, where the relative refractive index (i.e. the ratio of the refractive indices of the dispersed (droplet) phase to the continuous (bulk) phase $n'=n_d/n_c$) is given by Equation (4) [7 and 8].

3. Optimisation of the PDA arrangement

In order to determine the optimal arrangement of the two detectors to suit the measuring problem, one has to recall some fundamentals of light scattering by a spherical particle, starting with light scattering simulations based on geometrical optics (GO) and the *Mie* theory. Such simulation tools have been used, e.g. [9 and 10], plotting for instance polar diagrams, as given in **Fig. 2** for a water droplet in air ($n=1.333$; $k=0$) and a tin melt droplet in nitrogen ($n=2.100$; $k=4.5$). The laser beam (from the left) has a wavelength of $\lambda=0.632$ µm and the drop diameter is $d=50$ µm. The radial axis of each diagram shows the intensity of

Table 1 Equations for the droplet diameter, based on geometrical optics

$d=\frac{1}{2b}\left(\frac{\lambda}{\pi n_c}\right)\Delta\Phi$	(1)
$b_{\text{Reflex.}}=\sqrt{2}\left[\left(1+\sin\frac{\theta}{2}\sin\Psi-\cos\frac{\theta}{2}\cos\Psi\cos\varphi\right)^{\frac{1}{2}}-\right.$ $\left.-\left(1-\sin\frac{\theta}{2}\sin\Psi-\cos\frac{\theta}{2}\cos\Psi\cos\varphi\right)^{\frac{1}{2}}\right]$	(2)
$b_{\text{Brech.}}=2\left\{\left[1+n'^2-\sqrt{2}n'\left(1+\sin\frac{\theta}{2}\sin\Psi+\cos\frac{\theta}{2}\cos\Psi\cos\varphi\right)^{\frac{1}{2}}\right]^{\frac{1}{2}}-\right.$ $\left.-\left[1+n'^2-\sqrt{2}n'\left(1-\sin\frac{\theta}{2}\sin\Psi+\cos\frac{\theta}{2}\cos\Psi\cos\varphi\right)^{\frac{1}{2}}\right]^{\frac{1}{2}}\right\}$	(3)
$n'=\frac{n_d}{n_c}$	(4)

the scattered light in a logarithmic scale versus the off-axis angle φ.

Mie calculations make no distinction between the different light components (the results are given in **Fig. 2a** as sectional views in two main planes of a hemisphere around the scattering particle in its centre). On the other hand, under geometrically optimal conditions, the light intensities may be differentiated, being plotted as either diffracted (**Fig. 2b**), refracted (**Fig. 2c**) or reflected (**Fig. 2d**) light components. (The lower part of the diagram holds true for parallel polarised light, the upper part for perpendicular polarisation). Particle sizing has to be executed out of the diffraction domain (off-axis angles φ up to 10°), otherwise phase-differences do not appear.

The message from these plots (**Fig. 2 a to d**) is that transparent (pure) liquids should be measured under off-axis angles $10° < \varphi < 60°$ (70° for parallel polarised light) using the refraction domain.

In the case of non-transparent particles with an absorption factor $k > 0$ of the refractive index, where the intensity of the refracted light portion is diminished and reflection becomes more and more dominant, the comprehensive simulation of light scattering becomes compulsory in order to find the best off-axis configuration for the set-up. This will be discussed in detail below, when the Gain/φ-diagram [11 and 12] will be introduced.

Small droplets of molten metal are also spherical in shape because of their high surface tension. The high

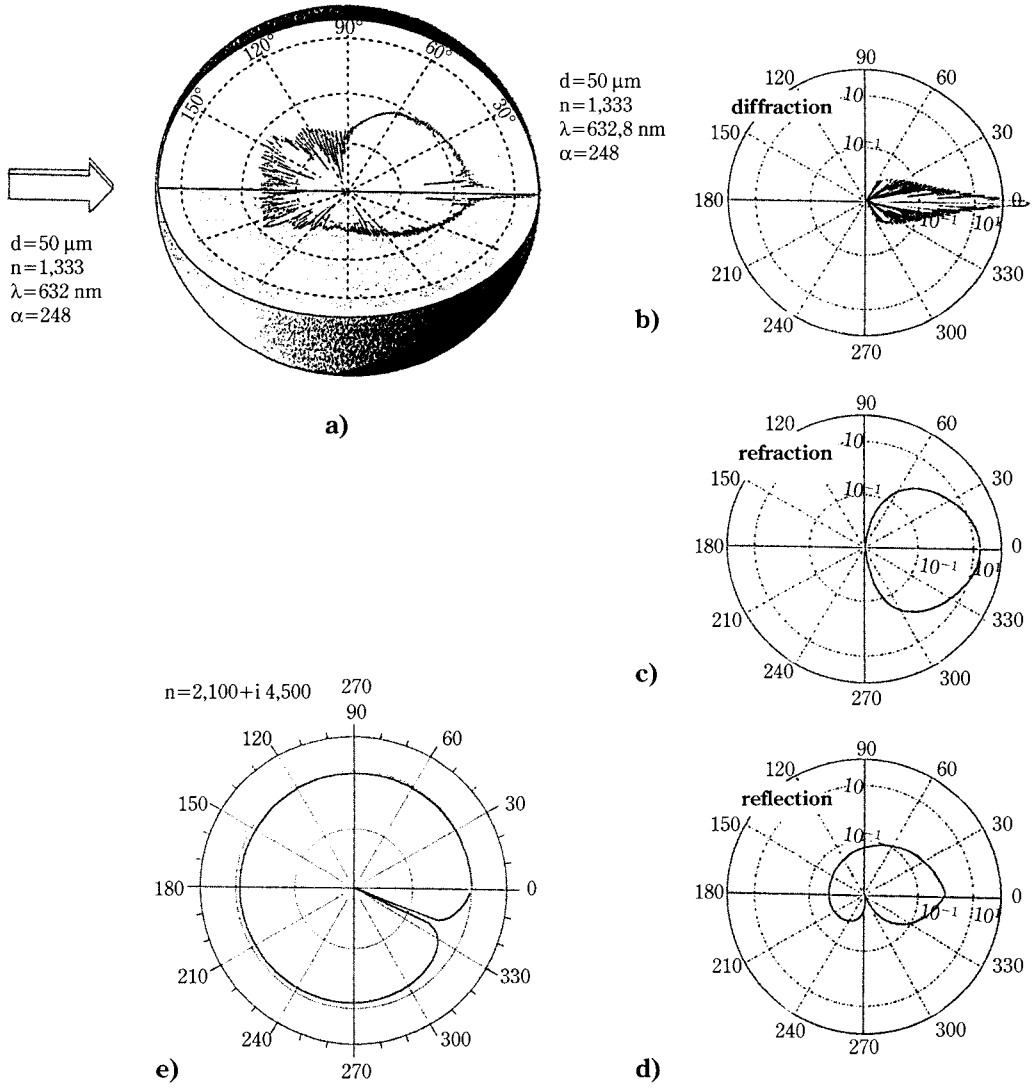

Fig. 2 Results from *Mie*-calculations a) and from GO-calculations b) to e) for light scattering of a droplet in air a) to d) $\{n=1.333; k=0\}$ and a tin melt droplet in nitrogen e) $\{n=2.100; k=4.5\}$ $d=50$ µm; $\lambda=0.632$ µm

imaginary part of their refractive index (e.g. for a tin droplet: $n=2.100+4.5$ i) causes a strong and sole domain of reflection for all off-axis angles in the polar diagram (**Fig. 2e**). This holds true for angles φ from 10° to 180°, enlarging the arrangement facility of the PDA receivers significantly, and allowing observation of the particles, for instance, from a back-scatter position [13 to 15].

Polar diagrams can even be plotted to specify the liquid droplet scattering behaviour in liquid environments, e.g. describing details of liquid/liquid extraction processes, where the relative refractive index ($n'=n_d/n_c$) approximates values of 1 [16 to 18]. Such plots allow a decision to be made on whether PDA measurements make sense, and if so, from which angular position the droplets should be observed, and whether the droplets have to be treated as refracting or reflecting particles. It is worth mentioning that the off-axis angles from these computations generally have to be set equal to those off-axis angles of the PDA detectors in relation to the measuring volume, i.e. to the droplet to be measured.

Prior to measurement, further simulation results (not shown here) may describe the expected phase-difference as $\Delta\Phi(\varphi, d)$ diagrams, the expected visibility as $V(\varphi, d)$ diagrams or the Gain (shown below), etc. Examples of these auxiliary diagrams are given in [19 and 20].

4. PDA for small particles

As can be seen from the more general **Fig. 3**, two intrinsic problems arise for the PDA technique with respect to small particles with diameters comparable to λ and below this value: a) there is a steady decrease of the scattered light intensity $I(d)$ with decreasing diameters; thus for a fixed detector sensitivity and with incident power restricted to a reasonable level, this fact limits the applicability of PDA as well as of any other optical sizing technique; and b) the phase-difference also decreases rapidly with decreasing particle diameters. Though $\Delta\Phi(d)$ can be shifted to higher values by increasing the elevation angles ψ of the two detectors, a minimum d-value obtained from the final minimum resolvable phase difference nevertheless ultimately results. Actual minimum values depend on set-up parameters and detector sensitivity. As can be concluded from **Fig. 3**, conductive (metallic) particles yield higher phase-differences than transparent ones in the submicron range, thus diminishing the above-mentioned difficulties significantly [21].

Two types of oscillations in the $\Delta\Phi(d)$ curves (**Fig. 3**) can be a severe hindrance to a direct conversion of a measured phase-difference to a sphere diameter. For transparent particles, interference between refracted and reflected scattering components causes these oscillations for $d < 10$ µm. The oscillations can be reduced to a minimum mainly by *Brewster* reflection suppression, via smoothing by means of large detector apertures or asymmetric set-up arrangements [22]. These "high-frequency" oscillations cause an increasing source of uncertainty in the data evaluation process.

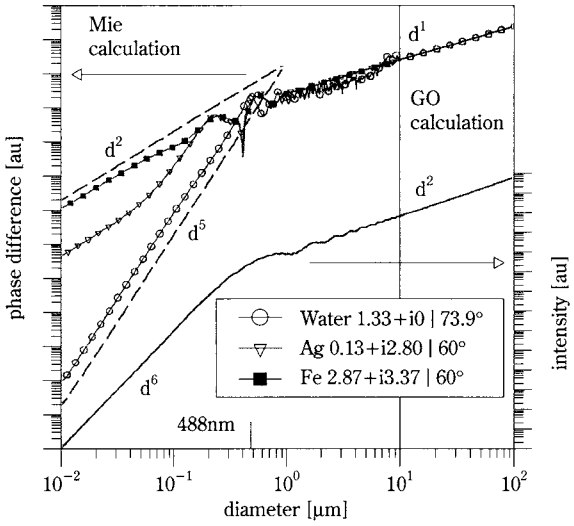

Fig. 3 ΔΦ (left axis) and scattered intensity I (right axis) versus particle diameter d for $\lambda=0.488$ µm, various materials and off-axis angles φ. *Mie* calculations have been performed for diameters $d < 10$ µm for water, Ag and Fe. For $d > 10$ µm, the geometrical optics results have been used

The other type of ambiguity can be observed from the small-particle limit for both transparent and absorbing particles. Here, rather "low-frequency" oscillations are obvious in the transition range between the exponential power law behaviour and the linear $\Delta\Phi(d)$ relation. This type of ambiguity can be reconstructed experimentally in detail [23]. Both types have to be considered during conversion of phase-difference to diameter.

Small-particle light scattering is associated with small scattering cross-sections, small phase-differences, and ambiguity in the form of oscillatory $\Delta\Phi(d)$ relations. This can be seen from **Fig. 3**, where $|\Delta\Phi|$ (holding true for both reflected and refracted light) and the scattered intensities I are depicted versus d

for a large diameter range in a log-log diagram [24]. *Mie* calculations have been performed for diameters $d < 10$ µm for water (transparent), Ag, and Fe (both with imaginary parts of the refractive index m). For $d > 10$ µm, the geometrical optics results (GO) have been used. Well-known limiting behaviour is obvious as well as *Mie*-specific resonances at $d \approx \lambda$ (0.488 µm, i.e. the laser wavelength).

5. Non-homogeneous droplets

5.1 Superfine inclusions

Although water atomization may play an important role for, e.g. cooling processes or model experiments, there is also a great demand for spray analysis of real process fluids such as paints, emulsions or suspensions, which have to be atomized in order to yield sufficiently smooth or colourful surfaces or to produce dry and small samples of good consistency. These types of process fluids contain inhomogeneities of varying materials and shapes and of mostly typical size ranges due to the previous process steps. As mentioned above, difficulties arise if the droplets to be measured contain such optical inhomogeneities, because the linear phase-difference/particle diameter relation may be limited or is no longer valid. The size of these inclusions in the bulk fluid differs greatly, but can be classified into superfine particles – of the order of, or smaller than, the wavelength of the laser light λ – and large particles – reaching the range of the droplet diameters. Their refractive index is different from that of the bulk fluid of the droplet, thus influencing the effective refractive index of the composite medium. Since the refractive index of the inhomogeneities usually contains an absorption term (factor $k > 0$ of the imaginary part), this consequently means that the composite medium behaves like a more or less absorbing fluid. As long as these emulsion or suspension droplets are spherical in shape without any bulge in the surface (which might be a result from higher concentrations), PDA can principally be used for spray or droplet analysis [25 to 27].

When using a PDA system to characterize inhomogeneous droplets, the size distributions that are measured are artificially broadened compared with those size distributions of droplets which contain only the pure bulk liquid (without any inhomogeneities). This artificial broadening effect can in most cases be reduced by the proper choice of the laser wavelength [28 and 11]. If not, it was shown that the application of highly sophisticated mathematical algorithms enables the PDA user to reconstruct the real size distribution from the measured one by using the information about the measured droplet size distribution of monosized droplets produced from the pure bulk liquid by a droplet generator, as shown in **Fig. 4** [29 to 31]. Using the Dual-Burst-PDA, it could be shown that it was possible to extract additional information about the concentration of the inhomogeneities from inside the droplet.

Due to the disturbing effect of the dispersed phase inside the droplet on the light scattering, a linear correlation between the phase-difference of the refracted light and the diameter of a single droplet does not, in most cases, exist any longer. Such a correlation only exists for the mean value of all the measured droplets. This effect is obvious when measuring high numbers of droplets of identical diameter. As can be seen from **Fig. 4**, the PDA measurements of 10,000 monosized droplets of either pure bulk liquid or bulk liquid con-

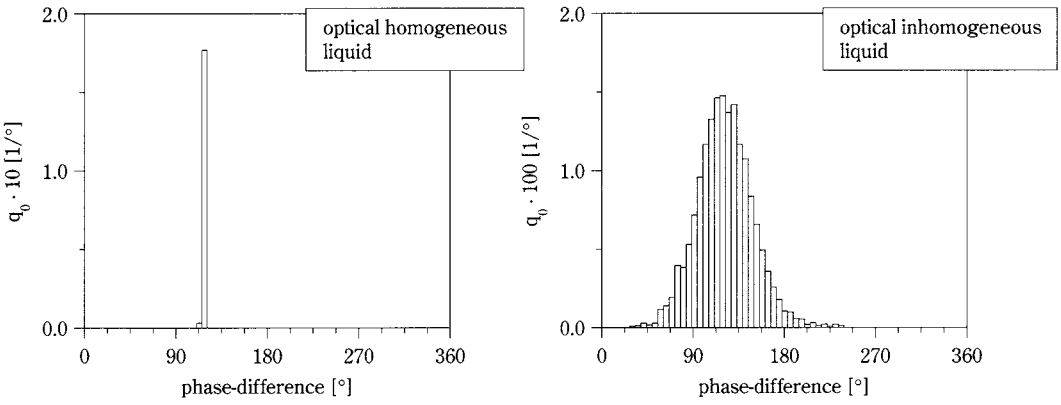

Fig. 4 PDA measurements from monosized optically homogeneous droplets and from droplets of the same bulk liquid – but containing fine inhomogeneities

taining fine inhomogeneities result in quite different distributions. In the case of optically homogeneous droplets, PDA detects nearly the same phase-difference for every droplet. In the case of optically inhomogeneous droplets, the measured phase-difference distribution is broadened into a *Gaussian* function. Using – as usual – only a linear $\Delta\Phi(d)$ correlation to compute the droplet diameter from these phase differences, nothing other than a *Gaussian* distribution is achieved, which is a false interpretation. On the other hand, the simultaneously measured droplet velocity is almost independent of the optical character of the droplets

The standard deviation of such a *Gaussian* distribution depends on the diameter of the dispersed inhomogeneities, on their concentration, and on the parameters of the PDA set-up. Regarding the phase-differences, their spreading can be influenced by the proper choice of a smaller beam-crossing angle ϕ and by off-axis angles φ, describing the domain of reflection (as will be discussed below). The standard deviation is not affected by the elevation angles of the detectors.

The *Mie* theory and other light scattering theories have been expanded in order to simulate the scattering behaviour, but their range of application is still limited either to a few larger particles in the droplet or to droplets with significantly smaller inclusions compared with λ. Recently, by using an independent scattering approximation [32], it was possible to simulate the broadening effect for a latex concentration (d=2 μm) of 2 vol.%. These simulation results agree perfectly with measurement results of the broadening obtained from monosized droplets of a latex suspension produced by a piezoelectric droplet generator.

In spite of this theoretical progress, in most technical applications, inhomogeneities cover a large section within the size range of the laser wavelength. While for monosized droplets the problem seems to be clear and quite easy to discuss, the broadening effect needs further interpretation of the PDA results in the case of polysized droplet sprays of optically inhomogeneous (process) liquids, which normally occur in industrial atomization processes.

Such sprays of solutions, e.g. of coffee and condensed dairy milk (inhomogeneous), in comparison with those of pure water and ink (homogeneous), have been analysed under various – but identical – atomization conditions, using laser wavelengths of between 0.488 and 0.830 μm [25, 26 and 11]. The question was whether the inhomogeneous liquids can be treated as homogeneous ones by using an effective complex refractive index of the composite medium instead of the refractive index of the bulk liquid (mostly water or an organic phase). The answer is that this can be done not only for spherical inclusions (milk), but also for non-spherical ones (coffee), as long as the inclusions are comparable to or smaller than the wavelength of the laser light. But the procedure to estimate the complex relative refractive index of an optically absorbent multicomponent liquid is complicated [11].

These results can be explained by **Fig. 5a)**, where the integrated light intensities per diffracted, refracted and reflected light components are given as Gain versus off-axis angle φ. An increasing value of the absorbent factor in the refractive index k (from 0.001 to 0.010) diminishes the importance of the refracted light, whereas the curves of the diffracted ($\varphi < 36°$) and reflected light ($0° < \varphi < 180°$) remain constant.

If one is forced to detect the scattered light of the droplet (multicomponent liquid) from a forward direction (i.e. the refracted light), this becomes more and more problematic caused, e.g. by an increase of concentration of the inhomogeneities.

Here, one gets another degree of freedom by changing the type of laser, i.e. by applying a laser with a different wavelength λ, thus one can change the *Mie* parameter $\alpha=\pi d/\lambda$, i.e. the ratio between particle circumference and wavelength. This can be explained by **Fig. 5b** where an increase of the particle diameter d causes nearly the same effect (as demonstrated in **Fig. 5a** by the augmentation of the k value). The particle size, given as a *Mie* parameter α varies from 25 to 250. The importance of the refracted light decreases with increasing particle diameter, whereas the curves of the diffracted ($\varphi < 36°$) and reflected light ($10° < \varphi < 180°$) remain constant. Vice versa this means, if the laser wavelength can be changed to higher values of λ, one can remove the problem of absorption of light in the range of visible wavelengths [29 and 33].

This depends – as demonstrated above – on the liquid's absorption properties and allows the linear $d(\Delta\Phi)$ correlation (Equation (1)) to be used. Extrapolating these results – in the case of optically absorbent inhomogeneous liquids – the use of a larger wavelength might be universally advantageous because it reduces scattering by these inhomogeneities inside the droplets. But, as has been shown in [29 and 33], changing to larger wavelengths does not always lead to more realistic results.

On the contrary, the proper selection of the laser

wavelength once again has to be based on *Mie* calculations of the extinction efficiency. Larger wavelengths are the better choice only for low *Mie* parameters ($\alpha \leq 5$), dependent on the refractive index. For larger values of the *Mie* parameter, the relation between the extinction efficiency and the wavelength is ambiguous. In other words, as long as the light intensity is sufficient for PDA analysis, droplets of optically absorbent multicomponent liquids should be analysed under off-axis angles where the reflected light component is dominant.

The experiments with optically absorbent multicomponent media [29 and 33] disclosed the tremendous potential for misinterpretation of PDA results and false droplet size distributions. In addition to milk and coffee and concentrated solutions of latex-water suspensions of definite monosized particles of 0.45, 0.72 and 3.50 µm, the laser wavelengths 0.488 and 0.830 µm, as well as 0.632 and 1.312 µm [33 and 34], were used. For each of these liquids, the results made

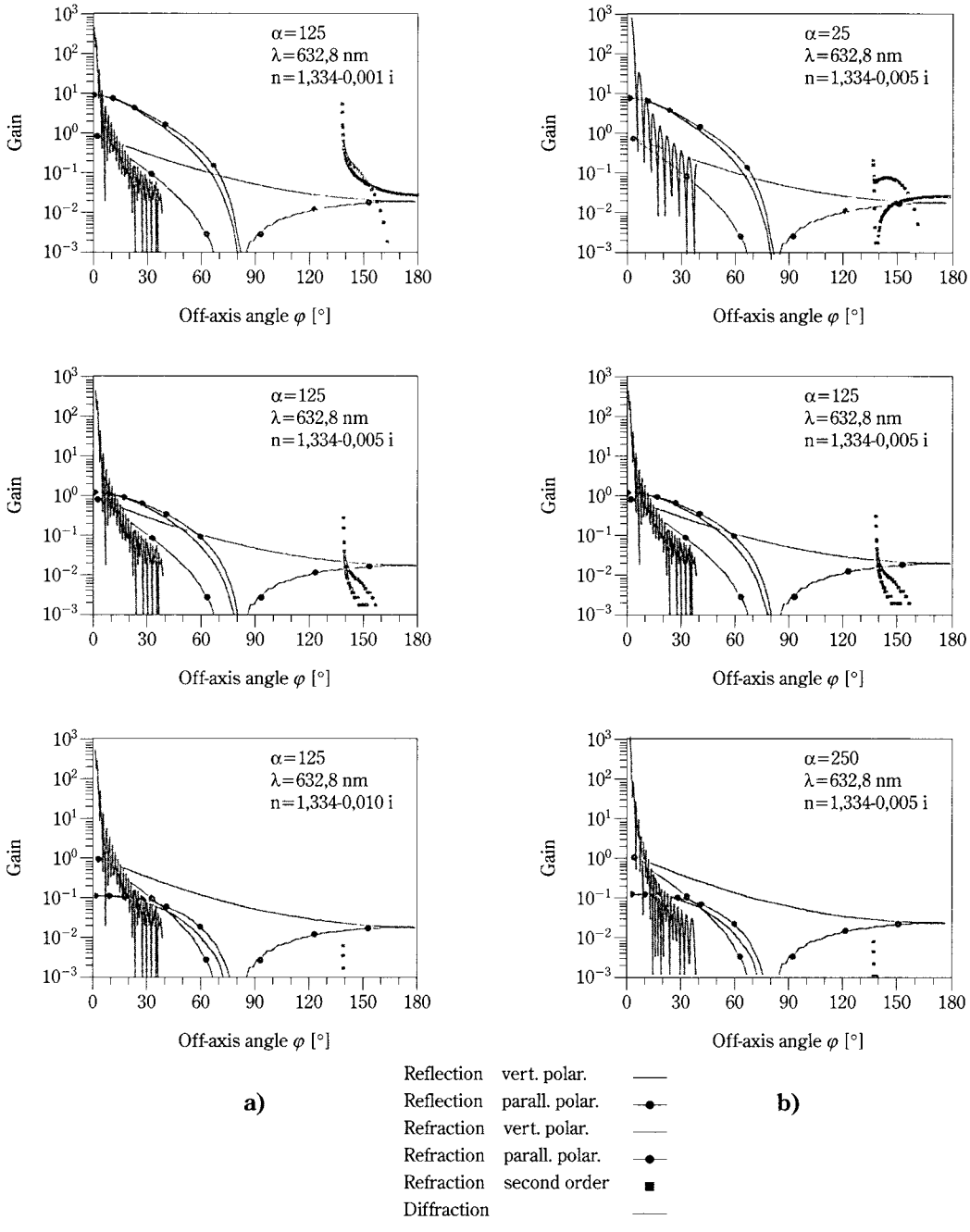

Fig. 5 Gain versus off-axis angle for different *Mie* parameters α and absorption factors k

it necessary to apply mathematical inversion algorithms to finally bring the widely spread data to a realistic droplet size distribution of the measured spray.

5.2 Inclusions in the diameter range of the droplet

Research work in meteorology, medicine, and pharmacy also deal with small droplets containing larger inclusions. PDA applications are, for instance, focused on generation processes of microcapsules which allow ultrasonic diagnostics of the blood circulation, or on capsules that include pharmaceuticals or coloured ink, as well as on coated spheres, e.g. water-coated carbon core particles. Such "droplets" with spherical inclusions that match the range of the droplet diameter cannot be treated as homogeneous ones with an effective complex refractive index (of the composite medium), because these inclusions reveal their own individuality. From the optical point of view, the material combinations of shell and core can be classified as a transparent or absorbent continuous phase including a transparent or absorbent dispersed phase. Research work has been carried out with several of these combinations, defined by their refractive index, respectively [35 to 39]. Using the generalized *Lorenz-Mie* theory, it could be shown by simulating the response of a PDA device that not only the core, but also the outer diameter of the particle could be detected as well as the refractive index profile of a multilayered particle [35].

Replacing the two detectors of the PDA system by a CCD line-scan sensor with, e.g. 256 pixels, allows the detection of 256 signals instead of two, thus capturing the scattered light with high spatial resolution. The phase-difference can be obtained 128 times, using two symmetrical (in relation to $\psi=0°$) pixels respectively as a pair. The CCD line-scan sensor can also be arranged with all its pixels in the ($\psi=0°$)-position, i.e. in the horizontal position instead of the vertical one (**Fig. 6**) [36]. Generally, the evaluation of the resulting signals can be performed in two different ways. The evaluation is either based on the entire signal or on selected parts of the burst, for example the lines of highest intensity in the temporal and spatial dimensions. Using the first alternative, detailed information can be obtained from the scattering process and thus from the particle passing the interference volume. The disadvantage is the high computational time required. The other option, evaluating just one line from the burst, is very fast but rather prone to error.

As outlined in a detailed previous description, using simulation results as well as results of various experiments [39], it is possible to analyse the diameter as well of the core as of the enclosing droplet, thus giving information on the shell thickness, preferring the horizontal arrangement of the CCD line-scan sensor, whereas both arrangements have the potential of exact size determination of, for instance, solid spheres with inhomogeneous composition (glass beads with cracks) or surface defects, whereas the measurable particle velocity for both arrangements is limited at present to approximately 10 ms^{-1}, because of the low scan rate of the CCD camera available.

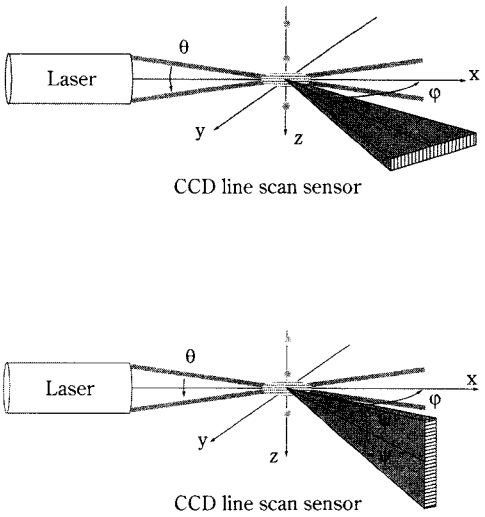

Fig. 6 PDA arrangements with a horizontal or vertical CCD line-scan sensor [39]

5.3 Droplets with radial gradients of the refractive index

Droplets of two or more completely miscible liquids, which are influenced by heat and mass transfer processes (liquid/liquid-extraction, spray combustion, evaporation), show a variation of their integral concentration (average value) with time, causing also a variation of their effective (average) refractive index with time. If their *Biot* number[1], *Bi*, exceeds values of about 1, radial concentration gradients (depending on the material properties of their components) also emerge that cause radial gradients of the effective refractive index of the composition. The change of the average value with time, as well as the variation of the

[1] $Bi=hd/K_{tp}$ for heat transfer with h=heat transfer coefficient and K_{tp}=thermal conductivity of dispersed phase
$Bi=\beta d/D_p$ for mass transfer with β=mass transfer coefficient and D_p=molecular diffusity of dispersed phase

gradients with time, depends on the intensity of the process and on the specification of the components. Both effects can be measured simultaneously, together with particle size and velocity [35; 40 and 41], and can be used for in-line process control. Since a direct correlation exists between the average refractive index and the droplet temperature, these PDA measurements are principally also suitable for in-flight temperature measurements. But improved precision can only be reached by using rainbow interferometry [42 to 44].

6. Deformed spheres

6.1 Spheroidal droplets

Deformation of spherical droplets takes place during droplet generation near a nozzle or within a gaseous atmosphere during accelerated and decelerated droplet motion, whereas even very small forces during droplet motion or during mass transfer may create deviations from the spherical shape within a liquid environment. In the case of axisymmetrical deformation one speaks of spheroids. Since light scattering is influenced mainly by the curvature of the particle surface (liquid/gas or liquid/liquid interface), these deformations create various light patterns from the same particle that result in deformed PDA bursts, leading to ambiguous signal interpretation. In addition, droplet oscillations (causing prolate or oblate shapes) or droplet deceleration and acceleration within the measuring volume give rise to similar burst deformations.

Using Fast-*Fourier*-Transform (FFT)-based signal processing allows an improvement of the signal validation, time-resolved frequency, and phase-difference analysis from the two bursts, and thereby the determination of the burst envelope and phase-difference changes, which results in additional information about the non-spherical droplet character while passing the measuring volume [45 to 47 and 44]. In **Fig. 7**, simulated results show the variation of the phase-difference $\Delta\Phi$ within the bursts of a prolate or oblate droplet with diameters d_v and d_h. In the case of $d_v = d_h$ with $E = d_h/d_v = 1$, the phase-difference $\Delta\Phi$ of an equivolumetric spherical droplet of a diameter of 2 mm is 254°.

A comparison between standard PDA and a planar detector arrangement [48], where the two detectors are placed at (two) elevation angles in the plane of the transmitting beams, demonstrated that non-sphericity of droplets leads to significant changes in the phase-difference, much more so for prolate than for oblate

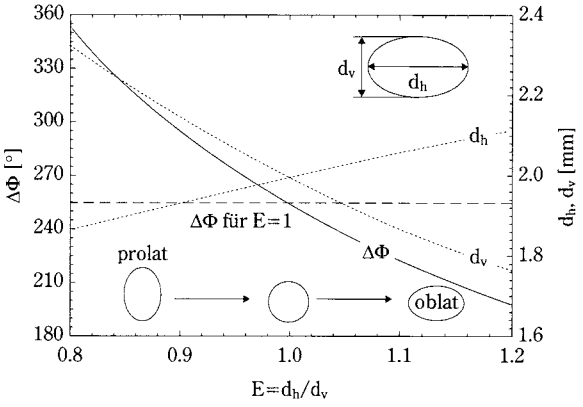

Fig. 7 Computed phase-difference $\Delta\Phi$ (and therefrom diameters d_v and d_h) of deformed droplets versus quotient E of horizontal to vertical droplet diameter after [44]

droplets, and stronger for the standard detector arrangement than for the planar detector arrangement. Increasing the investment, the combination of both standard and planar detector arrangements finally leads to more accurate information about the deformation [48].

6.2 Spheroidal fine particles

Theoretical [49] as well as theoretical and experimental work [50] has been directed at recognizing the potential and the limitations of PDA measurements of fine spheroids. Monodispersed polystyrene latex particles (equivolumetric spheres of diameters of 3.0 and 3.5 µm) were stretched to a predetermined extent in order to convert the spherical particles to spheroids with semi-axes $a = (d/2)\ \varepsilon^{2/3}$ and $b = (d/2)\ \varepsilon^{1/3}$ [49]. These particles were measured as single particles by means of an electrodynamic trap [23] as well as suspended ones in double-distilled water (as flowing suspensions). As can be seen from **Fig. 8**, the electron micrograph shows well-defined monodispersed (polystyrene) spheroids, and the frequency distributions of phase-differences show a good agreement between experiment and simulation.

While liquid droplets (or polystyrene particles) – due to their surface tension – are in general spherical or at least spheroidal in shape, solid (metal) particles show more or less (local) deviations from sphericity. Their surface exhibits structures resulting from the solidification and/or crystallization process. The real particle properties can neither be quantified in detail – in addition there are differences from one particle to another – nor can they be accounted for exactly in the light scattering computations. There-

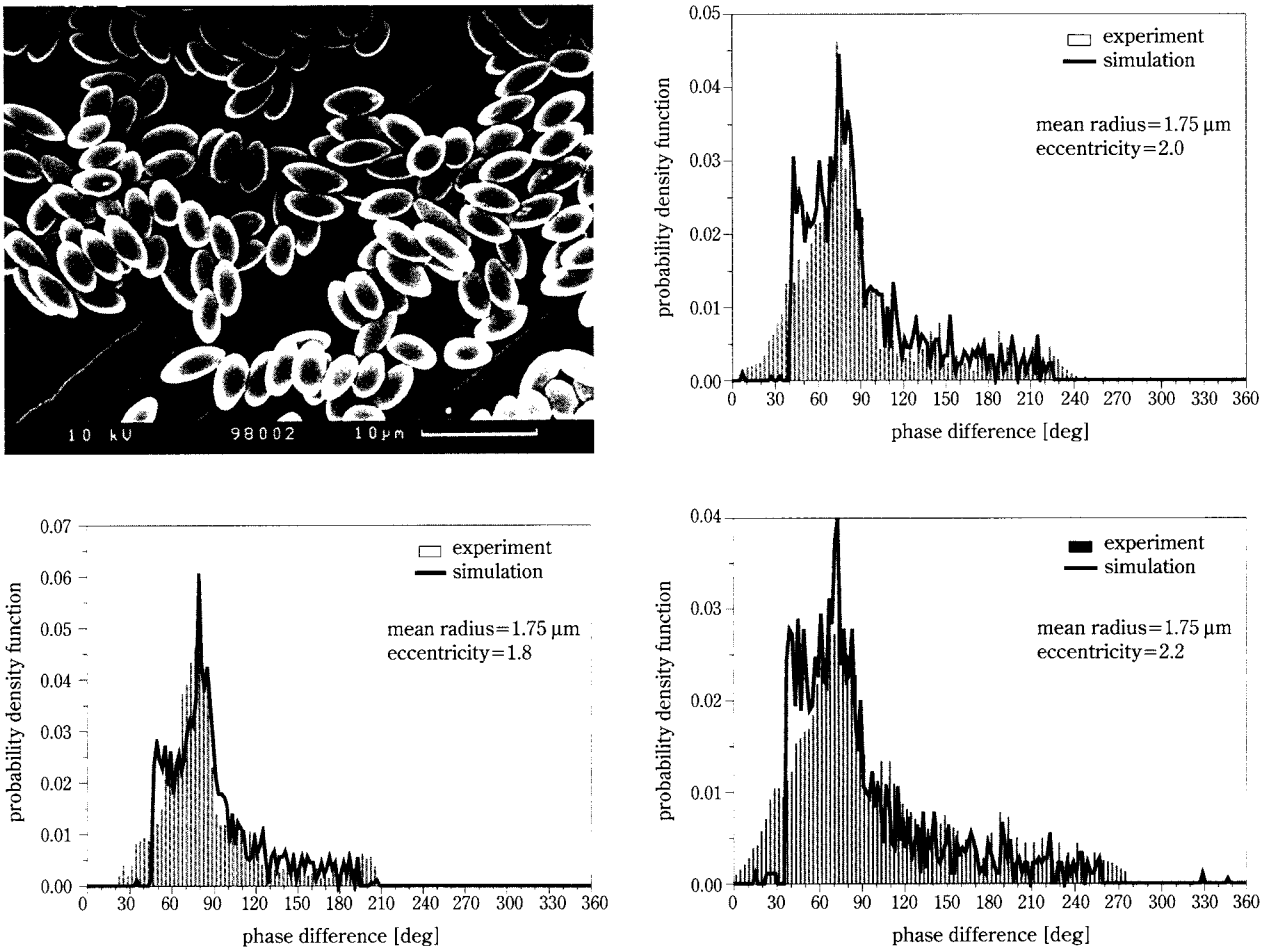

Fig. 8 Electron micrograph of monodispersed polystyrene spheroids and frequency distributions of phase-differences of these particles (measured and simulated results) for d=3.5 µm and ε=1.8, 2.0 and 2.2 in accordance with [49]

exactly in the light scattering computations. Therefore, an apparent decrease of precision during the PDA measurements of fine solid particles has to be tolerated which results in a broadening of the measured phase-difference distributions, thus leading to an apparent inaccuracy of diameter detection and corresponding particle size distribution.

6.3 Surface roughness and deviations from sphericity of solid particles

In order to analyse the influences of surface roughness and deviations from sphericity and to quantify the problems of apparent inaccuracy of diameter detection, single fine solid particles were measured several times using an electrodynamical particle trap [23]. After capturing the individual particles from the trap, the resultant mean particle characteristics were compared by electron microscopical observation [23, 51 and 52].

Several measurements on micron and submicron monospheres – both transparent and conducting – on monodisperse aerosols, and on fine metal particles verify the theoretical and numerical results. **Fig. 9** shows number density distributions $q_d(\Delta\Phi)$ (performed by 10^4 single diameter measurements on each particle) from four solid spherical particles: two steel particles (St2 and St4), a tin particle (Sn5), and a copper particle (Cu1). Although the same particles were analysed in each case, the results show typical number density distributions which can be regarded as an orientation-averaged PDA result in any case. Especially the width of the distributions gives a measure for the deviations from sphericity. In addition, the surface structures have a further broadening effect on the width of these distributions. Thus, the apparent decrease of precision during PDA measurements of solid particles has a complementary result: together with the information of the mean particle diameter,

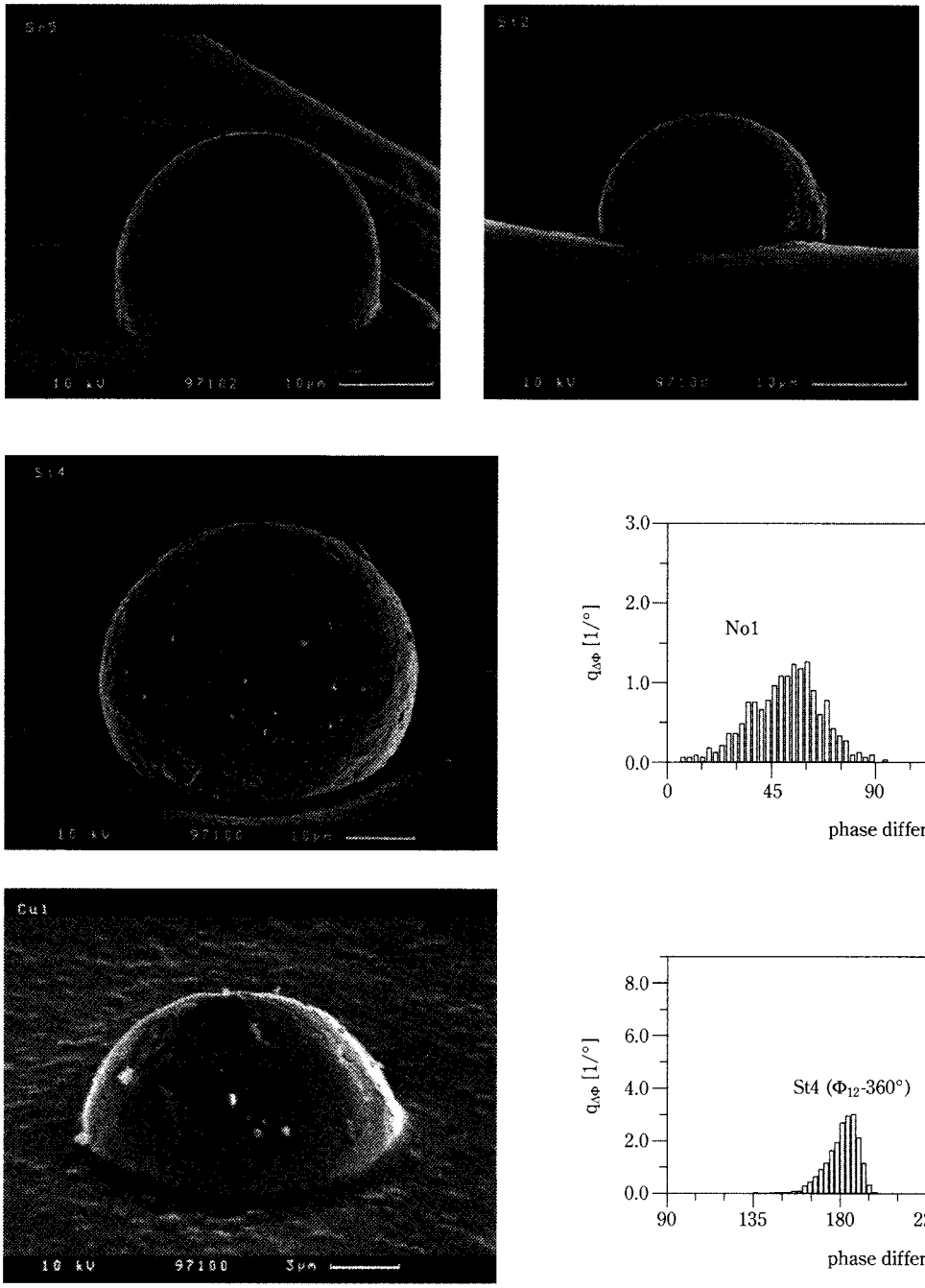

Fig. 9 PDA-measured number size distributions of three metallic particles as per [23]

one can obtain information about its sphericity and surface structures.

The particles were submerged in a conducting glue to some degree before electron microscopical photographs were taken. From these photographs, the mean particle diameter d_{REM} was extracted and compared with the PDA results d_{PDA}. The agreement is good in all cases, though the width of the PDA number density distributions varies from particle to particle. After correlating the width of each measured diameter distribution with the surface roughness, one could observe from the electron microscopical photographs (same figure) some surface structures as well as some impurities sticking on the surface. This was the explanation for the broadening effect.

Since the tin particle (Sn5) exhibits the smoothest

surface, the width of its diameter distribution is small [$d_{REM}=(28.2\pm0.5)\mu m$; $\Delta\Phi=335°$; $d_{PDA}=(27.8\pm1.6)\mu m$]. The surface roughness is slightly higher for the steel particle St2 [$d_{REM}=(23.6\pm0.5)\mu m$; $\Delta\Phi=291°$; $d_{PDA}=(24.2\pm1.3)\mu m$] and again for the steel particle St4 [$d_{REM}=(45.5\pm0.7)\mu m$; $\Delta\Phi=177°$; $d_{PDA}=(44.6\pm2.5)\mu m$]. The worst measurement result was from the copper particle [$d_{REM}=(14.4\pm0.2)\mu m$; $\Delta\Phi=167°$; $d_{PDA}=(13.9\pm0.8)\mu m$] and from a Novamet particle No1 with substructures in its surface, not shown here [$d_{REM}=(5.52\pm0.19)\mu m$; $\Delta\Phi=71.1°$; $d_{PDA}=(5.9\pm0.3)\mu m$]. Accordingly, the measured diameter distributions are broadened, which could be reconstructed by means of a ray theory model for spheres with random shapes and a computation of the far-distance electric fields and PDA phase-differences [51 and 52].

Because these results are in good agreement with the experimental data given above, one can conclude – generally speaking – that powders consisting of spherical particles can principally be measured by PDA, if it is sufficient to obtain information on the mean values of the particle diameter or about the average characteristics (quality) of the product.

7. Agglomerates of solid spheres

Since the formation of agglomerates in general gives rise to problematic size distributions of powders, and because substances such as solders, consisting of fine spherical metal powders, require particles free of agglomerates, there is a great demand for process control, e.g. of gas atomization of metal melts, where the metal powder production results in fine spherical particles. In principle, a tool for this process control, i.e. for the control of agglomeration or of agglomeration-free powder production, can be PDA (if further research work is performed). After solving the fundamentals of light scattering from a two-sphere system in the intersection field of the PDA (probe volume), mathematical tools, based on the approximate ray theory, were developed and the phase-differences simulated for a real three-sphere system and compared with such an agglomerate [53]. The agreement between simulation and experiment is good as long as the spheres are almost the same size. Otherwise, a single peak, corresponding to the largest sphere, occurs in the frequency distribution, and the smaller particles will broaden the phase distribution.

8. Dense sprays

The denser the sprays, i.e. the higher the particle fluxes (or concentrations) and the stronger the extinction of the atomized medium, the lower will be the probability of measuring realistic mass flux rates within the spray by PDA.

Dense sprays can be defined either as two-phase flows with high particle (mass or volume) fluxes of the droplet phase (e.g. water), thus increasing the probability of coincidences of droplets, passing the PDA probe volume, or – from an optical point of view – as two- or multi-phase flows with an increased optical extinction (i.e. absorption and scattering) of the entire dispersed phase, due to the material properties of the atomized droplets and their increased scattering probability. The scattered light from the droplet(s) in the probe volume will be influenced by other droplets, simultaneously passing either the probe volume or the laser beams or the light paths to the detectors, not to mention that the signal-to-noise ratio (SNR) will become worse in any case. The increased optical absorption of the entire droplet phase, also due to the increased droplet concentration, depends on the material properties of the atomized medium, originating from a high value of the factor k of the imaginary part in the refractive index, if the medium is homogeneous (e.g. metal melt droplets) or from inclusions of the droplets, when the effective refractive index results from a composite medium (described in Section 5.1). For instance, the atomized medium may be a process liquid like a suspension or an emulsion.

In general, the original size distribution of the droplets after atomization ranges over more than two decades, thus a low SNR may already cause an underrepresentation of the finest particles in particular. This tendency may be intensified by increased optical extinction and/or multiple scattering of high particle fluxes. Since in axisymmetrical sprays, the local particle flux changes with distance not only from the atomizer but also from the centre line, this causes longitudinal and radial gradients of density, of various local SNR, and of multiple scattering probability. In addition, some of the above-mentioned problems may also diminish the signal quality of the droplets: inclusions, pulsations together with deformations, or agglomerates and surface structures after solidification of melt droplets. Thus the assumption that PDA measurements from single particles may provide absolute measures has to be abandoned, because particle collectives such as sprays or powders in most cases show a strong tendency to have their finer particles under-represented and their larger particles over-represented (due to agglomerates).

In order to eliminate these types of errors, one can use additional instrumentation such as patternators or diffraction techniques or laser light sheet arrangements. Also, the choice of different lasers with appropiate wavelengths – as described in Section 5.1 – may solve some of these problems. An entirely different strategy is the use of post-processing programs, as have been developed, e.g. for dense metal melt sprays [54 and 55] and sprays of optical absorbing process fluids [33], or to combine special PDA arrangements with a post-processing program, in order to eliminate coincidence [56]. In any case, post-processing needs a fast signal acquisition for definite time periods without using any trigger criteria. Hence a kind of signal band is recorded, including bursts as well as noise. This signal band is stored on a hard disk (without any data evaluation) for subsequent signal analysis. It is intended to coordinate the various ways of data evaluation (described in the foregoing sections) and to implement them in a common evaluation scheme and upgraded post-processing program.

9. Conclusions

An extended application of standard phase-Doppler anemometry (PDA) to deformed or opaque (absorbing) particles, to metal melt droplets, or to droplets which contain inclusions – so called optical inhomogeneities – has been discussed. Since problems may also occur due to the surface roughness or to agglomeration of solid particles, it is in any case helpful to use light scattering simulations based on geometrical optics (GO) and the *Mie* theory for the design and arrangement, and finally for optimisation, of the optical set-up prior to measurements.

Experiments have been described with spherical particles of different materials: polystyrene, coffee suspensions, and milk emulsions, molten and solidified steel and tin. Since solid particles show more or less deviations from sphericity, the width of PDA-measured diameter distributions gives a measure for these deviations. Since the surfaces of solid particles also exhibit structures resulting from the solidification and/or crystallization process or even contain impurities, these too have a further broadening effect on the width of these distributions. Hence, the apparent decrease of precision of PDA measurements from fine solid particles had to be cleared up, ending in a complementary result: together with the information of the mean particle diameter, one also obtains information about its sphericity and surface structures or – generally speaking – of the product quality.

All these strategies have to be tested, and can be coordinated, in order to implement the various data evaluations in a common post-processing scheme.

10. References

1) E.D. Hirleman: Part. Part. Syst. Charac. 13 (1996) 59-67;
2) K. Bauckhage; H.-H. Flögel; U. Fritsching; R. Hiller: Part. Part. Syst. Charac. 5 (1988) part 1: pp. 16-22; part 2: pp. 66-71;
3) K. Bauckhage: Chem.-Ing.-Tech. 68 (1996) Nr. 3, S. 253-266;
4) C. Tropea; T-H. Xu; F. Onofri; G. Gre'han. P. Haugen; M. Stiegelmeier: Part. Part. Syst. Charac. 13 (1996) 165-170;
5) P. Lehmann; E.H. Schombacher; Th. Wriedt: Part. Part. Syst. Charac. 13 (1996) 27-33;
6) G. Gre'han; G. Gouesbet; A. Naqwi; F. Durst: Part. Part. Syst. Charac. 11 (1994) 133-144;
7) K. Bauckhage: Chem.-Ing.-Tech. 65 (1993) Nr. 10, S. 1200-1205;
8) H.-H. Flögel: Dissertation Universität Bremen (1987), Fortschr.-Ber. VDI Z. Reihe 3, Nr. 140, VDI Verlag, Düsseldorf, 1987;
9) SCATAP-Programm: WWW http://diogenes.iwt.uni-bremen. de/vt/laser/laser/htm1;
10) Z. Jiang: Dissertation Universität Bremen (1994);
11) U. Manasse: Dissertation Universität Bremen (1993), Fortschr.-Ber. VDI Z. Reihe 8, Nr. 353, VDI Verlag, Düsseldorf, 1993;
12) M. Willmann; A. Glahn; S. Wittig: Part. Part. Syst. Charac. 14 (1997) 122-128;
13) K. Bauckhage; F. Schöne; D. Dopheide: Int. Conf. on Laser Anemometry, Advances and Applications, Swansea, Wales 1989;
14) J. Tillwick: Dissertation Universität Bremen (1999);
15) J. Tillwick; V. Uhlenwinkel; K. Bauckhage: Int. J. Heat and Fluid Flow 20 (1999) 530-537;
16) P. Haugen; E.J. Hayes: 3rd Int. Congr. on Opt. Particle Sizing; Yokohama 1993;
17) P. Haugen; E.J. Hayes; H.-H. von Benzon: Part. Part. Syst. Charac. 11 (1994) 63-72;
18) H. Schombacher; Th. Wriedt; K. Bauckhage: PARTEC 1995-4th Int. Congr. on Opt. Particle Sizing; Nürnberg 1995;
19) Z. Jiang: Applied Optics 36, 6 (1997) 1367-1375
20) P. Buchhave; H.-H. von Benzon: Part. Part. Syst. Charac. 13 (1996) 68-78
21) G. Göbel; Th. Wriedt; K. Bauckhage; Journal of Aerosol Science, Vol. 29, No. 9, pp 1063-1073; 1998
22) H.-H. von Benzon; P. Buchhave: Part. Part. Syst. Charac. 11 (1994) 55-62;
23) G. Göbel: Dissertation, Universität Bremen 1998
24) G. Göbel; Th. Wriedt; K. Bauckhage: Rev. Sci. Instrum. 68 (8) August 1997; pp 3046-3052
25) U. Manasse; Th. Wriedt; K. Bauckhage: Part. Part. Syst. Charac. 9 (1992) 176-185
26) U. Manasse; Th. Wriedt; K. Bauckhage: Meas. Sci.

Technol. 4 (1993) 369-377
27) F. Onofri; L. Bergougnoux; J.-L. Firpo; J. Misguich-Ripault: Applied Optics; 20. July (1999), Vol 38, No 21, 4681-4690
28) U. Manasse; Th. Wriedt; K. Bauckhage: Part. Part. Syst. Charac. 11 (1994) 84-90
29) M. Mitschke; Th. Wriedt; K. Bauckhage: Meas. Sci. Technol. 9 (1998) 197-209
30) Th. Wriedt; M. Mitschke; P. Lehmann: SPIE, Proc. Optical Techniques, Thermal and Combustion Flow; San Diego, July 10-13; Vol. 2546; (1995)
31) Th. Wriedt; M. Mitschke; U. Fritsching; K. Bauckhage: 2nd Int. Conf. on Multiphase Flows; Kyoto, Japan; April 3-7; 1995
32) A. Doicu; M. Mitschke; Th. Wriedt; K. Bauckhage: Part. Part. Syst. Charac. Submitted.
33) M. Mitschke: Dissertation Universität Bremen (2000), Fortschr.-Ber. VDI Z. Reihe 8, Nr. 852, VDI Verlag, Düsseldorf, 2000
34) O. Köser; Th. Wriedt: Applied Optics 35, 15 (1996) 2537-2543
35) F. Onofri, D. Blondel; G. Gre'han; G. Gouesbet: Part. Part. Syst. Charac. 13 (1996) 104-111
36) J. Rheims; H. Dahl; Th. Wriedt; K. Bauckhage: PARTEC 1995-4th Int. Congr. on Opt. Particle Sizing, Nürnberg 1995
37) J. Rheims; Th. Wriedt; K. Bauckhage: Meas. Sci. Technol. 10 (1999) 68-75
38) J. Rheims; Th. Wriedt; K. Bauckhage: Part. Part. Syst. Charac. 15 (1998) 219-224
39) J. Rheims: Dissertation Universität Bremen (1998), Fortschr.-Ber. VDI Z. Reihe 8, Nr. 710, VDI Verlag, Düsseldorf, 1998
40) S. Sankar; K.M. Ibrahim; D.H. Buermann; W.D. Bachalo: 3rd Int. Congr. on Opt. Particle Sizing; Yokohama 1993
41) W.D. Bachalo: Part. Part. Syst. Charac. 11 (1994) 73-83
42) L. Kai; P. Massoli; A. D'Alassio: Part. Part. Syst. Charac. 11 (1994) 385-390
43) K. Anders; N. Roth; A. Frohn: Part. Part. Syst. Charac. 13 (1996) 125-129
44) H. Schombacher: Dissertation, Universität Bremen 1997; Fortschr.-Ber. VDI Z. Reihe 8, Nr. 648, VDI Verlag, Düsseldorf, 1997
45) P. Lehmann; Th. Wriedt; A. Schöne: SPIE, Proc. Optical Techniques, Thermal and Combustion Flow; San Diego, July 10-13; Vol. 2546; 246-257 (1995)
46) A. Doicu; Th. Wriedt; K. Bauckhage: Part. Part. Syst. Charac. 14 (1997) 3-11
47) P. Lehmann; H. Schombacher; Th. Wriedt: Part. Part. Syst. Charac. 13 (1996) 27-33
48) N. Damaschke; G. Guesbet; G. Gre'han; H. Mignon; C. Tropea: Applied Optics 37, 10 (1998) 1752-1761
49) A. Doicu; S. Schabel; F. Ebert: Part. Part. Syst. Charac. 13 (1996) 79-88
50) A. Doicu; J. Köser; Th. Wriedt; K. Bauckhage: Part. Part. Syst. Charac. 15 (1998) 257-262
51) Th. Wriedt; K. Bauckhage; A. Schöne: IEEE Transactions on Instrumentation and Measurement Vol. 38 No. 5; Oct. 1989; 984-990
52) G. Göbel; A. Doicu; Th. Wriedt; K. Bauckhage: Part. Part. Syst. Charac. 14 (1997) 283-289
53) A. Doicu; G. Göbel; Th. Wriedt; K. Bauckhage: Part. Part. Syst. Charac. 15 (1998) 225-229
54) J. Tillwick; V. Uhlenwinkel; K. Bauckhage: Int. J of Heat and Fluid Flow 20 (1999) 530-537
55) J. Tillwick: Dissertation Universität Bremen (1999)
56) H. Dahl: Dissertation Universität Bremen (1999)

Author's short biography

Klaus Bauckhage

K. Bauckhage is Professor of Chemical Engineering, Faculty of Process Engineering at the University of Bremen (since 1978). Since 1986 he is Director at the Stiftung Institut für Werkstofftechnik, Bremen. After receiving his diploma in Chemical Engineering in 1966 at the Technische Universität Berlin, he was with the FRIEDRICH UHDE GmbH from 1966 to 1968. He received his Dr.-Ing. from the Technische Universität Clausthal in 1973.

The packing coefficient: a suitable parameter to assess the flow properties of powders†

Marylène Viana[a], Cécile M.D. Gabaude-Renou[b], Catherine Pontier[a] and Dominique Chulia[a]

[a] *EA 2631, GEFSOD, Groupe d'Etude sur la Fonctionnalisation des Solides Divisés, Laboratoire de Pharmacie Galénique, Faculté de Pharmacie*

[b] *Sanofi-Synthelabo Recherche*

Abstract

A parameter, defined by Gabaude et al. in a previous work [1], was further investigated for its ability to evaluate flow properties of particulate materials. It is based on the volume reduction of the powder bed under low compaction pressure. Compaction data and the packing coefficient ($C_t=[(H_0-H_P)/H_0].100$) were analysed over a [0−1] MPa pressure range. Comparison of the C_t value with the flowability index (i) determined by Jenike shear cell measurements demonstrated the reliability of this packing coefficient to assess powder flow properties using small quantities of powder (<1 g). This method appeared to be helpful for an adequate determination of flowability in the early stages of drug development. Finally, because the packing assessment is performed in a compression die, improvement in the prediction of the weight variation of tablets is expected, as compared with other methods of flowability assessment.

Key words: powders, flow properties, shear cell measurements, packing coefficient

1. Introduction

There is a need in the pharmaceutical industry for easy tests to enable characterisation of the flow properties of materials to be used in tabletting or capsule filling. Indeed, poor flowability of powders or granules can result in irregular weight and low production performances. During the past 40 years, a lot of methods have been developed to assess the flow properties, including the measurement of angle of repose, mass flow rate or compressibility (reduction in volume of a powder bed due to the application of taps). Even though these methods are quite simple, they do have their limitations. The results obtained are significantly affected by experimental conditions [2], and a lack of accuracy has been reported in the case of cohesive powders [3, 4]. It is also admitted that these methods measure derived properties and are unable to represent the intrinsic flow properties of powders [5]. Finally, they also require large amounts of product (100 g at least are recommended in the European Pharmacopeia for the determination of tapped density, for example).

Against the inadequacy of the methods cited above, more sophisticated and accurate techniques such as shear cell measurements have been used for testing the flowability of powders [5, 6]. The flowability index measured by the Jenike shear cell in particular has been shown to correlate with tablet weight variations [2]. Despite the accuracy in predicting flowability during tabletting, shear measurements are seldom used in the development of a drug product because they are time- and product-consuming.

Another approach to assess flowability consists in investigating the first compression stage of a compression cycle. Actually, several stages have been identified during the compression of powders [7]: (i) filling of the die; (ii) densification by particle slippage and packing; (iii) elastic and plastic deformation of particles; (iv) cold welding, with or without fragmentation. York [7] used the Heckel equation to analyse compressional data and attributed the initial curvature of the Heckel plot to particle slippage and rearrangement. However, he did not correlate the packing fraction that quantified this part of the curve with

[a] 2 rue du Dr Marcland, 87025 Limoges Cedex, France
[b] 371 rue du Pr Blayac, 34184 Montpellier Cedex 04, France
† Accepted: May 7, 2001

the flow properties of the powders, but only linked the increase of the packing fraction to the decrease of the particle size. Furthermore, in our opinion, the breakage of aggregates to primary particles is likely to be included in this parameter as the pressure range taken into account in that paper can extend to 10 MPa.

In the present study, a parameter to assess flow properties, derived from the work of York [7] and presented in a previous work [1], is further investigated. The method is based on the volume reduction of the powder bed corresponding to the first part of the force-displacement compaction curve. The purpose of this complementary work is to determine more precisely the end-compaction pressure to be considered for the calculation of the packing coefficient:

$C_t = \frac{H_0 - H_P}{H_0} \times 100$ where H_P is the powder bed height under pressure P and H_0 the initial height.

Hence the C_t values of a large range of products (powders, mixtures and granules of various sizes, shapes and behaviour during compaction) have been investigated using as end-compaction pressure P, a pressure ranging from 0 to 1 MPa and correlated to the Jenike flowability index.

2. Materials and methods

2.1 Materials

The products used (**Table I**) constituted a representative selection of pharmaceutical products, with different densities, flow properties and behaviour under pressure.

Powders (drug and excipients) were used as received.

Mixture 1 (M1) is a ternary blend composed of 20% anhydrous theophylline, 60% α-lactose monohydrate (Pharma 200/70) and 20% microcrystalline cellulose (Avicel PH 101). This mixture has also been processed by dry granulation (G1D) and wet granulation (G1W). Details of the manufacturing processes are given in a previous work [8].

Mixture 2 (M2) is a binary mixture with the same chemical composition as mixture 1 but, in this blend, the two excipients (lactose and cellulose) are associated in the co-processed Cellactose®.

Mixture 3 is a formulation by simple blend supplied by the *Pharmaceutical Sciences Department of Sanofi-Synthelabo Recherche* (patented product). Dry granules (G3D) and lubricated dry granules (G3DL) of mixture 3 were also analysed. The compaction was manufactured on an Alexanderwerk WP 150 roller compactor followed by sizing of compact on a mesh screen of 1.25 mm, and hydrogenated oil was used as lubricant mixed with G3D leading to G3DL.

Stoichiometric hydroxyapatite $Ca_{10}(PO_4)_6(OH)_2$ (Ca/P=1.667) was synthesized according to the process described in [9]. Granulation was performed using an oscillating granulator equipped with a 2-mm screen (Erweka AR 400, Heusenstamm, Germany) after drying of the precipitate (5% (w/w) final moisture content). Granules with a mean diameter of 200

Table I Characteristics of the products under study

Product	Supplier	Median diameter (μm)	Pycnometric density (g/cc)	Bulk density (g/cc)
Powders				
Anhydrous theophylline	Boehringer-Ingelheim	17	1.493	0.267
Pharma 200/70	S.A. du Sucre de Lait	236	1.534	0.844
Avicel PH 101	FMC Corp.	71	1.534	0.303
Cellactose®	Meggle GmbH&CO	113	1.529	0.399
Mixtures				
Mixture 1 (M1)		162	1.523	0.483
Mixture 2 (M2)		79	1.522	0.346
Mixture 3 (M3)	Sanofi Recherche	60	1.536	0.400
Granules				
Dry granules 1 (G1D)		250	1.536	0.610
Wet granules 1 (G1W)		250	1.536	0.490
Dry granules 3 (G3D)	Sanofi Recherche	500	1.537	0.690
Lubricated dry granules 3 (G3DL)	Sanofi Recherche	462	1.527	0.720
Stoichiometric hydroxyapatite (HAP200)		200	2.832	0.640
Stoichiometric hydroxyapatite (HAP400)		400	2.786	0.570

μm (HAP200) and 400 μm (HAP400) were obtained after a calibration step using a 315-μm and a 800-μm screen, respectively.

2.2 Methods

Packing measurements

The evolution of the apparent density of a powder bed in a volumetric cylinder subjected to successive vertical vibrations was followed using the Erweka Model SVM2 unit (Erweka GmbH, Heusenstamm, Germany). The measurements were made in a 250-mL cylinder with 100 g of product, except for HAP200 and HAP400 which were only available in small quantities. For these granules, the experiments were conducted in a 125-mL cylinder with 25 g of product.

The reduction in powder volume was estimated by two parameters:

- the difference between the volumes after 10 and 500 shocks ($V_{10}-V_{500}$).
- the Carr index calculated as follows:

$I_{carr}=\frac{d_{max}-d_0}{d_{max}}\times 100$ where d_{max} is the maximum tapped density and d_0 the bulk density after filling

Flow rate measurements

Mass flow through a funnel was determined according to the European Pharmacopeia recommendations (3rd edition, 2.9.16 ‹‹écoulement››).

Shear cell measurements

The product flow properties were analysed using a shear cell designed by Jenike [5, 6] (**Figure 1**). The apparatus is composed of a base and a ring, which are filled with the tested material, and a cover on which a vertical force V is applied. Preconsolidation of the product is carried out by applying a vertical consolidation force V_c (corresponding to a consolidation stress σ_c varying between 3 and 10 kPa) and a number of oscillating twists. Consolidation is completed in a second stage by applying a shear force S and causing the specimen to flow under the same normal force V_c until a steady state is reached. When consolidation is completed, the vertical compacting force V_c is replaced by a smaller vertical force V, and a shearing force S is applied until a failure plane has developed corresponding to the shear strength τ. The measurement of several points (σ, τ) allows determination of a yield locus (**Figure 2**). From one yield locus, two Mohr semi-circles are drawn. The first one is drawn through the origin tangentially to the yield locus. The point of intersection of this semi-circle with the σ-axis determines the value of the unconfined yield strength f_c. The second Mohr semi-circle is drawn through the end-point (σ, τ) tangentially to the yield locus. The major consolidating stress σ_1 is determined by the intersection of the circle with the σ-axis.

The determination of the flowability of the bulk solid requires the determination of (f_c, σ_1) values for at least three consolidation stresses σ_c. From these points, the flow-function FF ($f_c=f(\sigma_1)$) can be drawn. As indicated on **Figure 3**, the flowability of bulk solids can be classified according to the flowability index (i), which corresponds to the inverse of the slope of the flow-function. This procedure has been retained in order to ensure a more accurate determination of the i-values and fit in a better way the experimental points, as the flow-function is not a straight line through the origin.

Compression

Compression was performed using a Lloyd 6000R uniaxial press, Lloyd instruments Ltd., Segensworth East, England, UK. The die, 1 cm^2 in surface and 1 cm in depth, was lubricated with magnesium stearate before compaction. The die (1 cm^3) was manually

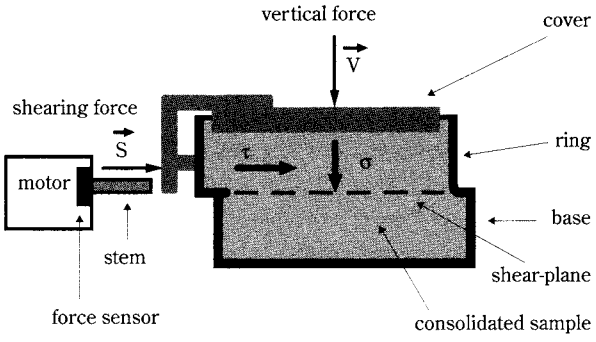

Fig. 1 Schematic diagram of Jenike shear cell

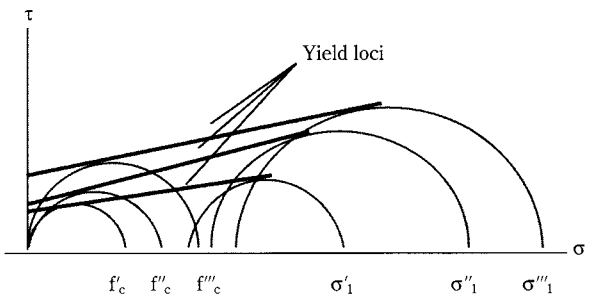

Fig. 2 Yield loci of a powder corresponding to three consolidation stresses (f'_c, σ'_1), (f''_c, σ''_1) and (f'''_c, σ'''_1)

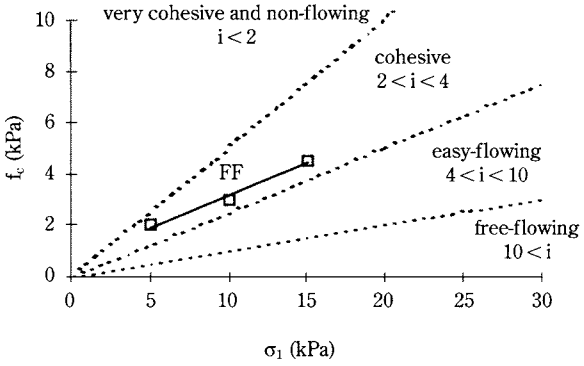

Fig. 3 Flow-function and classification according to the flowability index (i) [5]

filled with an accurate mass of product, calculated from the bulk density of the material. Compression was performed by the displacement of the upper punch at a speed set at 1.14 mm/min. The pressure was measured by an accurate gauge and the upper punch displacement was measured with an external LVDT extensometer. Compression data (displacement as a function of pressure) were collected until the predefined pressure was reached. Only the beginning of the curve will be discussed here (0 to 1 MPa). In the work of Gabaude [1], a packing coefficient C_t was defined to quantify the first compression period that was assumed to correspond to packing and slippage of the particles. It was suggested that this packing of the powders was fully achieved when the pressure at the upper punch had reached 0.5 MPa. The packing coefficient was based on the powder bed height:

$C_t = \frac{H_0 - H_{0.5}}{H_0} \times 100$ where $H_{0.5}$ is the powder bed height under pressure 0.5 MPa and H_0 is the initial height

In the present work, the packing coefficient has been calculated not only for 0.5 MPa but in steps of 0.05 MPa for pressures ranging from 0 to 1 MPa in order to determine more precisely the pressure influence on the calculation of the C_t value. Three compression cycles were analysed for each sample.

3. Results

3.1 Packing and flow rate measurements

It is generally accepted that a $V_{10}-V_{500}$ value greater than 20 ml indicates the presence of air entrapped between the particles and consequently a high compressibility which hinders the flowability of the product [10, 11]. Concerning the flow rate, a value of at least 10 g/s is required to ensure uniform flow. On the basis of these parameters and according to Carr's classification [12], results presented in **Table II** point to the poor flow properties of anhydrous theophylline and Avicel PH 101, whereas Pharma 200/70 and Cellactose® have good flow properties, due to their larger particle diameter and density. The three mixtures display poor flow properties, making a granulation step necessary or the addition of a lubricant for easy handling and manufacturing of solid dosage forms. In the case of mixture 2, the presence of 80%

Table II Packing results and mass flow rates through a funnel

Product	$V_{10}-V_{500}$ (mL)	I_{carr} (%)	Flow rate (g/s)	Classification
Powders				
Anhydrous theophylline	44.9	34.6	–	very poor flow
Pharma 200/70	3.5	13.9	11	good flow
Avicel PH 101	25.5	23.5	2.2	passable flow
Cellactose®	16.3	17.5	16.2	fair flow
Mixtures				
Mixture 1 (M1)	14.5	24.6	–	passable flow
Mixture 2 (M2)	44	27.2	–	poor flow
Mixture 3 (M3)	40	40.0	–	very poor flow
Granules				
Dry granules 1 (G1D)	13.3	21	12	passable flow
Wet granules 1 (G1W)	11.7	16	10	good flow
Dry granules 3 (G3D)	11	21.9	–	passable flow
Lubricated dry granules 3 (G3DL)	10	21.4	–	passable flow
Stoichiometric hydroxyapatite (HAP200)	2.7*	21.6	13	passable flow
Stoichiometric hydroxyapatite (HAP400)	2.2*	21	17	passable flow

* measured with 25 g in a 125 mL cylinder

of Cellactose®, a co-processed excipient especially designed for direct compression, is not sufficient to correct the very poor flow properties of anhydrous theophylline as shown by the high I_{carr} value of M2 (27.2%). All granules, except the wet granules of mixture 1 (G1W), are considered to have passable flow properties based on their I_{carr} index being higher than 18%.

3.2 Shear cell measurements

The flow properties of the products that were available in large quantities were only investigated using the shear cell method (**Figures 4** and **5** and **Table III**). From these measurements, the excipients appear to be free- (Cellactose® and Pharma 200/70) or easy-flowing powders (Avicel PH101), whereas theophylline is cohesive. The three mixtures are classified as easy-flowing according to their flowability index, but it must be said that the flow-functions of M1 and M3 are located in the cohesive area (**Figure 5**). As expected, granulation improved the flow properties of M1 and M3 since the flow-functions of G1D/G1W and G3D are located in the easy-flowing area. The effect of lubrication appears clearly with the improvement of the flowability index of G3DL versus G3D (from i=6.5 to 25.7).

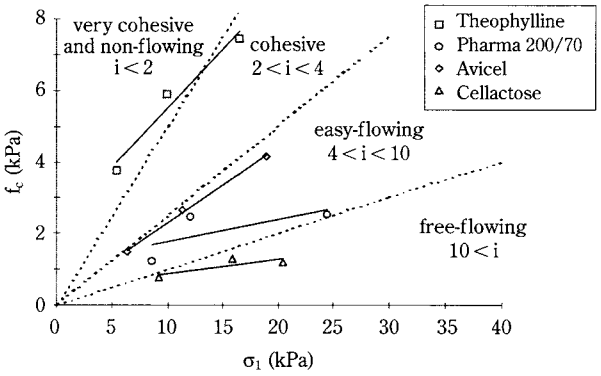

Fig. 4 Flow-functions of the powders

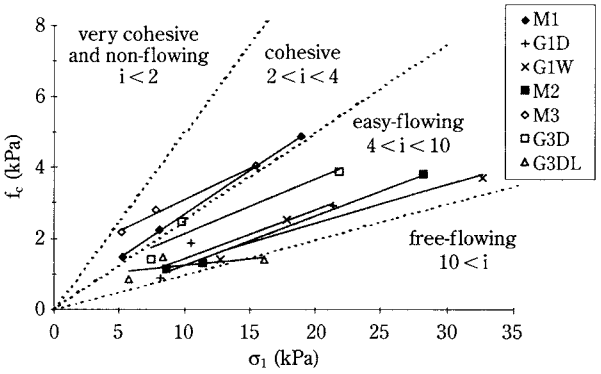

Fig. 5 Flow-functions of the mixtures and granules

Table III Flow-function equations and related flow characteristics of the products

Product	Flow-function equation	R^2	Index	Flowability
Powders				
Anhydrous theophylline	$f_c=0.327\sigma_1+2.230$	0.9614	3.06	cohesive
Pharma 200/70	$f_c=0.060\sigma_1+1.173$	0.4907	16.8	free-flowing
Avicel PH 101	$f_c=0.210\sigma_1+0.202$	0.9977	4.76	easy-flowing
Cellactose®	$f_c=0.040\sigma_1+0.479$	0.7139	25.0	free-flowing
Mixtures				
Mixture 1 (M1)	$f_c=0.247\sigma_1+0.228$	0.9997	4.04	easy-flowing
Mixture 2 (M2)	$f_c=0.140\sigma_1+0.150$	0.9948	7.14	easy-flowing
Mixture 3 (M3)	$f_c=0.178\sigma_1+1.332$	0.9919	5.64	easy-flowing
Granules				
Dry granules 1 (G1D)	$f_c=0.138\sigma_1+0.072$	0.8931	7.25	easy-flowing
Wet granules 1 (G1W)	$f_c=0.108\sigma_1+0.287$	0.9337	9.26	easy-flowing
Dry granules 3 (G3D)	$f_c=0.155\sigma_1+0.595$	0.9182	6.45	easy-flowing
Lubricated dry granules 3 (G3DL)	$f_c=0.039\sigma_1+0.869$	0.3863	25.7	free-flowing

3.3 Volume reduction on uniaxial press

The evolution of the packing coefficient as a function of the pressure is presented on **Figures 6** and **7**. All products display an inflection point P (mentioned in **Table IV**) in the curve between 0.2 and 0.5 MPa that indicates a change in the phenomena occurring in the powder bed. This point is considered as the end of the packing phenomena. The compaction pressure corresponding to this change is determined by adjusting the linearisation of the two parts of the curve to obtain optimal linear regression coefficients. The results are presented in **Table IV** with the C_t values calculated for 0.5 MPa. The comparison of the packing coefficients shows that the maximum varia-

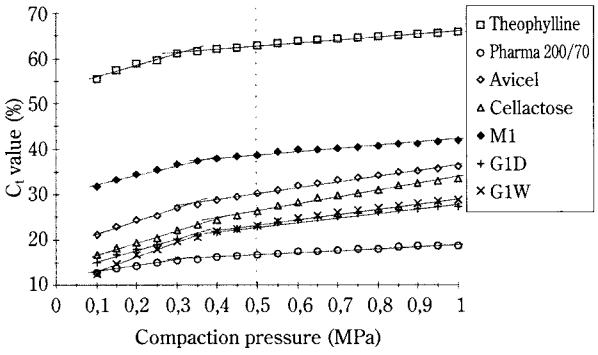

Fig. 6 Evolution of the C_t value (%) as a function of the compaction pressure (MPa)

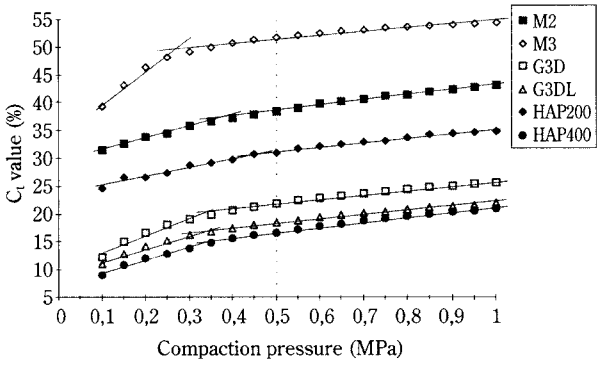

Fig. 7 Evolution of the C_t value (%) as a function of the compaction pressure (MPa)

Table IV Linear regressions and C_t values according to the pressure used for the packing coefficient calculation

Product	Linear regressions			P (MPa)	C_{tp} (%)	$C_{t0.5}$ (%)	$\frac{C_{t0.5}-C_{tp}}{C_{t0.5}}$ (%)
Powders							
Anhydrous theophylline	0.1–0.3 MPa 0.35–1 MPa	C_t=53.1+26.7P C_t=59.6+6.4P	R^2=0.9981 R^2=0.9821	0.32	61.6	62.9	2.1
Pharma 200/70	0.1–0.25 MPa 0.3–1 MPa	C_t=11.5+13.7P C_t=14.2+4.7P	R^2=0.9898 R^2=0.9756	0.30	15.6	16.6	6.0
Avicel PH 101	0.1–0.3 MPa 0.35–1 MPa	C_t=18.5+28.2P C_t=23.8+12.8P	R^2=0.9970 R^2=0.9889	0.34	28.1	30.2	6.9
Cellactose®	0.1–0.35 MPa 0.4–1 MPa	C_t=14+26.9P C_t=18.9+15P	R^2=0.9968 R^2=0.9868	0.42	25.2	26.25	4.0
Mixtures							
Mixture 1 (M1)	0.1–0.3 MPa 0.35–1 MPa	C_t=29.5+24.1P C_t=35.5+6.5P	R^2=0.9968 R^2=0.9781	0.34	37.7	38.8	2.8
Mixture 2 (M2)	0.1–0.35 MPa 0.4–1 MPa	C_t=29.5+20.7P C_t=33.3+10.1P	R^2=0.9941 R^2=0.9919	0.38	37.3	38.5	3.1
Mixture 3 (M3)	0.1–0.25 MPa 0.3–1 MPa	C_t=33.7+60P C_t=47.8+7.3P	R^2=0.9791 R^2=0.9485	0.27	49.8	51.8	3.9
Granules							
Dry granules 1 (G1D)	0.1–0.3 MPa 0.35–1 MPa	C_t=12.6+25.4P C_t=18+9.9P	R^2=0.9942 R^2=0.9769	0.35	21.5	21.6	0.5
Wet granules 1 (G1W)	0.1–0.35 MPa 0.4–1 MPa	C_t=9.6+32.7P C_t=17.2+12.1P	R^2=0.9866 R^2=0.9837	0.37	21.7	23.1	6.1
Dry granules 3 (G3D)	0.1–0.35 MPa 0.4–1 MPa	C_t=10.3+29.4P C_t=17.7+8.4P	R^2=0.9516 R^2=0.9868	0.35	20.6	21.9	5.9
Lubricated dry granules 3 (G3DL)	0.1–0.3 MPa 0.35–1 MPa	C_t=8.9+25.2P C_t=14.6+7.8P	R^2=0.9800 R^2=0.9854	0.33	17.2	18.6	7.5
HAP200	0.1–0.45 MPa 0.45–1 MPa	C_t=23.4+16.6P C_t=27.3+8.1P	R^2=0.9720 R^2=0.9845	0.45	30.9	31.05	0.5
HAP400	0.1–0.4 MPa 0.45–1 MPa	C_t=7.1+23.5P C_t=12+9.4P	R^2=0.9790 R^2=0.9894	0.35	15.3	16.6	7.8

P is the pressure at the intersection
C_{tp} is the C_t value at the intersection

tion between $C_{t0.5}$ and the C_t corresponding to the slope change is about 8%, but this leads only to a very small modification in the ranking of the products as shown in **Table V** (the classification of G1D and G3D only are modified). Furthermore, this variation has no consequence on the classification of the products: all powders (except pharma 200/70), the three mixtures, and HAP200 have a packing coefficient above 25%, whereas granules are classified as products having good flow properties, whatever the calculation method used.

For the purpose of defining a standardised parameter to compare the packing of different products, it seems that the choice of 0.5 MPa is appropriate. For most of the products, the packing stage can be considered as completed without any fragmentation or deformation of the particles as the applied pressure is very low.

Table V Ranking of the products according to their packing coefficient

Product	Classification C_{tp}	Classification $C_{t0.5}$
Powders		
Anhydrous theophylline	13	13
Pharma 200/70	2	2
Avicel PH 101	8	8
Cellactose®	7	7
Mixtures		
Mixture 1 (M1)	11	11
Mixture 2 (M2)	10	10
Mixture 3 (M3)	12	12
Granules		
Dry granules 1 (G1D)	5	4
Wet granules 1 (G1W)	6	6
Dry granules 3 (G3D)	4	5
Lubricated dry granules 3 (G3DL)	3	3
HAP200	9	9
HAP400	1	1

C_t value lower than 25%

4. Discussion

The comparison of the packing coefficient C_t with the flowability index i (**Figure 8**) confirms the possibility of evaluating the flowability by calculation of the packing coefficient, despite the difference in the

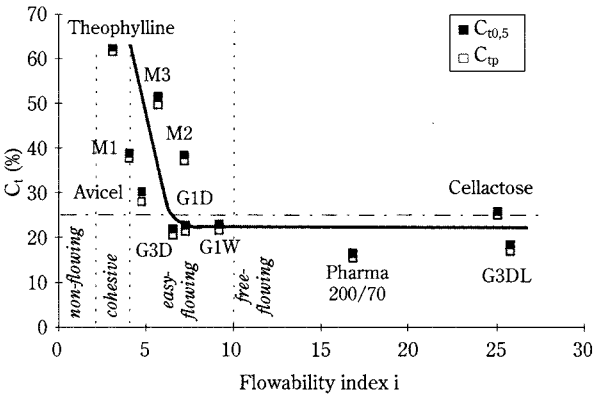

Fig. 8 Flowability index (i) and packing coefficient (C_t) calculated at 0.5 MPa (■) or at the pressure P corresponding to the slope change (□)

stress region applied. Globally, materials with a low C_t have easy- or free-flowing properties according to the Jenike classification, whereas products with a high packing coefficient have a low flowability index, which is characteristic of poor flow properties. Thus a rapid assessment of the flow properties of a product can be obtained from the analysis of the first part of its compression curve.

It should be noted that some products classified as easy-flowing (Avicel and the three mixtures) or free-flowing (Cellactose®) according to Jenike are considered to have inadequate flow properties according to their packing coefficient. This observation indicates that this new parameter seems to be more "reliable" than the flowability index determined by Jenike shear cell measurements. One hypothesis that could explain this discrepancy is the fact that considering only the flowability index reduces the information given by the flow-functions. In particular, the flow-functions of mixtures M1 and M3 (**Figure 5**), which are classified as easy-flowing products based on their flowability index, are situated in the cohesive area which is in accordance with their high C_t value. Likewise the flowability index of Cellactose® is one of the best of the products under consideration, whereas the C_t value is not as favourable (higher than 25%). In fact, mass flow through a funnel and tapped density measurements confirm this result; in spite of a high flow rate (16.2 g/sec), the flow properties of Cellactose® are not as good, as shown by the I_{carr} value (17.5%), which indicates relatively high compressibility of the product. This tabletting limiting characteristic is indicated by the packing coefficient of Cellactose® around the limit value of 25%. Thus, this method permits better discrimination of the products with poor flow properties, as for example M3 and G3D, than the

flowability index measured by Jenike shear cell, and fits rather well with our objective which is to characterise and classify products available in small quantities in the early stages of drug development.

Particulate materials with a C_t value below 25% can be considered to have adequate flow properties for industrial use, while a higher packing coefficient indicates too much compressibility that has to be corrected by the formulation and/or the manufacturing process.

5. Conclusion

This work has confirmed the possibility of investigating the flow properties of particulate materials by means of the packing coefficient calculated at 0.5 MPa. This new method has the advantage of being very easy, rapid and above all of requiring very small amounts of product. It has been shown to be in good correlation with flow-functions results and furthermore to better discriminate cohesive materials. In a recent paper, J.K. Prescott and R.A Barnum [13] specified that flowability is not an inherent material property, but is rather a result of the combination of material physical properties and the equipment used. As the packing assessment is performed in experimental conditions close to the industrial ones, i.e. in a compression die, improved prediction of the weight variation of tablets as compared to other methods may be expected, although parameters such as speed or punch shapes have not been taken into account. In addition, the flow properties assessed by the packing coefficient are less favourable as compared to the results from other methods, more efficiently preventing flow problems that can occur in a given application.

6. References

1) Gabaude, C.M.D.; Gautier, J-C.; Saudemon, P.; Chulia, D.: Validation of a new pertinent packing coefficient to estimate flow properties of pharmaceutical powders at a very early development stage, by comparison with mercury intrusion and classical flowability methods, J. Mater. Sci., 36, 2001, 1-11.
2) Ho, R.; Bagster D.F.; Crooks M.J.: Flow studies on directly compressible tablet vehicles, Drug Dev. Ind. Pharm., 3(5), 1977, 475-487.
3) York, P.: Application of powder failure testing equipment in assessing effect of glidants on flowability of cohesive pharmaceutical powders, J. Pharm. Sci., 64(7), 1975, 1216-1221.
4) Nyqvist, H.; Brodin, A.: Precision of a ring shear cell in determining flow properties of pharmaceutical powders, Acta Pharm. Suec., 17, 1980, 215-223.
5) Chulia, D.: Application aux poudres pharmaceutiques de méthodes d'investigation rhéologique empruntées à la mécanique des sols. A propos de l'écoulement, S.T.P. Pharma Pratiques, 1(5), 1991, 473-476.
6) Jenike, A.W.: Storage and flow of solids. Bull. 123, Utah Engineering Experiment Station, University of Utah, Salt Lake City, Utah, 1970.
7) York, P.: Particle slippage and rearrangement during compression of pharmaceutical powders, J. Pharm. Pharmacol., 30, 1978, 6-10.
8) Viana, M.; Caramigeas, E.; Vachon, M.G.; N'Dri, B.; Chulia, D.: Effect of formulation excipients and the manufacturing process for solid dosage form on the initial dissolution of theophylline, S.T.P. Pharma. Sciences, 10(5), 2000, 363-371.
9) Pontier, C.; Viana, M.; Champion, E.; Bernache, D.; Chulia, D.: Influence of chemical and manufacturing processes on apatitic calcium phosphates compressibility, 3rd World Meeting on Pharmaceutics Biopharmaceutics Pharmaceutical Technology, Berlin, 3-6 april 2000.
10) Guyot, J.C.: Critères technologiques de choix des excipients de compression directe, STP Pharma, 7, 1978, 551-559.
11) Delacourte-Thibaut, A.; Guyot, J.C.; Traisnel, M.: Formulation technologique des comprimés. Etablissement de fiches techniques, STP Pharma, 11, 1982, 131-140.
12) Carr, L.R.: Particle behaviour storage and flow, British Chem. Eng., 15, 1970, 1541-1549.
13) Prescott, J.K.; Barnum, R.A.: On powder flowability, Pharm. Technol. Eur., 13(1), 2001, 36-43.

Author's short biography

Marylène VIANA

Marylène Viana received her Ph.D. in biomaterials at the University of Nantes (France). She worked on the elaboration of calcium phosphate ceramics and their modifications in vivo. Currently, she is teaching pharmaceutical technology and biopharmaceutics at the University of Limoges (France). She joined the research team GEFSOD EA 2631 involved in the area of divided solids.

Cécile GABAUDE-RENOU

Cécile Gabaude-Renou is a chemical engineer with a master in Process Integration (UMIST, Manchester). She received her Ph.D in Pharmaceutical technology under the scientific direction of Prof. Dominique Chulia at the university of Limoges (France). She is now in charge of the development of new formulations and new processes for Sanofi-Synthélabo (Montpellier, France).

Catherine PONTIER

She is a pharmacist. She is Ph.D student in GEFSOD and she teaches pharmaceutical technology. Her research deals with the rationalization of the chemical nature of apatitic calcium phosphates used as direct compression excipients.

Dominique CHULIA

Prof. Dominique Chulia is a pharmacist. She is professor of pharmaceutical technology and biopharmaceutics at the University of Limoges (France). She is head of a research team (GEFSOD EA 2631) devoted to the functionalization of divided solids with a view to optimizing their processability and the bioavailability of active constituents from solid pharmaceutical dosage forms.

The On-Line Optical Investigation of Concentrated Dispersions in Precipitation and Grinding Processes†

Claire BORDES[1], François GARCIA[1], Christine FRANCES[1], Béatrice BISCANS[1] and Patrick SNABRE[2]

[1] *Laboratoire de Génie Chimique UMR 5503 CNRS/UPS/INPT*

[2] *Institut de Sciences et de Génie des Matériaux et Procédés, UPR 8521 CNRS*

Abstract

The present work reports new progress in the development of a multiple light scattering technique for investigating calcium carbonate precipitation and grinding processes. The optical analyser Turbiscan was used for the on-line analysis of light transmission and backscattering from a concentrated calcium carbonate dispersion. From a multiple scattering model based on the photon diffusion approximation, the size and mean refractive index of crystals or nuclei agglomerates are derived from measurements of the backscattered light flux. The time evolution of the particle mean diameter was determined with the on-line Turbiscan during the grinding process. In the precipitation process, the nucleation, growth and agglomeration of fine particles were investigated using this instrument. The crystal or nuclei agglomerate sizes derived from light flux measurements are compared with direct size determination by means of scanning electron microscopy. The multiple scattering technique was found to be highly sensitive to operating conditions (feed flow rate, calcium carbonate volume fraction, reactant concentration and stirring rate), and proved to be a powerful way of controlling precipitation or grinding processes and of optimising operating time.

Introduction

Optical techniques for the measurement of particle sizes and concentrations are usually carried out by elastic light scattering or diffractometry. Unfortunately, industrial and laboratory applications may require the use of optical diagnosis in densely laden flows for which multiple scattering phenomena are significant. Indeed, concentrated solid liquid dispersions such as food, detergents or pharmaceuticals are frequently encountered in industrial situations.

The aim of the present paper is to report new progress in the development of a measurement technique for studying precipitation and grinding processes. Solid liquid dispersions are often generated in an agitated batch vessel, for instance by precipitation. Sometimes, a more energetic dispersive action is needed when size reduction of particles is carried out. The control of precipitation and wet milling processes is of great interest for industrial applications.

Physico-chemical and processing conditions strongly influence the macroscopic behaviour of concentrated dispersions. Both physico-chemical and hydrodynamic interactions between particles determine densely laden flows. As a consequence, dispersions display non-Newtonian features and specific flow properties resulting from changes in the microstructure when increasing the shear stress [1]. However, microrheological models relating the dispersion viscosity and the aggregate mean size involve several structure parameters (packing concentration, fractal dimension and rupture parameter of aggregates) [1]. On the other hand, simple light scattering methods usually used for particle sizing require prior sampling and dilution that may change the macroscopic properties of the dispersion.

Recently, direct techniques were developed to characterise the on-line and in-line properties of concentrated dispersions in a non-intrusive and non-denatur-

[1] ENSIACET, 18 Chemin de la Loge, 31078 Toulouse-FRANCE

[2] BP 5, 66125 Font-Romeu-FRANCE

† Accepted: May 14, 2001

ing way. Ultrasonic spectrometry techniques provide advantages for on-line particle size analyses, particularly the ability to operate on undiluted and optically opaque media. The technique consists in propagating ultrasonic waves of variable frequency through the particulate system and measuring the frequency dependence of the attenuation to derive particle size [2-5]. The ultrasonic velocity method and the electroacoustic technique can also be used for particle size characterisation in concentrated systems. The ultrasonic velocity method consists in measuring the transit time of pulsed multiple frequency ultrasonic waves propagating through a medium [6]. In the electroacoustic method, an alternating electric field causes the electrically charged particles to move back and forth generating sound waves. Zeta potential and particle size are derived from the analysis of sound waves in relation to particle motions [7].

Multiple light scattering methods represent an alternative to acoustic spectrometry techniques for the characterisation of densely laden flows. In the multiple scattering regime, the transport mean free path representative of particle size can indeed be derived from the analysis of the light flux distribution in the incoherent backscattered spot light [8-10]. The present work concerns the study of calcium carbonate precipitation and grinding with an on-line optical device (Turbiscan On-Line instrument) that analyses multiple light scattered from a concentrated dispersion. Calcium carbonate is a soluble salt widely used in industry as a filler or a basic raw material in the manufacture of paint, coating, talc, adhesive, as well as in water treatment processes. Concentrated suspensions of calcium carbonate were produced by batch precipitation and the size reduction of a commercial calcite was carried out in a continuous stirred bead mill. During the grinding process, the analyser was used to characterise changes in particle size. During the precipitation process, the nucleation, growth and agglomeration of fine particles were investigated with the optical instrument. The size and mean refractive index of particles or nuclei agglomerates are derived from measurements of the backscattered light flux on the basis of a multiple light scattering model by Snabre *et al.* [8,9].

Multiple light scattering

Multiple light scattering methods are increasingly used to characterise concentrated dispersed media such as suspensions or emulsions. One considers the interaction of a focused light beam (light wavelength Λ, polarisation effects are ignored) with particles of diameter d randomly distributed in a fluid. Incident photons undergo multiple scattering events before absorption, backscattering or transmission through the sample. In the weak and multiple light scattering regime ($d > \Lambda$), interference effects are averaged out over the photon mean path λ and the photon diffusion approximation can be used because of the randomisation of scattered waves [11]. Monte Carlo simulations and statistical models are then suitable for predicting the spatial distribution of multiply scattered photons in the backscattered spot light [8].

Conservative multiple light scattering

In the framework of the diffusion approximation, the characteristic lengths involved in conservative multiple light scattering (no light absorption phenomena) are the photon mean path λ and the transport mean path λ^*, which are dependent upon the physical properties of the scattering medium (refractive index n_f of suspending fluid, refractive index n_p of particles, particle mean diameter d and particle volume fraction ϕ). The photon mean path λ is the average distance between two scattering events in the medium. All information about the initial direction of a wandering photon is further lost over the transport mean path λ^*, which represents a decorelation length between the direction of photon propagation and the incident direction. The scattering medium geometry and the transport mean path λ^* determine the photon path length distribution in the medium. For a random distribution of scatterers, the path lengths λ and λ^* are related to the particle mean diameter d and the particle volume fraction ϕ through the relations [8]:

$$\lambda = \frac{2d}{3\phi Q_s} \qquad \lambda^* = \frac{\lambda}{1-g} = \frac{2d}{3\phi(1-g)Q_s} \tag{1}$$

where $Q_s(n_p/n_f, d)$ is the scattering efficiency (ratio of total scattering cross-section and geometrical cross-section $\pi d^2/4$ of a particle). The asymmetry parameter $g(n_p/n_f, d)$ represents the average cosine of scattering angles from a single particle and describes the anisotropy of the scattering diagram ($g=0$ for isotropic Rayleigh scatterers and $0.5<g<1$ for Mie scatterers of sizes larger than the light wavelength). The optical parameters Q_s and g may be determined from the Mie theory. For large non-spherical particles ($d > \Lambda$), both the scattering efficiency and the asymmetry parameter no longer depend upon scatterer size. The mean diameter representative of scattering phenomena is the surface mean diameter or Sauter diameter:

$$d = \frac{\sum_i \phi_i}{\sum_i \phi_i / d_i} \qquad (2)$$

When illuminating the scattering medium with a focused beam, the normalised surface light flux $F(r)$ in the centre and outer regions of the backscattered spot light obey the scaling relations [8]:

$$F(r) \approx (1-B)\frac{0.03}{\lambda^{*2}}\left(\frac{\lambda^*}{r}\right)^{1.4} \quad \text{for } r < 4\,\lambda^*$$

$$F(r) \approx (1-B)\frac{\lambda^*}{\pi r^3} \quad \text{for } r > 4\,\lambda^* \qquad (3)$$

where r is the radial distance from the centre of the spot light and B accounts for boundary reflections at air/wall and liquid/wall interfaces ($B \approx 0.2$ for an aqueous suspension in a cylindrical glass tube [9,10]).

Turbiscan On-Line measurements

The Turbiscan On-Line device for the size characterisation of dispersed media is developed and sold by Formulaction (France). This device usually allows the characterisation of dispersions with a particle volume fraction to 70% and a particle surface mean diameter ranging from ten or so nanometres to a few millimetres, depending on the optical properties of the medium. A near-infrared focused LED (Λ=850 nm) illuminates the scattering medium flowing in a cylindrical glass tube (**fig. 1**) [9]. A transmission (detection angle θ=0) and a backscattering detector (detection angle θ=135°) of small aperture and rectangular cross-section (width dl and height $dh << dl$) detect both the transmitted and multiply backscattered light flux (**fig. 1**). The transmission level $T(\lambda) = e^{-2R_i/\lambda}$ only involves the tube radius R_i and the photon mean path λ. The integration of the normalised surface light flux $F(r)$ over the detection area $\delta S = dh\,dl$ further gives the backscattering level $BS(\lambda^*)$ or diffuse reflectance measured by the sensor:

$$BS(\lambda^*) \approx \frac{\int_{\delta S} F(r, \lambda^*)\,ds}{\int_{\delta S} F_o(r, \lambda^*_o)\,ds} \qquad (4)$$

where F_o is the light flux backscattered from a reference suspension (polystyrene spheres with diameter d_o=0.3 μm, particle volume fraction ϕ_o=10% and reference transport path λ^*_o=70 μm). From a numerical inversion of relation (4), the photon free path λ or transport free path λ^* are derived from the transmission rate $T(\lambda)$ or the diffuse reflectance $BS(\lambda^*)$. For known particle volume fractions, the Mie Theory then gives an estimate of the surface mean diameter d of scatterers [9].

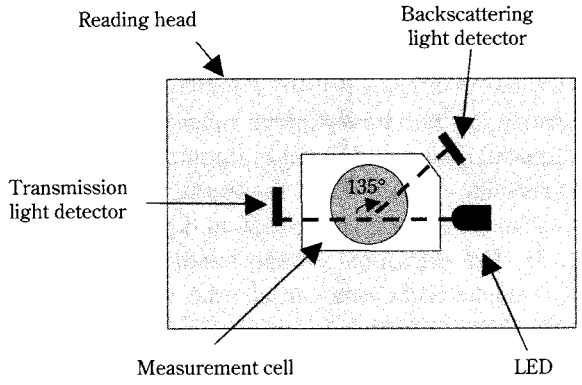

Fig. 1 Schematic representation of the Turbiscan On-Line reading head.

Both experiments with polystyrene spheres (refractive index n_p=1.59) and Monte Carlo simulations prove the model [9]. Indeed, the relation (4) describes the volume fraction dependence of the diffuse reflectance $BS(\phi)$ for suspensions of polystyrene spheres [9]. In the concentrated regime, independent scattering results in a continuous increase of the diffuse reflectance BS with particle volume fraction. However, departure from independent scattering occurs in concentrated dispersions of small particles (ϕ >10% and $d < \Lambda$) where the increase in correlation among particles induces short-scale interference of the scattered waves [11]. Dependent scattering effects cause an increase of the transport path length λ^* and a decrease of the diffuse reflectance BS [10-12]. For non-absorbing Rayleigh scatterers ($d << \Lambda$), the Percus-Yevick approximation for the pair distribution function gives an analytical expression of the transport mean path $\lambda^*(d, \phi)$ in the dependent scattering regime [5,12]:

$$\lambda^* = \frac{2d}{3\phi(1-g)Q_s}\frac{(1+2\phi)^2}{(1-\phi)^4} \quad \text{for } d < \Lambda \qquad (5)$$

Calcite crystals

Preliminary experiments were performed with calcium carbonate particles and compared with the predictions of the scattering model. Three crystalline forms for calcium carbonate are reported in the literature [13,14]: rhombic (calcite), spherical (vaterite) and needle-like (aragonite) particles. Precipitated pure calcite (>99%, Merck) corresponding to the rhombic form of the calcium carbonate is considered in this section. Electron microscopy observations show compact calcite crystals of a mean size around 10 μm and

larger open agglomerates (**fig. 2**).

The calcium carbonate volume fraction dependence of the backscattering level $BS(\phi)$ was investigated with the Turbiscan optical analyser. Experiments were performed in a batch well-stirred reactor. A peristaltic pump allows the suspension circulation at a constant flow rate (Q=40 l/h) through the optical analyser. The backscattering level of the suspension was measured for particle volume fraction up to 25%. A higher particle volume fraction results in unstable flows and poorly reproducible experiments for calcite aqueous suspensions without a dispersing agent.

Figure 3 shows the experimental and theoretical dependence of the transmission and backscattering levels upon the particle volume fraction ϕ for calcium carbonate aqueous suspension. In the diluted regime ($\phi < \phi_C$), the transmission level $T(\phi)$ decreases exponentially with particle volume fraction. The strong diffuse reflectance BS in the diluted regime results from the dominant boundary reflections on the inner tube interface. In the concentrated regime ($\phi > \phi_C$), the transmission level $T(\phi)$ becomes negligible and the diffuse reflectance $BS(\phi)$ increases with particle volume fraction as a result of independent scattering representative of scatterers larger than the light wavelength. The agglomeration of large and compact calcite particles weakly changes the scattering area per unit volume. As a consequence, transmission and backscattering levels are mainly sensitive to calcite crystals since light waves cannot resolve the structure of large agglomerates. Considering a refractive index n_p=1.52 for calcite rhombic crystals [15], the scattering model describes experimental data (**fig. 3**) for an average calcite crystal diameter d=9 μm and is in good agreement with electron microscopy observations (**fig. 2**). Because of multiple scattering phenomena and photon randomisation, the model remains suitable for describing the diffuse reflectance of a dense collection of irregularly shaped and polydispersed compact calcite crystals.

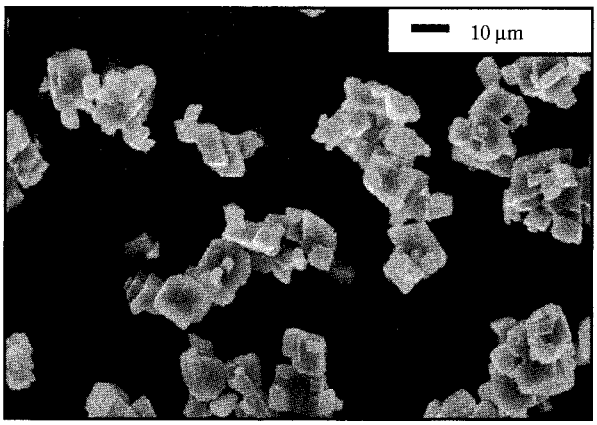

Fig. 2 Microphotograph of (unground) rhombic calcite particles.

The scattering model was used to determine the calcite crystal diameter dependence of the backscattering level BS for a particle volume fraction ranging from 4% up to 14% (**fig. 4**). In the case of Rayleigh scatterers smaller than the wavelength (nearly isotropic scattering), the diffuse reflectance BS increases with particle surface mean diameter. On the other hand, the anisotropic forward scattering of light from calcite crystals larger than the wavelength results in a decrease of the backscattering level with

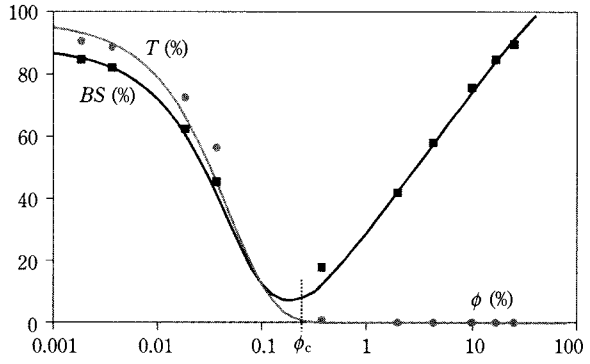

Fig. 3 Theoretical (full lines) and experimental backscattering (■) or transmission (●) levels versus particle volume fraction for calcite aqueous suspensions. Mean refractive index n_p=1.52, dh=500 μm and λ^*=70 μm. Particle surface mean diameter d=9 μm.

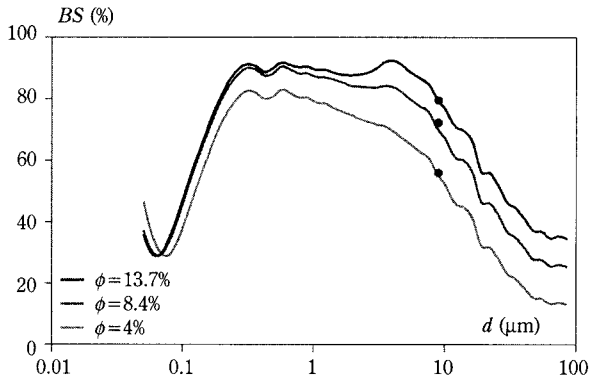

Fig. 4 Theoretical backscattering level BS versus particle surface mean diameter d for particle volume fraction ϕ=4%, ϕ=8.4% and ϕ=13.7%. Mean refractive index of the agglomerates n_p=1.52, dh=500 μm and λ^*=70 μm. Closed symbols (●) show experimental backscattering levels.

particle size (**fig. 4**) [9]. Backscattering level measurements and theoretical predictions show a reasonable agreement for a calcite crystal surface mean size $d \approx 9$ μm and particle volume fractions in the range from 4% up to 14% (black symbols in **fig. 4**).

These results show the ability of the multiple scattering model to describe the backscattering level of concentrated aqueous suspensions of calcium carbonate. Multiple light scattering is especially sensitive to the surface mean size of calcite crystals and is weakly influenced by agglomeration phenomena since crystals are larger than the light wavelength. In the following sections, the optical device is used to study changes in particle diameter or volume fraction during calcium carbonate precipitation and grinding processes. Experimental transmission or backscattering levels are interpreted within the framework of the scattering model.

Experimental set-up

Experimental set-up for grinding runs

Wet grinding of calcium carbonate was performed in a laboratory stirred bead mill (Drais Pearl Mill PML-V/H, 0.8 litre in capacity). The mill consists of a cylindrical grinding chamber agitated with four discs mounted on a driven shaft (**fig. 5**). About 80% of the chamber volume is filled with grinding zirconium beads (bead density 2300 kg/m^3) ranging from 400 to 600 μm in size. The stirring rate was kept constant at 2130 rpm. During the grinding runs, the beads are kept in the chamber by using a separating gap, which permits a continuous mill discharge. Cooling water circulating from a thermostatic bath through the mill jacket prevents overheating of the grinding chamber.

Grinding runs were performed initially with calcium carbonate particles suspended in distilled water without a dispersing agent for weight fractions of particles ranging from 10% to 30% (i.e. particle volume fraction $4\% < \phi < 14\%$). Then, more dense suspensions (60 wt.% equivalent to 35.6 vol.%) were used adding a dispersing agent (sodium polyacrylate). Under these conditions, the suspensions remain macroscopically homogeneous and can be pumped from a well-stirred reactor so that no settling occurs. A peristaltic pump circulates the calcium carbonate suspension from the feeding tank to both the grinding chamber and the optical analyser placed on-line at the outlet of the mill. In that case, direct measurements on the whole outlet flow were performed. A second feed reactor containing distilled water was used to clean the installation before each experiment.

Experimental set-up for precipitation runs

Calcium carbonate precipitation is realised by mixing a carbonate-salt aqueous solution with a calcium-salt solution. Batch experiments for calcium carbonate precipitation were performed in a well-stirred 1.2-litre crystalliser. **Figure 6** shows a schematic diagram of the experimental set-up. Cooling water circulating from a thermostatic bath through the reactor jacket is used to maintain a constant temperature $T_R = 21$°C in the reactor. Equimolar solutions of calcium nitrate and sodium carbonate were added to get the desired calcium and carbonate ion concentration in the reactor.

The time evolution of calcium carbonate precipitation was then followed with the optical analyser by measuring the time variation of the backscattering level *BS*. For this purpose, a peristaltic pump circulates the suspension at a constant flow rate $Q = 30$ l/h through the cylindrical cell of the optical analyser.

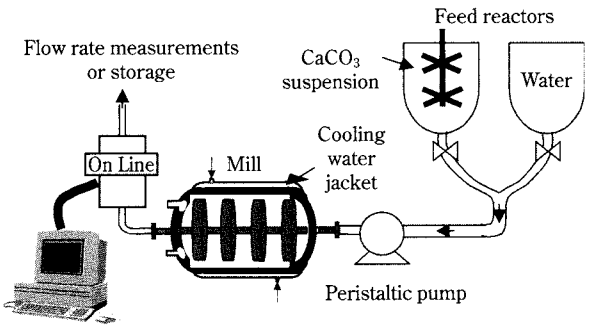

Fig. 5 Schematic representation of the grinding experimental set-up.

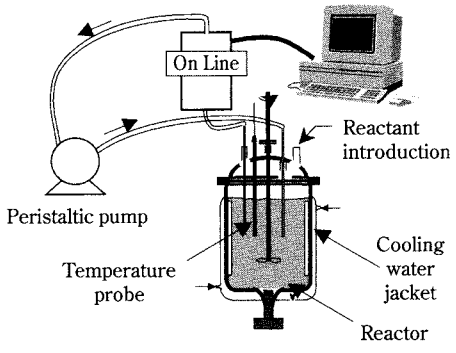

Fig. 6 Schematic representation of the precipitation experimental set-up.

Results

Grinding experiments without sodium polyacrylate

At the beginning of an experiment, a precise amount of calcium carbonate particles was injected into the feed reactor previously filled with distilled water to prepare a suspension of known particle volume fraction. Water from the second feed reactor circulates first through the installation. After a few minutes, the calcium carbonate suspension was pumped to the mill at a controlled flow rate. The flow rate can be changed by adjusting the peristaltic pump without stopping the flow during an experiment. The grinding process was followed with the Turbiscan On-Line by measuring the time variations of the backscattering level $BS(t)$. Samples were further taken during grinding experiments to determine the flow rate and the suspension density. Calcium carbonate particles were visualised by scanning electron microscopy at the beginning and the end of each experiment (**fig. 2** and **fig. 7**). Rhombic calcite crystal agglomerates as well as irregularly shaped fragments were always observed (**fig. 7**). X-ray analysis shows no polymorphism transformation during the wet grinding of calcite particles.

The experimental conditions regarding the calcite volume fraction ϕ, the feed flow rate Q and the mean residence time $\tau = V/Q$ of particles in the reactor of volume $V = 400$ ml are listed in **table 1**.

For the calcium carbonate volume fraction $\phi > 4\%$, the suspension flowing in the cylindrical tube of the optical analyser is optically thick and only the backscattering level was analysed since the transmission level becomes negligible. **Figure 8** shows time variations of the backscattering level $BS(t)$ for a calcium carbonate volume fraction $\phi = 13.7\%$ and a feed flow rate $Q = 22.2$ l/h. The mill was initially filled with water. The diffuse reflectance $BS(t)$ increases sharply as the process starts before stabilising at $BS \approx 92.4\%$ after a few hundred seconds with signal fluctuations less than 0.2%.

Influence of flow rate

Figure 9 shows the time variation of the backscattering level when gradually increasing the feed flow rate for a calcium carbonate volume fraction $\phi = 13.7\%$.

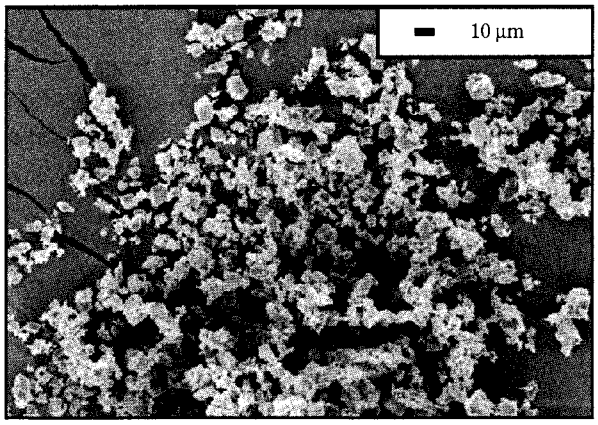

Fig. 7 Microphotograph of ground calcite particles after 30 s (initial calcium carbonate volume fraction $\phi = 13.7\%$).

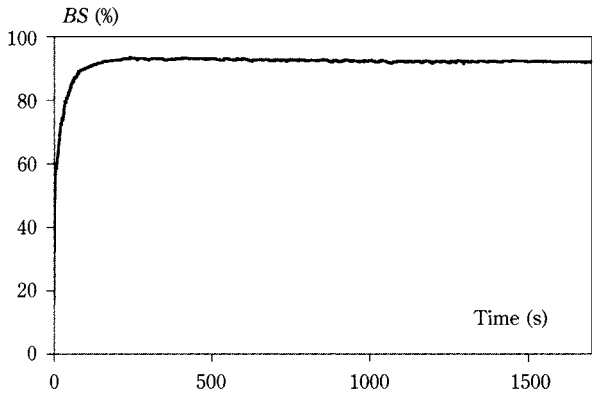

Fig. 8 Time dependence of the backscattering level $BS(t)$ for initial calcium carbonate volume fraction $\phi = 13.7\%$ and feed flow rate $Q = 22.2$ l/h.

Table 1 Operating conditions during the wet grinding process without additive

Experiment	G1		G2		G3		G4		G5		G6	
ϕ (%)	4		4		8.4		8.4		13.7		13.7	
	Q (l/h)	τ (s)	Q (l/h)	τ (s)	Q (l/h)	τ (s)	Q (l/h)	τ (s)	Q (l/h)	τ (s)	Q (l/h)	τ (s)
	21.2	67.9	19.8	72.7	22	65.5	22	65.5	22.2	64.9	20.4	70.6
	45.6	31.6	46.8	30.8	46.2	31.2	46.2	31.2			47.5	30.3
	72	20	73	19.7	72	20	73	19.7			72	20
			24	60	22.6	63.7	22.8	63.2				
							74	19.5				

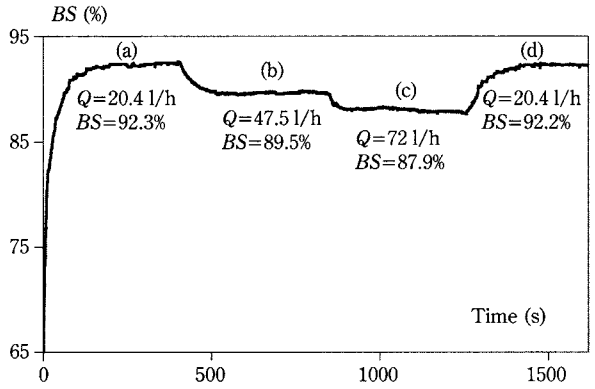

Fig. 9 Time dependence of the backscattering level $BS(t)$ for initial calcium carbonate volume fraction $\phi=13.7\%$ and feed flow rates $Q=20.4$ l/h (a), $Q=47.5$ l/h (b), $Q=72$ l/h (c) and $Q=20.4$ l/h (d).

At a constant flow rate $Q=20.4$ l/h, the backscattering level first reaches a steady level $BS=92.3\%$ (**fig. 9**(a)). After a steep flow rate increase from 20.4 to 47.5 l/h, the rise in the backscattering stationary level indicates larger particles (**fig. 3**) as a result of a reduced mean residence time of particles in the reactor and a weaker efficiency of the grinding process. The backscattering stationary level increases with feed flow rate $20\ \text{l/h} < Q < 72\ \text{l/h}$ and is representative of independent scattering from particles larger than the light wavelength. **Figure 9** further shows the reversibility of the experiments since an identical backscattering stationary level is observed when the flow rate is reduced to the initial value $Q=20.4$ l/h (**fig. 9** (a) BS=92.3% and (b) BS=92.2%). The reproducibility of the experiments was verified since differences in the backscattering levels never exceed 0.2% for identical hydrodynamic conditions.

Influence of calcium carbonate volume fraction

In this section, the effect of the particle volume fraction on the grinding efficiency is analysed. **Figure 10** shows the backscattering curves $BS(t)$ for the calcium carbonate volume fraction $\phi=4\%$, $\phi=8.4\%$ and $\phi=13.7\%$. For identical flow rate conditions, the backscattering stationary level increases with particle volume fraction, which indicates a reduced grinding efficiency at high solids concentrations.

The effect of the solids concentration on the grinding efficiency mainly depends on the solids mechanical properties and operating conditions. Concerning the grinding of limestone, experiments from Kwade et al. [16] showed that more mechanical energy is required to achieve a similar product fineness at very low limestone concentrations since the grinding probability of a particle becomes negligible. At intermediate solids concentrations, the grinding efficiency rises because of a higher presence probability of particles near the stressed region. For high solids concentrations and at constant rate of supplied mechanical energy, particle crowding reduces again the fragmentation rate and the grinding efficiency. Moreover, part of the mechanical energy is lost in viscous dissipation energy because of the viscosity increase of the suspension. In the case of calcium carbonate grinding, a higher fineness is achieved as the particle volume fraction decreases. The higher the solids concentration, the shorter is the interparticle distance, and the aggregation phenomenon in the absence of a dispersing agent is promoted, leading to an increase of the viscosity.

Grinding experiments with sodium polyacrylate

A dispersing agent was used to obtain denser calcium carbonate suspensions which were pumpable and able to flow in the grinding set-up pipes. Sodium polyacrylate is one of the most frequently used additives in the grinding of calcite, and prevents the aggregation phenomenon which takes place during the size reduction process and decreases the viscosity of the ground suspensions [17]. Grinding experiments were performed at a particle volume fraction of 35.6% (60 wt.%) using sodium polyacrylate (molecular weight 5100 g/mol) at a concentration of 1 wt.% relative to calcite dry matter. **Figure 11** shows the time evolution of the backscattering level $BS(t)$ for two feed flow rates $Q=7$ l/h and $Q=32$ l/h. As previously observed, the signal first increases sharply and then reaches a stationary level after a variable time depending on the flow rate. As expected, the BS values obtained are higher ($BS=97.5\%$ for $Q=7$ l/h i.e. $\tau=206$ s and $BS=95.3\%$ for $Q=32$ l/h i.e. $\tau=45$ s) than those corresponding to lower volume fractions (see **fig. 10**).

The optical system can also be used to determine the delay time τ^* necessary to reach a steady state when starting the process or changing the feeding conditions.

Hydrodynamic conditions in the grinding chamber (solids concentration and stirring rate) strongly influence the time interval τ^*. For the present experiments, this delay time necessary to reach a backscattering stationary level ranges between 50 and 300 s and indeed varies as the inverse of feed flow rate. However, τ^* is always shorter than the time interval $\tau^*=4\text{-}5\ \tau$ usually considered in a grinding process, where t is the mean residence time $\tau=V/Q$

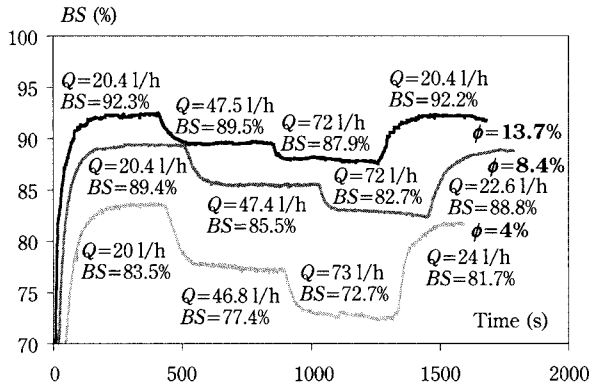

Fig. 10 Time dependence of the backscattering level $BS(t)$ for different initial calcium carbonate volume fractions $\phi=4\%$, $\phi=8.4\%$ and $\phi=13.7\%$ and variable feed flow rates.

[18]. A possible explanation is the small size of the laboratory grinding chamber (0.8 l) whose hydrodynamic behaviour can be assimilated with a good approximation to that of a perfect mixed reactor [19].

Precipitation experiments

The stirred reactor is first filled up with distilled water and the temperature is kept constant at 21°C. After a few minutes, the first reactant (sodium carbonate solution) is introduced into the reactor. Several minutes later, an equimolar calcium nitrate solution is added and the precipitation process starts immediately because of the high reactant concentrations ranging from 0.1 mol/l up to 0.4 mol/l. The time evolution of the backscattering level BS is recorded with the Turbiscan On-Line during the precipitation process.

Samples were taken from the reactor with a syringe during the precipitation process. A few drops of hydrochloric acid were added rapidly to the filtrated solution to stop calcium carbonate precipitation. The samples were dried at room temperature and characterised by scanning electron microscopy. The calcium concentration in the reactor was further determined by sample proportioning. The effects of reactant concentration c and stirring rate ω on the precipitation process were studied. The experimental conditions are shown in **table 2**.

For high reactant concentrations $c>0.1$ mol/l, precipitation occurs instantaneously as soon as a few drops of nitrate calcium solution are introduced into the sodium carbonate solution. The turbulent mixing time $t_m \approx 7{,}3(D_r^2/\bar{\varepsilon})^{1/3}$ is about six seconds where D_r is the reactor diameter and $\bar{\varepsilon}$ the viscous dissipation rate per unit mass of stirred suspension [20]. As a consequence, calcium carbonate precipitation takes place before complete mixing and a viscous gelatinous reaction product is formed during the first seconds of the precipitation process in agreement with reported

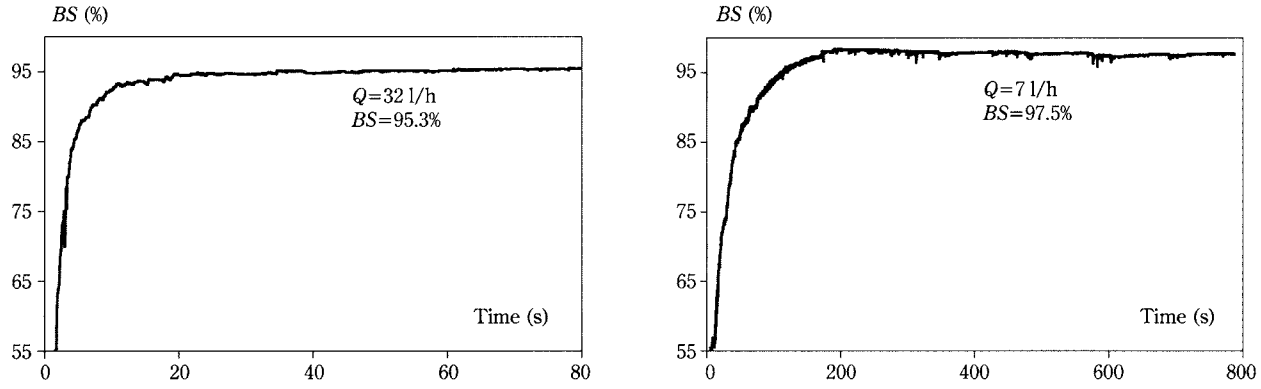

Fig. 11 Time dependence of the backscattering level $BS(t)$ for calcium carbonate volume fraction $\phi=35.6\%$ (adding dispersant agent) at two different feed flow rates: $Q=32$ l/h (a) and $Q=7$ l/h (b).

Table 2 Operating conditions during the precipitation runs ($T_R=21$°C)

Experiment	P1	P2	P3	P4	P5	P6	P7	P8	P9	P10
c (mol/l)	0.1	0.1	0.15	0.15	0.2	0.3	0.3	0.4	0.3	0.3
ω (rpm)	710	710	710	710	710	710	710	710	1000	500

observations from S. Kabasci [14].

Figure 12 shows the time evolution of the backscattering level $BS(t)$ for a reactant concentration c=0.3 mol/l and a stirring rate ω=500 rpm. The optically transparent aqueous carbonate salt solution displays a high backscattering level because of internal reflections (**fig. 12***a*). The introduction of the calcium nitrate reactant induces an instantaneous calcium carbonate precipitation and a steep decrease of the backscattering level as the scattering medium becomes optically thick. The backscattering level further rapidly increases before reaching a stationary level after a delay time of about 500 seconds.

The backscattering curves $BS(t)$ indeed show several stages just after reactant introduction and calcium carbonate precipitation (**fig. 12***b*). On a short time scale $t<10$s, the backscattering level increases steeply in relation to the nucleation phase since the crystal concentration rises and the medium scatters the incident light more strongly. During the nucleation phase, the observed decrease of the backscattering level (**fig. 12***b*) probably results from the mixing of the gelatinous reaction product. The nucleation phase can be considered complete after a few seconds as confirmed by sample proportioning during the precipitation process. After the nucleation phase, the nuclei species form spherical agglomerates and then the backscattering level $BS(t)$ displays a bell-shaped variation and a further decrease before reaching a stationary level after a few minutes (**fig. 12***b*). For similar operating conditions, the experiments are reproducible and the signal deviation remains less than 1% (**fig. 13**).

During the course of experiments, the calcium ion concentration remaining in the solution was determined and the particles were further visualised by scanning electron microscopy (**fig. 14**). Spherical vaterite crystals (agglomerates of nuclei) and porous

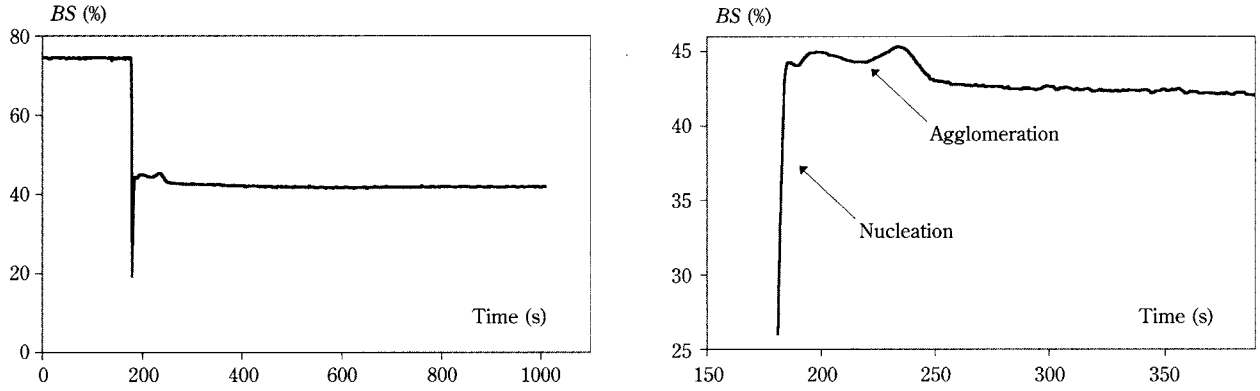

Fig. 12 Time dependence of the backscattering level $BS(t)$ for initial reactant concentration c=0.3 mol/l (T_R=21°C, ω=500 rpm) and time $t<1000$ s (a) or 150 s$<t<$400 s (b).

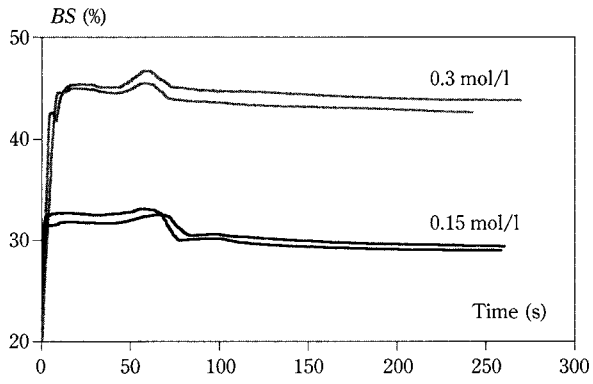

Fig. 13 Time dependence of the backscattering level $BS(t)$ for initial reactant concentration c=0.15 mol/l or c=0.3 mol/l (T_R=21°C, ω=710 rpm).

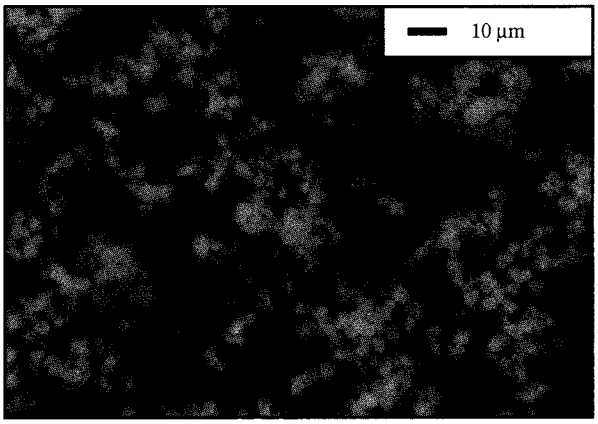

Fig. 14 Microphotograph of agglomerates of spherical vaterite crystals formed at time t=60s.

large aggregates were always observed briefly during calcium carbonate precipitation.

For a given nuclei and crystal concentration, the scattering model predicts a maximum backscattering level for agglomerates of a size close to the light wavelength Λ=0.85 μm (see **fig. 4**). Therefore, the bell-shaped backscattering curves $BS(t)$ probably reflect the formation of nuclei agglomerates which are larger than the wavelength in agreement with electron microscopy visualisation (**fig. 14**). Nuclei agglomerates can further stick and form large open structures or aggregates. Over a long time scale, the light wave cannot resolve the internal structure of large porous aggregates made of sub-units larger than the wavelength, and multiple light scattering becomes mainly sensitive to nuclei agglomerates.

Influence of reactant concentration

Figure 15 shows the backscattering curves $BS(t)$ for reactant concentrations ranging from 0.1 mol/l up to 0.4 mol/l. As a consequence of mixing phenomena during the nucleation phase and formation of a gelatinous phase, the backscattering curves $BS(t)$ display a first oscillation (more pronounced for the high reactant concentration c=0.4 mol/l) a few seconds after precipitation starts. During nucleation and agglomeration phases, the scattering behaviour and the maximum backscattering level increases with the reactant concentration since more nuclei are formed in the reactor (**fig. 15**). The optical signal $BS(t)$ further displays time oscillations near the maximum backscattering level except for the weakest reactant concentration c=0.1 mol/l.

Nuclei agglomeration promotes the formation of porous agglomerates which trap some liquid solution. One may thus expect calcium carbonate precipitation within nuclei agglomerates and a delayed compaction of structures. Size increase to above one micron lowers the backscattering level while the compaction of agglomerates results in a higher average refractive index and stronger scattering phenomena. Therefore, the observed oscillations near the maximum backscattering level probably results from the competition between growth and compaction of nuclei agglomerates. Indeed, the signal oscillation is more intense and occurs earlier in time when increasing the reactant concentration because high ionic concentrations promote the calcium carbonate precipitation within nuclei agglomerates. A small reactant concentration c=0.1 mol/l prevents the compaction of nuclei agglomerates and then the backscattering peak is no longer observed (**fig. 15**).

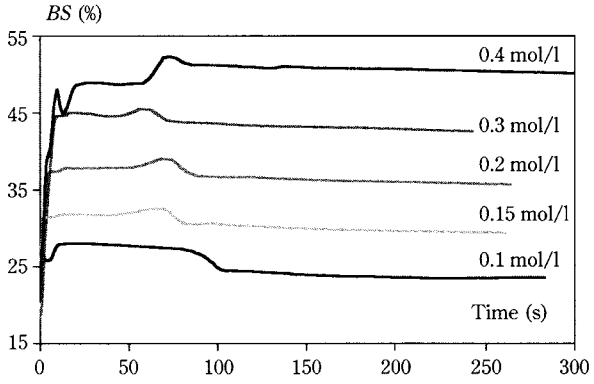

Fig. 15 Time dependence of the backscattering level $BS(t)$ for different initial reactant concentrations in the reactor (T_R=21°C, ω=710 rpm).

Influence of stirring rate

Calcium carbonate precipitation was performed under different flow conditions in the stirred reactor. For stirring rates in the range from 500 rpm to 710 rpm, the flow conditions have no significant influence upon the backscattering curves $BS(t)$ (**fig. 16**). On the other hand, a high stirring rate ω=1000 rpm greatly changes the scattering behaviour during the first minute. High shear gradients delay the nucleation phase and the growth of nuclei agglomerates. Over longer times t>1 min, the flow conditions have less influence both on the growth and the compaction of nuclei agglomerates. However, the backscattering stationary level is somewhat lower under strong stirring conditions.

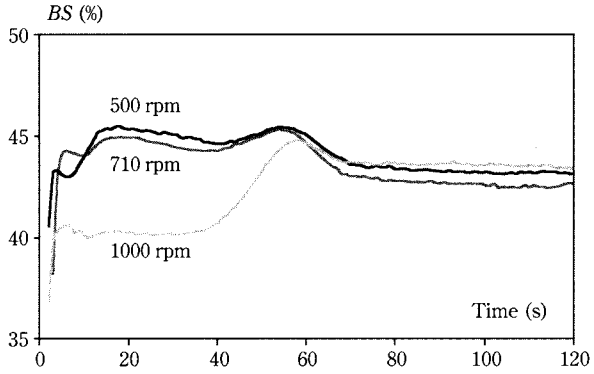

Fig. 16 Time dependence of the backscattering level $BS(t)$ for different stirring rates in the reactor (T_R=21°C, c=0.3 mol/l).

Discussion

Grinding experiments

For a known calcium carbonate volume fraction, the time evolution of particle surface mean diameter can be determined from the measurement of the backscattering level during the grinding process. **Figure 17** shows the particle volume fraction dependence on the surface mean particle diameter for backscattering stationary levels displayed in **figure 10** (experiments without additive). The surface mean particle diameter increases with calcium carbonate volume fraction and with the feed flow rate (i.e. reducing the mean residence time) because of the lower grinding efficiency. Whatever the operating conditions, the surface mean diameter of the ground particles always remain larger than the light wavelength Λ=850 nm, as confirmed by electron microscopy analysis of samples. One can further expect precise values of the average size of particles because of the high sensitivity of the backscattering level upon scatterer diameter for calcite crystals larger than the wavelength (**fig. 4**).

During grinding experiments, changes in the feeding rate significantly affect the backscattered light detected by the on-line optical sensor at the outlet of the mill. Thus, the optical device can be used to adjust the flow rate and control the grinding process. However, the on-line control of particle size from measurement of the backscattering level requires knowledge of the particle volume fraction. Indeed, the backscattering level is dependent both upon particle fineness and solid concentration. The analysis of the transient behaviour of multiple light scattering phenomena further gives information about the delay time required to reach steady state and can also be used to optimise the operating time during grinding processes.

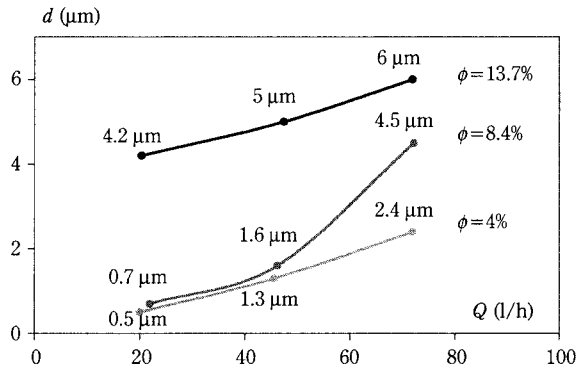

Fig. 17 Flow rate dependence of the mean diameter d for calcium carbonate grinding and different initial particle concentrations (T_R=21°C).

Precipitation experiments

Precipitation experiments can be analysed on the basis of the multiple scattering model. In the framework of a mean field approximation, porous nuclei agglomerates trap some liquid which reduces the mean refractive index of scatterers. Since the nucleation phase only takes a few seconds, a constant nuclei volume fraction is further assumed. Sample proportioning indeed indicates a roughly constant particle volume fraction after about 20 seconds. However, the mean refractive index of nuclei agglomerates appears to increase during particle growth as a result of carbonate calcium precipitation within agglomerates. **Figure 18** shows the particle diameter dependence of the backscattering level $BS(d, \phi)$ for a mean refractive index n_p=1.475 (*a*) or n_p=1.51 (*b*).

For an experimental particle volume fraction 0.3%< ϕ <1.6% and a mean refractive index n_p=1.475, the mean field scattering model predicts the maximum values of the backscattering level $BS(\phi)$ (**figs. 15** and **18***a*) very well. When compared to the refractive index n_p=1.52 of calcite crystals at wavelength Λ=0.65 μm [15], a mean refractive index n_p=1.475 indicates the formation of porous nuclei agglomerates.

During the first stage of the precipitation process, the rise of the backscattering level from an initial value BS≈20% (**fig. 15**) corresponds both to the nucleation phase and the growth of agglomerates from nuclei of initial size d≈0.15 μm. The limited backscattering level variation at a low particle volume fraction (ϕ=0.38%) results both from internal reflections and weak light scattering from diluted suspensions (**fig. 15**).

The scattering model considers monosized particles, and the theoretical backscattering level then displays an oscillating behaviour for particles of a size close to the light wavelength, because of interference effects (**fig. 18**). For polydispersed agglomerates formed during batch precipitation, the observed oscillation in the scattering behaviour cannot be a result of interference effects but is rather the result of a restructuration process of nuclei agglomerates as discussed above.

In a second stage, the growth of nuclei agglomerates beyond the light wavelength leads to a decrease of the backscattering level in agreement with experiments (**figs. 15** and **18***a*). Light scattering phenomena then become mainly sensitive to the porous nuclei agglomerates and cannot resolve the structure of aggregates larger than the light wavelength. In the framework of the mean field scattering model and for a refractive index n_p=1.475, the experimental back-

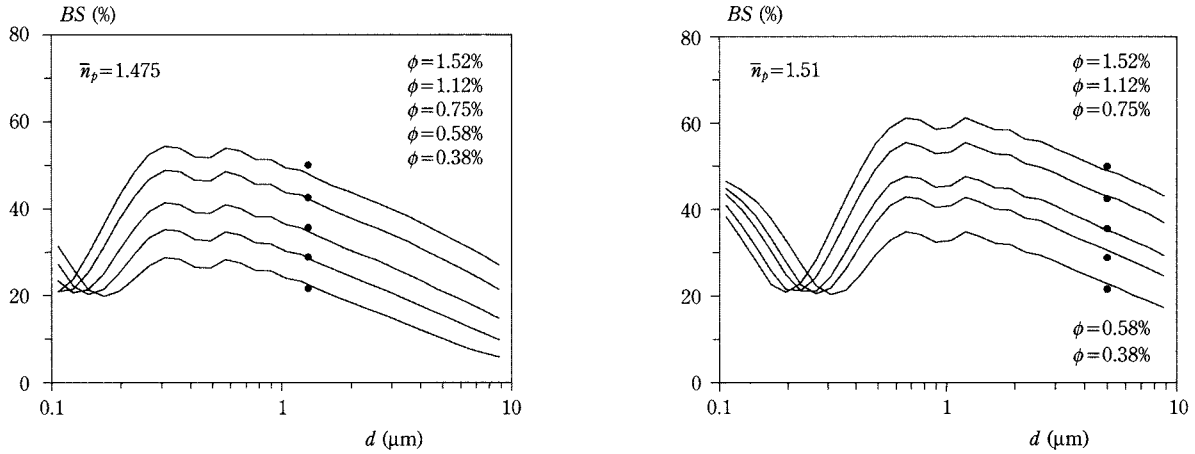

Fig. 18 Theoretical backscattering level $BS(d)$ versus surface mean aggregate diameter d for calcium carbonate precipitation and experimental initial volume fractions. Mean refractive index of the agglomerates n_p=1.475 (a) and n_p=1.51 (b) (dh=400 μm and λ^*=70 μm). Initial calcium carbonate concentration ϕ=0.38% (c=0.1 mol/l), ϕ=0.58% (c=0.15 mol/l), ϕ=0.75% (c=0.2 mol/l), ϕ=1.12% (c=0.3 mol/l) and ϕ=1.52% (c=0.4 mol/l). Closed symbols (●) show the experimental backscattering level.

scattering stationary values $BS(\phi)$ give a nuclei agglomerate size of about 1.3 μm (closed symbols in **fig. 18***a*). However, electron microscopy analyses of spherical vaterite crystals indicate larger agglomerates of the size 1 μm$<d<$20 μm. At the end of the precipitation process, one can expect a larger mean refractive index because of calcium carbonate precipitation within the agglomerates. A refractive index n_p =1.51 indeed enhances the backscattering level and then the scattering model predicts agglomerates of characteristic size $d\approx$5 μm (closed symbols in **fig. 18***b*) in better agreement with electron microscopy observations.

According to these results, the optical instrument is suitable for analysing precipitation processes. A rapid nucleation phase is followed by the formation of nuclei agglomerates and open aggregates after a few minutes. The time analysis of the backscattering curves shows crystal growth and a compaction process of the agglomerates. A mean field multiple scattering model predicts porous nuclei agglomerates with a mean refractive index $1.47<n_p<1.51$ and average size increasing from 0.15 μm up to 5 μm. Rapid stirring of the solution in the batch reactor was further shown to delay both nucleation and agglomeration phases during the first minute. The mean field scattering model proposed here assumes monosized homogeneous particles and neglects the multi-scale structure of porous and polydispersed agglomerates. Despite crude approximations, the model reasonably describes carbonate calcium precipitation in a batch reactor, because the statistical spatial distribution of multiply scattered photons mainly involves an average transport length depending on the mean scattering properties of nuclei agglomerates.

Conclusion

On-line optical experiments were performed with the Turbiscan On-Line to study concentrated calcium carbonate suspensions. The optical device is suitable for analysing calcium carbonate precipitation and grinding processes. During the continuous wet grinding process, the particle volume fraction remains constant and the particle average size was derived from the measurement of the backscattering level. In the case of calcium carbonate precipitation, assuming that the nucleation step lasts only a few seconds, a constant nuclei volume fraction for the agglomeration step was then considered. Moreover, porous nuclei agglomerates were considered as homogeneous spheres (mean field approximation). Despite crude approximations, the multiple scattering model reasonably describes the precipitation process and predicts nuclei agglomerate size in good agreement with electron microscopy observations. As a conclusion, the Turbiscan On-Line is well suited to analyse changes in particle diameter or volume fraction and estimate the optical properties of scatterers.

Acknowledgment

The authors would like to acknowledge the company Formulaction (Toulouse, France) for financially supporting this project.

Nomenclature

BS	Backscattering level	%
c	Reactant concentration	mol/l
d	Average particle diameter	m
d_o	Polystyrene sphere diameter	m
dh	Detector height	m
dl	Detector width	m
D_r	Batch reactor diameter	m
g	Asymmetry parameter	–
n_f	Fluid refractive index	–
n_p	Particle refractive index	–
Q	Feed flow rate	l/h
Q_s	Scattering efficiency factor	–
t	Time	s
T	Transmission level	%
t_m	Turbulent mixing time	s
T_R	Reactor temperature	°C
V	Volume of the grinding chamber	m^3
$\bar{\varepsilon}$	Viscous dissipation energy per unit mass of stirred suspension	J/kg
ϕ	Particle volume fraction	%
ϕ_c	Critical particle volume fraction	%
λ	Photon mean path	m
λ^*	Photon transport path	m
Λ	Light wavelength	m
τ^*	Delay time	s
ω	Reactor stirring rate	rpm

References

1) SNABRE, P.; MILLS, P.: Rheology of weakly flocculated suspensions of rigid particles, J. Physique III, Volume No 6, 1996, page 1811 – page 1834. Rheology of weakly flocculated suspensions of viscoelastic particles, J. Physique III, Volume No 6, 1996, page 1835 – page 1855.
2) GEERS, H.; WITT, W.: Opus ultrasonic extinction: fields of application, World Congress on Particle Technology 3, Brighton, UK, 1998.
3) STINTZ, M.; HINZE, F.; RIPPERGER, S.: Characterization of concentrated dispersions and colloidal systems by acoustic attenuation spectroscopy and colloid vibration potential, World Congress on Particle Technology 3, Brighton, UK, 1998.
4) ALBA, F.; CRAWLEY, G.M.; HIGGS, D.M.J.; KIPPAX, P.G.: Acoustic attenuation spectroscopy for particle sizing of high concentration dispersions, World Congress on Particle Technology 3, Brighton, UK, 1998.
5) SNABRE, P.; HAIDER, L.; BOYNARD, M.: Ultrasound and light scattering from a suspension of reversible fractal clusters in a shear flow, Eur. Phys. J.E., Volume No 1, 2000, page 41 – page 53.
6) COGHILL, P.J.; MILLEN, M.J.; RAINEY, S.; SOWERBY, B.D.: On-line measurement of particle size in fine slurries, World Congress on Particle Technology 3, Brighton, UK, 1998.
7) O'BRIEN, R.W.; ROWLANDS, W.M.; GIBBS, S.E.; WADE, T.E.; HUNTER, R.J.: The electroacoustic method for determining particle size and charge, World Congress on Particle Technology 3, Brighton, UK, 1998.
8) SNABRE, P.; ARHALIASS, A.: Anisotropic scattering of light in random media, Incoherent Backscattered spot light, Applied Optics, Volume No 37, 1998, page 211 – page 225.
9) SNABRE, P.; MENGUAL, O.; MEUNIER, G.: Optical Characterization of concentrated suspensions, Colloid and Surfaces A, Volume No 152, 1999, page 79 – page 88.
10) MENGUAL, O.; MEUNIER, G.; CAYRE, I.; PUECH, K.; SNABRE, P.: Concentrated dispersion instability characterised by multiple light scattering, The Int. J. of Pure and Applied Anal. Chem., Volume No 50, 1999, page 445 – page 446.
11) PINE, D.J.; WEITZ, D.A.; MARET, G.; WOLF, P.E.; HERBOLZHEIMER, E.; CHAIKIN, P.M.: Scattering and Localization of Classical Waves in Random Media, P. Sheng Editor. World Scientific, Singapore, 1990.
12) ISHIMARU, A.; KUGA, Y.: Attenuation constant of a coherent field in a dense distribution of particles, J. Opt. Soc. Am., Volume No 72, 1982, page 1317 – page 1320.
13) OHTAKI, H.: Crystallisation Processes, Ed. John Wiley & Sons, page 49 – page 67.
14) KABASCI, S.; ALTHAUS, W.; WEINSPACH, P.M.: Batch-precipitation of calcium carbonate from highly supersaturated solutions, Trans J chem E, Volume No 74, 1996, page 765 – page 772.
15) PERRY, R.H.; GREEN, D.W.: Perry's Chemical Engineer's Handbook, 7th Ed. Mc Graw & Hill, 1997, page 2 – page 11.
16) KWADE, A.; BLECHER, L.; SCHWEDES, J.: Motion and stress intensity of grinding beads in a stirred media mill, Part 2: stress intensity and its effect on comminution, Power Technology, Volume 86, 1996, page 69 – page 76.
17) GARCIA, F.; LE BOLAY, N.; FRANCES, C.: Physical and flow properties of dense aggregated suspensions, 7th International Symposium on Agglomeration, Albi, France, 2001.
18) STEHR, N.: Residence time distribution in a stirred ball mill and their effect on comminution, Chem. Eng. Process., Volume 18, 1984, page 73 – page 83.
19) BEL FADHEL, H.; FRANCES, C.; MAMOURIAN, A.: Investigations on ultra-fine grinding of titanium dioxide in a stirred media mill, Powder Technology, Volume 105, 1999, page 362 – page 373.
20) GEISLER, R.; MERSMANN, A.; VOIT, H.: Macro and micromixing in stirred tanks, International Chemical Engineering, Volume No 31, 1991, page 642 – page 653.

Author's short biography

Claire Bordes

Claire Bordes was born in 1975. She graduated from the Ecole Nationale Supérieure d'Ingénieurs de Génie Chimique of Toulouse (France) in 1998 and obtained her research degree in Chemical Engineering (DEA) from the Institut National Polytechnique of Toulouse in 1998. At present, she is working for her PhD degree at the Laboratory of Chemical Engineering of Toulouse (UMR 5503). Her main interest is the area of processes dealing with highly concentrated suspensions. She has developed methods of characterising dense suspensions under flow.

François Garcia

François Garcia was born in 1973. He graduated from the University Paul Sabatier of Toulouse (France) in 1997 and obtained his research degree in Chemical Engineering (DEA) from the Institut National Polytechnique of Toulouse in 1998. At present, he is working for his PhD degree at the Laboratory of Chemical Engineering of Toulouse (UMR 5503). His main interest is the area of comminution processes. His current research deals with the elaboration of finely ground suspensions in a stirred bead mill.

Christine Frances

Dr Christine Frances was born in 1965. She graduated from the Ecole Nationale Supérieure d'Ingénieurs de Génie Chimique of Toulouse (France) in 1988. She obtained her doctor's degree from the Institut National Polytechnique of Toulouse (France) in the field of crystallisation. In 1991, she became a researcher at the CNRS (French National Center of Research) in the field of comminution. Since 1991, she has developed and supervised several studies in that field, especially on wet ultrafine grinding. Her current research interest includes the elaboration and formulation of ground suspensions with defined properties.

Béatrice Biscans

Dr Béatrice Biscans was born in 1958. She graduated from the Ecole Nationale Supérieure d'Ingénieurs de Génie Chimique of Toulouse (France) in 1982. She prepared a PhD thesis on the separation of proteins by means of ion exchange chromatography in the Chemical Engineering Laboratory of Toulouse (UMR CNRS 5503) and obtained her doctor's degree in 1985. She then undertook post-doctoral research on the electrophoretic separation technique. She held a position at C.N.R.S. (French National Center of Research) in 1987 and was appointed Research Director in 1997. Since 1987 she has developed and supervised several studies in the field of crystallisation. Her current research interest includes the elaboration and formulation of crystals with controlled properties.

Author's short biography

Patrick Snabre

Patrick Snabre was born in Oran, Algeria, on October 30, 1955. He received his engineering degree from the "Ecole Supérieure de Physique et Chimie de Paris" (E.S.P.C.I.) in 1979 and a PhD degree in fluid mechanics from the University Paris VII in 1983. He held a position at C.N.R.S. (French National Center of Research) in 1983. Between 1983 and 1990, he was a researcher at the Laboratory of Biorheology and Physico-Chemical Hydrodynamics (L.B.H.P. C.N.R.S.), and received the French state doctorate in 1988. Since 1990, he has been a senior scientist at the Institute of Materials and Process Engineering (I.M.P. C.N.R.S.) and was appointed Research Director in 1998. He is the author of more than 80 publications in physico-chemical hydrodynamics and wave scattering from complex media. His current research interests include suspension rheology, radiative transfer in heterogeneous media (acoustic and electromagnetic waves), laser Doppler velocimetry in dense flowing dispersions, Doppler ultrasound, and LIDAR atmospheric detection.

The Influence of Carbon Dioxide on Ring and Ball Formation in a Pilot-Scale Rotary Kiln†

Josefina Lindblom
Department of Chemical Engineering Design
and Hans Theliander
Department of Forest Products and Chemical Engineering
*Chalmers University of Technology, Gothenburg, Sweden**

Abstract

The influence of carbon dioxide on ring and ball formation in a pilot-scale rotary kiln has been investigated. The balls were found to have a higher specific surface area and a higher content of residual carbonate compared with the rings and dusts: this was probably due to a lower heat transfer rate. The influence of carbon dioxide on sintering proved to be different for the two lime muds investigated. One of them reached a minimum in specific surface area at about 10 weight-% and the other decreased its specific surface area with increasing residual carbonate. The strength of the balls increased with increasing residual carbonate. At constant temperature and partial pressures of carbon dioxide, the strength of the balls increases with time and the specific surface area decreases. Also, as the partial pressure of carbon dioxide increases, the reduction of the specific surface area becomes slower and the increase in strength becomes more rapid.

Introduction

Lime mud reburning is one of the steps in the chemical recovery process in the kraft pulp mill. The reburning of lime mud is normally carried out in a rotary kiln. The rotating kiln is a long cylindrical furnace which is somewhat inclined to make it a continuous process (**Figure 1**). The moist lime mud is fed in at the upper end and, on its way down through the kiln, is dried, heated and calcined. Fuel is combusted at the lower end of the kiln and hot flue gases leave the kiln at the upper end, thus making the kiln a counter-current direct heat exchanger. During calcination, the calcium carbonate dissociates into calcium oxide (lime) and carbon dioxide. The porous lime also sinters because of the high temperature in the kiln. During sintering, the solid material may harden significantly, and rings and balls often form in the kiln. Ring and ball formation is a persistent problem in many mills and can easily affect the production capacity. In severe cases, it can also be the cause of shut-downs in order to clean the kiln. The results of an inquiry sent to all Swedish kraft pulp mills showed that ring formation was a real problem encountered by many mills (about 70%), and that they often did not know the cause of the problems.

The sintering atmosphere in a rotary kiln contains carbon dioxide, since hot flue gases supply the heat needed for calcination. Tran et al. (1992) and Skrifvars et al. (1992) studied the inter-particle gas-solid chemical reaction sintering as a mean of forming and hardening rings in rotary kilns. It was found in both studies that recarbonation is the most important mechanism in hardening mid-kiln rings (which are the most common and troublesome type of rings). The calcination reaction is reversible and recarbonation occurs when the temperature is lower than the equilibrium temperature. The mid-kiln rings are formed close to the maximum temperature where $CaCO_3$ (s) is still thermodynamically stable, which is, consequently, in the middle of the kiln (at the very end of the heating zone and the beginning of the calcination zone), where the concentration of carbon dioxide is high and the temperature not too high. Experimentally, Tran et al. (1992) and Skrifvars et al. (1992) calcined lime mud and limestone, respectively,

* Chalmers University of Technology SE-41296 Gothenburg, Sweden
hanst@sikt.chalmers.se
† Accepted: June 8, 2001

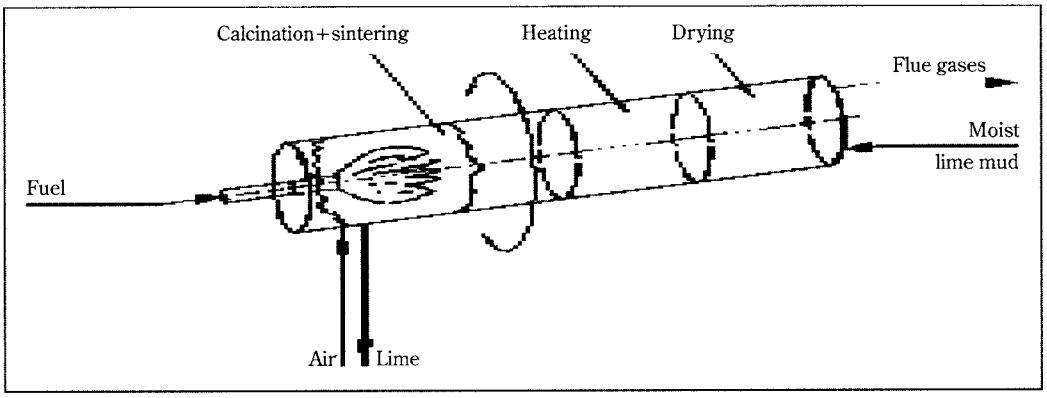

Fig. 1 The rotary kiln.

and then shaped cylindrical pellets, which were heat-treated in different temperatures and atmospheres. Sintering was measured as the compressive strength of the sintered pellets. The strength measured after recarbonation was by far the highest compared with the strengths obtained when using SO_2, O_2 and H_2O in the atmosphere (Skrifvars et al. 1992) or when doping the lime mud with different impurities (Tran et al. 1992); neither did high-temperature sintering yield as hard pellets (Tran et al. 1992). Tran et al. (1992) found that the relationship between the compressive strength and degree of recarbonation was linear, independent of reaction time, temperature and conditions at which the pellets had been treated.

The influence of carbon dioxide on the intra-particle sintering of calcined lime mud was investigated earlier by Lindblom et al. (1996). The sintering equipment was a quartz glass reactor, and a small sample of lime mud was placed on a fritted disc of quartz glass. Hot gases with different mixtures of nitrogen and carbon dioxide flowed through the solid, and the intra-particle sintering was determined by measuring the specific surface area. It was found that carbon dioxide strongly enhanced sintering, since it affected the decrease of the specific surface area. At equilibrium, the specific surface area decreased even more, probably due to recarbonation as well as sintering.

The objective of the current study was to investigate how the partial pressure of carbon dioxide in the sintering atmosphere influences the formation of rings and balls. This was done in a pilot-scale rotary kiln, where dried lime mud was treated at different temperatures in varying concentrations of carbon dioxide. Sintering was determined by measuring the specific surface area and, in addition, the strength of the formed balls was measured. The residual carbonate was also analysed.

Experimental

Equipment

The experiments were carried out in a rotary kiln with a heated length of 1125 mm and a diameter of 190 mm (Entech, Energiteknik AB). The inner tube is made of high-temperature steel (Avesta Sheffield 253 MA). Three electrical heating elements (type S) in three zones are used to heat the kiln electrically; it can be operated at temperatures up to 1000°C. The temperature is controlled with PID-controllers (Eurotherm 2116). Two extra thermocouples (Eurotherm, type N) are inserted through the ends of the kiln; they are located in the gas bulk and in the solid material, respectively. The kiln is horizontal and, consequently, is a batch reactor. It can be rotated at a speed of up to 6 rpm. Both ends are partly made of quartz glass to allow for visual control, and are easily removable.

The sintering atmosphere is nitrogen with different concentrations of carbon dioxide. The two gas flows are set with flowmeters (Platon A10HS786PC and EK-EB89, Kytölä Instruments AB) and then mixed in a static mixer. The total gas flow is 20 l/min, at STP and the total pressure is 1 bar. The mixed gas is preheated in a preheater (Entech, ETF 30/12) to about 500°C before entering the rotary kiln. The outgoing gas is cooled in a heat exchanger and passes two cyclones before leaving the system.

Lime mud

Two different lime muds had to be used. The first one was used in the extensive series at 850°C, and the second one was used when studying the influence of temperature. The composition of the two lime muds can be seen in **Table 1**. The specific surface area, mean particle size, initial density and the content of

carbonate and free calcium oxide of the lime muds are shown in **Table 2**.

SEM images were also taken to characterize the different lime muds: **Figure 2** shows that their microstructures are similar.

Table 1 Composition of the dried lime muds. The elements, with the exception of calcium, are expressed as their related oxides.

Component	Lime Mud I (weight-%)	Lime Mud II (weight-%)
$CaCO_3$	86	97
MgO	0.87	0.35
Na_2O	7.4	0.92
P_2O_5	5.8	0.67
Al_2O_3	0.28	<0.035
SiO_2	0.73	0.15
K_2O	0.057	<0.058
Fe_2O_3	0.18	0.033
TiO_2	0.018	0.0062
MnO	0.030	0.025

Table 2 Characteristics of the lime muds.

	Lime Mud I	Lime Mud II
Specific surface area (m^2/g)	2.2	1.0
Mean particle size (μm)	26	24
Density (kg/m^3)	2646	2630
Carbonate (weight-%)	79	88
Free calcium oxide (weight-%)	0.78	0.76

Procedure

Before heating the kiln, 2 kg of the dried lime mud was spread out evenly in the reactor. This was done through the openings in both of the ends. The ends were then mounted and it was ensured that the two extra thermocouples were positioned correctly. The gas flow was turned on and the heating of the gas and the kiln was started as well as the rotation of the kiln. The temperature increase in the gas bulk and the solid material was monitored, and it was found that it took about 1 hour for them to reach the predetermined temperature. This hour was subtracted from the total time in order to obtain the reported time.

When the experiment was over, the heating was turned off. The gas flow and rotation were continued, however, in order to achieve as rapid cooling of the solid material as possible. When the temperature had decreased to about 400°C, everything was turned off and left overnight. The following morning, the reactor was opened and the interior of the tube was inspected. Three different kinds of samples of the reburned lime mud were taken, i.e. balls, rings and powders. These were analysed with respect to carbonate and free calcium oxide. The specific surface area was measured by a five-point nitrogen adsorption method in Micromeritics Gemini 2370, and the theory of Brunauer, Emmet and Teller (Lovell and Shields 1984) was used to calculate the specific surface area. The balls were photographed and their sizes noted. For the sintering experiments that produced hard enough balls, the compression strength of the balls was measured with a granular strength testing unit from Etewe.

The variables were temperature, sintering time and partial pressure of carbon dioxide. The temperatures

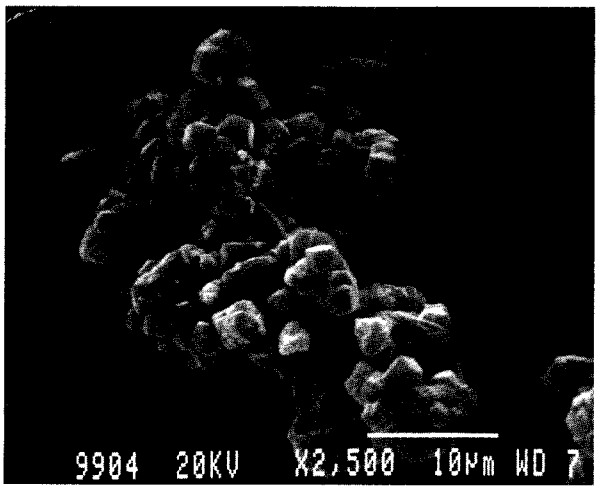

Fig. 2a Lime mud I.

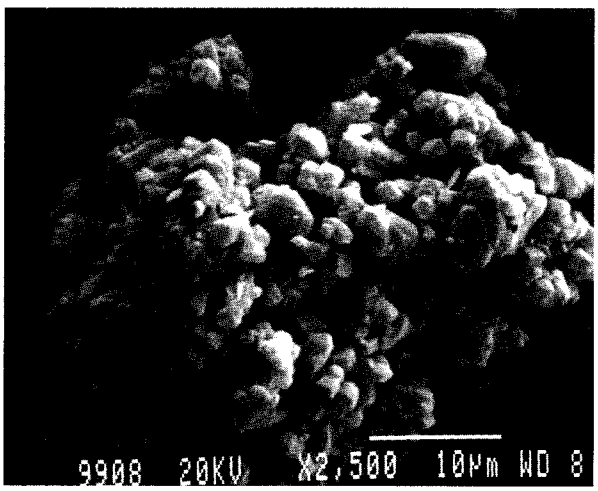

Fig. 2b Lime mud II.

investigated were 750, 850 and 950°C, with the emphasis on 850°C. The time ranged between one and seven hours. The partial pressure of carbon dioxide at equilibrium is a function of temperature, and was calculated with the help of an expression derived by Baker (1962). At 750°C, the partial pressure at equilibrium is 9 kPa and, at 850°C 48 kPa. Therefore, the partial pressure of carbon dioxide was chosen to vary from 0 to 60 kPa. At 950°C, the partial pressure at equilibrium is 190 kPa, which was impossible to use in the experiments since the total pressure was 100 kPa.

Results

The results were evaluated separately for dusts, rings and balls. The dusts and rings showed a similar behaviour in all aspects, while the balls behaved slightly differently in some tests. The balls generally had a larger specific surface area, and the calcination reaction was also slower, probably due to a lower heat transfer rate. In most of the graphs presented here, the results of the analysis balls are shown because, of the balls, rings and dusts, it was possible to measure the strength of the balls. The balls were chosen to be shown throughout the paper so that the strength could be compared with residual carbonate, specific surface area etc.

When comparisons between different temperatures are made, the powder, rather than the balls, is shown. This is because balls were seldom present after experiments at 750°C. It should also be remembered that during the experimental work, two different lime muds had to be used. Lime mud I was used in the first part of the study when the relationships between strength, specific surface area and residual carbonate at 850°C were investigated. In the latter part of the study, where the temperature dependence was examined, lime mud II was used. Several experiments at 850°C had to be rerun with the second lime mud for the purpose of comparing the results at different temperatures. The lime mud used is clearly indicated in each graph.

The first lime mud was used, and the temperature was 850°C, in the experiments referred to in the first part below. It is shown in **Figure 3** that the degree of calcination (a higher degree is shown by a low residual carbonate) is high at partial pressures of carbon dioxide up to 24 kPa in the sintering atmosphere. The degree of calcination is high, especially longer times, which can be seen in the low residual carbonate. When increasing the partial pressure of carbon dioxide above 24 kPa, the residual carbonate increases rapidly. At partial pressures between 48 and 60 kPa, equilibrium is obtained, and the high residual carbonate is the same after five and seven hours. Only results for the balls are shown in **Figure 3**. It should be mentioned, though, that for constant partial pressures below equilibrium (48 kPa), the range of the residual carbonate from one to seven hours is wider for the balls than for the dusts and rings. The wider range is mainly because of the poor calcination after one hour. It can also be seen that, at all partial pressures of carbon dioxide below equilibrium, the residual carbonate decreases with increasing time but, at and above equilibrium, there is no change between five and seven hours.

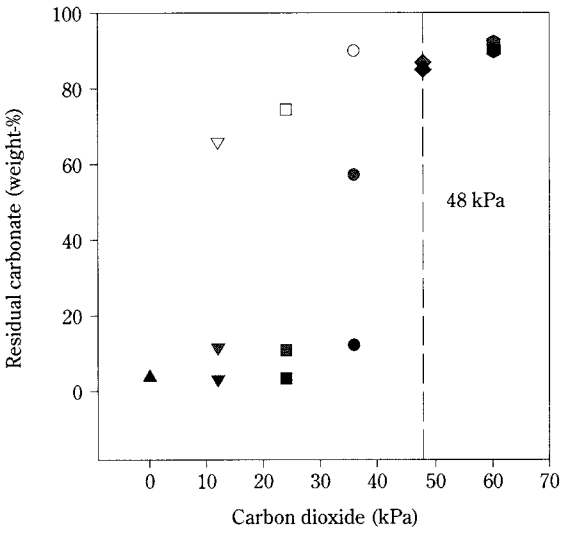

Fig. 3 Lime mud I. Balls.
All of the symbols described below are not necessary for this figure, but the same notation will be used for all other figures unless otherwise stated. They are therefore also included here, so that comparisons may be made.
Residence time: Open ("white")=1 hour, grey=5 hours and black=7 hours.
Partial pressures of carbon dioxide (kPa): Δ=0, ▽=12, □=24, ○=36, ▯=48 and hexagons=60.

When studying the change in specific surface area with the degree of calcination, two different behaviours can be observed (**Figure 4**). The largest specific surface areas can be found when pure nitrogen is used as the sintering atmosphere. If carbon dioxide is added up to a partial pressure of approximately 24 kPa, the specific surface area decreases rapidly as the residual carbonate increases slightly. Conversely, when a value of the residual carbonate of about 10 weight-% is reached, the specific surface area starts to increase again slowly as higher partial pressures of

carbon dioxide are used. Simultaneously, the residual carbonate increases rapidly up to equilibrium, as already shown in **Figure 3**. Moreover, it is evident that the specific surface area decreases with increasing time, which can be seen in **Figure 4**.

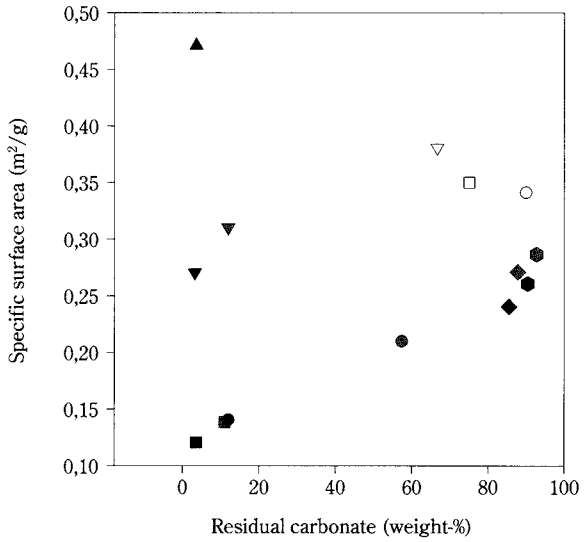

Fig. 4 Lime mud I. Balls. Symbols as in **Figure 3**.

The size of the balls seems very much dependent upon the residual carbonate. An almost linear relationship can be seen in **Figure 5**, with decreasing ball diameters as the residual carbonate increases. For low partial pressures of carbon dioxide in the sintering atmosphere, the results indicate that the size of the balls seems to increase with time. When equilibrium is reached, time does not seem to be as important to the size any more.

It is obvious that the size of the balls has a significant effect on their strength. In **Figure 6** it can be seen how, at constant time and increasing partial pressure of carbon dioxide, the strength increases and the balls decrease in size. At equilibrium and higher partial pressures of carbon dioxide, the strength increases with increasing time, even though the size of the balls is almost constant. In **Figure 7** it is evident that at constant time, as the residual carbonate increases with increasing carbon dioxide, so does the strength. The strength of the balls is plotted versus the specific surface area in **Figure 8**. It can be seen that with increasing time, the strength increases and the specific surface area decreases at constant, relatively high, concentrations of carbon dioxide. The increase in strength becomes more rapid, and the decrease in specific surface area slower at higher concentrations of carbon dioxide (the lines in the graph are there to make it easier to follow the trend described). The strength after five hours with a partial pressure of carbon dioxide of 36 kPa is high. When all kinds of comparisons were made, it was observed that this particular experiment gave unusually small balls, which results in a higher strength than could be expected.

In the second part of the study, the influence of temperature was investigated, whereby lime mud II was used. **Figure 9** shows how equilibrium is reached for two different temperatures. At a partial pressure of carbon dioxide of 90 kPa, the samples at 750°C reached a high level of carbonate and, at 850°C,

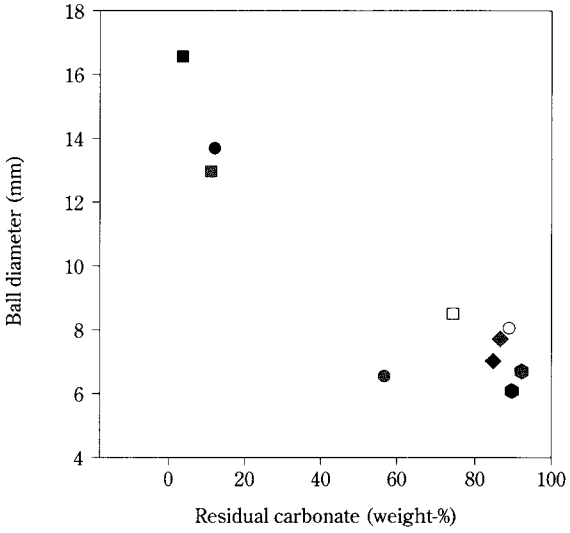

Fig. 5 Lime mud I. Balls. Symbols as in **Figure 3**.

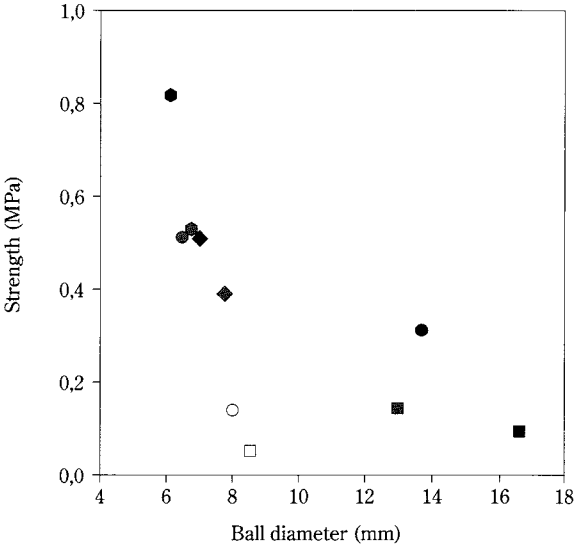

Fig. 6 Lime mud I. Balls. Symbols as in **Figure 3**.

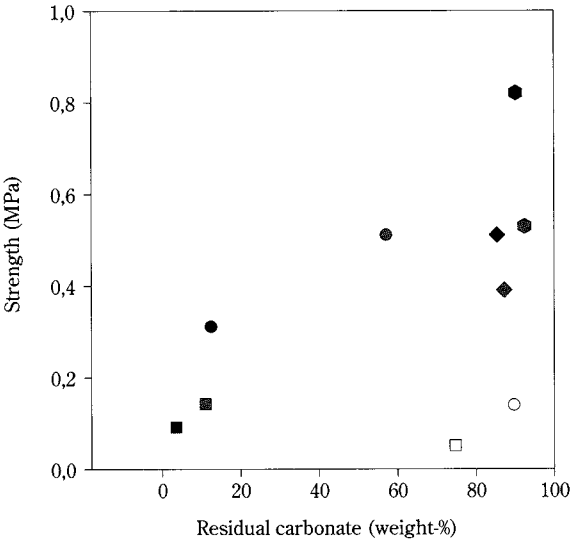

Fig. 7 Lime mud I. Balls. Symbols as in **Figure 3**.

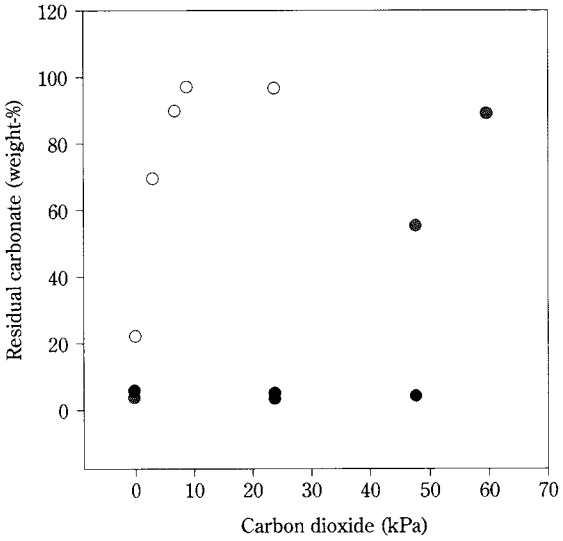

Fig. 9 Lime mud II. Powder. White=750°C, grey=850°C and black=950°C. Time: 7 hours.

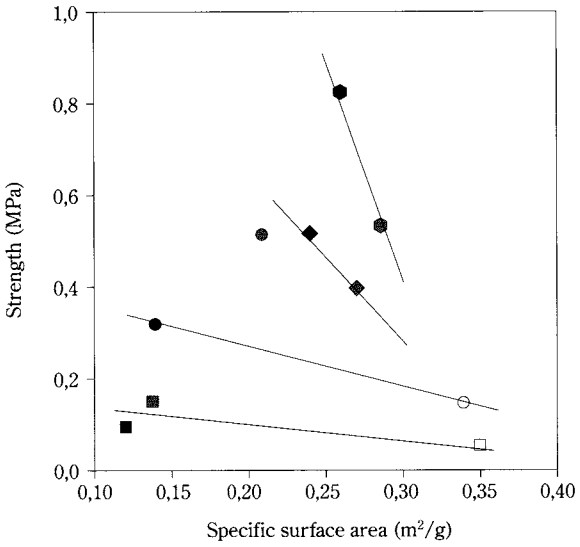

Fig. 8 Lime mud I. Balls. Symbols as in **Figure 3**.

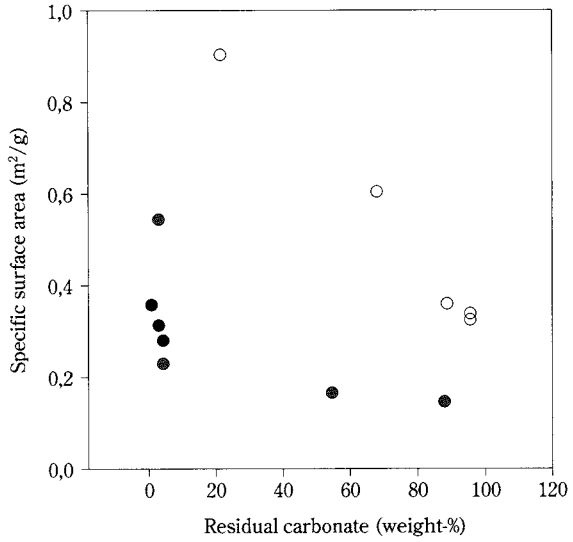

Fig. 10 Lime mud II. Powder. White=750°C, grey=850°C and black=950°C. Time: 7 hours.

the same level is reached at about 60 kPa. At 900°C, equilibrium is never reached.

The second lime mud was observed as having a different relationship between specific surface area and residual carbonate compared with the first lime mud (cfg. 4), **Figure 10**. Here, it can be seen how the surface area decreases with increasing residual carbonate over the whole range at both 750 and 850°C. It may seem as though the reduction of the specific surface area ceases when equilibrium is reached. The results shown in **Figure 10** represent powder, since not enough balls were created with the second lime mud. The few balls that were formed were not hard enough to withstand strength measurements, which is the reason why no comparisons in strength for the different temperatures could be made.

Discussion

It is shown that with the equipment used, the calcination reaction at partial pressures of carbon dioxide below equilibrium takes almost seven hours to be completed, but the residual carbonate value after five hours is close to the seven-hour value. After only 1

hour, the balls still have a high residual carbonate, probably as a result of a poor heat transfer rate. The equilibrium partial pressure of carbon dioxide, calculated using the expression of Baker (1962), agrees well with the measured data where, when using this partial pressure, it can be seen how the same high value of residual carbonate is obtained after both five and seven hours.

The behaviour of the specific surface area when varying the partial pressure of carbon dioxide and thus the residual carbonate is ambiguous, as the two different lime muds show different trends at 850°C. The first one showed a minimum in specific surface area at about 10 weight-% of residual carbonate. It looked as if calcium carbonate, with its larger particles, sinters more slowly compared with calcium oxide exposed to carbon dioxide. The second lime mud, on the other hand, decreases its specific surface area with increasing residual carbonate over the whole range investigated. This can be observed at both 750 and 850°C, and is in accordance with the findings of Lindblom et al. (1996), when the influence of carbon dioxide on the sintering of reburned lime mud in a tube reactor was studied. This equipment allowed a small amount of lime mud, placed on a porous quartz glass disc, to be penetrated by gas. The reduction in specific surface area with increasing carbon dioxide is thought to be caused by higher mobility in the solid when the reacting gas is present. It seems as though the reduction of the surface area finally slows down significantly. The particles involved have become large by then, and the sintering process is consequently slow.

The same trend as was seen for the two lower temperatures with decreasing surface areas with increasing residual carbonate could not be seen at 950°C, where the residual carbonate is low, independent of carbon dioxide. The specific surface area is higher at 950°C and low residual carbonate than for the samples with high residual carbonate at 850°C. A possible explanation could be that mobility is not as high for the first condition as the latter, since the calcination reaction is strongly favoured when compared to recarbonation at this high temperature. Tran et al. (1992) observed the same behaviour when they sintered formed pellets. They report that sintering at a high temperature without recarbonation gave a much lower strength than sintering at a low temperature with recarbonation.

There are substantial differences in the compositions of the two lime muds used in the present study. The first one has less calcium carbonate and significant amounts of sodium and phosphorus, but SEM images did not reveal any major differences in microstructure between them. The second one resembles the one used in the earlier study with the tube reactor; maybe that is why their behaviours can be compared. Furthermore, when using the first one, balls were formed under most of the conditions investigated, which was not the case for the second one. It may be that the first lime mud, because of some kind of surface phenomenon due to substantial concentrations of sodium and phosphorus, forms balls and rings more easily. Thus, the following discussion regarding balls is based on the results from lime mud I only. It should be noted that the results suggest that the balls are formed at an early stage, before calcination.

For partial pressures of carbon dioxide below equilibrium, the size of the balls increases with time. It is evident that, at those conditions, the lime keeps adhering to balls already formed, which makes them grow. When equilibrium is reached, neither the residual carbonate nor the ball size are affected by time after five hours, as the same values are obtained after seven hours. Calcium oxide seems more prone to form large balls than calcium carbonate.

The relation between ball size and its strength shows a decrease in strength with an increase in diameter. The same observation was made in a previous study (Lindblom and Theliander 1998), where the strength of several industrial reburned limes were tested, and balls of different sizes were used. The smaller balls have most likely been allowed to sinter more, because of homogeneous heating. It should be mentioned that the strength measurements give a high average error, about 50%. Considering the various ball sizes present after an experiment, and how they are picked manually for strength measurements, the high average error seems reasonable. All trends discussed here can, despite the high average error, still be discerned.

The strength was also shown to increase with increasing residual carbonate. Both Skrifvars et al. (1992) and Tran et al. (1992) formed pellets that were sintered under controlled conditions, and they both observed the same behaviour. According to Skrifvars et al. (1992), the greatest strength development occurs just before decomposition. Tran et al. (1992) claims a linear relationship between strength and degree of recarbonation. It is believed that the way in which the solid material closes its pores when it recarbonates accounts for the increased strength.

The strength of the balls, at constant partial pres-

sure of carbon dioxide and temperature, increases with time as the specific surface area decreases. The reduction in specific surface area with increasing time is in accordance with several earlier studies (Hanson 1993, Lindblom et al. 1996). The simultaneous increase in strength is probably due to the reduction in porosity as sintering proceeds. The exact same behaviour was identified in the study concerning the sintering of formed lime pellets (Lindblom and Theliander 1998).

When studying **Figure 8** it is obvious that, for higher partial pressures of carbon dioxide, the reduction of surface area slows down at the same time as the increase in strength accelerates. Different kinds of mechanisms seem to be involved during the sintering process, depending on the partial pressure of carbon dioxide. The results at low partial pressures with a rapid reduction in surface area, but not very strong agglomerates, could suggest that small particles have become large, but that the bonds between them are not very strong. Some kind of bulk diffusion process could be expected to make the particles grow in such a manner. Conversely, at higher partial pressures, a surface diffusion process may result in strong necks between particles without the same densification as at lower partial pressures. The high partial pressures, of course, result in extensive recarbonation, and this would make a surface diffusion process likely to occur.

The fact that strength increases with increasing residual carbonate means that, in an industrial rotary kiln, whenever the calcined material recarbonates, the strength is enhanced. Recarbonation occurs when either the temperature is low enough and/or the concentration of carbon dioxide is high enough. The conditions in the middle of the kiln, close to the beginning of the calcining zone, enhance recarbonation and, not surprisingly, severe ring problems are common in this region. In this area, even a small drop in temperature may lead to recarbonation.

Balls were used in the present study in order to measure agglomerate growth and strength. The results obtained could be used to explain ring growth and hardening in industrial rotary kilns. They show that, besides the fact that rings are able to grow with increasing time if the solid material is influenced by some kind of as yet unknown surface phenomenon, they will also become harder whenever recarbonation occurs. The combination of growing rings which become harder with time makes the middle of the industrial rotary kiln prone to severe ring formation.

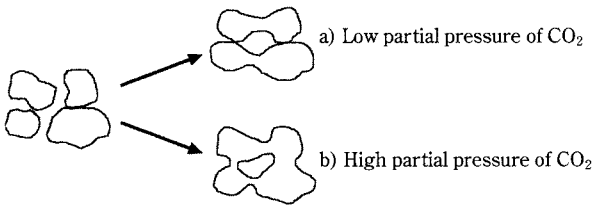

Fig. 11 Different kinds of mechanisms depending on the partial pressure of carbon dioxide.

Concluding remarks

The balls were found to behave slightly differently compared with the rings and dusts in that they generally had a larger specific surface area and a higher content of carbonate. This is thought to be due to a lower heat transfer rate. It was shown that, at 850°C, the degree of calcination is high at partial pressures of carbon dioxide up to 24 kPa in the sintering atmosphere. At higher partial pressures, the residual carbonate increases rapidly and, at as high partial pressures as 60 kPa, equilibrium is obtained.

The two lime muds showed different behaviours in terms of the influence of carbon dioxide on sintering. The first one reached a minimum in specific surface area at about 10 weight-% of residual carbonate, while for the second one, the specific surface area decreased with increasing residual carbonate over the whole range investigated. For the second lime mud, at the highest temperature used, i.e. 950°C, the residual carbonate was low at all partial pressures of carbon dioxide. For these samples, the specific surface area was higher than for those with a high residual carbonate at 850°C.

The strength of the balls decreases as they increased in size and, furthermore, the strength increased with increasing residual carbonate. At constant temperature and partial pressures of carbon dioxide, the strength of the balls increased with time and the specific surface area decreased. Also, as the partial pressure of carbon dioxide increased, the reduction of the specific surface area became slower and the increase in strength more rapid.

Acknowledgements

The skilful and extensive experimental work of Mr. Aslan Akbas is acknowledged here. The authors are indebted to The Swedish National Board for Industrial and Technical Development for financial support of the project.

References

1) Baker, E. H., "The calcium oxide – carbon dioxide systems in the pressure range 1-300 atmosphere", *J. Chem. Soc.* 464-469 (1962)
2) Hanson, C., "Lime mud reburning – Properties and quality of the lime produced", PhD Thesis, Chalmers University of Technology, Göteborg (1993)
3) Lindblom, J., Hanson, C. and Theliander, H., "Sintering of calcined lime mud – the influence of carbon dioxide", *Pulp and Paper Canada* 97:10, T355 (1996)
4) Lindblom, J. and Theliander, H., "The physical strength of lime pellets", TAPPI Proceedings, 1998 International Chemical Recovery Conference, 561-569 (1998)
5) Lovell, S. and Shields, J. E., "Langmuir and BET theories" in "Powder surface and porosity", Second edition, 14-29, Chapman and Hall, New York (1984)
6) Skrifvars, B.-J., Frederick, W. J. and Hupa, M., "Chemical reaction sintering as a cause for lime kiln rings", TAPPI Proceedings, 1992 International Chemical Recovery Conference, 161-167 (1992)
7) Tran, H., Mao, X. and Barham, D., "Mechanisms of ring formation in lime kilns", TAPPI Proceedings, 1992 International Chemical Recovery Conference, 169-179 (1992)

Author's short biography

Josefina Lindblom

The author received her M. Sc. and Ph. D. degrees from Chalmers university of Technology in 1993 and 1999. She is a researcher at the Institute for Prospective Technological Studies, a Joint Research Centre for the European Commission, Seville, Spain since 2000. Her research areas are sintering in the lime kiln and recovery boiler, and the impact on competitiveness of the use of best available technology in the pulp and paper industry.

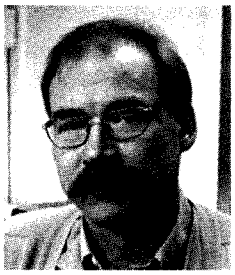

Hans Theliander

The author is Professor in Forest Products and Chemical Engineering at Chalmers University of Technology since 1999. His mayor research interests are heterogeneous reactions (gas-solid or liquid-solid), all aspects of dewatering of solid materials, systems engineering and recycling aspects.

On the Relationship between Torque and Flow Structure in Powder Mixers[†]

B.F.C. Laurent and J. Bridgwater
*Department of Chemical Engineering, University of Cambridge**

Abstract

This work establishes the link between direct measurement of powder flow in a horizontal mixer and shaft torque. Three agitator designs were used: one featured six long flat blades, one a long flat blade and the third, four series of short paddles. With the single long flat blade agitator, the amount of powder moved by the blade was related to the torque. The relationship between torque and non-dimensional mean tangential velocity was demonstrated using phase diagrams. These remained unchanged with increase of agitator speed. The fluctuations of the torque with the long flat blade agitator were logically related to those for the single blade. The torque on the short-paddle agitator exhibited larger fluctuations which were strongly affected by the level of fill and the agitator speed. Powder cohesion had a significant influence on the mean and standard deviation of the instantaneous torque. Instantaneous torque measurement may be seen as a valuable method for process control.

Introduction

Developing fundamentals from laboratory experiments to industrial scale often represents a challenge in particle technology. This is particularly true in devices in which powders are mixed. However, there is now a range of activity in the literature as witnessed in recent papers. In 1995, McCarthy *et al.* developed a theory of powder behaviour in rotary drums. Metcalfe *et al.* (1998), provided some insights into powder flow in the cross-section of a rotating cylinder using MRI. Moakher *et al.* (2000), and Cleary *et al.* (2001), presented a comparative study between experimental results in tumbling blenders and results given by a discrete element model.

In the literature, it is argued that the mean torque <T> and an angular velocity ω can be correlated using a power number $N_p=\frac{P}{\rho_b\omega^3D^5}\frac{D}{L}$ where P=<T> ω is the power, D the mixer diameter, L the mixer length, ρ_b the bulk density of the bed. N_p is a function of the Froude number $Fr=\frac{\omega^2D}{2g}$, where g is the acceleration due to gravity, and of dimensionless variables and parameters linked to powder properties. This has been employed by Müller and Rumpf (1967) amongst others. For a regime in which interparticle friction is dominant, they propose for a free-flowing powder that N_p is proportional to Fr^{-1}. For a mixer of given diameter and length, this expression indicates that the torque is independent of speed and is proportional to bed density.

Positron Emission Particle Tracking (PEPT), a non-invasive method of investigation liquid or solid systems, provided much more information on powder flow patterns than other methods commonly used such as sampling. In PEPT, the motion of a single positron-emitting tracer is followed. The typical output is a data file containing the spatial co-ordinates of the tracer as a function of time. Particles moving at up to 20m/s have been followed. For the present work, the uncertainty of the positron camera in three dimensions or spatial resolution is approximately 2 mm for a speed of 0.2 m/s, and increases with the speed of the positron emitter to about 5 mm at a speed of 1 m/s (Parker *et al.*, 1993). The tracer used here was a 0.6-mm-diameter resin particle containing absorbed water with ^{18}F atoms produced by bombarding the water with ^{3}He ions.

Studies using the PEPT technique include that of Broadbent *et al.* (1993) and of Jones and Bridgwater (1997), who investigated powder mixing in a plough-

* Pembroke Street, Cambridge, CB2 3RA, UK
† Accepted: July 7, 2001

share mixer. Experiments were also performed on fluidised beds (Parker *et al.*, 1997). More recently, Laurent *et al.* (2000) provided for the first time the general description of the mixing patterns created by a single-blade agitator in a cylindrical shell. In the course of such studies on internal flow in mixers, information was also obtained on the torque. Here, this information is analysed and presented. It comprises instantaneous torque for a single-blade system, mean torque and torque fluctuations as the agitator moves through the particle bed. The study continues by examining how the blade structure determines the instantaneous torque, and offers proposals to assist the understanding of internal behaviour using information delivered by the authors in the previous work relying on PEPT.

Experimental Equipment and Materials

Experiments were conducted in a horizontal cylindrical mixer of diameter 270 mm and of length 650 mm. Three types of agitators were used. The first one, agitator A, is a simplified version of an industrial mixer, having six 53-mm-wide blades with an angular separation of 60°. The plane of each blade is inclined by 45° in radial direction. Each blade is supported at six points along its length by radial supports. Each of these supports has three radial plates with open space between and is fixed onto a 90-mm-diameter rotor shaft (**fig. 1**). Since two of the radial supports are close to the ends of the mixing chamber, the series of radial supports defines five axial compartments. The clearance between the tip of the blade and the inside of the cylindrical shell is 8 mm, and that between the blade tip and the inside of the end of the shell is 4 mm. The second device, agitator B, is a simplified version of the first agitator. Here, the radial supports carry one single flat blade as opposed to six. The third device, agitator C carries radial arms separated by 90° with mixing elements fastened to a rotor shaft of diameter 110 mm (**fig. 2**). The mixing elements are paddles of 97 mm by 46 mm inclined to form a 45° angle with the radial direction of the arms. Two sets of arms separated by 180° carry two series of five paddles each. The arms carry a further four rectangular bars, these being 104 mm long and of cross-section 19 mm by 19 mm. The clearance between the end wall and the paddles is 10 mm, that between the paddles and the cylindrical shell is 2 mm. A further two sets of arms, set at 90° to the others, carry four paddles and three rectangular bars.

The torque applied to the agitator shaft was measured by a torque gauge consisting of a set of strain gauges fixed on the surface of the rotating shaft and mounted to form a measuring bridge. The difference of potential created when a torque was applied was measured by a voltmeter to give a measure of the torque, the value being converted into a digital signal for acquisition by computer using an analogue-digital converter having a frequency of acquisition of 10 kHz. The linear range of measurement of the torque gauge was 0 to 200 Nm with a precision of 0.1%. The torque gauge was calibrated statically by a sequence of eight

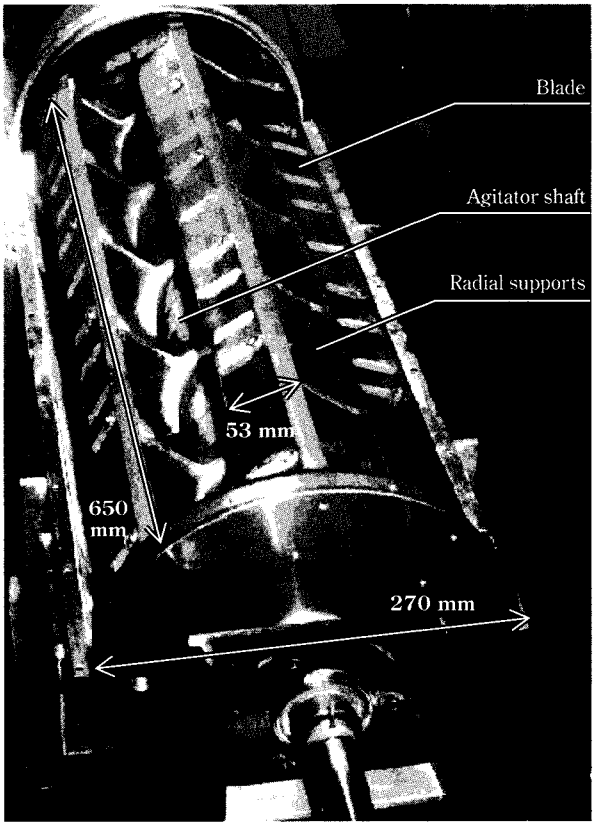

a) General view of agitator A

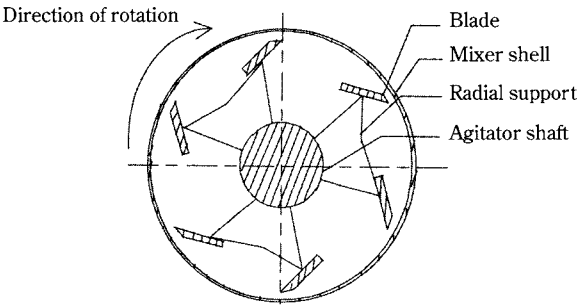

b) Cross-sectional view

Fig. 1 Agitator A

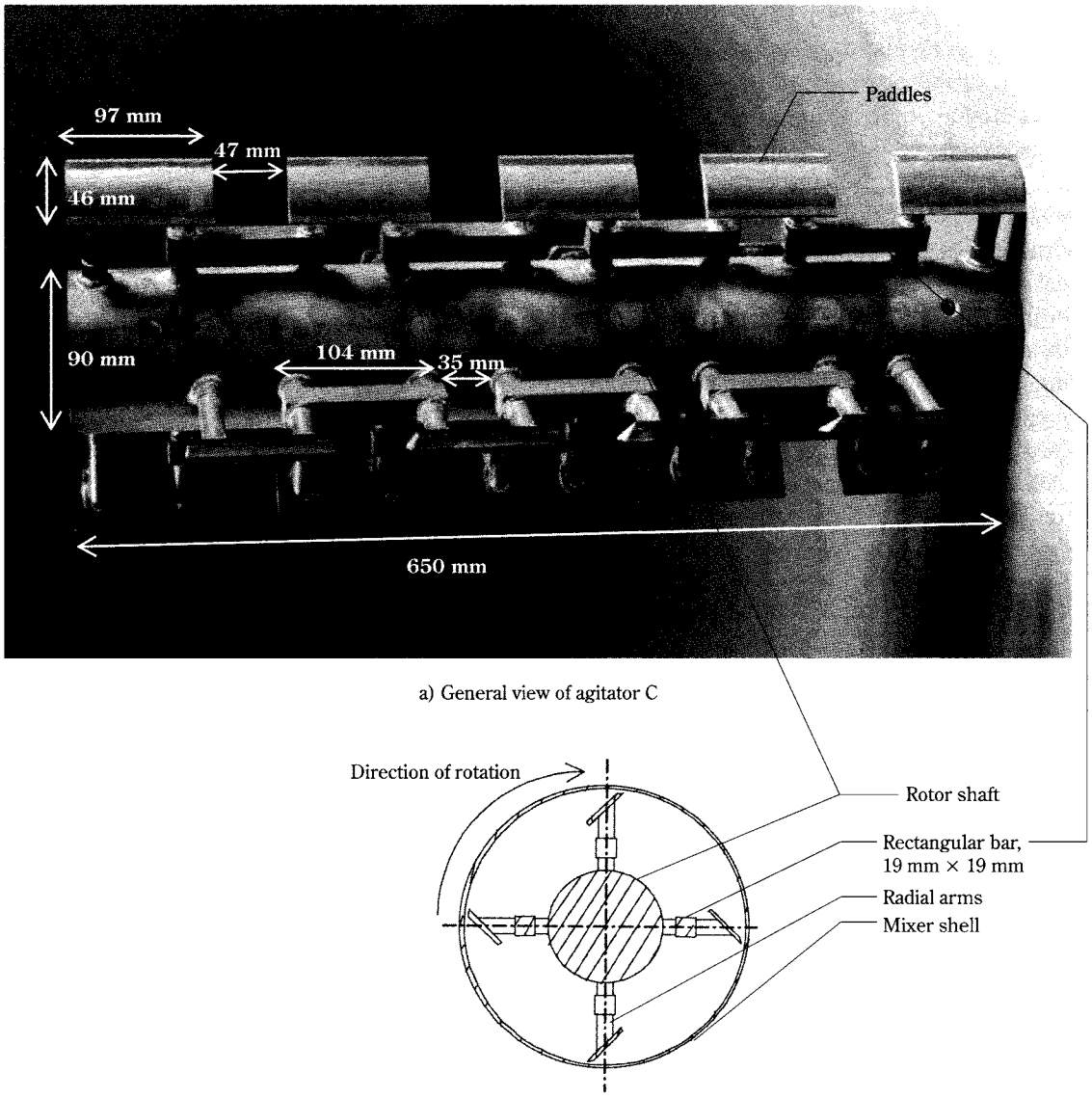

Fig. 2 Agitator C

weights fixed at the end of a horizontal bar fixed radially to the rotation axis. The digital signal produced by the converter corresponded to the known applied torque. This gave a linear relationship between the digital signal and the torque. Instantaneous torque was measured typically twenty times per second.

Two principal powders were used. Powder 1 had a bulk density of 510 kg/m^3 with a mean particle diameter of 520 μm and an internal angle of friction of 30°. The powder was free flowing. Powder 2 had a bulk density of 420 kg/m^3 with a mean particle diameter of 550 μm and was cohesive. The radioactive tracer had a diameter of 0.6 mm and true density close to that of the bulk particles, its motion thus representing the behaviour of the bed.

Analysis of results

The principal results employ powder 1; the effect of powder type is discussed at the end of this section.

Mean torque

Here, experiments conducted in the laboratory horizontal mixers are compared as a function of level of fill. The results are presented using the power number $N_p = \frac{P}{\rho_b \omega^3 D^5} \frac{D}{L}$ in **figure 3**. This shows the influence of the agitator type on the power number for

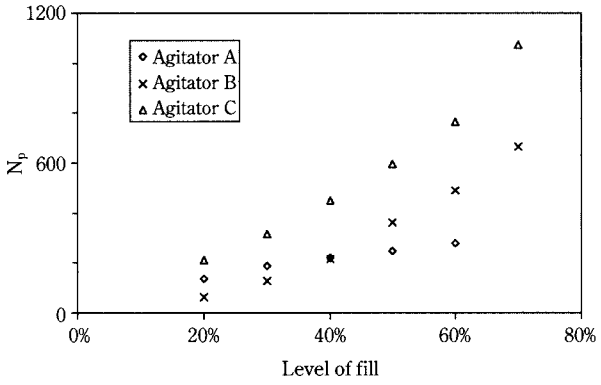

Fig. 3 Power number N_p vs. level of fill for the three agitator designs; 38 rpm

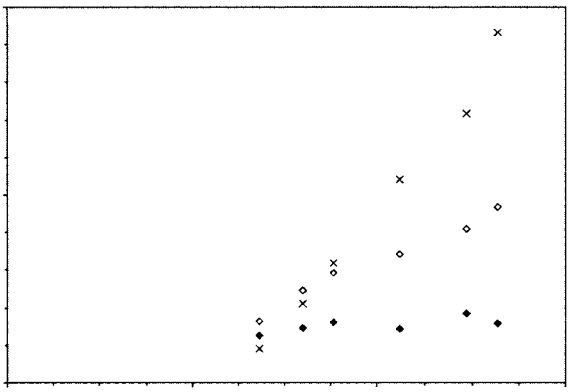

Fig. 4 Mean torque vs. circumferential length $\mathcal{L}$, agitators A and B; 38 rpm

F_r=0.22. The power consumption is higher for agitator C and the difference between the agitators A and C increases with the level of fill. Thus at a fill of 60%, the power consumption of agitator A is around a third that of agitator C. In order to seek an explanation for this difference, consider the area of the mixing elements (including the blades, the rectangular bars and their supports) projected onto a plane passing through the axis of rotation. The projected surface of the mixing elements is 960 cm^2 for agitator C and 1520 cm^2 for agitator A. One thus sees that the projected surface of the mixing elements is not the dominant factor; this matter is pursued below.

If the level of fill is below 40%, then the mean torque needed for the single blade (agitator B) is less than the six-blade agitator A, whereas the converse is found if the level of fill exceeds 40%. This is ascribed to the existence of slip surfaces within the material for the single-blade system whereas for the six-blade agitator, the powder moves as a block around the inner surface of the mixer shell.

Figure 4 compares the mean torque as a function of $\mathcal{L}$ for the six-blade agitator A with the single-blade agitator B, where $\mathcal{L}$ is the length of the circumference of the mixer in contact with the particle bed. The level of fill corresponding to $\mathcal{L}$ is also represented on a double axis. The circumferential length is thought to be a significant parameter since the application of a torque on the shaft results in frictional forces on the mixer bowl which might be expected to be proportional to the surface area in contact with the powder bed.

At 20% of fill, the mean torque for agitator A is roughly twice that for agitator B, this suggesting that two blades of agitator A are in the bed at the same time. At 40% of fill, the mean torque is the same for agitators A and B. At 60% of fill, the mean torque for agitator B is around twice that for agitator A. Hence, increasing the number of blades does not increase the torque in a proportional manner. For the single-blade agitator B it may be suggested instead that the bed reconsolidates between each blade pass. This means that the single blade of agitator B has to overcome the stress necessary to put the material in a state of incipient failure, whereas the bed is continuously stirred by the six-blade agitator A. This implies that the local bulk density of the bed is lower with agitator A and that stresses in front of each blade will be less with more blades stirring the bed, leading to a lower torque due to each blade.

Flow structure and instantaneous torque

Agitator B

Figure 5 shows the influence of the level of fill on the torque reported as a function of blade position. The results plotted have been adjusted by subtracting

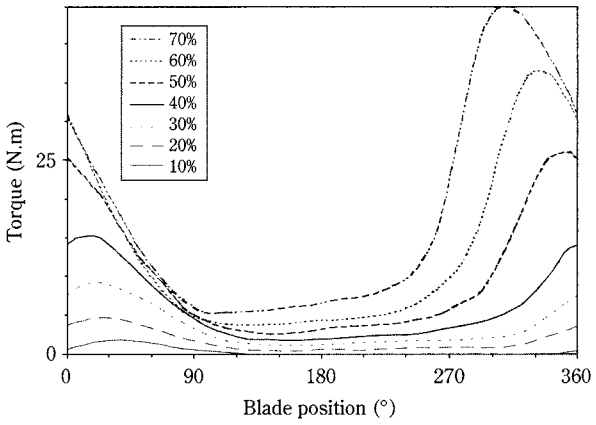

Fig. 5 Influence of blade position and level of fill on the torque; agitator B, 38 rpm

the torque measured with no fill in order to take into account the lever effect exerted by the single blade; the associated fluctuation has an amplitude of 1 Nm. The blade angle co-ordinate is defined to be zero when the leading edge of the blade is directly below the centre of the shaft. The position of the powder bed in the mixer is obtained using PEPT (**fig. 6**).

Consider first the torque corresponding to a level of fill of 20%. The signal is low when the blade is out of the particle bed, i.e. blade position of 120° to 315°. As the blade penetrates into the bed, the torque increases and reaches its maximum when the blade position is 30°. It then decreases as the blade moves towards the free surface and then out of the bed. **Figure 6** shows the occupancy, i.e. probability of finding the tracer particle, integrated along the whole length of the mixer, and gives a measure of the local bulk density. Thus **figure 6 b)** corresponds to a blade position of around 30° for 20% of fill. The bed is being pushed along the wall and is also being slightly raised. Material does not flow over the shaft, and cascading over the blade is about to start. The maximum value of the torque increases with level of fill; the blade position at which the torque is a maximum changes its phase, this changing from 25° at 20% of fill to 330° at 60% of fill.

Figure 7 shows the occupancy for a level of fill of 60%. The dotted line marks the approximate position of the free surface of the bed. Thus **figure 7 b)** corresponds to the approximate blade position where the torque is maximum for 60% of fill, and shows the blade being engaged into the whole bed and sliding it along the wall. Most of the material is pushed over the shaft.

At all levels of fill, the torque decreases and reaches a value which is not zero when the blade is out of the bed. This is due to the action of the friction forces on the radial supports of the blades described in **figure 1**. As the level of fill increases, this value increases since the contact area between the particle bed and the radial supports increases. **Figure 4** also presents the mean of the torque for both agitators A and B from which the base of the signal for agitator B, as just defined, has been subtracted. This procedure is correct for agitator B but an approximation for agitator A, as the particle bed does not relax to rest and may even be fluidised. The resulting signal is independent of fill for agitator A and follows the same trend for agitator B. This demonstrates that the single-blade agitator B has to overcome a reconsolidation effect after each blade pass, whereas the bed is constantly stirred by agitator A, leading to a torque that is independent of the amount of material in the mixer.

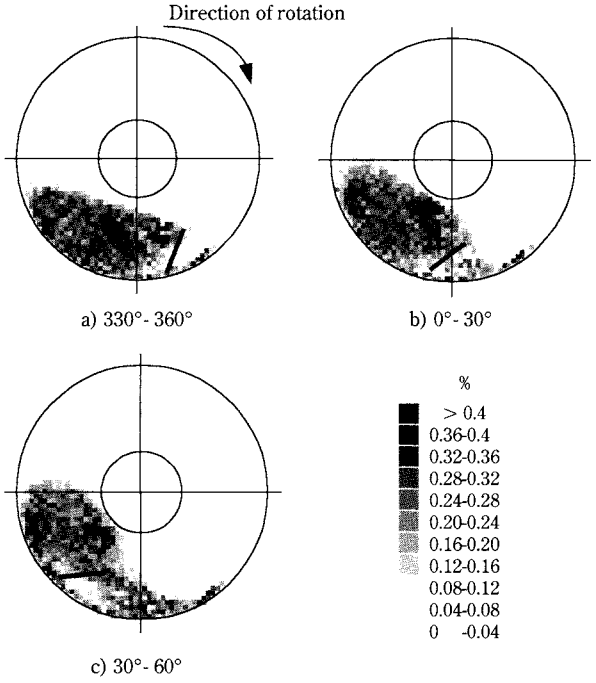

Fig. 6 Cross-sectional view of agitator B for six different blade positions, 20% of fill, 38 rpm

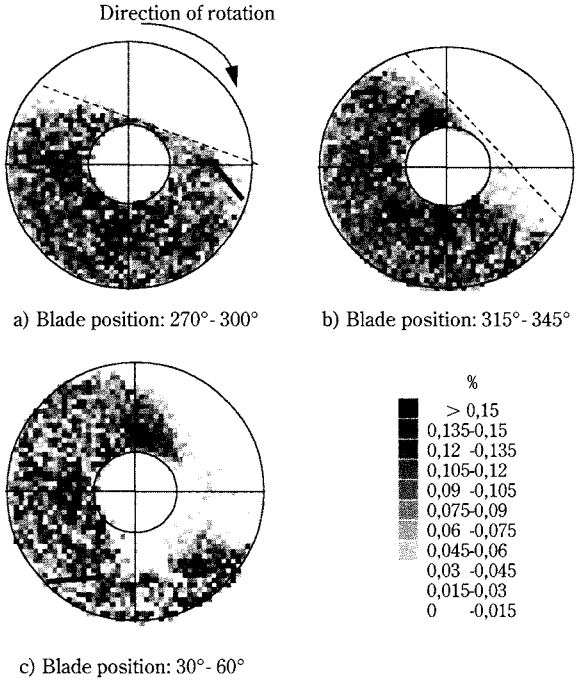

Fig. 7 Cross-sectional view of agitator B for six different blade positions, 60% of fill, 38 rpm

In both cases (i.e. with/without the base signal), the curves for the two agitator types intersect for a fill of around 40%, which is thought to be a critical value as the flow patterns switch from pure cascade mode to channelled flow between the agitator shaft and the cylinder wall. For the six-blade system, the blades in the bed have an associated but strongly non-additive effect. The signal corresponding to the base of the single-blade agitator B is mainly believed to be due to the friction forces of the radial supports. The signal for agitator A, from which the base value has been subtracted, shows that the value of the torque is practically independent of the amount of fill in the system. It follows that the material rotates as a core around the central shaft. This means that the number of blades does not then have any influence on the torque necessary to rotate the core of material. It is to be expected that there is a critical value of angular spacing of blades below which the system returns to rest between each blade pass.

Analysis of PEPT data provides direct access to the mean tangential velocity of the tracer, offering this parameter as a way of characterising the powder flow. **Figure 8** presents the mean tangential velocity and the torque measured on the agitator shaft versus the blade position for three levels of fill 20%, 40% and 60%. Between 180° and 270°, the blade is always out of the particle bed, the tangential velocity is low since the bed is in or close to a rest state at all levels of fill. As the blade moves into the bulk and reaches 315° for 20% of fill, 300° for 40% of fill and 250° for 60% of fill, the tangential velocity increases progressively. The tangential velocity then increases progressively to reach a maximum for a blade position of 0°, 345° and 330° at a fill level of 20%, 40% and 60%, respectively. At a blade position of 90° for 20% fill, the velocity decreases to reach a minimum. As the blade moves further out of the particle bed, the tangential velocity increases and reaches a value close to zero when the bed returns to the rest state.

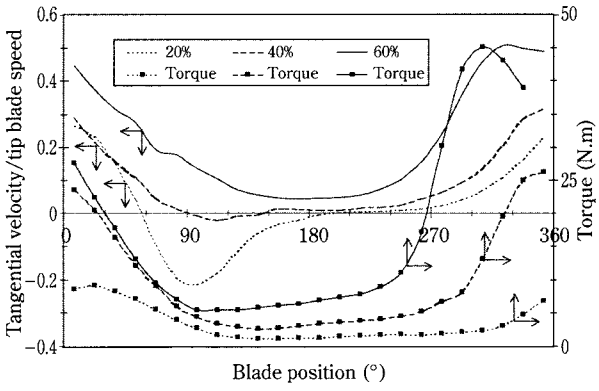

Fig. 8 Mean tangential velocity of the tracer and torque vs. blade position, agitator B, 38 rpm

Compare now the torque with the tangential velocity for one blade rotation. Between 180° and 270°, the tangential velocity is very low and the bed is at rest. Over this angular interval, the torque is low as the blade is out of the particle bed at all levels of fill. The signal is then due to the frictional forces between the bed and the radial supports (**fig. 1**), to the friction at the bearings supporting the rotating shaft together with the torque due to asymmetry of the radial arms and blade. The torque starts to increase for a blade position of 315° for 20% of fill, 270° for 40% of fill and 250° for 60% of fill; this corresponds to the blade entering the particle bed. This is in agreement with the approximate position of the lower point of the free surface (**figs. 6, 7**).

At 20% fill, the torque increases further as the blade moves through the bulk and reaches a maximum when the blade position is 30°. This can be related to **figure 6 c)** showing how part of the bed is lifted by the blade. The maximum in the torque occurs when all the material is being lifted by the blade before it cascades into the void behind the blade. As material cascades down the free surface of the bed, less material is lifted by the blade and the torque decreases; the tangential velocity becomes negative since, at this level of fill, material is flowing down the free surface in anti-clockwise direction below the centre of the agitator. As the blade moves out of the bulk, the mean tangential velocity reaches a minimum. Most of the motion in the bed then occurs at the free surface. Once the blade is completely out of the particle bed, the torque is low and the mean tangential velocity increases to reach a value close to zero. This phase brings the bed back to its initial state.

As the fill increases, most of the material moves over the agitator shaft in clockwise direction; the tangential velocity stays positive as a result. The torque can be again related directly to the flow structure developed.

Phase diagrams offer a way of relating the torque to the tangential velocity. The parametric curve quantifies the phase between the two signals. **Figure 9** shows the influence of the fill on the phase diagram of the torque vs. mean tangential velocity, the agitator speed being 38 rpm. At 20% of fill, the parametric curve of torque vs. tangential velocity is a flattened ellipse, the direction of rotation being anticlockwise, implying that the tangential velocity is ahead of

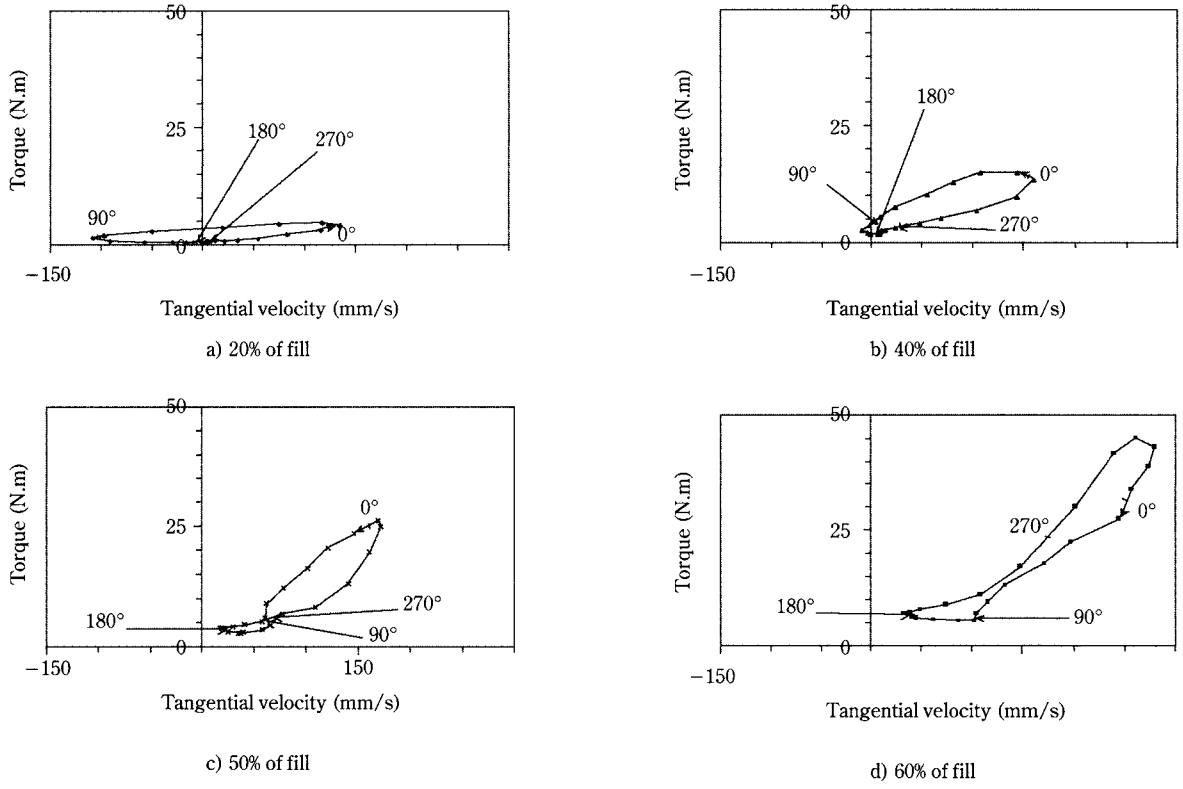

Fig. 9 Influence of fill on the phase diagram (torque vs. tangential velocity), agitator B, 38 rpm
Parameters on curves: blade position in the bed; 0° origin: blade in lower vertical position

torque. The diagram indicates the position of the blade in the bed. Both the tangential velocity and the torque reach their minimum in the range of blade positions 180° to 270° as the bed is then at rest. The shape of the curve remains the same up to 40% of fill, although the ellipse is here less flattened, i.e. the phase between the tangential velocity and torque has increased. At 50% of fill, the shape of the curve has dramatically changed and becomes octagonal. This level of fill is considered to represent a change in the patterns inside the cylinder, being at the transition point below which the powder cascades essentially onto the free surface below the agitator shaft and above which the powder rotates mainly around the agitator shaft. At 70% fill, the shape of the curve has reverted to an ellipse which rotates here in clockwise direction, showing that tangential velocity is now lagging behind torque.

Using the same presentation, **figure 10** shows the influence of the agitator speed on the phase diagram of the scale torque vs. the non-dimensional tangential velocity, the level of fill being 60%. Here, the amplitude of the curve is not affected by the agitator speed. This feature is related to the general non-dimensional structure of the flow being kept invariant with respect to the agitator speed, i.e. flow displacements scale with the number of blade passes. However, close observation of the shape of the curves shows that the shape is not kept invariant with increase of speed. At 20 rpm and 25 rpm, the curve is slightly elliptic, rotating in clockwise direction, showing that the tangential velocity is lagging slightly behind the torque. At 38 rpm and 45 rpm, the curve becomes octagonal.

Agitator A

Figure 11 illustrates the torque for agitator A; data for the single-blade agitator B are included for comparison purposes, the level of fill being 60% and the rotation speed 38 rpm. The signal for agitator A exhibits six peaks, each of these being spaced by 60°. These peaks correspond to the six flat blades of the agitator. The amplitude of the fluctuations of the torque for agitator A is here around 3% of its average of 8 Nm. The torque measured with the single-blade agitator reaches a maximum for a blade position of 330°, for which a peak in the torque for the six-blade agitator A also appears.

The time-occupancy diagram for agitator A is pre-

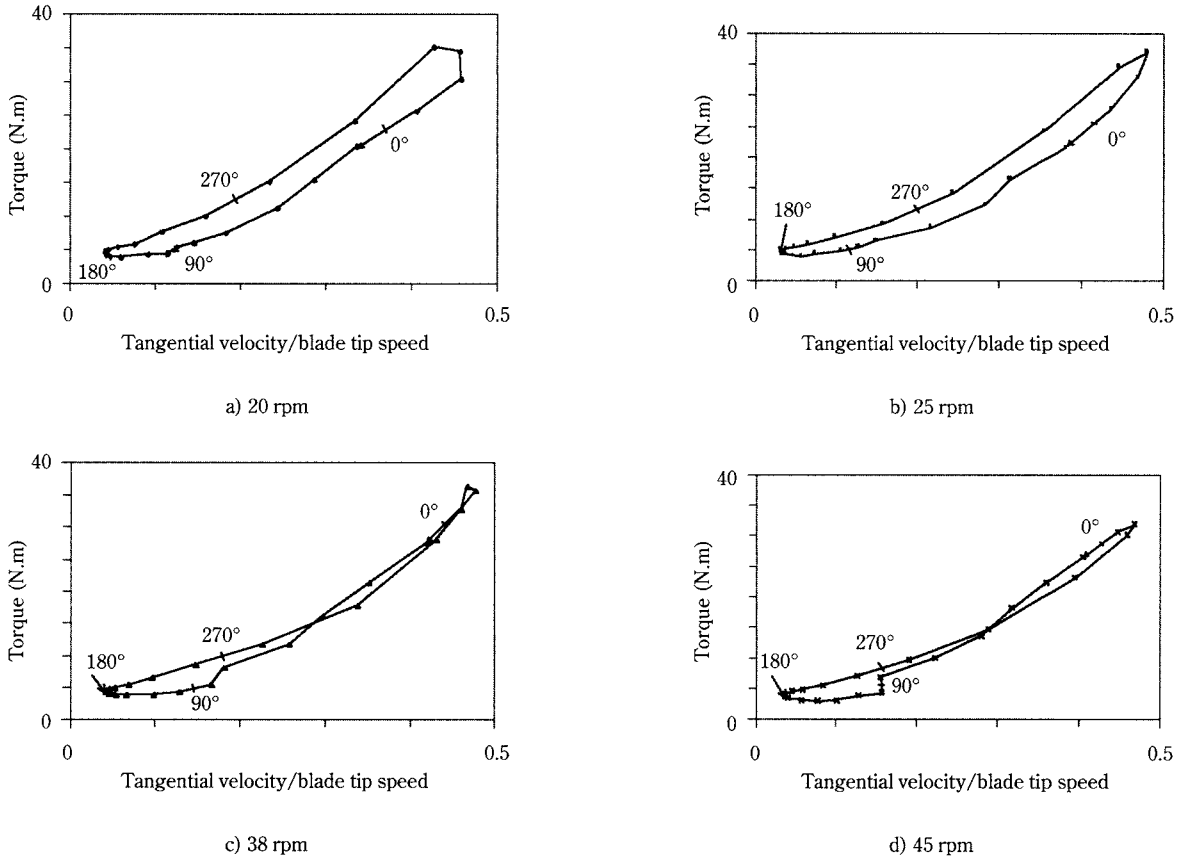

Fig. 10 Influence of speed on the phase diagram (torque vs. tangential velocity), agitator B, 60%
Parameters on curves: blade position in the bed; 0° origin: blade in lower vertical position

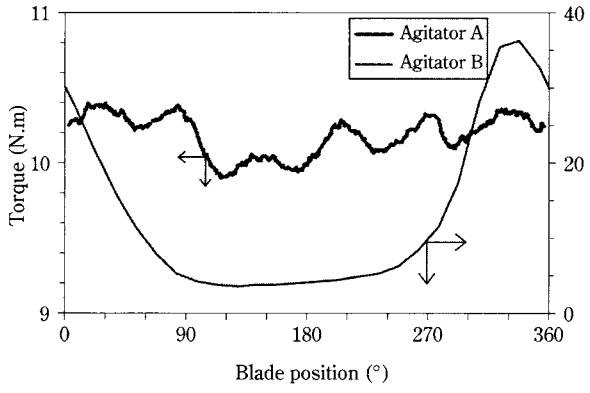

Fig. 11 Torque vs. blade position; agitators A and B, 38 rpm; level of fill: 60%

sented in **figure 12 a)** and shows the existence of two zones of higher probability of presence of the tracer. The first zone is situated beneath the rotating shaft, immediately above the dotted line showing the locus of the inner radius of the rotating blades. The second region of higher occupancy lies in the clearance between the locus of the tip of the blade and the inside of the shell. By comparison, **figure 12 b)** shows the time-occupancy diagram for the single-blade agitator B. This diagram is integrated over all the blade positions. It exhibits similar regions of higher density as for the six-blade agitator A, although these regions appear less clearly. The region of higher density situated beneath the agitator shaft corresponds to a loop of circulation where agitation is poorer, as reported in an earlier work by Laurent *et al.* (2000).

Agitator C

For the short-paddle agitator C, the torque observed is periodic at all levels of fill investigated. **Figure 13 a)** gives an example of the signal as the fill varies from 20% to 70%. The periodicity of signals being π, we show only half of the full cycle. For a level of fill of 60%, the amplitude of the fluctuations of the torque is in this case 50% of its average compared to 3% for the six-blade agitator A for the same fill. The peaks of the torque correspond to the paddles and rectangular bars fixed on the four series of arms sepa-

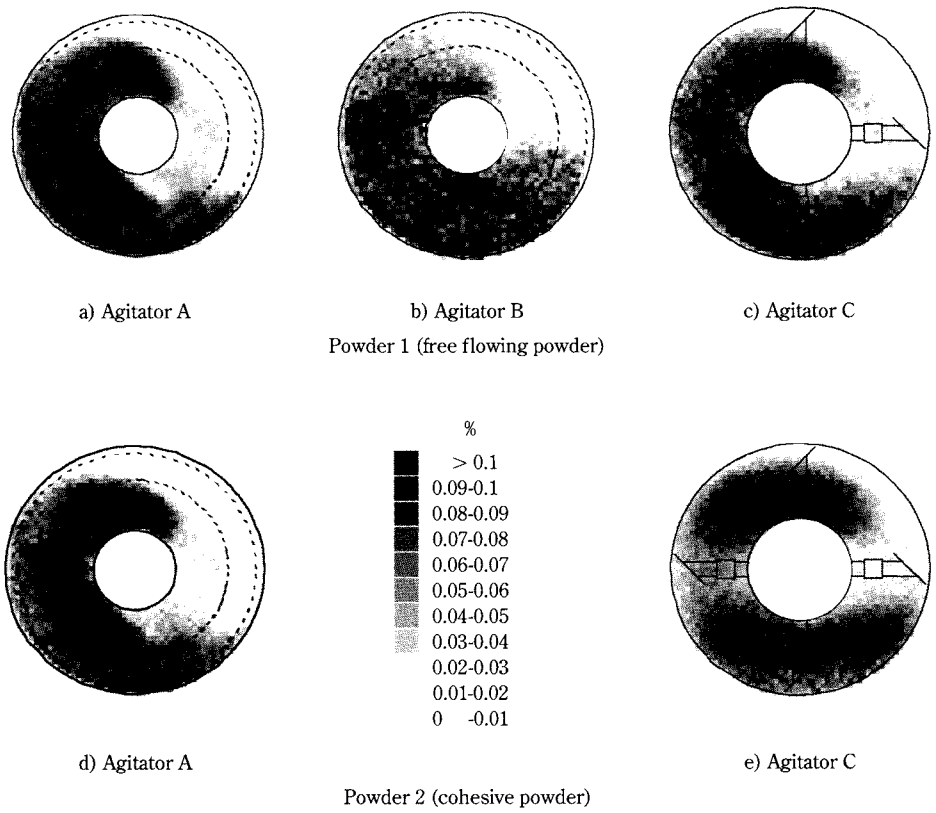

Fig. 12 Time-occupancy diagram, transaxial view of the three agitators, 38 rpm; 50% of fill

rated by 90° each. The angular position of each peak corresponds to a radial arm forming an angle with the vertical of 60°.

Consider the torque for 20% of fill. The blade position of 0° corresponds to the lower vertical position of one of the series of arms carrying four paddles. The signal increases and reaches its maximum for a blade position of 30°, which corresponds to four paddles being in the particle bed. Then the torque decreases as the blades move out of the bed. It increases again, here due to the five paddles penetrating into the material, and peaks for a blade position of 120°. The cycle then resumes with the other set of four and five paddles. The signal shows that the peak corresponding to the five paddles being in the middle of the bed is slightly higher than the other peak corresponding to the four paddles.

With increase of fill, the difference of amplitude between the two peaks increases. The position of the peaks is altered, the maximum of the torque corresponding to the five paddles being 120° at 20% of fill and 60° at 70% of fill. At this fill, the peak corresponding to the four paddles has been absorbed into the other peak.

Figure 14 a) shows the influence of the agitator speed on the angular distribution of the torque for powder 1. The mean torque is not affected by an increase of speed. However, the shape of the signal changes dramatically. At low speed, the signal exhibits two peaks, corresponding to the two different series of arms carried by agitator C. The ratio of the two peaks is around 0.86. By comparison, the ratio of projected surface of the mixing elements (paddles and rectangular bars) of the arms carrying five paddles to those carrying four paddles is about 0.81. As the agitator speed increases, the ratio of the two peaks decreases and reaches 0.65 for a rotation speed of 60 rpm. By then, the lower peak has been practically absorbed into the other dominant peak. The maximum has also been shifted towards a higher blade position in the bed, corresponding to a delay in phase.

Figures 12 a), b) and **c)** show comparative performances for agitators A, B and C at 50% of fill. Two

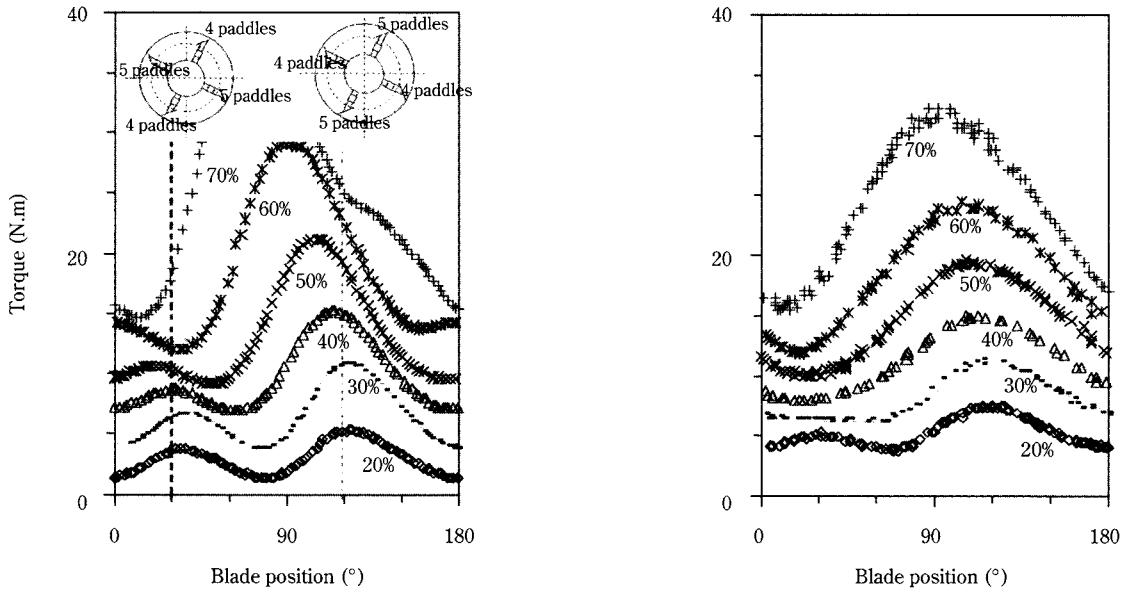

a) Powder 1, free flowing

b) Powder 2, cohesive

Fig. 13 Influence of the level of fill on the torque; 20 rpm, agitator C

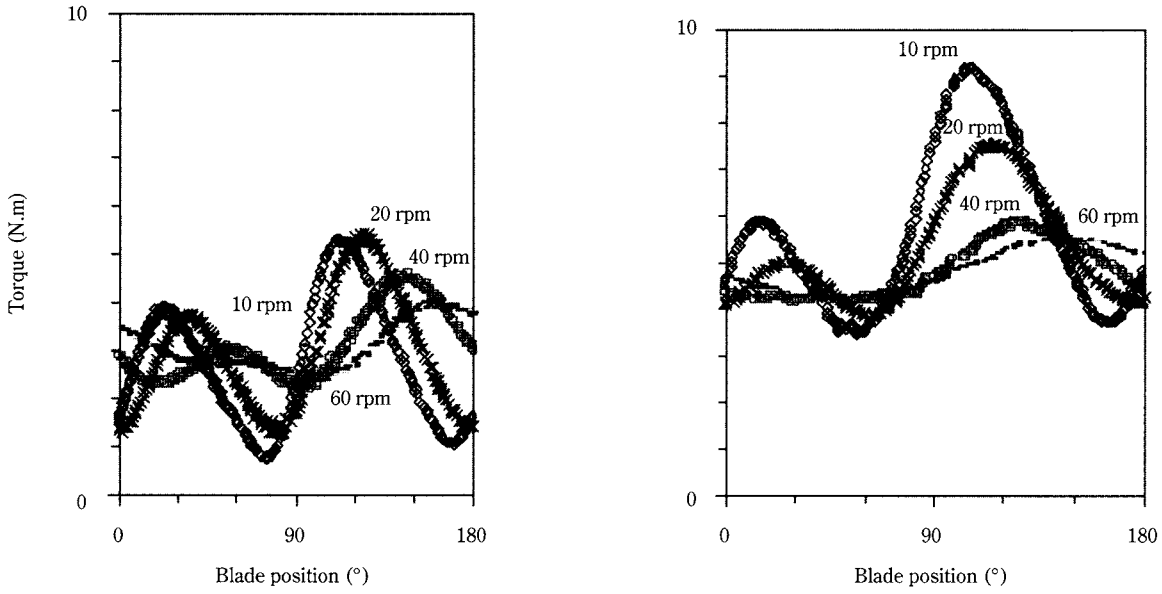

a) Powder 1, free flowing

b) Powder 2, cohesive

Fig. 14 Influence of the agitator speed on the torque; 20% of fill, agitator C

zones of higher density appear with agitator C, one beneath the shaft and the other immediately above it. As the agitator rotates, material is able to escape to the rear of a paddle of this agitator through the space between adjacent blades. The boundaries are not as distinct as those of the higher density zones for agitator A because the mixing elements of agitator C leave less material in the mixer cross-section unaffected by the blades and the rectangular bars. This is a likely explanation of the higher power consumption with the short-paddle agitator C. Thus the rectangular bars of agitator C operate between radial positions of 70

mm and 90 mm, and the paddles between ones of 100 mm and 133 mm. These rectangular bars eliminate the zone of little radial agitation observed with agitator A. These observations suggest that material has more even radial distribution in the cross-sectional plane with agitator C, as confirmed in **figure 13 a)** and **c)**.

Influence of the powder

The experiments reported in **figures 13 a)** and **14 a)** for powder 1, the free-flowing powder material, were repeated for powder 2, the cohesive material. The findings are given in **figure 13 b)** and **14 b)**. From **figure 13**, we see that the mean torque at 20% fill is greater for powder 2 and the amplitude of the fluctuations is reduced. On increasing the fill, the second peak corresponding to the four paddles is lost even at 30% fill. Allowing for the difference in bulk densities by supposing that torque is proportional to the bulk density enhances the differences. With powder 2, a cohesive material, we deduce that the correlation established by Müller and Rumpf (1966) is incomplete. **Figure 14 b)** shows the effect of speed; the behaviour of the two systems is again markedly different. The mean torque could be used as a characterisation of the material in the mixer. However, the standard deviation is also a sensitive parameter.

Figure 15 presents the standard deviation of the torque vs. fill for both powders 1 and 2. It shows a remarkable linear relationship, particularly for the cohesive powder 2. It also shows that the amplitude of the oscillations is lower for the cohesive powder 2 than for the free-flowing powder 1. This demonstrates

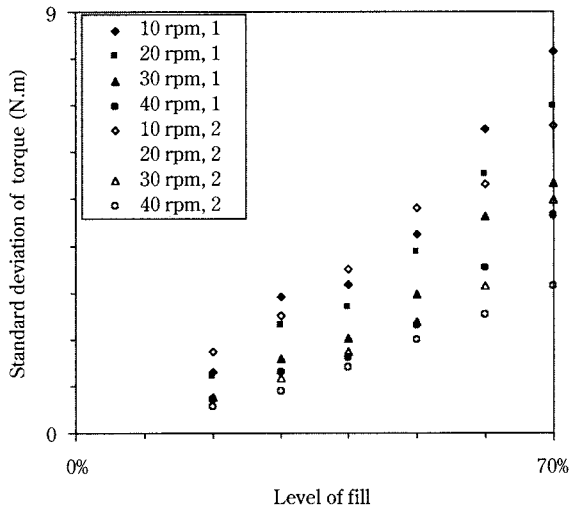

Fig. 15 Influence of the rotation speed on the standard deviation of the torque, agitator C, powders 1 and 2

the potential for on-line instantaneous torque measurement to control an industrial process. Indeed, these diagrams can be used to relate the mean torque and torque fluctuations to the operating parameters of the system as well as the quality of the product.

When PEPT experiments are performed with powder 2 (**fig. 12 d)** and **e)**), we find with agitator A that the material is more concentrated between the inner shaft and the inner tip of the blades; the region of bed less influenced by the blade is emphasised. For agitator C, a body of material is found above the shaft with a more open region in the horizontal plane of the inner shaft.

Conclusions

Experiments have been carried out here with three horizontal cylindrical mixers. The systems have been discussed using the mean torque, instantaneous torque, particle tangential velocity and powder occupancy of each mixer. Three designs have been employed.

Investigations using a single-blade agitator showed that as the blade progresses into the particle bed, the increase of torque corresponds to an increase in the mean tangential velocity. The torque is a maximum for a blade position corresponding closely to the maximum of the mean tangential velocity. In this system, the powder is moved in a series of pulses by the blade and comes back to rest after each blade pass.

The torque measured with a six-blade agitator was found to be periodic, having a frequency six times that of the agitator speed. Each peak of the torque corresponded to the same blade position as for the single-blade agitator. However, the mean could be less than the mean torque for just a single blade because the whole of the material is kept in constant motion by the multi-blade agitator. The torque was found to be 30% lower at 20% of fill with the six-blade agitator than with the short-paddle agitator. This difference increased with the level of fill.

The instantaneous torque and the mean tangential velocity can be conveniently related using phase diagrams. It can happen that the mean tangential velocity leads the torque, as well as the converse. The variations of speed, level of fill and cohesion of the material are all manifest in the relationship between instantaneous torque and blade position.

For the future, instantaneous torque can thus be used as a simple and effective means of monitoring and controlling process operation. The knowledge of the mean and fluctuations of torque at drive and

vessel support, or even internally on the mixing elements, would be of further theoretical and industrial interest. Analysis of instantaneous torque provides a means of gaining insight into the scale-up of vessel diameter, a significant and unresolved issue.

Acknowledgments

The authors would like to express their gratitude towards Elf for the financial support.

Notation

D	[m]	Mixer diameter
L	[m]	Mixer length
$\mathscr{L}$	[m]	Circumferential length
N	[rpm]	Agitator speed
P	[W]	Power
<T>	[Nm]	Mean torque
ρ_b	[kg/m^3]	Powder bulk density
ω	[rad/s]	Agitator angular velocity

Bibliography

Broadbent C.J.; Bridgwater J.; Parker D.J.; Keningley S.T.; Knight P.: "A phenomenological study of a batch mixer using a positron camera", *Powder Technol.*, **76**, (1993), 317-329

Cleary P.W.; Debroux F.; Morton D.: "Advanced DEM modelling of industrial granular flows" *World Congress of Chemical Engineering, Melbourne, in preparation* (2001)

Jones J.R.; Bridgwater J.: "A case study of particle mixing in a ploughshare mixer using Positron Emission Particle Tracking", *Int. J. Miner. Processing*, **53**, (1997), 29-38

Laurent B.F.C.; Bridgwater J.; Parker D.J.: "Motion in a particle bed agitated by a single blade" *AIChE J.*, **46**, (2000), 1723-1734

Malhotra K.; Mujumdar A.S.: "Particle mixing and solids flowability in granular beds stirred by paddle-type blades", *Powder Technol.*, **61**, (1990), 155-164

McCarthy J.J.; Shinbrot T.; Metcalfe G.; Wolf J.E.; Ottino J.M.: "Mixing of granular materials in slowly rotated containers", *AIChE J.*, **42**, (1995), 3351-3363

Metcalfe G.; Lachlan G.; Liffman K.; Cleary P.; Shattuck M.: "Imaging of laboratory-scale industrial granular flows", *World Congress on Particle Technology 3, Eds. IChemE*, Rugby, UK, (1998), paper 349

Moakher M.; Shinbrot T.; Muzzio F.J.: "Experimentally validated computations of flow, mixing and segregation of non-cohesive grains in 3D tumbling blenders", *Powder Technol.*, **109**, (2000), 58-71

Müller W.; Rumpf H.: "Das Mischen von Pulvern in Mischern mit axialer Mischbewegung" (Powder mixing in mixers with axial agitation), *Chem. -Ing. Tech.*, **39**, (1967), 365-373

Parker D.J.; Broadbent C.J.; Fowles P.; Hawkesworth M.R.; McNeil P.: "Positron emission particle tracking – a technique for studying flow within engineering equipment" *Nucl. Instr. and Meth.*, **326**, (1993), 592-607

Parker D.J.; Dijkstra A.E.; Martin T.W.; Seville J.P.K.: "Positron emission particle tracking studies of spherical particle motion in rotating drums", *Chem. Eng. Sci.*, **52**, (1997), 2011-2022

Author's short biography

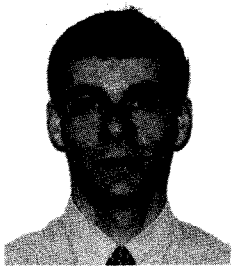

Bruno Laurent

Bruno Laurent is Research Associate at the Department of Chemical Engineering of the University of Cambridge and is a Junior Member of the Isaac Newton Institute (University of Cambridge). His research interest is in the processing of granular materials, mainly in the area of mixing and segregation of powders. He graduated from the ENSIC-INPL in Nancy (France) in 1993 and subsequently obtained a Diplomarbeit at the Department of Mechanical Processing at the University of Karlsruhe (Germany). His PhD thesis, supervised by Professor Bridgwater, was concerned with the study of powders flowing inside a scaled-down version of an industrial mixer. Since the completion of his PhD, his main research interest has been the fundamentals of granular flow.

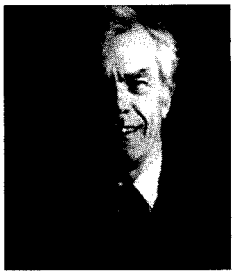

John Bridgwater

John Bridgwater is Shell Professor of Chemical Engineering at the University of Cambridge. He has had a research interest centred in Particle Technology throughout his career, recently having worked on paste flow and extrusion, powder attrition and the fundamentals of powder mixing, He was Chairman of the World Congress on Particle Technology held in the UK in 1998. He is Chairman of the Board of Executive Editors of Chemical Engineering Science.

The Measurement of Adhesion Forces using the Centrifuge Method and AFM†

B. Hoffmann[a], G. Hüttl[b], K. Heger[c], B. Kubier[a], G. Marx[c] and K. Husemann[a]

[a] *TU Bergakademie Freiberg, Institut für Mechanische Verfahrenstechnik und Aufbereitungstechnik*

[b] *TU Bergakademie Freiberg, Institut für Keramische Werkstoffe*

[c] *TU Chemnitz, Institut für Chemie*

Abstract

Many studies have been made on the theoretical and practical aspects of the several adhesion forces which determine the properties of bulk solids of fine and finest particles. The aim of this work is the defined modification, especially minimisation, of the adhesion forces measured at the model adhesion system sphere-plate by the centrifuge method and AFM. The sphere diameter, surface roughness and chemical surface properties were varied in a controlled manner. In the observed diameter region (several nanometres to several tens of micrometres) and ambient conditions (25 to 80% relative humidity), the adhesion can be described as a combination of van der Waals forces and capillary forces according to well-known theories [1, 2]. Because of the combination of the force spectroscopy with the imaging of surface topography in atomic force microscopy (AFM), it is possible to interpret measured forces as a function of the locally resolved curvature of the surface, which can be influenced by cleaning or etching procedures and surface modification or deposition, respectively.

1. Introduction

The control of the interaction forces between adjacent particles as well as between particles and neighbouring walls of the apparatus plays an important role for the process optimisation in particle technology. The aim of this work is the controlled modification, especially minimisation, of the adhesion forces of fine and finest particles.

Apart from other influences, the adhesion of fine and finest particles strongly depends on particle size and shape, plus the physical and chemical properties of surfaces – especially roughness. These parameters can modify the adhesion forces over decades. In general, different forces must be taken into account: van der Waals force, capillary force, adsorption layer bondings, electrostatic force, and others. To measure the influence of each of several parameters on the adhesion force at given ambient conditions, it is necessary to choose an almost ideal adhesion system which allows the defined variation of sphere diameter, surface roughness, and chemical surface properties. These requirements can be realised with the model adhesion system micro glass spheres on silica glass plates and oxidised silicon wafers.

The adhesion force distributions between particles in narrow diameter fractions in the range from 2 up to 20 μm and a plate were measured by means of the centrifuge method [3, 4].

Furthermore, it is possible to record force versus distance curves by use of atomic force microscopy (AFM). In this case, the spring force in the moment of the jump out of the cantilever from the surface is a measure for the adhesion force at the contact point, so that the adhesion forces of single contacts can be measured directly [5].

To model the sphere-plate system for different

[a] Agricolastrasse 1, D-09599 Freiberg, Germany
[b] Gustav-teuner-Strasse 3, D-09599 Freiberg, Germany
[c] D-09107 Chemnitz, Germany
† Accepted: July 19, 2001

sphere diameters, silicon tips were used whose radii were varied by a special oxidation mechanism between 50 nm and 1 μm. Besides this, glass spheres having diameters between 3 and 15 μm were glued on the tip of the cantilever. In this way, it is possible to measure the local interaction forces at rough and partially covered samples, respectively. In addition, this measuring principle has the advantage that there are no uncertainties in determination of the sphere diameter because after finishing the AFM measurements, the individual diameter of each particle can be determined by scanning electron microscopy (SEM).

2. Experimental

2.1 Methods

The centrifuge method

The centrifuge method is an almost classic technique for measuring adhesion force distributions between particles and a plane [3, 4]. This method has been used for fundamental research in particle technology as well as for the solution of practical questions, for instance in pharmaceutics [6, 7, 8].

Flat substrates covered with particles of a known and a very narrow mass or size distribution are placed in a centrifuge in such a manner that the centrifugal force acts as a pull-off force. Prior to the beginning of the experiment and after each centrifugal step with increasing angular velocity ω, the number of adherent particles is counted. The angular velocity is increased until all particles are taken off.

The percentage of pulled-off particles as a function of the angular velocity is called "pull-off distribution". Taking the average mass or average particle size of the known particle mass or size distribution, it is possible to calculate the adhesion force distribution according to equation (1):

$$F=\frac{\pi}{6}\rho\cdot l\cdot\omega^2\cdot x^3 \qquad (1)$$

One disadvantage of this method is that the adhesion force distributions obtained do not depend on the adhesion mechanisms and on the contact geometry only, but also on the particle size distribution, which should be as narrow as possible to reduce this influence.

The adhesion measurements were carried out using an ultra centrifuge Optima TL-100 CE (Beckman Instruments Inc., Fullerton, California) with a titanium vertical tube rotor TLV-100. The distance l between the rotor axis and the surface of the plate carrying particles to be pulled off was fixed at a value of 30 mm by a special design. The speed range from 5000 to 10^5 rpm allows a maximum acceleration of $3\cdot10^5$ g. By means of a video system (camera Kappa CF 15/2 and CCD module sony XC-77CE), images of the substrate with still adhering particles are recorded after each centrifuge step. This allows application of the computer-aided image analysis to determine the pull-off distribution and adhesion force distribution, respectively.

To prepare the model sphere-plate adhesion system, very small amounts of microspheres were powdered through a microsieve onto the substrate surfaces. Each substrate carried between 100 and 200 separated spheres. Four substrates were centrifuged simultaneously. The experiment was repeated under the same conditions until at least 3000 particles had been centrifuged. Agglomeration and oversize or undersize particles have to be neglected by a suitable image analysing and particle counting system.

During sample preparation and measurement of adhesion forces using the centrifuge method, the ambient conditions were kept constant by means of a climatic room NCZ 3025N (Nema Industrietechnik GmbH, Netzschkau, Germany). The relative humidity was adjusted to controlled values (±2% r.h.) in the range between 10 and 90% relative humidity at a constant temperature of 21°C. The adhesion systems were prepared, stored and measured under the same conditions.

Force spectroscopy and surface analysis by AFM

The possibility of measuring adhesion forces with atomic force microscopy has been known since this surface imaging method was developed [9]. Reviews on force microscopy are given by CAPELLA [10] and by MEYER and HEINZELMANN [11], for instance. BURNHAM [12] discussed the interactions occurring on the tip-surface microcontact in connection with the corresponding force-versus-distance curves. BUTT [5] gave a review about the possibilities of this method known as force spectroscopy.

During earlier experimental works in ambient air, relatively large adhesion forces were measured due to capillary effects [13, 14]. The influence of adsorbed layers on force-distance curves recorded by using commercial AFM tips have also been discussed [13].

The spring force at the moment of the snap-back of the cantilever from the surface is a measure for the adhesion force at the contact point, so that the adhesion forces of single contacts can be measured directly [5].

In this work, a commercial AFM (NanoScope III,

Digital Instruments Inc., Santa Barbara, California, located at Institut für Polymerforschung, Dresden, Germany) was used to record force-versus-distance curves as well as topographic images of the surface. Silicon cantilevers with a spring constant in the range of 0.2−0.4 N/m were applied. Force-distance curves were detected at 64×64 scan points in the force volume mode of the AFM.

To interpret AFM images quantitatively, it is possible to compute for instance the root mean square roughness (RMS roughness) or average roughness (R_a) of line scans of equal length or of the whole image areas if the areas are equal. From a previous work [15] describing measurements on thin polycrystalline gold films, it is known that the values of RMS roughness and average roughness correlate. Therefore in the following, we consider only the average roughness of areas ($R_{a,F}$) which is defined for ($N \times M$) image points with heights $z_{i,j}$ and the average height $\bar{z}$:

$$R_{a,F}=\frac{1}{N}\cdot\frac{1}{M}\sum_{i=1}^{N}\sum_{j=1}^{M}\left|\left(z_{ij}-\bar{z}\right)\right| \qquad (2)$$

To obtain reasonable results, it is important that the image area is significantly larger than the lateral extension of the typical surface or hillock structure. Statistical reliability demands a lot of images from different locations of the sample. In the same way, we also saw the average hillock diameter and average hillock height in the interpretation of the images of the modified surfaces. In this context, all given values of roughness arose from 5×5 μm^2 images.

AFM experiments were carried out under ambient conditions of 50% relative humidity and a temperature of 21°C.

2.2 Materials

Polished silica glass plates of 3 mm in diameter and a thickness of 1±0.1 mm (Hellma Optik GmbH, Jena, Germany) and 4×4 mm^2 pieces of p-Si wafers covered with 500-nm thermal oxide were used as substrates for the adhesion measurements. The glass material has a content of 99.9% SiO_2 and a density of 2.2 g/cm^3.

Micro glass spheres with a mass density of 2.49 g/cm^3 and contents of 71.2% SiO_2 and 15.4% Na_2O (distributor: Topas GmbH Dresden, Germany) were classified by air classification with the impeller classifier 100 MZR (Alpine AG, Augsburg, Germany) and by microsieving. The particle size distributions were analysed by laser diffraction with the HELOS system (producer: Sympatec GmbH, Clausthal-Zellerfeld, Germany).

2.3 Variation of the properties of the adhesion partners

2.3.1 Sphere diameter

Narrow diameter distributions in the range of 2 to 20 μm were employed to measure the adhesion force as a function of the sphere diameter by means of the centrifuge method. To find out the force dependence on the other parameters, we used the two particle size fractions 10−15 μm and 15−20 μm, respectively.

To measure adhesion forces by means of AFM, it is possible either to take the original AFM cantilever or to modify it. Glass spheres with diameters between 3 and 15 μm were glued on the tip of the cantilever by using a micromanipulator. This method has been described by other authors [5].

Commercial silicon tips were oxidised to yield a tip radius of between 50 nm and 1 μm [16]. A heat treatment in a muffle furnace at a temperature of 1150°C under normal atmosphere leads to formation of an oxide layer and the tip rounds itself. The geometry of the oxidised tip is almost ideally spherical and the radius depends on the oxidation time.

2.3.2 Surface morphology of the substrate covered with surfactants or thin metal films

The local curvature of the surface depends on the bulk material, the origin of the surface and its history, especially surface polishing procedures as well as cleaning and etching processes. It can be estimated by AFM. Standard characterisation values are the root mean square value of the roughness and the average roughness, respectively.

The heights and latitudes of the hillocks of the typical hillock structure of many surfaces can be determined from cross-sectional images of the surface in height contrast. Simple geometric considerations allow calculation of the locally resolved curvature of the surface.

Experimental data of several surfaces with and without additional surfactant layers demonstrate that the hillock structure of the surfaces can be described by spherical segments instead of the half-spheres assumed years ago in the literature [17].

The modification of surfaces with surfactants and other (specially modified) hydrocarbon films changes the local curvature as well as the surface properties (surface tension).

The glass substrates were cleaned in an aqueous H_2SO_4/H_2O_2 solution with a volume ratio of 70:30 at a temperature of about 90°C. The duration of the cleaning and etching procedure was varied between five

minutes and one hour. The optimal duration was found to be 30 mins to get the cleanest possible surfaces characterised by a small value of roughness and a low surface energy. Finally, the substrates were rinsed with bidistilled water several times and dried in air at a temperature of 100°C for one hour. Before use, the substrates were stored in a dry atmosphere. The static contact angles (correlating to the surface energies) were measured with distilled water by means of the contact measuring system G10 (Krüss GmbH, Hamburg, Germany).

The surfaces of the glass plates were coated with several surfactants to influence the adhesion. Here, the adsorption of dodecyl ammonium chloride is shown as an example. The glass substrates were exposed to aqueous solutions of varying concentration of dodecyl ammonium chloride at a *p*H of 9 and a temperature of 25°C for two hours. The concentration was varied between $3 \cdot 10^{-7}$ and $6 \cdot 10^{-3}$ mol/l. After this treatment, the substrates were dried in air at a temperature of 60°C. The coverage of the surface was detected photometrically using a UV/VIS spectral photometer lambda 3 (Perkin Elmer, Norwalk, Connecticut). For this purpose, glass spheres with particle sizes in the range of 10–20 μm and a specific surface of 2300 cm^2/g were treated in the same way as the glass substrates to get adsorption isotherms (see **Fig. 1**). The adsorbed amount of surfactant was detected indirectly from the change of concentration of the surfactant in the solution. The quantitative analysis of amines was described by SINGEWALD [18]. The red complex arose from the amine. It can be detected by the photometer at a wavelength of 529 nm. The coverage of the solid surface was calculated from the estimated adsorption density given by the amount of adsorbed surface active agent in relation to the mass of the solid spherical particles. The molecular mass of dodecyl ammonium chloride is 185 g/mol.

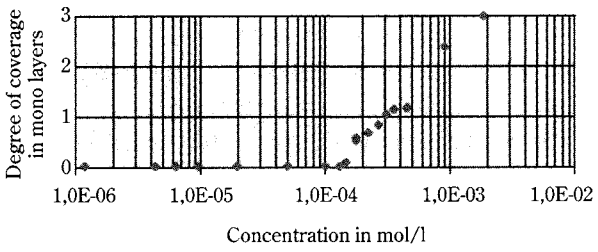

Fig. 1 Degree of coverage of glass surfaces (microspheres 10 ... 20 μm diameter) with dodecyl ammonium chloride (DAC) as a function of the concentration during the adsorption process

A space requirement of $20 \cdot 10^{-20}$ m^2 for each adsorbed molecule at the surface was assumed.

The deposition of a specially selected material (Bi) on oxidised silicon wafers leads to a surface morphology distinguished by a nearly flat or a half-sphere-like hillock structure.

Thin bismuth films were prepared in a simple high vacuum process by thermal evaporation at a pressure of 10^{-3} Pa onto p-Si wafer, <100> orientation, 28–53 Ωcm, covered with 500 nm thermal oxide or onto polycrystalline Ti/Au or Ti/Pt underlayers. The 20-nm-thick titanium adhesion layers were deposited by electron beam evaporation followed by at least 60 nm of platinum deposited also by electron beam evaporation or by thermal evaporation of a gold film of a minimum 80 nm in thickness. The preparation of the underlayers previously described [19, 15] demands a substrate temperature of 650 K in the case of the Ti/Au system to obtain sufficient adhesion of the Au film on the substrate. The Ti/Pt system adheres well at substrate temperatures close to room temperature. During bismuth evaporation, the substrate temperature was fixed at 300 K or 650 K. The film thickness was varied between 20 nm and 2 μm at a constant deposition rate of 20 nm per second.

By means of AFM and SEM investigations in a previous work [15], it had been shown that on average, 500-nm-thick bismuth layers cover the substrate completely. The presence of noble metal underlayers and their interface properties (surface and interface tension) determine whether a flat or hillock-like topography of the evaporated bismuth layer develops. Dependent on the evaporation conditions, the radius of the half-spheres can be varied in the range between 50 and 500 nm at least.

2.3.3 Surface properties modified by gaseous chemical treatment

The real surface of silicon dioxide is always covered with silanol groups giving rise to its hydrophilic character. This was changed into a hydrophobic surface by the following reactions. The isolated silanol groups were replaced by hydrogen in the gas phase at 1223 K, resulting in the formation of hydride groups on the surface. Phenyl groups were formed by the reaction of benzene with these hydride groups at 873 K. The modification reactions were carried out in a flow unit. Unfortunately, the spectroscopic detection of the groups on the quartz glass was not successful due to the small specific surface area of the samples.

However, identical modifications were carried out

using highly disperse silica Aerosil® 300 (Degussa AG, Frankfurt/Main, Germany) with an average particle size of 7 nm and a specific surface area of 300 ±30 $m^2\ g^{-1}$ as previously described [20, 21]. This modified silica can be characterised by, e.g., transmission infrared spectroscopy. **Figure 2** shows the spectra of the modified samples. The spectra contain the O-H-stretching vibration of the isolated silanol groups at 3748 cm^{-1}, the Si-H-stretching vibration of the hydride groups at 2293 cm^{-1}, and the combination vibrations of silica at 1973 cm^{-1}, 1862 cm^{-1} and 1635 cm^{-1}. In addition, the spectrum of the sample modified with phenyl groups still contains the aromatic C-H-stretching vibrations of the phenyl groups at 3028 cm^{-1}, 3068 cm^{-1}, 3084 cm^{-1} and 3104 cm^{-1}, as well as the strong C-C-stretching vibrations of the phenyl groups at 1600 cm^{-1} and 1432 cm^{-1}.

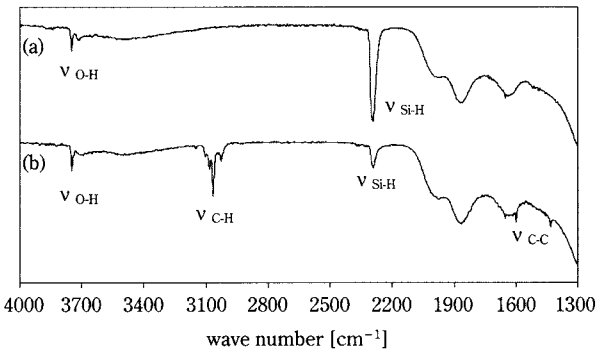

Fig. 2 Infrared spectra of Aerosil® 300 modified with hydride (a) and phenyl (b) groups

3. Results and discussion

3.1 Theory

The adhesion of a rigid sphere of radius R on a flat plate is a well-known standard model for the adhesion of a particle on a wall. To describe the different adhesion forces (van der Waals, capillary, electrostatic and so on), various models have been developed [1, 2, 17].

Adhesion is caused by van der Waals and capillary forces especially in the size range of fine and finest particles investigated here. Van der Waals forces at the sphere-plate adhesion system can be described according to the microscopic theory of HAMAKER [22] and the macroscopic theory of LIFSHITZ [23] by the simple equations

$$F=\frac{C_H}{6a_0^2}\cdot R \tag{3}$$

$$F=\frac{\hbar\omega}{8\pi\cdot a_0^2}\cdot R \tag{4}$$

summarised by KRUPP [1].

According to the DERJAGUIN approximation [24], the adhesion force between two curved surfaces is related to their work of adhesion. In the case of forces between a rigid sphere and a plate, that means

$$F=4\pi R\gamma \tag{5}$$

the so-called "DMT limit" of the Derjaguin-Muller-Toporov theory [25, 2].

The additional capillary force due to the LAPLACE pressure of condensed water in the contact region can be approximated by [2]

$$F=4\pi R\gamma_{l,v}\cos\theta \tag{6}$$

On the whole, the force is given by the sum of equation (5) describing the direct solid-solid contact inside the liquid annulus and equation (6) due to capillary effects [2]. Using the YOUNG equation, it can be added to

$$F=4\pi R(\gamma_{l,v}\cos\theta+\gamma_{s,l})=4\pi R\gamma_{s,v} \tag{7}$$

In the general case of two adhering spheres with radii R and r, the radius R in the equations (3) to (7) has to be replaced by the term $\frac{R\cdot r}{R+r}$, the so-called reduced radius. The noted equations (3) to (7) are the limit values for $r>>R$, that means one of the adhesion partners may be considered as a flat plate. In the experimental set-up, it was initially attempted to realise this case. On the other hand, the radius r may be used to describe the local curvature of the rough solid surface. Especially if the roughness exceeds a certain value and the surface is characterised by a hillock structure with small radii, the radius of these hills determines the adhesion behaviour.

3.2 Particle size

Figures 3 and 4 show the dependence of adhesion force on particle size measured by the AFM and centrifuge method. The particle size was varied by oxidation of AFM tips, by pasting on different size particles, and by variation of the particle size in centrifuge measurements. All experiments were carried out at a constant relative humidity of 50% using the same quartz glass substrates. Every point in **Figs. 3 and 4** is a result of several thousand single contacts. The linear dependence of adhesion forces on particle size theoretically known was confirmed using cleaned substrates (**Fig. 3**) as well as substrates deposited

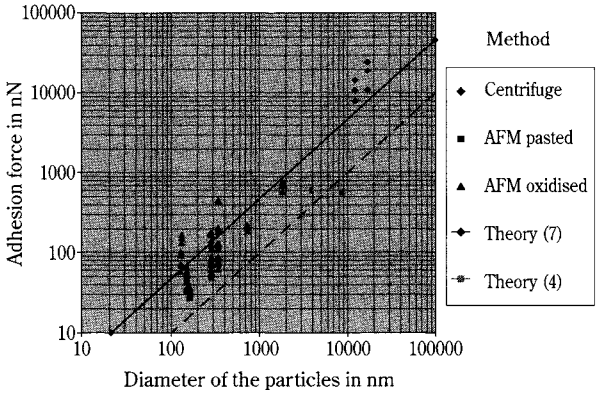

Fig. 3 Adhesion force as a function of the sphere diameter; glass spheres and oxidised AFM tips on cleaned quartz glass plates; theory according to the adhesion system sphere - plate (equations 4 and 7)

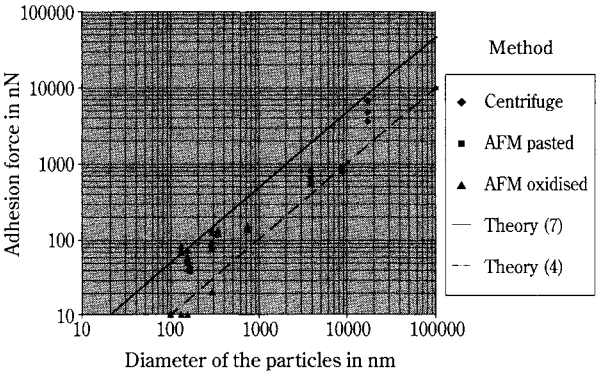

Fig. 4 Adhesion force as a function of the sphere diameter, glass spheres and oxidised AFM tips on surfactant-covered quartz glass plates (DAC concentration during the adsorption $3 \cdot 10^{-3}$ mol/l); theory according to the adhesion system sphere - plate

with surfactants (**Fig. 4**). The lower straight lines in **Figures 3 and 4** correspond to the van der Waals force in the contact distance with $a_0 = 0.4$ nm and a Lifschitz-van der Waals constant of $\hbar\omega = 5$eV (equation 4), and the upper ones to thermodynamic consideration, including the capillary force with a surface tension $\gamma_{s,v} = 72$ mN/m (equation 7).

The adhesion mechanism may be described as a combination of van der Waals and capillary forces. Due to the surface roughness the real adhesion forces lie below the theoretically values.

The average roughness $R_{a,F}$ of cleaned quartz glass substrates was measured at 0.4−0.6 nm with commercial AFM tips in contact mode. Adsorption of dodecyl ammonium chloride from a $3 \cdot 10^{-3}$ mol/l solution raised the roughness to 0.7−1.4 nm, in some cases to 2.1 nm.

The diminution of forces due to the deposition of surface active agents might be explained by the increasing roughness or by the decrease of surface energy as a result of hydrophobic surface properties or better by a combination of both effects.

To determine the influence of the hydrophilic and hydrophobic properties of any surface on their adhesion behaviour alone, it is necessary to create almost ideally flat surfaces which can be covered with a monolayer of a surface active agent. In this way, random hillock structures are excluded.

3.3 Surface energy

The surfaces of quartz glass plates and oxidised silicon wafers were cleaned and modified by chemical gas-phase reactions or by the adsorption of surfactants from aqueous solution. Force-distance curves were recorded with AFM in force volume mode using original as well as specially oxidised AFM tips.

By chemical modification of the surface (substitution of silanol groups by hydride or phenyl groups [20, 21]), it is possible to reduce the adhesion force between substrate and AFM tip to almost the same degree over the whole surface. AFM images prove that in this case, no additional roughness arises due to the treatment of the solid surface. Therefore, the geometric distance between the adhesion partners has not been changed, meaning that the alteration of adhesion forces arises only from varying surface energies and capillary forces.

The adhesion forces diminish in the same relation as the cosine function of the boundary angles θ, if the boundary angles lie under the limit of about 60°. In this range, capillary forces dominate because of a high surface tension $(\gamma_{s,v} - \gamma_{s,l})$. The capillary force decreases and the adhesion force contribution inside the liquid annulus (the term $4 \pi R \gamma_{s,l}$ in equation 7) becomes important when the boundary angle increases because of a strongly reduced surface tension.

The slight surface roughness of oxidised silicon wafers ($R_{a,f} = 0.31$ nm for an 5×5 μm^2 image scanned in contact mode with an original AFM tip) was preserved for instance by the substitution of silanol groups by hydride groups ($R_{a,f} = 0{,}28$ nm). The very smooth surfaces result in homogeneous surface forces measured by AFM in force volume mode with commercial cantilevers to 38 nN±3%. The adhesion forces of oxidised wafers were 60 nN±15%.

Figure 5 shows the adhesion force measured by AFM as a function of the boundary angle. The variation of the tip radius yields to the different slops according to equation (7). The surface tension of the liquid was assumed to be $\gamma_{l,v}$= 72 mN/m for water.

Minimal adhesion forces of about 25% of the original value (at cos $\theta \approx 0$) were found by gas-phase methylisation of the surface with hexamethyl disilazane (HMDS).

The adhesion force of micro glass spheres (diameter: 10−15 μm) on cleaned and chemically modified glass and silicon wafer surfaces was measured with the centrifuge method as a function of the relative humidity of the environment (**Figure 6**). The diminution of the modal value of the adhesion force due to the hydrophobic behaviour of the modified surfaces is proved especially in the case of high humidity (80% r.h.). In all other cases, the confidence intervals of the measured values (not drawn in **Figure 6**) overlap and therefore only the tendency of force reduction to about a half of the original value can be perceived.

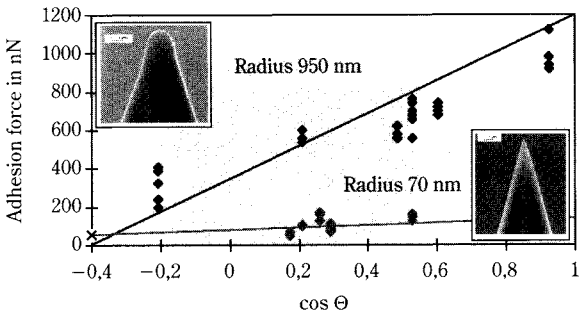

Fig. 5 The adhesion force between a quartz glass plate and the AFM tip as a function of the boundary angle Θ, measured with different tip radii

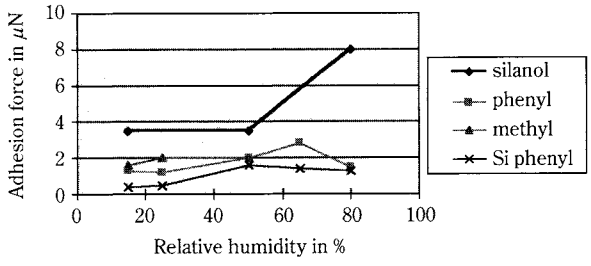

Fig. 6 Modal value of the adhesion forces between micro glass spheres (10 ... 15 μm) and chemically modified glass surfaces and Si/SiO_2 wafers as a function of the relative humidity

3.4 Surface roughness

3.4.1 Combination of developing hillock structure and changes in surface energy due to the adsorption of surface active agents

The decrease of adhesion forces by the adsorption of dodecyl ammonium chloride (DAC) mentioned above should be considered further.

The properties of the glass surfaces coated with DAC were modified by varying the concentration of the surfactant during deposition. AFM images not shown here demonstrate that these adsorption conditions allow the full spectrum of thin-film growth to be reached. At low concentrations ($c \leq 3 \cdot 10^{-5}$ mol/l), first nucleation occurs and the clusters of molecules grow. At a concentration of about $c \approx 3 \cdot 10^{-4}$ mol/l, an adsorption monolayer originates. At higher concentrations ($c \approx 3 \cdot 10^{-3}$ mol/l), this monolayer is superimposed by a hillock structure (see the adsorption isotherm in **Figure 1**). The different stages of growth are correlated with changes in surface roughness and adhesion.

Figure 7 shows the dependence of typical adhesion forces measured by AFM in force volume mode with commercial AFM tips on the concentration of DAC during the adsorption process. The forces are given in relation to the force measured at untreated pure glass substrates. In cases of a small coverage below one monolayer, the adhesion force differs over the whole surface in the order of 10% (see also **Fig. 8**, top). The adsorption of greater amounts of surfactants leads at first to a smoothness of the surface characterised by nearly constant or softly increasingly adhesion forces due to the sphere-plate model, and secondly to a hillock growth. The hillocks act as spacers and decrease the locally resolved forces according

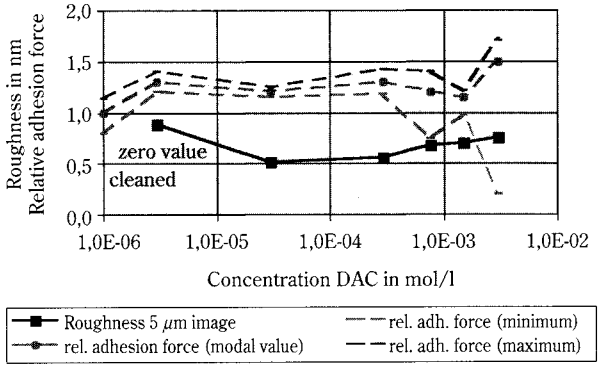

Fig. 7 Relative adhesion force measured with commercial AFM tips and roughness $R_{a,F}$ of surfactant-covered quartz glass surfaces

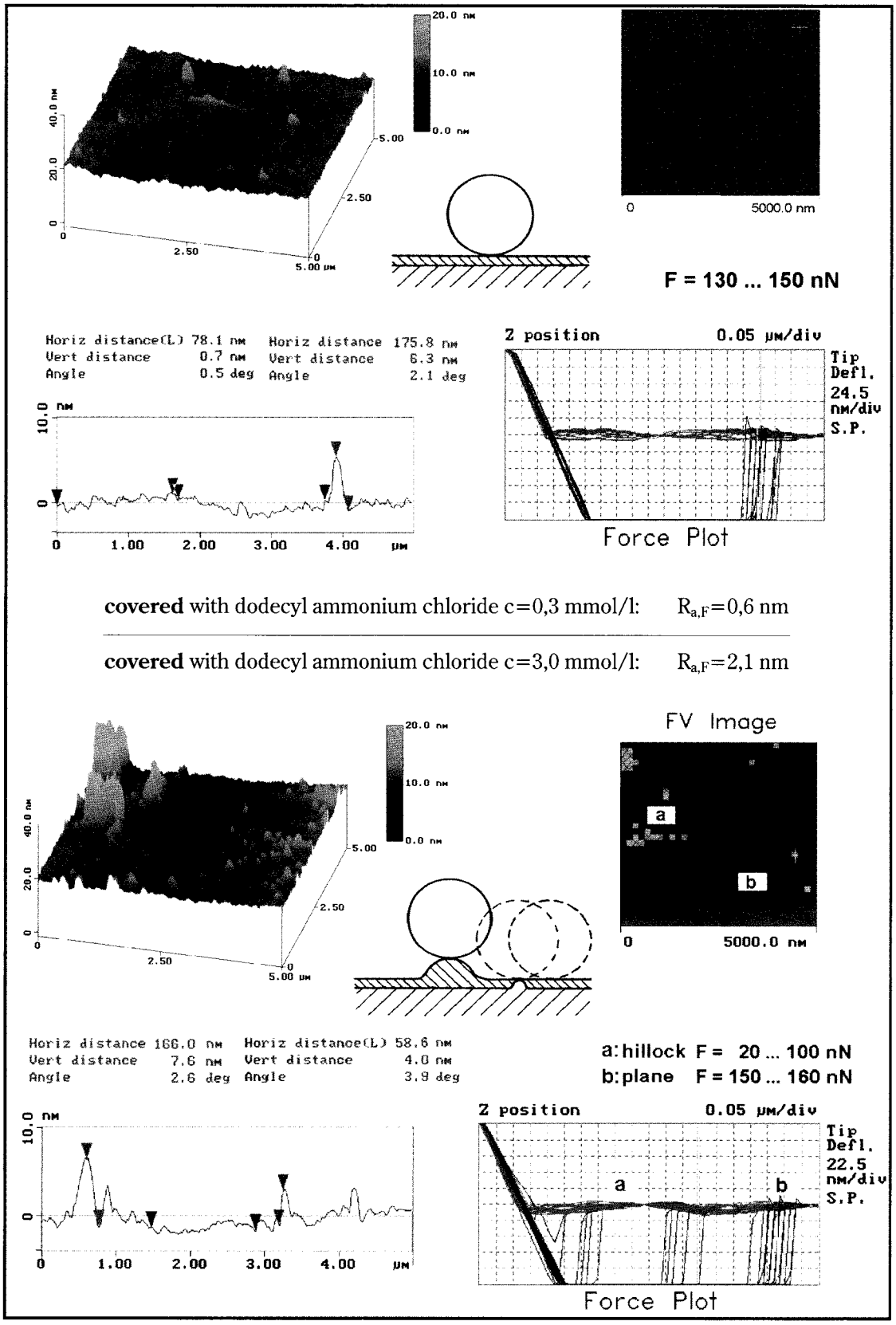

Fig. 8 Surface morphology and adhesion forces of surfactant-covered quartz glass surfaces measured by AFM; adsorption from solution containing $3 \cdot 10^{-4}$ mol/l DAC (top) and from $3 \cdot 10^{-3}$ mol/l (bottom)

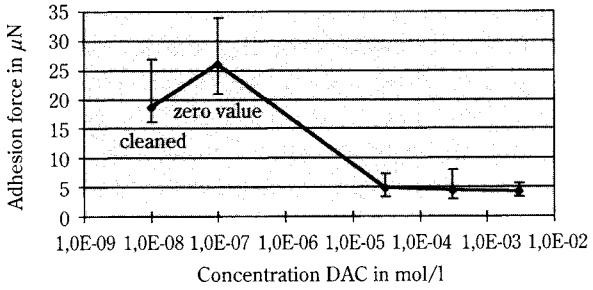

Fig. 9 Modal value of the adhesion force between micro glass spheres (diameter 15 ... 20 μm) and covered glass surfaces as a function of the concentration of DAC during the adsorption process; relative humidity 50%

to their dimensions down to 10% (see also **Fig. 8**, bottom). The roughness $R_{a,F}$ of the modified surfaces is also given in **Figure 7**. Essential results of the coating of glass substrates with dodecyl ammonium chloride (DAC) are summerited in **Figure 8**. It can be seen in each case in detail: the surface topography in height contrast scanned over an area of 5×5 μm^2 in contact mode; a principal representation of the adhesion system; the force volume image with marked points at which the shown force displacement curves were recorded; typical cross-sections with hillock heights and widths; the force displacement curves (the so-called Force Plot).

The adhesion force of micro glass spheres (diameter: 15–20 μm) on glass surfaces covered with different amounts of the surfactant DAC was also measured by means of the centrifuge method. **Figure 9** shows the modal values of the adhesion force including the confidence intervals at a relative humidity of the environment of 50%.

This result seems to be in contradiction to the slope of the curve measured with AFM (**Figure 7**). The apparent contradiction can be explained by the different influence of the small hillocks of surfactant material deposited on the surface as a function of the radius of the spherical adhesion partner. A small hillock in a plane is detected by AFM using a tip with a sharp apex as a small hillock, and the average adhesion force is relatively large according to the sphere-plate model. The hillock acts as a spacer inside a small area. This area increases if the tip radius increases or much greater microspheres are used. For this reason, the average adhesion force measured over the whole surface is influenced more by the hillocks when the radius increases (see also **Figure 11** in section 3.4.2). In conclusion, the same partial coverage of substrates can result in different changes of the adhesion force in proportion to the radius of the adhesion partner.

Centrifuge measurements were repeated at varied relative humidity in the range 10–90%. At low humidity up to 25%, the adhesion force is nearly constant over a wide range of DAC concentration and rises slowly at concentrations above $3 \cdot 10^{-4}$ mol/l in the same way as measured with AFM under the condition of 50% r.h. (see also **Figure 7**). At a high humidity of 80%, a decrease of the adhesion force with increasing DAC concentration during the adsorption process was measured. But in all cases (low as well as high humidity), only the measured force at the high concentration of $3 \cdot 10^{-3}$ mol/l differed from the confidence interval of the other forces significantly. The results of force measurements as a function of the humidity are summarised in **Figure 10**. Parameter is the concentration of DAC during the adsorption process and the resultant coverage with surface active agents discussed above.

The adhesion behaviour as a function of the relative humidity of the ambient air is known from other adhesion systems in principle [26]. As shown for the chemical modification of the surfaces, the increase of adhesion force with increasing humidity of the ambient air can be reduced by coating the substrate surfaces with surfactants. To reduce the adhesion forces caused by capillary effects primarily at high humidity, it is necessary to cover the surface completely. This was the case when the DAC concentration during the deposition process exceeded $3 \cdot 10^{-4}$ mol/l.

3.4.2 The half-sphere-like hillock structure of deposited thin films

The surface of real, almost flat substrates can be described by an ideally flat plane in combination with a segment of a sphere. To calculate the adhesion force at such a surface, it is necessary to modify the theory given by RUMPF [17], but this is not the aim of

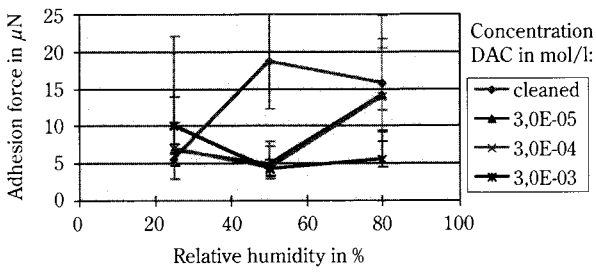

Fig. 10 Modal value of the adhesion force between micro glass spheres (diameter 15 ... 20 μm) and covered glass surfaces as a function of the relative humidity; parameter is the concentration of DAC during the adsorption process

this work. RUMPF [17] calculated the van der Waals adhesion force at the sphere-plate system and assumed that the surface of the sphere with radius R is covered with a small half-sphere-like roughness with the radius r:

$$F = \frac{\hbar\omega}{8\pi} \cdot \left(\frac{R}{(r+a_0)^2} + \frac{r}{a_0^2} \right) \tag{8}$$

This sum of the forces acting between sphere and plate and roughness and plate exceeds the real force. The systematic error is caused by taking a spherical roughness instead of a hemisphere. It can be neglected since the radius r is small in comparison to the sphere radius R. By geometrical consideration, it can be shown that the same equation is valid for the force between a plate with a half-sphere-like roughness of the radius r and a sphere of radius R since $r \ll R$. Such a surface was created by bismuth deposition on oxidised silicon wafers. The formula changes into

$$F = \frac{\hbar\omega}{8\pi} \cdot \left(\frac{R}{(r+a_0)^2} + \frac{1}{a_0^2} \cdot \frac{R \cdot r}{R+r} \right) \tag{9}$$

if the limiting condition $r \ll R$ is not valid (**Figure 11**). If the radius of the roughness exceeds the contact distance in orders ($r \gg a_0$), the contribution of the plate (the first term in formula 9) can be neglected and the force can be described equivalently to the sphere-sphere adhesion system

$$F = \frac{\hbar\omega}{8\pi} \cdot \frac{1}{a_0^2} \cdot \frac{R \cdot r}{R+r} \tag{10}$$

The adhesion force is a function of the reduced radius only (**Figure 12**), if the Lifshitz-van der Waals constant and the contact distance or, in thermodynamical consideration, the surface energy is constant.

The adhesion force between AFM tips of different radius and thin bismuth films characterised by a hemisphere-like hillock structure was measured by AFM in force volume mode. The hillock radius of the thin film investigated was about 1 μm. The adhesion force measured with commercial tips ($R \approx 10$ nm) was about 10 nN at the top of the spheres as well as at the flat areas of the bismuth-covered substrate. Using an AFM tip with a radius of 875 nm, for instance, the force at the bismuth spheres rose to 16–30 nN and forces of 25–44 nN were measured at the flat areas. **Figure 13** shows a scanning electron microscope (SEM) image of the bismuth-covered Si/SiO_2 substrate [15]. The locally resolved adhesion force lies between 16 and 36 nN, if an oxidised tip with 450 nm radius is used.

The measured adhesion forces correspond in principle to the calculated values according to equation (10) (**Figure 12**). The slope with the parameter $r=1$ μm is valid for the bismuth spheres and $r \to \infty$ for the flat areas.

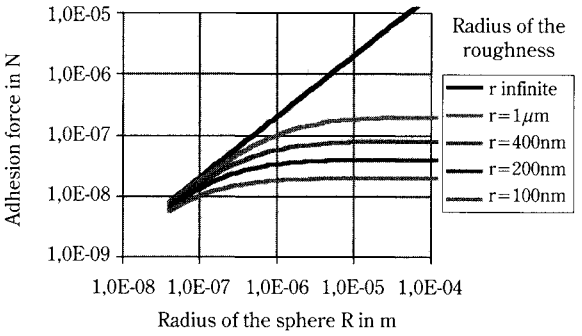

Fig. 12 Van der Waals force according to equation (9) as a function of the sphere radius R; adhesion system sphere - plate with hemisphere-like roughness; a_0=0,4 nm, $\hbar\omega$=5 eV, Parameter: hillock radius r

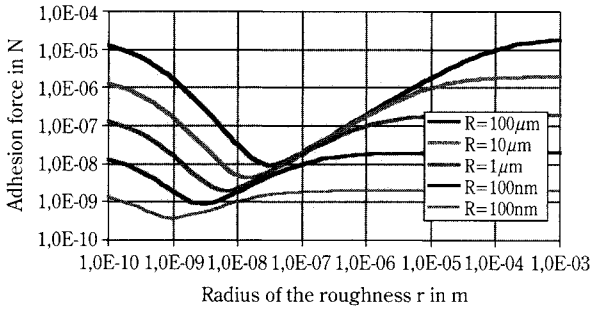

Fig. 11 Van der Waals force according to equation (9) as a function of the hillock radius r; adhesion system sphere - plate with hemisphere-like roughness; a_0=0,4 nm, $\hbar\omega$=5 eV, Parameter: sphere radius R

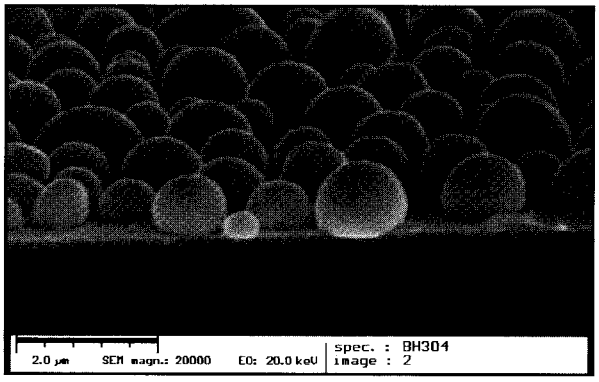

Fig. 13 SEM image of a bismuth thin film deposited at elevated substrate temperature onto an oxidised Si wafer with a Ti/Pt under-layer

4. Summary

It is possible to coat flat glass surfaces and silicon wafers, respectively, in different ways with surfactants, chemically functional groups and other deposition materials so that the surface morphology can be changed over a wide range from almost ideally flat surfaces and separate cap-like hillocks to a whole hemispherical hillock structure. Adhesion forces measured by the centrifuge method and by AFM using these defined substrates and spherical particles in the nanometre and micrometre range correspond to the model sphere-plate adhesion system. Each of the parameters: sphere radius, surface roughness (curvature), and surface energy was varied separately. The adhesion force can be described as a combination of van der Waals and capillary forces according to known theories [1, 2, 17, 25].

The analysis of the AFM force-vs.-distance curves at differently pre-treated surfaces allows measurement of the interaction forces in a locally high resolution. In combination with topographic AFM images and the analysis of the roughness of the substrate surfaces, this facilitates interpretation of the mean adhesion forces measured by the centrifuge method between glass spheres and quartz glass or SiO_2 substrates, respectively.

By chemical modification of the surface, it is possible to reduce the adhesion force between substrate and AFM tip to almost the same degree over the whole surface. AFM images prove that in this case, and in contrast to the covering with surfactants, no additional roughness arises due to treatment of the solid surface. Therefore, the geometric distance between the adhesion partners has not been changed, meaning that the alteration of adhesion forces arises only from varying surface energies and capillary forces.

Altogether it is shown that it is possible to influence adhesion forces directly by changing the relief of the solid surface and by varying the physical and chemical surface properties by suitable treatment. This can be done by deposition of hill-like structures in the range of nanometres and by chemical modification of the surface, respectively.

Acknowledgements

The authors thank the graduate students Mrs Mende and Mrs Spindler for realisation of the adhesion force experiments using the centrifuge method.

The work was embedded in the research project "Sonderforschungsbereich 285" of the Deutsche Forschungsgemeinschaft. The authors thank the Deutsche Forschungsgemeinschaft for its financial support.

Nomenclature

a_0	contact distance; $a_0=4\cdot10^{-10}$ m	(m)
C_H	Hamaker constant	(Nm)
F	adhesion force; Laplace pressure	(N)
g	gravity constant; $g=9.81$ m s^{-2}	(m s^{-2})
$\hbar\omega$	Lifshitz - van der Waals constant	(Nm)
l	distance between rotor axis and surface of the plate	(m)
R	radius of the rigid model sphere	(m)
r	radius of the hemisphere like roughness	(m)
$R_{a,F}$	average roughness of area	(m)
x	particle diameter	(m)
γ	interfacial tension	(kg s^{-2})
$\gamma_{l,v}$	interfacial tension liquid - vapour	(kg s^{-2})
$\gamma_{s,l}$	interfacial tension solid - liquid	(kg s^{-2})
$\gamma_{s,v}$	interfacial tension solid - vapour	(kg s^{-2})
θ	contact angle	(°)
ρ	particle density	(kg m^{-3})
ω	angular frequency	(s^{-1})

References

1) KRUPP, H.: Particle Adhesion. Theory and Experiment. Adv. Coll. Interf. Sci., **1** (1967), 111-239
2) ISRAELACHVILI, J.N.: Intermolecular and Surface Forces, Academic Press, London, 1992
3) BÖHME, G., KRUPP, H., RABENHORST, G., SANDSTEDE, G.: Adhesion measurements involving small particles. Trans. Instn. Chem. Engrs. (London) **40** (1962), 252-259
4) BÖHME, G., KLING, W., KRUPP, H., LANGE, H., SANDSTEDE, G.: Haftung kleiner Teilchen an Feststoffen. Teil I: Messungen der Haftkraft in gasförmigen Medien Z. angew. Phys. **16** (1964) 6, 486-490
5) BUTT, H.-J., JASCHKE, M., DUCKER, W.: Measuring surface forces in aqueous electrolyte solution with the atomic force microscope. Bioelectrochem. and Bioenergetics **38** (1995), 191-201
6) KRUPP, H., SPERLING, G.: Haftung kleiner Teilchen an Feststoffen. Teil II: Theorie. Z. angew. Phys. **19** (1965) 3, 259-265
7) LAM, K.K., NEWTON, J.M.: Influence of particle size on the adhesion behaviour of powders, after application of an initial press-on force. Powder Techn., **73** (1992), 117-125
8) PODCZECK, F., NEWTON, J.M., JAMES, M.B.: The influence of constant and changing relative humidity of the air on the autoadhesion force between pharmaceutical powder particles. Int. J. Pharm. **145** (1996), 221-229
9) BINNIG, G., QUATE, C.F., GERBER, C.: Phys. Rev. Lett., **56**

(1986) 9, 930
10) Capella, B., Dietler, G.: Force-distance curves by atomic force microscopy. Surf. Sci. Rep. **34** (1999) 1-104
11) Meier, E., Heinzelmann, H., in: Güntherodt, H.-J., Wiesendanger, R. (Ed.): Scanning Tunneling Microscopy II. Springer-Verlag, Berlin, Heidelberg, New York, 1992
12) Burnham, N.A., Colton, R.J., Pollock, H.M.: Interpretation of force curves in force microscopy. Nanotechnology **4** (1993), 64-80
13) Weißenhorn, A.L., Hansma, P.K., Albrecht, T.R., Quate, C.F.: Forces in atomic force microscopy in air and water. Appl. Phys. Lett. **54** (1989) 2651-2653
14) Burnham, N.A., Colton, R.J., Pollock, H.M.: Interpretation issues in force microscopy. J. Vac. Sci. Technol. **A 9** (1991) 4, 2548-2556
15) Hoffmann, B.: Dünnschicht-Metallelektroden für Chemo- und Biosensoren. Thesis. TU Chemnitz - Zwickau, 1996
16) Hüttl, G., Klemm, V., Popp, R., Simon, F., Müller, E.: Tailored colloidal probes and their easy way TEM investigation. Surf. Interf. Anal. 2001 (in press)
17) Rumpf, H.: Die Wissenschaft des Agglomerierens. Chem.-Ing.-Technik, **46** (1974) 1, 1-11
18) Singewald, A.: Quantitative Mikroanalyse von Fettaminen und ihre Anwendung bei der Salzflotation. Kali und Steinsalz **9** (1959), 281-300
19) Hintsche, R., Neumann, G., Dransfeld, I., Kampfrath, G., Hoffmann, B., Scheller, F.: Polyurethane Enzyme Membranes for Chip Biosensors Anal. Letters, **22** (9) (1989) 2175-2190
20) Heger, K., Marx, G., Brendler, E., Thomas, B.: Characterization of chemically modified silica by infrared and solid state nuclear magnetic resonance spectroscopy. Fresenius J. Anal. Chem. **358** (1997) 240-241
21) Heger, K., Marx, G.: Determination of the molar decadic absorptivities of the stretching vibrations of the hydride and phenyl groups on Aerosil® 300. Mikrochim. Acta **133** (2000) 187-189
22) Hamaker, H.C.: The London-van der Waals Attraction between Spherical Particles. Physica **4** (1937) 1058-1072
23) Lifshitz, E.M.: The Theory of Molecular Attractive Forces between solids. Soviet Physics **2** (1956) 73-83
24) Derjaguin, B.: Untersuchungen über die Reibung und Adhäsion, IV. Theorie des Anhaftens kleiner Teilchen. Koll. Z. **69** (1934) 155-164
25) Derjaguin, B.V., Muller, V.M., Toporov, Yu.P.: Effect of Contact Deformations on the Adhesion of Particles. J. Coll. Interf. Sci. **53** (1975), 314-326
26) Chikazawa, M., Kanazawa, T., Yamaguchi, T.: The Role of Adsorbed Water on Adhesion Force of Powder Particles. KONA **2** (1984), 54-61

Author's short biography

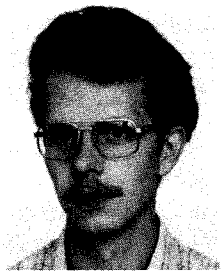

Bernd Hoffmann

Bernd Hoffmann studied physics at the University of Technology in Chemnitz, Germany. He completed his graduate studies with a Ph.D. thesis titled "Thin-film metal electrodes for use in chemical and biosensors" in 1996. His main research fields at the Institute of Physics of the Chemnitz University were thin-film technology, electrochemical sensors and the characterisation of solid surfaces by scanning probe microscopy.
He currently investigates adhesion forces, especially by AFM. He is a member of the research group "Sonderforschungsbereich 285" located at the Freiberg University of Mining and Technology, Germany.

Grit Hüttl

Grit Hüttl graduated in materials science from the Freiberg University of Mining and Technology, Germany. She studied one semester at the Mining Academy of Krakow, Poland. After studying, she worked as a scientific assistant at the Institute of Ceramic Materials in Freiberg. During this time, her research activities were focused on force measurements in liquids by using AFM.

Author's short biography

Katrin Heger

Katrin Heger finished her Ph.D. thesis at the University of Technology in Chemnitz, Germany, in 1998. Her main research field was the surface modification of silica. She worked on the same topic in cooperation with Degussa AG at the Chemnitz University for two years. She then investigated the compounding of polypropylene and organically modified layered silicates (development of nanocomposites) at the Institute of Polymer Research in Dresden, Germany. She is now employed as a process engineer in the Department of Process & Transfer CVD/PVD at Infineon Technologies SC300 GmbH & Co. KG in Dresden.

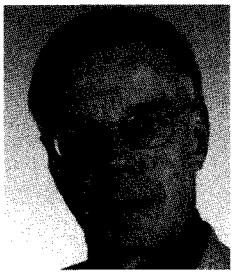

Bernd Kubier

Bernd Kubier graduated in physics from the Dresden University of Technology in 1972. In 1979, he obtained a Ph.D. degree in physics at the Freiberg University of Mining and Technology.
Since 1981, he has been working at the Institute of Mechanical Process Engineering and Mineral Processing at the same university. He is managing assistant to the chair for mechanical process engineering and works mainly in the fields of particle size measurement and classification.

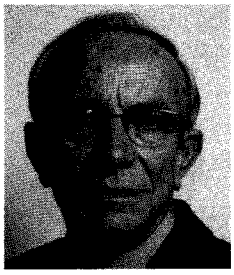

Günter Marx

Study of chemistry in Jena, Germany (1958 – 62), Ph.D. thesis in the group of Dr. Dr. h.c. H. Dunken at the institute of physical chemistry of the University of Jena.
Professorship in chemical kinetics (1972) and habilitation (1975) at the Jena University.
Professorship in chemistry and physical chemistry at the University of Technology in Chemnitz, Germany (1976).
1993 – 2000, head of the institute of chemistry, Chemnitz University, chairman of the international conferences of solid-state analysis.
Research areas:
Interface chemistry on solids, layers and films, thermodynamics, kinetics, analysis of thin film growth processes.

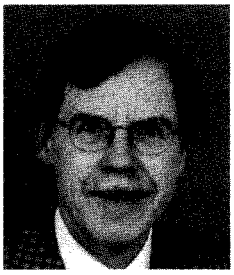

Klaus Husemann

Graduated in mechanical engineering, specialisation chemical engineering, from the Magdeburg University of Technology.
Senior researcher at the Mineral Processing Research Institute (FIA) Freiberg. Professor for mechanical process engineering at the Freiberg University of Mining and Technology. Speaker of the special research project "Particle interaction in mechanical process engineering" sponsored by the DFG (Deutsche Forschungsgemeinschaft).

Analysis of Feed Shoe Powder Deposition Method Using a Real-time Cumulative Mass Deposition Tester†

B. Mittal[1], V.M. Puri[1] and W. Shaffer[2]
[1] *Department of Agricultural and Biological Engineering*
*The Pennsylvania State University**
[2] *Process Control Manager, Magnetics Inc.*
*A Division of Spang and Company***

Abstract

A real-time cumulative mass deposition tester (MDT) was fabricated and tested to study the deposition profiles of powders in complex-shaped dies. The deposition behavior of two different powders (manganese zinc ferrite – MZF[1] and microcrystalline cellulose – MCC[2]) was studied in an "E" shaped die. The feed shoe deposition method was used to deposit the powders in the die via two different fill directions. The MDT was used to develop real-time fill trends, deposition profiles, contour plots and databases of spatial powder mass distribution in the die. From the results, it was ascertained that both fill direction and die shape affect a powder's deposition behavior. It was observed that the average MCC powder masses deposited in both fill directions were roughly one-seventh the average MZF powder mass. Also, the average voids volume fraction of MCC was roughly double the average voids volume fraction of MZF. Due to its favorable particle characteristics (spherical-shaped particles and low cohesion), the MZF powder filled better compared to MCC. In the case of MZF, the coefficient of variation (COV) values for powder mass were mostly in the range of 5-20%, compared to 25-50% for MCC. Therefore, MCC is expected to be a more difficult powder to process due to its poor flowability and large variations in powder masses during deposition. Overall, the experimental results clearly show that the MDT is an effective and reliable tool that can be used for the real-time measurement of powder deposition profiles in a die.

Keywords: Mass Deposition Tester, spatial powder mass distribution, die filling, complex die shapes, feed shoe deposition method

1. Introduction

Powders play a major role in a variety of industries (such as ceramic, chemical, food, pharmaceutical, etc.) where they must be handled, stored, compacted or otherwise processed in large volumes. All phases of those operations require precise knowledge of the behavior of powder systems in order to improve the quality of the components produced. For example, in the powder compaction process, it is known that the quality of green compacts (unsintered, pressed particulate assemblies) is dependent upon factors such as intrinsic material properties, nature of applied load, die geometry, and a variety of operational parameters. Many compact-quality issues (such as cracking, low green strength, shrinkage or warpage) can be influenced by the anisotropic compaction of powder. This anisotropic mechanical response of powder during compaction is further attributable, in part, to non-uniform, pre-compaction fill-density of the powder within a die (Li and Puri, 1996). Localized weight or density gradients may arise from the die geometry, die-wall friction or even from the method used to deposit powder in the die. Since manufacturing processes have a tendency to magnify variation, ensuring a uniform pre-compaction particulate deposition will be an effective method of enhancing the quality of the green compacts (Mittal and Puri, 1999a, b).

Although the above facts are well documented in the literature, no effective tool that is capable of mea-

* University Park, PA 16802, USA.
** East Butler, PA 16029, USA.
† Accepted: August 17, 2001

[1] Courtesy of Spang and Company, Butler (PA)
[2] Courtesy of FMC Corporation, Newark (DE)

suring the uniformity of powder deposition in complex-shaped dies is yet available. Therefore, the objective of this research was to fabricate and test a real-time cumulative mass deposition tester (MDT) for two different powders (with varied physical characteristics) in an "E" shaped die. The design of the MDT was based on the concept demonstrated by Puri and Dhanoa (2000). Puri and Dhanoa postulated that an anisotropic fill density distribution would result in an uneven vertical pressure distribution at the bottom surface of the die. This uneven vertical pressure distribution could then be detected and analyzed by placing multiple, sensitive and high precision load cells on the inside surface of the die-bottom.

2. Theory

2.1 Selected Literature Review

Dhanoa and Puri (1998) have summarized the results of much of the work done in the area of powder deposition. Some of the key studies mentioned, among others, were Molenda et al. (1994), Moysey (1984), Moriyama and Genji (1985), Bocchini (1987) and Faikin et al. (1976). All the above-mentioned studies show that deposition methods are significant contributors to the variation observed in the bulk density of powder in a die. This variation is dependent on the rate of die fill, die-geometry and die-size. Therefore, in order to maintain homogeneity of a compact's quality, a deposition method that gives the most uniform bulk density of powder should be used.

Dhanoa and Puri (1998) proposed a radical concept for quantifying the uniformity of powder fill in simple shaped dies. They developed a low-cost tester capable of acquiring real-time data for experimental analysis of the die-filling process. The underlying principle of their proof-of-concept tester was that an anisotropic fill density distribution would result in an uneven vertical pressure distribution at the bottom surface of the die. This uneven vertical pressure distribution could be detected and analyzed by placing multiple, sensitive and high precision load cells on the inside surface of the die-bottom. Using their tester, Dhanoa and Puri provided a qualitative data interpretation for the deposition of a spray-dried alumina powder in simple geometric cavities (i.e., circular, square and diamond-shaped in cross section). They studied two different die fill methods, namely funnel fill and sieve fill. The results indicated that their tester had the ability to quantify variations in spatial deposition of powder mass as a consequence of the differing fill methods.

2.2 Concept of Mass Deposition Tester (MDT)

The Mass Deposition Tester (MDT) was designed to acquire real-time data for complex die shapes using high precision semiconductor load cells that were sensitive enough to measure powder mass values in the range of 0 to 2.5 g (**Figure 1**). These load cells operate on a 10-volt DC excitation and the voltage changes (due to mass differences) are measured using a high precision data acquisition (DAQ) system. The signals acquired by the DAQ system are recorded using a program written in LabVIEW. This program displays the real-time spatial accumulation of powder mass in the die. The quantitative data obtained from the MDT can be used to develop iso-mass contours in a die.

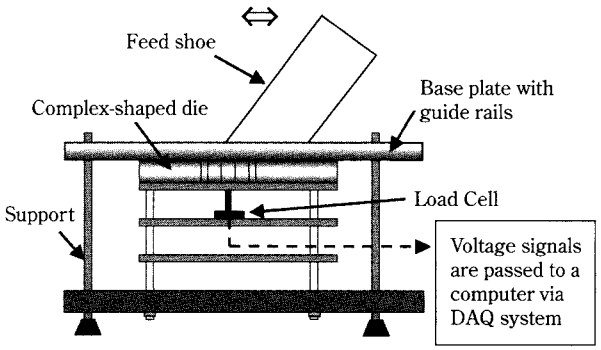

Fig. 1 Schematic of MDT along with feed shoe deposition method

3. Methodology

3.1 Experimental Materials

Two powders, a manganese zinc ferrite-based (MZF) and a microcrystalline cellulose-based (MCC), were selected as test materials in this research because of the contrasting nature of their characteristic properties (**Table 1**). The MZF powder used in this study was a cohesionless, spray-dried powder and is widely used for dry pressing magnetic components. On the other hand, microcrystalline cellulose (MCC) is a relatively cohesive powder that is widely used in the pharmaceutical industry and to a lesser extent in the food industry. The particle size distribution of the two test powders is shown in **Figure 2** and the micrographs are shown in **Figure 3**.

The shape difference between the particles of the two powders is quite evident from **Figure 3**. The MZF powder particles are round, whereas, MCC particles are irregular and elongated (length to diameter ratio of 6). In this research, these two powders were

Table 1 Comparison of characteristic properties of the two test powders

	Particle Shape	Median Size (d_{50})	Density (g/cc)		Granule Strength	Cohesion (kPa)	Internal friction angle
			Bulk	Particle			
MZF	Spherical	150 μm	1.45	5.03	Rigid	≈0	35°
MCC	Needle-shaped	113 μm	0.33	1.55	Fragile	≈1.5	46°

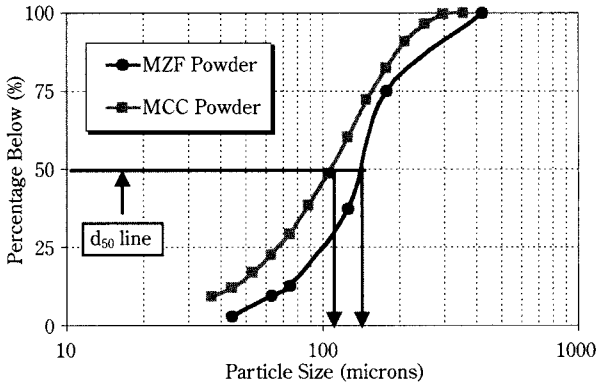

Fig. 2 Particle size distribution of the two test powders

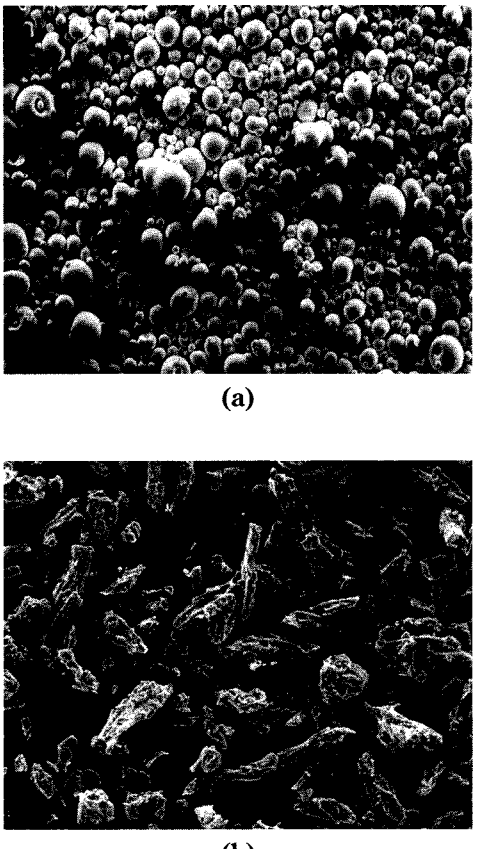

Fig. 3 Micrographs of the test powders (a) MZF powder (b) MCC powder

tested at environmental conditions of 22°C±2°C and 40%±5% RH.

3.2 Die Shape

An E-shaped die was instrumented as described in **Figure 4**. This particular shape was chosen because it represents a complex, yet, industrially relevant geometry that is being dry pressed in large quantities for ultimate use as a magnetic component. A nomenclature was developed for the E-shaped die, which is also explained in **Figure 4**.

The E-die was made of aluminum and had fourteen different hole locations where the load cell could be placed. The dimensions of the E-die were 5 (length) × 2.5 (width) × 1.8 cm (depth). Each of the holes was 0.5 cm in diameter. This was the smallest diameter hole that could be used, with load cell stem diameter of 0.3 cm. Smaller size holes would make the placement of multiple load cells, as originally planned, difficult to achieve due to the required precision in

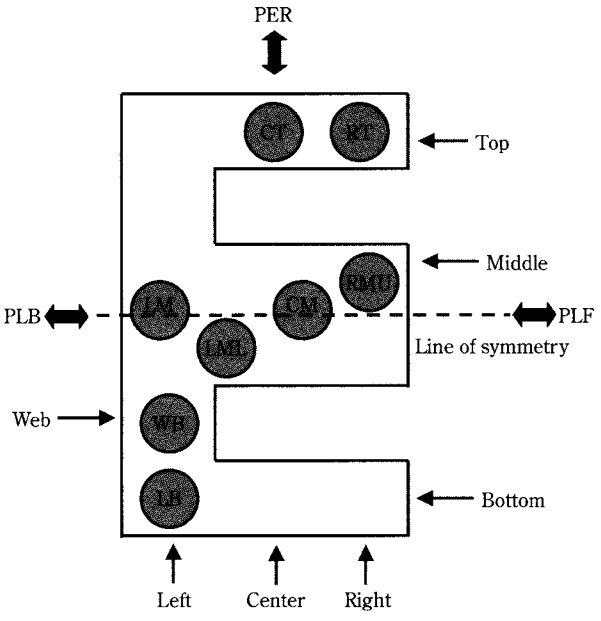

Fig. 4 E-die with description of fill directions and selected hole locations
(PER = Perpendicular to Leg; PLB = Parallel to Leg from Back; PLF = Parallel to Leg from Front)

hole-to-hole alignment. The width of the top, middle and bottom legs of the "E" was 0.7, 1.4 and 0.7 cm, respectively. There were three practical directions from which the powder could be deposited into the E-die. These fill directions namely, perpendicular to leg from front (PLF), perpendicular to leg from back (PLB) and perpendicular to leg (PER), are also shown in **Figure 4**. Data were collected for all three fill directions, however, only the PLB and PLF fill directions were assumed to result in a symmetric fill with respect to the centerline of the middle leg of the "E". This assumption is not valid for PER fill direction; consideration of that data is therefore excluded from this paper.

Due to symmetry and time considerations, data were collected only for 8 different shaded locations (**Figure 4**). Also, based on prior experience with pressed parts, these eight measurement locations were identified as candidate regions of large powder mass variations. The results from these eight locations were then extrapolated to other locations due to symmetry of E-die. The nomenclature of these eight locations is given in **Table 2**.

Table 2 Nomenclature of eight shaded locations where data was collected

CM = Center Middle	LM = Left Middle
CT = Center Top	LML = Left Middle Lower
LB = Left Bottom	RMU = Right Middle Upper
RT = Right Top	WB = Web Bottom

Five runs were done for each fill direction and for each of the shaded hole locations. Only one load cell was active during a given run due to instrument limitations and cost constraints. In total, 160 runs (2 powders * 8 hole locations * 5 replicates * 2 fill directions) were conducted. Results of these experiments are presented and discussed in this paper.

3.3 Powder Deposition Method

The feed shoe deposition method is widely used in powder processing industries to rapidly deposit powder into a die. Therefore, this powder deposition method was chosen in this research to simulate an industrial powder-processing situation. In this method, a feed shoe (made out of Plexiglas®) was manually moved forward and backward on guide rails (as shown in **Figure 1**). The guide rails had an opening that channeled the powder flow into the die cavity. During the forward stroke, due to the trajectories of particles moving at high velocity, powder tended to deposit on the die's forward-end. This resulted in the partial filling of the die. Rearrangement of particles took place during the brief period of rest. During the backward stroke, trajectories of the particles were reversed resulting in deposition at die's leeward-end, resulting in complete filling of the die. This deposition process schematic is shown in **Figure 5**.

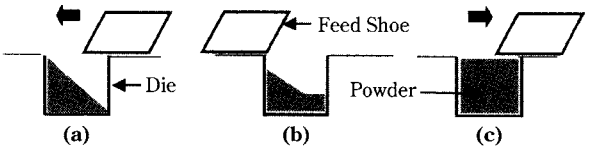

Fig. 5 Stages in feed shoe deposition method: (a) Forward stroke – partial die-filling (b) Rest period – particle rearrangement (c) Backward stroke – complete die filling

The total time taken to deposit the powder into the die using the feed shoe method was in the order of 1.5-3 seconds (includes time to reach a steady value after the deposition process is completed). This also includes a period of rest of approximately 1 second. The dimensions of the feed shoe used were: outer diameter – 10 cm, inner diameter – 9.2 cm. The angle of feed shoe tube with respect to the base plate was 44.5 degrees.

4. Results and Discussion

The following subsections discuss the various applications of the mass deposition tester (MDT) based on the data collected on the E-die. **Figure 6** summarizes some of the key benefits and applications of the MDT. A detailed explanation of each of the MDT's applications is presented in the following subsections.

4.1 Generation of Fill Trends in Real-Time

The MDT load cells generate real-time fill trends as the feed shoe moves back-and-forth across the die-cavity. These fill trends quantify the mass of powder deposited at any location during the deposition process. This valuable information from the fill trends can be used to study the effect of die-shape, powder flowability, particle shape and fill-speed on the entire process of powder deposition. For example, in the case of feed shoe deposition, the effect of the forward and backward stroke can be studied independently using the fill trends. A typical real-time fill trend obtained for the feed shoe method is shown in **Figure 7**.

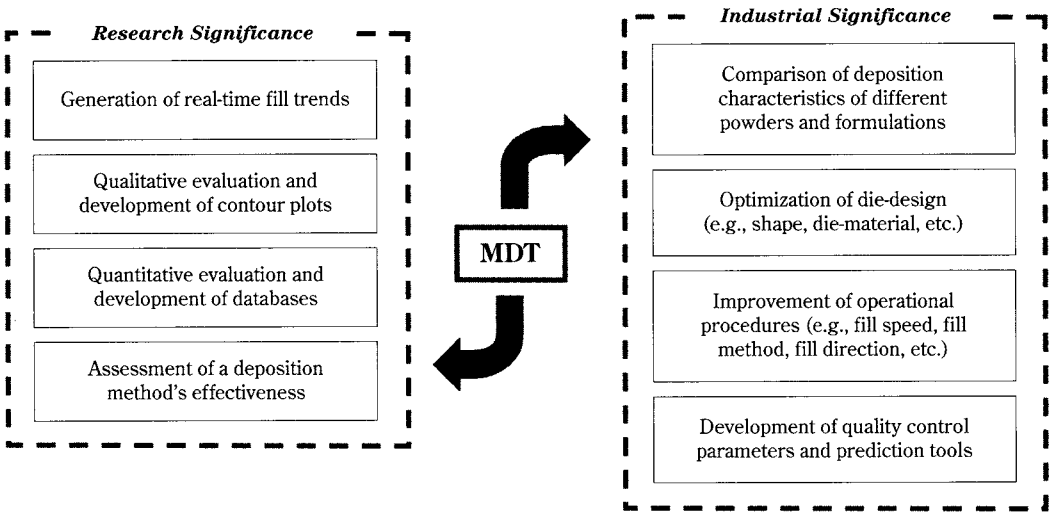

Fig. 6 Applications and benefits of the MDT

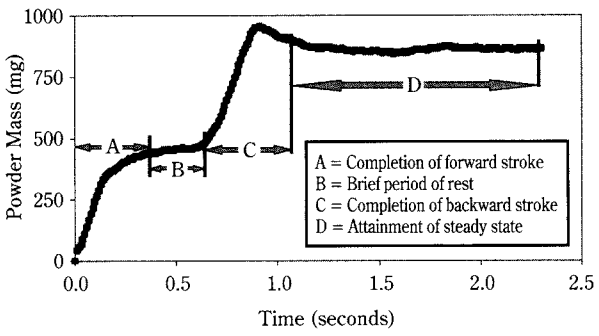

Fig. 7 A typical fill trend explaining the feed shoe deposition method

In all the fill trends generated for the feed shoe, it was observed that the data series go from a position of zero mass (initiation of the deposition process) to some intermediary mass value. This intermediate mass value is generally observed as a plateau in the fill trends defining the end of the feed shoe's forward stroke. The forward stroke is followed by a brief period of rest that appears as a horizontal line in the fill trend. Finally, the backward stroke of the feed shoe is completed. This backward stroke leads to the formation of a peak in the fill trends that is followed by a steady response. This peak represents the maximum powder mass value measured by the load cell just before the excess powder is scrapped off from the die during the retraction of feed shoe. The steady response value is the measure of final mass at a particular location.

Different real-time fill trends can be generated by placing a load cell at various locations in a die. These real-time fill trends can then be pooled to develop a real-time deposition profile for the entire die. These deposition profiles can be used for the qualitative assessment of a deposition process in a given die shape. The quantitative information from the fill trends can be used to optimize the deposition process in order to obtain a uniform fill.

4.2 Qualitative Evaluation of Deposition Method

The deposition profiles obtained by pooling the different real-time fill trends can be used 1) to evaluate various operational procedures in die-filling process, 2) to study the effect of various powder characteristics on the powder deposition process, and 3) to develop mass/fill density contour plots for a given die shape. The data obtained from the manganese zinc ferrite (MZF) and microcrystalline cellulose (MCC) powders are used to highlight the importance of this information.

4.2.1 ***Evaluation of Operational Procedures:*** The deposition profiles can be used to study the effect of various operational procedures (such as fill-speed, direction of fill, die material, etc.) on the powder deposition process. In this paper, only the effect of fill-direction on the spatial powder mass distribution in E-die was studied.

Manganese zinc ferrite (MZF) powder: The MZF powder's deposition profiles obtained for the PLB and PLF fill directions are compared in **Figures 8** and **9**. These figures clearly indicate that there is a significant difference in the way MZF powder deposits in E-

die for the two fill directions. Also, each fill direction has certain unique characteristics that are further examined.

In case of PLB fill direction, the observed maximum mass of MZF was concentrated at the right middle upper (RMU) location, followed by center middle (CM), left middle lower (LML) and left middle (LM) locations. This clearly indicates that the powder mass is concentrated in the middle leg of the E-die. This apparent mass concentration was expected because the middle leg was wider (1.4 cm) compared to the other two legs (0.7 cm). Therefore, the powder encountered less influence from die-walls during deposition in the middle leg. MZF powder's final mass at various locations varied from 500-1700 mg. The average recorded powder mass in the PLB fill direction was 1017 mg. The voids volume fraction (volume of solids/total volume) values varied from 0.05 (in the middle leg) to 0.70 (in the outer legs). The average voids volume fraction was 0.42. Voids volume fraction values were theoretically calculated for each measuring location. These values should be used qualitatively to study the distribution of the voids volume fraction in the entire die. The actual values are expected to be somewhat different from the calculated values. Although the absolute values are likely to differ, the ratios of any two values are expected to be nearly the same when using the numbers in this paper and those obtained using actual values. The void fraction analysis confirms that the powder was much tightly packed in the middle leg compared to the outer legs.

In case of PLF fill direction, it was observed that the fill-trends were quite different from those observed in the PLB fill direction. The maximum concentration of powder mass was again observed in the middle leg. However in PLF, the maximum mass was concentrated at center middle (CM), followed by right middle upper (RMU) and left middle (LM)[8]. The MZF powder mass at various locations varied from 500-1700 mg. The average recorded powder mass in PLF fill direction was 957 mg. The voids volume fraction varied from 0.04 (in the middle leg) to 0.71 (in the outer legs). The average voids volume fraction was 0.46. A thorough quantitative evaluation of the two fill directions is done in **Table 3** (discussed further in section 4.3).

Microcrystalline cellulose (MCC) powder: Observations similar to the MZF powder were noted for the MCC powder. The MCC fill-trends obtained in PLB and PLF fill direction are shown in **Figures 10** and **11**. Nomenclature is shown in **Figure 4** and summarized in **Table 2**.

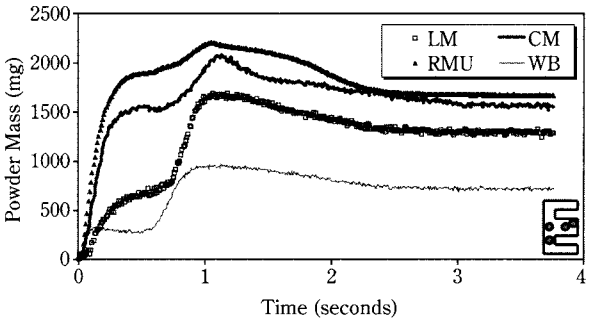

Fig. 8 Deposition profile of MZF powder in typical locations for PLB fill direction (**Figure 4, Table 2**)

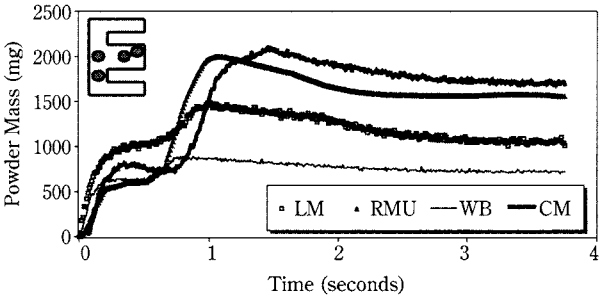

Fig. 9 Deposition profile of MZF powder in typical locations for PLF fill direction

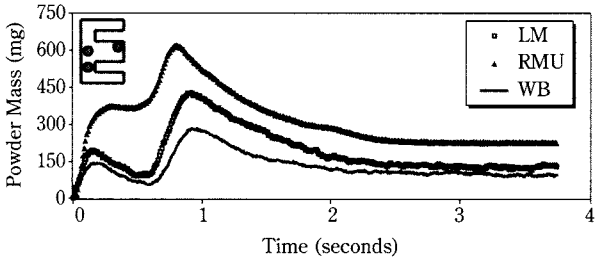

Fig. 10 Deposition profile of MCC powder in typical locations for PLB fill direction

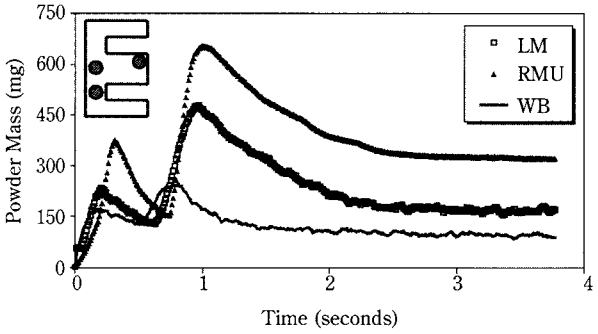

Fig. 11 Deposition profile of MCC powder in typical locations for PLF fill direction

It was observed that the fill trends of MCC in PLB and PLF fill direction are very different. In addition, the MCC powder's final mass varied from 50-330 mg in both cases. The average masses in the PLB and PLF fill directions were 150 and 143 mg, respectively. The quantitative results for MCC are tabulated in **Table 4** (discussed further in section 4.3). The voids volume fraction varied from 0.40 (in the middle leg) to 0.90 (in the outer legs) for both fill directions. The average voids volume fraction was 0.71 in both PLB and PLF fill directions.

4.2.2 ***Effect of Powder Characteristics on Deposition Process:*** The mass deposition tester (MDT) can be used to study the deposition behavior of different powders and powder formulations. This information can be helpful in the development of quality control measures and prediction tools in an industrial powder-processing unit. For example, even before attempting to press a part, the MDT can give significant information regarding whether the powder will deposit uniformly into the die. Corrective measures (such as changing fill direction, tailoring particle shape, etc.) can then be applied to enhance the deposition. The data collected on the manganese zinc ferrite (MZF) and microcrystalline cellulose (MCC) powder highlight these salient features of the MDT.

Die filling: It was observed that in certain runs of the data collection process, the MCC powder was unable to completely fill the E-die cavity. This behavior of MCC was unlike that of MZF that completely filled the E-die cavity during every run. This effect can be attributed to the cohesive nature of MCC powder.

Fill trends: It can be observed from **Figures 8** to **11** that the fill trends in both the powders are very different. These variations can be attributed to differing cohesion, angle of internal friction, particle shape, etc. The MZF particles are spherical in shape and flow readily. Therefore, the MZF powder was able to pack (or fill) better compared to MCC during deposition, thus leading to differences in the fill trends. It was also observed that the spatial powder mass distribution was markedly different for the two powders.

Amount of powder deposited: The average MCC powder mass deposited (for either fill directions) was roughly one-seventh that of the average MZF powder mass. The reason for such a variation in final masses can be attributed to the differences in bulk and particle densities of the two powders. Since MZF has a higher bulk and particle density, the average MZF powder mass was expected to be higher than that of MCC. However, the bulk and particle density ratios of the two powders (MZF:MCC) are only 4:1, which does not fully explain the observed mass ratio differences. The observed high ratio of 7:1 is clearly related to powder particle characteristics.

Voids volume fraction: In order to compare the deposition behavior of the two powders irrespective of the particle density, it was necessary to calculate the voids volume fraction (volume of solids/total volume) at various locations in the die. From the data it was observed that the voids volume fraction of MZF powder varied from 0.05-0.70. The volume voids fraction of MCC powder varied from 0.4-0.9. The average voids volume fraction for MZF and MCC was 0.42 and 0.71, respectively. Therefore, it is clear that the MZF powder packs more tightly compared to MCC. These differences in voids volume fraction can be attributed to the particle shape differences.

4.2.3 ***Development of Contour Plots for Given Die-Shape:*** The quantitative information from the MDT can be used to develop iso-mass contour plots of a particular die-shape at any given instant in time. These contour plots are helpful in ascertaining the regions of high and low mass. They are also useful in identifying certain locations that might lead to defects during powder pressing. These contour plots can be easily generated for any given die-shape using commercially available software such as Matlab® or SigmaPlot®. One such contour plot is developed for MZF in the PLF fill direction (**Figure 12**) based on the quantitative information tabulated in **Table 3** of section 4.3.

Figure 12 strengthens the qualitative observations made in section 4.2. It is clear that the powder mass is concentrated in the middle leg and is roughly twice the mass in the other two legs. The contour plot also clearly demonstrates the anisotropy in spatial powder mass distribution in the E-die.

4.3 Quantitative Evaluation of Deposition Method

The mass deposition tester (MDT) can be used for the quantitative evaluation of a given deposition method and can be utilized to develop databases for practicing engineers. The quantitative information obtained from the deposition behavior of MZF and MCC in the E-die is tabulated in **Tables 3** and **4**.

From **Table 3**, it is observed that the high mass

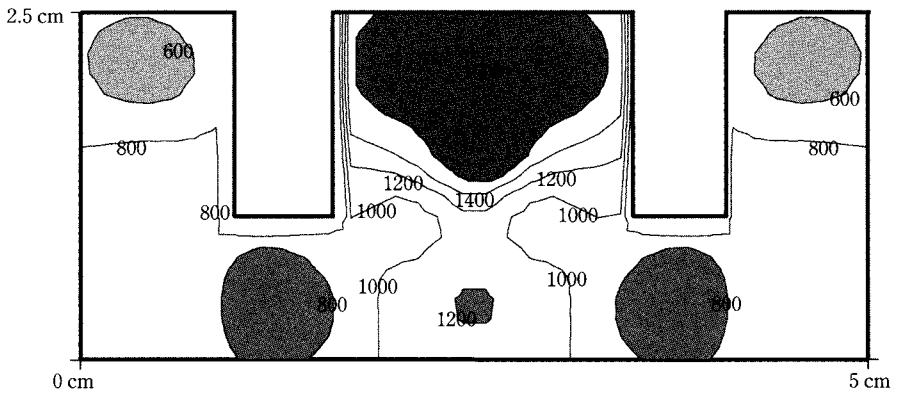

Fig. 12 MZF's spatial mass distribution at the end of fill process in PLF fill direction

zones are concentrated in the middle leg of the E-die (**Figure 12**). The middle leg roughly had twice the mass present in the outer legs. This trend was observed with both fill methods and in both powders. This clearly emphasizes that the presence of die-walls affects the spatial powder mass distribution in a die. These differences in spatial mass distribution will result in anisotropic powder compaction. From **Table 3**, the coefficient of variation (COV) values were mostly in the range of 5-20% for MZF powder.

From **Table 4**, the COV values for MCC generally ranged from 25-50%. This clearly emphasizes that MCC is much more difficult to process than MZF. It does not deposit as readily, i.e., its low flowability (compared with that of MZF) leads to large variations in deposited powder masses. This quantitative information supplements the observations made in section 4.2.2.

From **Tables 3** and **4**, it can be concluded that fill direction does not affect the average powder mass deposited in the E-die. For example, the average MZF powder mass deposited in the PLB and PLF fill directions was 1017 mg and 957 mg, respectively. On the other hand, the average MCC powder deposited in the PLB and PLF fill directions was 150 mg and 143 mg, respectively. The average voids volume fraction

Table 3 Comparison of MZF powder's final mass and voids volume fraction values at various locations in E-die+

Hole Locations^		PLB Fill Direction				PLF Fill Direction			
		Average Mass (mg)	Std. Dev.	COV*	Voids Volume Fraction**	Average Mass (mg)	Std. Dev.	COV	Voids Volume Fraction
Top Leg	*RT*	528	143	27	0.70	503	105	21	0.71
	CT	752	119	16	0.57	851	109	13	0.52
Middle Leg	*LM*	1291	154	12	0.27	1008	308	31	0.43
	LML	1293	95	7	0.27	963	102	11	0.45
	CM	1553	98	6	0.12	1691	158	9	0.04
	RMU	1671	343	21	0.05	1559	84	5	0.11
Bottom Web	*WB*	717	123	17	0.59	645	132	20	0.63
Lower Leg	*LB*	737	132	18	0.58	830	177	21	0.53
***Average*++**		***1017***			***0.42***	***957***			***0.46***

\+ Five runs were done for each location. However, in certain locations, three or four out of five runs were acceptable.

^ Description of hole locations is given in **Figure 4** and **Table 2**.

* COV % = (Average/Standard Deviation)* 100

** Voids volume fraction values were theoretically calculated for a given location. These values should be used qualitatively to study the distribution of the voids volume fraction in the entire die. The real values are expected to be higher than the quoted theoretical values.

++ Average values for mass and voids volume fraction were calculated using the values obtained for all 14 locations.

Table 4 Comparison of MCC powder's final mass and voids volume fraction values at various locations in E-die+

Hole Locations^		PLB Fill Direction				PLF Fill Direction			
		Average Mass (mg)	Std. Dev.	COV*	Voids Volume Fraction**	Average Mass (mg)	Std. Dev.	COV	Voids Volume Fraction
Top Leg	*RT*	54	29	55	0.90	***			***
	CT	64	30	47	0.88	56	28	49	0.90
Middle Leg	*LM*	123	71	58	0.77	173	57	33	0.68
	LML	317	106	33	0.42	120	68	56	0.78
	CM	302	111	37	0.44	308	73	24	0.43
	RMU	231	79	34	0.57	325	71	22	0.40
Bottom Web	*WB*	91	26	28	0.83	93	44	48	0.83
Lower Leg	*LB*	82	41	50	0.85	115	34	29	0.79
***Average*++**		***150***			***0.72***	***143***			***0.71***

+ Five runs were done for each location. However, in certain locations, three or four out of five runs were acceptable.
^ Description of hole locations is given in **Figure 4** and **Table 2**.
* COV % = (Average/Standard Deviation)* 100
** Voids volume fraction values were theoretically calculated for a given location. These values should be used qualitatively to study the distribution of the voids volume fraction in the entire die. The real values are expected to be higher than the quoted theoretical values.
*** Data for this particular location did not turn out to be acceptable.
++ Average values for mass and voids volume fraction were calculated using the values obtained for all 14 locations.

values for MZF and MCC are roughly 0.43 and 0.71, respectively.

Also, there were a few locations where the localized powder masses deposited in the two fill directions were quite different. These differences in spatial powder mass distribution clearly indicate that the direction in which the feed shoe approaches the die-cavity can affect the deposition process. These differences in spatial mass distribution make it difficult to use final part weight or final part density as a quality criterion and would, instead, necessitate a measurement of "sectional weight or density". Therefore, it can be concluded that the MDT is an effective tool that is capable of quantifying the sectional differences that actually exist during filling of complex-shaped dies.

4.4 Assessment of a Deposition Method's Effectiveness

From the fill trends in **Figures 8-11**, the forward and backward strokes of the feed shoe can be readily delineated and quantified (**Table 5**). As the feed shoe moves forward, the die is filled partially. Some rearrangement of the particles takes place during the brief period of rest. Finally, the unfilled portions of the die are filled during the backward stroke (as shown in **Figure 5**).

A quantitative evaluation of how a die is filled during the forward and backward strokes of the feed shoe can help in ascertaining the effectiveness of the feed shoe fill method in a given processing situation. For example, it may be possible that if the die gets completely filled during the forward stroke, then there is no need for the backward stroke. On the other hand, if more uniform spatial powder mass distribution is obtained during forward stroke compared to the backward stroke, then a deposition method can be developed that incorporates two feed shoes with only forward strokes. Also, suitable adjustments in the fill-speed and the shoe design can result in a better spatial powder mass distribution. In **Table 5**, the MZF powder's final mass values along with the masses obtained at the end of the forward stroke at the various hole locations are compared. Similar tables can also be developed for MCC.

From **Table 5**, it can be observed that average mass of powder deposited during the forward stroke of the feed shoe is less than average powder mass deposited after the completion of one cycle of feed shoe. Therefore, it can be concluded that the forward stroke only fills the die partially. The complete filling of the die takes place during the backward stroke. It can also be observed that even though the powder's average final mass is the same in both fill directions, differences in spatial mass distribution are present even in the forward stroke. This analysis provides quantitative credence to the observations made in

Table 5 Comparison of MZF powder mass deposited during various strokes of feed shoe[+]

Hole Locations^		MZF Powder Mass (in mg)					
		PLB Fill Direction			PLF Fill Direction		
		FS*	FM**	Diff %***	FS	FM	Diff %
Top Leg	*RT*	813	528	154	659	503	131
	CT	460	752	61	461	851	54
Middle Leg	*LM*	658	1291	51	1022	1008	101
	LML	988	1293	76	583	963	60
	CM	1557	1553	100	788	1691	47
	RMU	1892	1671	113	603	1559	39
Bottom Web	*WB*	284	717	40	621	645	96
Lower Leg	*LB*	627	737	85	903	830	109
Average Mass (mg)[++]		***882***	***1017***		***676***	***957***	

[+] The shaded portions indicate the locations where FS was greater than FM
^ Description of hole locations is given in **Figure 4** and **Table 2**.
* FS = Powder mass deposited after completion of forward stroke
** FM = Powder mass deposited after completion of 1 complete cycle of feed shoe (forward + backward)
*** Diff % = 100 * FS/FM
[++] Average values for mass were calculated using the values obtained for all 14 locations.

section 4.1.1 where it was mentioned that fill directions lead to differences in the spatial powder mass distribution in E-die.

In **Table 5**, it was observed that there were certain locations where the mass deposited during forward stroke was greater than the total mass deposited. The reasoning behind such an effect is that during the forward stroke, the particles collide with the die-walls at high velocities. Due to the impact, the particles tend to pack more closely. However, during the brief period of rest, the MZF particles rearrange under the influence of gravity or vibrations and tend to slide over each other due to the low cohesion and angle of internal friction value. Due to this rearrangement of particles, the powder mass becomes more evenly distributed in the die. During the backward stroke, additional powder is deposited into the die. But since the trajectories of the particles in the backward stroke are different from those in the forward stroke, reduced packing of particles occurs. Hence, for certain locations it was observed that the mass deposited during forward stroke was greater than the total mass deposited.

5. Conclusions

From the data collected on the manganese zinc ferrite (MZF) and the microcrystalline cellulose (MCC) powder for E-die, it is concluded that the mass deposition tester (MDT) is an effective tool capable of generating a real-time deposition profile of a powder in a die. The die shape can either be complex or simple. The information obtained from the MDT is very helpful in comparing the deposition characteristics of different powders and powder formulations. Based on this study, the following conclusions were drawn:

1. Fill directions affect the deposition profiles. This was observed for both MZF and MCC powders. Also, each fill direction has certain unique characteristics.
2. The powder mass was highly concentrated in the middle leg of the E-die. This effect of high mass concentration in this leg was expected because the middle leg was wider (1.4 cm) compared to the other two legs (0.7 cm). Therefore, the powder experienced considerably less influence from die-walls during deposition in the middle leg.
3. The average MCC powder mass deposited in both fill directions was roughly one-seventh the average MZF powder mass. The reason for such a variation in final masses can be attributed partially to the differences in bulk and particle densities of the two powders. However, the bulk density ratio of the two powders (MZF:MCC) is only 4:1, which does not fully explain the observed mass ratio differences. The observed high ratio of 7:1 is clearly related to powder particle characteristics.
4. MZF powder was able to pack better compared to

MCC during deposition and hence the differences in the voids volume fraction values were observed.

5. From the quantitative evaluation of MDT results, it was observed that the coefficient of variation (COV) values were mostly in the range of 5-20% for MZF powder. On the other hand, the COV values for MCC generally ranged from 25-50%. This clearly demonstrates that MCC is a more difficult powder to process.

6. Assessment of MDT

From the data collected on the two powders, it is concluded that the mass deposition tester (MDT) is an effective tool capable of generating a real-time deposition profile of a powder in a die. The MDT can be used to develop fill trends, contour plots and databases for any powder's behavior during a given deposition process. The MDT is also very useful in comparing the effect of various operating parameters (such as feed shoe design, fill directions, etc.) on a powder's spatial mass distribution in complex-shaped dies. The MDT can be used to identify a deposition process that minimizes the localized density/weight differences even before attempting to press a part. In the long run, the MDT can lead to the development of quality control parameters and prediction tools for die-filling scenario during powder processing.

References

- G.F. Bocchini, "Influence of Small Die Width on Filling and Compacting Densities", *Powder Metallurgy.* **30** [4] 261-266 (1987).
- P.S. Dhanoa and V.M. Puri, "Deposition of Particulate Materials into Confined Spaces – New Tester Development and Experimental Results", *KONA (Powder and Particle)* **16** 150-160 (1998).
- V.I. Faikin, V.P. Levin and Y.N. Gribenyuk, "Influence of the Rate of Die Filling on the Density of the Powder", *Soviet Powder Metallurgy and Metal Ceramics.* **15** [8] 590-592 (1976).
- F. Li and V.M. Puri, "Measurement of Anisotropic Behavior of Dry Cohesive and Cohesionless Powders Using a Cubical Triaxial Tester", *Powder Technology.* **89** 197-207 (1996).
- B. Mittal and V.M. Puri, "Correlation Between Deposition Methods, Powder Compression Response and Green Compact Quality: Part I Mechanical Properties of Powders". *Particulate Science and Technology.* **17** (4) 283-299 (1999 a).
- B. Mittal and V.M. Puri, "Correlation Between Deposition Methods, Powder Compression Response and Green Compact Quality: Part II Compact Quality and Correlations". *Particulate Science and Technology.* **17** (4) 301-315 (1999 b).
- M. Molenda, J. Horabik and I.J. Ross, "Effect of Filling Method on Load Distribution in Model Grain Bins". ASAE Paper No. 94-4517. St. Joseph, MI (1994).
- R. Moriyama and J. Genji, "Effect of Filling Methods on the Wall Pressure Near the Transition in a Bin", *Bulk Solids Handling.* **5** [3] 603-609 (1985).
- E.B. Moysey, "The Effect of Grain Spreaders on Grain Friction and Bin Wall Pressures", *J. Agric. Engg. Res.* **30** 149-156 (1984).
- V.M. Puri and P.S. Dhanoa, "Real-time Cumulative Mass Deposition Tester". US Patent No. 6,089,100 (2000).

Author's short biography

Bhavishya Mittal

Bhavishya Mittal is a Ph.D. candidate in the Materials Program at The Pennsylvania State University from where he graduated in 1999 with a M.S. in Agricultural and Biological Engineering. He received his Bachelor of Technology degree in Chemical and Bio Engineering from Regional Engineering College, Jalandhar (India) in 1997. His research interests include powder deposition, dry powder compaction and finite element modeling.

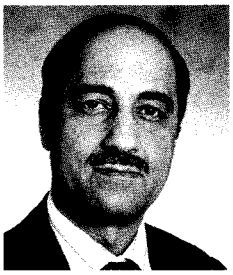

Virendra M. Puri

Dr. Virendra M. Puri is Professor in the Department of Agricultural and Biological Engineering at the Pennsylvania State University. Professor Puri also served as the Acting Director of the Particulate Materials Center, a National Science Foundation's Industry/University Cooperative Research Center. He is also the research thrust leader of Powder Mechanics group of the Particulate Materials Center. Dr. Puri received his B.S. from Indian Institute of Technology and M.S. and Ph.D. from the University of Delaware in Mechanical Engineering. Professor Puri's research interests include: measurement of fundamental engineering properties of powders, development and validation of constitutive models, and use of numerical methods to model flow and compaction behavior of powders. He has served as the chairperson of the Bulk Solids Storage Systems Committee of the American Society of Agricultural Engineers. Professor Puri is a Co-Editor-in-Chief of the Particulate Science and Technology, An International Journal. Dr. Puri regularly offers a postgraduate course in the area of powder mechanics and several hands-on industrial short courses. Professor Puri has received several teaching and research awards.

Walter Shaffer

E. Walter Shaffer is Manager, Process Development, Improvement and Control for Magnetics, Inc., a division of Spang & Co. located in Butler, PA. Magnetics is a manufacturer of ferrites and other soft magnetic components for the electronics industry. At Magnetics, Mr. Shaffer has held positions as Manager, Analytical Services and Manager, Chemical Processing and Control. Prior to joining Magnetics in 1988, he was previously employed as Group Leader, Analytical Services for Brockway Glass Co., a manufacturer of glass containers. Mr. Shaffer earned a BS degree in Ceramic Engineering from Alfred University and an MS degree in Ceramics and Material Science from Case Western Reserve University. He is actively engaged in the synthesis and processing of powders utilized in the manufacture of MnZn Ferrites.

Combustion Synthesis of Nanopowder Ceramic Powders†

Ruth H.G.A. Kiminami
*Federal University of São Carlos – Department of Materials Engineering**

Abstract

The combustion process is an important powder preparation process by which several hundred compounds may be prepared. The process is, in the simplest sense, the exploitation of an exothermic and usually very rapid chemical reaction to produce a useful material. It is a versatile process to synthesize any kind of single phase, multiphase or composite on a nanophase-scale. This review presents the thermochemical concepts and aspects of the mechanism that occurs under conditions of the combustion and examples of powders synthesized by this process.

Introduction

A number of synthesization techniques for oxide and non-oxide ceramic powders, starting from precursor solutions, have been developed over the last few decades. The "Auto Ignition" process or "Combustion Synthesis" is one of such process to synthesize crystalline ceramic nanopowders using the precursor route. In these synthesization techniques, an intermediate amorphous solid is formed from the liquid precursor. The desired crystalline phase is formed directly from an amorphous solid by local rearrangement of the ions with no interdiffusion of species. The process of "Combustion Synthesis" originated from rocket propellant technology and consists of an oxidizer and a fuel [1]. As the name suggests, high temperatures can be generated by exothermicity of the redox reaction between the decomposition of the oxidizer and the fuel. The process is controlled by the heating rate, the stoichiometry, mass of the combustion mixture, the volume of the container and the fuel. Characterization of the reaction is especially necessary for materials in which nucleation and growth occur during the combustion reaction. However, the mechanism of the reaction in a gaseous mixture is much more complex than in a simple condensed system and the resulting high purity products consist of loose agglomerates. Other variations of combustion synthesis are, for example, "Flame synthesis" [2] and "Spray conversion process" [3].

Combustion Synthesis Process

Combustion synthesis is a processing technique by which exothermic reactions are used to produce a variety of ceramic powders. The process is based on the principle that, once initiated by an external source, an exothermic reaction occurs, becoming self-sustained and resulting in the end product within a short period of time. In a conventional combustion process, e.g., "Forced Combustion", ignition occurs due to the addition of local energy from an external source such as an electric wire, spark or flame, etc. [4]. A combustion zone is initiated locally near the ignition source and propagated throughout the mixture. On the other hand, spontaneous combustion occurs when the temperature of a considerable volume of a gas mixture is raised by containing it in hot boundaries or by subjecting it to adiabatic compression, causing the generation rate to exceed the loss rate, which in turn leads to spontaneous ignition. Hence, the name "Auto Ignition". Despite the many differences, all combustion reactions share a common denominator, i.e., the heat required to drive the chemical reaction is supplied by the reaction itself. Several oxide powders have been synthesized by this "Auto Ignition" process. The technique is usually an easy, safe and fast way to produce ceramic powders, and its potential advantages are that it requires less energy than conventional ceramic synthesization processes

* P.O.Box 676 – CEP 13565-905, São Carlos/S.Paulo – Brazil
ruth@power.ufscar.br
† Accepted: August 17, 2001

and that the processing time is reduced to a few minutes. In addition, the high temperature of the combustion wave may expel volatile impurities, leading to higher purity products [5, 6]. It has been demonstrated that this quick, straightforward process can be used to produce homogeneous, high-purity, crystalline oxide nanopowder ceramic powders. The method uses an exothermic, usually rapid and self-sustaining, chemical reaction between the desired metal salt and a suitable organic fuel. Typically, the dish containing the solution (metal-nitrate and fuel) is heated directly on a hot plate at 350°C + 10°C [5, 6, etc.], in a muffle furnace maintained at 500°C + 10°C [7, 9, 10, 17, etc.], using both procedures sequentially [6, 8, 11, 12, etc.], or in a microwave oven [13, 14, 15].

Mechanism

The mechanism of the combustion synthesis the metal nitrate-fuel mixture reaction involve dehydration, decomposition, swelling and burn. In the case when the fuel is urea $CO(NH_2)_2$, for example, the probable mechanism involves melting and dehydration in the first few minutes, then the mixture decomposes, with frothing that may be due to the formation of metal- $(OH)(NO_3)_2$ gel along with other products such as $CO(NH_2)_2$ (urea nitrate), (H_2N-CO-NH-CO-NH_2) (biruet), HNCO, and NH_3. It then foams, due to the gaseous decomposition products of the intermediates, causing enormous swelling of the reaction product. The gaseous decomposition product is a mixture of N_2, NH_3 and HNCO, which are combustible. The foam itself most likely consists of polymers such as cyanuric acid $(HNCO)_3$ and polymeric nitrates, which are also combustible. Finally, the accumulation of the combustible mixture of gases causes the foam to burst into flame and burn to incandescence, with further swelling, producing an oxide powder [16, 6]. **Fig. 1** illustrates the development of the combustion synthesis of the ZnO-varistor powders using both procedures sequentially (hot plate at 350°C + 10°C and muffle furnace maintained at 500°C + 10°C) [17].

After the reaction begins, the above described method is self-sustaining, reaching high temperatures that ensure crystallization and the formation of oxides in a short period of time and releasing large amounts of gases, which prevent less agglomeration of the particles that are formed. This method is therefore considered simple; involving few steps and producing powders with the desired composition and crystalline structure. Temperature and reaction time are the two most important factors to control phase transformation during the process of combustion synthesis. Optimal temperature/time conditions vary from one material to another and the intrinsic phase transformation is fixed and characteristic of each system. General theoretical studies of the self-sustaining reaction system demonstrate that increasing the density of the medium and the reaction heat and reducing the mediums heat loss by convection and radiation can facilitate the combustion synthesis reaction. The reaction conditions a be adjusted by adjusting the fuel content

(a)

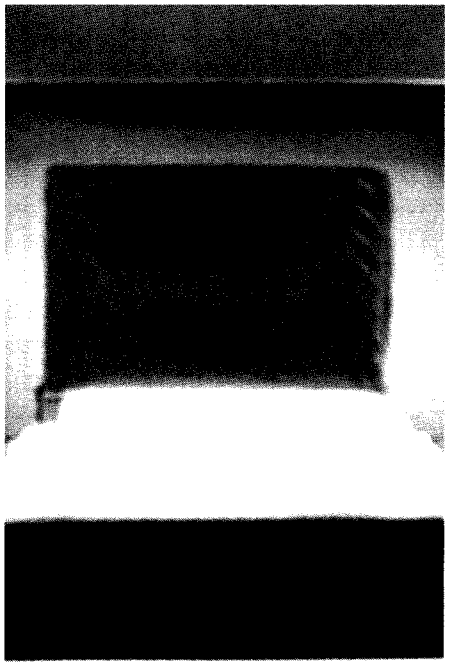

(b)

Fig. 1 Development of the combustion synthesis of the varistor powders using (a) a hotplate at 350°C and (b) a muffle furnace at 500°C [17, 18].

and the surrounding temperature. Thus, the properties of combustion-prepared powders depend on the fuel and on the combustion flame employed. **Fig. 2** shows the foam after burn to incandescence as prepared mullite obtained by combustion reaction [18].

Fig. 2 Mullite foams as formed by combustion reaction [18].

The limits of flammability depend on the direction of flame propagation and on the dimensions of the vessel employed [19] and occur after ignition has begun. The limit of flammability in most fuels is higher the higher the temperature is. This parameter has a considerable influence on the reactive character of the combustion reaction. Mixtures containing gases and vapors with air or oxygen explode spontaneously when the temperature is sufficiently high. This influence is clearly illustrated in **Fig. 3**, from which the point of ignition can be predicted. This figure relates the variation of fuel content with temperature, showing that, for ignition to occur, it must be ensured that the fuel content and the temperature are at a level that allows for self-ignition. Self-ignition does not occur above these limits because with excess fuel, although the gases that are formed show strong bonding, they tend to absorb heat and reduce temperature, thus preventing self-ignition. On the other hand, with low fuel content there is insufficient heat to cause self-ignition [19].

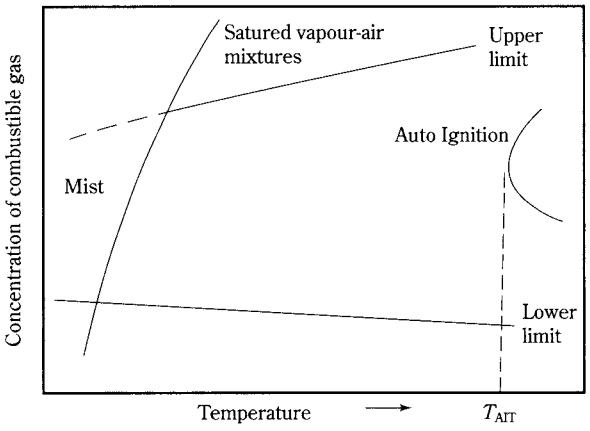

Fig. 3 Effects of the temperature on limits of flammability of combustible vapor in air at constant pressure [19].

The limits of flammability remain practically unaltered under 1 atm., but the energy required producing ignition increases as pressure decreases, and the ignition temperature decreases when pressure exceeds atmospheric pressure [19].

The combustion process can be characterized in several ways, one of which relates to the thermodynamic behavior and the temperature reached by the reaction. Thermodynamics allow one to determine the state and the properties of the gases produced by combustion. This is considered an important tool in view of the fact that the thermodynamic properties of combustion products and overall chemical balance must be taken into account [5].

Thermochemical Concepts

Combustion synthesization techniques are based on the thermochemical concepts used in propellant chemistry [20]. The composition of a fuel-oxidizer mixture is important in the field of propellants and explosives for various reasons; thus, whatever parameters are used to express it, it must clearly indicate the closeness to stoichiometry of the mixture, i.e., if it is fuel-lean, stoichiometric or fuel-rich.

Combustion mixtures consist of a fuel (reducer) and an oxidizer commonly characterized by parameters such as the φ_m ratio of the mixture and the stoichiometric coefficient of the ϕ_e elements. The greater or lesser richness of a fuel's mixture is determined by the equivalent ratio, which is defined by the expression:

$$\phi = \frac{\phi_s}{\phi_m} \qquad \text{Equation I}$$

where ϕ_s is the stoichiometric ratio (stoichiometric fuel/oxidizer relation). $\phi > 1$ values correspond to fuel-lean mixtures, $\phi < 1$ to fuel-rich mixtures, and $\phi = 1$ to stoichiometrically mixed systems [21].

For Backman [21], the expression that defines ϕ does not take into account the elementary energy contained simultaneously in the oxidizer and the reducer, particularly in cases where the fuel contains both oxidizer and combustible elements, i.e., reducer elements. Thus, to include the effect of the energy of the elements that constitute a combustion mixture,

Backman proposed another parameter, ϕ_e, denoted by the stoichiometric coefficient of the elements and defined by:

$$\phi_e = \frac{Total\ composition\ in\ oxidant\ elements}{Total\ composition\ in\ reducer\ elements}$$

Equation II

or

$$\phi_e = \frac{\sum(coeff.\ oxidant\ elements\ in\ the\ especific\ formula\ vs\ valence)}{(-1)\sum(coeff.\ reducer\ elements\ in\ the\ specific\ formula\ vs\ valence)}$$

Equation III

This coefficient (ϕ_e) considers the weight and valence of each element present in the chemical equation. The fuel (reducer) and the oxidizer are mixed in a stoichiometric relation when $\phi = \phi_e = 1$. Hence, the calculation of φ_e can be used to adjust combustion equations, i.e., the stoichiometric relation between the fuel and the oxidizer. The ϕ_e coefficient will be less than one for fuel-rich mixtures and more than one for fuel-lean mixtures. However, the Backman method is rather complicated, requiring the solution and adjustment of chemical equations. Jain et al. [22] proposed a simpler method, also applicable to systems with more than two components, to quickly determine the system's stoichiometry. The method is based on the calculation of the total valence of the fuel and the oxidizer. A mixture is stoichiometric when the value of the respective valences is the same, i.e.,

$$\phi_e = 1 = \frac{\sum(coeff.\ of\ the\ oxidant\ elements\ vs\ valence)}{(-1)\sum(coeff.\ of\ the\ reducer\ elements\ vs\ valence)}$$

Equation IV

In other words, a mixture is stoichiometric when the total value of its positive valences is equal to the value of its negative valences, as shown in the following equation:

$$\sum(\text{coefficient of oxidant vs. valence}) + \sum(\text{coefficient of reducer vs. valence}) = 0$$

Equation V

Thus, for this calculation, the elements are considered together with their valences in the gaseous products. For CO_2, H_2O and N_2, carbon is $+4$, hydrogen is $+1$, oxygen is -2 and nitrogen is zero. The values of the mixture parameters calculated by this method are very close to those reported by Backman [21]. Jain et al. demonstrated that, in a stoichiometric mixture, there is a relationship between the total oxidizer and reducer forces and the heat of the reaction, calculated from the heat produced by the formation of the reagents and reaction products. Extrapolating these concepts to ceramic oxide synthesis corresponds to considering metallic cations with the valences they will have in the end oxides.

Then, in order to release the maximum energy for the reaction, the stoichiometric composition of the redox mixture for the combustion synthesis is calculated based on the total oxidizing and reducing valences of the oxidizer and the fuel.

From the thermodynamic point of view, several synthesis reactions between the nitrates in the stoichiometric molar proportion can be possible, all endothermic. All leading to the formation of the oxide (s) and water (g), together with a variety reaction of products containing nitrogen and oxygen gases. In order to estimate which is the reaction most favored and check the validity of the assumed elemental valences in the propellant chemistry calculations, thermodynamic data are necessary to calculate the free energy changes ΔG, as well as enthalpy ΔH and entropy ΔS, involved in each reaction, as a function of temperature [7]. From the thermodynamic point of view, the decomposition reaction for example, of 2 mol of aluminium nitrate to produce 1 mol of alumina can occur by any one of the following reactions leading to the evolution of different gases:

$$2Al(NO_3)_3 \cdot 9H_2O_{(s)} \Rightarrow Al_2O_3 + 18H_2O_{(g)} + 3N_2O_{2(g)} + 4.5O_{2(g)} \quad (1)$$

$$Al_2O_3 + 18H_2O_{(g)} + 5NOO_{2(g)} \quad (2)$$

$$Al_2O_3 + 18H_2O_{(g)} + 3N_2O_{5(g)} \quad (3)$$

Using the thermodynamic data [7, 13], the change in free energy, ΔG, for the reactions can be calculated as a function of temperature. These curves (**Fig. 4**) show that, while the combustion of urea is always exothermic, the three alternative reactions that pro-

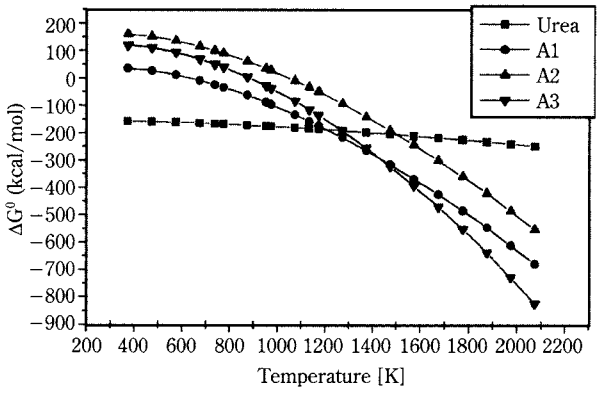

Fig. 4 Effect of temperature on the Gibbs free energy change various alternative reactions [13].

duce Al_2O_3 are endothermic at low temperatures. The reaction described as alternative (1) becomes spontaneous above 407°C, remaining the most favored reaction up to ≈1100°C at which the alternative (3) becomes the favored reaction [13].

The various reactions involved in the combustion synthesis process (**Table I**) and the corresponding enthalpy change show that the reaction R1 describes the combustion reaction of urea which, being exothermic, should supply the heat needed for the synthesis reaction. Reactions R2 and R3 are the decomposition reactions of the precursor nitrate, leading to the corresponding Al_2O_3 for alternative (1) and (3).

Then, according to propellant chemistry criteria, the urea quantity necessary to balance the total oxidizing and reducing valences in the mixture of oxidizer and fuel is 5 mol ($-30+n6=0$, $n=5$ mol). Based on the thermodynamic data, only $n=2.73$ mol of urea would be necessary in the reaction RA1, [$\Delta H°$ (25°C, kcal) $= n\ (-129.9) + 354.5 = 0$]. However, more urea is necessary ($5-2.73=2.27$ mol) to raise the temperature from 25°C to the required minimum temperature of 407°C for spontaneous decomposition of the nitrate.

Experimentally, the reactions carried out with the molar proportion of 2:5 of $Al(NO_3)_3 \cdot 9H_2O$ and $CO(NH_2)_2$ were found to permit suitable ignition/combustion conditions to yield α-Al_2O_3. The gases produced in the combustion of the extra moles of urea (2.27 mol) dissipated some of this heat and the remaining thermal energy was spent in the synthesis of the alumina. These 5 moles of urea were sufficient to promote a controlled combustion reaction of aluminium nitrate with urea [13].

Fuels

Several fuels have been employed in oxide syntheses, among them tetraformol triazine (TFTA) ($C_4H_{16}N_6O_2$) [22], hydrazide in the form of maleic hydrazide ($C_4H_4N_2O_2$) [24] and carbohydrazide $CO(N_2H_3)$ [2], and the carbamide better known as urea ($CO(NH_2)_2$) [6]. These fuels differ in their reducing power and the amount of gases that they generate. Their total valences are +6, +28, +16, and +8, respectively, and the amounts of gases generated by one mole of fuel are 4 mol, 15 mol, 7 mol and 6 mol, respectively. This obviously affects the characteristics of the reaction product. The reaction is not isothermal and large amounts of gases dissipate more heat, thereby preventing the oxides from sintering, because the temperature reached is not so high. The coincident sintering effect in the higher-temperature reactions may result in a loss of submicron features of the powders. But the product tends to be microporous and less crystalline. Another fuel used in the combustion reaction is the glycine $32NH_2CH_2COOH$ [25, 26].

Some Examples of Powders Oxides Prepared by Combustion Reaction

Urea has been used to produce powders, such as mullite [27, 28, 29, 30], lithium and zirconic aluminate [28], chromite [31], calcium aluminates [5, 3], zirconium-mullite [33], perovskite [7], alumina titanate [12, 34], materials of the NZP structural type [35], Al_2O_3/ZrO_2 [36] alumina [8] and others. Carbohydrazide has been used to obtain zirconium-alumina powders [37], colored zirconium and zircon [38]; tetraformol triazine (TFTA) to synthesize ferrites and orthoferrites with a superficial area of 5-15 m^2/g [39], chromites [40], perovskite oxides [41], dielectric materials [42] and superconductors [43].

Patil and his group have carried out extensive studies on the combustion synthesis of ceramic oxides with different fuels [6, 8, 29, 30, 37, 38, 39, 41, etc]. One of them demonstrated the production of fine particles of dielectric materials of the $MTiO_3$ type, $MZrO_3$ (M = Ca, Sr, Ba and Pb), $Pb(Zr_{0,53}Ti_{0,47})O$ and $Pb_{0,92}La_{0,08}(Zr_{0,65}Ti_{0,35})_{0,98}O_3$, obtained through the

Table I Reactions involved in the combustion synthesis [13].

Reactions (Alternatives A1 and A3)	$\Delta H°$ (25°C, kcal)
R1: $CO(NH_2)_{2(s)} + 1.5O_{2(g)} \Rightarrow CO_{2(g)} + 2H_2O_{(g)} + N_{2(g)}$	−129.9
R2: $2Al(NO_3)_3 \cdot 9H_2O_{(s)} \Rightarrow Al_2O_{3(s)} + 18H_2O_{(g)} + 3N_{2g)} + 7.5O_{2(g)}$	354.5
RA1: $2Al(NO_3)_3 \cdot 9H_2O_{(s)} + CO(NH_2)_{2(s)} + 1.5O_{2(g)} \Rightarrow Al_2O_{3(s)} + (18+2n)H_2O_{(g)} + (3+n)N_{2g)} + (7.5-1.5n)O_{2(g)} + nCO_{2(g)}$	345.5 + n(−129.9)
R3: $2Al(NO_3)_3 \cdot 9H_2O_{(s)} \Rightarrow Al_2O_3 + 18H_2O_{(g)} + 3N_2O_{5(g)}$	362.5
RA3: $2Al(NO_3)_3 \cdot 9H_2O_{(s)} + CO(NH_2)_{2(s)} + 1.5O_{2(g)} \Rightarrow Al_2O_{3(s)} + (18+2n)H_2O_{(g)} + n)N_{2g)} + 3N_2O5_{(g)} + nCO_{2(g)}$	362.5 + n(−129.9)

combustion of metallic nitrate mixtures corresponding to tetraformol triazine (TFTA) in an aqueous solution at 350°C [42]. Combustion synthesis produced dielectric oxides with high specific surface (12 and 30m^2/g) that, after sintering at 1200°C for 1 hour, reached 92 to 95% of the theoretical density. These authors concluded that it is possible to produce dielectric oxide materials such as titanates, zirconates, PZT and PZLT by the combustion process, the greatest advantage being time and energy gains. In another study, Patil [43] demonstrated the feasibility of synthesizing rare earth cuprites, La_2CuO_4, Nd_2CuO_4, $La_{1.8}M_{0.2}CuO_4$ (M = Ca, Sr) and $Nd_{1.85}Ce_{0.15}CuO_4$, prepared by the combustion of the redox mixture containing the nitrates of the metals corresponding to maleic hydrazine at 350°C. The combustion products he used were submicrometric amorphous powders which, after thermal treatment at 700°C for 30 min, formed the desired crystalline cupric phases. Cupric lanthanum doped with the strontium obtained, $La_{1.8}M_{0.2}CuO_4$, presented initial superconductivity at 36K (−237°C). Thus, the process of combustion synthesis has proved to meet expectations for the production of technologically significant superconductors owing to its controllable stoichiometry, homogeneity and the pureness of the resulting products. The process has proved to be simple and safe, with all the advantages of conventional chemical methods, and requires no sophisticated equipment.

Another study demonstrated the production of fine chromite particles of the MCr_2O_4 type, in which M = Mg, Ca, Mn, Fe, Co, Ni, Cu and Zn through the use of nitrates of the corresponding metal plus chromo III nitrate and urea in stoichiometric proportions [31]. The exothermicity of the redox reaction in the nitrate-urea mixture produced a temperature of approximately 1000°C, as shown by the formation of the α-$CaCr_2O_4$. The end products of the process were ceramic oxides with specific surface varying from 5 to 25m^2/g. Fumo et al. [5, 45] produced submicrometric (CA, CA_2 and $C_{12}A_7$) aluminates using an aluminum and calcium nitrate mixture with urea. The effect of the oxidizer/fuel ratio in the redox mixture was investigated with the purpose of ascertaining the smallest stoichiometric quantity of urea needed to trigger combustion and to what extent this reaction affected the formation of phases, the morphology and particle size of the powder produced. It was ascertained that the desired phases were obtained during the combustion reaction and that, in regard to the fuel content needed to obtain them, if the fuel content is below that required by propellant chemistry, the reaction simply fails to occur (decomposition of the nitrates is not completed).

The SEM micrographs (**Fig. 5**) shows the morphological aspects of alumina foam obtained by combustion reaction using two different effects of heating, the conventional combustion reaction (CCR) using a hot plate and furnace and the microwave-induced combustion reaction (MICR) using a hot plate and microwave [13]. The different morphologies of the foam reflected the different effects of heating. The particles of the powders obtained by the MICR route were thinner, finer and softer (a), characteristics believed to be due to the effect of homogeneous heating associated with the microwave process. The alumina powders obtained by CCR route showed a different agglomerate morphology, confirming the high density of these powders (b) [13, 14].

The **Table II** show the characteristics of both alu-

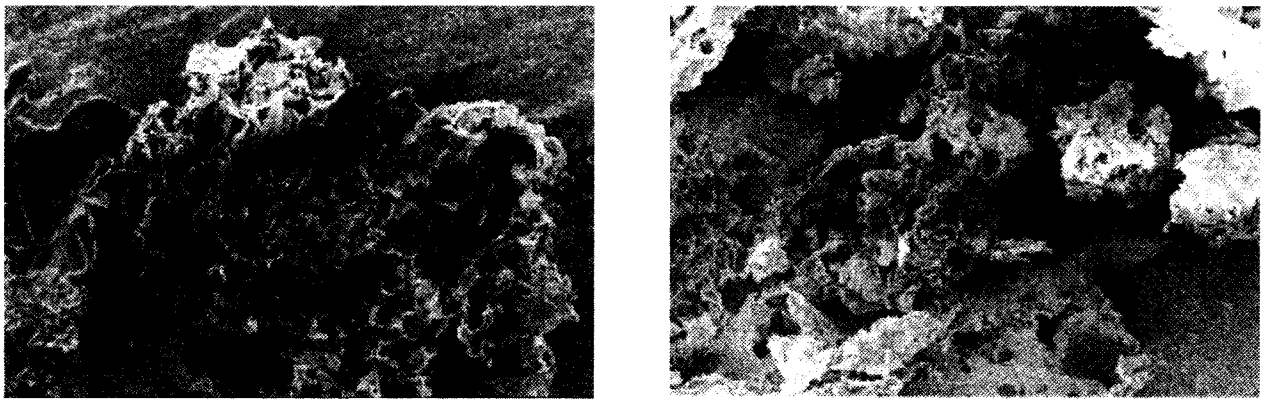

Fig. 5 SEM micrographs of the stoichiometric as prepared alumina powders, showing (a) less dense foam and fine particles obtained by the MICR route and (b) more dense foam (CCR).

Table II Characteristics of the alumina powders [13].

Routes	Powder density [g/cm^3] (% from the theoretical density)	Specific surface area [m^2/g]	Particle size* [μm]	50% average agglomerate size [μm]
MICR	3.78 (95.7)	25	0.06	1.9
CCR	3.89 (98.5)	13	0.12	1.8

* From surface area

minas after desagglomeration of the foam. The benefits of the microwave over conventional combustion reaction were to obtain finer powders, softer foam and faster reaction (2 min – MICR and 5 min – CCR) [13].

Another example is the preparation of the ZnO powders for varistor ceramics obtained with exit by the combustion synthesis technique [17, 46]. The combustion synthesis route enables synthesis at low temperature and the products obtained are in a finely divided state with large surface area. The additives (Bi_2O_3, Sb_2O_3, MnO_2, CoO and Cr_2O_3) introduced during the powder synthesis reaction were found to be already playing their expected roles (i.e. sintering aids, grain growth inhibitors, etc.) which are normally observed only during the sintering stage of powders compacts. The SEM micrographs (**Fig. 6**) show the typical morphology of combustion synthesis powders of ZnO powders and ZnO powders with additives (powders for varistor). Can be observed in the SEM photographs typically morphology aspects of (a) ZnO powder and (b) ZnO-varistor powder. The ZnO-varistor powders have high surface area specify (20,5 m^2/g) and small particle size (<300nm) and after processing and sintering at 1050°C/1.5h these varistor have been excellent electric properties ($\alpha = 41$) [17, 46].

Another study reported the production of ceria-zirconia solid solutions [26]. The exothermicity of the reaction in the nitrates-carbohydrazode/oxalyl dihidrazide mixture was produced into a muffle furnace preheated to 350+10°C. The combustion products have high surface area of 36-120 m^2/g. Calcination of $Ce_{1-x}Zr_xO_2$ at 1350°C showed three distinct solid solution regions: single phase cubic ($x \leq 0.2$), biphasic cubic-tetragonal ($0.2, x \leq 0.8$) and tetragonal ($x > 0.8$). When $x \geq 0.9$, the metastable tetragonal phase formed transforms to monoclinic phase on cooling after calcination above 1100°C.

The Al_2O_3-dispersed Cu prepared by the combustion synthesis was studied by Park et al. [48]. In this study, the mixed solution aluminium and cupper nitrate with urea was heated until the mixture was ignited to form black colored Al_2O_3 – CuO powder. This results showed by TEM that the primary particles of < 100 nm are agglomerated and that the combustion process is expected to have a definitive advantage in producing homogeneous oxide dispersion strengthened copper. Recently, C.H. Yan et al. [49] obtained nanophased $CoFe_2O_4$ using an iron and cobalt nitrate mixture with glycine dissolved in deionized water to obtain the precursor solution. The effect of the G/N (glycine to nitrates) ratio in the range

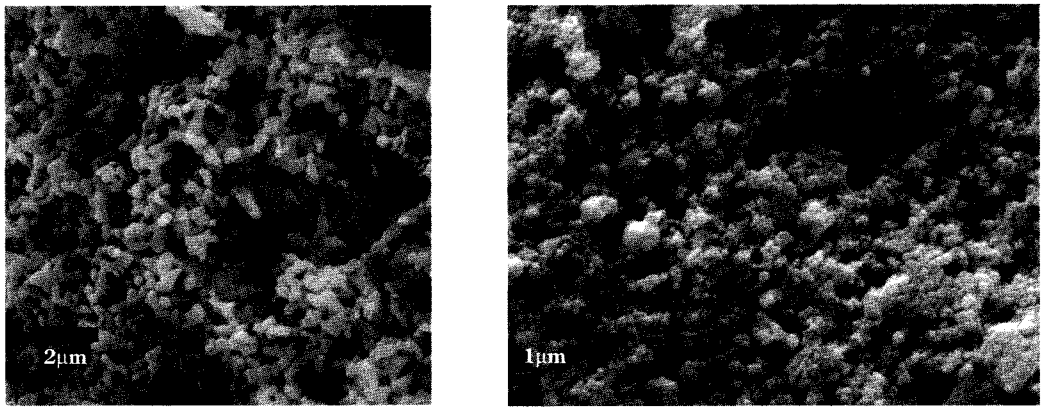

Fig. 6 Morphological aspects of (a) ZnO powders (b) ZnO-varistor powders obtained by combustion synthesis [17].

from 0.2 to 1.0 was investigated. The purpose was to investigation the ascertaining the smallest quantity of glycine needed to trigger combustion, and to what extent this reaction affected the formation of phases and the dependence of the satured magnetization (M_s) and the coercive force (H_c) of the samples produced.

Many other studies besides this one have been reported [50-55 etc.] to produce ceramic powders by combustion synthesis. However, very few of these studies have focused on the control of process parameters, i.e., maximum reaction temperature and duration of the flame, which are both very important factors in phase formation, phase crystallization and in the characteristics of final powders. Combustion synthesis is a very fast process requiring only low energy to produce ceramic powders. Several patents have already been registered in the first step toward industrial applications of this process.

Summary

Combustion synthesis has attracted much attention in recent years because it allows for synthesis of ceramic powders and because the technique is usually simple, safe and fast. The main potential advantages of combustion synthesis are that the process requires less energy than in conventional syntheses and that processing time is reduced to minutes. Combustion synthesis produce high purity powders with nanophase particle sizes and narrow size distribution, which are desirable properties for sintering of advanced ceramic materials.

Acknowledgments

The author would like to thank FAPESP – State of São Paulo Research Support Foundation for the Visiting Professor grants (Process No. 98/05783-1) and express their gratitude to Prof. Dr. M.R. Morelli, Dra. V.C. de Sousa and W.A. Mariano for their cooperation in preparations for several experiments, data analysis, and other tasks associated with this theme.

References

1) Zhang, Y. and Stangle, G.: Ignition Criteria for Self-Propagation Combustion Synthesis, J. Mater. Res., 8, 1703 (1993).
2) Mcmillin, B.K., Biswas, P. and Zachariah, M.R.: In Situ Characterization of Vapor Phase Growth of Iron Oxide-Silica Nanocomposites 1.2-D Planar Laser-Induced Fluorescence and Mie Imaging, J. Mater. Res., 11, 1552 (1996).
3) Kear, B.H. and McCandlish, L.E.: Nanostructured W-base Materials Synthesis Processing and Properties, J. Ad. Mater. 25, 11 (1993).
4) Kanury, A.M.: Introduction to Combustion Phenomena, Published by Gordon and Breach Science Publishers, One Park Avenue, NY 10016.1. R.C. Garvie and R.H. Hannick, Nature, 228, 703 (1975).
5) Fumo, D.A., Morelli, M.R. and Segadães, A.M.: Combustion Synthesis of Calcium Aluminates, Mater. Res. Bull, 31, 1243 (1996).
6) Manoharan, S.S. and Patil, K.C.: Combustion Synthesis of Metal Chromite Powders, J. Am. Ceram. Soc., 75, 1012 (1992).
7) Fumo, D.A., Jurado, J.R., Segadães, A.M. and Frade, J.R.: Combustion Synthesis of Iron-Substituted Strontium Titanate Perovskites, Mater. Res. Bull., 32, 1459 (1997).
8) Kingsley, J.J. and Patil, K.C.: A Novel Combustion Process for the Synthesis of Fine Particle α-Alumina and Related Oxide Materials, Mater. Lett., 6, 427 (1988).
9) Sato, T., Ozawa, F. and Ikoma, S.: Thermal Decomposition of Aluminium Salts-Hydrates of the Chloride, Nitrate and Sulphate, and of Ammonium Alum., Appl. Chem. Biotechno., 28, 811 (1978).
10) Bhaduri, S., Zhou, E. and Bhaduri, S.B.: Combustion Synthesis of Nanocrystalline Powders in Al_2O_3-MgO Binary System, Ceram. Eng. & Sci., 18, 645 (1997).
11) Breval, E. and Agraval, D.K.: Synthesis of [NZP]-Structure-Type Materials by the Combustion Reaction Method, J. Am. Ceram. Soc., 81, 1729 (1998).
12) Segadães, A.M., Morelli, M.R. and Kiminami, R.H.G.A.: Combustion Synthesis of Aluminium Titanate, J. Eur. Ceram. Soc. 18, 771 (1998).
13) Kiminami, R.H.G.A., Morelli, M.R., Folz, D. and Clark, D.E.: Microwave Synthesis of Alumina Powders, Amer. Ceram. Soc. Bull. 79, 63 (2000).
14) Kiminami, R.H.G.A., Morelli, M.R., Folz, D. and Clark, D.E.: Microwave Synthesis of Al_2O_3/SiC Powders by Microwave Reaction, accepted to be publish in the Proceedings of the 2nd World Congress on Microwave an RF Processing (2000).
15) Park, H.K., Han, Y.S., Kim, D.K. and Kim, C.H.: Synthesis of $LaCrO_3$ Powders by Microwave Induced Combustion of Metal Nitrate-Urea Mixture Solution, J. Mater. Sci. Letters, 17, 785 (1998).
16) Kingsley, J.J.: Ph D. Thesis, Indian Institute of Science (1989).
17) Sousa, V.C. de: Ph D. Thesis. Federal University of São Carlos – Brazil (2000).
18) Mariano, W.A.: Master Dissertation, Federal University of São Carlos, Brazil (1998).
19) Rose, J.W. and Cooper, J.R.: Technical Data on Fuel. Published by the British National Committee – Worl Energ. Conference – London (1977).
19) Barrere, M., Jaumote, A., Deveubeke, B.F. and Vandenkerekhove: Rocket Propulsion, Elsevier, Amster-

dam, 132 (1960).
21) Backman, N.N.: Combustion Explosion Shock Waves, 4, 9 (1968).
22) Jain, S.R., Adiga, K.C. and Pai Verneker, V.R.: A New Approach to Thermochemical Calculations of Condensed Fuel-Oxidizer Mixtures, Combustion and Flame 40, 71 (1981).
23) Dhas N.A. and Patil, K.C.: Combustion Synthesis and Properties of Fine Particle Spinel Manganites, J. Solid State Chem 102, 440 (1993).
24) Zhang, Y. and Stangle, G.C.: Preparation of Fine Multicompnent Oxide Ceramic Powder by a Combustion Synthesis Process, J. Mater. Res., 9, 1997 (1994).
25) Chick, L.A., Pederson, L.R., Maupin, G.D. Bates, J.L., Thomas, L.E. and Exarhos, G.J.: Glycine-Nitrate Combustion Synthesis of Oxide Ceramic Powders, Mater. Letters, 10, 6 (1990).
26) Aruna, S.T. and Patil, K.C.: Combustion Synthesis and Properties of Nanostructured Ceria-Zirconia Solid Solutions, NanoStructured Mater. 10, 955 (1998).
27) Hong, C.S., Ravindranathan, P., Agrawal, D.K. and Roy, R.: Synthesis and Sintering of Mullite Powders by the Decomposition Combustion of Aluminum-Nitrate Amorphous Fumed Silica Urea Mixtures, J. Mat. Sci. Letters, 13, 1072 (1994).
28) Ravindranathan, P., Komarneni, P. and Roy, R.: Synthesis of Lithium Aluminate, Mullite and Colored Zirconia by Combustion Process, J. Mat. Sci. Letters, 12, 369 (1993).
29) Chandran, R.G. and Patil, K.C.: A Rapid Combustion Process for the Preparation of Crystalline MullitePowders, Mat. Letters, 10, 291 (1990).
30) Chandran, R.G., Chandrashekar, B.K., Ganguly, C. and Patil, K.C.: Sintering and Microstructural Investigation on Combustion Processed Mullite, J. Eur. Ceram. Soc., 16, 843 (1996).
31) Manoharan, S.S. and Patil, K.C.: Combustion Synthesis of Metal Chromite Powders, J. Am. Ceram. Soc., 75, 1012 (1992).
32) Tag A.C.: Chemical Preparation of Binary Compounds in the Calcia-Alumina System by Self-Propagation Combustion Synthesis, J. Am. Ceram. Soc., 81, 2853 (1996).
33) Chandran, R.G., Chandrashekar, B.K. and Patil, K.C.: Combustion Synthesis and Properties of Mullite-Zirconia Composites, J. Mat. Sci., 31, 5773 (1996).
34) Segadães, A.M., Morelli, M.R. and Kiminami, R.H.G.A.: Microstructure Development and Sintering of SHS Aluminium Titanate Powders, Sixt Inter. Conf. Sci. Hard Mat., 1, 59 (1998).
35) Breval, E. and Agraval, D.K.: Synthesis of [NZP]-Structure-Type Materials by Combustion Reaction Method, J. Am. Ceram. Soc., 81, 1729 (1998).
36) Bhaduri, S., Bhaduri, S.B. and Zhou, E.: J. Mater. Res., 13, 156 (1998).
37) Dhas, N.A. and Patil, K.C.: Combustion Synthesis and Properties of Zirconia-Alumina Powders, Ceram. Inter., 20, 57 (1994).
38) Muthuraman, M. Dhas, N.A. and Patil, K.C.: Preparation of Zirconia-based Color Pigments by Combustion Route, J. Mater. Synthesis and Processing, 4, 115 (1996).
39) Suresh, K. Kumar, N.R.S. and Patil, K.C.: A Novel Combustion Synthesis of Spinel Ferrites, Orthoferrites and Garnets, Advanced Mat., 3, 148 (1991).
40) Merzhanov, A.G. In: Rao, C.N.R.: Chemistry of Advanced Materials. London: Oxford-Blackwell, 704 (1976).
41) Manoharan, S.S. and Patil, K.C.: Combustion Route to Fine Particule Perovskite Oxides, J. State Chem., 102, 267 (1993).
42) Sekar, M.M.A. and Patil, K.C.: Combustion Synthesis and Properties of Fine-Paricle Dielectric Oxide Materials, J. Mater. Chem., 2, 739 (1992).
43) Manoharan, S.S., Prasad, V., Subramanyam, S.V. and Patil, K.C.: Combustion Synthesis and Properties of Fine particle La_2CuO_4, Physica C, 190, 225 (1992).
44) Sekar, M.M.A. and Patil, K.C.: Hydrazine Carboxylate Precursors to Fine Particle Titania, Zirconia and Zirconium Titanate, Mater. Res. Bull., 2, 485 (1993).
45) Fumo, D.S. Ph D. Thesis – Universidade de Aveiro, Portugal (1997).
46) Sousa, V.C., Segadães, A.M., Morelli, M.R. and Kiminami, R.H.G.A., Combustion Synthesized ZnO Powders for Varistor Ceramics, J. Inorg Mater. 1, 235 (1999).
47) Greca, M.C. et al.: Ni/Alumina Catalysts Produed by Combustion Synthesis, Key Eng. Mater., 132, 205 (1997).
48) Park, J.Y., OH, S.J., Jung, C.H., Hong, G.W. and Kuk. I.H.: Al_2O_3-Dispersed Cu Prepared by the Combustion Synthesized Powder, J. Mater. Sci. Letters 18, 67 (1999).
49) Yan, C.H., Xu, Z.G., Chen, F.X., Wang, Z.M., Sun, L.D., Liao, S. and Jia, J.T.: Nanophased $CoFe_2O_4$ Prepared by Combustion Method, Solid State Commun. 111, 287 (1999).
50) Ekambaram, S. and Patil, K.C.: Combustion Synthesis of Ytria, J. Mater. Chem., 5, 905 (1995).
51) Castro, S., Gayoso, M., Rivas, J., Greneche, J.M., Mira, J. and Rodríguez, C.: Structural amd Magnetic Properties of Barium Hexaferrite Nanostructured Particles Prepared by Combustion Method, J. Magn. Magn. Mater. 152, 61 (1996).
52) Muthuraman, M., Patil, K.C., Senbagaraman, S. and Umarji, A.M.: Sintering, Microstructural and Dilatometric Studies of Combustion Synthesized Synroc Phases, Mater. Res. Bull., 31, 1375 (1996).
53) Aruna, S.T. and Patil, K.C.: Synthesis and Properties of Nanosize Titania, J. Mater. Synthesis and Processing, 4, 175 (1996).
54) Ye, T., Zhao G.W., Zhang W.P.: Combustion Synthesis and Photoluminescence of Nanocrystalline Y_2O_3: Eu Phosphors, Mater. Res. Bull., 32, 501 (1997).
55) Jose, R., James, J., John, A.M., Sundararaman, Divakar, R. and Koshy, J.: A New Combustium Process for Nanosized $YBa_2ZrO_{5.5}$ Powders, NanoStructured Mater., 11, 623 (1999).

Author's short biography

Ruth H.G.A. Kiminami

Ruth H.G.A. Kiminami received the B.A.Sc. degree in Materials Engineering from the Federal University of São Carlos, Brazil in 1979, the M.Sc. degree in Chemical Engineering from the Federal University of Paraiba, Brazil in 1981. She received the Ph.D. degree in Ceramic Engineering in 1986, from the Rheinisch-Westfalischen Technischen Hochschule Aachen, Germany.

She is Professor Adjunto of the Department of Materials Engineering in the Federal University of São Carlos, Brazil.

Her research interests include: synthesis of ceramic powders by conventional combustion reaction and microwave-induced combustion reaction, carbothermal reduction in conventional and microwave oven, and processing of ceramic structural and nonlinear electrical ceramics (varistors). She is member of the American Ceramic Society and Brazilian Ceramic Society.

Continuum-based FEM Modeling of Alumina Powder Compaction†

J. Guadalupe Argüello, A. F. Fossum, D. H. Zeuch and K. G. Ewsuk
*Sandia National Laboratories**

Abstract

Software has been developed and extended to allow finite element (FE) modeling of ceramic powder compaction using a cap-plasticity constitutive model. The underlying, general-purpose FE software can be used to model even the most complex three-dimensional (3D) geometries envisioned. Additionally, specialized software has been developed within this framework to address a general subclass of axisymmetric compacts that are common in industry. The expertise required to build the input deck, run the FE code, and post-process the results for this subclass of compacts is embedded within the specialized software. The user simply responds to a series of prompts, evaluates the quality of the FE mesh that is generated, and analyzes the graphical results that are produced. The specialized software allows users with little or no FE expertise to benefit from the tremendous power and insight that FE analysis can bring to the design cycle. The more general underlying software provides complete flexibility to model more complicated geometries and processes of interest to ceramic component manufacturers but requires significantly more user interaction and expertise.

Introduction

Conventional ceramic component manufacturing often involves processing and fabrication with raw materials in powder form. Granulated powder is formed into a "green" body of the desired size and shape by consolidation, often by simply pressing nominally dry powder. Ceramic powders are commonly pressed in steel dies or rubber bags with the aim of producing a near-net-shape green body for subsequent sintering. Density gradients in these compacts, introduced during the pressing operation, are often severe enough to cause distortions in the shape of the part during sintering due to nonuniform shrinkage. In such cases, extensive green machining or diamond grinding may be required to produce a part with the desired final shape and size. In severe cases, density gradients and nonuniform shrinkage may even create cracks in the parts during sintering. Likewise, severe density gradients can result in green bodies that break during ejection from the die or that are too fragile to be handled during subsequent processing.

While empirical relationships (i.e., rules of thumb) exist to describe powder compaction, they do not provide the understanding necessary to control die design or compaction parameters to eliminate density gradients; consequently, the designer is forced to use expensive and time-consuming trial and error procedures to develop new components. The problem with this traditional approach is that compaction density gradients of unknown and uncontrolled magnitude are inevitably introduced in the process, contributing to warping and uncontrolled sintering, and ultimately to unpredictable component performance and reliability. For this reason, interest has grown in developing and applying computational tools to address the problem [1, 2].

The technical approach that we have taken in this work has been to apply fundamental scientific understanding to develop an overall predictive model for powder compaction. A scientifically-based model should help us to design cost-effective processes to manufacture improved performance and reliability ceramics by providing the insight needed to control die design and/or compaction to minimize density

* P. O. Box 5800 – MS 0847
Albuquerque, New Mexico, USA 87185-0847
† Accepted: August 17, 2001

gradients. The objective of this work, therefore, has been to develop an overall predictive model for powder compaction that will aid in producing components of accurate shape and size, as-sintered, without the need to perform extensive machining. We call this a "model-based design and processing" approach.

Development of our macroscopic, continuum-based, FE technology has involved four distinct steps:

- We identified and further developed a mathematical material description (i.e., constitutive model) capable of predicting ceramic powder consolidation response in the form of a multisurface plasticity model that is typically referred to as a cap-plasticity model [3];
- We identified, extended, and implemented a testing methodology to characterize ceramic powders in a manner consistent with the mathematical description to estimate parameters for the constitutive model;
- We implemented the constitutive model within a more general-purpose, established, and accepted numerical simulation technique (i.e., the finite element method, FEM) as embodied within the nonlinear, inelastic, large-deformation FE program, JAS3D [4]; and
- We validated the predictive capability afforded by the overall model to ceramic powder compaction.

The resulting tool is a powerful, predictive tool for ceramic powder compaction.

Beyond this, we also developed specialized software that wraps around various tools from Sandia's FE toolkit, including the more general-purpose software. The specialized software targets a general subclass of axisymmetric compacts, typical of many commonly pressed parts. Its purpose is to provide a user-friendly, simple interface to the various tools in the FE toolkit that are typically needed to perform an analysis and to visualize/interpret the results from the FE analysis within the context of ceramic component manufacturing.

This paper will describe and discuss the details of each of the steps identified above to develop the underlying general FE technology and will delve into the specialized software that has been developed for nonexperts in the field of FE analysis.

Cap-plasticity constitutive model

Geotechnical engineers have had a rich and extensive history of providing tools to help evaluate soils behavior in the context of soil-structure interaction, a process that is analogous to the interaction of a ceramic powder with a metal die and/or rubber bag. For this reason, we began the search for a mathematical model of material behavior that might be applicable to ceramic powder compaction in the geotechnical literature. Among the many mathematical descriptions available, we sought one that could capture both the hydrostatic and deviatoric response of the powder; namely, one that could capture the compaction due to mean stresses (pressure) as well as the plastic flow and enhancement of compaction due to deviatoric stresses (shear). The justification for this is based on the analysis of a typical powder compaction curve obtained by uniaxial pressing relative to the measured density gradients in a die-pressed compact (**Figure 1**). The compaction curve in **Figure 1a** represents the average relative density obtained for a 94 wt% alumina body as a function of the applied compaction pressure. The fringe plot of relative density in **Figure 1b** was obtained by removing a central slice from a pressed alumina compact and determining spatial density using ultrasound velocity measurements. In this particular case, a 94 wt% alumina compact, 22.2 mm in diameter by 35.1 mm tall, was formed using a pressure of 68.9 MPa applied from the top. The highest relative density of 0.56 is measured in the upper right corner, as seen in the fringe plot. To reach such a compacted state implies that either the local "pressure" in that region was *significantly* higher than the applied 68.9 MPa or that the consolidation behavior of the powder is also influenced by the high deviatoric stresses occurring in that area due to friction between the powder and the die-wall. Because it is unlikely that higher pressure alone could account for the higher degree of compaction, a mathematical description of material behavior that allowed for the enhancement of compaction was deemed necessary.

A model that captures the mechanical behavior of granular materials during consolidation, allowing for this enhancement of compaction, is the "cap-plasticity" model of Sandler and Rubin [3], shown schematically in **Figure 2**. The ordinate in this figure is the first invariant of stress (three times the mean stress or hydrostatic "pressure") and the abscissa is the second invariant of the deviatoric stress (a measure of the shearing stresses). Features of this model include two yield surfaces, one a stationary shear failure envelope, F_s, and the other a non-stationary strain-hardening cap, F_c, that bound the elastic regime. This allows for an initially "small" cap that grows and hardens during loading (compaction), an elastic rebound upon unloading (springback), and the possibility for

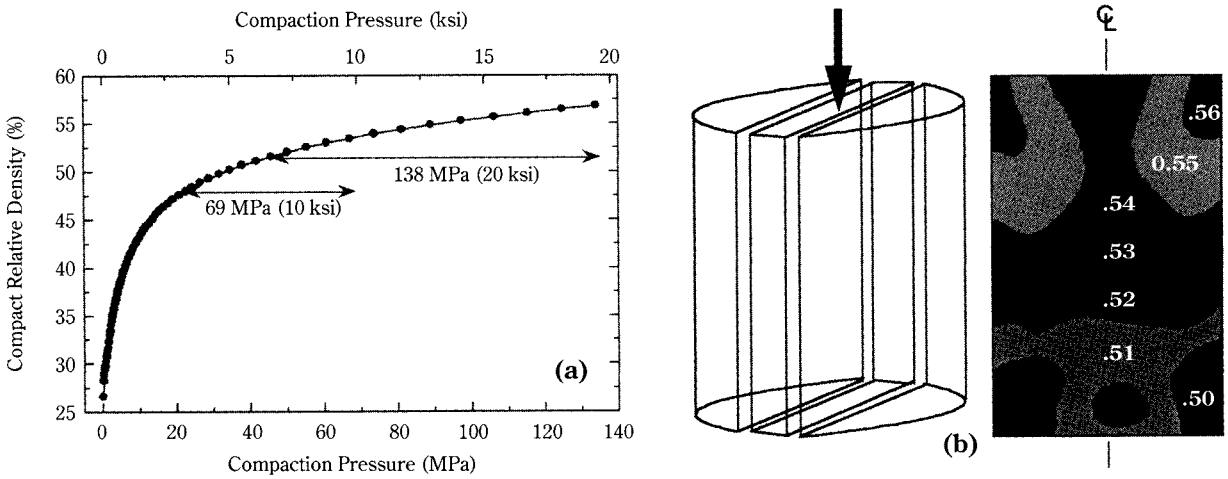

Fig. 1 Measured (a) Powder Compaction Curve and (b) Density Gradients for a 94 wt% Alumina Compact Top-Pressed to 68.9 MPa.

secondary yielding (delamination) if unloading results in an intersection with the failure envelope. In **Figure 2**, material subjected to a stress state "Q" located on the cap would undergo the same effective compaction that material subjected to a stress state "X" on the cap; however the compaction of material at "Q" would be enhanced by the deviatoric component beyond what could be achieved by the hydrostatic component alone. Effectively, it "appears" that the material at "Q" is subjected to the higher purely hydrostatic stress state at "X."

The cap-plasticity model implemented and used in this work is a generalization of the Sandler-Rubin constitutive model. It was generalized so that it incorporates Lode-angle dependence of yield in the deviatoric plane and nonassociativity in the meridional plane on the shear failure surface. Details of this generalized model can be found in Argüello *et al.* [5]. The material model also includes a modified functional form of the pressure versus volumetric strain response to better-capture ceramic powder behavior.

The material parameters that define the surfaces and other pertinent characteristics of the model come from a combination of laboratory hydrostatic compression tests and from confined triaxial compression tests. Fossum *et al.* [6] have outlined the techniques by which hydrostatic and triaxial compression experiments are used to obtain parameters for models of the foregoing type.

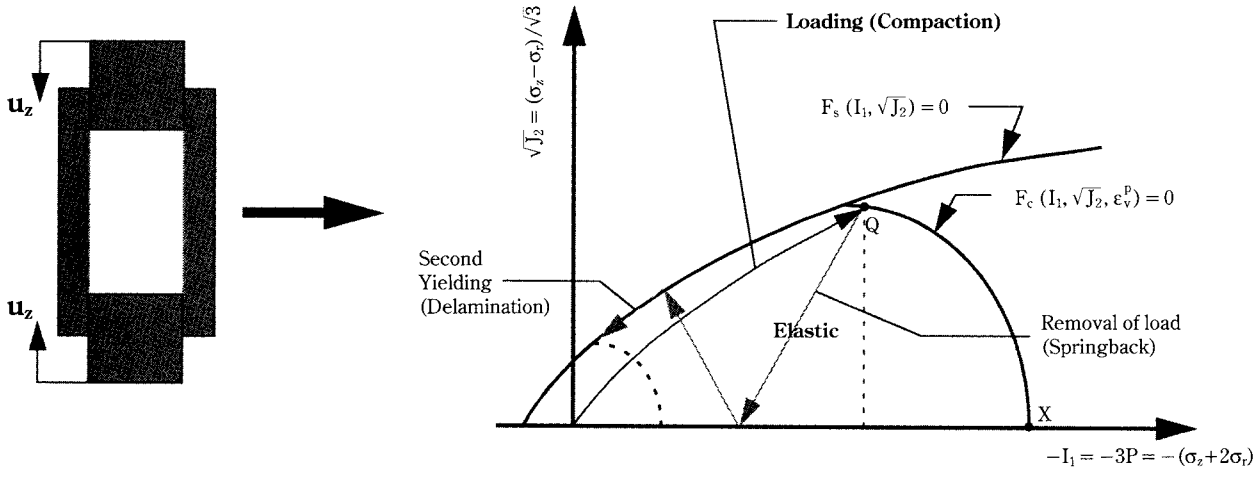

Fig. 2 Schematic of Material Response Captured by Cap-Plasticity Model.

Characterization of ceramic powder material response

The 94 wt% alumina powder is comprised of nominally micrometer-size primary particles that has been granulated with organic binder through spray drying to produce nominally 100 micrometer agglomerates. After firing, the finished product is a debased alumina body comprised of alumina and a silicate-based glass phase. The designation for the powder signifies that 94% of the inorganic matter present in the green powder is alumina, and 6% is glass. Additionally, the powder contains several percent of organic matter, some of which is intentionally added as a binder to aid in forming and to provide the compacted powder (tensile) strength after press forming. A theoretical green density of 3.54 g/cc is calculated from the constituents for the powder.

Hydrostatic compression experiments are performed to determine the evolution of the cap along the I_1 ($\sqrt{J_2} = 0$) axis, and to measure the bulk modulus at the pressure(s) of interest. The onset of permanent volume strain marks the initial location of the cap on the I_1 axis, and subsequent increases in pressure result in permanent hardening. The initial bulk modulus, and those of the hardened states, are measured by monitoring strains during small depressurization/repressurization cycles at the corresponding pressures [7].

Triaxial compression experiments are used for several purposes. First, they are used to locate the position of the shear failure surface in $\sqrt{J_2} - I_1$ space. The shear failure surface is usually (but not always) taken to be the loci of points in $\sqrt{J_2} - I_1$ space outside of which the specimen will no longer support increasing deviatoric loads. Second, during deviatoric loading, small unload/reload cycles can be performed to measure Young's modulus and Poisson's ratio for the corresponding stress state [7]. Finally, by overhardening the specimens with a hydrostatic pressure sufficiently great to cause permanent strain, and then dropping to a lower pressure before deviatoric loading, the off-axis shape and evolution of the cap can be probed: Deformation within the cap-failure envelope wedge is elastic; when the "new" cap is reached, permanent shear and volumetric strain begin to accumulate.

Knowing the bulk and Young's moduli, and Poisson's ratio, the shear modulus can be calculated. Thus, all required parameters for the model can be obtained from these two types of experiments.

Our experiments, described in more detail in Zeuch *et al.* [8], were performed using a standard, liquid-medium, triaxial cell [7]. The cell consisted of a cylindrical, 200 MPa pressure vessel with one end of the closure penetrated by a moveable piston. The piston permitted application of a deviatoric load to a test specimen concurrent with a separately controlled hydrostatic pressure. For triaxial testing, this cell was mounted in a servo-controlled, 979 kN-capacity MTS frame that permitted transfer of load from the frame to the specimen. The cell was equipped with electrical feed-throughs that permitted direct strain measurements using various types of transducers, in this instance, linear variable displacement transducers (LVDTs).

Loose ceramic powders have very high porosities, so strains are large and inhomogeneous even under hydrostatic compression. Direct triaxial compression experiments on such specimens would not be useful because the initial state of the specimen (other than its density) would be poorly defined. For this reason, experiments on ceramic powders were conducted in two separate steps, which we call the hydrostatic and triaxial stages. In the first stage, the loose powders were compacted under a succession of hydrostatic pressures to establish pressure-density curves for each of the powders and to create a suite of pre-compacted specimens of known density and dimensions for the triaxial series. The specimen assembly consisted of a cylindrical, 44.5 mm inner diameter by 133.4 mm long Viton jacket, sealed with two aluminum endcaps fitted with O-rings. One endcap was vented to the atmosphere via a tube that penetrated the lower end closure to permit gas to escape from the specimen and test in the "drained" condition [7].

To prepare a specimen, a known weight of powder was poured into the rubber jacket-endcap assembly and vibrated for 60 seconds, followed by carefully assembling the vented endcap to the rubber jacket.

Volume measurements were then made on the assembly using Archimedes' method. The known volume of the jacket plus endcaps was subtracted out to determine the volume and density of the powder. The assembled specimen was then loaded into the pressure vessel, and successively pressurized to several different pressures. At the maximum pressure for each pressurization stage, a vacuum was applied to the specimen to keep the rubber jacket compressed tightly against the powder and the sample was removed from the vessel. Volume measurements were then made on the compacted specimen, and a density corresponding to that particular pressure was determined. The sample was then returned to the pressure vessel, and the specimen was pressurized to the next

value in the series, until the final (*target*) pressure was reached. Typically, our target pressures were 6.9, 20.7, 34.5, 51.7, and 68.9 MPa. In this way, we determined the pressure-density curves for the powders up to 68.9 MPa and also obtained a suite of pre-compacted specimens of known density that were subsequently machined into cylinders of known length and diameter for triaxial testing.

For triaxial testing, the hydrostatically pressed cylindrical specimens were jacketed in polyolefin tubing and sealed with endcaps, with the lower endcap again vented. The endcaps were equipped with holders for a pair of diametrically opposed LVDTs to measure axial strain. A single spring-loaded LVDT held in a clip-on fixture measured diametral strain.

This assembly was returned to the triaxial test cell, and pressurized back to the highest pressure that the specimen experienced during the hydrostatic stage. Once the target pressure was reached, a depressurization/pressurization cycle was performed to measure the bulk modulus. The absolute magnitude of the pressure cycle depended on the target pressure, with larger loops possible at higher pressures. To preserve the original state of the specimen, it was never completely depressurized during the depressurization-pressurization loop.

For triaxial testing, the moveable piston was brought into contact with the specimen endcap and then moved at a constant displacement rate corresponding to a nominal axial strain rate of 1×10^{-4} s^{-1}. During the course of the axial deformation, the specimen was partially unloaded and reloaded periodically to measure Young's modulus and Poisson's ratio. Again, the magnitude of the cycle depended on the confining pressure and strength of the specimen. Pronounced "barreling" of the specimens was observed under all test conditions, and axial stresses were continuously corrected for the change in cross-sectional area.

Finite element discretization

The cap-plasticity constitutive model described can be incorporated into simple mathematical algorithms to model specific simple geometries and compacts of academic interest; however, for application to problems that are of interest to ceramic component manufacturers, a much more general tool was needed. Realistically, a useful tool has to be able to capture the varied and complex geometries of real pressed parts; the general loading and unloading conditions that are imposed when those parts are manufactured; and the general initial and boundary conditions that must be imposed to yield a desired part. A general-purpose, established, and accepted numerical simulation technique that provides this functionality is the finite element method. In particular, the advanced quasistatic FE technology developed by Sandia National Laboratories that is based on iterative solvers has been a key element in our program. This technology has been specifically and extensively developed under defense programs to handle large problems involving large deformations, exactly the type of problem typically encountered when simulating the pressing of ceramic components. The use of iterative solvers and the extensive experience with non-linear material response that exists at Sandia provided a base technology that offered an efficient solution to this type of problem.

For the displacement-based FEM used in this work, the field equations governing deformation of a body can be discretized and written as [5]:

$$\left\{\sum_{N}\int_{ve}\mathbf{B}\sigma dV\right\}=\{\mathbf{F}\},\ \text{or}\ [\mathbf{K}(\mathbf{u})]\{\mathbf{u}\}=\{\mathbf{F}\}, \tag{1}$$

where the term on the left-hand side of each form of the equation is the internal force vector, and {**F**} is the external force vector. In the first form, **B** is the strain-displacement transformation matrix, N is the number of elements in the FEM discretization, σ is an ordered vector of stress components in each element at a Gauss point, and *ve* is the volume of each element. In the second form of Equation (1), on the right, [**K**(**u**)] represents the global stiffness matrix in the traditional FEM [9] and {**u**} represents the global vector of unknown nodal displacements. Both forms of the equation are included to highlight the differences in approach between the traditional FEM approach and the explicit approach used in this work within the quasistatic nonlinear FE program, JAS3D [4]. The stress-strain relationship (constitutive model) is incorporated via the integrand product in the left-hand side of the first form of Equation (1) and is similarly incorporated within the left-hand side of the second form as well. The cap-plasticity constitutive model described above was implemented within JAS3D in the form of a material subroutine and constitutes one of many material models available in the code for simulating various advanced industrial processes.

The explicit technology that forms the basis of the present work approaches the solution of Equation (1) in a manner different from that used in the traditional FEM [9]. First, a global stiffness matrix is never formed. Instead, at the element level, the divergence

of the stress is found, and the contributions to each node in the overall structure are summed (i.e., the vector described by the left side of the first form of the equation). A residual force vector comprised of the internal minus the external forces,

$$\{\mathbf{R}\} = \left\{\sum_{N}\int_{ve}\mathbf{B}\sigma dV\right\} - \{\mathbf{F}\}, \quad (2)$$

is computed, and the solution procedure is then one of reducing the residual to zero using an iterative technique. Because the quantities being manipulated are vectors, there is no need to store a global stiffness matrix and factor it. Consequently the storage requirements are small when compared to the traditional FEM approach and larger problems can be solved more efficiently. The two iterative techniques that are currently used in JAS3D are a pre-conditioned Conjugate Gradient (CG) technique [10] and an adaptive Dynamic Relaxation (DR) technique [11].

Model validation for simulating powder compaction

Once the cap-plasticity model was implemented within JAS3D, confidence needed to be established in the accuracy of the overall model for predicting powder compaction response. Although JAS3D continuously undergoes many specific processes to improve software quality (e.g., change control, configuration control, regression testing, etc.), its predictive capability using the newly implemented constitutive model needed to be ascertained.

The first check performed was to simulate one of the laboratory tests performed on the 94 wt% alumina. The triaxial test at 68.9 MPa confining pressure was chosen and the entire loading history of the material was simulated, i.e., hydrostatic loading to target confining pressure followed by an increasing axial load thereafter. The simulation was performed using the material parameters obtained from all the hydrostatic and triaxial tests completed on this specific powder. **Figure 3a** shows the results of the JAS3D simulation overlaid on the data from the laboratory experiment. Axial stress is plotted as a function of the axial and radial components of strain. With the obvious exception that the JAS3D simulation did not include any of the unload/reload cycles seen in the data, the figure shows that there is good agreement between the simulation and the experiment. During the phase of hydrostatic loading to the target confining pressure of 68.9 MPa, all components of strain are equivalent. However as the axial stress increases beyond the confining pressure, during the actual triaxial phase of the test, the axial strain continues to increase while the radial strain begins to decrease. In both the simulation and experiment, the maximum value of axial stress reached is about 172.4 MPa.

With confidence that the cap-plasticity model had been implemented correctly within JAS3D, a more complex simulation was performed. The uniaxial com-

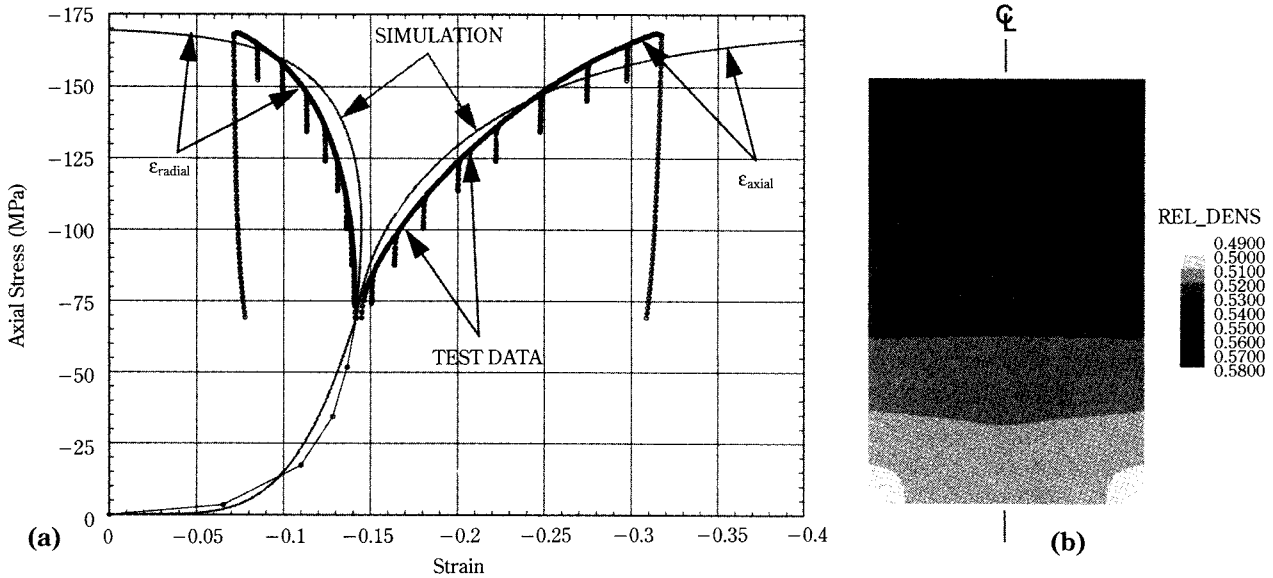

Fig. 3 (a) Comparison of Data from Confined (68.9 MPa) Triaxial Compression Test with a JAS3D Simulation (b) Fringe Plot of Computed Relative Density for the Uniaxially Compacted Cylinder in **Figure 1b.**

paction of the cylindrical specimen shown in **Figure 1b** was undertaken assuming a compaction ratio of about 1.9 (i.e., the powder fill height was 67 mm). This is more complicated because we have to account for the interaction of the powder with the die-wall. The contact interaction in JAS3D was modeled simply with Coulomb friction and the coefficient of friction between the die-wall and the powder was assumed to be 0.2, which is in the range of values measured for the interaction of ceramic powders with various die-wall materials. Because of symmetry and an assumption of uniformity in die-filling, only a wedge of the cylinder needed to be modeled with JAS3D. The fringe plot of computed relative density from this simulation is shown in **Figure 3b**. The computed relative density at the outer top of the compact is 0.56-0.57, while that at the outer bottom is 0.50-0.51. These predictions compare quite well with the respective measured values of 0.56 and 0.50 in **Figure 1b**. The spatial distribution of relative density, however, is somewhat different, particularly in the radial direction near the top and bottom of the cylinder. This may be attributable to several things, among them the manner in which the upper and lower boundaries were specified in the simulation. In the simulation, material was free to move radially but not axially relative to the vertically moving boundary at the top and the stationary boundary at the bottom. In the real pressing scenario, there are platens at the top and bottom that also interact with the powder and will induce shearing stresses. Furthermore, a uniform die-fill was assumed in the simulation that is undoubtedly not the case in the real part: this can be inferred by the presence of asymmetry in the density distribution relative to the axis of the cylinder in **Figure 1b**. Finally, the coefficient of friction between the die-wall and the powder may be different from the assumed value, or the frictional interaction may not be simple Coulomb friction.

Additional simulations have been performed on more complex geometry compacts to gain further confidence in the predictive capability of the overall model, and we have had a similar degree of success in predicting density distributions. Ultimately, however, the real test of the model's predictive capability will be at the hands of ceramic component manufacturers who must gain confidence in this tool by comparing code predictions with measured data from a wide range of production parts.

Specialized software

The resulting tool above can be used to predict forming stresses, density gradients, and material flow to investigate the effects of compact geometry; compaction ratio; pressing conditions (single, dual, hydrostatic pressing); die-wall friction coefficient; and die design (tapers, corner radii, etc.). As such, it constitutes part of the general underlying software, that we will refer to as the Sandia FE "toolkit" that is available to model even the most complicated 3D ceramic compacts envisioned. Effective use the software at this level, however, requires significant FE modeling expertise, insight into the underlying mechanics of the compaction process, and experience in using the cap-plasticity constitutive model and the JAS3D code. Furthermore, constructing the FE mesh that is part of the required input to JAS3D as well as visualizing results from the database output from JAS3D depends on several additional pre- and post-processing tools from the toolkit.

These significant requirements and potential impediments for using the underlying software, by the typical engineer on the production floor, called for a more user-friendly tool than the general-purpose capability described. To achieve this goal, it became essential to limit the scope of the class of problems to be handled by the software without being overly restrictive. The flexibility to model simple and complex geometry dies was achieved by developing higher-level specialized software to wrap around the general toolkit to address geometry variability within the axisymmetric subclass of compacts that are quite common in the industry.

This was accomplished by allowing multiple concentric cylinders to be stacked axially, as depicted schematically for three cylinders in **Figure 4**. The cylinders are interconnected using smaller transition radii that can be varied systematically. The individual cylinders, which can be solid or hollow, are allowed to have variable inner and outer diameters and heights. By linking the different size and shape cylinders axially, it is possible to model geometric features like counter-bores and bushing stems that are common in complex-geometry ceramic components fabricated by powder pressing. In addition to the geometric variables mentioned, the software also provides some capability to realistically vary the properties of the die and powder compact materials, as well as the loading applied to the compacts.

At the heart of the software we call "UNIPACK" is a top-level driver that queries the user, builds and

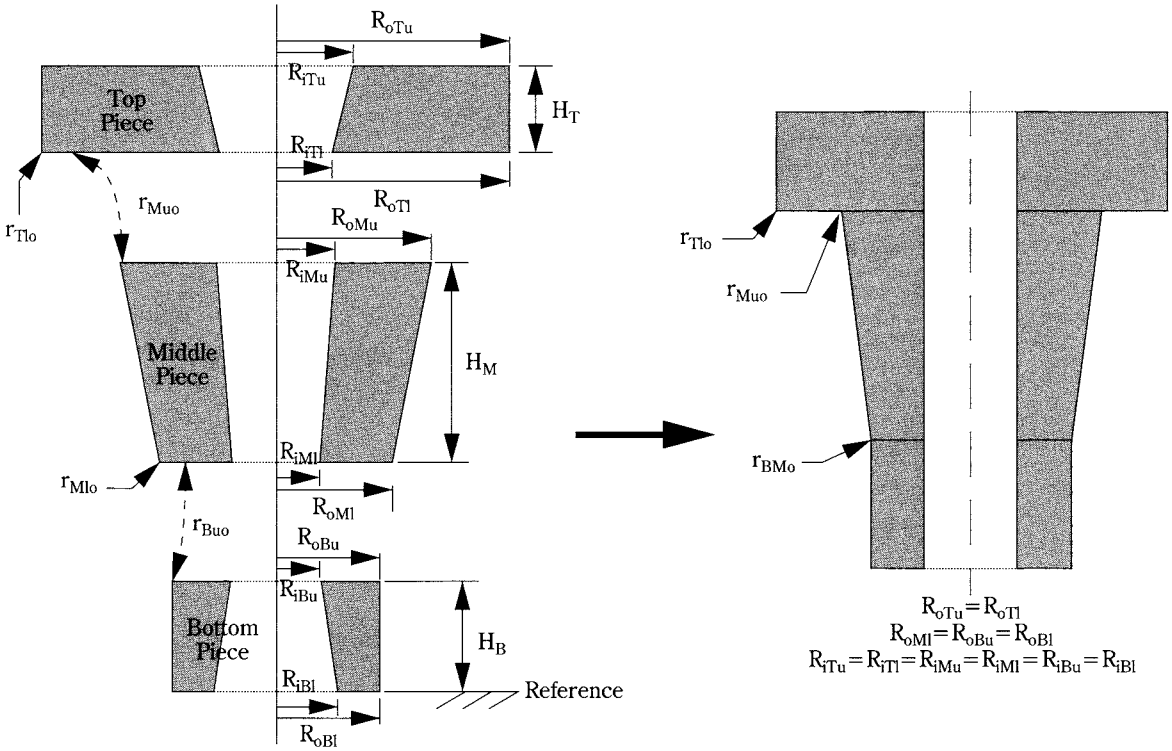

Fig. 4 Schematic of a Complex Part Built Up from Three Stacked Axisymmetric Pieces.

parses input parameter files, and wraps around Sandia's existing FE analysis toolkit to automatically perform a ceramic powder compaction analysis. In addition, there are key, pre-built files that contain the logic to generate the mesh for the compact in question from the input geometric quantities.

The overall flow of the specialized UNIPACK software package is depicted in **Figure 5**. There are three distinct phases that are automatically handled by the software:

- Geometry Definition Phase – Queries user for geometry information, builds user parameter files, and parses these files to the FE pre-processing tools to build the FE mesh for use in the analysis.
- Run Definition Phase – Queries user for parameters that define pressing conditions and type of material (specific powder) being pressed; builds a file of user parameters, and parses this file to a pre-processing tool to build an input deck for JAS3D.
- Solution & Post-processing Phase – Submits the FE analysis run; after the analysis finishes, it calls the FE post-processing tool to query the FE results database and generates a postscript file of select results; it then launches a postscript viewer to display this file to the user.

Thus, the expertise required to build the input deck, run the FE analysis code, and post-process the results resides in the specialized package. The user simply responds to a series of prompts, evaluates the quality of the FE mesh that is generated automatically, and analyzes the graphical results generated from the simulation. **Figure 6** shows a two-piece part simulated with the specialized software. **Figure 6a** is a schematic of the problem, showing that very few parameters are needed by the software to perform the simulation (ten radii, two heights, etc.). **Figure 6b** is an actual postscript image of results from the simulation that is presented to the user at the end of the simulation. In this case, it is a fringe plot of relative density; i.e., relative to the starting density. This relatively small simulation takes about 30 minutes of CPU time to run under the Linux OS on a 450 MHz Pentium III PC.

This specialized software tool allows users with little or no FE expertise to benefit from the tremendous power and insight that FE analysis can bring to the design cycle. Furthermore, as the user develops expertise in modeling the powder compaction process with the specialized software package, the more general underlying software is available to him to allow modeling of more complicated geometries and processes.

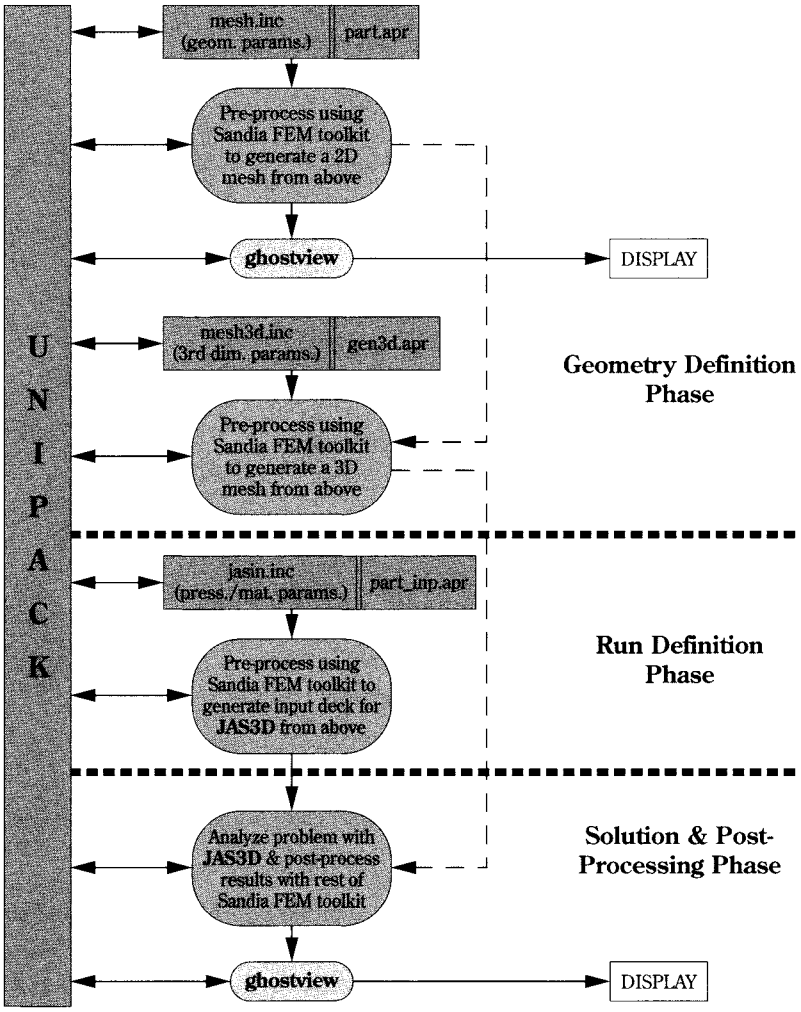

Fig. 5 Flow Diagram Depicting How Unipack Drives and Wraps Around Existing Tools from the Sandia Finite Element Toolkit.

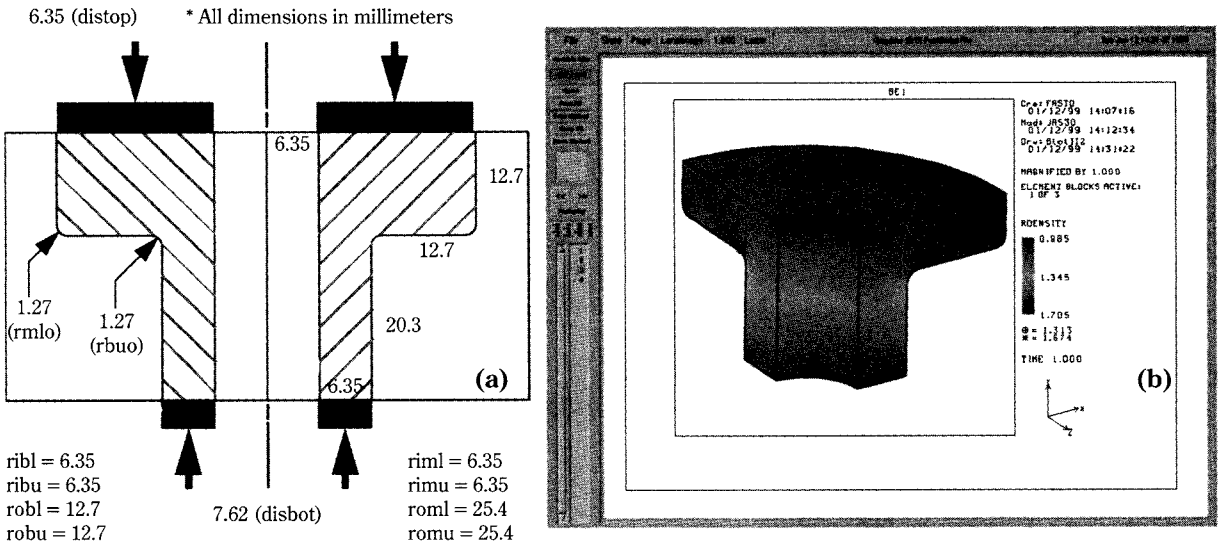

Fig. 6 Sample Two-Piece Compact Simulated with Specialized Software (a) Parameters Needed by Package (b) Postscript Image of Density Fringe Plot from the Simulation.

Summary and conclusions

A cap-plasticity constitutive model, originally developed to predict the geomechanical response of soils, has been adapted to simulate the compaction of ceramic powders. The parameters for the constitutive model are obtained from an extensive suite of hydrostatic and triaxial compression "soils-like" laboratory tests on specific ceramic powders. The constitutive model has been implemented in a finite element program for simulating the quasistatic, nonlinear, large deformation, inelastic response of solids. The overall tool has been used to predict and investigate the response of different powder compacts to various die-design details and parameters and pressing conditions. Thus the overall model has been at least qualitatively validated for ceramic powder compaction, and additional efforts are underway to further exercise and obtain increased confidence in its predictive capability.

Recent efforts have focused on developing a "user-friendly" powder compaction "package" in which the "expertise" required to perform the highly nonlinear analyses on a subclass of axisymmetric "complex" parts is embedded within the system and invisible to the user. A "test-of-concept" version of the software package for die-pressed compacts, running under Linux on a PC, has been demonstrated and was released to our industrial partners. In turn, they will exercise the specialized software; compare its predictive capability to production parts; and suggest improvements for the package. Generalization of the specialized software to include biaxial-pressing and bag-pressing is also currently underway.

Acknowledgments

The authors thank Mark Grazier of Sandia National Laboratories for completing the hydrostatic and triaxial compression tests on the alumina powder, Donald Ellerby and C. M. Stone of Sandia National Laboratories for providing a critical review of this manuscript, and the members of AACCMCI, Inc. for their assistance with testing and validating the compaction model. This work was funded by the US Department of Energy under contract No. DE-AC04-94AL85000. Sandia is a multiprogram Laboratory operated by Sandia Corporation, a Lockheed Martin Company.

References

1) Aydin, I., B. J. Briscoe, and K. Y. Sanliturk, "The Internal Form of Compacted Ceramic Components: A Comparison of a Finite Element Modelling with Experiment," *Powder Technology*, 89:239-254, 1996.
2) Coube, O., *Modelling and Numerical Simulation of Powder Die Compaction with Consideration of Cracking*, Ph.D. Thesis, University Pierre et Marie Curie, Paris VI, 1998.
3) Sandler, I. and D. Rubin, "An Algorithm and a Modular Routine for the Cap Model," *Int. J. Numer. Anal. Methods Geomech.*, 3:173-186, 1979.
4) Blanford, M. L., *JAS3D – A Multi-Strategy Iterative Code for Solid Mechanics Analysis, User's Instructions, Release 1.6*, Internal Sandia Report, Sandia National Laboratories, Albq., NM, 1999.
5) Argüello, J. Guadalupe, C. M. Stone, and A. F. Fossum, "Progress on the Development of a Three-Dimensional Capability for Simulating Large-Scale Complex Geologic Processes," *Int. J. Rock Mech. Min. Sci.*, Vol. 35 4/5:469-470, Paper No. 083, 1998.
6) Fossum, A. F., P. E. Senseny, T. W. Pfeifle, and K. D. Mellegard, "Experimental Determination of Probability Distributions for Parameters of a Salem Limestone Cap Plasticity Model," *Mech. of Mat.*, 21:119-137, 1995.
7) Jaeger, J. C. and N. G. W. Cook, *Fundamentals of Rock Mechanics*, 3rd ed., Chapman and Hall, London, England, 1979.
8) Zeuch, D. H., J. M. Grazier, J. G. Argüello, and K. G. Ewsuk, "Measurement of the Mechanical Properties and Shear Failure Surfaces of Two Alumina Powders in Triaxial Compression," submitted to *J. Mat. Sci.*, 2000.
9) Crisfield, M. A., *Non-linear Finite Element Analysis of Solids and Structures (Vol. 1)*, John Wiley & Sons, Chichester, UK, 1991.
10) *Biffle, J. H., *JAC3D – A Three-Dimensional Finite Element Computer Program for the Nonlinear Quasistatic Response of Solids with the Conjugate Gradient Method*, SAND87-1305. Sandia National Laboratories, Albq., NM, 1993.
11) *Stone, C. M., *SANTOS – A Two-Dimensional Finite Element Program for the Quasistatic, Large Deformation, Inelastic Response of Solids*, SAND90-0543, Sandia National Laboratories, Albq., NM, 1997.

*Available from: National Technical Information Services
U. S. Department of Commerce
5285 Port Royal Rd.
Springfield, VA 22161

Author's short biography

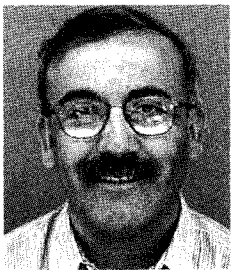

J. Guadalupe Argüello

J. Guadalupe Argüello is a principal member of the technical staff in the Solid Mechanics Engineering Department of Sandia National Laboratories in Albuquerque, New Mexico. He is responsible for computational mechanics R&D and support in the areas of Oil & Gas reservoir and basin-scale geomechanical behavior, nuclear waste repository behavior, and granular materials processing. His research interests include advanced computational mechanics, numerical methods, geomechanics, powder mechanics, nonlinear dynamics, soil/structure and fluid/structure interaction. He has held previous R&D and engineering positions in the Offshore Technology Section at Amoco Production Company in Tulsa, OK and with Jefferson Chemical Company, a Subsidiary of Texaco, in Port Neches, TX. He is a member of the American Ceramic Society and the Society of Petroleum Engineers. He holds a Bachelor of Science, a Master of Engineering, and a Ph.D. from Texas A&M University. Argüello can be reached at: Sandia National Laboratories, MS 0847, P.O. Box 5800, Albuquerque, NM 87185-0847, USA; phone 505-844-1482; fax 505-844-9297; e-mail jgargue@sandia.gov.

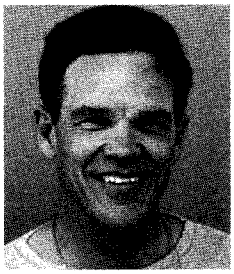

Arlo F. Fossum

Arlo F. Fossum is a principal member of the technical staff in the Materials Mechanics Department at Sandia National Laboratories in Albuquerque, New Mexico. e-mail: affossu@sandia.gov. His interests include nonlinear constitutive law development, material parameter estimation for modern constitutive laws, and uncertainty modeling in large-scale structural analyses. He earned a Ph.D. degree in Solid Mechanics from Brown University.

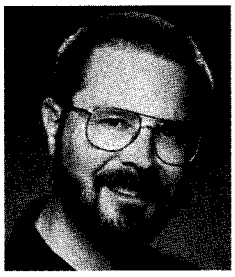

David Zeuch

David Zeuch received his Ph.D. in Geology from the University of California at Davis. For his dissertation, he used transmission electron microscopy to characterize the creep mechanisms of upper mantle rocks that he had experimentally deformed at high temperatures and confining pressures. Subsequently, he joined Cornell University as a postdoctoral associate in the Department of Materials Science and Engineering, investigating the effects of superimposed confining pressures on deformation mechanisms of glass-ceramics. In 1980 he joined the Geomechanics Research Department at Sandia National Laboratories where he is now a Principal Member of the Technical Staff. Over most of the past twenty years, he has experimentally investigated the deformation processes of materials ranging from geomaterials such as rock salt and oil shale to engineering materials like lead-zirconate-titanate ceramic (PZT 95/5-2Nb) and ceramic powder-binder systems used in sintering. Dr. Zeuch is author or coauthor on twenty-two peer-reviewed articles in the geomechanics and materials science literature.

Author's short biography

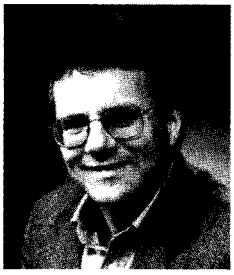

Kevin G. Ewsuk

Kevin G. Ewsuk is a Principal Member of the Technical Staff in the Ceramic Materials Department (1843) of Sandia National Laboratories in New Mexico, where he is responsible for ceramic powder characterization and processing R&D, including modeling ceramic processing. He has worked on advanced composite processing and characterization, powder and powder compact characterization, and characterizing and modeling powder compaction and sintering. Before joining Sandia, he was a technical staff member of the Central Research and Development Department of E. I du Pont de Nemours and Co, Inc. in the Corporate Ceramics Program. He received his Ph.D. and M. S. degrees in Ceramic Science from the Pennsylvania State University. He currently leads a major R&D effort to characterize and model ceramic powder sintering at Sandia. He spearheaded a successful Cooperative Research & Development Agreement (CRADA) with industrial partners, focused on powder compaction, that developed and applied computer modeling and advanced characterization technology to aid ceramic component design and manufacturing. His interests are in: materials engineering, research, and development of glass, ceramic, and composite materials/systems; materials processing, including powder synthesis, fabrication, and densification (compaction and sintering); characterizing and modeling processing and materials composition-microstructure-property relationships; and composite and composite system design and development. He has over 170 technical presentations and over 60 technical publications, including an invited contribution on "Ceramics (Processing)" in the Kirk-Othmer Encyclopedia of Chemical Technology, Fourth Ed., Vol. 5. He was the Guest Editor of the December 1997 MRS Bulletin (Vol. 22 No. 12) on Compaction Science and Technology. Kevin can be reached at Sandia National Laboratories, MS 1349, 1001 University Boulevard, SE, Albuquerque, NM; phone (505) 272-7620; FAX (505) 272-7304; email kgewsuk@sandia.gov.

On the sensitivity of the maximum explosion pressure of a dust deflagration to turbulence†

A.E. Dahoe[1,2,4], K. van der Nat[1], M. Braithwaite[3] and B. Scarlett[1]

[1] *Department of Chemical Engineering, Delft University of Technology*

[2] *Department of Engineering, University of Cambridge*

[3] *Royal Military College of Science, Cranfield University*

[4] *University of Cambridge, Department of Engineering*

Abstract

The maximum explosion pressure of a deflagration is often regarded as a thermodynamic quantity and it is believed to be insensitive to the flow conditions of the combustible mixture involved. While this is true for premixed gases, the present work demonstrates that the opposite is the case when powder-air mixtures are ignited to deflagration. In order to illustrate this disparate behavior, experiments were conducted with methane-air and cornstarch-air mixtures of a fixed fuel to air ratio, at varying turbulence levels. The maximum explosion pressure of cornstarch-air mixtures was observed to increase by a factor of 1.5 when the turbulence level of the dust cloud was varied. An explanation for this behavior is proposed by considering the effect of turbulence on the liberation of volatile matter from the particles.

1 Introduction

The assessment of the severity of an accidental dust explosion is of crucial importance when it concerns the safe operation of industrial processes involving combustible particles. Due to the absence of a comprehensive description of the transient combustion behavior of any particular dust-air mixture under arbitrary conditions (pressure, temperature, flow properties), it is common practice to measure the explosion severity in laboratory test vessels (1 m^3-vessel, 20-liter sphere) and to predict what would happen if a similar mixture exploded in an industrial plant unit. A typical result of a laboratory explosion severity test is shown by **Figure 1**. The figure shows the behavior of the pressure in the explosion chamber when a combustible mixture is ignited to deflagration. At the beginning of the explosion the pressure is equal to the atmospheric pressure and increases up to a maximum value of about 7 bar. During this process the pressure increases progressively until the rate of pressure rise achieves a maximum, after which the pressure continues to increase with a progressively decreasing rate of pressure rise. For the assessment

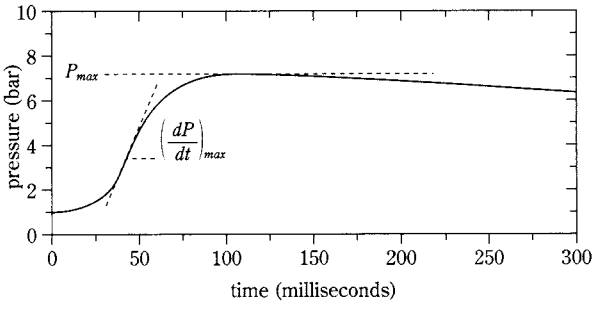

Fig. 1 Explosion curve of a 500 gm^{-3} cornstarch-air mixture in a standard 20-liter sphere.

[1] Delft, The Netherlands
[2] Cambridge, United Kingdom
[3] Shrivenham, Swindon, United Kingdom
[4] Trumpington Street, CB2 1PZ, Cambridge, United Kingdom
Telephone: +44-1223-332603. FAX: +44-1223-332662.
Email: aed23@eng.cam.ac.uk

† Accepted: September 17, 2001

of the severity of a dust explosion, two quantities are extracted from the explosion curve, namely, the maximum explosion pressure, P_{max}, and the maximum rate of pressure rise, $(dP/dt)_{max}$. The reasons for choosing these quantities to characterize dust explosion severity are evident: the maximum explosion pressure gives an indication of the magnitude of the damaging pressures that may be caused by accidental deflagrations and the maximum rate of pressure rise indicates how fast these damaging pressures can develop.

From a practical point of view, the maximum explosion pressure can be used to determine the design strength of industrial equipment so that it can withstand damaging explosion pressures. The maximum rate of pressure rise can be used to size pressure relief systems to counteract the development of damaging pressures so that they do not exceed a particular design strength. Since the containment of explosion pressures requires equipment to be capable of withstanding pressures of up to 7−10 times the operating pressure, this approach is financially prohibitive and therefore applied to small industrial equipment only. Whilst explosion relief venting is the most commonly used protection method against explosion hazards because of its convenience and economical attractiveness, there are circumstances where it may not be applied. Such circumstances are those where the siting is such that spreading of burning material to other plant units may occur, or where highly toxic combustibles and combustion products will be released in the environment, or that the internal geometry of the industrial equipment is such that a transition from deflagration to detonation will occur due to the enhancement of turbulence in the presence of a vent relief area. When this is the case, containment becomes an important safety measure and accurate determination of the maximum explosion pressure becomes of great importance.

Knowing that the rule of the thumb in the case of containment is to design industrial equipment at a strength which is such that it can withstand at least 1.5 times the expected explosion pressure, the importance of accurate knowledge of the maximum explosion pressure becomes even greater when industrial processes are carried out at elevated pressures. For example, when the maximum explosion pressure is known with an inaccuracy of 10%, and the ratio between the maximum explosion pressure and the initial pressure is assumed to be 10, then this inaccuracy would result in an error margin of 3 bar in the design strength of the equipment. In other words, if the expected maximum explosion pressure is expected to be 10 bar, it can be anywhere between 9 and 11 bar, and when this is multiplied by a factor of 1.5 then one finds a design strength which is anywhere between 13.5 and 16.5 bar. When the industrial operating conditions are such that an explosion may occur at an initial pressure of 10 bar then one finds a design strength between 135 and 165 bar along the same lines of reasoning; a difference of 30 bar. It is therefore not only important to know the maximum explosion pressure of a combustible mixture with great accuracy, but it also important to know which factors influence this quantity, and, to which extent these factors may affect the maximum explosion pressure.

When a fuel-air mixture burns adiabatically in a closed vessel, with the additional assumptions that kinetic and potential energy changes are negligible and that there is no shaft work, the first law of thermodynamics requires that the internal energy of the reactants at the initial state equals the internal energy of the products at the final state. In the final state, the entire vessel is filled with combustion products whose temperature is equal to the constant volume adiabatic flame temperature, T_f^{ad}, and the pressure is at its maximum attainable value, P_{max}. This final state is independent of the path followed from the initial state and the ideal gas law may be used to express it as

$$P_{max} = \frac{n_e}{n_0} \frac{T_f^{ad}}{T_0} P_0, \tag{1}$$

where P_0 denotes the initial pressure, T_0 the initial temperature, n_0 the moles of gas present before the explosion, and n_e the moles of gas present after the explosion. This equation implies that the maximum explosion pressure is determined by the initial state of the reactant mixture (T_0, P_0), variations in the number of moles of gas due to the chemical conversion process and the value of the adiabatic flame temperature due to the release of chemical energy by the reactants. Since both n_e/n_0 and T_f^{ad} are determined by chemical equilibria and caloric properties of the species involved (e.g. heats of formation, specific heats), the maximum explosion pressure is regarded as a thermodynamic property of the reactant mixture. And, owing to the fact that kinetic energy changes are negligible with respect to the heat release by the reactants, the maximum explosion pressure is considered to be insensitive to the flow conditions of the reactant mixture. While this expectation is confirmed by experiments with gaseous fuel-air mixtures (see **Figure 2**), the opposite appears to be true for dust-air mixtures (see **Figure 3**).

Leuckel *et al.* [1] ignited turbulent stoichiometric

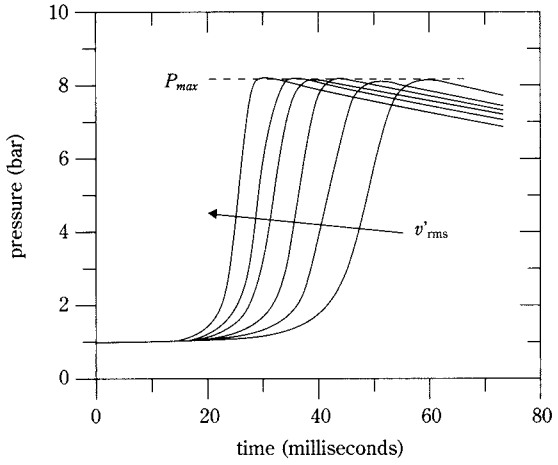

Fig. 2 Explosion curves of stoichiometric methane-air mixtures ignited at various turbulence levels: v'_{rms}=2.40 ms^{-1}, 1.92 ms^{-1}, 1.44 ms^{-1}, 1.20 ms^{-1}, 0.96 ms^{-1}, and 0.72 ms^{-1} [1].

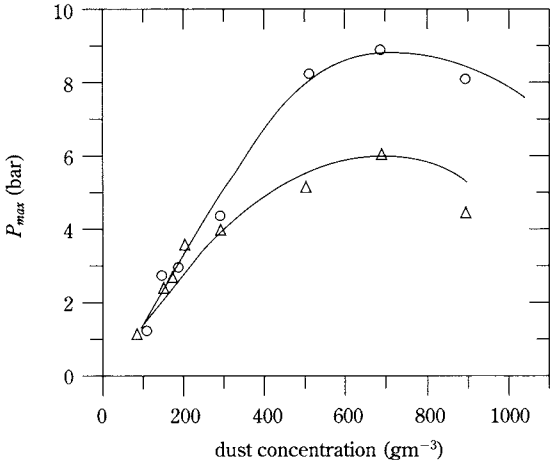

Fig. 3 The maximum explosion pressure of cornstarch-air mixtures ignited at two different turbulence levels: v'_{rms}=4.2 ms^{-1} (○) and v'_{rms}=1.5 ms^{-1} (△) [2].

methane-air mixtures to deflagration in a 65-liter fan-stirred spherical bomb and the resulting pressure-time curves are shown in **Figure 2**. The turbulence level of the reactive mixtures was varied by means of four symmetrically opposed ventilation fans and ranged from $v'_{rms} = 0.72$ ms^{-1} to $v'_{rms} = 2.40$ ms^{-1}. In all cases, an increase of the turbulence level resulted in a faster explosion, while the maximum explosion pressure remained at a constant value of about 8.2 bar.

Kauffman *et al.* [2] used a 950-liter jet-stirred spherical bomb to measure the explosion characteristics of turbulent cornstarch-air mixtures. Experiments were conducted at two different turbulence levels, namely, $v'_{rms} = 1.5$ ms^{-1} and $v'_{rms} = 4.2$ ms^{-1}, while the dust concentration was varied between 100 and 900 gm^{-3}. Conditions of turbulence were established by flushing the sphere continuously with air through a manifold of six inlet ports, located in the lower hemispherical wall, and a manifold of eight exhaust ports, located in the upper hemispherical wall. The dust was supplied continuously by means of a dust feeder with an adjustable feed rate so that the dust concentration and the turbulence level could be varied independently. These researchers found that, unlike in the case of gaseous fuel-air mixtures, the maximum explosion pressure of dust-air mixtures was sensitive to the turbulence level. Their findings are plotted in **Figure 3** and it is seen that the sensitivity of the maximum explosion pressure to turbulence increases with increasing dust concentration. When the dust concentration is below 200 gm^{-3}, turbulence seems to have little to no effect. At the optimum concentration of about 700 gm^{-3} the maximum explosion pressure increases by a factor of 1.5 when the turbulence level is increased by a factor of about 3. At a dust concentration 900 gm^{-3}, the maximum explosion pressure was found to increase by a factor of 1.8 when the turbulence level was changed from $v'_{rms} = 1.5$ ms^{-1} to $v'_{rms} = 4.2$ ms^{-1}. This sensitivity of the maximum explosion pressure of dust-air mixtures to the turbulence level may result in serious shortcomings in the current practice of applying laboratory explosion severity data to industrial circumstances, as will be discussed below.

Taking the observed sensitivity of the maximum explosion pressure of dust-air mixtures to turbulence into consideration, it is evident that laboratory test data are only applicable to industrial circumstances when the laboratory test conditions are such that the turbulence levels are higher than those which may be encountered in industrial equipment under both normal operating conditions as well as during the occurrence of an accidental explosion. Currently accepted technical guidelines for protection methods against dust explosion hazards [3, 4] prescribe the use of the so called standard 20-liter explosion sphere and the 1 m^3-explosion vessel as laboratory test devices for dust explosion severity testing. Unlike the test methods used by Leuckel *et al.* and Kauffman *et al.*, which maintain quasi-steady conditions of turbulence at the moment of ignition, these devices generate turbulence by means of an air blast. This air blast is necessary to suspend the dust and to ensure that the dust particles remain airborne in the explosion chamber and that they do not settle out due to gravity. How-

ever, as soon as the air blast is completed, the intensity of the turbulence decreases with time. Test procedures therefore stipulate precise time values at which certain operations must occur. In the 1 m^3-vessel, for example, ignition must occur at 600 milliseconds after the injection air blast has started (i.e. ignition delay time = 600 milliseconds), while in the 20-liter cell, ignition must occur after an ignition delay time of 60 milliseconds. The use of these ignition delay times was based on the belief that by adhering to the specified procedure, unknown, but reproducible turbulence levels could be established at the moment of ignition. It was furthermore assumed that when the air blast was vigorous enough, the turbulence level at the moment of ignition would supersede those which may be encountered under industrial operating conditions. With the standard 20-liter explosion sphere, for example, the explosion chamber is partially evacuated to a pressure 0.4 bar and compressed air at a pressure of 21 bar is injected into it so that a turbulent flow field at conditions of atmospheric pressure and room temperature exists at the moment of ignition.

This conservative approach, which was initially adopted because the maximum rate of pressure rise was generally known to increase with increasing turbulence, is obviously not the most optimal design basis for explosion protection methods. It may lead to unacceptable over-estimations of the required design strength of plant units in situations where turbulence levels are much lower than those created in laboratory test vessels. It may also lead to dangerous underestimations of the required design strength under circumstances where additional turbulence is generated by the explosion itself. These shortcomings are not only due to the application of laboratory test data, obtained under conditions of unknown turbulence, to industrial situations where the turbulence levels are unknown. Even if the conditions of turbulence in the laboratory tests vessels and in the industrial equipment would be known quantitatively, there appears to be a lack of quantitative relationships between the maximum explosion pressure and turbulence. Hence it is the purpose of this work to investigate the sensitivity of the maximum explosion pressure to turbulence.

In the present work methane and cornstarch were used as test fuels because of their use by previous researchers, and the constant composition and narrow size distribution of the latter. In order to verify the observations of previous researchers, namely, that the maximum explosion pressure of a gaseous fuel is insensitive to turbulence while that of a particulate solid fuel is a function of turbulence, experiments were done by igniting both methane-air mixtures and cornstarch-air mixtures to deflagration at various turbulence levels. The experiments were performed by means of a standard 20-liter sphere since it is the recommended laboratory test equipment, prescribed by the technical guidelines for dust explosion severity testing [3, 4].

2 Experimental

The experiments reported in this work were conducted by means of the standard 20-liter sphere, shown in **Figure 4**. In essence the equipment consists of three major components, namely, an explosion chamber, a storage canister and an injection valve.

The explosion chamber is a hollow sphere made of stainless steel, with a volume of 20-liters, and is surrounded by a cooling jacket, which allows the circulation of a cooling liquid. It is designed to house a removable top cover, a port for evacuation and admission of gases, an outlet port for combustion products, two flanges so that sensors can be placed, and a port to allow the inflow of compressed air and to hold a dust dispersion device. The top cover contains the holes for introducing the electrodes for the ignition system. With these electrodes it is possible to ignite the combustible mixtures by means of a spark or a chemical igniter at the center of the sphere with an inaccuracy of only a few millimeters. In order to measure the pressure two piezo-electric pressure sensors were installed in one of the flanges mounted in the wall of the explosion chamber. A temperature-controlled heat transfer fluid was circulated through the cooling jacket so that the combustible mixtures investigated were at an initial temperature of 20°C in all experiments.

The storage canister has a volume of 0.6 liter and is connected to the explosion chamber by means of a duct which can be opened and closed very quickly by means of a pneumatically driven injection valve. The dust must be placed in the storage canister and be dispersed via the duct which leads to the explosion chamber, with a dispersion device attached to the outflow end of the duct. The dispersion device used in this work is the so called rebound nozzle.

As mentioned in the Introduction, according to the guidelines for dust explosion severity testing, the explosion chamber must be partially evacuated to 0.4 bar and the storage canister has to be filled with pressurized air of 21 bar, prior to dispersing the dust. This

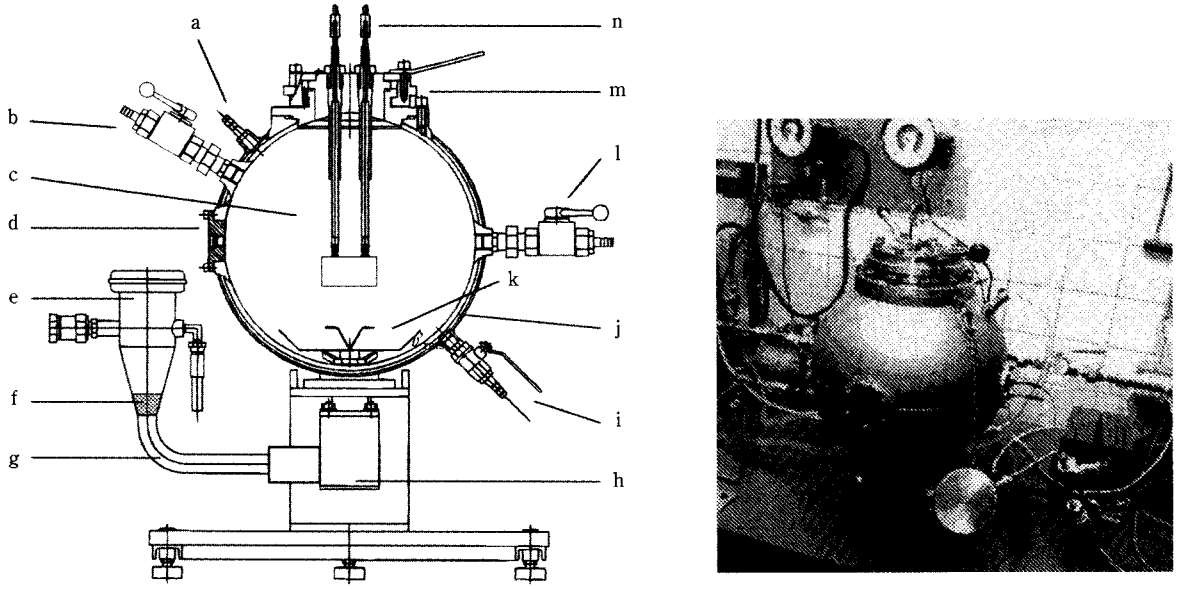

(a) inlet for cooling fluid (b) port to evacuate the explosion chamber or to admit gases (c) explosion chamber (d) flange which holds pressure sensors (e) storage canister (f) powder (g) duct which connects the storage canister to the explosion chamber (h) injection valve (i) outlet for cooling fluid (j) cooling jacket (k) rebound nozzle (l) outlet valve for combustion products (m) removable top cover (n) electrode

Fig. 4 A schematic overview of the standard 20-liter sphere (left) and a photograph of the equipment (right).

pressure difference between the storage canister and the explosion chamber forms the driving force of the air blast which disperses the dust into the explosion chamber. When the injection valve is opened, the compressed air within the storage canister develops an expansion flow, which drags the dust particles into the explosion chamber. Turbulence is generated by friction with the wall of the duct and the dispersion device, and this process continues until the pressure in the storage canister and the explosion chamber have become equal. When this occurs there is no longer a driving force present which leads to the generation of additional turbulence and the existing turbulence level starts to decay. In case of the standard 20-liter sphere, standardized guidelines prescribe a precise time value for ignition to occur during this turbulence decay process, namely, at 60 milliseconds after the very beginning of the injection process. In the present work this so called ignition delay time was varied so that combustible mixtures were ignited at various turbulence levels.

The turbulent cornstarch-air mixtures were generated according the procedure described above and ignited to deflagration at various ignition delay times. The turbulent methane-air mixtures were also created following this procedure by injecting compressed air into the explosion chamber containing a pre-mixture of methane and air of such a composition that a stoichiometric methane-air mixture would be present after completion of the injection process. The methane-air mixtures were ignited by means of a spark and the cornstarch-air mixtures were ignited by means of a chemical igniter with an energy of 180 J. The measured pressure-time curves of the mixtures investigated are shown in **Figures 5** and **6**.

The behavior of the turbulence characteristics of the transient flow field generated by the injection process were also investigated [5]. Since a detailed account of this investigation falls beyond the scope of this paper, only the results and conclusions relevant to this work are presented here. The transient flow field during and after the injection process, without

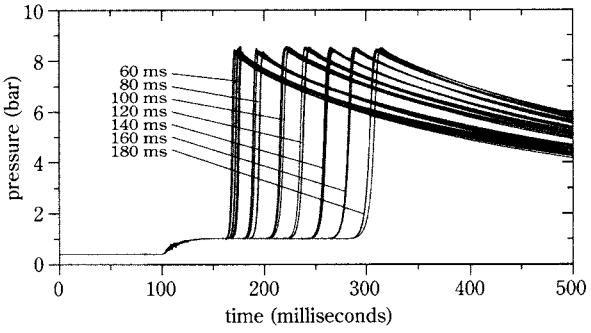

Fig. 5 Pressure-time traces of turbulent stoichiometric methane-air mixtures ignited at different ignition delay times.

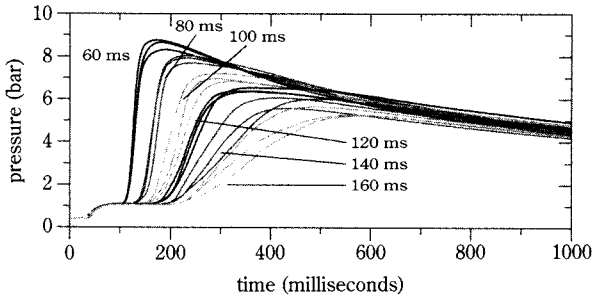

Fig. 6 Pressure-time traces of 625 gm^{-3} cornstarch-air dust explosions ignited at different ignition delay times.

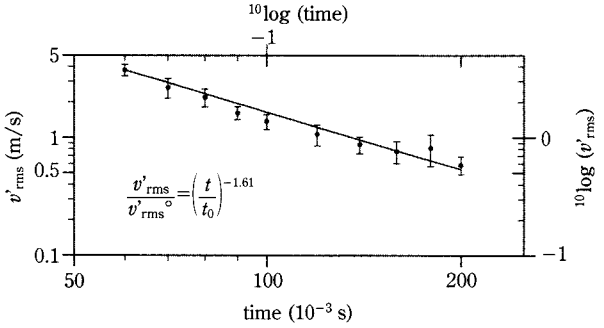

Fig. 7 Decay of the root-mean-square velocity in the 20-liter sphere with the rebound nozzle.
$t_0 = 60$ ms and $v'^{\circ}_{rms} = 3.75$ ms^{-1}.

dust, was investigated by means of laser Doppler anemometry. Two instantaneous velocity components were measured simultaneously in order to quantify the turbulence characteristics of the flow field as a function of time. From this information the root-mean square value of the velocity fluctuations, v'_{rms}, and the turbulence macro length scale, ℓ_t, could be determined. The spatial homogeneity of the turbulence was investigated by performing measurements at various locations in the explosion chamber. Directional isotropy of the turbulence was investigated by comparing the root-mean-square values of the velocity fluctuations measured simultaneously in two independent directions. This research showed that conditions of spatially homogeneous and directionally isotropic turbulence exist in the explosion chamber, after an initial period of about 40 milliseconds with inhomogeneous and non-isotropic turbulence present. The value of the root-mean-square of the velocity fluctuations and the length scale of the turbulence macro structure as a function of the time are respectively shown in **Figures 7** and **8**. It appeared to be possible to correlate the temporal behavior of these quantities by means of the decay-law expressions presented in these figures.

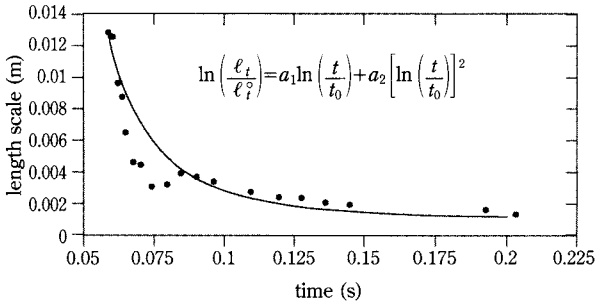

Fig. 8 The behavior of the length scales of the macro structure in the period of 60 to 200 milliseconds.
$\ell_t^{\circ} = 12.845 \cdot 10^{-3}$ m, $a_1 = -3.542$, $a_2 = 1.321$ and $t_0 = 58.8 \cdot 10^{-3}$ s.

Knowing that a 20-liter sphere at a pressure of 1 bar contains about 21 grams of air, while explosion severity testing involves dust loadings ranging from 2.5 to 25.0 grams, one may reasonably ask whether the decay of turbulence of a dust cloud will deviate significantly from the behavior shown in **Figures 7** and **8**. To shed some light on this issue injection experiments were conducted with different loadings of cornstarch dust [5]. For safety reasons nitrogen was used instead of air. The results of this investigation are shown in **Figures 9** to **11**. The pressure curves in the first two figures indicate that the presence of dusts at the bottom of the storage canister has a

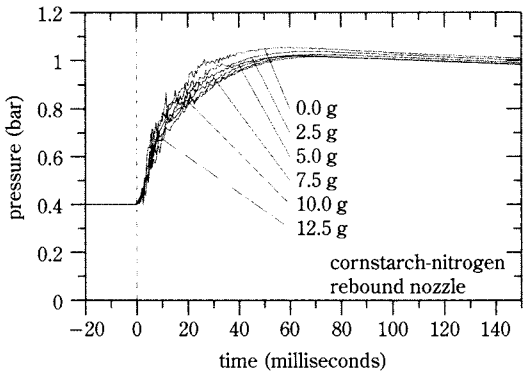

Fig. 9 Behavior of the pressure in the explosion chamber during the injection of various quantities of dust.

systematic effect on the behavior of the pressure, namely, that increasing amounts of dust tend to decrease the curvature of the pressure curves during the injection process. In order to get an impression of what this means for the turbulence conditions in the explosion chamber, it was attempted to measure the vertical velocity component at the center and to de-

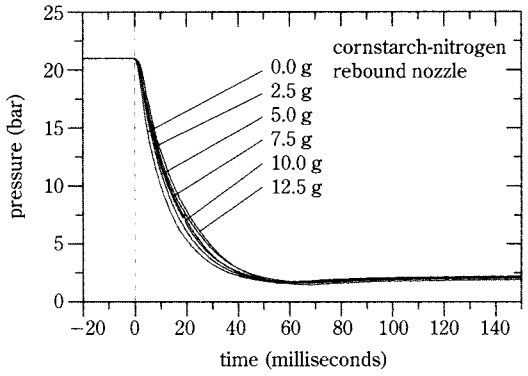

Fig. 10 Behavior of the pressure in the storage canister during the injection of various quantities of dust.

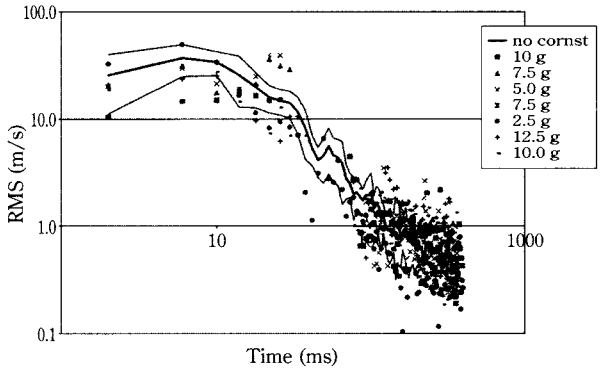

Fig. 11 Root-mean-square values of the vertical velocity component during the injection of cornstarch dust.

termine the root-mean-square value of the velocity fluctuations as a function of time. Although these measurements were conducted under conditions that are beyond the range of applicability of laser Doppler anemometry, the authors believe that these measurements may give a qualitative idea of the effect of the particulate phase on the gas phase fluctuations. As in the case of the gas injection experiments discussed previously, small particles, capable of following the gas phase fluctuations, were added to the flow field and the settings of the laser Doppler anemometer were optimized so that the signals arising from the larger, and hence slower, cornstarch particles would be rejected. The results obtained with various cornstarch dust loadings are presented in **Figure 11**. The thick line in this figure shows the behavior of the root-mean-square value of the velocity fluctuations generated by the injection of nitrogen only. The thin lines indicate the deviation from the thick line when different amounts of cornstarch dust are being injected. From these results it is concluded that the turbulent fluctuations of the gas phase behave more or less independently of the presence of a solid phase (apart from the larger scatter in the presence of cornstarch dust) and that the decay law expressions discussed previously may be used as an approximation for their behavior.

It is worth noting that this observation is consistent with the implication of the Hinze-Tchen equation [6]. This equation states that the turbulent kinetic energy per mass unit of the particulate phase, k_p, relates to that of the gas phase, k, as

$$\frac{k_p}{k} = \left[1 + \frac{\tau_p}{2\tau_t}\right]^{-2}, \tag{2}$$

where τ_t denotes the time scale of the turbulent fluctuations and τ_p denotes the response time of a particle to a change in the velocity or the magnitude of the gas velocity. Since the response time of the cornstarch particles is much larger than the time scale of the gas-phase fluctuations, the particles pick up little kinetic energy from the gas phase. Owing to the larger response time of the particles, the local velocity of the gas phase will have changed its direction many times before the particles can pick up a significant amount of momentum in one preferential direction.

3 Effect of turbulence on the maximum explosion pressure of dust-air mixtures

The pressure-time curves shown by **Figures 5** and **6** indicate that the maximum explosion pressure of methane-air mixtures is insensitive to turbulence (it remains at a constant value of about 8.4 bar) while that of cornstarch-air mixtures appears to be a function of turbulence. This result is consistent with the observation made by other researchers, as mentioned in the Introduction. According to **Figure 13**, the maximum explosion pressure of the investigated cornstarch-air mixtures increases from 5.3 bar to 8.5 bar when the turbulence level is increased from 0.75 ms^{-1} to 3.75 ms^{-1}. In other words, the maximum explosion pressure increases by a factor of 1.6 when the turbulence level increases by a factor of about five. This change is less drastic than that observed with the equipment used by Kauffman *et al.* [2], namely, an increase of the maximum explosion pressure by a factor of 1.5 when the turbulence intensity is increased by a factor of about three. This difference may be attributed to the existence of turbulence with a different length scale in the equipment used by Kauffman *et al.*

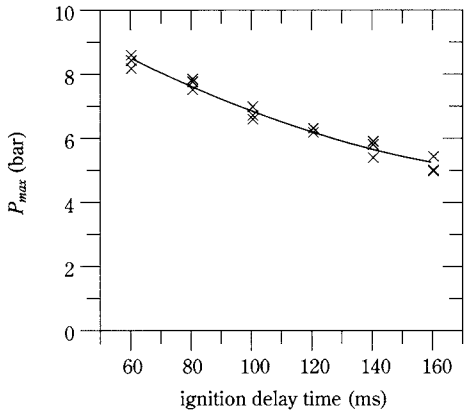

Fig. 12 The maximum explosion pressure of cornstarch-air mixtures ignited at various turbulence levels (data are taken from **Figure 6**).

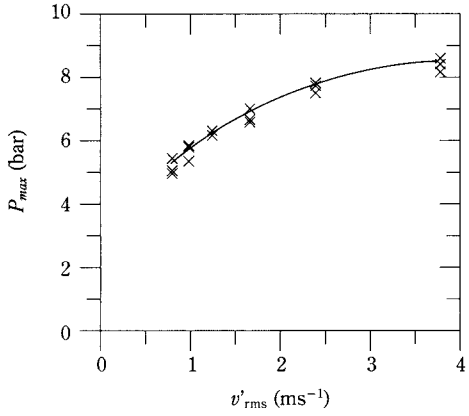

Fig. 13 The maximum explosion pressure of cornstarch-air mixtures as a function of the turbulence level at the moment of ignition. This figure is essentially the same as **Figure 12** with the horizontal axis rescaled according to the correlation presented in **Figure 7**.

In our work, as well as in the work of Kauffman *et al.*, the maximum explosion pressure was observed to increase with more than 3 bar when turbulence was varied. Since this is a significant difference when it concerns the assessment of the design strength of industrial equipment, and since laboratory test data are being applied to industrial circumstances where the conditions of turbulence are different from those existing in laboratory test vessels, it is of great importance to know why and how turbulence affects the maximum explosion pressure.

It was mentioned in the Introduction that the maximum explosion pressure of premixed gases of fuel and air may be regarded as a thermodynamic property which is a function of the initial pressure, the initial temperature, and the chemical composition only. It is insensitive to flow conditions because the kinetic energy of the fluid motions is negligible in comparison with the heat effects associated with the combustion reactions, and flow conditions do not affect the chemical composition of the reactant mixture which is consumed by the flame. In the case of dust-air mixtures, turbulence does have an effect on the maximum explosion pressure because it affects the liberation of volatile components from the particles, as will be discussed below.

When a combustible mixture is ignited to deflagration in a spherical enclosure, an initially spherical flame is created which propagates radially into the surrounding reactant mixture. During this flame propagation process reactants enter the flame at the downstream side in order to be burned in the flame zone, and expanding hot combustion products are left behind in the wake of the flame. Prior to entering the flame these reactants are being heated at the downstream side. In case of a gaseous fuel-air mixture the chemical composition is established down to the molecular scale and the partial pressures of the reactant gases that compose it remains the same during this heating process. In the case of a dust-air mixture, which may be regarded as a homogeneous mixture of fuel and oxidizer on a macroscopic scale, the heat released by the flame affects the chemical composition of the reactants that are actually being consumed. As the particle temperature increases in the preheat zone of the flame, volatile components begin to be emitted and mix with the surrounding oxidizer. This leads to the formation of a primary reaction zone which is largely sustained by gaseous combustion [7]. The emission of volatile components and the mixing process continues into the reaction zone and is largely completed before the end of the reaction zone. Hence, in comparison with premixed gases, the flame temperature of a dust cloud additionally depends on the rate of evolution of volatile components, and the residence time of the particles in the preheat zone and the flame zone.

With lignites, bituminous coals, vegetable grains and powdered foodstuffs, remaining char burns in the hot oxygen beyond the preheat zone. Particles of less than 1 μm can be oxidized entirely in the primary reaction zone and the effect of the chemical heat release of the oxidation of these particles on the flame temperature is additive to that of the volatile species. For particle sizes greater than 10 μm, the oxidation of char in the primary reaction zone is slow in compari-

son with the gaseous combustion process. In this case the oxidation of char within the primary reaction zone hardly affects the flame temperature. Since the cornstarch particles used in this work have a narrow size distribution with a modal diameter of 15 μm, the combustion of char will not be considered here.

The liberation of volatiles can be considered by means of a simplified analysis of particle devolatilization with the following assumptions:

- The particle is surrounded by a infinite quiescent medium with a constant temperature, denoted by T_g.
- The particle has a uniform temperature, and the heat resistance is located at the gas side of the interface between the particle and the medium that surrounds it.
- The devolatilization process is steady, and all physical properties, such as the density, thermal conductivity and specific heat, are constant.
- During the devolatilization process, the particle has a constant devolatilization temperature, denoted by T_d.

The objective of this analysis is to find a relationship between the volatile production rate, $\dot{m}$, and the temperature to which the particles are being exposed. This is done by means of a gas-phase energy and a surface energy balance [8]. In spherical coordinates, the gas phase-energy balance reads,

$$\frac{d}{dr}\left(4\pi\lambda_g r_p \frac{dT}{dr}\right)-\dot{m}\hat{C}_{Pg}\frac{dT}{dr}=0 \tag{3}$$

and can be solved with the boundary conditions

$$r\to\infty:\ T=T_g \quad \text{and} \quad r=r_p:\ T=T_d \tag{4}$$

to give the temperature profile of the gas phase (see **Figure 14**):

$$T(r)=\frac{T_d-T_g\exp\left(-\dfrac{\hat{C}_{Pg}\dot{m}}{4\pi\lambda_g r_p}\right)+(T_g-T_d)\exp\left(-\dfrac{\hat{C}_{Pg}\dot{m}}{4\pi\lambda_g r}\right)}{1-\exp\left(-\dfrac{\hat{C}_{Pg}\dot{m}}{4\pi\lambda_g r_p}\right)}. \tag{5}$$

The surface energy balance may be stated as

$$4\pi\lambda_g r_p^2\frac{dT}{dr}\Big|_{r=r_p}=\dot{m}\Delta_d H, \tag{6}$$

where $\Delta_d H$ denotes the required enthalpy per unit mass to devolatilize the solid fuel. The temperature gradient at the gas phase side of the particle surface is found by differentiating equation (5) and setting r equal to r_p:

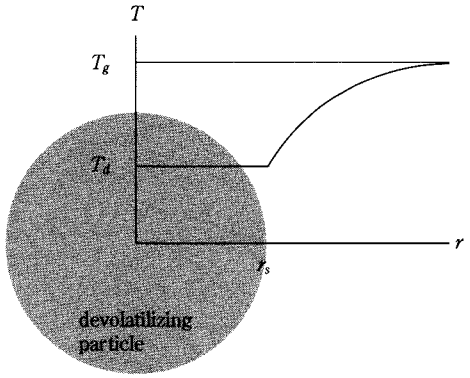

Fig. 14 Temperature profile around a spherical particle according to equation (5).

$$\frac{dT}{dr}\Big|_{r=r_p}=\frac{\hat{C}_{Pg}\dot{m}}{4\pi\lambda_g r_p^2}\left[\frac{(T_g-T_d)\exp\left(-\dfrac{\hat{C}_{Pg}\dot{m}}{4\pi\lambda_g r_p}\right)}{1-\exp\left(-\dfrac{\hat{C}_{Pg}\dot{m}}{4\pi\lambda_g r_p}\right)}\right]. \tag{7}$$

Insertion of this expression into equation (6) leads to the following relationship,

$$\dot{m}=\frac{4\pi\lambda_g r_p}{\hat{C}_{Pg}}\ln\left[1+\frac{\hat{C}_{Pg}(T_g-T_d)}{\Delta_d H}\right] \tag{8}$$

$$=\frac{4\pi\lambda_g r_p}{\hat{C}_{Pg}}\ln[1+\mathrm{Sp}], \tag{9}$$

which describes the influence of the preheat temperature on the devolatilization rate. The quantity denoted by Sp is known as the Spalding number.

It will now be shown how turbulence affects the amount of volatile components released from the particles. In the case of the preheat zone this is done by considering the enthalpy equation of a multi-component reacting mixture consisting of N species,

$$\frac{\partial(\rho h)}{\partial t}+\nabla\cdot(\rho\boldsymbol{v}h)=\frac{\partial p}{\partial t}+\boldsymbol{v}\cdot\nabla p+\boldsymbol{\tau}:\nabla\boldsymbol{v}-\nabla\cdot\boldsymbol{j}_h-\sum_{i=1}^{N}\rho Y_i\boldsymbol{f}_i\cdot(ID_i\nabla Y_i). \tag{10}$$

The heat flux vector,

$$\boldsymbol{j}_h=-\lambda\nabla T+\boldsymbol{q}+\sum_{i=1}^{N}\rho Y_i h_i\boldsymbol{V}_i+RT\sum_{i=1}^{N}\sum_{j=1}^{N}\left(\frac{X_j\alpha_i}{\mathcal{M}_i\mathcal{D}_{ij}}\right)(\boldsymbol{V}_i-\boldsymbol{V}_j), \tag{11}$$

is the sum of four contributions, namely, thermal diffusion, the radiant energy flux, the Soret flux and a Dufour flux, of which the last two phenomena make very small contributions.

With turbulence present, in the absence of external

body forces, and on the assumption of a negligible effect of turbulence on the radiant energy flux, the Favre-averaged form of this equation becomes,

$$\frac{\partial(\bar{\rho}\tilde{h})}{\partial t}+\frac{\partial}{\partial x_j}\left(\bar{\rho}\tilde{v}_j\tilde{h}\right)=\frac{\partial\bar{p}}{\partial t}+\tilde{v}_j\frac{\partial\bar{p}}{\partial x_j}+\bar{\tau}_{ij}\frac{\partial\tilde{v}_i}{\partial x_j}-\frac{\partial\bar{j}_{hi}}{\partial x_j}+\overline{v_j''\frac{\partial p}{\partial x_j}}+\overline{\tau_{ij}\frac{\partial v_i''}{\partial x_j}}-\frac{\partial}{\partial x_j}\left(\overline{\rho h''v_j''}\right). \quad (12)$$

which contains three additional terms, namely,

$$\overline{v_j''\frac{\partial p}{\partial x_j}},\ \overline{\tau_{ij}\frac{\partial v_i''}{\partial x_j}}\ \text{and}\ \frac{\partial}{\partial x_j}\left(\overline{\rho h''v_j''}\right). \quad (13)$$

These additional terms are respectively identified as

i. pressure work due to turbulence,
ii. dissipation due to molecular friction,
iii. and turbulent diffusion of fluid enthalpy.

If the turbulence would disappear suddenly in a mysterious way, these terms would reduce to zero, and the Favre-averaged equation would become identical to the instantaneous equation. If, on the other hand, the turbulence is intensified, then the magnitude of these terms increases. Since it is evident that one or more of these terms must be responsible for the influence of turbulence on the maximum explosion pressure, their relative importance will be considered.

Since the spatial pressure distribution in the 20-liter sphere is almost uniform during the course of a deflagration, the contribution of the pressure work term, $\overline{v_j''\,(\partial p/\partial x_j)}$, to the microscopic enthalpy balance is negligible. The dissipation due to molecular friction, $\overline{v_j''\,(\partial p/\partial x_j)}$, may also be neglected because of the low viscosity of air. Moreover, the spatial derivatives of the velocity fluctuations in this term are small due to the spatial homogeneity of the turbulent flow field. These considerations leave $\partial\overline{\rho h''v_j''}/\partial x_j$ as the only remaining possibility to account for the effect of turbulence on the maximum explosion pressure.

It is indeed possible to deduce a mechanism for the effect of turbulence on the release of volatile components in the preheat zone by treating the turbulent flux of enthalpy by analogy with the molecular flux of heat. In an ideal gas the following relationship exists between the heat flux and the driving force that governs it [9, Chapter 26],

$$j_{hi}=-\lambda\frac{\partial T}{\partial x_i}, \quad (14)$$

where

$$\lambda=(3/32\pi)^{1/2}\bar{\ell}\,\bar{v}'k\mathcal{N}. \quad (15)$$

Here λ denotes the thermal conductivity, k the Boltzmann constant, $\mathcal{N}$ the number density, $\bar{\ell}$ the mean free path and $\bar{v}'$ the root mean square velocity of the molecules. By analogy with equations (14) and (15) the turbulent diffusion of fluid enthalpy is modelled here as

$$\overline{\rho h''v_j''}=-\lambda_t\frac{\partial\tilde{T}}{\partial x_j}=-\ell_t\,v'_{\mathrm{rms}}\frac{\partial\tilde{T}}{\partial x_j}, \quad (16)$$

where the turbulent thermal conductivity, λ_t, is expressed as the product of the turbulence length scale, ℓ_t, and the root mean square of the fluid velocity fluctuations, v'_{rms}. The product $\lambda_t=\ell_t\,v'_{\mathrm{rms}}$ simply implies that turbulent heat conduction is enhanced as v'_{rms} and ℓ_t are being increased.

During an explosion, the system pressure and the mean quantities in the Favre-averaged energy equation change slowly in comparison with the localized process of turbulent fluid enthalpy diffusion from the flame into the unburnt mixture. The Favre-averaged energy equation may therefore be simplified to

$$\frac{\partial}{\partial t}\left(\bar{\rho}\hat{C}_{Pm}\tilde{T}\right)+\frac{\partial}{\partial x_j}\left(\bar{\rho}\tilde{v}_j\hat{C}_{Pm}\tilde{T}\right)=\frac{\partial}{\partial x_j}\left(\ell_t\,v'_{\mathrm{rms}}\frac{\partial\tilde{T}}{\partial x_j}\right). \quad (17)$$

For a fixed planar flame which is sustained by a steady, isotropic turbulent flow of a combustible mixture, the convective velocity $\tilde{v}_j$ may be replaced by the turbulent burning velocity, S_{uT}, at which the unburnt mixture enters the flame. Together with the assumption of a constant $\hat{C}_{Pm}$, equation (17) may be simplified to

$$\frac{d^2\tilde{T}}{dx^2}+\frac{\bar{\rho}\hat{C}_{Pm}S_{uT}}{\ell_t\,v'_{\mathrm{rms}}}\frac{d\tilde{T}}{dx}=0. \quad (18)$$

When this equation is solved with the boundary conditions $x=0:\tilde{T}=T_f$ and $x=\infty:\tilde{T}=T_\infty$, one obtains

$$\frac{T-T_\infty}{T_f-T_\infty}=\exp\left(-\frac{\bar{\rho}\hat{C}_{Pm}S_{uT}}{\ell_t\,v'_{\mathrm{rms}}}x\right). \quad (19)$$

This solution is plotted in **Figure 15** to illustrate how the width of the preheat zone depends on the turbulence characteristics of the dust cloud. The turbulence measurements discussed in the previous section indicate that both v'_{rms} and ℓ_t are increasing when the ignition delay time is decreased (see **Figures 7** and **8**). If the turbulent burning velocity, S_u, were constant, shortening the ignition delay time would always increase the width of the preheat zone. The turbulent burning velocity of premixed gases and dust-air mixtures, however, is known to be a function of the turbulence level and the turbulence length scale. Since the turbulent burning velocity and the

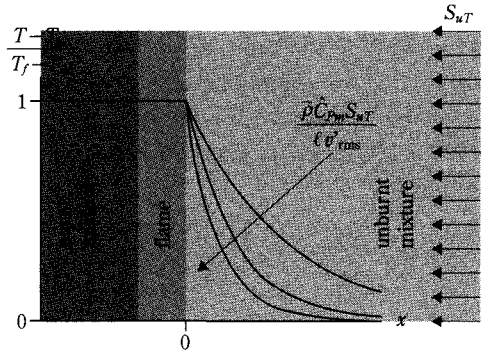

Fig. 15 The effect of turbulence on the temperature profile of the preheat zone.

product $\ell_t v'_{rms}$ have opposite effects on $\bar{\rho}\hat{C}_{Pm}S_{uT}/\ell_t v'_{rms}$ it is necessary to know the precise dependence of the former quantity on turbulence.

Trautwein *et al.* [10] measured the turbulent burning velocity of several gaseous fuels in a single stroke compression-expansion machine. Reactive mixtures were ignited at various turbulence intensities and the measured turbulent burning velocities were correlated by (see **Figure 16**)

$$\frac{S_{uT}}{S_{uL}} = 1 + C\left(\frac{v'_{rms}}{S_{uL}}\right)^n. \tag{20}$$

Tezok *et al.* [11] measured the turbulent burning velocity of cornstarch-air mixtures in the 950-liter explosion vessel mentioned in the Introduction and the results are shown in **Figure 17**. The turbulence intensity of the reactant mixture was varied between 1.0 and 4.2 ms^{-1} and experiments were done at two dust concentrations, namely, 300 gm^{-3} and 700 gm^{-3}. The ratio of turbulent to laminar burning velocities was found to correlate to the ratio of the turbulence intensity to the laminar burning velocity according to equation (20). The laminar burning velocities that were used in this correlation were derived from the turbulent burning velocities by means of extrapolation to zero turbulence. In all cases the turbulent burning velocity was found to increase with increasing turbulence levels. With the gaseous fuels investigated, the exponent n appears to have a value between 0.48 and 0.71. The ratio of the turbulent to the laminar burning velocity of cornstarch-air mixtures appears to have a linear dependence on v'_{rms}/S_{uL}. Owing to this linear dependence, the first term on the right hand side of equation (20) is made negligible by the second term for high values of v'_{rms}/S_{uL} and hence, $S_{uT} \propto v'_{rms}$. When this result is substituted into the expression for the temperature profile of the preheat zone (19) it is seen that the width of the preheat zone principally depends on the behavior of the turbulence length scale, ℓ_t. **Figure 8** then implies that a shorter ignition delay time leads to a wider preheat zone. As a result the amount of volatiles released from the particles is increased as follows:

- As the preheat zone extends *further* into the unburnt mixture, the fuel particles are *longer* exposed to a *higher* temperature and consequently release more volatiles.
- A greater amount of volatiles increases the flame temperature, which in turn enhances the devolatilization rate.

The residence time of the particles in the preheat zone does depend on the turbulence intensity since it is equal to the ratio between the width of this zone and the turbulent burning velocity. The mass change,

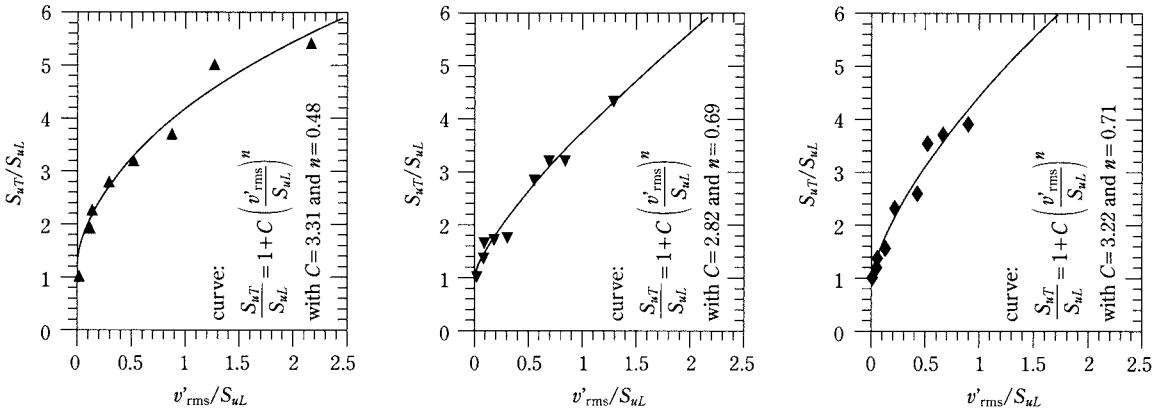

Fig. 16 The turbulent burning velocity of various gaseous fuels. The data in this figure were taken from Trautwein *et al.* [10].

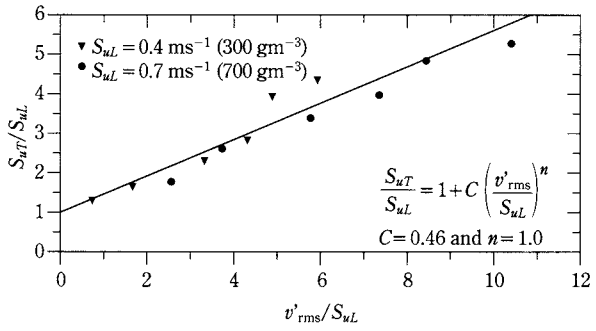

Fig. 17 The turbulent burning velocity of cornstarch-air mixtures. The data in this figure were taken from Tezok *et al.* [11].

Δm, of a particle may thus be expressed as

$$\Delta m=\dot{\bar{m}}\frac{x^*}{S_{uT}}, \tag{21}$$

where the average release rate of volatiles, $\dot{\bar{m}}$, and the width of the preheat zone where the temperature exceeds the particle devolatilization temperature, x^*, principally depend on the turbulence length scale.

When the release of volatiles from the particles continues in the reaction zone, it is also necessary to consider the residence time of the particles in the flame zone. In this case the release of volatiles in the flame zone is additive to that in the preheat zone and may be described by extending equation (21) to

$$\Delta m=\dot{\bar{m}}\frac{x^*}{S_{uT}}+\dot{m}\frac{\delta_T}{S_{uT}}, \tag{22}$$

where δ_T denotes the turbulent flame thickness. Tezok *et al.* [11] performed some indicative measurements of the turbulent flame thickness of cornstarch-air mixtures. These researchers observed that the turbulence intensity has a significant effect on the turbulent flame thickness. At a dust concentration of 300 gm^{-3} the turbulent flame thickness increased from 13 cm to 21 cm when the turbulence intensity was changed from 1.5 to 4.2 ms^{-1}. At a dust concentration of 700 gm^{-3} an increase from 34 cm to 44 cm was observed when the turbulence intensity was changed from 1.5 to 4.2 ms^{-1}. This emphasizes the necessity for a correlation between the turbulent flame thickness and the turbulence characteristics of the dust cloud. Due to the absence of such a correlation, an attempt will be undertaken here to derive one. In fact, a set of correlations will be derived here for both the turbulent burning velocity and the turbulent flame thickness.

At every instant of time during the flame propagation process, the departure of the burning velocity from its laminar value, $S_{uT}-S_{uL}$, can be expressed as a function of the laminar burning velocity at the actual pressure and temperature, S_{uL}, the laminar flame thickness at the actual pressure and temperature, δ_L, the root-mean-square value of the velocity fluctuations, v'_{rms} and the macro length scale of the turbulence, ℓ_t, as

$$S_{uT}-S_{uL}=f(S_{uL},\,\delta_L,\,v'_{rms},\,\ell_t) \tag{23}$$

$$=(S_{uL})^a\,(\delta_L)^b\,(v'_{rms})^c\,(\ell_t)^d. \tag{24}$$

Substitution of the dimensions of the quantities involved leads to

$$\frac{m}{s}=\left(\frac{m}{s}\right)^a(m)^b\left(\frac{m}{s}\right)^c(m)^d \tag{25}$$

$$\Longleftrightarrow\begin{cases} m: & 1=a+b+c+d,\\ s: & 1=a+c \end{cases} \tag{26}$$

which can be solved to give

$$a=1-c,\quad b=b,\quad c=c,\quad d=-b. \tag{27}$$

Substitution of equation (27) into equation (24) results into

$$\frac{S_{uT}-S_{uL}}{S_{uL}}=\left(\frac{v'_{rms}/\ell_t}{S_{uL}/\delta_L}\right)^b\left(\frac{v'_{rms}}{S_{uL}}\right)^{c-b} \tag{28}$$

$$\Longleftrightarrow\frac{S_{uT}}{S_{uL}}=1+\left(\frac{v'_{rms}/\ell_t}{S_{uL}/\delta_L}\right)^{a'}\left(\frac{v'_{rms}}{S_{uL}}\right)^{b'}. \tag{29}$$

Similarly, the turbulent flame thickness, δ_T, can be expressed as

$$\delta_T-\delta_L=f(S_{uL},\,\delta_L,\,v'_{rms},\,\ell_t) \tag{30}$$

$$=(S_{uL})^a\,(\delta_L)^b\,(v'_{rms})^c\,(\ell_t)^d \tag{31}$$

$$\Longrightarrow m=\left(\frac{m}{s}\right)^a(m)^b\left(\frac{m}{s}\right)^c(m)^d \tag{32}$$

$$\Longleftrightarrow\begin{cases} m: & 1=a+b+c+d\\ s: & 0=a+c \end{cases} \tag{33}$$

$$\Longrightarrow a=-c,\quad b=1-d,\quad c=c,\quad d=-d \tag{34}$$

$$\text{and hence}\quad\frac{\delta_T-\delta_L}{\delta_L}=\left(\frac{v'_{rms}/\ell_t}{S_{uL}/\delta_L}\right)^c\left(\frac{\ell_t}{\delta_L}\right)^{d+c} \tag{35}$$

$$\Longleftrightarrow\frac{\delta_T}{\delta_L}=1+\left(\frac{v'_{rms}/\ell}{S_{uL}/\delta_L}\right)^{a''}\left(\frac{\ell_t}{\delta_L}\right)^{b''}. \tag{36}$$

Thus, the turbulent burning velocity and the turbulent flame thickness are related to the laminar burning velocity and the laminar flame thickness by means of the following two equations,

$$\frac{S_{uT}}{S_{uL}} = 1 + \mathrm{Da}^{a'} \left(\frac{v'_{\mathrm{rms}}}{S_{uL}} \right)^{b'} \tag{37}$$

$$\frac{\delta_T}{\delta_L} = 1 + \mathrm{Da}^{a''} \left(\frac{\ell_t}{\delta_L} \right)^{b''}, \tag{38}$$

of which the independent variables, v'_{rms}/S_{uL} and ℓ_t/δ_L, are the same as the ordinates of the Borghi diagram [12, 13], and in which the Damköhler number, $\mathrm{Da} = (\ell_t S_{uL}/v'_{\mathrm{rms}}\delta_L)$, serves as an indicator for the combustion regime in which the flame propagation process occurs. Notice that $S_{uT} \to S_{uL}$ and $\delta_T \to \delta_L$ if $v'_{\mathrm{rms}} \to 0$, and that equation (37) is a generalized form of expression (20) for the turbulent burning velocity. Although the exponents in equations (37) and (38) are still unknown, one may get an impression of the magnitude of a' and b' by inspecting **Figures 16** and **17**, and from the work reported by Leuckel *et al.* [1].

Leuckel *et al.* investigated the dependency of the inclination of equation (20) on the laminar burning velocity using methane-air, hydrogen-air, and methane-hydrogen-air mixtures. With all mixtures C was found to correlate with the laminar burning velocity as

$$C \propto S_{uL}^{1/4}. \tag{39}$$

This result implies that a' has a value of 1/4 and owing to this weak dependence of C on the turbulence characteristics of the flow field, **Figures 16** and **17** indicate that b' ranges between 1/2 and 1. Since the Damköhler number is a measure of the coupling between the flame and the flow field, it is reasonable to expect that the exponent a'' has the same value as the exponent a'.

The estimation of a value for b'' is more difficult since Tezok *et al.* reported turbulent flame thicknesses, but did not mention anything about the length scales of the turbulence in their equipment. Leuckel *et al.*, on the other hand, state that the turbulence length scales associated with various turbulence intensities were found to be independent of the ventilator speed which sustained the turbulent flow field in their equipment. These turbulence length scales were observed to have a size of about 20 mm. Since Tezok *et al.* also worked with non-decaying turbulent flow fields it is assumed here that there was no large variation in the turbulence length scales present in their equipment. Due to the fact that the diameter of the vessel used by Tezok *et al.* was 2.4 times that of the vessel used by Leuckel *et al.* it is assumed here that the turbulence length scale is also greater by the same factor. With the turbulence length scale being about 50 mm and the laminar flame thickness of cornstarch-air mixtures being about 3 mm [14], insertion of the turbulent the flame thicknesses reported by Tezok *et al.* into equation (38) reveals that the of b'' ranges between 1.6 and 2.0 (the quantity $\mathrm{Da}^{a''}$ is taken to be equal to 0.51; see **Figure 17**).

Equations (9) and (22) will now be used to derive an expression for the effect of turbulence on release of volatile matter from the particles. For this purpose the average release rate of volatiles, $\bar{\dot{m}}$, is defined as

$$\bar{\dot{m}} = \frac{1}{T_f - T_d} \int_{T_d}^{T_f} \dot{m}\, dT = \frac{4\pi\lambda_g r_p}{\hat{C}_{Pg}} \frac{1}{\mathrm{Sp}_f} [(1+\mathrm{Sp}_f)\ln(1+\mathrm{Sp}_f) - \mathrm{Sp}_f], \tag{40}$$

and, based on equation (19), the width of the region inside the preheat zone where the temperature exceeds the devolatilization temperature of the particles is approximated by

$$x^* = \frac{\ell_t v'_{\mathrm{rms}} (T_f - T_d)}{\bar{\rho} \hat{C}_{Pm} S_{uT}}. \tag{41}$$

The quantity denoted by Sp_f is the Spalding number based on the flame temperature. A final expression may then be obtained by combining equations (9), (22), (40) and (41) into

$$\Delta m = \frac{4\pi\lambda_g r_p}{\hat{C}_{Pg}} \times \left[\frac{\Delta_d H}{\bar{\rho} \hat{C}_{Pg} \hat{C}_{Pm}} \frac{\ell_t v'_{\mathrm{rms}}}{S_{uT}^2} [(1+\mathrm{Sp}_f)\ln(1+\mathrm{Sp}_f) - \mathrm{Sp}_f] + \frac{\delta_T}{S_{uT}} \ln(1+\mathrm{Sp}_f) \right]. \tag{42}$$

This expression unveils the various factors that affect the release of volatiles from the particles, and hence the maximum explosion pressure of a dust-air mixture. These factors include flow properties of the mixture (turbulence level and length scale), physical properties of the mixture (specific heat, density), properties of the flame (flame temperature, burning velocity, flame thickness), physical properties of the particles (particle size, devolatilization temperature, devolatilization enthalpy), and physical properties of the gas phase (specific heat, thermal conductivity). Notice that this equation would also be valid for flames propagating through laminar dust clouds since, according to equations (37) and (38), the turbulent burning velocity and the turbulent flame thickness would reduce to the laminar burning velocity and the laminar flame thickness, and, by the analogy between equations (14) and (15), the product, $\ell_t v'_{\mathrm{rms}}$, would transform into the thermal conductivity of the

mixture.

Owing to the simplifying assumptions made earlier, equation (42) may only be used for a qualitative explanation of observed trends in the behavior of the maximum explosion pressure of dust-air mixtures. Hence, equation (42) is reduced into a scaling relationship,

$$\Delta m \propto \frac{\Delta_d H}{\bar{\rho}\hat{C}_{Pg}\hat{C}_{Pm}} \frac{\ell_t v'_{\mathrm{rms}}}{S_{uT}^2}[(1+\mathrm{Sp}_f)\ln(1+\mathrm{Sp}_f)-\mathrm{Sp}_f] + \frac{\delta_T}{S_{uT}}\ln(1+\mathrm{Sp}_f) \tag{43}$$

$$\propto A\frac{\ell_t v'_{\mathrm{rms}}}{S_{uT}^2}+B\frac{\delta_T}{S_{uT}}, \tag{44}$$

which can be used for a qualitative explanation for the effect of turbulence on the maximum explosion pressure and to assess the relative importance of the release of volatiles from the particles in the preheat zone and in the flame zone. With $\hat{C}_{Pm}\approx 10^3$ Jkg^{-1} K^{-1}, $\hat{C}_{Pg}\approx 10^3$ Jkg^{-1} K^{-1}, $\Delta_d H\approx 10^7$ Jkg^{-1}, $\bar{\rho}\approx 1$ kgm^{-3}, and an assumed temperature difference of 1000 K between the particles and the surrounding medium, one finds that $\mathrm{Sp}_f = 0.1$, and that the quantities A and B have a value of about 0.1. When the temperature difference between the particles and the surrounding gas is assumed to be 2000 K then one finds that $A = 0.16$ and $B = 0.18$. With an assumed $\Delta_d H$ of 10^6 Jkg^{-1} and a temperature difference of 2000 K one finds that $\mathrm{Sp}_f = 2$ and that $A = 0.3$ and $B = 1.1$. Since $\ell_t v'_{\mathrm{rms}}/S_{uT}^2$ and δ_T/S_{uT} are in the same order of magnitude, these values indicate that with increasing Spalding numbers the release of volatiles in the preheat zone becomes less important than in the flame zone.

Figure 18 shows the solution of equation (44) at various ignition delay times, together with the maximum explosion pressure of cornstarch-air mixtures. Equal values were assigned to A and B, and the values of v'_{rms} and ℓ_t were calculated by means of the correlations presented in **Figures 7** and **8**. The turbulent burning velocity and flame thickness were calculated by means of equations (37) and (38). The laminar burning velocity and the laminar flame thickness in these correlations were respectively assumed to have a value of 20 cms^{-1} and 3 mm. In all cases the turbulent flame thickness was calculated with $\mathrm{Da}^{a''} = 0.51$ and $b'' = 2$. The upper-left part of **Figure 18** was obtained with $\mathrm{Da}^{a'} = 0.51$ and $b' = 1$ in the turbulent burning velocity correlation, like the work of Tezok *et al.* suggests (see **Figure 17**). The amount of volatiles released from the particles is seen to decrease up to an ignition delay time of 120 milliseconds and increases slightly thereafter. This behavior is inconsistent with the monotonously decreasing trend of the maximum explosion pressure. According to the upper-right part of **Figure 18** this inconsistency arises from the behavior of the residence time of the particles in the flame zone, δ_T/S_{uT}. Hence, its cause must be sought in the accuracy of the correlations which describe the turbulent burning velocity and the turbulent flame thickness.

In order to achieve a better consistency between the trends of the maximum explosion pressure and the release of volatiles from the particles, the turbulent burning velocity correlation (37) was re-evaluated as shown by **Figure 19**. The solid lines in this figure depict the behavior of equation (20) when it is fitted to the experimental data in two distinct regions, namely, when $v'_{\mathrm{rms}}/S_{uL} \leq 5$ and when $v'_{\mathrm{rms}}/S_{uL} > 5$. Since the turbulent cornstarch-air mixtures investigated in this work were ignited at a turbulence level of 3.75 ms^{-1} while the laminar burning velocity is in the order of 20 cms^{-1}, the solution of equation (44) was calculated again with $\mathrm{Da}^{a'} = 0.68$ and $b' = 0.79$. This solution is shown in the lower-left part of **Figure 18** and its monotonously decreasing behavior is found to be more consistent with that of the maximum explosion pressure.

For a number of reasons equation (42) can not be used as a correlation which predicts the effect of turbulence on the maximum explosion pressure in a quantitative sense, but only as one which explains the global trend in a qualitative manner. This is partly due to the simplifying assumptions on which its derivation rests, and partly due to deficiencies in our knowledge of the turbulent flow field and its interaction with the flame.

It was assumed that a particle in the preheat zone is surrounded by a quiescent medium, that the particle size does not change (notice that equation (40) relies on this assumption), and that all physical properties, including the temperature at which devolatilization occurs, are constant. In reality there is a relative velocity between the particle and the surrounding medium and the particle size may change considerably during the devolatilization process. Since the temperature in the preheat zone varies from that of the cold unburnt mixture to the high temperature of the flame zone, the particles are continuously exposed to a greatly varying temperature during their passage through this region. The physical properties of the particles and the surrounding medium are known to vary greatly over such a wide temperature range. The devolatilization temperature is further-

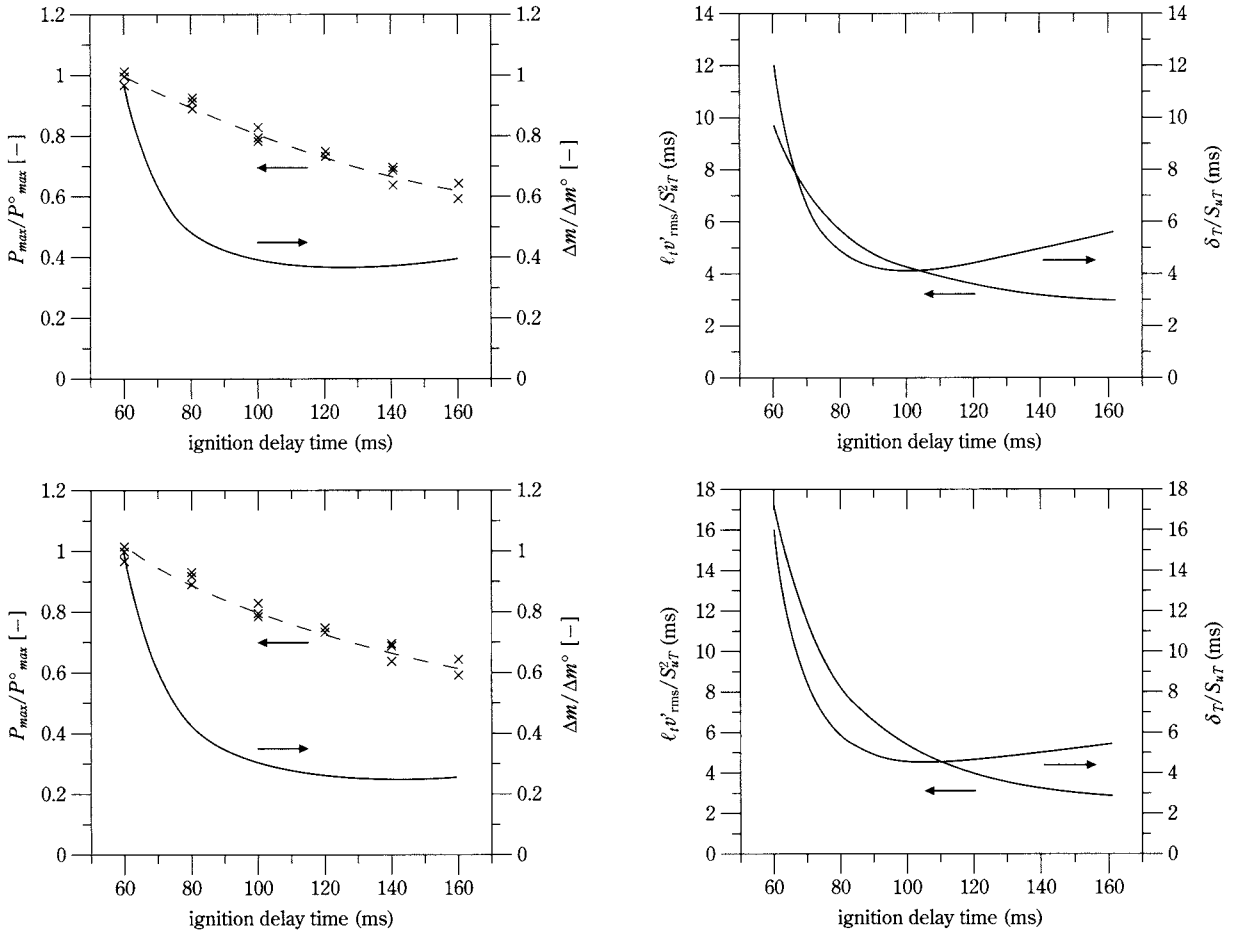

Fig. 18 The solution of (44) and the behavior of $\ell_t v'_{rms}/S_{uT}^2$ and δ_T/S_{uT} as a function of the ignition delay time. The upper-left and the upper-right figure were obtained with $Da''=0.51$ and $b'=1$. The lower-left and the lower-right figure were obtained with $Da''=0.68$ and $b'=0.79$.

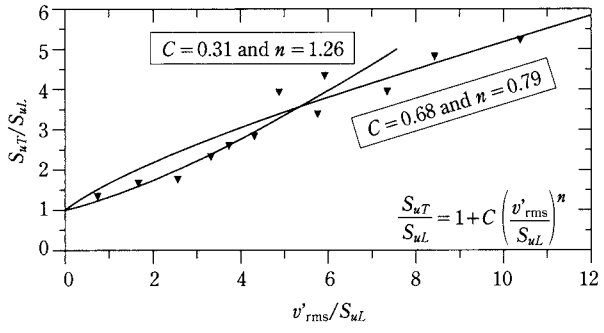

Fig. 19 The turbulent burning velocity of cornstarch-air mixtures. The data points in this figure are the same as those in **Figure 17**.

more not constant, like in the case of a pure compound, but may vary over a temperature trajectory.

The residence time in the preheat zone and the flame zone, respectively denoted by $\ell_t v'_{rms}/S_{uT}^2$ and δ_T/S_{uT}, are of crucial importance in the estimation of the amount of volatiles released from the particles. In order to have good estimates of these quantities, it is not only important to have accurate knowledge of the flow properties. Accurate relationships are also needed which express the turbulent burning velocity and the turbulent flame thickness in terms of the flow properties. In this work two such relationships have been developed (equations (37) and (38)) and the constants in these expressions were evaluated on the basis of experimental data reported by Tezok *et al.* A comparison between the graphs presented in **Figure 18**, in conjunction with **Figures 17** and **19**, shows that accurate knowledge of these constants is of great importance. An additional source of inaccuracy is due to the fact that the magnitudes of the turbulence properties (v'_{rms} and ℓ_t) which were used to calculate the residence times are those at the moment of ignition. Hence, their values are no more than a crude esti-

mate of the values we are supposed to know during the course of the flame propagation process.

4 Conclusions

The effect of turbulence on the maximum explosion pressure of dust-air mixtures was investigated by igniting turbulent cornstarch-air mixtures to deflagration at various turbulence levels in the standard 20-liter sphere. Turbulence was created by means of a blast of compressed air and the turbulence level was varied by changing the ignition delay time. A comparative study was also undertaken by deflagrating stoichiometric methane-air mixtures at different turbulence levels. The conclusions arising from this investigation are summarized as follows.

- The maximum explosion pressure of a dust-air mixture is sensitive to flow properties. It was observed to increase by a factor of 1.6 when the turbulence level was increased by a factor of about five (see **Figure 13**). This observation is consistent with the findings of Kauffman *et al.*, namely, that the maximum explosion pressure of cornstarch-air mixtures increases with increasing turbulence levels (see **Figure 3**).
- The comparative experiments with stoichiometric methane-air mixtures show that the maximum explosion pressure of gaseous fuel-air mixtures is not being affected by turbulence. This observation is consistent with the findings of Leuckel *et al.* (see **Figure 2**) and with the general view that the maximum explosion pressure of a gas mixture may be regarded as a thermodynamic property which is insensitive to flow properties.
- The controversy between the previous two items has important consequences for the safe design of industrial equipment. It is common practice to assess the maximum explosion pressure of combustible mixtures experimentally by means of laboratory test vessels, or, theoretically by calculating the product mixtures composition, temperature and pressure. In the experimental approach combustible mixtures are ignited to deflagration in laboratory test vessels and the resulting maximum explosion pressure is used as a design basis for industrial equipment. In the theoretical approach the final explosion pressure is calculated on the basis of the chemical composition of the reactants, the chemical composition of the products, and the chemical and thermodynamic properties of the species involved. When the effect of turbulence is not taken into account, these approaches may lead to underestimations or over estimations of the design strength of industrial equipment.
- The availability of quantitative correlations between the experimental maximum explosion pressure or the product mixture composition on one hand, and the flow properties of a dust cloud on the other hand, would greatly enhance our capability to predict what would happen if a dust-air mixture exploded under industrial circumstances. This would lead to a more optimal design basis for industrial equipment. In case of the experimental approach, the maximum explosion pressure can be measured at a particular turbulence level and such correlations could be used to extrapolate this result to the flow conditions which exist under industrial circumstances. The accuracy of the theoretical approach can be improved by such correlations since they enable one make a better estimate of the reactant mixture composition and the resulting product mixture composition.
- In this work an explanation is proposed for the effect of turbulence on the maximum explosion pressure of dust-air mixtures by considering the release of volatiles from the particles. Although this explanation rests on a picture which is too simplified to yield an accurate quantitative relationship between the maximum explosion pressure, the release of volatiles from the particles, and the effect of turbulence on the latter, a number of important issues which require further improvement have been singled out by this analysis.
- A relationship was established between the instantaneous release rate of volatiles from the particles, the physical properties of the particles, and the physical properties of the gas that surrounds them (see equation (9). Its derivation is based on the assumption that the gas which surrounds the particles is quiescent. Since there is a velocity difference between the particles and the surrounding gas, an improved expression ought to be derived by describing the heat transfer from the latter to the former by means of the Ranz-Marshall equation.
- In order to estimate the total amount of volatiles released from the particles, it is necessary to know their residence time in the preheat zone and the flame zone. It is shown that these residence times depend entirely on the flow properties of the dust cloud. In this work, experimental

values of the turbulence level and the turbulence length scale at the moment of ignition were presented and used. Since the release of volatiles occurs after the ignition has occurred, it is necessary to extrapolate these flow properties to what they would be during the flame propagation process. Ideally, turbulence measurements would have to be performed in the unburnt mixture at the downstream side of the advancing flame front.

- The residence time of the particles in the preheat zone and the flame zone were found to depend also on the turbulent burning velocity and the turbulent flame thickness. A set of generalized correlations (see (37) and (38)) have been derived for these quantities and the mixture specific constants in these correlations were estimated on the basis of experimental burning velocities and flame thicknesses, using turbulence levels and length scales at the moment of ignition. The constants in these correlations would have to be re-evaluated on the basis of flow properties as they exist during the course of the flame propagation process.

5 List of symbols

The symbols used throughout this work are explained below. When a symbol represents something else than stated here, or when a symbol in the text is not explained here, or when a symbol represents more than one quantity, its precise meaning is clarified by the text.

LATIN SYMBOLS

$\hat{C}_{Pg}$	gas phase specific heat	$Jkg^{-1}K^{-1}$
$\hat{C}_{Pm}$	mixture specific heat	$Jkg^{-1}K^{-1}$
$\boldsymbol{f}_i$	sum of body forces per unit mass acting on the i-th species	Nkg^{-1}
h	microscopic enthalpy per unit mass	Jkg^{-1}
	heat transfer coefficient	$Wm^{-2}K^{-1}$
$\boldsymbol{j}_h$	enthalpy flux vector	Wm^{-2}
k	turbulent kinetic energy per unit volume of the gas phase	Jm^{-3}
k_p	turbulent kinetic energy per unit volume of the particulate phase	Jm^{-3}
$\dot{m}$	release rate of volatiles	kgs^{-1}
$\overline{\dot{m}}$	average release rate of volatiles	kgs^{-1}
p	microscopic pressure	Nm^{-2}
P	macroscopic pressure	Pa
P_{max}	maximum explosion pressure	Pa
n_0	moles of gas present before explosion	[−]
n_e	moles of gas present after explosion	[−]
$\boldsymbol{q}$	radiant flux	Wm^{-2}
r	radial coordinate	m
R	universal gas constant	$Jmol^{-1}K^{-1}$
r_p	particle radius	m
S_{uL}	laminar burning velocity	ms^{-1}
S_{uT}	turbulent burning velocity	ms^{-1}
T	temperature	K
T_d	devolatilization temperature	K
T_f	flame temperature	K
T_f^{ad}	flame temperature	K
T_g	gas phase temperature	K
$\boldsymbol{v}$	velocity vector	ms^{-1}
$\boldsymbol{V}_i$	diffusion velocity vector of the i-th species	ms^{-1}
v'_{rms}	root-mean-square value of the velocity fluctuations	ms^{-1}
X_i	i-th species mole fraction	[−]
Y_i	i-th species mass fraction	[−]

GREEK SYMBOLS

α_i	interaction parameter of the i-th species	$kgm^{-2}s^{-1}$
δ_L	laminar flame thickness	m
δ_T	turbulent flame thickness	m
$\Delta_d H$	devolatilization enthalpy	Jkg^{-1}
λ	thermal conductivity	$Wm^{-1}K^{-1}$
λ_g	thermal conductivity of the gas phase	$Wm^{-1}K^{-1}$
ρ	density	kgm^{-3}
$\boldsymbol{\tau}$	shear stress tensor	Nm^{-2}
τ_p	response time of a particle	s
τ_t	turbulence macro time scale	s

OTHER SYMBOLS

ID_i	diffusion coefficient of the i-th species	m^2s^{-1}
$\mathcal{D}_{ij}$	binary diffusion coefficient between the i-th and the j-th species	m^2s^{-1}
$(dP/dt)_{max}$	maximum rate of pressure rise	Pas^{-1}
ℓ_t	turbulence macro length scale	m
$\mathcal{M}_i$	molecular mass of the i-th species	$kgmol^{-1}$

DIMENSIONLESS GROUPS

Sp	Spalding number	[−]
Sp_f	Spalding number based on the	

	flame temperature	[−]
Da	Damköhler number	[−]

References

[1] Leuckel W., Nastoll W., and Zarzalis N. Experimental investigation of the influence of turbulence on the transient premixed flame propagation inside closed vessels. In *Proceedings of the Twenty-Third Symposium (International) on Combustion*, pages 729−734. The Combustion Institute, 1990.

[2] Kauffman C.W., Srinath S.R., Tezok F.I., Nicholls J.A., and Sichel M. Turbulent and accelerating dust flames. In *Proceedings of the Twentieth Symposium (International) on Combustion*, pages 1701−1708. The Combustion Institute, 1984.

[3] National Fire Protection Association (NFPA). Venting of deflagrations, 1988. NFPA 68, 1988 edition.

[4] Verein Deutcher Ingenieure (VDI). Pressure venting of dust explosions, 1995. VDI 3673.

[5] Dahoe A.E. *Dust Explosions: a Study of Flame Propagation*. PhD thesis, Delft University of Technology, May 2000.

[6] Zhou Lixing. *Theory and numerical modeling of turbulent gas-particle flows and combustion*. Science Press, 16 Donghuangchenggen North Street, Beijing 100717, China, 1993. Distributed by CRC Press outside China.

[7] Bradley D. and Lee J.H.S. Proceedings of the first international colloquium on the explosibility of industrial dusts. volume 2, pages 220−223, 1984.

[8] Turns S.R. *An Introduction to Combustion*. McGraw-Hill Series in Mechanical Engineering. McGraw-Hill, 1996.

[9] Atkins P.W. *Physical Chemistry*. Oxford University Press, Oxford, third edition, 1987.

[10] Trautwein S.E., Grudno A., and Adomeit G. The influence of turbulence intensity and laminar flame speed on turbulent flame propagation under engine like conditions. In *Proceedings of the Twenty-Third Symposium (International) on Combustion*, pages 723−728. The Combustion Institute, 1990.

[11] Tezok F.I., Kauffman C.W., Sichel M., and Nicholls J.A. Turbulent burning velocity measurements for dust/air mixtures in a constant volume spherical bomb. In *Dynamics of Reactive Systems, Part II: Modeling and Heterogeneous Combustion*, volume 105 of *Progress in Astronautics and Aeronautics*, pages 184−195, 1986.

[12] Borghi R. Turbulent combustion modelling. *Progress in Energy and Combustion Science*, 14: 245−292, 1988.

[13] Peters N. *Length scales in laminar and turbulent flames*, volume 135 of *Progress in Astronautics and Aeronautics*, chapter 6, pages 155−182, 1991.

[14] Proust C. and Veyssiere B. Fundamental properties of flames propagating in starch dust-air mixtures. *Combustion Science and Technology*, 62: 149−172, 1988.

Author's short biography

A.E. Dahoe

Arief Dahoe is a postdoc at Delft University of Technology and an invited scholar at the University of Cambridge.

K. van der Nat

Koen van der Nat is a chemical engineering student at Delft University of technology.

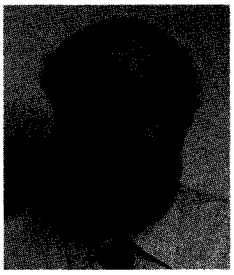

M. Braithwaite

Martin Braithwaite is a Professor at the Royal Military College of Science, Cranfield University.

B. Scarlett

Brian Scarlett is a Research Professor at the Engineering Research Center for Particle Science and Technology at the University of Florida.
He is currently Chairman of ISO TC24/SC4, the committee for particle size measurement. He is also the Series Editor of the Kluwer Powder Technology Series of books and an editor of the journal Particle and Particle Systems Characterisation.

Accurate Wet-type Centrifugal Classification Using an Almost Rigidly Rotating Flow†

Koichi Nakabayashi and Yoichi Tsuchida
Department of Mechanical Engineering,
*Nagoya Institute of Technology**

Abstract

The authors propose a new system for accurate wet-type centrifugal classification that employs an almost rigidly rotating through-flow. This flow can be produced within a rapidly rotating double-walled container, without producing any turbulent fluctuation. We have conducted both batch and continuous classification using a double-walled cylinder-sphere container in classification experiments and in theoretical and numerical flow analyses. The batch type exhibited decreasing cut size and increasing classification accuracy when the Ekman number decreased (i.e., rotation rate increased) while the Rossby number remained constant, or when the Rossby number decreased (i.e., through-flow rate decreased) and the Ekman number remained constant. With the continuous type, achieved by extracting the coarse product continuously, the cut size decreased as the extraction rate increased, but the sharpness index was almost as high as that for the batch type when the extraction rate was below the threshold value, which was reduced when the Ekman and Rossby numbers decreased.

1. Introduction

Increasing the sophistication and functionality of the material characteristics of IC circuit boards, as well as membrane materials, fine ceramics, and the other new materials that support advanced technology fields including the semiconductor industry makes it important to control the grade of the feed powders used in those materials. With the greater sophistication and diversification of user needs in recent years, there are increasingly rigorous demands for particle size to be more uniform and in submicrometer sizes, and that will increasingly be the trend.

Powder manufacturing processes can be roughly categorized as breaking down processes (melt sprays, mechanical comminution, etc.) and building up processes (chemical synthesis), but despite the differences in product grade between these two process types, both unavoidably yield particle size distributions. Consequently, classification to produce precision fine powders is required as the final stage of making products for the advanced technologies mentioned above.

For these reasons a number of dry and wet classifiers have been developed [1-3], but they do not perform precision fine powder classification well enough to satisfy the previously noted demands for grade control. A satisfactory method has to meet all the following four conditions: a sustained and powerful separation force; a turbulence-free flow (stratified flow); good particle dispersion; and prevention of classification product (coarse and fine product) mixing [4]. However, the conventional centrifugal classifier's operating principle does not allow it to completely meet the requirement of a turbulence-free flow during high-speed rotation that creates a strong separation force.

The authors for this reason propose a new wet-type centrifugal classification method that by principle classifies particles within an almost rigidly rotating flow (a stable stratified flow) without turbulence no matter how fast the rotation. This classification method can be expanded to both the batch and continuous methods.

Figure 1(a) shows the flow structure of the classification field and the particle trajectories in the batch

* Gokiso-cho, Showa-ku, Nagoya 466-8555, Japan
Tel: +81-52-735-5323, Fax: +81-52-735-5342
E-mail: nakabaya@cfd.mech.nitech.ac.jp

† This report was originally in J. Soc. Powder Technology, Japan. **36**, 881-896 (1999) in Japanese, before being translated into English by KONA Editorial Committee with the permission of the editorial committee of the Soc. Powder Technology, Japan.

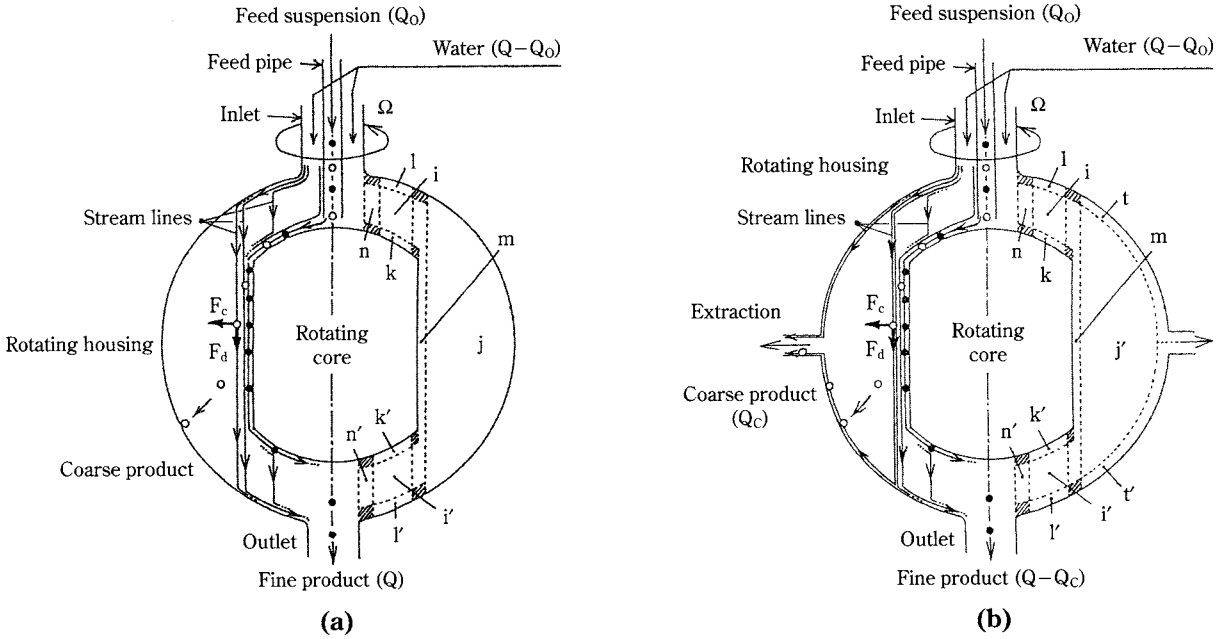

Fig. 1 Schematic of the almost rigidly rotating flow structure and particle paths within the rotating double-walled container
k, l, k′, l′: Ekman layers; m, n, n′: Stewartson layers; i, i′: interior regions; hatching: Ekman extensions of Stewartson layers; ○: coarse particles; •: fine particles; F_c, F_d: centrifugal and drag forces
(a) Batch-type classification (j: rigid rotation region)
(b) Continuous-type classification (t, t′: Ekman layers; j′: interior region)

method. While a detailed discussion shall come below, note here that the almost rigidly rotating flow is formed by running a small amount of fluid (water) through an axisymmetric double-walled container (comprising a housing and core) that rotates at high speed. Precision fine powder classification is rendered possible by running a feed suspension through the flow field of this perfectly axisymmetric stratified flow. The flow structure consists of Ekman layers, Stewartson layers, an interior region, and a rigid rotation region. The fine product is collected at the rotating double-walled container's bottom outlet, and the coarse product is collected in the rigid rotation region (j).

Figure 1(b) shows the flow structure of the classification field and the particle trajectories in the continuous method. While there is a detailed discussion below, suffice it to say that this method achieves continuous processing while maintaining the high classification performance of the batch method because it continuously extracts product from the coarse product collection region (i.e., the rigid rotation region) without disrupting the basic flow structure of the batch method.

This classification method is suitable when the suspension's mass concentration is dilute (no more than several percent).

Compared with conventional methods (those whose flow fields have turbulence), this method is far more advantageous in terms of classification accuracy, the reason being that while the principle influencing the classification limit of conventional methods is turbulence diffusion, that of this method is determined by Brownian diffusion. For example, the Brownian diffusion coefficient $\kappa TC_c/(3\pi\mu D_P)$ of spherical particles with diameter $D_P = 0.1$ μm in water (viscosity $\mu = 1.002\times10^{-3}$ Pa·s, Cunningham compensation coefficient $C_c = 1$) at one atmosphere and 20°C ($T = 293$ K) is 4.28×10^{-12} m^2 s^{-1} (Boltzmann constant $\kappa = 1.38\times10^{-23}$ J/K), while the turbulence diffusion coefficient is, for example, about 10^{-6} m^2 s^{-1} for a wet type horizontal flow gravitational classifier. The Brownian diffusion coefficient is far smaller than the turbulence diffusion coefficient.

In addition to these characteristics, our new method also features a sustained and powerful separation force, and prevention of classification product mixing. As explained below, classification is achieved by widening inter-particle gaps with a strong shearing flow in the Ekman layers, and then separating the particles still further with a rapidly rotating flow in the neighboring Stewartson layers. The post-classifi-

cation coarse product is confined in the rigid rotation region in the batch method, while in the continuous method the coarse product is extracted continuously from the housing's equatorial section, which keeps it from mixing into the fine product.

Research on the gas centrifuge process used in uranium enrichment [5] indicates that it mainly uses only the Stewartson layers formed in the rotating cylindrical container, and that no research has been performed on separation methods such as ours, which actively use all four areas: the Ekman layers, Stewartson layers, interior region, and rigid rotation region.

With respect to the batch method this paper will discuss its classification principle and characteristics, a performance assessment according to classification tests, and the almost rigidly rotating flow that is employed in classification. For the continuous method this paper describes a classification performance assessment using extraction, and the limits to extraction.

2. Batch Method

2.1 Classification Principle

Figure 1(a) shows the particle trajectories and the structure of the stable axisymmetric almost rigidly rotating flow in the rotating double-walled container. Ω is the angular velocity of the rotating container, and Q is the through-flow rate (total of the flow rate Q_O of the feed suspension and the flow rate of water $Q-Q_O$). As detailed below, this almost rigidly rotating flow consists of Ekman layers k, l, k′, and l′, Stewartson layers m, n, and n′, the interior regions i, i′, and the rigid rotation region j. Hatched areas are overlaps of Ekman and Stewartson layers (Ekman extensions of the Stewartson layers). The feed suspension is fed in over the core's rotation axis through a feed pipe, then moves to k (near the core wall) via the Ekman extension of the Stewartson layer below n. Water is supplied through the inlet and passes via n to k (near the interior region i) or l. At k and m the powder particles undergo classification according to their size by centrifugal force $\boldsymbol{F}_c$ and fluid drag $\boldsymbol{F}_d$. Those forces take fine particles (represented by solid circles) from m to either k′ or l′, and particles are then collected from the outlet as fine product. Coarse particles (hollow circles) enter the rigid rotation region j from m and adhere to the housing wall adjacent to j. After classification is finished, those coarse particles are collected from the outlet as coarse product. Owing to the flow structure, coarse particles cannot leave region j once they have entered, making it impossible for coarse particles to mix into the fine product.

The centrifugal force $\boldsymbol{F}_c$ and fluid drag (Stokes resistance) $\boldsymbol{F}_d$ acting on fine spherical particles are given by these equations.

$$\boldsymbol{F}_c = (\rho_P - \rho_f)(\pi D_P^3/6)\Omega^2 r^* \boldsymbol{i} \tag{1}$$

$$\boldsymbol{F}_d = 3\pi\mu D_P(\boldsymbol{v}^* - \boldsymbol{u}^*) \tag{2}$$

$$\therefore |\boldsymbol{F}_c|/|\boldsymbol{F}_d| = (\gamma-1)(D_P/a)^2 r/(18ER_S|\boldsymbol{v}-\boldsymbol{u}|) \tag{3}$$

Where:
Variables r, $\boldsymbol{v}$, and $\boldsymbol{u}$ without superscripted asterisks are non-dimensional quantities according to characteristic length a or characteristic velocity U_E.

In this research, a is the radius of the core cylinder, and U_E is $Q/\{4\pi a\ (\nu/\Omega)^{0.5}\}$, the benchmark for the average radial velocity within an Ekman layer whose thickness is $O((\nu/\Omega)^{0.5})$. E and R_S are flow control parameters defined in the following equation; the first is the Ekman number (the ratio of viscous force to Coriolis force acting on the fluid) and the second is the Rossby number (the ratio of inertial force to Coriolis force). γ is the ratio of true particle density ρ_P to fluid density ρ_f.

$$E = \nu/(\Omega a^2) \sim 1/n,$$
$$R_S = U_E/(\Omega a) \sim Q/n^{0.5} \quad (n = 30\,\Omega/\pi) \tag{4}$$

As discussed below, the almost rigidly rotating flow arises under conditions in which E and R_S are small. That is to say, when through-flow rate Q is a small value, no turbulence at all will appear in the flow no matter how fast the rotation rate n becomes. As long as the through-flow is maintained, the rotation rate can be freely accelerated or slowed, and the ratio of centrifugal force to fluid drag in Eq. 3 can be set at any desired value. Therefore highly accurate submicrometer classification is possible by decreasing E (or increasing n) or by decreasing R_S (or decreasing $Q/n^{0.5}$) and increasing the centrifugal force to fluid drag ratio.

2.2 Performance Assessment According to Classification Tests

2.2.1 Experimental Apparatus and Method

Figure 2(a) is an experimental classification apparatus for both batch and continuous use. It consists of these elements: rotating container C; drive system D; a slip ring; feed suspension tank T_O; water supply tank T_W; overflow tanks O_O and O_W, which supply constant amounts of the feed suspension and water, respectively; and a mechanism that extracts the coarse product suspension (extraction flow rate Q_C) from the

equatorial section of the rotating housing and discharges it to the static system. In the batch mode the extraction mechanism is not used when $Q_C = 0$. The pump and nozzle N_O were used to prevent agglomeration of the suspension during the experiment.

Figure 2(b) is a detailed view of the rotating container C and the slip ring. The inside of the housing (made of clear acrylic resin) is a spherical surface with a radius of 94.49 mm, and the outside of the core (made of duralumin) consists of a spherical surface (87.90 mm) and a cylindrical surface ($a = 72.64$ mm). The feed pipe is fixed to the slip ring's stationary section.

The feed suspension comprises the feed powder, a dispersion medium, and a dispersant which were, respectively, polymethyl methacrylate spherical particles with a true specific gravity (γ) of 1.19; water; and liquid synthetic detergent. In this experiment we used a feed powder mass concentration C_O of 0.5% for the feed suspension, and a dispersant mass concentration of 0.6% for the feed suspension.

Our classification test procedure for the batch method was as follows [6]. First, we supplied water in place of the feed suspension, and set container rotation rate n, through-flow rate Q, and feed suspension flow rate Q_O. In this way Ekman number E, Rossby number R_S, and the feed suspension flow rate ratio k_O (i.e., Q_O/Q) were set. Next the classification test was initiated by switching the water to feed suspension, and then concluded by switching back to water. When using 20°C water with this apparatus (characteristic length $a = 0.07264$ m), the following equations show the relationship among E, R_S, n (rpm) and Q ($m^3\ s^{-1}$).

$$E = 1.82\times10^{-3}/n,\ Rs = 4.65\times10^{4}\,Q/n^{0.5} \quad (5)$$

$$n = 1.82\times10^{-3}/E,\ Q = 9.16\times10^{-7}\,Rs/E^{0.5} \quad (6)$$

In this experiment flow rate ratio k_O was set at a constant 0.15. At this value, feed suspension flow rate Q_O is about 30% of the theoretical value of the flow rate passing through Ekman layer k (Ekman transport quantity q, discussed below), into which the feed suspension is delivered.

Particle size was measured with a light transmission centrifugal particle size analyzer (SA-CP4L), by which we determined the cumulative oversize distrib-

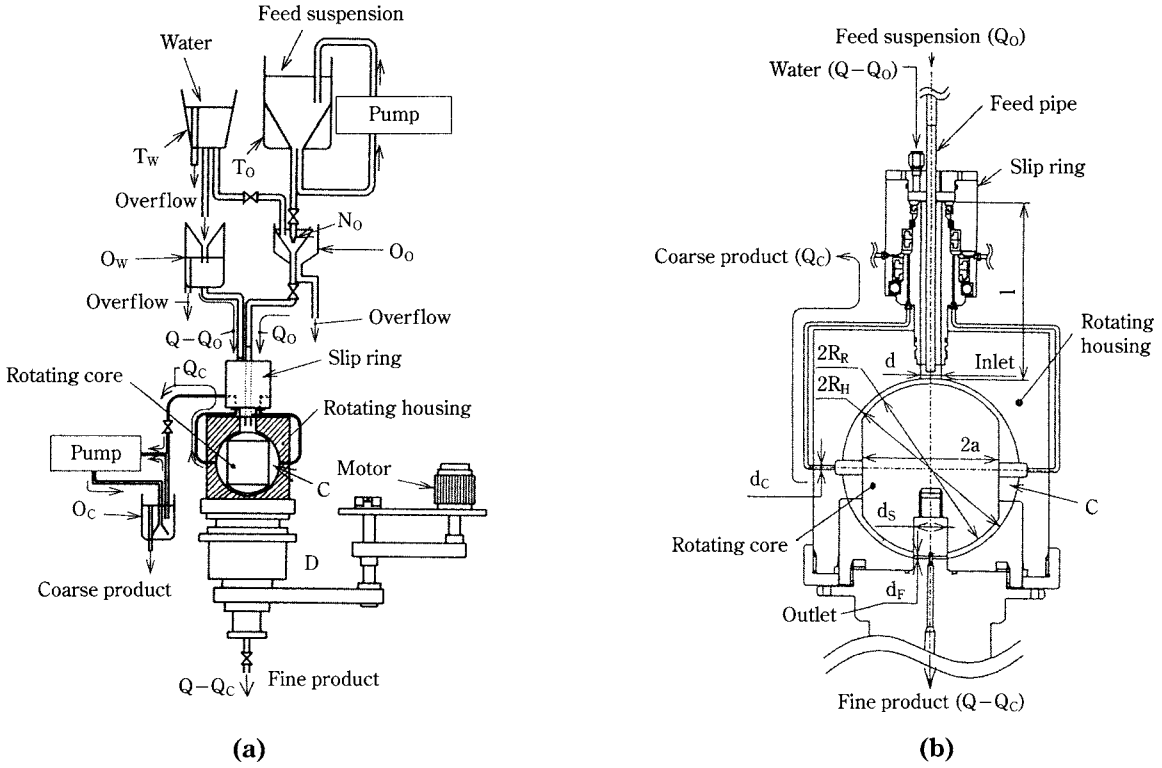

Fig. 2 Experimental apparatus

(a) Total system (C: rotating container; D: drive system, T_O, T_W: tanks for feed suspension and water; O_O, O_W, O_C: overflow tanks for feed suspension, water, and coarse product; N_O: dispersion nozzle)

(b) Rotating container C and slip ring
Dimensions (mm): housing: $R_H = 94.49$; core: $a = 72.64$, $R_R = 87.90$; inlet: $d = \phi21.8$, $l = 179.5$; extraction: $d_C = 4-\phi4$; outlet: $d_F = 4-\phi4$, $d_S = \phi34$)

ution $R(D_P)$ (mass base).

The fine powder yield, which is defined by this equation,

$$\eta_F = \text{mass flow rate of fine product / mass flow rate of feed powder} = \rho_f Q C_F / (\rho_f Q_O C_O) = C_F / (k_O C_O) \quad (7)$$

was found by measuring the mass concentration C_F of the fine product because k_O and C_O are values set as previously noted.

2.2.2 Classification Performance Assessment Method

In order to assess classification performance more accurately, we functionally approximated, as in the following equation, the discrete data for the cumulative oversize distributions $R_O(D_P)$ and $R_F(D_P)$ of the feed powder and fine product, respectively, obtained by particle size measurements (the subscripts O and F are omitted).

$$R = 10\exp(-10\exp y) \quad (\text{i.e., } y = \log_{10}\{\log_{10}(1/R)\}),$$
$$y = A_1 x + A_2 \sin(A_3 x) + A_4,\ x = \log_{10} D_P \quad (8)$$

A_1, A_2, ... are constants determined by the least squares method. As shown in **Figure 3**, this functional approximation is more accurate than the linear approximation $y = A_5 x + A_6$ (corresponding to a Rosin-Rammlar approximation) on a Rosin-Rammlar diagram (x–y plane). We were able to bring the R approximation error down to less than the error of repeated particle size measurements (under 5%).

The frequency distributions of the feed powder and fine product, f_O and f_F, which are defined by the following equations, are determined from the differential coefficient dR/dD_P obtained from Eq. 8, and the fine powder yield η_F of Eq. 7.

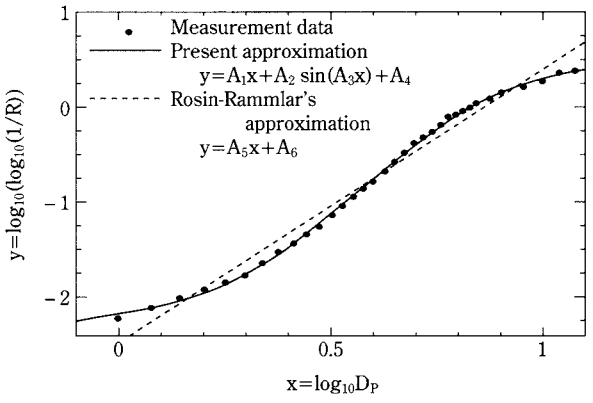

Fig. 3 Approximation of the mass-base oversize distribution $R(D_P)$ on a Rosin-Rammlar diagram of the x-y plane ($D_P(\mu m)$, $R(-)$)

$$f_O(D_P) = -dR_O/dD_P,$$
$$f_F(D_P) = -\eta_F dR_F/dD_P \quad (9)$$

Eq. 10 gives the fine product's partial fractional efficiency.

$$\Delta\eta(D_P) = f_F(D_P)/f_O(D_P) \quad (10)$$

The coarse product's cumulative oversize distribution and frequency distribution are determined using these two equations from the law of conservation of mass before and after classification.

$$R_C = (R_O - \eta_F R_F)/(1-\eta_F) \quad (11)$$

$$f_C(D_P) = f_O(D_P) - f_F(D_P) \quad (12)$$

2.2.3 Results and Discussion of Classification Test

Figure 4 shows the cumulative oversize distribution $R(D_P)$, frequency distribution $f(D_P)$, and partial fractional efficiency $\Delta\eta(D_P)$ obtained with an Ekman number of $E = 7.0\times10^{-6}$ and a Rossby number of $R_S = 8.3\times10^{-3}$ ($n = 260$ rpm and $Q = 2.87\times10^{-6}$ m^3 s^{-1} from Eq. 6). Discrete data for cumulative oversize distribution are quite accurately approximated by the curves in the above approximation functions (Eqs. 8 and 11). As the frequency distribution shows, the cut size D_{P50} (the particle size at which $f_F = f_C$) was 4.40 μm and therefore on the micrometer order, but that is because the rotation rate n was low as noted above. But as one can see from the partial fractional efficiency, the sharpness index S (the particle size ratio D_{P25}/D_{P75}, at which $\Delta\eta$ is 25% and 75%; $S = 1$ for perfect classification) is 1.49, showing that comparatively high accuracy was obtained despite the low rotation rate.

Figure 5 shows the dependence of partial fractional efficiency on the Ekman number E (rotation rate n) when the Rossby number was constant ($R_S = 8.3\times10^{-3}$, $Q/n^{0.5} = 1.78\times10^{-7}$ m^{3}s$^{-0.5}$). In response to an E decrease (an n increase), partial fractional efficiency decreased considerably for large particle sizes, while it increased slightly for small particle sizes. The plot approaches the efficiency curve for perfect classification perpendicular to the horizontal axis.

Figure 6 shows the dependence on the Ekman number E of the sharpness index S and cut size D_{P50} (the particle size at which $\Delta\eta = 50\%$) from **Figure 5**. D_{P50} became smaller as E decreased (as rotation rate

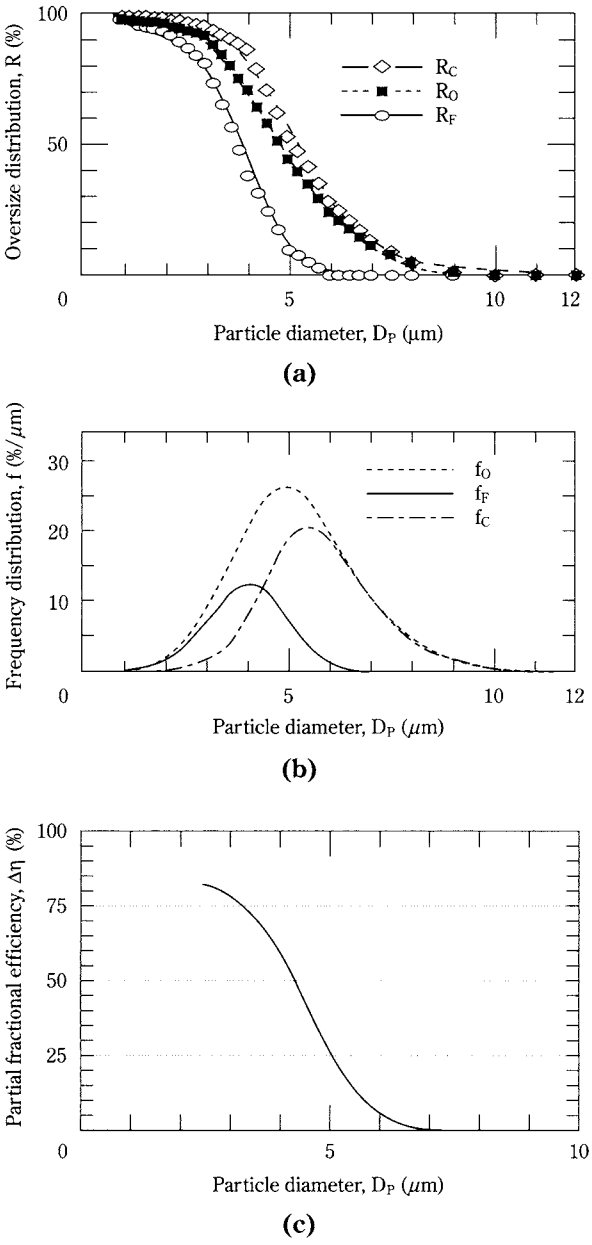

Fig. 4 Classification performance when $E = 7.0\times10^{-6}$ and $R_S = 8.3\times10^{-3}$
(a) Oversize distributions
(b) Frequency distributions
(c) Partial fractional efficiency of the fine product

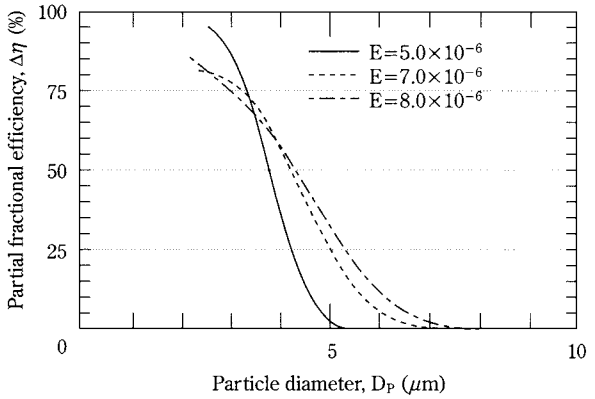

Fig. 5 Dependence of partial fractional efficiency on Ekman number E when $R_S = 8.3\times10^{-3}$

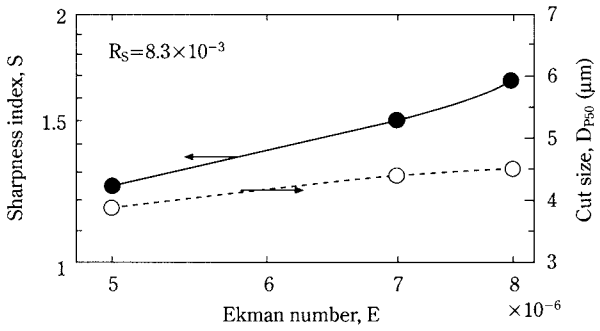

Fig. 6 Dependence of sharpness index and cut size on the Ekman number when $R_S = 8.3\times10^{-3}$

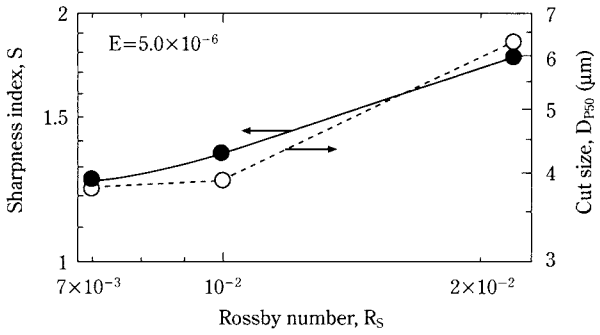

Fig. 7 Dependence of sharpness index and cut size on the Rossby number when $E = 5.0\times10^{-6}$

n increased), which is because the ratio of centrifugal force to the fluid drag acting on particles (Eq. 3) increased as E decreased. Meanwhile, S approached the value for perfect classification ($S = 1$) as E decreased, which shows that an increase in the effect of centrifugal force increased classification accuracy.

Figure 7 shows the dependence on the Rossby number R_S (through-flow rate Q) of the sharpness index S and the cut size D_{P50} obtained when the Ekman number was constant ($E = 5.0\times10^{-6}$, $n = 363$ rpm). D_{P50} became smaller as R_S decreased (Q decreased) because the ratio of centrifugal force to fluid drag (Eq. 3) increased as R_S decreased. In other words, a decrease in the through-flow rate induced a decrease in fluid drag, bringing about a relative increase in the centrifugal force effect, which resulted in a smaller cut size. Meanwhile, S approached 1 as R_S decreased. This increase in classification accuracy was also due to the heightened centrifugal force effect.

Figure 8 shows the dependence of the fine powder yield η_F on Ekman number E and Rossby number R_S. η_F became smaller when E diminished (n increased) while R_S remained constant ($Q/n^{0.5}$ was constant), and when R_S decreased (Q decreased) while E remained constant (n was constant). The reason is that because, as noted above, the ratio of centrifugal force to fluid drag increased as either E or R_S decreased, causing smaller particles to appear among the coarse product and decreasing the proportion of fine product.

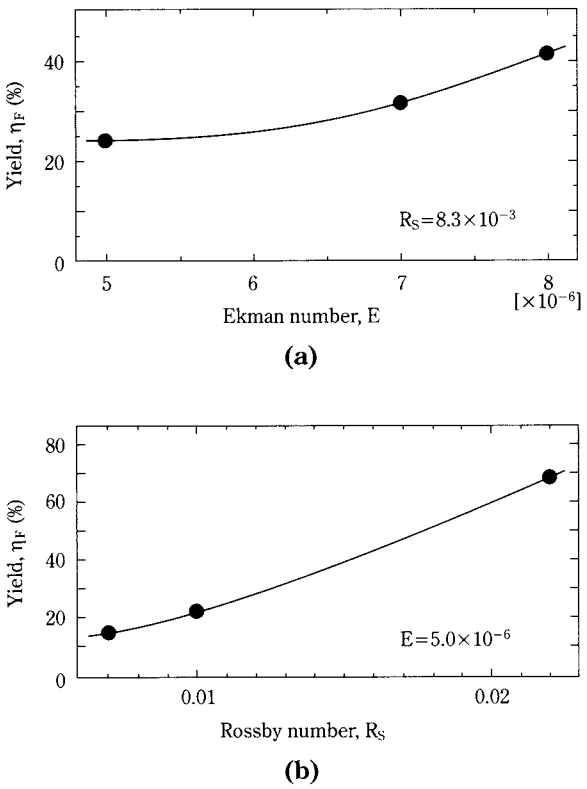

Fig. 8 Dependence of fine product yield on the Ekman and Rossby numbers
(a) Ekman number dependence for $R_S = 8.3\times10^{-3}$
(b) Rossby number dependence for $E = 5.0\times10^{-6}$

2.3 Application of an Almost Rigidly Rotating Flow to Classification

2.3.1 Almost Rigidly Rotating Flow Overview

When the feed suspension has a low mass concentration, it is possible to treat the flow as a single-phase flow of the medium fluid (the incompressible viscous fluid water). The dimensionless governing equation (made dimensionless as before) of this steady flow (velocity $\boldsymbol{u}$, pressure p reduced by centrifugal force) in a rotating coordinate system is given by the following Navier-Stokes equation (meaning of each term is shown) and continuity equation.

$$R_S(\boldsymbol{u}\cdot\nabla)\boldsymbol{u}+2\boldsymbol{k}\times\boldsymbol{u} = -\nabla p+E\nabla^2\boldsymbol{u} \tag{13}$$

(inertial force) (Coriolis force)
(pressure gradient) (viscous force)

$$\nabla\cdot\boldsymbol{u} = 0 \tag{14}$$

The almost rigidly rotating flow [7, 8] is the flow when the Rossby number R_S is small (small throughflow, rapid rotation), and is given by the following equation.

$$2\boldsymbol{k}\times\boldsymbol{u} = -\nabla p+E\nabla^2\boldsymbol{u} \tag{15}$$

This equation is the governing equation in the boundary layers, i.e., the Ekman layers and Stewartson layers, that arise near walls and where flow shearing is great. Because the influence of viscous force can be ignored in the interior regions, which are the regions other than the boundary layers, there is a geostrophic balance in which Coriolis force and the pressure gradient balance each other. This is where the Taylor-Proudman theorem works, i.e., velocity does not change in the rotation axis direction.

The Ekman layers (k, l, k′, and l′ in **Figure 1**), which are boundary layers that form near the walls that are not parallel to the rotation axis, function to harmonize the velocity distributions of the interior regions (i, i′) with the no-slip conditions on the walls. By contrast, the Stewartson layers (m, n, and n′) are boundary layers formed near walls parallel to the rotation axis (the part of m near the core's cylindrical wall) and areas that are parallel to the rotation axis and have an azimuthal velocity gradient (the remaining parts of m, plus n and n′). The former Stewartson layer along the wall functions to harmonize the velocity distribution of the region on one side of this layer with no-slip conditions on the wall, while the function of the latter free Stewartson layers is to harmonize the velocity distribution in the regions on both sides of this layer.

2.3.2 Flows of Ekman Layers and Interior Region

We shall begin by explaining the flow structure of Ekman layers and the interior region, which affect partial fractional efficiency. Theoretical solutions of the steady and axisymmetric flows of Ekman layers, and the interior region shown by Eqs. 14 and 15 can be derived with the singular perturbation method as shown below, because of a small coefficient E for the highest-degree differential in Eq. 15 [9].

Velocity components of the interior regions (i and i′ in **Figure 1**)

$$u_I = 0 + O(E) \tag{16a}$$

$$v_I = -4C_Q r^{-1}[(1+b_L'^2)^{0.25} + (1+b_U'^2)^{0.25}]^{-1} + O(E^{0.5}) = O(E^0) \tag{16b}$$

$$w_I = -C_Q E^{0.5} r^{-1} \times (1+b_L'^2)^{-0.75}(1+b_U'^2)^{-0.75} \times \{b_L' b_L''(1+b_U'^2) - b_U' b_U''(1+b_L'^2)\} \times [(1+b_L'^2)^{0.25} + (1+b_U'^2)^{0.25}]^{-2} + O(E) = O(E^{0.5}) \tag{16c}$$

Velocity components of the Ekman layers (k, l, k′, and l′)

$$u = -(1+b'^2)^{-0.5} v_I \exp(-\tau)\sin\tau = O(E^0) \tag{17a}$$

$$v = v_I[1 - \exp(-\tau)\cos\tau] = O(E^0) \tag{17b}$$

$$w = -b'(1+b'^2)^{-0.5} v_I \exp(-\tau)\sin\tau = O(E^0) \tag{17c}$$

$$G = (1+b'^2)^{-0.5}(b'w+u) = -v_I \exp(-\tau)\sin\tau = O(E^0) \tag{17d}$$

Where:

b is an arbitrary function of r, which indicates the axisymmetric wall shape;

L and U subscripts denote variables relating to the Ekman layers near walls (upper and lower) where the value of b is large and small, respectively, in flow fields;

C_Q is the non-dimensional flow rate between the upper and lower walls; and

τ (next equation) is the stretched coordinate perpendicular to each wall and rendered non-dimensional by $(\nu/\Omega_N)^{0.5}$, equivalent to Ekman layer thickness, given below.

$$\tau = \tau^*/(\nu/\Omega_N)^{0.5} = (\pm 1)E^{-0.5}(z-b)(1+b'^2)^{-0.75}$$
$$(\pm 1: +1 \text{ (for lower wall) and } -1 \text{ (for upper wall)} \tag{18}$$

Figure 9 shows the velocity distribution of the interior region i ($C_Q = 1$) between the upper and lower walls

$$\text{Lower wall: } b_L = \{1.21^2 - r^2\}^{0.5},$$
$$\text{Upper wall: } b_U = \{1.30^2 - r^2\}^{0.5} \ (0.15 < r < 1, z > 0) \tag{19}$$

of the concentric double-walled sphere surface of the experimental apparatus in **Figure 2(b)**. Azimuthal velocity v_I approaches the velocity of the rotating system ($v_I = 0$) as radius r increases, the reason being that in Eq. 16b the absolute values of the slopes b_L' and b_U' increase with r due to the nature of the upper and lower spherical surfaces. On the other hand, the axial velocity w_I (Eq. 16c), which is the small amount of $O(E^{0.5})$, and is dependent not only on wall slope but also on rates of change b_L'' and b_U'', exhibits negative values (downward axial flow) whose absolute values increase as r increases. As long as the flow is axisymmetric, radial velocity u_I is zero without regard to wall shape because there is a balance between the Coriolis force, which is dependent on u_I, and the pressure gradient ($u_I = -r^{-1}\partial p_I/\partial\phi$).

Figure 10 plots the distributions in the direction (τ) normal to the wall of azimuthal velocity v in the Ekman layer arising near the concentric double-walled sphere surface described above, and of tangential velocity G. The τ distribution forms of $v/(-v_I)$ and $G/(-v_I)$ are the same as those of the two rotating disks ($b_L' = b_U' = 0$), and thus the influence of wall

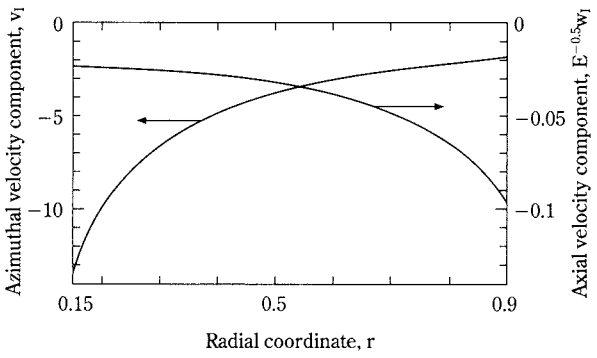

Fig. 9 Radial distributions of the azimuthal and axial velocity components v_I and w_I in the interior region

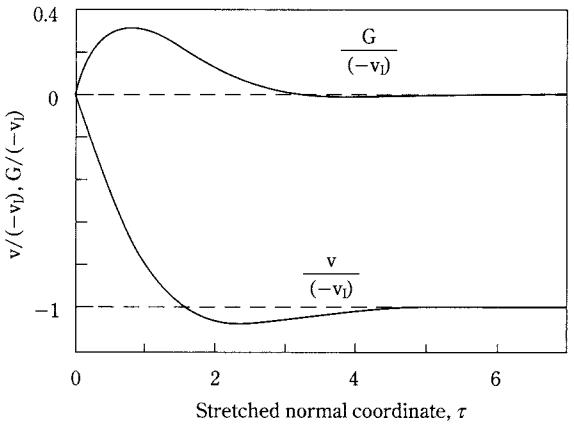

Fig. 10 Normal (τ) distributions of the azimuthal and tangential velocity components v and G, divided by $-v_I$, in the Ekman layer

shape (slope b', curvature b'') does not appear explicitly. This is because, as we know from Eqs. 17b and 17d, the influence of wall shape is completely included in v_I (Eq. 16b) and τ (Eq. 18). Further, b' and b'' appear explicitly in the distribution forms of radial and axial velocity u and w.

In **Figure 10** both v and G gradually approach the values (G_I is the small quantity of $O(E^{0.5})$) in the interior region for $\tau \cong \pi$ ($\tau^* \cong \pi\ (\nu/\Omega_N)^{0.5}$ in the dimensional quantity). Hence the following equation is obtained with regard to Ekman layer thickness (dimensional δ^*, non-dimensional δ).

$$\delta^* \fallingdotseq \pi\ (\nu/\Omega_N)^{0.5},$$
$$\delta = \delta^*/a \fallingdotseq \pi E^{0.5}(1+b'^2)^{0.25} = O(E^{0.5}) \tag{20}$$

To further examine Ekman layer flow, we introduce Ekman transport quantity q (the flow rate that passes through the cylindrical surface at r in each Ekman layer, non-dimensionalized by Q), which is defined by the following equations.

$$q = 0.25\int_0^\infty 2ru(1+b'^2)^{0.75}d\tau$$
$$= C_Q(1+b'^2)^{0.25}[(1+b_L'^2)^{0.25}+(1+b_U'^2)^{0.25}]^{-1} + O(E^{0.5}) = O(E^0) \tag{21a}$$

$$\therefore q_L+q_U = C_Q,\quad q_L'+q_U' = 0 \tag{21b}$$

Based on Eqs. 20 and 16c, the relationship among Ekman transport quantity q, Ekman layer thickness δ, and interior region axial velocity w_I is that shown in the following equations.

$$q_L/q_U = (1+b_L'^2)^{0.25}/(1+b_U'^2)^{0.25} \sim \delta_L/\delta_U \tag{22a}$$

$$w_I = -2E^{0.5}r^{-1}q_L' = 2E^{0.5}r^{-1}q_U' = -E^{0.5}r^{-1}(q_L'-q_U') \tag{22b}$$

Figure 11 shows the above relationship for Ekman layers k and l, and interior region i, when the upper and lower walls have arbitrary shapes. In accordance with Eq. 20, δ is inversely proportional to $\Omega_N^{0.5}$. Accordingly, when the curvature of the lower wall is greater than that of the upper wall as shown in **Figure 11**, $\Omega_{NL} < \Omega_{NU}$ at r, so $\delta_L > \delta_U$. It follows that $q_L > q_U$ according to Eq. 22a (a large δ indicates large Ekman transport q). At radii larger than the above r, the thickness of the upper wall Ekman layer δ_U becomes thicker than at r (because Ω_{NU} decreases), but the thickness δ_L at the lower wall becomes even greater, and thus q_U becomes smaller than its value at r, while q_L grows larger (because $q_L'+q_U' = 0$ as in Eq. 21b). These increases and decreases in Ekman transport are induced by the downward axial flow w_I in the interior region, as shown by Eq. 22b.

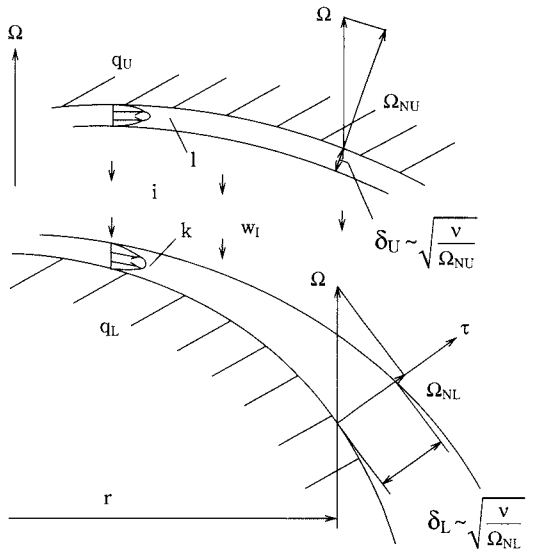

Fig. 11 Schematic of the relationship among Ekman transport q, thickness δ of the Ekman layer, and interior axial velocity component w_I

2.3.3 Conditions for Rigid Rotation Region Formation

The rigid rotation region (j in **Figure 1(a)**) is indispensable as a region for coarse product capture. The conditions for its formation are as follows. As long as the flow field is closed on the outside as seen in area j of **Figure 1(a)** (unrelated to the functional shape of wall shapes b_L and b_U), flow rate C_Q passing by the cylindrical surface at r in region j is zero. Thus from Eqs. 16 and 17 all velocity components become zero, and j becomes a rigid rotation region. In other words, to form this region the flow field is given as a concave shape facing the rotation axis.

2.3.4 Stewartson Layer Flow Structure

The flows of Ekman layer k and Stewartson layer m in **Figure 1(a)** play the most important roles in partial fractional efficiency. Because the Ekman layers have already been explained, this section will give a general description of the Stewartson layer flow structure. **Figure 12** shows the stream lines of the axisymmetric almost rigidly rotating flow in relation to the container shape of the experimental apparatus and obtained with a numerical analysis procedure from a previous paper [10]. The left figure is an enlargement of the right, but shows stream lines produced by different stream function values. A Stewartson layer arises along the core's cylindrical surface and near the extensions of that surface, and it consists of the through-flow region along the cylinder's surface

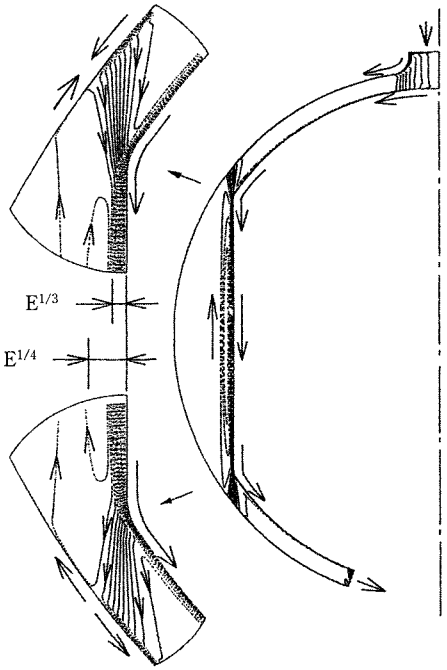

Fig. 12 Numerically simulated stream lines of the axisymmetric almost rigidly rotating flow when $E=5.0\times10^{-6}$ and $R_S=1.22\times10^{-2}$

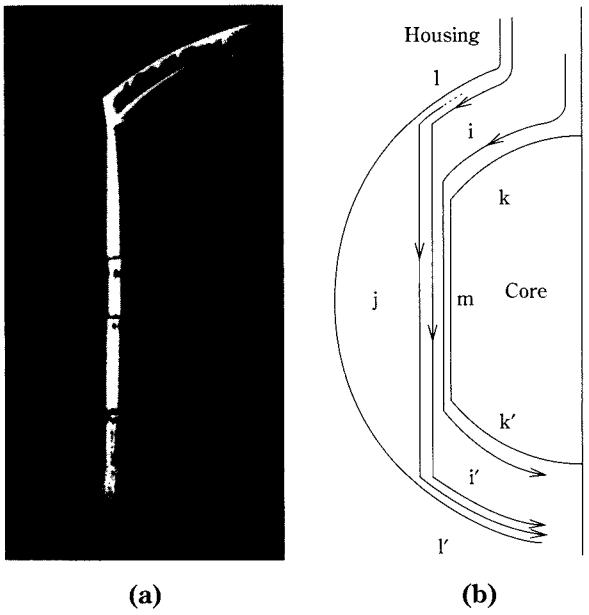

Fig. 13 Stable axisymmetric regime of the almost rigidly rotating flow when $E=5.0\times10^{-6}$ and $R_S=1.5\times10^{-2}$
(a) Visualized streak lines
(b) Schematic of stream lines

and the circulating flow region outside of the through-flow. The Stewartson layer is generally a compound layer comprising the $E^{1/3}$ and $E^{1/4}$ layers, whose thicknesses are, respectively, $O(E^{1/3})$ and $O(E^{1/4})$. **Figure 12** shows the thicknesses of the values of $E^{1/3}$ and $E^{1/4}$, which correspond to the value of E. From this it is evident that the $E^{1/3}$ layer corresponds to the through-flow region and the $E^{1/4}$ layer to the circulating flow region.

2.3.5 Conditions for the Formation of a Stable Almost Rigidly Rotating Stratified Flow

We employed the laser-induced fluorescence method to experimentally determine the formation conditions of a stable axisymmetric almost rigidly rotating flow. This entailed training an argon laser on fluorescein sodium coloring ($C_{20}H_{10}O_5Na_2$) injected into the through-flow, and observing fluorescent coloring streak lines. **Figure 13(a)** is a photograph taken when using water instead of feed suspension. Because of the suspension's low concentration, there was no clear difference between the results from water and the suspension. Observations revealed that under flow conditions of $0<R_S\leq2.5\times10^{-2}$ and $4.0\times10^{-6}\leq E\leq8.0\times10^{-6}$, a stable axisymmetric almost rigidly rotating flow arose as shown in **Figure 13(b)** (a sketch of the stream lines determined from streak lines).

2.3.6 Relationship Between Flow Structure and Classification Performance

As explained above, it is necessary to introduce the feed suspension over the core's rotation axis and put it into Ekman layer k because if the suspension is fed into the entire gap, it will also enter Ekman layer l (see **Figures 1** and **12**), allowing fine particles that arrive near the housing wall to advance into rigid rotation region j from Stewartson layer m. Fine particles would thus be captured as coarse product, thereby impairing classification accuracy.

Feed particles fed into Ekman layer k are subject to the strong azimuthal shearing effect (see $v/(-v_I)$ in **Figure 10**) along the core wall due to the wall's tangential velocity ($G/(-v_I)$ in **Figure 10**), resulting in particle trajectory separation. And because the interior region's axial velocity (w_I in **Figure 9**) is negative, there is a flow proceeding from the housing toward the core (see **Figure 11**), making it impossible for fine particles to be carried to Ekman layer l on the housing side. Trajectory separation of particles that make their way from Ekman layer k to Stewartson layer m is facilitated by the $E^{1/3}$ or $E^{1/4}$ layer (**Figure 12**), and ultimately coarse particles are confined in the rigid rotation region, while fine particles are emitted from the outlet.

As this discussion shows, this classification meth-

od makes synergistic use of the powerful shearing flow in Ekman layers and the fast rotational flow in Stewartson layers to effectively facilitate particle trajectory separation, and it uses the interior region flow and the rigid rotation region to achieve highly accurate classification.

The effects of E and R_S on the sharpness index, cut size, and fine powder yield (section 2.2.3) obtained in classification testing are qualitatively the same, as shown by the ratio of the centrifugal force to the fluid drag acting on particles (Eq. 3). However, the reason that experimental results show a quantitative difference is that, due to the difference in particle size D_P in Eq. 3, and the particle disparity at the inlet, differences arise in the trajectories of particles, resulting in a different $|\boldsymbol{v}-\boldsymbol{u}|$ for each particle.

3. Continuous Type

3.1 Flow Structure Changes and Particle Movement Induced by Extraction

The right half of **Figure 1(b)** shows the flow structure of the continuous method, and the left half is a simplified representation of the flow's stream lines and particle trajectories. The housing is spherical while the core's outer surface is spherical and cylindrical. Both parts rotate together at angular velocity Ω. The feed suspension is fed into this rotating container via the feed pipe (flow rate Q_O), and water is fed in through the inlet (flow rate $Q-Q_O$). While this procedure is the same as that for batch processing, the difference is that coarse product suspension is extracted from the housing's equatorial section (extraction flow rate Q_C). Accordingly, the fine product's suspension flow rate at the outlet is $Q-Q_C$. The flow control parameters, the Ekman number E and the Rossby number R_S, are obtained with the same defining equation (Eq. 4) as in the batch method, and extraction ratio k_C is defined by this equation.

$$k_C = Q_C/Q \ (<1) \tag{23}$$

If product is extracted at Q_C from the housing's equatorial position, the Ekman transport quantities arising in Ekman layers t and t′ along the upper and lower walls are, according to Eq. 21a, both 0.5 Q_C because the housing wall shape is symmetrical to the equatorial surface. Assuming that this Ekman transport is supplemented from region j′, the supplement would have to be supplied from interior region j′ as Ekman suction. But because the Taylor-Proudman theorem works, and because of this flow region's equatorial symmetry, the axial flux component is zero. If the walls were flat, the axial vorticity component of interior region j′ would be proportional to its axial velocity component, and therefore zero due to Ekman compatibility conditions, but when the wall is a spherical surface, the axial vorticity component is not zero but a function of r alone due to the curvature effect [11]. Therefore the value of the azimuthal velocity component of interior region j′ is unrelated to z, and changes only in relation to r. As this shows, the region that was the rigid rotation region in the batch method is transformed by extraction into interior region j′ and Ekman layers t and t′.

Meanwhile, the flow rate of Stewartson layer m becomes $Q-0.5Q_C$ by extraction, but in the downstream part of m the $0.5Q_C$ portion is carried by Ekman transport to Ekman layer t′, while the remaining $Q-Q_C$ divides and flows into Ekman layers k′ and l′, ultimately exiting from the outlet. Thus the E and R_S conditions for a stable rotating stratified flow, which were ascertained in batch method testing, do not change in regions n, k, l, and i, but in regions n′, k′, l′, and i′ Rossby numbers alone decrease, while Ekman numbers do not change, and thus the flow moves to the stable side [12]. For this reason the flow stream lines discussed above assume the configuration in the left half of **Figure 1(b)**.

Owing to the flow change induced by coarse product extraction, powder particle motion from Stewartson layer m and thereafter differs from that of the batch method. When the values of R_S and E are the same as in the batch method, the axial velocity in Stewartson layer m is lower than that in the batch method, as noted above. This increases the particle residence time in m, as well as the time that centrifugal force acts on particles, thereby pulling particle trajectories farther outward than in the batch method. This tendency increases as Q_C increases.

3.2 Performance Assessment by Classification Testing

3.2.1 Experimental Method

The classification testing method consisted of the batch method illustrated in **Figure 2(a)**, to which we added an operation using the extraction mechanism described above. Specifically, we first fed in water instead of the feed suspension, and set rotation rate n, through-flow quantity Q, feed suspension flow rate Q_O, and extraction flow rate Q_C. The classification test was then initiated by switching from water to feed suspension, and the test was concluded by switching back to water.

Because of the extraction of flow rate Q_C (extrac-

tion ratio k_C), fine powder yield η_F is:

$$\eta_F = \text{mass flow rate of fine product / mass flow rate of feed powder}$$
$$= \rho_f(Q-Q_C)C_F/(\rho_f Q_O C_O)$$
$$= (1-k_C)C_F/(k_O C_O) \quad (24)$$

Because k_C, k_O, and C_O are set values as above, η_F was determined by measuring the mass concentration C_F of the fine product as in the batch method.

The rest of the experimental method was the same as that for batch processing.

3.2.2 Results and Discussion of Classification Testing

First we shall discuss the effects of extraction ratio k_C on classification performance when Ekman number E and Rossby number R_S are constant.

Figure 14 presents an example ($k_C = 0.4$) of the cumulative oversize distribution $R(D_P)$ obtained by varying extraction ratio k_C when $E = 5.0\times10^{-6}$ and $R_S = 1.2\times10^{-2}$ ($n = 363$ rpm and $Q = 4.92\times10^{-6}$ m^3 s^{-1} according to Eq. 6). The curves in the graph are approximation function curves of measured data determined as in Eqs. 8 and 11 in order to accurately assess classification performance.

Figure 15 shows the change induced by extraction ratio k_C in the frequency distribution $f(D_P)$ determined from the functions of the approximation curves in **Figure 14**. When the extraction ratio was increased to $k_C = 0.4$ (**Figure 15(a)**), which is greater than the no-extraction ratio $k_C = 0$ (of the batch method), the frequency increased in the range where particle size D_P of the fine product f_F was small (around 2 μm), but frequency decreased at larger particle sizes, and the percentage of coarse particles in the fine product decreased as k_C increased. The reason that coarse particles in the fine product decreased as k_C increased is that, as noted previously, because non-dimensional Ekman transport (0.5 k_C) in Ekman layer t (**Figure 1(b)**) increases with k_C, the non-dimensional flow rate (1−0.5 k_C) in Stewartson layer m, which is the classification field, decreases; axial flow velocity in m thus becomes smaller, and the time that centrifugal force acts on particles increases with k_C. Because of the increase or decrease in f_F depending on particle size, which occurred in conjunction with the above-mentioned k_C increase, and the corresponding increase or decrease in f_C ($=1-f_F$) depending on particle size, the particle size at which $f_F = f_C$ (cut size D_{P50}) and the graph area sandwiched between the f_F curve and the horizontal axis (fine powder yield η_F) decreased as k_C increased. Increasing the extraction ratio to $k_C = 0.6$ (**Figure 15(b)**) decreased the frequency of not only the fine product's larger particles but also its finer particles (increased frequency in the coarse product), and there were further decreases in cut size and fine powder yield.

Figure 16 shows the change that extraction ratio k_C brought about in the partial fractional efficiency $\Delta\eta(D_P)$ of the fine product as determined from the frequency distribution in **Figure 15**. **Figure 17** plots the dependence of the sharpness index S and cut size D_{P50}, sought from **Figure 16**, on extraction ratio k_C. As **Figure 17** shows, the sharpness index S was nearly

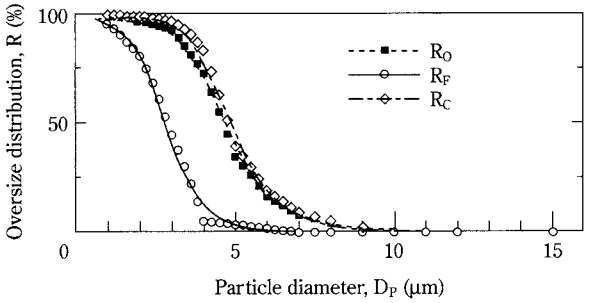

Fig. 14 Oversize distribution for $k_C = 0.4$, $E = 5.0\times10^{-6}$, and $R_S = 1.2\times10^{-2}$

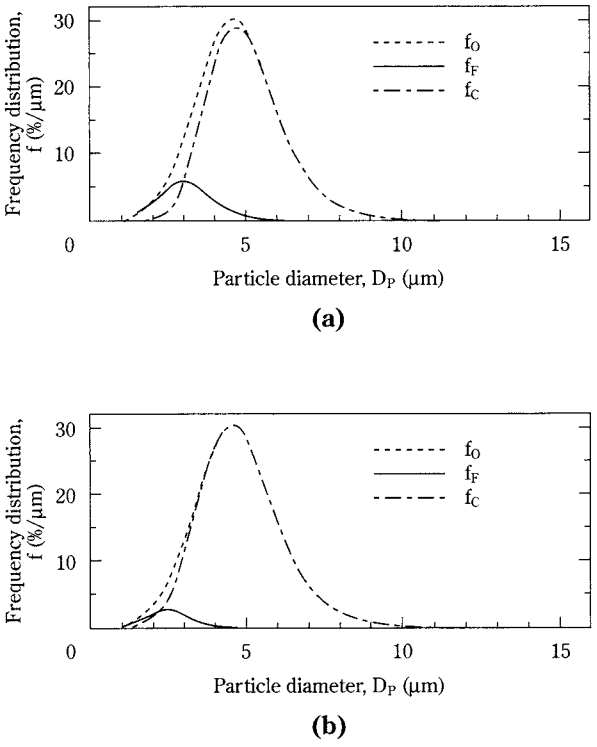

Fig. 15 Change in frequency distribution caused by extraction ratio k_C when $E = 5.0\times10^{-6}$ and $R_S = 1.2\times10^{-2}$
(a) $k_C = 0.4$
(b) $k_C = 0.6$

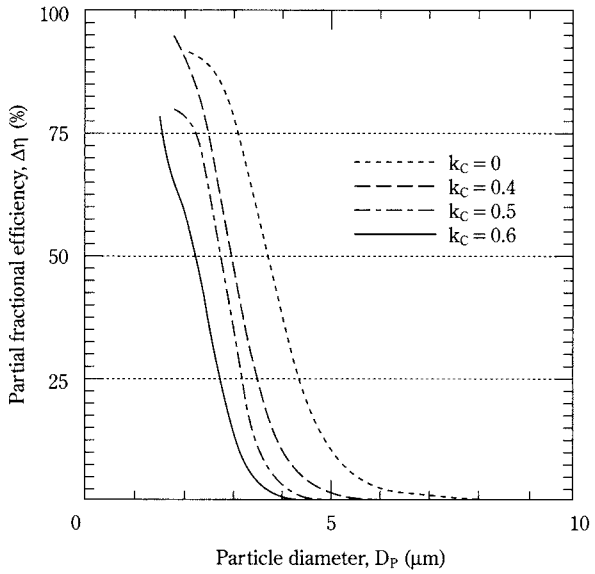

Fig. 16 Change in partial fractional efficiency caused by extraction ratio k_C when $E = 5.0\times10^{-6}$ and $R_S = 1.2\times10^{-2}$

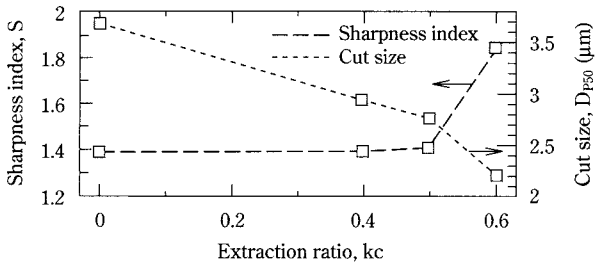

Fig. 17 Dependence of sharpness index and cut size on extraction ratio k_C when $E = 5.0\times10^{-6}$ and $R_S = 1.2\times10^{-2}$

constant at 1.39 when k_C was under 0.5, thereby exhibiting the same high classification accuracy as in the batch method ($k_C = 0$). But when $k_C = 0.6$, S rose to 1.84 and accuracy quickly declined. Meanwhile, cut size D_{P50} fell at a nearly steady rate as k_C increased while staying under 0.5, but it plummeted when $k_C = 0.6$. These results came about for this reason: When k_C is under 0.5, the partial fractional efficiency curves in **Figure 16** (which would be perpendicular to the horizontal axis if classification were perfect) shift toward smaller particle sizes as k_C increases while maintaining about the same highly accurate distribution as in the batch method, but when k_C is 0.6 the said shift degenerates because of the decreased partial fractional efficiency at particle sizes under approximately 2 μm.

The cause of this sudden cut size drop at $k_C = 0.6$ (i.e., the sudden increase in the proportion of fine particles captured as coarse product) and the rapid worsening of classification accuracy is likely that part of the flow (that near interior region i) passing through Ekman layer k (**Figure 1(b)**) over the rotating core into which the feed suspension is fed, is extracted when $k_C = 0.6$. Accordingly, maintaining high classification accuracy in continuous processing as in batch processing necessitates keeping extraction ratio k_C under a certain threshold value (called the critical extraction ratio k_{CS} concerning the sharpness index). In the foregoing example k_{CS} is about 0.5.

Now let us examine the effect of Ekman number E and Rossby number R_S (i.e., the effect of rotation rate n and through-flow Q) on the relationship between classification performance and extraction ratio as noted above.

Figure 18(a) plots the relationship between the sharpness index S and k_C under three sets of E and R_S conditions: A ($E = 5.0\times10^{-6}$, $R_S = 1.0\times10^{-2}$), B ($E = 7.0\times10^{-6}$, $R_S = 1.0\times10^{-2}$), and C ($E = 5.0\times10^{-6}$, $R_S = 1.2\times10^{-2}$). Set C conditions were the E and R_S conditions given above ($n = 363$ rpm, $Q = 4.92\times10^{-6}$

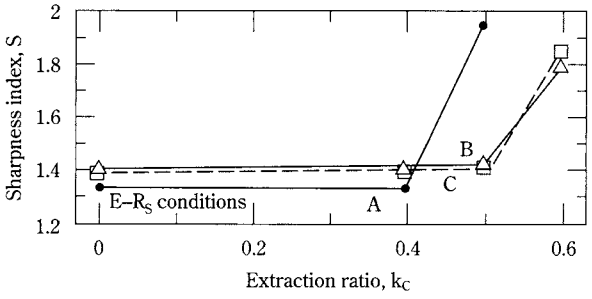

(a)

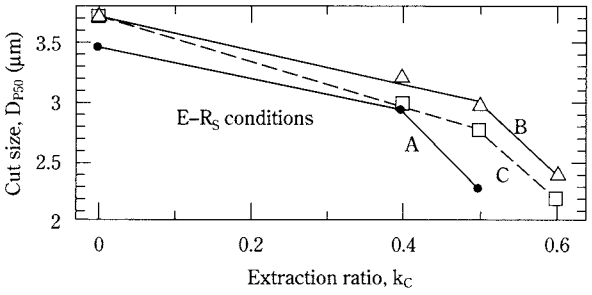

(b)

Fig. 18 Relationship between classification performance and extraction ratio for three sets of conditions of Ekman and Rossby numbers, A ($E = 5.0\times10^{-6}$, $R_S = 1.0\times10^{-2}$), B ($E = 7.0\times10^{-6}$, $R_S = 1.0\times10^{-2}$) and C ($E = 5.0\times10^{-6}$, $R_S = 1.2\times10^{-2}$)
(a) Relationship between sharpness index and extraction ratio
(b) Relationship between cut size and extraction ratio

$m^3\ s^{-1}$); set A had a smaller R_S (smaller through-flow Q) than C ($n = 363$ rpm, $Q = 4.10 \times 10^{-6}\ m^3\ s^{-1}$), and set B had a larger E (decreasing rotation rate n while holding $Q/n^{0.5}$ steady) than A ($n = 260$ rpm, $Q = 3.46 \times 10^{-6}\ m^3\ s^{-1}$). It is evident from the graph that the relationship between S and k_C under the conditions for A and B was the same as that under the aforementioned C conditions. However, the value of critical extraction ratio k_{CS} became larger with the increase in Ekman number (decrease in rotation rate n) from A to B, or the increase in Rossby number (increase in through-flow) from A to C ($k_{CS} \approx 0.4 \rightarrow 0.5$). The k_{CS} increase in the former case (from A to B) happened because slower rotation causes decreased centrifugal force, which made it more difficult for fine particles to be extracted as coarse product; in the latter case, increased through-flow made particles traverse the classification field faster, which reduced the time they are subject to centrifugal force, and made it harder for fine particles to be extracted. **Figure 18(b)** plots the relationship between cut size D_{P50} and k_C for the above three sets of conditions in relation to E and R_S. This relationship likewise exhibits changes corresponding to those in k_{CS} engendered by the conditions of E and R_S.

Figure 19 shows the critical extraction ratio k_{CS}, obtained from **Figure 18(a)**, on a parameter plane for Ekman number E and Rossby number R_S. As described above, the value of k_{CS} becomes smaller when the Ekman number decreases (rotation rate n increases) and the Rossby number decreases (through-flow decreases).

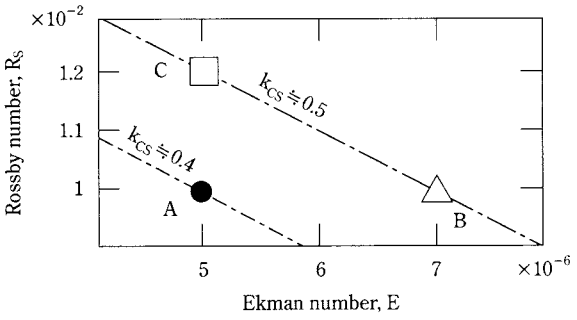

Fig. 19 Critical extraction ratio k_{CS} concerning the sharpness index on the $E-R_S$ parameter plane
(A, B, and C have the same $E-R_S$ conditions as in **Figure 18**)

4. Conclusion

We explored a new wet centrifugal classification system employing a stable, axisymmetric almost rigidly rotating flow that arises when making a small amount of water flow through a rapidly rotating double-walled container. We arrived at the following conclusions.

(1) In the batch (no-extraction) method, we found that the smaller the through-flow when the rotation rate is constant, and the larger the rotation rate when the through-flow is constant, the smaller the cut size and fine powder yield, and the more the sharpness index approaches the value of perfect classification.

(2) The condition for creating the rigid rotation region, which is the region where coarse product is captured in the batch method, is to give the flow field a form that is closed on one side that has an arbitrary concave shape facing the rotation axis.

(3) Extraction changes the rigid rotation region in the batch method into an Ekman layer and an interior region. Thus in continuous processing, this Ekman layer and interior region flow quickly expel coarse particles from the classification field, and thus, just as in batch processing, it is impossible for coarse particles to be mixed into the fine product.

(4) In continuous processing the cut size and fine powder yield decrease as the extraction flow rate increases, but the sharpness index has the same high accuracy as in the batch method without exceeding the critical extraction ratio. However, when the critical extraction ratio is exceeded, the sharpness index quickly rises and accuracy falls.

(5) In continuous processing the critical extraction ratio's value becomes smaller as the Ekman number decreases (rotation rate increases) or the Rossby number decreases (through-flow decreases).

(6) Highly accurate classification performance obtained under the critical extraction ratio is achieved through a detailed understanding of the flow structure. Particle trajectory separation is facilitated by the synergistic effect of: supplying feed suspension into Ekman layer k near the rotating core wall; particle dispersion by the strong shearing flow in the Ekman layers; the effect of the flow in interior region i heading from the housing toward the core, which works to keep fine particles near the core wall; and the rapidly rotating flow of Stewartson layer m.

The authors wish to express their appreciation for research assistance under Ministry of Education Grant-in-Aid for Developmental Research B2 (project number 03555037).

Nomenclature

A	Constants (Eq. 8)	(−)
a	Radius of the cylindrical part of the rotating core (characteristic length)	(m)
b	Dimensionless arbitrary function of r, indicating an axisymmetric wall configuration	(−)
C	Mass concentration of suspension	(−)
C_Q	Flow rate, non-dimensionalized by Q, of the flow passing by the cylindrical surface at r between the lower and upper walls	(−)
D_P	Spherical particle diameter	(m)
D_{PN}	Particle diameter for $\Delta\eta = N(\%)$ (D_{P50}: cut size)	(m)
E	Ekman number, $\nu/(\Omega a^2)$	(−)
$\boldsymbol{F}_c$	Centrifugal force acting on particles (Eq. 1)	(N)
$\boldsymbol{F}_d$	Drag acting on particles (Eq. 2)	(N)
$f(D_P)$	Frequency distribution (mass base, Eqs. 9 and 12)	(m^{-1})
G	Dimensionless velocity component tangential to the wall (Eq. 17d)	(−)
$\boldsymbol{i}, \boldsymbol{k}$	Unit vectors in the radial and axial directions	(−)
k_C	Extraction ratio, Q_C/Q	(−)
k_{CS}	Critical extraction ratio concerning the sharpness index, Q_C/Q	(−)
k_O	Feed suspension ratio, Q_O/Q	(−)
n	Rotation rate of the rotating container, $30\,\Omega/\pi$	(rpm)
p	Pressure reduced by centrifugal force, non-dimensionalized by $\rho_f \Omega a U_E$	(−)
Q	Through-flow rate	($m^3\,s^{-1}$)
Q_C	Extraction flow rate	($m^3\,s^{-1}$)
Q_O	Feed suspension flow rate	($m^3\,s^{-1}$)
q	Ekman transport at r on each wall, non-dimensionalized by Q (Eq. 21a)	(−)
$R(D_P)$	Oversize distribution (mass base, Eqs. 8 and 11)	(−)
(r^*, ϕ, z^*)	Rotating cylindrical coordinate system (radial, azimuthal, and axial coordinates), (ar, ϕ, az)	(m, −, m)
R_S	Rossby number, $U_E/(\Omega a)$	(−)
S	Sharpness index, D_{P25}/D_{P75}	(−)
$\boldsymbol{u}^*$	Flow velocity vector, $U_E\boldsymbol{u}$	($m\,s^{-1}$)
(u, v, w)	Dimensionless velocity components in the rotating cylindrical coordinate system	(−)
U_E	Characteristic velocity, $Q/\{4\pi a(\nu/\Omega)^{0.5}\}$	($m\,s^{-1}$)
$\boldsymbol{v}^*$	Particle velocity vector, $U_E\boldsymbol{v}$	($m\,s^{-1}$)
x	$\log_{10} D_P$ (Eq. 8)	(−)
y	$A_1x+A_2\sin(A_3x)+A_4$ (Eq. 8)	(−)
γ	ρ_P/ρ_f	(−)
η_F	Fine product yield (Eqs. 7 and 24)	(−)
$\Delta\eta(D_P)$	Partial fractional efficiency of the fine product (Eq. 10)	(−)
δ	Dimensionless Ekman layer thickness at r, δ^*/a (Eq. 20)	(−)
μ	Viscosity of fluid	(Pa·s)
ν	Kinematic viscosity of fluid, μ/ρ_f	($m^2\,s^{-1}$)
ρ_f, ρ_P	Densities of fluid and particles, respectively	(kgm^{-3})
τ	Dimensionless stretched coordinate normal to the wall in each Ekman layer (Eq. 18)	(−)
Ω	Angular velocity of the rotating container	($rad\,s^{-1}$)
Ω_N	Angular velocity component normal to the wall at r, $(1+b'^2)^{-0.5}\Omega$	($rad\,s^{-1}$)

Subscripts

C, F	Denote the coarse and fine products, respectively
I	Denotes interior regions
L, U	Denote the lower and upper walls with small and large axial coordinates, respectively
O	Denotes feed suspension
W	Denotes water feed

Superscripts

' Derivatives with respect to r

* Variables with dimensions corresponding to the dimensionless variables

References

1) Tanaka, Z., T. Inoue, J. Hitaka and S. Miwa. "Basic Lectures of Powder Technology 2, Chapter 2 Classification," *J. Soc. Powder Technol., Japan*, **25**, 221-230 (1988).
2) Tanaka, Z., T. Miya and T. Takahasi. "Wet Size Classification for Fine Particles in Centrifuges," *J. Soc. Powder Technol., Japan*, **29**, 750-754 (1992).
3) Isshiki, Y., K. Fukui, H. Yoshida and A. Kobayashi. "The Control of Particle Size Separation by the Use of a Hydrocyclone," *J. Soc. Powder Technol., Japan*, **34**, 690-696 (1997).
4) Okuda, S. "On Accurate Classification of Fine Particles," *J. Soc. Powder Technol., Japan*, **26**, 451-458 (1989).
5) Harada, I. and N. Ozaki. "A Numerical Study of Source-Sink Flows in a Rotating Cylinder," *J. Phy. Soc. Jap.*, **45**,

1400-1409 (1978).
6) Nakabayashi, K. et al. "Basic Study on Fine Particles in Almost Rigidly Rotating Flow (4th Report, Experimental Consideration of Classification Efficiency)," *Trans. Japan Soc. Mech. Eng.*, **594**, 586-592 (1996).
7) Kimura R. *Introduction to Geophysical Fluid Dynamics*, pp. 27-45, Tokyodo Press (1987).
8) Greenspan, H. P. *The Theory of Rotating Fluids*, pp. 28-118, Cambridge University Press (1968).
9) Nakabayashi, K. and Y. Tsuchida. "Basic Study on Fine Particles in Almost Rigidly Rotating Flow (1st Report, Theoretical Consideration of Flow)," *Trans. Japan Soc. Mech. Eng.*, **591**, 3989-3995 (1995).
10) Morinishi Y. et al. "Computational Method for Almost Rigidly Rotating Flow," *Trans. Japan Soc. Mech. Eng.*, **572**, 1234-1241 (1994).
11) Nakabayashi, K. and Y. Tsuchida. "Basic Study on Fine Particles in Almost Rigidly Rotating Flow (1st Report, Theoretical Consideration of Flow)," *Trans. Japan Soc. Mech. Eng.*, **591**, 3989-3995 (1995).
12) Nakabayashi, K. et al. "Basic Study on Fine Particles in Almost Rigidly Rotating Flow (3rd Report, Conditions of Occurrence of a Stable Regime of Almost Rigidly Rotating Flow)," *Trans. Japan Soc. Mech. Eng.*, **591**, 4004-4010 (1995).

Author's short biography

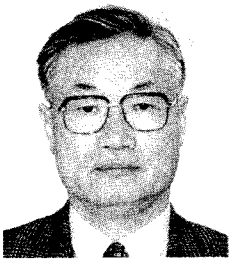

Koichi Nakabayashi

The author is Professor of Mechanical Engineering Department at Nagoya Institute of Technology since 1980. He received a B. S. degree from Nagoya Institute of Technology in 1961, a M. S. degree from Osaka University in 1964 and a Dr. of Engineering degree from Nagoya University in 1970. His major research interests are new accurate centrifugal classification of fine particles using an almost rigidly rotating flow, Couette-type turbulent flow, and rotating turbulence in the system rotation and laminar-turbulent transition in spherical Couette flow between two concentric rotating spheres.

Yoichi Tsuchida

The author is Assistant Professor of Mechanical Engineering Department at Nagoya Institute of Technology since 1991. He received B. S. and M. S. degrees from Nagoya Institute of Technology in 1976 and 1978, and a Dr. of Engineering degree from Osaka University in 1988. His major research interests are centrifugal classification of fine particles, almost rigidly rotating flow structure and particle motion within a rotating double-walled container shaped arbitrarily, and laminar-turbulent transition of spherical Couette flow.

Motion Characteristics of a Fine-Particle Assembly in a Laterally Vibrated Box under Microgravity†

Yasushi OHYAMA, Hiromi TAKEUCHI, A. T. PYATENKO, Shigeo CHIBA, Izumi UCHIDATE
National Institute of Advanced Industrial Science and Technology *
and Kunio SHINOHARA
*Division of Material Science & Engineering, Hokkaido University***

Abstract

The present work describes the behavior of fine particles in a laterally vibrated box under microgravity and shows the effects of vibrating conditions and particle concentration on particle motion characteristics. During the 10 seconds of microgravity provided by a drop capsule, particles 51 μm in mass median diameter rose along walls vibrating at 75 to 150 Hz and dispersed into the box's central region. Propagation of momentum from the vibrating walls to the particles was controlled by frequency and particle concentration in the dispersed phase. With a small charge, static clusters were formed due to the restricted propagation of momentum. But with a high particle concentration or at a high frequency, the enhanced propagation resulted in the formation of dynamic clusters, which were transitional assemblies of moving particles. It was found that there was a saturated concentration of dispersed particles in the fully developed vibrating state. High particle concentration caused supersaturation and the formation of new beds from dispersed particles.

1. Introduction

It is important for the future industrial use of space to elucidate the behavior and other phenomena of powders and to explore the ways of their manipulation, when they are exposed to external forces in a microgravitational field. Microgravitational fields can be effectively used for basic research on terrestrial powder phenomena, because it is possible, for example, to observe only the effects of cohesion and other forces that on Earth always coexist with gravity. As reported previously[1], the dispersion structure of a coarse particle assembly was investigated in a container subjected to lateral vibration under microgravity. The results showed that particle assemblies in the vibrating field exhibited repetition of collision and rebounding motions between individual particles, and formed a vertically oriented saddle-shaped concentration distribution in the container. Generally, it is anticipated that the motion of coarse particles with diameters larger than 100 μm is close to that of rigid spheres because of their separation force far stronger than their cohesive force, while fine particles will exhibit different behaviors owing to the cohesion, friction, and other kinds of interaction between particles. Various findings on the behavior of fine particles on vibrating walls have been attained through previous experiments[2,3] and simulations[4], but many of them pertain to particle movement under gravitational influence, and nothing is known about the behavior of fine particles in vibrating containers under microgravity. Elucidating the motion characteristics of fine powder under microgravity will form the basis for a variety of microgravity industrial technologies, such as manipulation of industrial feedstock in space, management of environmental fine particles like dusts in orbiting craft, and processing of resources extracted from other planets. In addition, it possibly provides useful findings for terrestrial technologies such as pneumatic transport and fluidized beds in high-concentration dispersed systems. In the present paper,

* 2-17-2-1 Tsukisamu-Higashi, Toyohira-ku Sapporo 062-8517, Japan
** Kita 13, Nishi 8, Kita-ku, Sapporo 060-8628, Japan
† This report was originally printed in J. Soc. Powder Technology, Japan. **36**, 742-749 (1999) in Japanese, before being translated into English by KONA Editorial Committee with the permission of the editorial committee of the Soc. Powder Technology, Japan.

generating a microgravity environment with a drop capsule, the behavior of fine particles in a vibrating box is observed, and the relationship is experimentally examined among the motion characteristics of particle beds, the dispersing and aggregation characteristics of particles and particle concentration, and vibration parameters.

2. Experimental Apparatus and Method

The same apparatus and microgravity environments were used in this experiment as in a previous paper (about 10 s; Japan Microgravity Center in Kamisunagawa Town, Hokkaido). The sample was loaded into a glass observation box (20 mm wide, 20 mm deep, and 28 mm high) shown in **Fig. 1**, and then the box was mounted on the platform of a vibrator. As vibration is applied laterally, the right and left walls as viewed from the front are to be called the vibrating walls. The sample used is silica-alumina particles with a mass median diameter of 51 μm (tapping bulk density, 516 kg/m^3). The experiment entailed starting the vibration of the observation box under prescribed conditions, and then placing it under microgravity by dropping the capsule. The particles' dispersion state and motion under microgravity was observed by taking sequential photographs with a still camera at 1/3 s intervals, and by using a video camera.

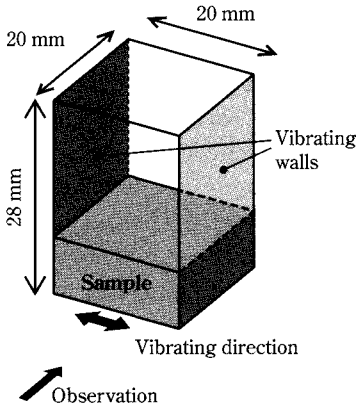

Fig. 1 Schematic Drawing of Vibrating Box

3. Results and Discussion

3.1 Particle Dispersion Patterns and Deformation of Particle Bed

A representative dispersion pattern appears in the sequential photographs in **Fig. 2**, showing the observation results for 75 Hz frequency, 300 μm displacement amplitude, and 1.2 g particle feed weight. Under normal gravity the particles form a bed at the bottom of the container as they are vibrated laterally ($t=0$ s). As the microgravity condition begins, particles begin to move upward starting with the parts of the particle bed in contact with the vibrating walls ($t=1.4$ s). After the particles rise along the vibrating walls from the bed, they change course at the ceiling and descend through the approximate center ($t=2.7$ s). **Fig. 3** is an enlargement of the upper right portion of this photograph. Here the differences in dispersion state can be observed according to position. At the place where particles have just emerged from the bed (area A) and near the vibrating wall (B) the particles are well dispersed, but particles aggregate far from the vibrating wall (C) and form clusters. The video recording

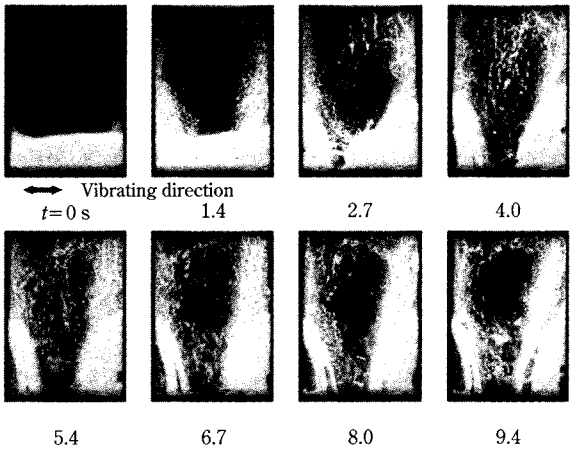

Fig. 2 Typical Pattern of Particle Dispersion under Microgravity
$f=75$ Hz, $A_d=300$ μm, $M=1.2$ g

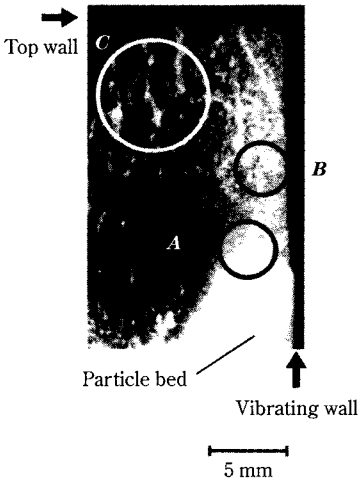

Fig. 3 Static Cluster Formation in Dispersed Particles
$t=2.7$ s, $f=75$ Hz and $A_d=300$ μm. A and B: moving particles, C: static clusters

shows that at positions A and B near the wall the particles moved as they made random local motions, while the particles and clusters seen at position C slowly moved away from the wall without any local motion. Generally when weak external forces act on particles under microgravity the cohesion effect, which is not affected by gravity, is more easily manifested. Particles just emerged from the particle bed and those near the vibrating walls have enough energy to achieve motion as single particles because of the continual kinetic energy, and thus can maintain a dispersed state. By contrast, at the position far from the wall, collision motion propagation is moderated by the inelasticity of collisions between particles, which eventually agglomerate due to cohesive force. The term static cluster will be used for the clusters that form due to the abatement of motion and to cohesive force. In **Fig. 2** it can be observed that particles dispersed along the vibrating walls, and also that the particle bed remaining at the bottom without dispersing is deformed instead of being just motionless. In order to track deformation, we extracted the particle bed portion of the **Fig. 2** images and presented them in **Fig. 4**, which shows that the particle bed split in the middle ($t = 2.7$ s) and climbed up the vibrating walls with the elapse of time. The lateral vibration-caused bed deformation and the mechanism of particle dispersion can be understood as follows: The right and left vibrating walls, which are endowed with their movement by the vibrator, compress the particle bed laterally on each cycle. Owing to this repeated compression, the particle bed deformed vertically along the walls, and at the surface of the bed near the vibrating walls the particles flow upwards from the bed and disperse because of the vibration. These dispersed particles likely rise along the vibrating walls for the following reason: Because particles collide with one another, ideally they try to isotropically diffuse so as to homogenize the particle concentration distribution produced by dispersion, with the homogenization occurring primarily at particle emergence locations, i.e., the bed surface and the place where particles come in contact with the vibrating walls. But in the process of collision propagation, particle motion is abated by air drag and collision inelasticity before the concentration distribution is evened. At places very near the vibrating walls, momentum is propagated when particles colliding with and rebounding from the walls collide with one another, which is the reason diffusion continues. Thus, particles move more readily near the vibrating walls, and particles rise from the bed surface along the walls.

Making the displacement small, the bed absorbs vibration by inter-particle friction without any macrodistortion. **Fig. 5** shows the observation result of a particle assembly at such a time. During the approximate 10 s duration of the experiment the bed hardly deformed and maintained a level surface. A few particles separated from the bed surface near the vibrating walls, but as compared with **Fig. 3** the just-separated particles form a larger powder mass. This is probably because under microgravity the particle bed is in a packed state maintained by weak contact, and some parts simultaneously lose all contact with surrounding particles due to vibration depending on the local packed structure near the bed surface. The powder mass in **Fig. 5** appears to have resulted owing to this separation of parts.

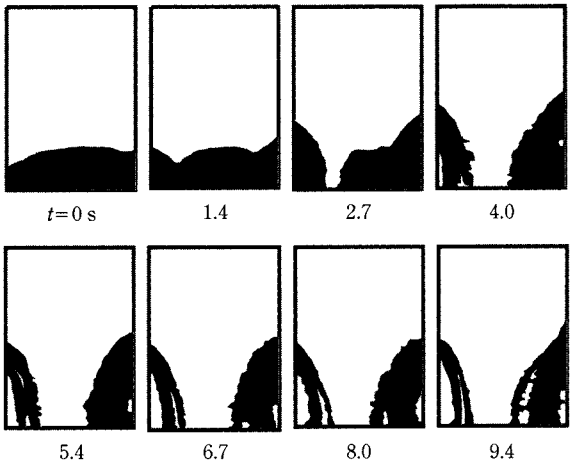

Fig. 4 Transformation of Particle Bed
$f = 75$ Hz, $A_d = 300$ μm and $M = 1.2$ g

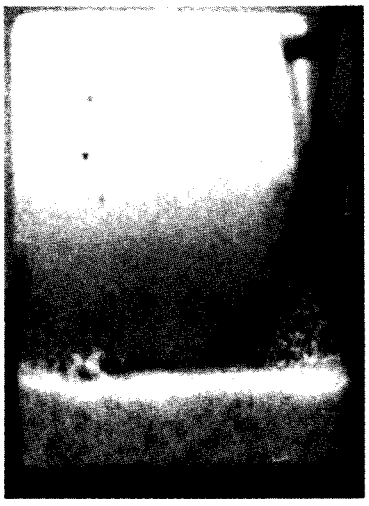

Fig. 5 Dispersion Behavior with Small Displacement Amplitude
$t = 8.7$ s, $A_d = 84$ μm, $f = 75$ Hz and $M = 1.2$ g

3.2 Effects of Frequency on Particle Bed Disruption

It was found that even under microgravity, particle beds deform due to vibration-caused compression and tend to form aggregates. In the dispersion of powders it is therefore important how to disrupt the initial packing structure. It is anticipated that if a particle bed relaxes external compressive stress through its deformation, before relaxation discipates, recompression by shortening the vibration frequency will yield the bed disruption without being able to deform. To test this the frequency was doubled to $f = 150$ Hz and the results appeared in **Fig. 6** were observed. Even though the displacement amplitude was smaller than that in **Fig. 2**, the particle bed was disrupted in all places over the vibrating walls, thereby demonstrating that a high frequency is effective at disrupting particle beds. Despite the formation of voids between the particle bed and vibrating walls after disruption, the bed sides continued being slightly disrupted, and the particle dispersion continued. This is probably because the dispersed particles inside the voids moved from the vibrating walls and collided with the particle bed sides to induce the separation of other particles.

3.3 Occurrence of Dynamic Clusters

The formation of dynamic clusters is believed to occur when the propagation of vibration with dispersed particles discontinues and particle motion abates. Here, it was investigated whether constraining this phenomenon makes it possible to obtain a homogeneous dispersed state. One conceivable way of propagating vibration well is to increase the collision frequency by raising the concentration of a dispersed particle group. Thus, the particle dispersion state was observed in a high-concentration system. **Fig. 7(a)** shows the results obtained when increasing by 2.5 the feed weight used in **Fig. 2**. The central region is nearly filled with dispersed particles, showing that dispersibility in the container was improved macroscopically by increasing feed weight. Likely this is because inter-particle distances were shorter and there was less air drag in the collision propagation process. Furthermore, greater collision frequency results in supplying of sufficient momentum even to locations away from the vibrating walls. A detailed examination reveals that the particle dispersion state is not uniform; instead, the particles are aggregated in an arborescent pattern. In the video image, the branches of these arborescent aggregates meander with energetic movements in which they appear to be joining and separating from other branches in their vicinity. Thus, it can be inferred that these aggregates clearly differ from static clusters in which particles are energetically entering and leaving. In other words, while the particles in static clusters touch one another in a static manner, in these aggregates the particles are in dense formations but have a compressed state that maintains inter-particle collisions and rebounding. We therefore called these aggregates dynamic clusters to distinguish them from static clusters.

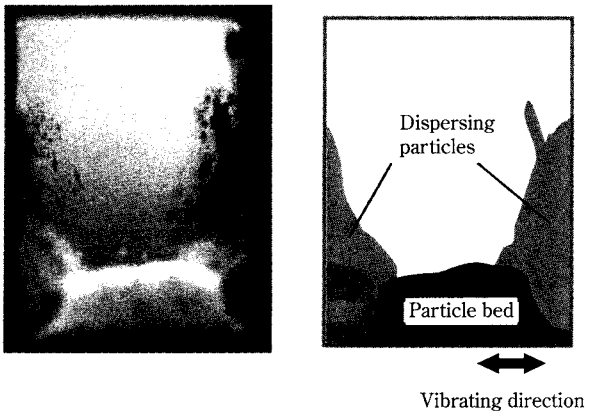

Fig. 6 Effect of Frequency on Bed Collapse
$t = 7.4$ s, $A_d = 86$ μm, $f = 150$ Hz and $M = 1.2$ g

3.4 Relationship Between Saturated Particle Concentration and New Particle Bed Formation

Next we turned our attention to particle bed behavior. The vertically oblong particle bed along the container's left side in **Fig. 7(a)** is a bed newly generated from particles that had dispersed. **Fig. 7(b)** shows the diachronic change in particle bed shape. After the start of microgravity the initial particle bed had split into left and right parts, and although the left side disappeared, new beds were subsequently generated in the upper and lower left corners of the container. These grew and joined, becoming a vertically oblong particle bed with a gap from the left vibrating wall. This newly generated particle bed remained stable as it slightly varied its position, inclination, and surface shape, while dynamic clusters moved about energetically in its vicinity. It was not possible to determine the particle bed's depth. For the sake of convenience, the term dispersed phase is used to describe the space in the system other than the initial particle bed and new particle beds. It is evident that the particle concentration in the dispersed phase increased because the disruption of the initial particle bed continued with the passage of time. Ideally the concentration

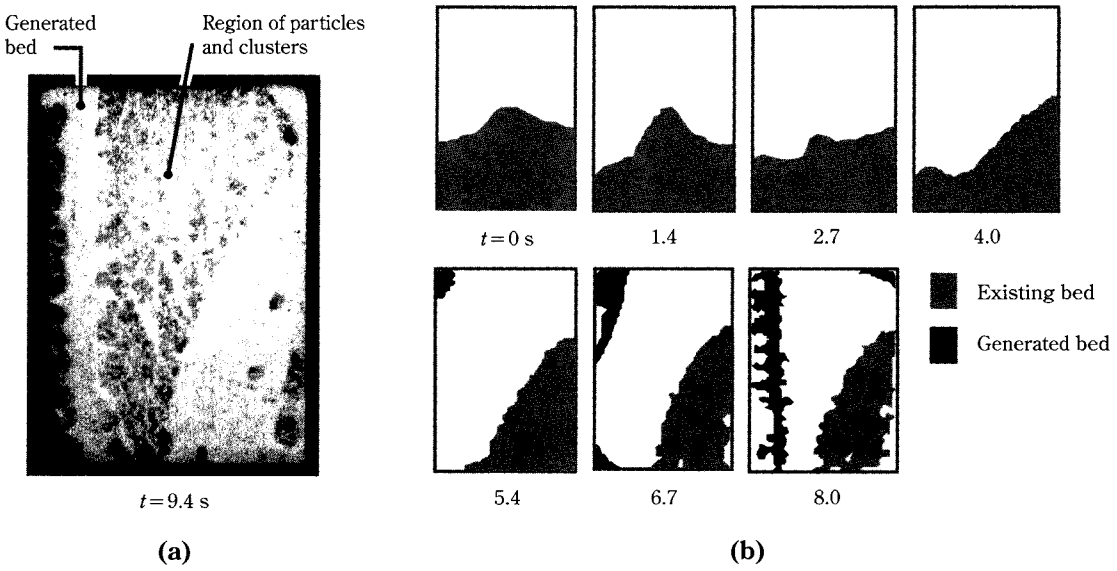

Fig. 7 Dispersion and Formation of Particle Bed at High Concentration
f=75 Hz, A_d=300 μm, M=3 g
(a) Photograph at t=9.5 s
(b) Illustrated bed motion in t=0 to 8.0 s

can assume any arbitrary value from a particle-free state to a completely dispersed one where all the particles in the system are evenly distributed. But our experimental results showed that when the particle concentration of the dispersed phase increased to a certain level, a new particle bed began to be generated from the dispersed phase.

For that reason a smaller container with a space of 5.0 to 5.6 mm between the vibrating walls was used next so that the initial particle bed would be quickly disrupted, and the effect of dispersed phase concentration was investigated on the state of particle dispersion, as shown in **Fig. 8**. In (a) and (b) for feed weights of 0.6 g and 0.25 g, respectively, particle bed height decreased due to dispersion for about 5 s after microgravity started, but subsequently maintained a more or less constant height. In (c) for feed weight of 0.05 g, all particles dispersed and the particle bed disappeared. It is evident from the photographs that while arborescent dynamic clusters were generated in (a) and (b), particles were uniformly dispersed in (c). Dispersed phase concentration is here assessed by the mass concentration ρ_d (kg/m^3) as the weight of particles per unit volume in the dispersed phase. The particle beds' longitudinal areas were assumed not to change according to depth and to be equal to their projected areas. ρ_d was calculated from the dispersed particle amount, and from the dispersed phase volume, which was determined from the container's longitudinal area and the projected areas of particle beds at each moment in time. The average values of ρ_d during t=7.4 to 10.0 s, which is the span of time from when the bed height becomes fairly steady to the end of microgravity, were (a) 58 kg/m^3, (b) 56 kg/m^3, and (c) 19 kg/m^3. Even though feed weights were different in (a) and (b), where the bed height decrease stopped before the beds completely dispersed, they both had about the same ρ_d. It suggests that dis-

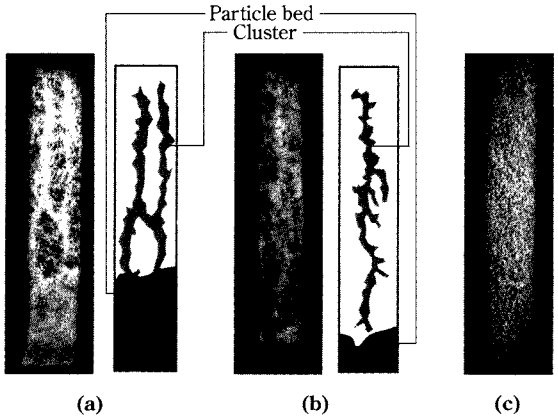

Fig. 8 Cluster Formation and Bed Deformation at High Concentration
t=7.4 s, f=75 Hz, A_d=300 μm
(a) M=0.6 g, D_w=5.6 mm
(b) M=0.25 g, D_w=5.0 mm
(c) M=0.05 g, D_w=5.0 mm

persed particle assemblies have a limit at which they can maintain dispersion, i.e., a saturated particle concentration. Particles in the dispersed phase repeatedly collide and rebound, and at the same time collide with the particle bed surface, while some particles accumulate on the bed surface. This is considered to have the effect of suppressing the separation of more particles due to collapse of the bed. Thus, as the bed collapses and the dispersed phase concentration increases, in time there arises a balance between the separation and collision/rebounding of particles on the bed surface to stop changing the bed height. This is a saturation state in a system comprising a dispersed phase and a particle bed. In a strict sense, the particle concentration that produces this saturation state seems to change depending on vibration conditions. But a detailed discussion is avoided here and the relationship is investigated with dispersion behavior by disregarding vibration conditions and treating the (a) and (b) average value of 57 kg/m^3 as the ρ_d in a saturated state, i.e., the saturated particle concentration ρ_{ds}. **Fig. 9** plots the change over time in dispersed phase concentration ρ_d after the beginning of microgravity for the experiment in **Fig. 7**. The dotted line indicates the complete dispersion concentration calculated as if the entire feed were dispersed. When microgravity started, the dispersed phase concentration rose, but after about 2 s the rate of increase slowed and then fell after peaking at 5.4 s. This was followed by irregular rising and falling. Such changes in particle concentration can be explained in the following way by the saturated particle concentration ρ_{ds}, which is represented by the straight solid line. At the time microgravity begins, the particle bed collapses by a mechanism like those studied previously and approaches a complete dispersion concentration. When the feed weight is large as under these conditions, i.e., the complete dispersion concentration is near the bulk density of packed bed, even a very small collapse of the particle bed will easily cause a sudden increase in the dispersed phase density. For this reason, immediately after microgravity begins, the particles in the dispersed phase assume a supersaturated state that far exceeds the saturated particle concentration, and the particles repeatedly collide and rebound at very close quarters. Powerful collisions and rebounding in the dispersed phase suppress the separation of particles from the bed surface, and slow the rise in dispersed phase concentration. Further, the formation of a new particle bed from particles in a supersaturated state causes the movement of particles from the dispersed phase to the particle bed, thereby decreasing dispersed phase concentration. In **Fig. 9** the thick arrow indicates the point in time when the new particle bed was observed to start formation. Subsequently the dispersed phase concentration declined with variation in the neighborhood of the saturation concentration. This behavior corresponds to the present investigation. Little is known about the mechanisms by which new particle beds form, and particularly the mechanisms that arise near the vibrating walls where kinetic energy is input. It is possible that when a preliminary particle assembly arises within a supersaturated particle one, growth will occur due to the accumulation of particles from the dispersed phase, just as with the initial particle bed. **Fig. 10** illustrates a model on the situation, what is believed to occur, when a preliminary particle assembly arises near a vibrating wall. When particle concentration is high near the vibrating wall, there forms a group of very closely spaced particles that are forcibly compressed by the wall movement. Because this results in very high collision frequency, the particle assembly tends to expand, but sometimes it is impossible to fast expand owing to the surrounding concentration. Particle assemblies like this quickly lose their kinetic energy because of high collision frequency. In other words, an assembly of particles near a vibrating wall will form into a preliminary particle assembly when the energy dissipation rate is greater than the expansion rate, and this makes it possible that a new particle bed will form.

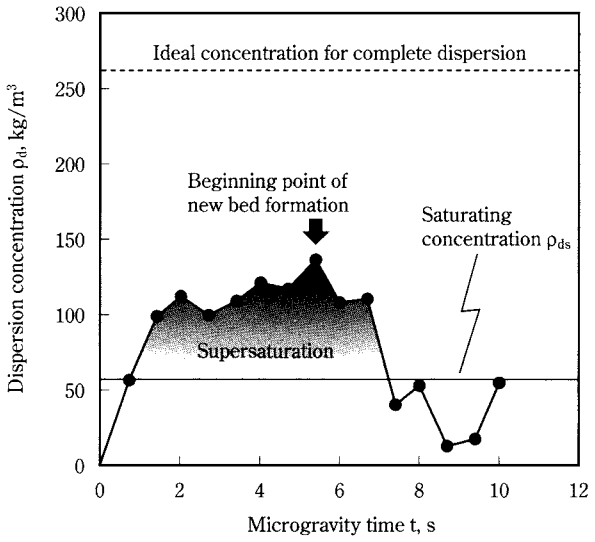

Fig. 9 Dispersed Particle Supersaturation
A_d = 300 μm, f = 75 Hz and M = 3 g

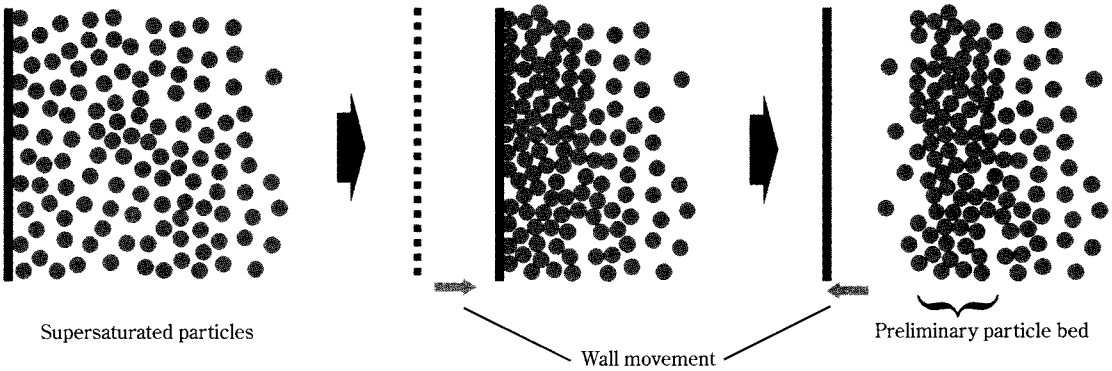

Fig. 10 Conception of Preliminary Particle Bed Formation among Supersaturated Particles

3.5 Effects of Frequency on Dynamic Cluster Formation

Section 3.3 described how augmenting the feed weight created a high-concentration field to increase collision frequency and lead to the formation of dynamic clusters. By contrast, it is anticipated that if vibration frequency is enhanced while keeping feed weight constant, particles will exhibit the same behavior, because collision frequency increases under these conditions as well. In **Fig. 2**, static clusters formed in the container's central region at $f = 75$ Hz, and the motion from the wall did not sufficiently propagate throughout the whole container. **Fig. 11** shows the results obtained when increasing to $f = 95$ Hz. As expected, particles are spread throughout the dispersed phase, and arborescent dynamic clusters have formed. **Fig. 12** compares the changes in dispersed phase concentration at $f = 75$ and 95 Hz. Data for $f = 75$ Hz and the time span under $t = 4.0$ s are not plotted because as a result of image analysis the values fluctuated near zero and were sometimes negative. At 75 Hz it took time for vibration to collapse the bed, and the concentration rose slowly, while at 95 Hz the concentration attained the saturated particle concentration. But because the complete dispersion concentration was low at this feed weight, the dispersed phase concentration increased slowly in relation to the particle collapse rate. For that reason the gradient lessened after about $t = 4.5$ s when the saturated particle concentration was exceeded, and at no time did the dispersed phase concentration become high enough to exceed the saturation concentration, as it did in **Fig. 9**. Observation results on particle bed behavior show that even if a new particle bed formed temporarily along a wall, it did not last long. This contrasted with **Fig. 7**, in which a new particle bed

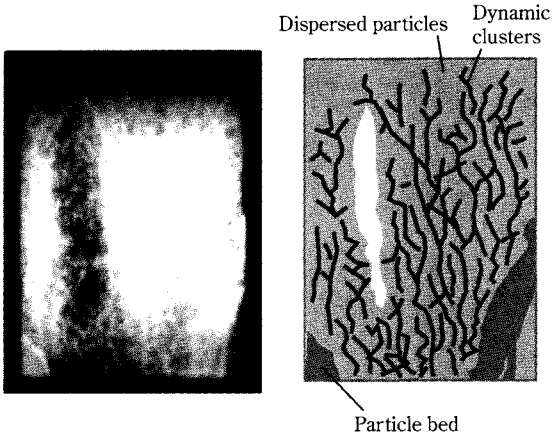

Fig. 11 Particle Behavior at High Frequency
$A_d = 300$ μm, $f = 95$ Hz and $M = 3$ g

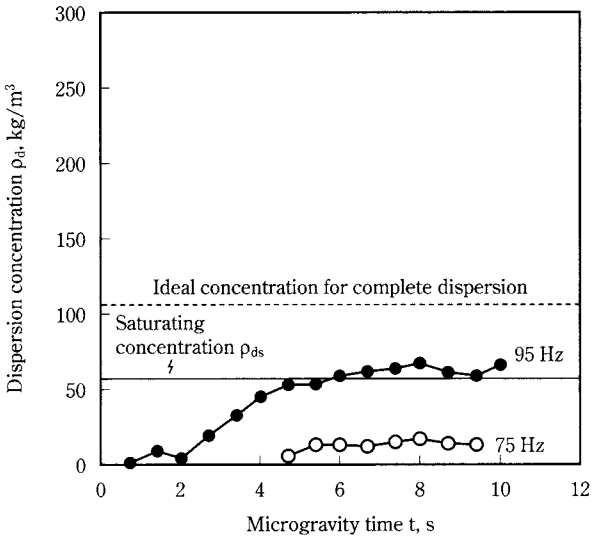

Fig. 12 Effect of Frequency on Particle Dispersion
$A_d = 300$ μm and $M = 1.2$ g

grew over time. This difference appears to depend on whether or not a state of supersaturation arises. At 95 Hz it was not until approximately $t = 4.0$ s and thereafter that dynamic clusters appeared throughout the entire dispersed phase. This roughly corresponds to the moment in **Fig. 12** when the concentration attained the saturation amount. Therefore, it suggests that the attainment of the saturated particle concentration is a condition for the formation of both new particle beds and dynamic clusters.

4. Conclusion

A bed of fine particles (silica-alumina with a 51 μm mass median diameter) and the dispersed particles were observed in a box-shaped container subjected to lateral vibration under microgravity, and particle motion and behavior stemming from vibrating conditions and dispersed phase particle concentration was examined to obtain the following findings.

(1) At a 75 Hz frequency the fine particle bed underwent fluid deformation at the vibrating wall surfaces, but at 150 Hz it was disrupted near the vibrating walls without being able to deform.

(2) Fine particles broke away from the part of the particle bed in contact with the vibrating walls, and dispersed along those walls, and then into the container's interior. At a 75 Hz frequency with small feed weight, the dispersed phase concentration was low, and at locations away from the vibrating walls, static clusters formed by cohesive force to abate particle motion. But with a large feed weight the particles dispersed throughout the entire container while colliding and rebounding, and arborescent dynamic clusters formed. Even when feed weight was low, raising the frequency to 95 Hz facilitated collisions and rebounding, which led to the generation of dynamic clusters.

(3) Under conditions in which vibration was well propagated into the container's interior, there was a saturated particle concentration in the dispersed phase. When this concentration was exceeded, particles were taken into the bed from the dispersed phase. Especially when supersaturation occurred, new particle beds were formed within the dispersed phase.

Acknowledgment

The authors wish to thank Mr. Masahiro Oshima and others at Kawasaki Heavy Industries Ltd. Gifu Technical Research Center for their cooperation with this research.

Nomenclature

A_d	Displacement amplitude	(μm)
D_w	Distance between vibrating walls	(mm)
f	Frequency	(Hz)
g	Acceleration due to gravity	(m/s^2)
M	Particle feed weight	(g)
t	Microgravity time	(s)
ρ_d	Particle concentration in dispersed phase	(kg/m^3)
ρ_{ds}	Saturated particle concentration in dispersed phase	(kg/m^3)

References

1) Ohyama, Y., H. Takeuchi, A. T. Pyatenko, S. Chiba and K. Shinohara. "The Dispersion Behavior of Coarse Particles by Lateral Vibration under Microgravity," *J. Soc. Powder Technol., Japan*, **34**, 834-839 (1997).
2) Matsusaka, S., K. Yamamoto and H. Masuda. "Micro Feeding of a Fine Powder Using a Vibrating Capillary Tube," *J. Soc. Powder Technol., Japan*, **32**, 83-88 (1995).
3) Matsusaka, S., S. Nakamura and H. Masuda. "Behavior of Fine Particles on a Plate under Ultrasonic Vibration," *J. Soc. Powder Technol., Japan*, **36**, 16-22 (1999).
4) Matsusaka, S., M. Furutate and H. Masuda. "Distinct Element Simulation of Vibrating Behavior of Adhesive Powder," *J. Soc. Powder Technol., Japan*, **35**, 168-173 (1998).

Author's short biography

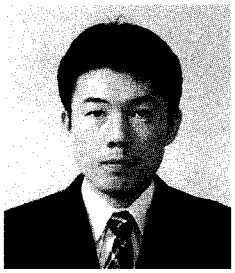

Yasushi Ohyama

Yasushi Ohyama obtained a bachelor of engineering and a master of engineering degree in Chemical Process Engineering from Hokkaido University, Japan in 1989 and 1991. He has been engaged in research work on powder handling in microgravity at Hokkaido National Industrial Research Institute(*) from 1991 as a researcher. Currently he is focusing on computing simulation of particle behavior, and applying it other field such as coal gasification.
(* The Hokkaido National Industrial Research Institute was reorganized into the National Institute of Advanced Industrial Science and Technology (AIST) in 2001)

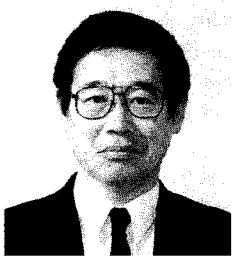

Hiromi Takeuchi

Hiromi Takeuchi graduated in Chemical Engineering from the Kyoto University, Japan, in 1980. And then, he studied at the same university as an assistant researcher for 3 years. In 1983, he obtained a Ph. D and the title of the thesis is "Gross behavior of vertical buoyant jet". In 1983 he moved to the Hokkaido National Industrial Research Institute and started research on circulating fluidized bed. Since 1996, he has been a chief of microgravity section. Takeuchi specialises in heat transfer and hydrodynamics in fluidized bed, but has carried out, or supervised, projects in a variety of other areas such as cold energy transportation and humidity control under the freezing point.

Alexandr T. Pyatenko

A. Pyatenko graduated in Chemical Physics from Moscow Institute of Physics and Technology, Russia in 1978. After completed his doctor course at the same Institute he was awarded a Ph. D in 1981. From 1981 to 1991 he worked as a researcher, then a senior researcher at the Institute for High Temperatures Academy of Science of the USSR. Since April 1993 up to now he is working as a senior researcher at HNIRI. He specializes in a study of powder handling process under microgravity, as well in a study of low-temperature (~0°C) −high humidity process.

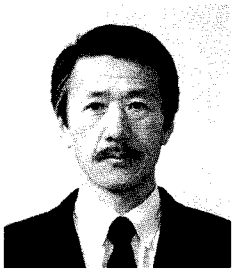

Shigeo Chiba

Shigeo Chiba graduated in Chemical Engineering from the Murolan Institute of Technology in 1975, and completed his Masters degree in Chemical Process Engineering at Hokkaido University in 1977 and was awarded a Dr. tech. degree by the University for his thesis entitled "Basic Study on Solid Mixing and Segregation in Gas-Fluidised Beds" in 1981. He jointed Hokkaido National Industrial Research Institute (HNIRI) under AIST, MITI, immediately afterwards, and was late awarded a Post-Doctoral Researchship to study on solid particle behavior in fluidised bed systems by the Fluidised Bed Cooperative Research Center at West Virginia University in 1984. He specialises in biotechnology, but has carried out projects in areas such as powder handling in microgravity and synthesis for particulate nanoparticles.

Author's short biography

Izumi Uchidate

Izumi Uchidate graduated in faculty of liberal arts from the University of the Air, Chiba, Japan, in 1995. She joined a project on powder handling in microgravity at Hokkaido National Industrial Research Institute in 1995 as a research assistant.

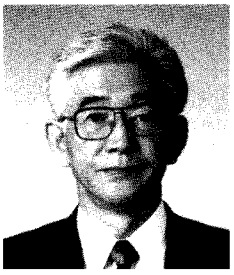

Kunio Shinohara

Kunio Shinohara graduated from Chemical Process Engineering, Hokkaido University, Sapporo, Japan, in 1965. He got M.Sc. in the course of Powder Technology, King's College London, England in 1970. He was awarded D.Eng. from Hokkaido University in 1973 for a thesis entitled "Mechanism of Gravity Flow of Particulate Materials". He was a research and teaching staff and became a professor at the same University in 1992. During these periods he made cooperative researches on agglomerate strength at NRC in Canada and on particle segregation at CMI & Telemark College in Norway.

He works on Preparation of surface modified particles by mechanical and chemical treatments, Analyses on packing characteristics and solids flow mechanism in storage vessels and reactors including segregation and transportation, and Production of functional compact materials including ceramics, hard materials and cosmetics.

Entrained Air Flow Characteristics due to the Powder Jet†

Koichiro OGATA[1], Katsuya FUNATSU[2] and Yuji TOMITA[2]

[1] *Satellite Venture Business Laboratory*

[2] *Department of Mechanical Engineering*

*Kyushu Institute of Technology**

Abstract

We experimentally and numerically examine the flow characteristics of powder jet and entrained air. A phase-Doppler anemometer is used for the measurement of axial velocity profiles of particle and entrained air. It is found that the axial velocity profile of the entrained air takes a maximum at the center-line and decreases toward outer edge. A flow region of the entrained air extends transversely into a particle free region. The center-line velocity of entrained air at first increases with increasing distance from the orifice outlet and then decreases after it remains a plateau. The transverse dispersion of the entrained air is very small as compared with that of a single-phase turbulent jet. The numerical simulation is performed based on the Lagrangian modeling for particles and Eulerian modeling for air flow. We consider particle-particle collision, gravity force, drag force and transverse force due to the particle spin and to the velocity gradient of air flow, and apply a k-ε model. The present simulation qualitatively explains our measurement in terms of velocity profiles and dispersion of particle and air.

1. Introduction

There are various kinds of particle fluid two-phase flow phenomena in natural and industry. In engineering application, there are typically pneumatic transport, powder handling, combustion system and chemical processes. To understand these phenomena, it is important to accurately investigate the particle behavior influenced by particle-fluid and particle-particle interaction and fluid motion.

Many studies have been done on the particle-fluid interaction. Now, we consider the hindered settling and the fluidization as a confined flow where the particle-particle interaction is also important due to high particle concentration. When particles are uniformly settling in a vessel, the terminal settling velocity is smaller than that of a single particle in an unbounded fluid[1-3]. In the case of fluidization, the fluidization velocity decreases with increasing particle concentration. These phenomena are approximately explained by assuming that the relative velocity between the particle and the fluid is equal to the terminal settling velocity of a single particle $v_{s\infty}$. Then, in the former, the settling velocity becomes small by the upward fluid velocity caused by displacement due to particle settling[4]. In the latter, the superficial fluidization velocity reduces with particle concentration since the upward fluid velocity through the particles is $v_{s\infty}$. In the pneumatic transport, the suspension velocity of particles is important for the design, which is larger than $v_{s\infty}$ and increases with increasing particle concentration[5].

As an important powder handling, there is particle discharge from a hopper through an orifice by gravity. The particle flow from the orifice, which we calls powder jet below, is different from that in a vessel. In this case, if there is no constraint for the motion due to the wall, the ambient air can be entrained into the powder jet. In addition to air entrainment, various motions are induced by this operation[6]. The air entrainment is important in the following powder handling processes.

To study this phenomenon, we have measured the

* 1-1 Sensui-cho, Tobata, Kitakyushu, 804-8550, Japan
TEL: +81-93-884-3157, FAX: +81-93-871-8591

† This report was originally printed in J. Soc. Powder Technology, Japan, **37**, 160-167 (2000) in Japanese, before being translated into English by KONA Editorial Committee with the permission of the editorial committee of the Soc. Powder Technology, Japan.

axial velocity of powder jet by using laser-Doppler velocimeter and we found that the falling velocity of powder jet is larger than that of a single particle $v_{s\infty}$, which is in contrast to the hindered settling[7]. The air entrained into the powder jet forms a downward air stream and the particles are falling relative to this air stream. If we infer this phenomenon by using the same assumption as to the hindered settling, then the falling velocity of powder jet is approximately equal to a sum of the terminal settling velocity of a single particle and the entrained air velocity in the powder jet. However, it seems that there is no measurement of entrained air in the powder jet. Therefore, in this research, we have measured the velocity of entrained air by using a phase-Doppler anemometer (P.D.A.). Furthermore, we perform a numerical simulation to investigate effects on the dispersion of powder jet of particle-particle collision and forces acting on the particle.

2. Experimental method

Fig. 1 shows a schematic diagram of the present experimental apparatus. The inside diameters of upper and lower conical hoppers are 490mm and 80mm and those heights are 1000mm and 180mm, respectively, the half-angle being 60 degrees. The detail of the circular orifice of lower hopper is also shown in **Fig. 1**. The mass flow rate of powder $\dot{m}$ is measured by load cell attached on the receiving tank. To change the mass flow rate of powder, we used two different orifice plates whose diameters D are 4 and 6 mm, and we have 1.969×10^{-3}kg/s and 5.747×10^{-3}kg/s, respectively. The particles used are glass beads of which mean diameter by number d_p is 454μm, geometric standard deviation σ is 0.116 and material density ρ_p is 2590kg/m^3.

Smoke chips are used as the tracer particles in P.D.A. measurement. The chips are burnt to produce smoke, which is introduced near the orifice outlet. The mean diameter of tracer particles is about 3μm. **Fig. 2** shows a schematic representation of the measuring method by a phase-Doppler anemometer. The focal lengths of lenses for the probe and the receiver are 400mm and 600mm, respectively. We can measure both velocities of particle and air. The measuring

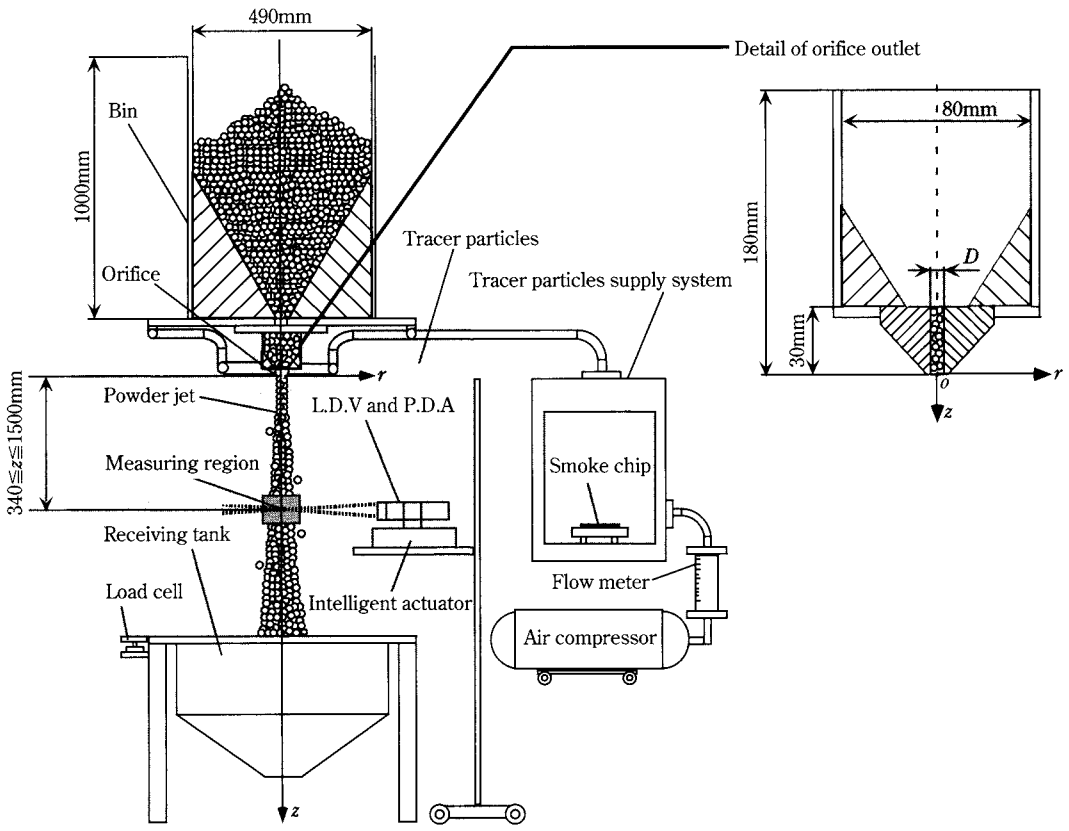

Fig. 1 Experimental apparatus

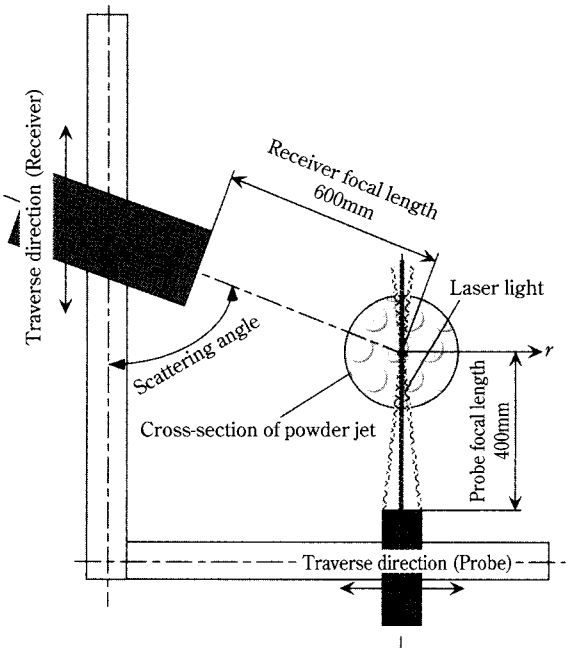

Fig. 2 P.D.A. traverse system

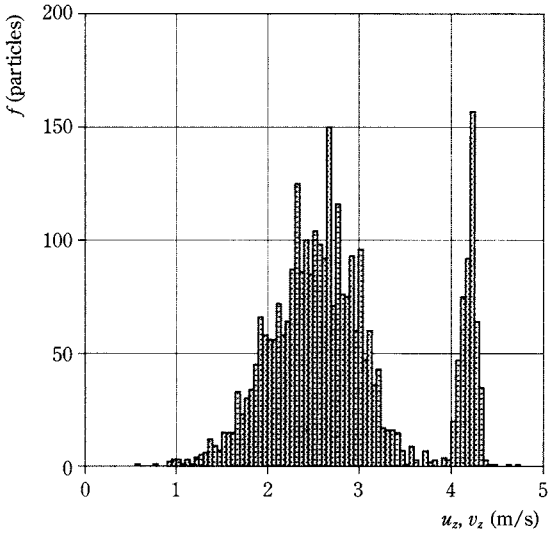

Fig. 3 Measured data of the axial velocities of entrained air and particle

range of entrained air flow is from 340mm to 1500mm in z, which is the vertically downward coordinate from the orifice outlet, and is ±150mm in the radial direction from z-axis. The measurement of entrained air velocity has been done only for $\dot{m}=5.747\times10^{-3}$ kg/s.

The signals from particles and tracers through the laser measuring volume were treated with a signal processor, and the measured velocities and diameters were stored in a personal computer. **Fig. 3** shows an example of measured particle and air velocities at z=1000mm and r=1mm. In the figure, the ordinate is the number of particles f and the abscissa is the axial velocities of particle and entrained air. However, in this case, it is not easy to identify the velocities in the valley between two peaks as those from particle or air. We identify the velocities by using the information of particle diameters. We confirmed by laser-Doppler velocimeter that the horizontal velocity component of powder jet at orifice outlet is almost equal to zero.

3. Numerical simulation

We trace the motion of all the particles in powder jet by the Lagrangian approach and model the forces acting on the particle by the gravity force, drag force, Magnus force and Saffman force[8]. The effect of particles on air is considered as a source term in the equation of motion for air flow and the drag force is considered. The detail of the present simulation and the treatment of particle-particle collision are found in the previous papers[9-10]. In the particle-particle collision, we consider the cases where the relative sliding between particles continues and ceases.

The particle motion is calculated by the Cartesian coordinate, where we take z as the vertically downward direction from the center of orifice and x and y in the horizontal plane. The equations of motion for particles are given as follows.

$$\frac{dv_x}{dt}=\frac{3\rho_a V_r}{4\rho_p d}\left\{-C_D(v_x-u_x)+\frac{C_L\omega_y}{|\omega|}(v_z-u_z)+\frac{4.1x(v_z-u_z)}{rV_r}\sqrt{\nu_l\left|\frac{\partial u_z}{\partial r}\right|}\right\} \tag{1}$$

$$\frac{dv_y}{dt}=\frac{3\rho_a V_r}{4\rho_p d}\left\{-C_D(v_y-u_y)-\frac{C_L\omega_x}{|\omega|}(v_z-u_z)+\frac{4.1y(v_z-u_z)}{rV_r}\sqrt{\nu_l\left|\frac{\partial u_z}{\partial r}\right|}\right\} \tag{2}$$

$$\frac{dv_z}{dt}=-\frac{3C_D\rho_a V_r}{4\rho_p d}(v_z-u_z)+g \tag{3}$$

where v_i is the instantaneous velocity of particle and u_i is that of air. If we put $u_i=\bar{u}_i+u_i'$, $\bar{u}_i$ is the mean velocity of air, u_i' is give as $\sqrt{2k/3}$ where k is the turbulent energy of air. V_r is the relative velocity between particle and air, and is given by $\sqrt{(v_x-u_x)^2+(v_y-u_y)^2+(v_z-u_z)^2}$. Furthermore, ρ_p is the particle density, d is the particle diameter, ρ_a is the air density, ν_l is the kinematic

viscosity of air, g is the gravitational acceleration, r is the radial coordinate given by $\sqrt{x^2+y^2}$, ω is the angular velocity of particle, C_D is the drag coefficient of particle which we calculate by using Morsi et al. correlation[11] and C_L is the coefficient of Magnus force which we calculate by using the correlation due to Tsuji et al.[12], being given by

$$C_L=\begin{cases}0.3\gamma\ (\gamma\leq 0.7)\\ 0.21\ (\gamma>0.7)\end{cases}\qquad \gamma=\frac{|\omega|d}{2V_r} \tag{4}$$

The rotation of a particle is generated by the particle-particle and particle-wall collisions. In the simulation, we consider the attenuation of particle rotation in free flight by air viscosity and ω is calculated by

$$\frac{d\omega}{dt}=\frac{-15\rho_a|\omega|\omega}{16\pi\rho_p}\left(\frac{C_1}{\sqrt{R_\omega}}+\frac{C_2}{R_\omega}\right) \tag{5}$$

where $R_\omega=d^2|\omega|/4\nu_l$ and we use the value by Dennis et al.[13] for C_1 and C_2.

We assume that the air flow is isothermal, steady and incompressible flow, and is calculated by using the Reynolds equation including the source terms by particles where we use a cylindrical coordinate system $(r,\ \theta,\ z)$, and we take z as vertically downward direction[14]. The turbulent stress in the Reynolds equation is calculated by using a k-ε model. We modify the model due to Jones et al.[15] for low Reynolds number flow by considering the particle effect as follows [16].

$$\bar{u}_z\frac{\partial k}{\partial z}+\bar{u}_r\frac{\partial k}{\partial r}=\frac{1}{r}\left[\nu r\frac{\partial k}{\partial r}\right]+G-\varepsilon-2\nu_l\left(\frac{\partial\sqrt{k}}{\partial r}\right)^2+nDk(CR_p-2) \tag{6}$$

$$\bar{u}_z\frac{\partial \varepsilon}{\partial z}+\bar{u}_r\frac{\partial \varepsilon}{\partial r}=\frac{1}{r}\left[\Gamma r\frac{\partial \varepsilon}{\partial r}\right]+C_{\varepsilon1}f_{\varepsilon1}\frac{\varepsilon}{k}G-C_{\varepsilon2}f_{\varepsilon2}\frac{\varepsilon^2}{k}+2\nu_l\nu_t\left(\frac{\partial^2\bar{u}_z}{\partial r^2}\right)^2-nD\varepsilon \tag{7}$$

where $\nu=\nu_t/\sigma_k+\nu_l$, $\Gamma=\nu_t/\sigma_\varepsilon+\nu_l$ and ε is the turbulent dissipation. The last terms of right hand in Equations (6) and (7) show the effect of particles. We derived these terms based on a dimensional analysis[16], considering the particle number density n, the particle drag D, k, ε, d and ν_l as governing variables, and D is given by

$$D=\frac{\pi}{8}C_D d^2\rho_a|\tilde{v}_z-\bar{u}_z|$$

where $\tilde{v}_z$ is the mean particle velocity in a calculating cell volume. Furthermore, R_p is the mean particle Reynolds number $R_p=d|\tilde{v}_z-\bar{u}_z|/\nu_l$ in cell and C is a constant and is put as 0.02, which is the same as our previous paper[16]. The generation term G is given by

$$G=\nu_t\left[2\left(\frac{\partial\bar{u}_r}{\partial r}\right)^2+2\left(\frac{1}{r}\frac{\partial\bar{u}_\theta}{\partial\theta}+\frac{\bar{u}_r}{r}\right)^2+2\left(\frac{\partial\bar{u}_z}{\partial z}\right)^2+\left(\frac{\partial\bar{u}_z}{\partial z}+\frac{\partial\bar{u}_z}{\partial r}\right)^2+\left(\frac{\partial\bar{u}_z}{r\partial\theta}+\frac{\partial\bar{u}_\theta}{\partial z}\right)^2+\left(\frac{\partial\bar{u}_r}{r\partial\theta}+\frac{\partial\bar{u}_\theta}{\partial r}-\frac{\bar{u}_\theta}{r}\right)^2\right] \tag{9}$$

The turbulent eddy viscosity is calculated by $\nu_t=C_k f_\mu k^2/\varepsilon$ and the coefficients of Jones et al. are $C_k=0.09$, $C_{\varepsilon1}=1.55$, $C_{\varepsilon2}=2.0$, $\sigma_k=1.0$, $\sigma_\varepsilon=1.3$, $f_{\varepsilon1}=1.0$, $f_{\varepsilon2}=1.0-3.0\exp(-R^2)$, $f_\mu=\exp[-2.5/(1+R/50)]$ and $R=k^2/\nu_l\varepsilon$. The air flow is calculated by a forward difference scheme in the axial direction and an upwind scheme in the cross-section.

4. Simulation conditions

We set a cylindrical calculating region. Based on the previous experiment, we found that the radial dispersion of powder jet is about 40mm at z=1500mm from an orifice of D=8mm. Therefore, we fix the radius of calculation cylinder R_d as 100mm and the axial length as 4000mm to avoid the particle-wall collision. We allow a slip for air flow at the cylinder wall and assume that the upper boundary of cylinder is open to the atmosphere.

The calculation time is taken as 4 seconds to have a steady condition of particles motion in the calculation region.

The diameter and density of particle used in the simulation are 1.0mm and 902kg/m^3 which gives the same terminal velocity of a single particle $v_{s\infty}$ as that of particle used in the experiment. This is because there is a problem about memory in our computer when we used the same particle as the measurement.

Since we set an origin at the orifice outlet of lower hopper in the experiment, the particles have a finite velocity there. We found that the axial velocity of powder jet at the orifice outlet is almost equal to $\sqrt{2gz_0}$ independent of $\dot{m}$ by our previous measurement[7], where z_0 is the length of orifice and is 30mm as shown **Fig. 1**. Therefore, we give the initial velocity of particle at the orifice outlet as 0.767m/s. Furthermore, we set ρ_a as 1.205kg/m^3, ν_l as 1.512×10^{-5}m^2/s, the coefficient of restitution between particles as 0.9 and $\dot{m}$ as 1.969×10^{-3}kg/s that is obtained by orifice diameter of 4mm.

5. Results and discussions

5.1 Flow characteristics of the powder jet and entrained air

Fig. 4 shows the measured axial velocity profiles of the powder jet $\bar{v}_z$ and the entrained air $\bar{u}_z$ where measuring stations from the orifice z are 500mm, 1000mm and 1500mm and the mass flow rate of powder $\dot{m}$ is 5.747×10^{-3}kg/s. It is found that the air velocity takes a maximum near the axis where the particle concentration is large, and that it decreases toward the outer edge like a powder jet. If the drag force acting on the particle is independent of the particle concentration, it becomes that the entrained air velocity is large near the axis when the particle velocity is large. Therefore, the entrained air velocity shows to a maximum near the axis. The boundary where the entrained air velocity becomes zero increases with increasing z and extends to the region where the particles are absent. As to the dispersion of entrained air flow, we discuss in later.

Fig. 5 shows the dimensionless axial velocity profiles of the powder jet and the entrained air, where the ordinates are $(\bar{v}_z-v_s)/(v_{zmax}-v_s)$ for the powder jet and $\bar{u}_z/u_{zmax}$ for the air flow, the abscissa is r/b, v_s is the local free falling velocity of a single particle, v_{zmax} and u_{zmax} are the center-line values of $\bar{v}_z$ and $\bar{u}_z$ at the measuring cross-section, b is the half-radius where the ordinate values become 0.5. For the air flow b is the radius where $\bar{u}_z/u_{zmax}$ is 0.5 and for the powder jet the radius where $(\bar{v}_z-v_s)/(v_{zmax}-v_s)$ is 0.5, this is because there is no particle at the radius where v_z/v_{zmax} is 0.5.

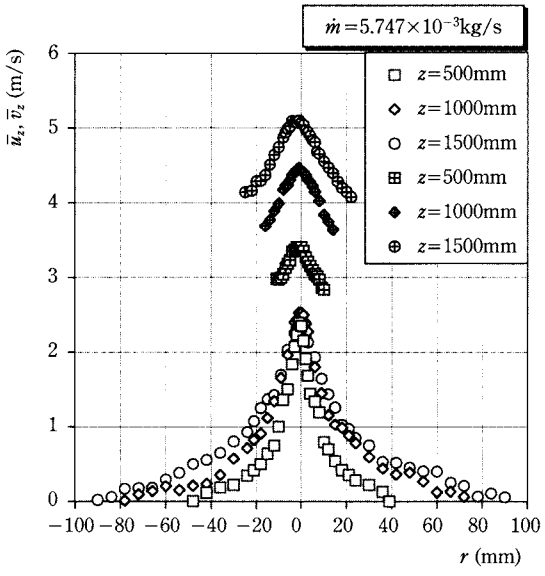

Fig. 4 Axial velocity profiles of entrained air and powder jet. open symbol: Entrained air $\bar{u}_z$, cross symbol: Powder jet $\bar{v}_z$

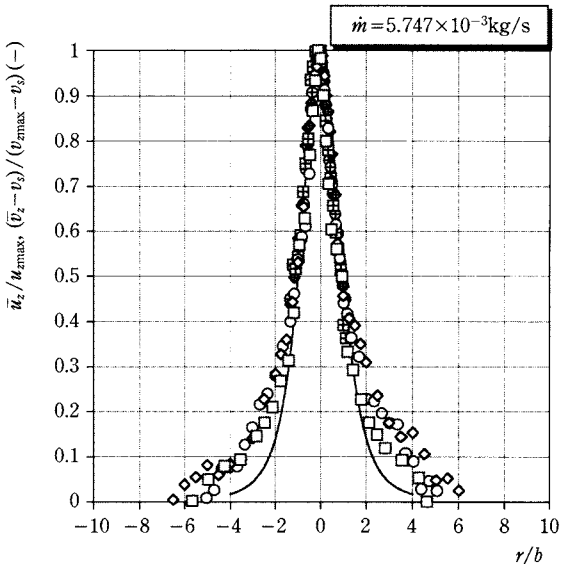

Fig. 5 Dimensionless axial velocity profiles of entrained air and powder jet.
open symbol: Entrained air $\bar{u}_z/u_{zmax}$, cross symbol: Powder jet $(\bar{v}_z-v_s)/(v_{zmax}-v_s)$, solid line: the constant eddy viscosity model

This figure includes all the experimental data in **Fig. 4** and the keys are the same. It is found that $\bar{u}_z/u_{zmax}$ is similar and independent of z where z is far from the orifice. The solid line in the figure shows a dimensionless profile for a single-phase turbulent jet by the constant eddy viscosity model[17]. Near the axis, the data of air and powder jet collapse this model.

Fig. 6 shows the relation of the center-line velocities of powder jet v_{zmax} and the entrained air u_{zmax} to the falling distance z. The solid line is the calculated local free falling velocity of a single particle v_s. The dotted line is the terminal free falling velocity of a single particle $v_{s\infty}$. The chain line represents the free falling velocity of a single particle without the drag force v_g. It shows that u_{zmax} at first increases with increasing z like v_{zmax} and seems to decrease after it takes a maximum. At the orifice outlet, the air entrainment is very small and then the drag force acting on the particle is also small. Therefore, v_{zmax} is nearly equal to v_g. The downward air stream forms in the powder jet when z increases, and then v_{zmax} becomes larger than v_s since the particles fall relative to the air flow under the gravity. It seems that v_{zmax} converges on a value between v_g and v_s.

It is found that $v_{zmax}-u_{zmax}$ is smaller than v_s at a long distance of z. If we assume that the drag coefficient of a particle in powder jet is the same as that of a

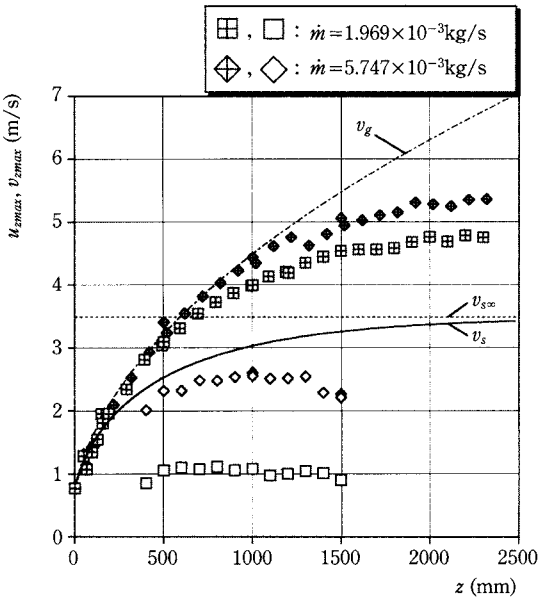

Fig. 6 Relationship between u_{zmax}, v_{zmax} and z.
open symbol: Entrained air u_{zmax}, cross symbol: Powder jet v_{zmax}

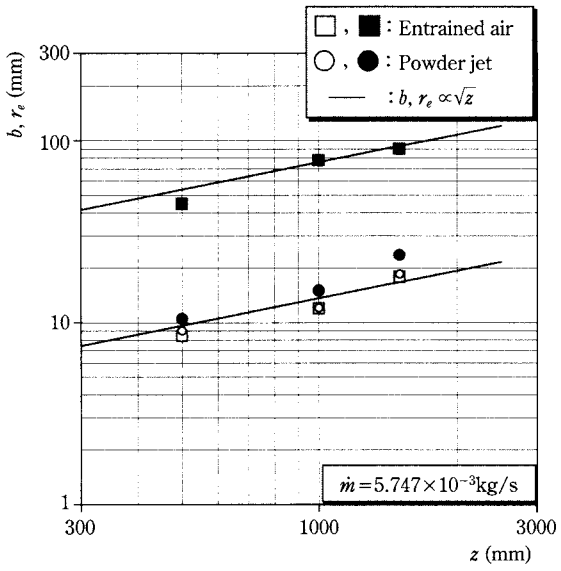

Fig. 7 Dispersion of entrained air and powder jet.
open symbol: half radius b, closed symbol: outer edge radius r_e

single particle in an unbound fluid, then we can infer that the drag force acting on a particle in powder jet is smaller than that of a single particle. Therefore, the acceleration of powder jet becomes smaller than that of a single particle.

In addition, for small $\dot{m}$, $v_{zmax}-u_{zmax}$ is large, which suggests that the drag force acting on a particle for small $\dot{m}$ is larger than that for large $\dot{m}$ and that acceleration for small $\dot{m}$ is faster.

Furthermore, u_{zmax} increases with increasing $\dot{m}$, which means that the volumetric flow rate of entrained air increases with increasing $\dot{m}$.

5.2 Dispersions of powder jet and entrained air

Fig. 7 shows that the relation of the half radius b and the outer edge r_e of the powder jet and entrained air to z. The outer edge of the powder jet r_e is defined as the radius of measuring limit of $\bar{v}_z$ and r_e of entrained air is as the radius where $\bar{u}_z$ becomes zero. The solid line in the figure represents $\sqrt{z}$. It is found that b and r_e of powder jet and entrained air are approximately proportional to $\sqrt{z}$. The dispersion angle for r_e of entrained air is about 3.5 degrees. It is well-known that the dispersion of a single-phase turbulent jet is between 12 and 15 degrees. Therefore, it is said that the dispersion of entrained air is very small.

Fig. 8 shows the dispersion of powder jet in r-z plane by the numerical simulation. The transverse force acting on the particles and the particle-particle collision influence the dispersion of powder jet. When the axial velocity of air is smaller than that of particle and decreases in the direction of outside, then the transverse force, that is known as the Saffman force, acting on the particles to move in the direction of out-

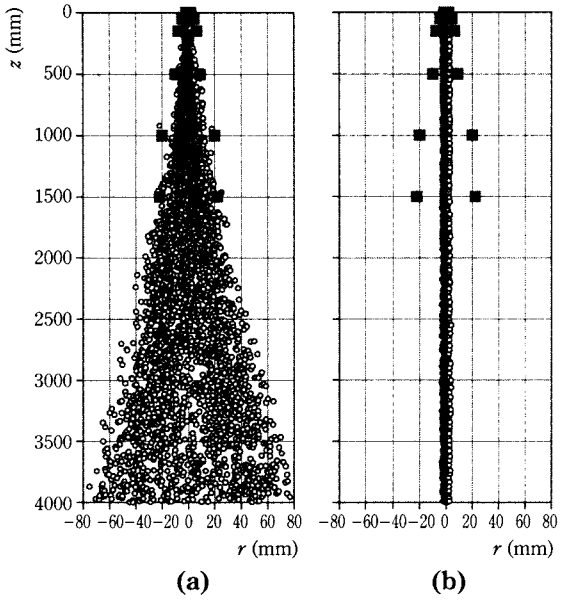

Fig. 8 Numerical simulation of dispersion of powder jet with Saffman force (a) and without Saffman force (b).
open symbol: Numerical simulation, closed symbol: Experiment

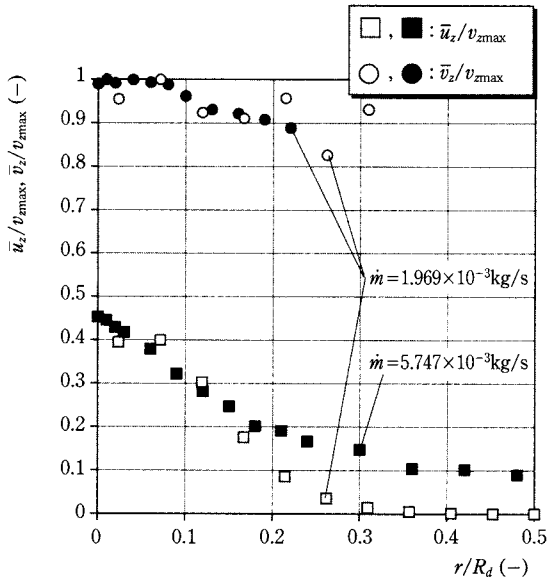

Fig. 9 Dimensionless axial velocity profiles of entrained air and powder jet.
open symbol: Numerical simulation, closed symbol: Experiment

side[8]. Therefore, the Saffman force acts to disperse the powder jet. **Fig. 8 (a)** is the case when considering the Saffman force and **Fig. 8 (b)** is the case when ignoring it. In these cases, the particle-particle collision and Magnus force are considered.

Comparison between **Figs. 8 (a)** and **(b)** shows that the Saffman force contributes the dispersion and the effect slowly increases toward the downstream. However, it should be noted that the particle size and number are different between the simulation and the measurement. The calculation without the Saffman force for the same particle as measurement for one second showed that the dispersion was promoted due to the particle-particle collision since the particle number is increased for the same particle mass flow rate. If the Saffman force is considered in this case, the dispersion was furthermore promoted to approach to the measurement.

The Saffman force is theoretically derived when the particle Reynolds number is small. Therefore, the applicability to high Reynolds number flow is not justified since the particle Reynolds number reaches to about 100 in this experiment. By the measurement of lift force on particle near the wall, the transverse force like the Saffman force is found when the particle Reynolds number is larger than unity[18]. Then, we can infer that a transverse force like the Saffman force exists in high particle Reynolds number flow as well. It is noted that the particle-particle collision number in **Fig. 8 (a)** is larger than that in **Fig. 8 (b)**, indicating the effect of the Saffman force.

Thus, the Saffman force is one of possible sources to disperse the powder jet. We are still continuing to examine the effect of particle-particle collision, the particle size distribution and the collision model for the particle.

Fig. 9 shows the dimensionless axial velocity profiles of the powder jet and the entrained air by the simulation and the measurement. However, it should be noted that the entrained air velocity profile was measured only for $\dot{m}=5.747\times10^{-3}$kg/s and that the simulation for this case could not carried out. The calculated axial velocity profile of the powder jet shows a similar behavior to the measurement, but is smaller than that of the measurement in the magnitude. It is found that the entrained air velocity in calculation reduces rapidly to zero in radial direction as compared with the measurement and the simulation does not predict accurately the dispersion of the entrained air flow. Furthermore, we will carry out the calculation considering the transverse force in the source term in the equation of motion for air flow as well.

6. Conclusion

To understand air entrainment phenomenon into the powder jet, we measured air flow by the using phase-Doppler anemometer. It was shown that the axial velocity profiles of entrained air become similar where the distance from the orifice is increased, show a maximum near the center-line and decrease toward the outer edge of powder jet, and that the entrained air flow region extends to the particle free region.

The center-line velocity of the entrained air increases at first with an increase in axial distance from the orifice, and then decreases after a plateau. The center-line velocity of powder jet is larger than the settling velocity of a single particle but smaller than that of free fall without the drag force, and it seems to converge a constant value.

The half radius and the outer edge of the entrained air increase in proportion to the square root of the axial distance from the orifice at a long distance. The dispersion of entrained air is very small as compared with that of a single-phase turbulent jet.

The present simulation shows that the Saffman force contributes to disperse the powder jet.

Acknowledgements

We wish to thank Mr. Hidehiro Kawanami of the graduate student in Kyushu Institute of Technology

for his cooperation to this work. This work was supported by grant-in-aid for Scientific Research (C) (2) 09650195 of the Ministry of Education, Science, Sports and Culture of Japan.

Nomenclature

b	: half radius	(mm)
C_D	: drag coefficient	(−)
d	: particle diameter	(μm)
g	: gravitational acceleration	(m/s^2)
k	: turbulent energy	(m^2/s^2)
r_e	: outer edge radius of powder jet and entrained air	(mm)
u	: entrained air velocity	(m/s)
v	: particle velocity	(m/s)
x, y, z	: Cartesian coordinates	(mm)
r, θ, z	: cylindrical coordinates	(mm),(rad)
$\dot{m}$	: mass flow rate of particles	(kg/s)
ε	: dissipation rate of turbulent energy	(m^2/s^3)
ν_l	: kinematic viscosity of air	(m^2/s)
ρ_a	: air density	(kg/m^3)
ρ_p	: particle density	(kg/m^3)
ω	: angular velocity of particle	(rad/s)

References

1) Richardson, J.F. and W.N. Zaki: "Sedimentation and Fluidisation, Part 1", *Trans. Inst. Chem. Eng.*, **32**, 35-53, (1954)
2) Famularo, J. and J. Happel: "Sedimentation of Dilute Suspension in Creeping Motion", *AIChE J.*, **11**-6, 981-988, (1965)
3) Steinour, H.H.: "Rate of Sedimentation, Nonflocculated Suspensions of Uniform Spheres", *Ind. Eng. Chem.*, **36**-7, 618-624, (1944)
4) Watanabe, H.: "Voidage Function of Sedimentation in Particulate Suspension", *J. Soc. Powder Tech., Japan*, **13**-10, 546-555, (1976)
5) Stinzing, H.D.: "Fluid Drag on Clouds Consisting of Solid Particle Enclosed in a Pipe", *Pneumotransport* 1, C6, 69-80, (1971)
6) Boothroyd, R.G.: "Flowing Gas-Solids Suspensions", Chapman and Hall Ltd., 24, (1971)
7) Ogata, K., K. Funatsu and Y. Tomita: "Characteristics of Free Falling Powder Jet and the Air Entrainment Phenomenon", *Trans. Jpn. Soc. Mech. Eng.*, **65**-633, 1629-1635, B(1999)
8) Saffman, P.G.: "The Lift on a Small Sphere in a Slow Shear Flow", *J. Fluid Mech.*, **22**-2, 385-400, (1965)
9) Tashiro, H. and Y. Tomita: "A Numerical Simulation of a Gas-Solid Two-Phase Flow(1st Report)", *Trans. Jpn. Soc. Mech. Eng.*, **56**-526, 1611-1614, B(1990)
10) Tashiro, H., X. Peng and Y. Tomita: "Numerical Simulation for Prediction of Saltation Velocity for Gas-Solid Two-Phase Flow in a Horizontal Pipe", *Trans. Jpn. Soc. Mech. Eng.*, **61**-589, 3210-3214, B(1995)
11) Morsi, S.A. and A.J. Alexander: "An Investigation of Particle Trajectories in Two-Phase Flow Systems", *J. Fluid Mech.*, **55**-2, 193-208, (1972)
12) Tsuji, Y., Y. Morikawa and O. Mizuno: "Experimental Measurement of the Magnus Force on Rotating Sphere at Low Reynolds Numbers", *Trans. ASME J. Fluids Eng.*, **107**, 484-488, (1985)
13) Dennis, S.D.R., S.N. Singh and D.B. Ingham: "The Steady Flow due to a Rotating Sphere at Low and Moderate Reynolds Numbers", *J. Fluid Mech.*, **10**-2, 257-279, (1980)
14) Ogata, K., K. Funatsu and Y. Tomita: "Flow Behaviors of Powder Jet and Entrained Air", *Prepr. of Jpn. Soc. Mech. Eng.*, No.998-1, 181-182, (1999-3)
15) Jones, W.P. and B.E. Launder: "The Prediction of Laminarization with a Two-Eqation Model of Turbulence", *Int. J. Heat Mass Transfer*, **15**, 301-313, (1972)
16) Peng, X., H. Tashiro and Y. Tomita: "Flow of Coarse Particles in Horizontal Pneumatic Pipes", *Trans. Jpn. Soc. Mech. Eng.*, **63**-612, 2645-2651, B(1997)
17) Townsend, A.A.: "The Structure of Turbulent Shear Flow", *Cambridge Univ. Press*, 189-205, (1976)
18) Hall, D.: "Measurements of the Mean Force on a Particle near a Boundary in Turbulent Flow", *J. Fluid Mech.*, **187**, 451-466, (1988)

Author's short biography

Koichiro Ogata

Koichiro Ogata graduated in mechanical engineering of Kyushu Institute of Technology (KIT) in 1996. He also received a master's degree and doctoral degree in mechanical engineering from KIT in 1998 and 2001. He is now a Research worker at Satellite Venture Business Laboratory of KIT. His major research interests are the effect of particle-particle and particle-fluid interaction for powder handling process, the evaluation of dynamic physical properties of powder.

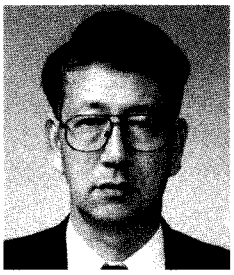

Katsuya Funatsu

Katsuya Funatsu is a Research engineer in the department of mechanical and control engineering of KIT.

Yuji Tomita

Yuji Tomita academic background involves a bachelor's degree in mechanical engineering from KIT in 1965. From there he went to the University of Tokyo, and received a master's degree in mechanical engineering and his doctoral degree in mechanical engineering doing a study in pipe flows of dilute aqueous polymer solution. He decided then to go into teaching and went back to KIT in 1970. His work has been primarily in the field of fluid mechanics with specialization in the areas of drag reduction and gas-solid two-phase flow. Since 1970 when he came back to KIT, he also has been deeply involved in work on pneumatic transport of solid and solids feeders. Recently he started studies of hydraulic capsule transport and fluidization of powder by mechanical means. He has been acting as the head of powder technology laboratory in the department of mechanical and control engineering of KIT since our late Professor T. Jotaki retired in April in 1979.

Zeolite Synthesis from Coal Fly Ash Prepared by Hydrothermal Treatment Method and Effect of Particle Size on Its Reaction Mechanism†

Kunihiro FUKUI, Hideto YOSHIDA, Hironori SAKAGUCHI and Mitsuhiro ARITA
*Department of Chemical Engineering, Hiroshima University**

Abstract

We investigated an effect of fly ash particle size on the synthesis of zeolites from coal fly ash, proposed and formulated the formation mechanism of zeolite.

It is found that the treatment time for the zeolites to synthesize decreases with a decrease in feed fly ash particle size. When the feed size is small, both phillipsite and hydroxysodalite are synthesized by hydrothermal treatment with NaOH solution. Only phillipsite is synthesized when large fly ash particles are used. The zeolite from the fly ash having 2.1 μm mass median diameter indicates the maximum $NH4^+$-adsorption capacity.

The change in liquid ion concentrations calculated by the newly proposed model agrees with the experimental results. It is assumed that dissoluble silica is contained by about twice the mass of dissoluble alumina in the large fly ash particles, while in the case of small ones, they are almost equal.

Keywords: Fly ash, Hydrothermal synthesis, Particle size, Zeolite

Introduction

Fifty-four percent of the fly ash generated by thermal power plants and other facilities is reused as concrete admixture, in building materials, and in many other ways, but the rest is currently landfilled as industrial waste (Kankyou Gijyutsu Kyoukai and Nihon Fly Ash Kyoukai, 1995a). In view of the anticipated difficulty of finding large landfill sites, as well as the problems of resource depletion and environmental damage, high-added-value, effective ways to reuse this fly ash need to be quickly developed. One new way to reuse fly ash (Kankyou Gijyutsu Kyoukai and Nihon Fly Ash Kyoukai, 1995b) by making zeolites with hydrothermal synthesis has been proposed (Haruna, 1989). This consists in attempts to synthesize zeolites (Takasaka et al., 1977; Matsukata et al., 1996), which have high added value as adsorbents, catalysts, and other materials whose raw materials are the silica and alumina that are the main components of fly ash (Takahashi et al.; 1977, Kato et al., 1986). However, hardly any detailed quantitative investigation has been done on the influence of feed fly ash particle size or on reaction mechanisms (Uchida, 1987; Haruna, 1991; Touyama et al., 1996).

For these reasons the purpose of our research was to investigate the influence of differences in fly ash particle size on the rate of zeolite formation and on its crystallization form, and to speculate on the reaction mechanism of zeolite formation.

1. Experiment

Our sample powders were four fly ash types (Samples A through D) whose mass median diameters were adjusted by classifying clinker fly ash from Chugoku Electric Co.'s Shin-Onoda Power Plant. As **Table 1** shows, they are mostly the same in component composition and crystal structure (SiO_2: powder diffraction file, inorganic volume, 34-1382; $Al_6Si_{12}O_{13}$: powder diffraction file, inorganic volume, 15-776; Al_2SiO_5: powder diffraction file, inorganic volume, 44-27), while the samples differ only in particle size.

Fig. 1 is a schematic diagram of the hydrothermal synthesis reactor. We hydrothermally treated the fly ash by suspending 40.0 g of test powder in 1.0 l of

* Higashi Hiroshima, 739-8527

† This report was originally printed in Kagaku Kougaku Ronbunshu, **25**, 987-991 (1999) in Japanese, before being translated into English by KONA Editorial Committee with the permission of the editorial committee of Soc. Chemical Engineers, Japan.

Table 1 Properties of tested powders

		Sample A	Sample B	Sample C	Sample D
Mass median diameter [μm]		1.4	2.1	10.8	19.8
Percent of whole	SiO_2	51.0	51.0	52.5	52.5
	Al_2O_3	37.0	37.0	37.0	37.0
	CaO	3.8	3.7	3.1	3.0
	Fe_2O_3	3.4	3.0	3.7	3.8
	Others	4.8	5.3	3.7	3.7
Crystal structure		SiO_2, $Al_6Si_{12}O_{13}$, Al_2SiO_5			

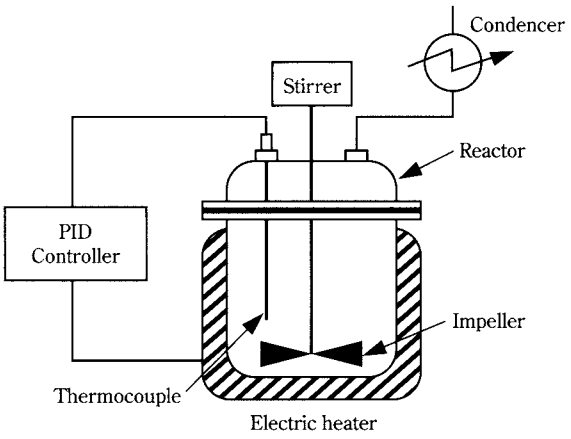

Fig. 1 Schematic diagram of hydrothermal synthesis reactor

aqueous 2N NaOH solution maintained at a reaction temperature of 373 K. Reaction pressure was 1 atm, and stirrer speed was 200 rpm. When the reaction was done, the reactor vessel was allowed to cool to room temperature in the atmosphere, and the suspension was then filtered. After fully washing the separated product with distilled water, we dried it at 393 K for 48 h.

We evaluated the mass of ammonium ion adsorption of product and crystal structure of it. The apparatus in **Fig. 2** was used to send a 200 ppm aqueous solution of NH_4Cl at 1.0 ml/min through a column packed with 0.5 g of product. A spectrophotometer (Shimadzu UV-1200) was used to measure the ammonium ion concentration of the solution passed through the column, and then the mass of ammonium ion adsorption was calculated with the following equation.

$$A = \frac{V(C_I - C_E)}{m_p} \quad (1)$$

Where:

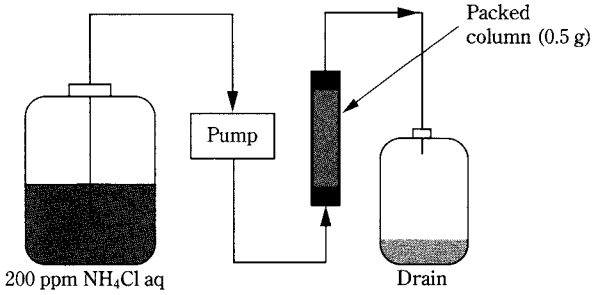

Fig. 2 Experimental setup (adsorption of NH_4^+)

A is the ammonium ion adsorption amount per unit mass of product,
V is the total amount of solution passed through the column,
C_I is the ammonium ion concentration before passage through the column, and
C_E is the ammonium ion concentration of the whole solution after passing through the column.

We observed the crystal structure with an x-ray diffraction (XRD) analyzer (Rigaku RINT-1000).

An atomic absorption analyzer (Shimadzu AAG-6400G) was used to measure the ion concentration in the hydrothermal synthesis reaction solution.

2. Results and Discussion

2.1 Effects of Feed Particle Size on the Formation of Zeolites from Fly Ash

Fig. 3 presents the SEM photographs of the original fly ash and the product yielded from fly ash after 12 h of hydrothermal synthesis. Although the feed ash is spherical and hardly agglomerated, in the product many new scale-like or parallelepiped substances are precipitated onto the surface of the fly ash, and there are associated particles.

Fig. 4 shows some of the XRD peak charts for fly ash and products obtained from it after 12 h of hydrothermal synthesis. The fly ash is a mixed crystal of $Al_6Si_{12}O_{13}$ and Al_2SiO_5, while the products exhibit peaks not seen in the fly ash plot. The product from Sample B has the peaks for kinds of zeolite called phillipsite ($Na_6Al_6Si_{10}O_{32}H_2O$; powder diffraction file, inorganic volume, 26-1310; 2.7, 3.3, 4.1, and 7.2 Å) and for hydroxysodalite ($Na_4Al_3Si_3O_{12}OH$; powder diffraction file, inorganic volume, 11-401; 3.3, 3.7, 4.1, and 6.4 Å), and the product from Sample C has the peaks for phillipsite only.

These results show that, under the same treatment conditions, differences in feed fly ash particle size

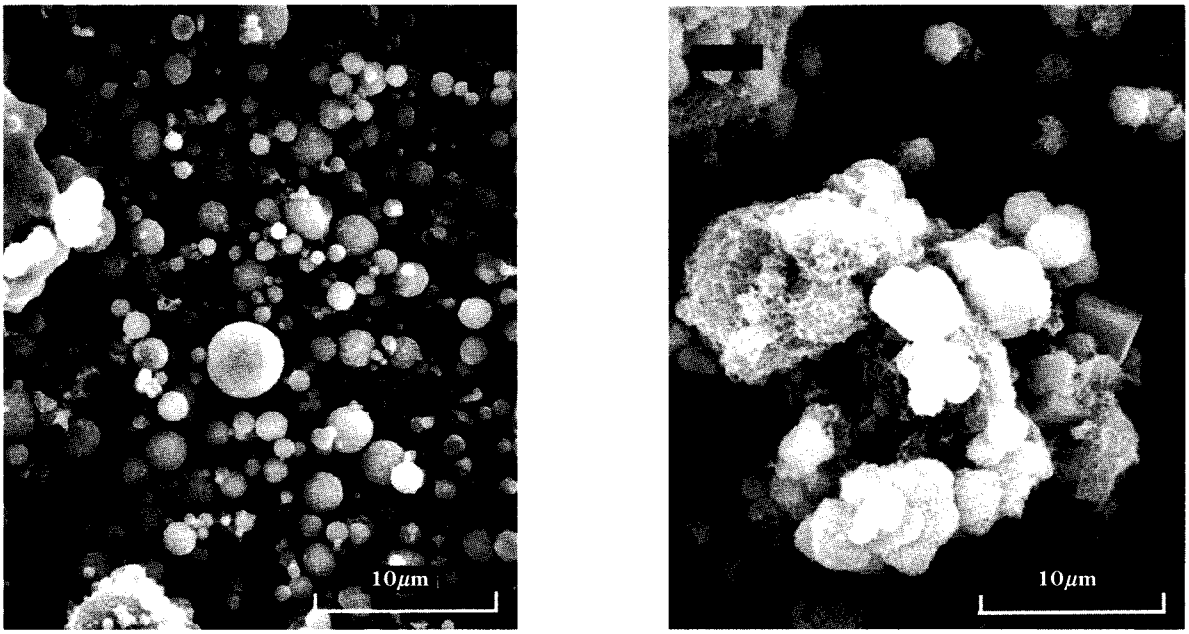

(a) Original fly ash (Sample C)

(b) Product from Sample C (Treatment time, 12 h)

Fig. 3 SEM photographs of original fly ash and product

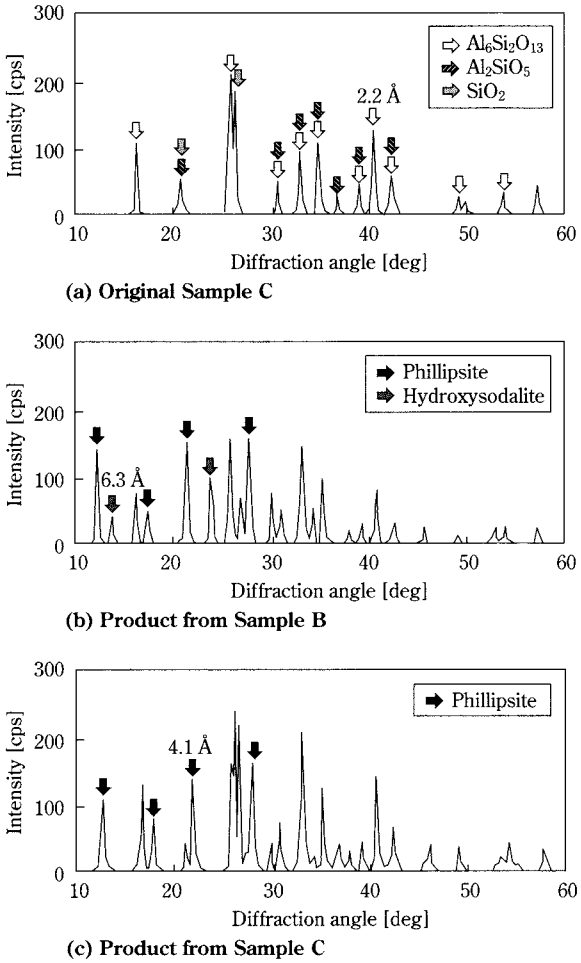

Fig. 4 XRD peak charts for original fly ash and products (treatment time, 12 h)

will yield different kinds of zeolite.

Fig. 5 shows the relationship between hydrothermal treatment time and the relative intensities of phillipsite peaks for a plane spacing of 4.1 Å, and a 6.3 Å peak for hydroxysodalite. Our standard for relative intensity was the fly ash peak for plane spacing of 2.2 Å, which exhibited a nearly constant height whether or not treatment had occurred. In the case of Samples A and B, whose particle sizes were small, the phillipsite relative intensity rapidly increased immediately after starting hydrothermal treatment, then later tended to decline. The relative intensity of hydroxysodalite increased with treatment time. At 10 h treatment time and thereafter, the decline in phillipsite's relative intensity and the rise in hydroxysodalite's relative intensity proceeded simultaneously, which suggests that the phillipsite that had been formed was transforming into hydroxysodalite. But with Samples C and D, whose particle sizes were relatively large, the relative intensity of phillipsite began to increase after about 3 h of treatment, and then later became nearly constant. Hydroxysodalite was not formed at all from these samples. These results show that if smaller fly ash particle sizes are used, it is possible to synthesize crystalline zeolite with a shorter treatment time. Additionally, we found that the crystal morphology distribution of the zeolite product differs according to particle size.

Fig. 6 shows the relationship between hydrothermal treatment time and the ammonium ion equilib-

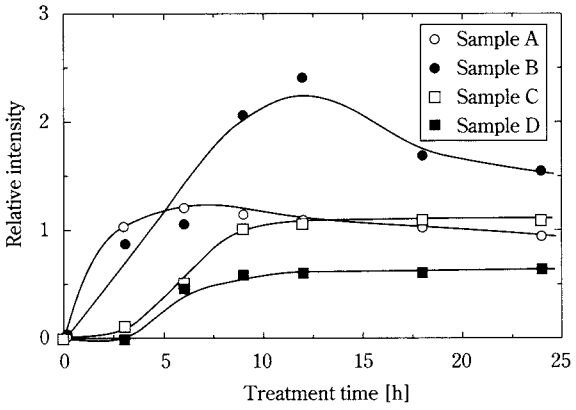

(a) Phillipsite

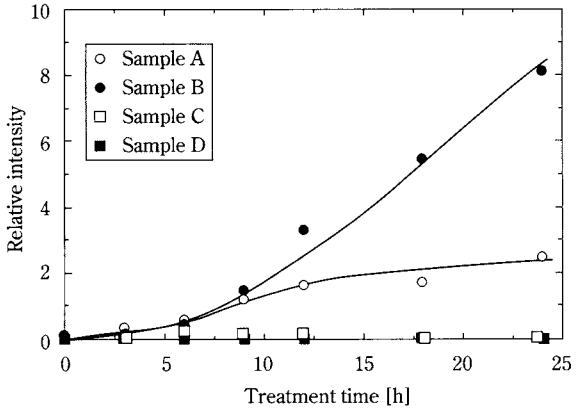

(b) Sodium silicate hydrate

Fig. 5 Change in relative intensity of zeolites according to treatment time

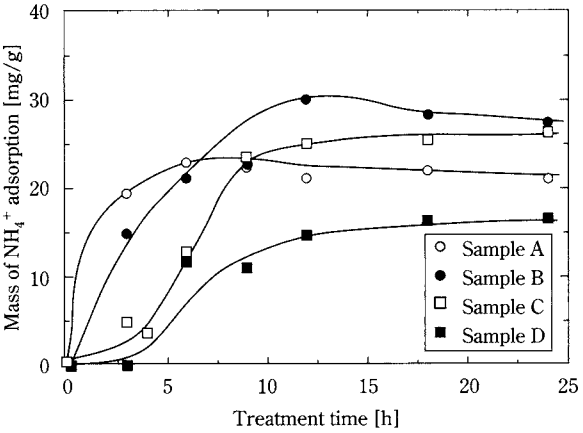

Fig. 6 Change in mass of ammonium ion adsorption according to treatment time

rium adsorption amount. For all fly ash samples, adsorption first increased with hydrothermal treatment time, and then attained a nearly constant rate or gradually decreased. As the fly ash particle size is smaller, the adsorption increase rate is larger during the early part of the reaction period. Also, the larger the fly ash particle size, the more adsorption declined in the latter part of the reaction period, with Sample B showing the largest adsorption. This means that using fly ash of a suitably small size makes it possible to synthesize zeolites with a high adsorption capacity with a shorter hydrothermal treatment time. Further, comparing this graph with **Fig. 5** reveals that the relationship between adsorption amount and hydrothermal treatment time resembles the relationship between phillipsite's relative intensity and hydrothermal treatment time. It is therefore likely that mainly the phillipsite product was adsorbing the ammonium ions.

We next measured the change over time in the ion concentration of the reaction solution to investigate the reason that different zeolite types are formed depending on fly ash particle size, and to infer the mechanism of zeolite formation.

Fig. 7 shows the relationship of concentration for

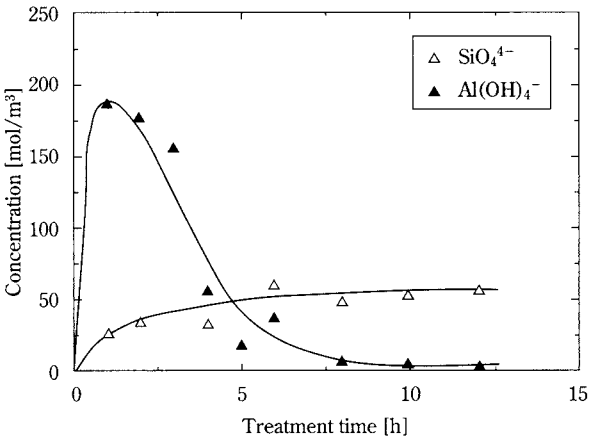

(a) Sample B

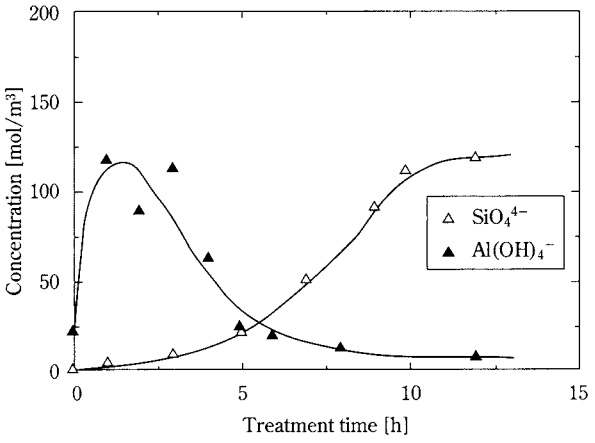

(b) Sample C

Fig. 7 Change in anion concentration according to treatment time

two samples of the silicate ion (SiO_4^{4-}) and the aluminate ion ($Al(OH)_4^-$) to treatment time. The graph for Sample B, from which hydroxysodalite formed, shows that the $Al(OH)_4^-$ concentration rose sharply as soon as the reaction began, then fell after reaching its maximum, finally coming to nearly zero. The SiO_4^{4-} concentration increased with treatment time and then leveled off. With Sample C, the $Al(OH)_4^-$ concentration produced the same curve as that of Sample B, while the SiO_4^{4-} concentration was very low until about the fourth hour of treatment, and then increased. Further, the SiO_4^{4-} concentration after 10 h of processing, when the formation of hydroxysodalite is pronounced, was about twice that of Sample B. This showed that the original fly ash particle size was responsible for considerable differences in not only the kind of zeolite formed, but also the ion behavior in the reaction solution. Experiments indicated similar ion behavior for Samples A and B, and for Samples D and C.

2.2 Modeling Zeolite Formation from Fly Ash

Based on the ion concentration change described above, we used the model described below (Tominaga, 1996) to quantitatively evaluate the reaction process by which fly ash becomes zeolite. When fly ash is suspended in an aqueous NaOH solution, the SiO_2 and Al_2O_3 in the fly ash become SiO_4^{4-} and $Al(OH)_4^-$ by the formulas shown in Eqs. 2 and 3, and dissolve into the solution. The dissolved ions form intermediate products such as aluminosilicate gel (Eq. 4). We postulate that bonding continues and forms bulks of a certain size, which then crystallize (Eq. 5).

$$SiO_2 + 2OH^- \longrightarrow SiO_4^{4-} + 2H^+ \quad (2)$$

$$Al_2O_3 + 2OH^- + 3H_2O \longrightarrow 2Al(OH)_4^- \quad (3)$$

$$SiO_4^{4-} + Al(OH)_4^- \longrightarrow HO\text{-}Si(OH)_2Al(OH)\text{-}(OH) \quad (4)$$

$$HO^- \cdots Si(OH)_2 \cdots Al(OH) \cdots OH + Na^+ + OH^- \longrightarrow Na_6Al_6Si_{10}O_{32}H_2O \quad (5)$$

We postulate the following reaction rate equations from the reactions in Eqs. 2 through 5. First of all, the rate equations for the dissolution reaction given by Eqs. 2 and 3 are zero-order reactions as shown in the following equations.

$$\frac{d\,M_{Si}}{dt} = -k_{Si} \quad (6)$$

$$\frac{d\,M_{Al}}{dt} = -k_{Al} \quad (7)$$

Assuming that the formation rate (r_{Gel}) of the intermediate product appears to be proportional to the product of $Al(OH)_4^-$ concentration (C_{Al}) and SiO_4^{4-} concentration (C_{Si}), and that the zeolite crystallization rate is proportional to the gel concentration (C_{Gel}), the following equations are obtained.

$$r_{Gel} = k_{Gel}\, C_{Al}\, C_{Si} \quad (8)$$

$$\frac{d\,M_{Cry}}{dt} = k_{Cry}\, C_{Gel} \quad (9)$$

Where:

k_{Si} and k_{Al} are constants for the dissolution rates of SiO_2 and Al_2O_3, respectively,

k_{Gel} and k_{Cry} are rate constants of gelation and crystallization reactions, respectively,

M_{Si} and M_{Al} indicate moles of SiO_2 and Al_2O_3 in the fly ash, respectively, and

M_{Cry} indicates moles of zeolite crystal.

Based on Eqs. 6 through 9, the concentrations of ions and intermediate products in the reaction solution are given by the following equations.

$$\frac{d\,C_{Si}}{dt} = k_{Si} - k_{Gel}\, C_{Al}\, C_{Si} \quad (10)$$

$$\frac{d\,C_{Al}}{dt} = k_{Al} - k_{Gel}\, C_{Al}\, C_{Si} \quad (11)$$

$$\frac{d\,C_{Gel}}{dt} = k_{Gel}\, C_{Al}\, C_{Si} - k_{Cry}\, C_{Gel} \quad (12)$$

Using the previously given reaction rate equations to explain the changes in ion behavior and zeolite formation amount in the reaction solution makes it necessary to determine six unknowns: the four reaction rate constants noted above, and the moles of soluble SiO_2 and Al_2O_3 (M_{SiO} and M_{AlO}) in the fly ash.

We measured k_{Si} and k_{Al} because these unknowns are experimentally determinable. Specifically, because XRD measurements revealed that zeolite crystals do not form at reaction temperatures below 333 K, it seems safe to assume that under such conditions only SiO_2 and Al_2O_3 dissolve out. **Fig. 8** presents the results obtained from measuring ion behavior in the reaction solution at 313 K. Experimental conditions other than reaction temperature were the same as those for the hydrothermal synthesis reaction at 373 K. Increases in SiO_4^{4-} and $Al(OH)_4^-$ ion concentrations were both proportional to treatment time. This confirms our assumption that at low temperatures only the reaction for dissolution from fly ash occurs. The dissolution rate constants can therefore be calculated from this gradient.

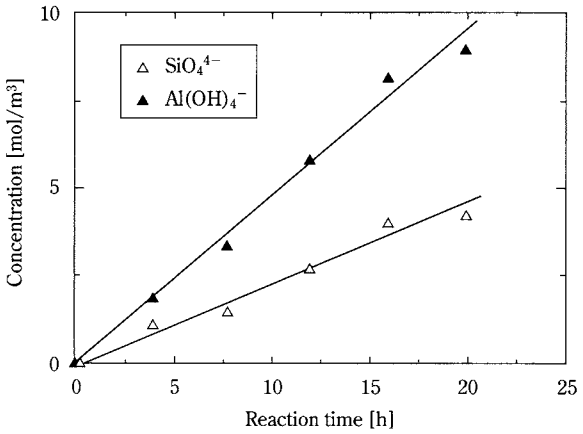

Fig. 8 Change in anion concentration according to reaction time at 313 K

Fig. 9 is an Arrhenius' plot of the dissolution rate constants at 313 to 333 K. As both display linear relationships, it is possible to determine the dissolution rate constants at 373 K. **Table 2** gives the constants obtained in this manner. Exactly the same procedure was used for all samples other than Sample C.

Because the dissolution rate constant had been determined, that reduced the needed unknowns to four. We determined those unknowns by numerical calculations based on our experimental results. We optimized the unknowns so as to minimize the error between the numerical solutions and experimental results, then determined the unknowns. Conditions used for these calculations were the same as the experimental conditions, i.e., 40 kg of fly ash were added to 1 m^3 of 2N aqueous NaOH solution. We set the maximum moles of SiO_2 and Al_2O_3 that can be dissolved at 394 and 290 moles, respectively. These values are the composition analysis results given in **Table 1**, converted to moles. Variables at the reaction's start (t=0) were as follows.

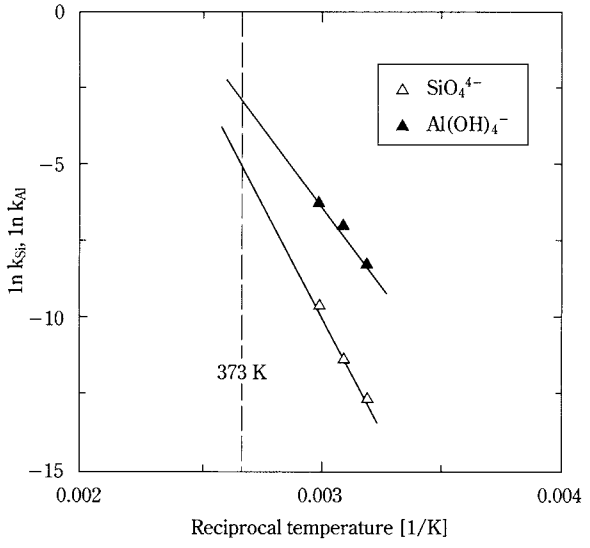

Fig. 9 Arrhenius plot for dissolution from Sample C

Table 2 Rate constants of dissolution at 373 K calculated from the Arrhenius plot

	k_{Si} [mol/m³s⁻¹]	k_{Al} [mol/m³s⁻¹]
Sample A	2.3×10^{-2}	2.3×10^{-1}
Sample B	1.9×10^{-2}	2.0×10^{-1}
Sample C	6.2×10^{-3}	6.3×10^{-2}
Sample D	2.0×10^{-2}	9.5×10^{-3}

$$t=0;\ C_{Al}=0,\ C_{Si}=0,\ C_{Gel}=0,\ M_{Cry}=0 \quad (13)$$

$$M_{SiO} \leq 394 \quad (14)$$

$$M_{AlO} \leq 290 \quad (15)$$

Relative intensity shown in **Fig. 5** was used as the representative value for the zeolite product amount.

Fig. 10 shows the relationship of reaction solution

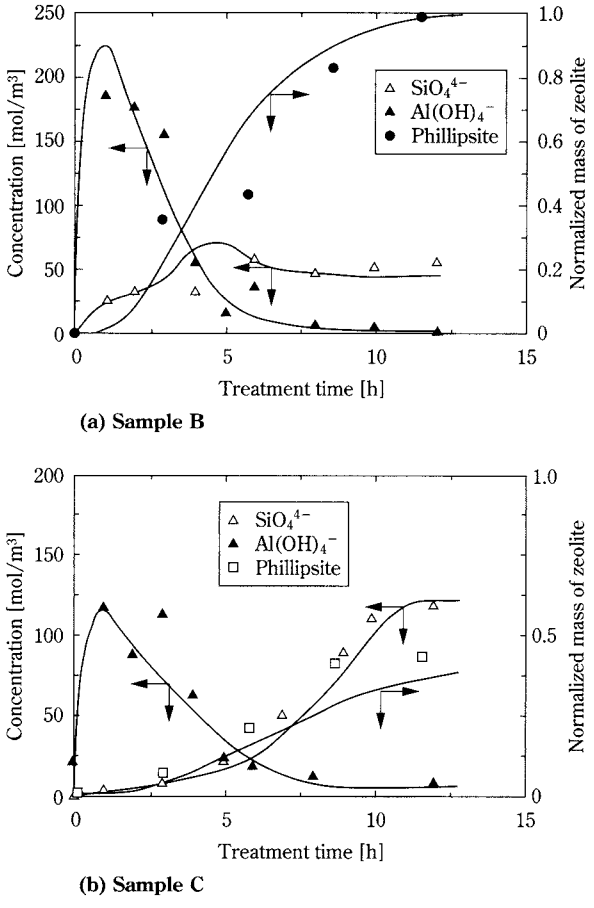

Fig. 10 Comparison between experimental and calculated results for concentration and normalized mass change

Table 3 Values of parameters optimized by numerical calculation

	k_{Gel} [mol/m^{3}s^{-1}]	k_{Cry} [m^{3}s^{-1}]	M_{SiO} [mol]	M_{AlO} [mol]
Sample A	9.3×10^{-6}	3.4×10^{-3}	310	264
Sample B	2.9×10^{-6}	6.9×10^{-3}	314	269
Sample C	1.0×10^{-5}	2.8×10^{-3}	244	128
Sample D	6.8×10^{-5}	2.3×10^{-3}	218	110

ion concentration to zeolite product amount and treatment time. The results are reproduced by numerical calculations. The amount of zeolite produced is shown normalized with the benchmark being the zeolite amount produced from Sample C after 12 h of processing. No matter which fly ash sample was used, we were able to make calculation results closely match our experimental results. This suggests that, using the reaction formulas and reaction rate equations postulated above, we have to an extent suitably described the reaction mechanism by which zeolites are formed from fly ash.

Table 3 presents the unknowns determined by numerical calculations. In Samples A and B, from which hydroxysodalite was produced, the soluble SiO_2 and Al_2O_3 components in the fly ash have nearly the same number of moles, while by contrast Samples C and D, from which no hydroxysodalite growth was observed, have about twice as much soluble SiO_2 as soluble Al_2O_3. The reason that different types of zeolite form depending on particle size even when classifying all the clinker fly ash samples and adjusting their particle sizes seems to be that the ratio of soluble SiO_2 to Al_2O_3 components differs for each particle size, which brings about different ion behavior in the reaction solution.

Conclusion

1) The hydrothermal treatment of fly ash whose particle size has been reduced through classification makes it possible to synthesize, in a short treatment time, crystalline zeolites with a higher ammonium ion adsorption capacity.
2) When the fly ash examined in our experiment had a particle size of under approximately 2 μm, phillipsite and hydroxysodalite were formed, but at particle sizes of 10 μm and above only phillipsite was obtained.
3) According to our reaction mechanism model, the SiO_2 and Al_2O_3 in fly ash dissolved into the aqueous NaOH solution, passed through an intermediate product stage, and then crystallized. This model can to an extent quantitatively explain the change over time in ion behavior in the reaction solution, and in the amount of zeolite product.
4) The type of zeolite formed depends on the particle size of the feed fly ash. A reason for this is that the difference according to particle size in the ratio of soluble SiO_2 to Al_2O_3 brings about differences in ion behavior in the reaction solution.

Nomenclature

A	Ammonium ion adsorption amount per unit mass of product	[g/g]
C_{Al}	Concentration of $Al(OH)_4^-$	[moles/m^3]
C_E	Concentration of NH_4Cl aq. at packed bed outlet	[moles/m^3]
C_{Gel}	Concentration of gel	[moles/m^3]
C_I	Concentration of NH_4Cl aq. at packed bed inlet	[moles/m^3]
C_{Si}	Concentration of SiO_4^{4-}	[moles/m^3]
k_{Al}	Rate constant of Al_2O_3 dissolution	[moles/m^3 s^{-1}]
k_{Cry}	Rate constant of crystallization	[moles s^{-1}]
k_{Gel}	Rate constant of gelation	[moles/m^3 s^{-1}]
k_{Si}	Rate constant of SiO_2 dissolution	[moles/m^3 s^{-1}]
m_p	Mass of packed bed	[g]
M_{Al}	Moles of Al_2O_3 in feed fly ash	[moles]
M_{AlO}	Moles of soluble Al_2O_3 in feed fly ash	[moles]
M_{Cry}	Moles of zeolite crystals	[moles]
M_{Si}	Moles of SiO_2 in feed fly ash	[moles]
M_{SiO}	Moles of soluble SiO_2 in feed fly ash	[moles]
t	Reaction time	[s]
V	Volume of NH_4Cl aq. discharged from packed bed	[m^3]

Literature Cited

Haruna, J. Japan Patent 01-24014 (1989).

Haruna, J. Japan Patent 03-45512 (1991).

Kankyou Gijyutsu Kyoukai and Nihon Fly Ash Kyoukai, ed. *Coal Ash Handbook*, p. II-4, Tokyo, Japan (1995a).

Kankyou Gijyutsu Kyoukai and Nihon Fly Ash Kyoukai, ed. *Coal Ash Handbook*, p. II-219, Tokyo, Japan (1995b).

Kato, Y., K. Kakimoto, H. Ogawa, M. Tomari and E. Sakamoto. "An Application of Hydrothermal Crystallized Coal Ashes to Waste Water Treatment 1," *Industrial Water*, **33**, 27-33 (1986).

Matsukata, M., N. Nishiyama and K. Ueyama. "Crystallization of FER and MFI zeolites by a vapor-phase transport method," *Microporous Material*, **7**, 109-117 (1996).

Takahashi, H. and S. Sanga. "Zeolite as a Removing Material for Ammonium Ions in Waste Water," *Seisan Kenkyuu*,

29, 3, 92-95 (1977).
Takasaka, A., M. Sato, T. Okuyama and Y. Matsuda. "Removal of H^+, NH_4^+, Cu^{2+} and Cd^{2+} by Using Itaya-Zeolite," *Zairyou*, **27**, 628-631 (1977).
Tominaga, H. *Zeoraito no Kagaku to Ouyou*, pp. 75-79, Kodansha, Tokyo, Japan (1996).
Touyama, Y., K. Katayama and M. Meguro. "NH_4^+ Adsorption Characteristics of Zeolites Synthesized from Fly Ash," *J. of Chem. Soc. of Japan*, **2**, 136-140 (1996).
Uchida, H. and A. Sato. "A Study on the Ammonium Isotherms of Zeolite," *J. of Japan Water Association*, **56**, 41-47 (1987)

Author's short biography

Kunihiro Fukui

The author received his B.S. and M.S. degrees from Kyoto University in 1991 and 1993. He earned his Ph.D. degree in Chemical Engineering in 1998 from Kyoto University. He is Research Instructor of Chemical Engineering Department at Hiroshima University since 1996. His major research interests are accurate size classification of fine particles, measurement of particle size distribution and recycling of coal fly ash.

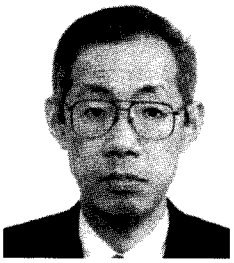

Hideto Yoshida

The author is Professor of Chemical Engineering Department at Hiroshima University since 1994. His major research interests are fine particle classification, numerical simulation of cyclone separator, cut size control of dry and wet cyclones and development of particle size distribution with automatic liquid sedimentation method.

Hironori Sakaguchi

He is now working as a engineer at Okayama prefectural office. He received his B.S. and M.S. degrees from Hiroshima University in 1996 and 1998.

Mitsuhiro Arita

He received his B.S. degrees from Hiroshima University in 1997.

An Evaluation of the Mixing Performance of Adhesive Fine Powders in a Tumbling Fluidized Bed Granulator Equipped with an Opposed Pulsed Jet Assembly†

Hiroyuki Tsujimoto and Toyokazu Yokoyama
*Hosokawa Micron Corp.**
Peter G. J. van der Wel
*Hosokawa Micron B.V***
and Isao Sekiguchi
*Department of Applied Chemistry, Chuo University****

Abstract

An optical sensor and adhesive fine powders were used to quantitatively evaluate the mixing performance of a tumbling fluidized bed granulator with an opposed pulsed jet (PJ) assembly. The effects of operating conditions were investigated in terms of the ratio of light intensity reflected from the powder mixture to that in the ultimately dispersed state, η_I. Mixing performance was then compared with that of other mixer types in terms of mixing degree η_I and processing energy consumption. The granulator's mixing performance was equal to or better than that of a high-speed stirring mixer.

Keywords: Tumbling fluidized bed, pulsed jet assembly, degree of mixing, mixing performance, optical measurement

1. Introduction

A tumbling fluidized bed granulator consisting of a batch fluidized bed granulator into which tumbling granulation and agitation granulation mechanisms have been incorporated [1] has functionality allowing a single granulator to continuously perform the operations of mixing the feedstock powder, granulating, and drying, and it can easily control size, shape, bulk density, and other product characteristics by adjusting granulation operating conditions. Tumbling fluidized bed granulators are now used in a wide variety of industries such as pharmaceuticals, ceramics, and food processing.

In conjunction with the rapid growth of the new materials, IT equipment, and other industries over the last few years, industry is actively developing composite particles used as functional materials for electronic components and rechargeable batteries. These general powder processes comprise a series of individual operations for making and drying granules for the purposes of: controlling particle size and shape through comminution and classification; control of particle dispersibility by kneading and precision mixing; and particle surface modification and coating, or making granules finer. An objective of these processes is to create composite particles with new functions by actively controlling the powders' particle structures and physico-chemical properties. The usual practice has been to use single-function devices suited to each individual operation. One recent trend is to improve efficiency by concatenating these individual operations, while another is the emerging idea of using tumbling fluidized bed granulators for the three individual operations of mixing, granulation, and drying for improvement of yield and product quality, and for process labor-saving and simplification.

These applications have some interesting points in common: the starting feedstock powders for tumbling fluidized bed granulators are multi-component powders containing fine, highly adhesive particles, and the improvement of final product characteristics requires that both the feedstock powders themselves and the resultant particles have excellent characteristics, but most importantly, the mixed state of feedstock powders is vital. The use of tumbling fluidized

* 1-9 Shoudai-Tajika, Hirakata Osaka 573-1132, Japan
** Doetinchem, Holland
*** 1-13-27 Kasuga, Bunkyo-ku Tokyo 112-8551, Japan
† This report was originally printed in J. Soc. Powder Technology, Japan. **36**, 756-767 (1999) in Japanese, before being translated into English by KONA Editorial Committee with the permission of the editorial committee of the Soc. Powder Technology, Japan.

bed granulators is now often considered also for making and processing the granules used for forming and sintering in the manufacturing processes of alloys and ceramics. For example, in the manufacture of WC/Co alloys with superlative metal compositions, it has been observed that the mixing techniques used for feedstock powders are of extremely great importance to improving product quality. [2] And in the manufacture of ceramic capacitors using quickly mixed dielectric feedstock powders, there are reports of quality problems in final products due to segregation when mixing. [3] A similar example would be the process of making solid pharmaceutical preparations, which involve the handling of fine, strongly adhesive main powders and for which tumbling fluidized bed granulators are often used. Over the last few years the implementation of validation has induced the pharmaceutical industry to recognize an important area for research in how to assure uniform amounts of the main powders in the granules made with tumbling fluidized bed granulators, and in the tablets made from those granules, [4, 5] but there have been no evaluations that focus on the mixing performance of tumbling fluidized bed granulators, which affect the uniformity of main powder amounts in products.

The foregoing examples suggest that the precise mixing of feedstock powders is crucial to improving final product quality. Further, in trying to apply tumbling fluidized bed granulation to the process of functional composite particle (granule) manufacturing, which entails the mixing-granulation-drying series of processes, several considerations will be very important from the perspective of determining this granulator's range of applicability and its optimum operating conditions, and obtaining guidelines for purposes such as increasing the operational scale. These are: quantifying the mixing performance and particle dispersibility of tumbling fluidized bed granulators, comparing characteristics with those of ordinary mixers, and considering how such granulators stack up against others in view of their mixing performance.

Hence in this research the authors used a tumbling fluidized bed granulator fitted with an opposed pulsed jet disperser (PJ assembly) developed by the authors [8-12], and attempted the evaluation of mixing performance and dispersion capability by using an index that was defined, in accordance with a method described in previous reports [6, 7], by the lightness of an adhesive powder (calcium carbonate/iron oxide) mixture.

In this section we begin by experimentally investigating how this index is affected by differences in the operating conditions and fluidization type of the tumbling fluidized bed granulator. In the next section we compare the results obtained in this section with the results for different types of mixers [13], and present the results obtained by exploring the possibilities for using this granulator in the mixing, granulation, and drying processes for the functional materials required in the precision mixing of feedstock powders.

2. Experimental Apparatus and Method

2.1 Experimental Apparatus

Fig. 1 is a schematic diagram of the tumbling flu-

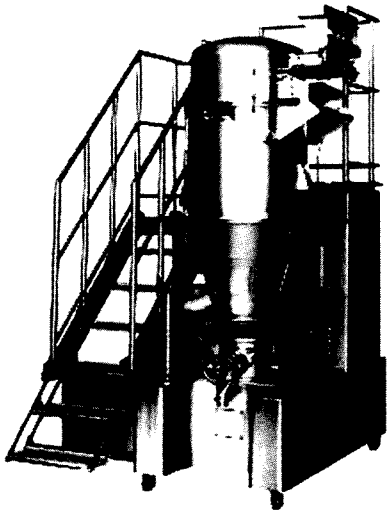

Photo of the Experimental Apparatus

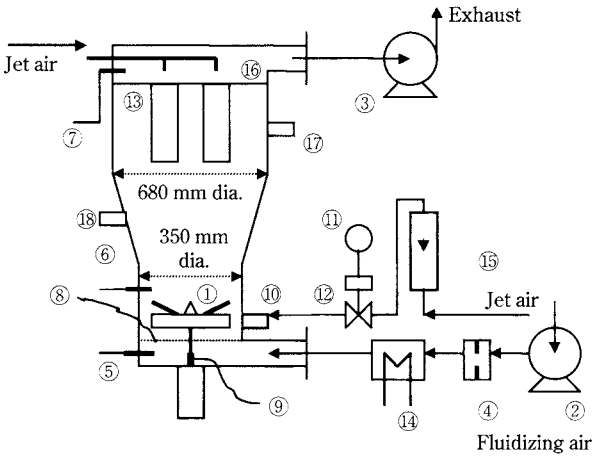

① Granulation chamber, ②, ③ Fan, ④ Orifice flow meter, ⑤, ⑥, ⑦ Pressure tap, ⑧ Distributor, ⑨ Motor shaft, ⑩ Opposed pulsed jet nozzle (three nozzles in all), ⑪ Timer, ⑫ Electromagnetic valve, ⑬ Filter bag (16 bags in all), ⑭ Heater, ⑮ Flow meter, ⑯ Jet nozzles for filter bag cleaning, ⑰ Knocker, ⑱ Knocker

Fig. 1 Schematic Diagram of Experimental Apparatus

idized bed granulator (AGGLOMASTER, AGM-35PJ, made by Hosokawa Micron) used in this experiment. The fluidized bed comprises three SUS304 stainless steel chambers: the granulation chamber (a cylinder, 350 mm inside diameter and 340 mm high), a freeboard (a truncated cone, 585 mm high with inside diameter between 680 and 350 mm), and a filter bag unit (a cylinder, 680 mm inside diameter and 650 mm high). An orifice flow meter measured the airflow rate from the two blowers, and air temperature was maintained at a constant 308 K. Digital manometers measured static pressure in the fluidized bed at three locations: the bottom of the distributor, the top of the fluidized bed, and the exhaust section. Exhaust was filtered through the filter bags (16 bags with a 2.3 m^2 filtration area). Particle masses adhering to these filter bags were dislodged from four bags at a time by intermittent blasts of compressed air (0.6 MPa) discharged at 1 s intervals from a jet nozzle into the bags, and this dislodging operation was repeated at 12 s intervals. Two air knockers were used together at 5 s intervals to minimize adhesion of feedstock powder to the unit's inside walls during operation.

This unit makes it possible to choose among three different ways to fluidize feedstock powder by changing the device configuration at the bottom of the granulation chamber, where a sintered stainless steel plate is fixed to serve as the distributor. Depending on the granulation purpose, it is possible to affix to the central shaft a rotor with a tumbling fluidization agitator (30.0° tilt angle; agitator and rotor rotate coaxially) or an agitating fluidization agitator (10.0° tilt angle). To investigate the effects of differences in unit type on mixing performance, this experiment compared the mixing capabilities of the three different fluidizing types shown in **Fig. 2**: (a) a fluidized bed (FB, distributor only), (b) a tumbling fluidized bed (TFB, distributor and rotor with agitator), and (c) an agitating fluidized bed (AFB, distributor and agitator). The experiment also studied the effects of the additional use of a PJ assembly, which promises to effectively disperse particle masses within these particle beds. **Fig. 3** shows the flow diagram and configuration of the three compressed air nozzles (4 mm dia.) used as the PJ assembly. The nozzles are located 85 mm above the distributor. Nozzle spray and stop times were set at 0.5 s and 2.5 s, respectively, and controlled by a timer-operated solenoid valve. Firing the air jet in this manner caused an intermittent energetic fluidization phenomenon to appear in the powder bed. [8-12] Specifically, it was expected that the jet effect would expedite mixing and dispersion by exercising a

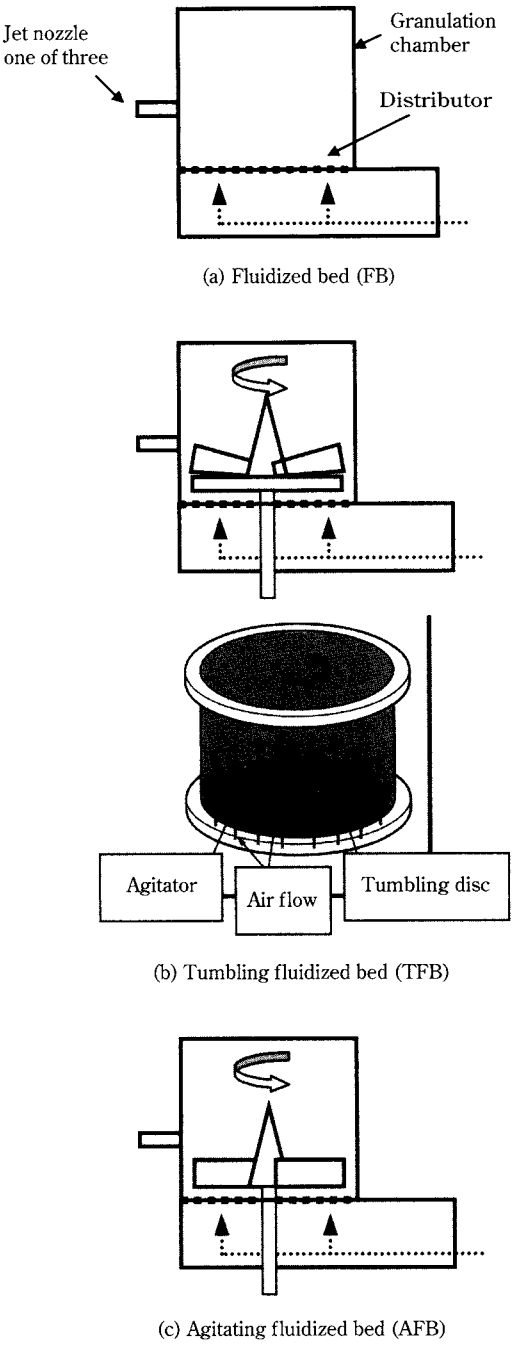

(a) Fluidized bed (FB)

(b) Tumbling fluidized bed (TFB)

(c) Agitating fluidized bed (AFB)

Fig. 2 Variations in Experimental Set up for Fluidization

periodic localized shear effect on the particle mass. **Fig. 4** shows the air jet's pulse-time instantaneous flow rate, as measured with a flow meter, in relation to changes in air-jet pressure, and the maximum static pressure change inside the granulator. As the air jet's pressure was raised, instantaneous flow rate and static pressure increased proportionately. At the granulator's standard air jet pressure of 600 kPa, those values were 3.83×10^{-2} m^3 s^{-1} and 2,120 Pa, respectively.

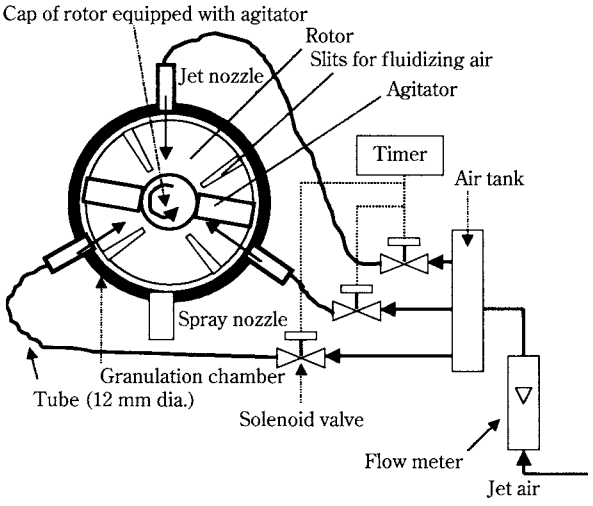

Fig. 3 Location of Pulsed Air-jet Nozzles

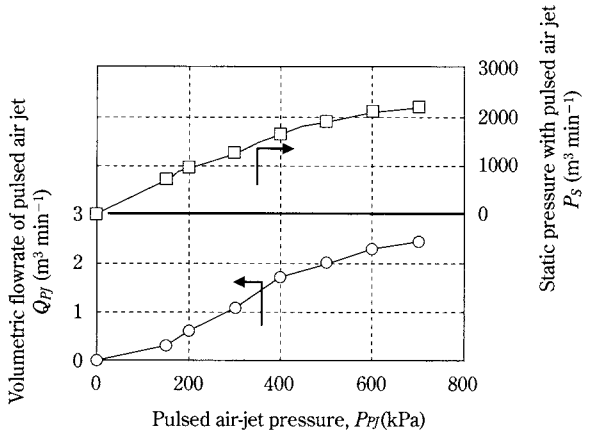

Fig. 4 Relationship between the opposed pulsed air-jet pressure and its volumetric flow rate and the static pressure in the fluidized bed granulator

2.2 Experimental Samples and Evaluation Method

The binary powder samples used in the experiment were calcium carbonate (white, Super #1500 made by Maruo Calcium) to which iron oxide (brown, Toda-color 140ED made by Toda Industries) had been added to an exact 5.00% by mass. These sample components were the same grades as those in previous reports, [5, 6] and **Table 1** shows their main physical properties, as well as the 50% particle diameter on a volume basis measured as particle size by a laser diffraction particle size distribution measuring device (a Honeywell Microtrac HRA), and the geometrical standard deviation of particle size distribution.

The experiment method entailed putting a prescribed amount of powder sample into the granulator, and mixing in accordance with the operating conditions in **Table 2**. The granulator was temporarily stopped after each prescribed length of mixing time, and differences in mixture color were detected as lightness using an optical mixing degree sensor (Photometer Model PM-III made by Minamide Systems). As shown in **Fig. 5**, we chose a total of 15 measuring points comprising five points each on three levels in the powder bed (20, 50, and 80 mm above the distributor with a 5 kg feed weight; 30, 100, and 180 mm with a 10 kg feed weight; and 80, 180, and 280 mm with a 20 kg feed weight). The degree of unevenness in mixing according to position is calculated as standard deviation σ_I, defined in the following equation. The smaller this value, the further dispersion has proceeded. [6, 7]

$$\sigma_I = \{\frac{1}{N-1}\sum_{J=1}^{N}(V_{IJ}-V_{AV})^2\}^{1/2} \quad \text{(V)} \tag{1}$$

Where:
N is the number of measuring points,
V_{IJ} is the measured value at point J at time θ_I, and
V_{AV} is the average of N V_{IJ} values

And just as in previous reports [6, 7], in this experiment we used a mixed sample which had been adjusted to 5.00% iron oxide by mass, wet dispersed it in a mortar until the mixture's lightness became constant, and used that lightness, V_{WET}, as the criterion for comparison. We decided to use the indicator η_I for the attainment of V_{WET}, to indicate the degree to

Table 1 Materials Used in the Experiments

Powder	50% particle diameter on a volume basis* (μm)	Geometrical standard deviation (−)	True density** (kgm^{-3})	Loose density** (kgm^{-3})	Tapped density** (kgm^{-3})	Compressibility** (%)
$CaCO_3$	3.092	2.75	2600	595	1026	42.0
Fe_2O_3	0.717	1.39	5200	680	1223	44.4
Mixture 5 wt% Fe_2O_3	2.974	1.69	2730	499	980	49.1

* Measured by Microtrac model HRA ** Measured by Powder Tester model PT-R

Table 2 Experimental Conditions

Run Nos.	Type of fluidization*	Tumbling rotor with agitator	Agitator	Rotational speed of rotor or agitator (min^{-1})	Fluidizing airflow rate ($m^3\ min^{-1}$)	Opposed pulsed airjet	Po (kPa)	Feed weight (kg)	Height of fixed bed (m)
1	FB	not used	not used	–	5	not used	0	10	0.19
2	FB	not used	not used	–	7.85	not used	0	10	0.19
3	FB	not used	not used	–	7.85	used	600	10	0.19
4	TFB	used	not used	350	6	not used	0	10	0.19
5	TFB	used	not used	700	6	not used	0	10	0.19
6	TFB	used	not used	350	6	used	600	10	0.19
7	TFB	used	not used	350	6	used	200	10	0.19
8	TFB	used	not used	350	6	used	400	10	0.19
9	TFB	used	not used	150	6	not used	0	10	0.19
10	TFB	used	not used	350	6	used	600	5	0.095
11	TFB	used	not used	350	6	used	600	20	0.32
12	AFB	not used	used	350	6	not used	0	10	0.19
13	AFB	not used	used	700	6	not used	0	10	0.19
14	AFB	not used	used	150	6	not used	0	10	0.19
15	AFB	not used	used	350	6	used	600	10	0.19
16	AFB	not used	used	350	6	used	400	10	0.19
17	AFB	not used	used	350	6	used	200	10	0.19
18	AFB	not used	used	350	6	used	600	20	0.32
19	AFB	not used	used	350	6	used	600	5	0.095

* FB: fluidized bed; TFB: tumbling fluidized bed; AFB: agitating fluidized bed

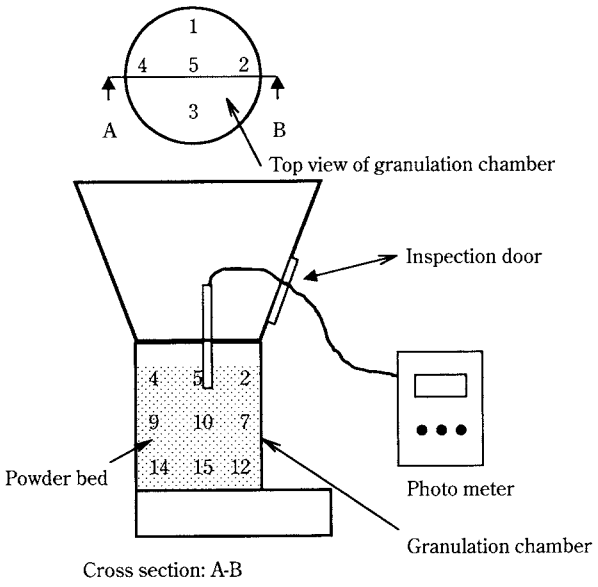

Fig. 5 Lightness Measuring Points in Powder Bed

which the mixture had been dispersed in the granulator, and this indicator is defined by the following equation using the lightness V_C of calcium carbonate. The closer η_I is to 1, the further dispersion has proceeded. [6, 7]

$$\eta_I = \frac{V_C - V_{AV}}{V_C - V_{WET}} \quad (-) \quad (0 \leqq \eta \leqq 1) \qquad (2)$$

3. Results and Discussion

3.1 Fluidized Bed (FB) Mixing Performance

In the FB experiments (runs 1 through 3) the indicator of dispersion degree η_I in all cases exceeded 0.9 at 600 s mixing time. Especially in R-2, η_I ultimately attained the very high value of about 0.98. These results yielded values that are high even in comparison with the η_I values obtained in the TFB and AFB experiments, discussed below, which were expected to provide highly effective mixing and dispersion, and therefore FB values likely were not indicative of the actual mixing state. Careful observation of particle mass fluidization during the experiments revealed that although the powder bed overall became a fluidized bed with stable expansion, immediately after operation began there was pronounced formation of agglomerates measuring several mm to 40 mm in the lower zone of the fluidized bed about 70 mm above the distributor. After operation finished we recovered and examined these agglomerates, and found that they were agglomerates of calcium carbonate particles covered completely with adhering iron oxide particles. Their strength was such that light finger pressure was enough to crush them. This formation of agglomerates by adhesive powders was likely caused when the agglomeration of particles was facilitated by the compaction effect that is a characteristic of fluidized beds in their lower regions. In contrast to R-2 operating conditions, this agglomeration tendency

was slightly weaker in R-1, in which the fluidization airflow rate had been set lower, and the tendency was significantly mitigated in R-3, which added the PJ assembly-supplied air jet to the conditions of R-2. Nevertheless, in all three runs we observed, in the lower zone of the fluidized bed, large agglomerates that were several mm in size and had high ratios of calcium carbonate particles.

To visually observe the degree of dispersion in the final mixture, we used an Aggrobt (AGR made by Hosokawa Micron) to perform compression tensile fracture tests [12] on final mixture samples, as shown in **Fig. 6**. Sample (a) is the reference sample, prepared with the wet dispersion method, while (b) and (c) were prepared using the mixture samples from R-2 and R-3. **Fig. 6** includes the ultimately dispersed states η_I. obtained in the previous mixture evaluations. In the reference sample ($\eta_I = 1.000$) the iron oxide particles are evenly dispersed throughout the calcium carbonate particles. In the R-2 sample, however, agglomerates of calcium carbonate particles are prominently visible in the cross section. In the R-3 sample, by contrast, we observed that the addition of the PJ assembly to the R-2 conditions provided a dispersive air-jet effect that considerably mitigated the formation of calcium carbonate agglomerates.

These observations demonstrated that the η_I values obtained above are not a basis for correctly assessing the overall mixing degree of samples due to the effects of agglomerates formed in the powder bed's lower zone. In other words, the formation of agglomerates with high ratios of calcium carbonate particles makes the concentration of iron oxide particles in the fluidized bed particle mass higher than the feed weight ratio, and η_I was measured at higher values than anticipated. For this reason, agglomerate formation made it impossible to correctly evaluate FB mixing performance when using adhesive powders.

3.2 Mixing Performance of Tumbling Fluidized Beds (TFBs) and Agitating Fluidized Beds (AFBs)

(a) Effects of Agitator Speed

Fig. 7 shows the results obtained when graphing the degree of dispersion η_I against mixing time. The parameter was the speed of the TBF rotor with agitator or the AFB agitator, and other conditions were the standard bed feed weight of this granulator ($W = 10$ kg) and the fluidizing airflow rate at which stable fluidization is maintained ($Q = 1.00 \times 10^{-1}$ m^3 s^{-1}). Owing to the agitation/shearing effect on the powder bed of the rotor and agitator rotation in the lower zone of the fluidized bed, in none of these cases did we note the formation of agglomerates like those observed in FB mixing.

Although results are not known from the standard deviation σ_I, which indicates the degree of mixing unevenness by zone, it assumes a nearly constant value (for example, $\sigma_I = 0.012$ in R-4, $\sigma_I = 0.010$ in R-12) after mixing time attains about 600 s no matter what fluidization method is used. This led us to reason that the concentration of iron oxide, which is the component of concern at the measuring point, would undergo no greater dispersion by zone. But the η_I values in **Fig. 7** continue to rise even after 600 s and attain their maximums at between 2400 and 3200 s. This is likely because even after dispersion by zone concludes, further dispersion occurs as agglomerates

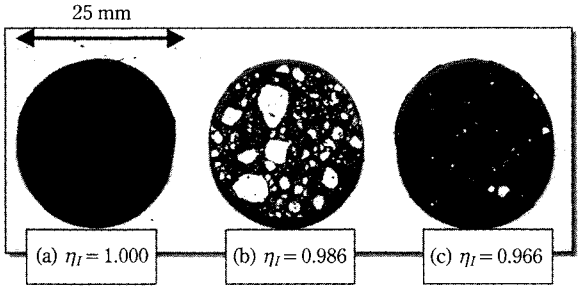

(a) Standard sample prepared by mortar
(b) R-2 product prepared by FB mixing
(c) R-3 product prepared by FB mixing with PJ assembly at $P_{PJ} = 600$ kPa

Fig. 6 Photographs of Powder Bed Cross Sections after Compression Tests at $\sigma_p = 4$ MPa

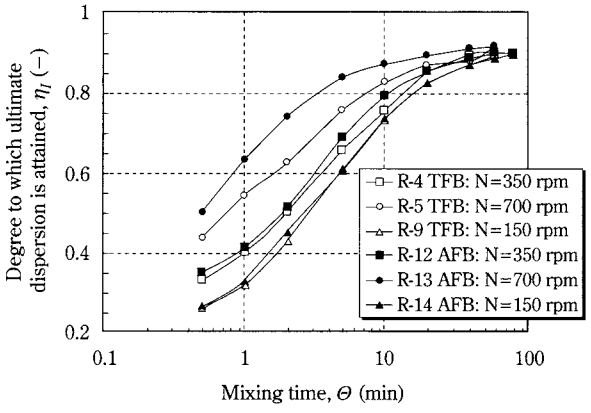

Fig. 7 Changes in the Degree of Mixing Attainment According to Mixing Time at Various Rotor or Agitator Speeds (Run nos. 4, 5, 9, 12, 13, and 14)

of very fine iron oxide particles disintegrate. [7] The effects of the speed of rotating devices on η_I and σ_I subjects the powder bed to an increasingly powerful shearing effect by operating at higher speeds. As a result, at the same mixing time the η_I value is larger and the σ_I value is smaller. We also noted that σ_I tends to attain a constant value more quickly as rotational speed is increased. A comparison of TFB and AFB fluidization methods showed that at the same mixing time the AFB η_I increased at overall high values, and that its ultimate value was somewhat higher than the TFB value. σ_I was also higher for the AFB overall. This means that the AFB method, which directly agitates the powder bed, applies a larger shearing force on the powder bed and produces less zonal unevenness than the TFB method, which agitates the powder bed by holding it above the rotor. This is because the AFB method requires more motive force for the motor, and it is that force which is actually measured. **Fig. 8** shows final mixture cross section samples prepared in the same way as in **Fig. 6**. As speed increases, iron oxide particles are more dispersed within the calcium carbonate particles, and fewer agglomerates of calcium carbonate particles are observed in the cross sections. Also, the AFB method produces fewer agglomerates than the TFB method. Even such visual assessments clearly show the influence of operating conditions on η_I in **Figure 7**.

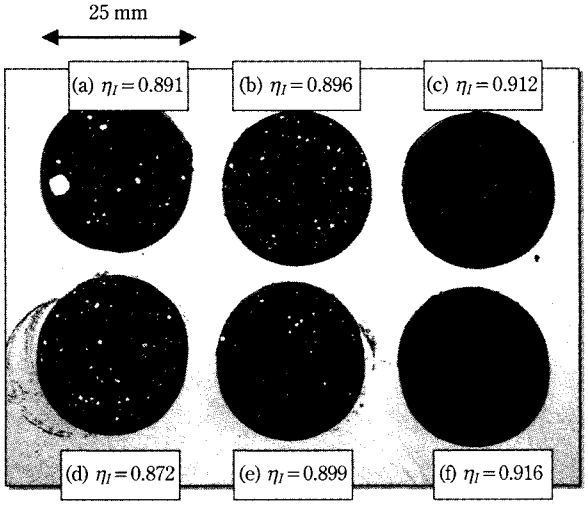

(a) R-9 product prepared by TFB mixing at N=150 rpm
(b) R-4 product prepared by TFB mixing at N=350 rpm
(c) R-5 product prepared by TFB mixing at N=700 rpm
(d) R-14 product prepared by AFB mixing at N=150 rpm
(e) R-12 product prepared by AFB mixing at N=350 rpm
(f) R-13 product prepared by AFB mixing at N=700 rpm

Fig. 8 Photographs of Powder Bed Cross Sections after Compression Tests at σ_p = 4 MPa

(b) Effects of PJ assembly Air-Jet Pressure

Figs. 9 and **10** show the effect of PJ assembly air-jet pressure on η_I and σ_I under the granulator's standard operating conditions. As in the results of 3.2(a), the zonal dispersion of iron oxide particles finished after about 600 s mixing time. Just as expected, the higher the air-jet pressure P_{PJ} during operation, the greater the value of η_I, and the sooner the ultimate degree of dispersion (η_I = 0.90 to 0.96) was attained. Additionally, the higher the P_{PJ}, the smaller the value of σ_I, showing that the iron oxide particle unevenness among zones further decreased. The main reason is likely that the air-jet effect which acts on the powder bed as a shearing effect became stronger as its pres-

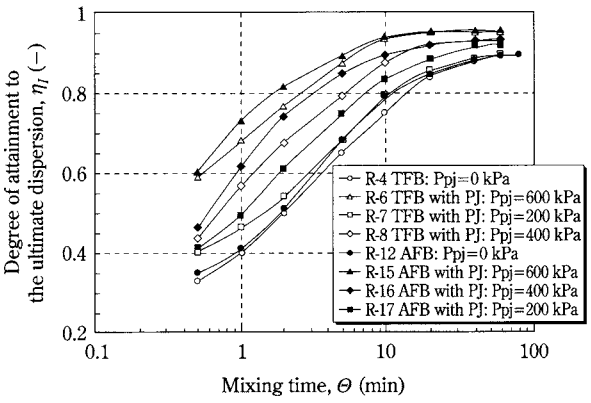

Fig. 9 Changes in the Degree of Mixing Attainment According to Mixing Time at Various Opposed Pulsed Jet Pressures (Run nos. 4, 6, 7, 8, 12, 15, 16, and 17)

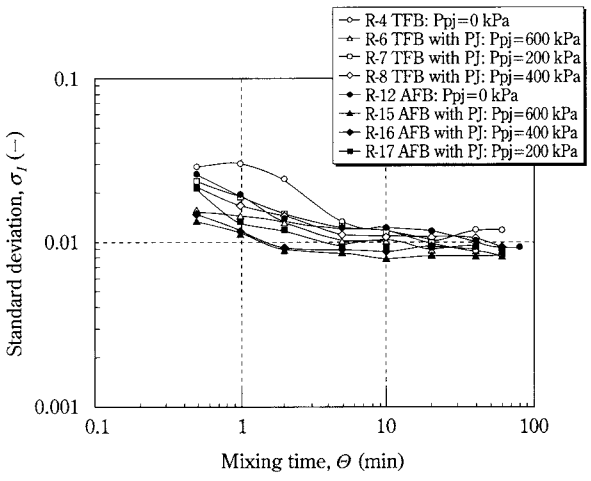

Fig. 10 Changes in Standard Deviation According to Mixing Time at Various Opposed Pulsed Jet Pressures (Run nos. 4, 6, 7, 8, 12, 15, 16, and 17)

sure setting increases, thereby facilitating dispersion of the iron oxide particles.

In connection with these results, **Fig. 11** shows cross sections of final mixtures like those in **Fig. 8**. Calcium carbonate agglomerations are seen in the results for both the TFB method ((a) through (d) in the figure) and the AFB method ((e) through (h) in the figure) under standard operating conditions for a conventional tumbling fluidized bed granulator, i.e., $P_{PJ} = 0$ kPa ((a) and (e) in the figure). Presumably, if one were to granulate an unevenly mixed powder bed with agglomerates like these samples, then sinter after filling and molding, the product's composition would be uneven, and one could not expect adequate sintered strength.

But adding the PJ assembly to these standard conditions facilitated iron oxide particle dispersion, and we observed no agglomerations at all of calcium carbonate itself at P_{PJ} values of at least 600 kPa for the TFB and 200 kPa for the AFB. As this shows, adding the PJ assembly limits the zonal unevenness of fine particles, and is very effective in preparing mixtures with better dispersion.

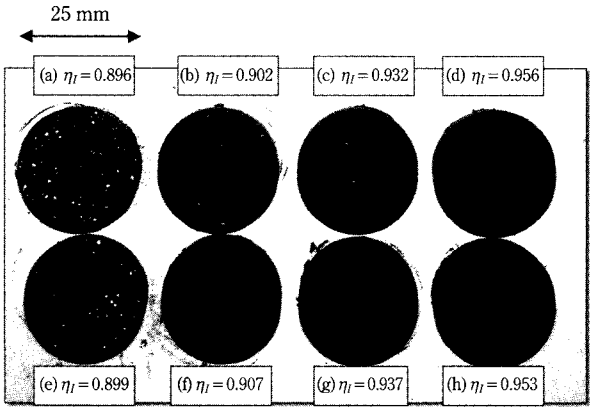

(a) R-4 product prepared by TFB mixing without PJ assembly
(b) R-7 product prepared by TFB mixing with PJ assembly at P_{PJ}=200 kPa
(c) R-8 product prepared by TFB mixing with PJ assembly at P_{PJ}=400 kPa
(d) R-6 product prepared by TFB mixing with PJ assembly at P_{PJ}=600 kPa
(e) R-12 product prepared by AFB mixing without PJ assembly
(f) R-17 product prepared by AFB mixing with PJ assembly at P_{PJ}=200 kPa
(g) R-16 product prepared by AFB mixing with PJ assembly at P_{PJ}=400 kPa
(h) R-15 product prepared by AFB mixing with PJ assembly at P_{PJ}=600 kPa

Fig. 11 Photographs of Powder Bed Cross Sections after Compression Tests at $\sigma_p = 4$ MPa

(c) Effects of Bed Feed Weight

Fig. 12 shows the effects of bed feed weight on η_I when PJ assembly air-jet pressure P_{PJ} is set at 600 kPa. Comparing the results of a 5 kg feed weight (R-10 and 19) with those for this granulator's standard 10 kg feed weight (R-6 and 15) shows that with the same mixing time, η_I has a higher value for the 5 kg feed weight up to about 600 s, after which both feed weights have about the same ultimately dispersed state ($\eta_I = 0.95$ to 0.96). With a feed weight of 20 kg (R-11 and 18) and the same mixing time, η_I is smaller than that of 10 kg, then at a mixing time of about 3600 s it attains a constant value. Using a 20 kg feed weight we subsequently continued the mixing operation for 6000 s, but the ultimately dispersed state was η_I = 0.942.

Examining differences between fluidization methods showed that at all feed weights the AFB method yielded a higher η_I for dispersion degree per mixing time, but we found no salient difference with the TFB method in terms of the ultimately dispersed state. Although the effect on standard deviation σ_I is not shown here, it tended to decrease faster when the granulator was operated with a smaller feed weight. In terms of fluidization type differences, the AFB method produced a smaller σ_I value with the same mixing time.

These results yielded the following findings. Reducing the powder bed feed weight increases the dispersion occurring in conjunction with the disintegration of iron oxide particle agglomerates, but in the mixing/dispersion range exceeding $\eta_I = 0.9$, which is unattainable for conventional tumbling fluidized bed

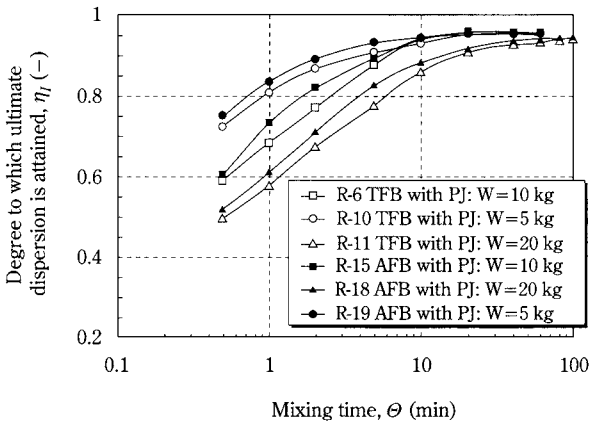

Fig. 12 Changes in the Degree of Attainment According to Mixing Time at Various Feed Weights (Run nos. 6, 10, 11, 15, 18, and 19)

granulators, the dominant contribution to the impelling force needed to disintegrate and disperse the iron oxide particle agglomerates is the effect of the PJ assembly's air jet, regardless of the fluidization type used. Hence if the granulator has an appropriate feed weight and uses an agitator that suppresses the formation of agglomerates in the fluidized bed's lower zone, the ultimate η_I value obtained with an air-jet pressure of 600 kPa was estimated at 0.95 to 0.96. But when powder bed feed weight was increased to 20 kg, it was difficult for the spouting of the agitator's shearing effect and the PJ assembly's air jet, which act mainly on the fluidized bed's lower zone, to act effectively on the entire fluidized bed so as to increase bed expansion, and the ultimately attained dispersion was estimated at a somewhat lower value ($\eta_I = 0.942$).

3.3 Mixing Performance Comparisons with Several Mixers

Another consideration regarding this granulator is the great importance of the feed powder's precisely mixed state to the improvement of final product quality, and, when exploring the granulator's use in the process of manufacturing functional materials, which involves the series of mixing, granulation, and drying processes, it is of the greatest importance to assess the degree of mixing and to weigh the economic perspective, which is indicative of powder processing costs.

We therefore compared the foregoing experimental results with the results obtained with mixers of other types [13] to determine how the mixing performance of this granulator compares with that of other devices and study the energy consumed in mixing operations as it relates to powder processing cost.

(a) Comparing the Granulator's Mixing Degree with That of Other Mixers

The relationships between mixing degree and mixing time, and that between standard deviation and mixing time under the standard operating conditions for this granulator are shown in **Figs. 13** and **14**, in comparison with results from several other mixers. [7] **Table 3** presents the mixers' operating conditions. As the mixers all have different working capacities, their feed weights also differ. We classified the mixers compared in this experiment as shown below, in a manner corresponding to types A, B, and C in the mixer classification used by Satoh et al. [6, 7]

Type A was a conical mixer with low-speed agitator (Nauta mixer made by Hosokawa Micron; symbol CV in **Table 3**), which exerts a moderate and compara-

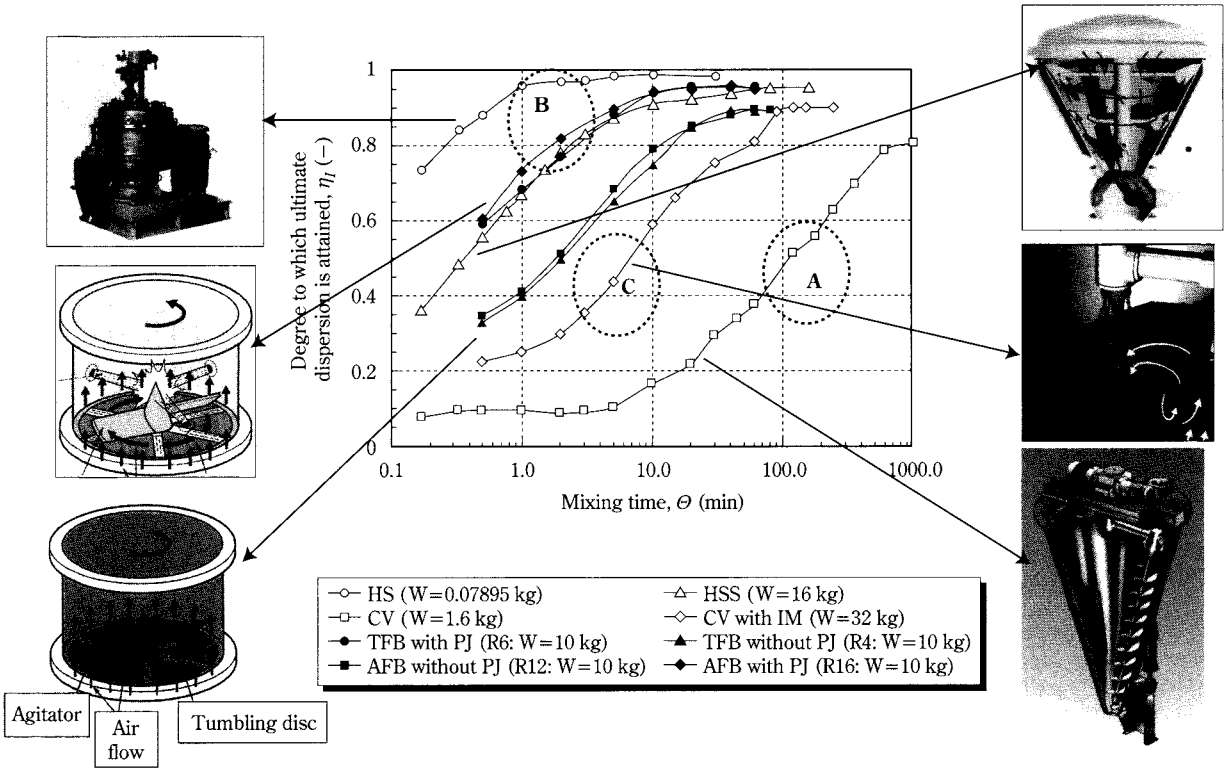

Fig. 13 Characterization of Mixers Based on Changes in Lightness According to Mixing Time

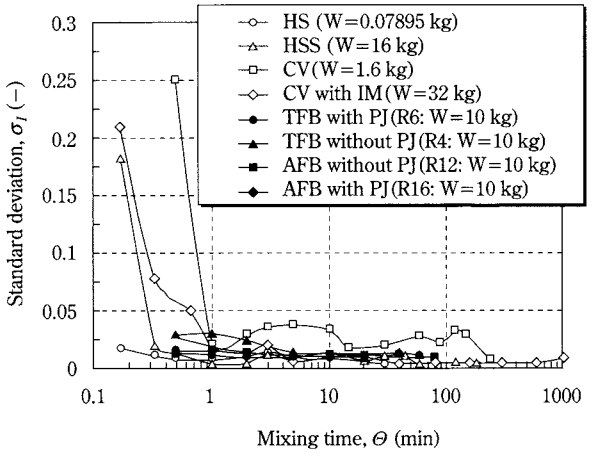

Fig. 14 Characterization of Mixers Based on Changes in Lightness According to Mixing Time

tively gentle mixing effect on particles. Type B mixers were a high-speed shearing surface modifier with powerful compaction, collision, and other effects (Mechanofusion made by Hosokawa Micron; symbol HS) and a high-speed stirring mixer (Cyclomix made by Hosokawa Micron; symbol HSS). Type C was the type A mixer into which we had installed a high-speed rotary impeller (Nauta mixer and Intensifier made by Hosokawa Micron; symbol CV with IM).

The relationship in **Fig. 13** shows that the conventional tumbling fluidized bed granulator without the PJ assembly (R-4, 16) yielded results falling between those of types B and C. Compared with the type C mixer, which had an impeller, the tumbling fluidized bed granulator provided compound mixing with more powerful convection and collisions by virtue of the fluidization effect caused by the spinning of the rotor and agitator, and by aeration. Results yielded by the tumbling fluidized bed granulator with the PJ assembly (R-6, 12) belong to the category for type B because, owing to the powerful spouting effect of the air jet, nearly all the fine agglomerates are disintegrated into primary particles with the passage of time. This demonstrated that the addition of PJ assemblies to conventional tumbling fluidized bed granulators provides a degree of mixing that is equal to or better than that of high-speed stirring mixers, which mix by causing powerful collisions. **Fig. 14** shows that the higher the mixing degree of a mixer, the smaller value for standard deviation σ_I it has, and the results for the tumbling fluidized bed granulator with the PJ assembly were about the same as those for the high-speed stirring mixer.

(b) Comparison by Power Requirements and Energy Inputs

The results of comparison by mixing performance suggest that it is possible to use a tumbling fluidized bed granulator with an internal PJ assembly for tasks that were difficult for conventional tumbling fluidized bed granulators: precision mixing at η_I values of about 0.95, and the subsequent individual operations of granulation and drying. In consideration of using this granulator in conventional manufacturing processes, we assessed mixing degree and examined the economic perspective, which is indicative of powder processing costs. Following is an exploration of the energy consumed in mixing, which is related to power processing costs.

In relation to the degree of mixing attainment, which increases as mixing proceeds, **Fig. 15** plots the results obtained when calculating, as the cumulative energy input per kg feed weight, the cumulative effective energy ([actual power − idling power] × running time) consumed in the process of reaching various mixing attainment degrees (η_I = 0.6, 0.7, 0.8, 0.9, and 0.95), and then standardizing them using the data for the conical mixer with low-speed agitator (CV) as

Table 3 Specifications of the Mixers and the Fluidized Bed Granulator

Mixing principle	Fluidized bed type with tumbling rotor or agitator	Fluidized bed equipped with PJ assembly with tumbling rotor or agitator	Conical vessel type with screw	Conical vessel type with screw and impeller	High-speed stirring, shearing type	High-speed shearing
Symbol	TFB, AFB	TFB with PJ AFB with PJ	CV	CV with IM	HSS	HS
Classification of mixer			A	C	B	B
Working capacity (m^3)	0.03	0.03	0.025	0.08	0.05	0.0002
Feed weight (kg)	5, 10, 20	5, 10, 20	1.6	32	16	0.07895
Rotation speed (rpm)	150, 350 and 700	150, 350 and 700	120	100	750	1500
Revolution speed (rpm)	–	–	4	3.5	–	–
Impeller speed (rpm)	–	–	–	1500	–	–

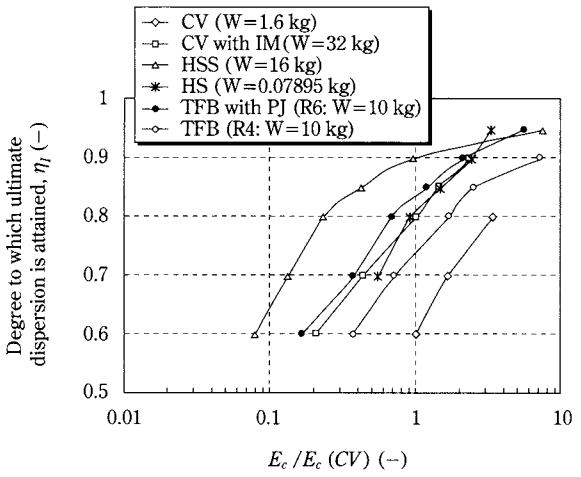

Fig. 15 Relationship Between the Degree of Mixing Attainment and Cumulative Energy Input Per Unit Weight of Product Obtained with Various Mixers

the reference.[1] For the tumbling fluidized bed granulator we assumed that the power needed by the two blowers and the compressor was completely converted to effective energy. From the graph one can see a tendency in which the more power a device needs per kg of feedstock,[2] the smaller energy input is used in mixing. This is likely because the larger the power needed by a machine, the shorter the time in which mixing and dispersion proceed as the powder bed is subjected to powerful shearing, compaction, collisions, and other effects.

Namely, the high-speed stirring mixer (HSS) shows to be more efficient than the other mixer types over the entire range of energy inputs with the exception of the point at maximum dispersion ($\eta_I = 0.95$), here the tumbling fluidized bed granulator with an added PJ assembly and the high-speed shearing equipment (HS) become more effective.[2]

Fig. 16 plots the ultimate degree of attainment as a mixer on the vertical axis, and the effective energy input into the powder bed to attain that degree of attainment on the horizontal axis. The data have been converted to per-kg values and standardized using the data for the conical mixer with low-speed agitator (CV) as the reference.[1] A comparison of the conical mixer, designated with white circle (CV) and white triangle (CV+IM) symbols, shows that if additional use is made of a high-speed rotary impeller (intensifier), then, as indicated by the arrow in the graph, a higher degree of attainment is achieved with a lower energy input. Similarly, the tumbling fluidized bed granulator with an added PJ assembly (black triangle plot) yields a higher degree of attainment with lower energy consumption than the same granulator without the PJ assembly (black circle), as shown by the arrow. The reason for these tendencies is that the use of an impeller in a conical mixer, which has high dispersive and disintegration effects, and the added use of a PJ assembly in a tumbling fluidized bed granulator require more power to run the devices, but mixing proceeds faster, and the mixing time needed to attain the ultimate degree of dispersion is considerably shortened, thereby reducing overall energy consumption. Especially when the tumbling fluidized bed granulator used the PJ assembly (R-6), it was able to attain the same or better degree of dispersion as the high-speed stirring mixer (HSS in the graph) with about half the energy input in this experimental conditions,[1] which demonstrated that the air jet is highly effective in assisting the mixing and dispersion of adhesive fine powders.

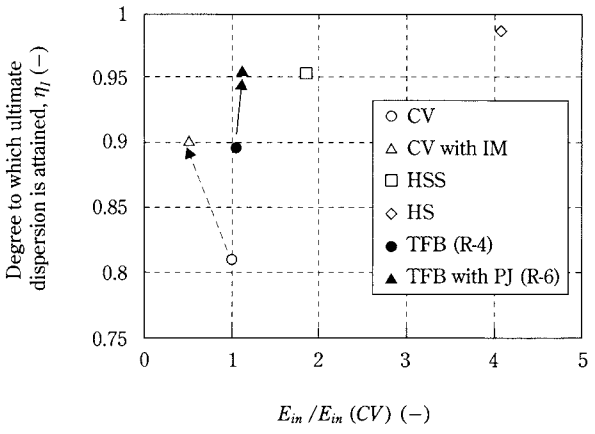

Fig. 16 Relationship Between the Maximum Degree of Mixing Attainment and the Total Energy Input Per Unit Weight of Product Obtained with Various Mixers

1. In this paper we could not consider directly in what respect the differences in weights of feed material in the different mixers do effect the results. It is well known that small-scale machines are usually less effective than larger units. Therefore, continued studies will investigate this effect.
2. The mixers used for comparison in this experiment exhibited correlative relationships between the power required per kg of powder feedstock (kW/kg) and the ultimately dispersed state. Standardizing the power required with CV data as the reference yields 1 for CV, 4.71 for CV with IM, 20 for HSS, and 831 for HS.

   The tumbling fluidized bed granulator with the PJ assembly required three to five times the power of the high-speed stirring mixer (HSS), which had about the same ultimately dispersed state (about $\eta_I = 0.95$). This is because the auxiliary devices that maintain the powder bed require more power than the high-speed stirring mixer.

4. Conclusion

For the purpose of quantifying the mixing and dispersive capacity of tumbling fluidized bed granulators, we used a previously reported method [5, 6] to assess mixtures of binary powder samples comprising calcium carbonate and iron oxide by measuring the lightness of mixtures obtained under various operating conditions. Results were compared with those from mixers of other types, and the following findings were obtained.

(1) The ultimate degree of dispersion attained by a conventional tumbling fluidized bed granulator without a PJ assembly was 0.89 to 0.9.

(2) Additional use of a PJ assembly raises the ultimate degree of dispersion to between 0.95 and 0.96.

(3) As the rotational speed of the rotor and agitator in this granulator were increased, the degree of mixing increased, and the observed difference in fluidization types was that the AFB type achieved a higher mixing degree than the TFB type.

(4) The conventional tumbling fluidized bed granulator without a PJ assembly yielded results ranking between those of mixer types B and C according to the classification scheme in previous reports. [5, 6]

(5) The results obtained with the granulator when using a PJ assembly were equal to or better than those of a high-speed stirring mixer, and we determined that it belonged to type B in the mixer classification.

(6) These results indicate that it might be possible to achieve both considerable process simplification and labor reduction by using tumbling fluidized bed granulators with internal PJ assemblies for precision mixing of about $\eta_I = 0.95$, which is difficult for conventional tumbling fluidized bed granulators, and also for the individual operations of granulation and drying, which constitute a series of operations with mixing.

Nomenclature

Volume median diameter of particles or granules	(m)
Cumulative input energy per unit weight of feed	(J)
Cumulative input energy per unit weight of feed in the conical vessel type mixer with screw	(J)
Total input energy per unit weight of feed	(J)
Total input energy per unit weight of feed in the conical vessel type mixer with screw	(J)
Rotational speed of rotor or agitator	(s^{-1})
Power requirement per unit weight of feed	(W)
Power requirement per unit weight of feed in the conical vessel type mixer with screw	(W)
Pressure of the opposed pulsed air jet	(Pa)
Static pressure in the fluidized bed	(Pa)
Volumetric flow rate of fluidizing air	($m^3\ min^{-1}$)
Volumetric flow rate of opposed pulsed air jet	($m^3\ min^{-1}$)
Average output voltage of V_{IJ}	(V)
Output voltage corresponding to the bulk powder, $CaCO_3$ (white component)	(V)
Output voltage after time, I at J-th sampling point	(V)
Output voltage corresponding to the completely dispersed powder	(V)
Feed weight	(kg)
Mixing time	(s)
Degree to which ultimate dispersion has been attained	(−)
Standard deviation, Eq. (1)	(V)
Pre-compressive stress in tensile strength test	(V)

References

1) Sekiguchi, I. "Recent Trend in Powder Technology 1991, Granulation," *Funtai to Kougyou*, 23, no. 1, 27-33 (1991).

2) Gulliver, E., E. Riman and J. Friel. "Mixedness engineering for advanced multicomponent materials," *Int. J. Powder Metall*, 33, no. 6, 29-36 (1977).

3) Satoh, H., Y. Nakano and T. Nomura. "Effect of the Mixing Procedure on the Reliability of Multilayer Ceramic Capacitors with Ni Electrode," *Journal of the Japan Society of Powder and Powder Metallurgy, Japan*, 42, 1103-1107 (1995).

4) Kurimoto, I., K. Terashita and K. Miyanami. "Ganryokinitsusei ni Sugureta Zouryubutsu wo Eru tame no Fukugou-gata Zouryuuki no Sousa Jouken," Preprints of 15th Symposium on Particulate Preparations and Designs, Soc. of Powder Technol., Japan, pp. 195-200, Shiga (1998).

5) Natsuyama, S., K. Hasegawa, H. Matsura and H. Sakamoto. "Tendouryuudousou no Kongoutokusei to Zouryuubutsu Butsusei," Preprints of 15th Symposium on Particulate Preparations and Designs, Soc. of Powder Technol., Japan, pp. 232-236, Shiga (1998).

6) Satoh, M., T. Yamashita, T. Yoshida, O. Hasegawa and K. Miyanami. "An Evaluation of the Mixing Characteristics of Solid Mixers Using Adhesive Fine Powders," *J. Soc. Powder Technol., Japan*, 30, 390-396 (1993).

7) Satoh, M., T. Yoshida, K. Miyanami and Y. Okudaira. "Evaluation of the Performance of a High-speed Elliptical-rotor-type Powder Mixer," *J. Soc. Powder Technol., Japan*, 31, 789-794 (1994).

8) Tsujimoto, H., and T. Yokoyama. "Fluidized Bed Granulator Equipped with Opposed Pulsed Jet Assembly," *J. Soc. Powder Technol., Japan*, 33, 476-480 (1996).
9) Tsujimoto, H., and T. Yokoyama. "Palusujetto Bunsankikou wo tousaisita ryuudousou zouryu koutingu souti niokeru zouryuu koutingu gijyutu," *Funsai*, 40, 57-64 (1996).
10) Tsujimoto, H., T. Yokoyama and I. Sekiguchi. "The Characterization of Microgranules Produced by a Tumbling Fluidized Bed Granulator with an Opposed Pulsed Jet Assembly," *J. Soc. Powder Technol., Japan*, 35, 256-264 (1998).
11) Tsujimoto, H., T. Yokoyama and I. Sekiguchi. "The Characterization of Microgranules Produced by a Tumbling Fluidized Bed Granulator with an Opposed Pulsed Jet Assembly," *KONA*, 16, 241-249 (1998).
12) Tsujimoto, H., Y. Inoue and T. Yokoyama. "Funtaisou asshuku hippari kyoudo jidoukeisoku sisutemu AGGROBOT," *Funsai*, 38, 57-64 (1994).
13) Ohishi, A. "Kousokusendangata Kongouki Cyclomix," *Kagaku Souchi*, 3, 65-68 (1998).

Author's short biography

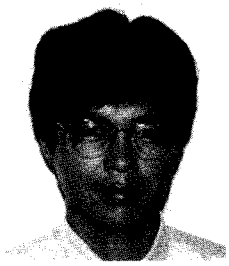

Hiroyuki Tsujimoto

Dr. Hiroyuki Tsujimoto graduated from the Department of Industrial Chemistry, Chuo University and received M.S. in 1988. At the same University he obtained his Doctor degree of Engineering in 2001 on the subject of new fluidized bed granulation and coating methods. Since 1988, he has been working at Hosokawa Micromeritics Laboratory, where he developed "Tumbling Fluidized Bed Granulator with Opposed Pulsed Jet Assembly" in 1994 and Advanced Spray Agglomarator realizing "Direct Granulation Method of Liquid Material in a Fluidized Bed Granulator" in 1998 as senior research engineer. Since 1999, he is a section manager of Hosokawa Micromeritics Laboratory. In 2000 he received "Japan Society for the Promotion of Machine Industry Prize" by the development of the above two types of advanced fluidized bed granulators.

Toyokazu Yokoyama

Toyokazu Yokoyama graduated in Chemical Engineering from Kyoto University and received M.S. in 1975. Then he spent six years in Europe to study powder technology at Karlsruhe University and to work as an engineer for Hosokawa Europe Ltd. in Cologne and near London. After another six year work in the engineering division and laboratory of Hosokawa Micron Corp. in Osaka, he was engaged in research at Nagoya University, where he received Ph.D. on the subject of fine wet grinding by ball media mills. Since 1992, he is a manager of Hosokawa Micromeritics Laboratory. His major interests are particle design and processing for advanced functioning by mechanical composing and granulation methods as well as fine grinding and particle characterization.

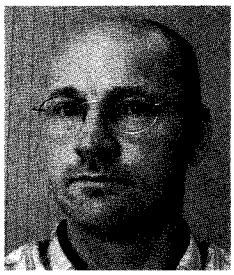

Peter G. J. van der Wel

Peter van der Wel is working as Research & Development Manager at Hosokawa Micron BV in Doetinchem, the Netherlands. His main responsibility is the development and improvement of powder process equipment in the field of mixing, drying and agglomeration. In 1987 he graduated from Delft University of Technology in the field of Chemical Engineering – Powder Technology. At the same university he obtained his Ph.D. in 1993 on the subject of Dust Explosions.

Author's short biography

Isao Sekiguchi

Dr. Isao Sekiguchi graduated from the Department of Industrial Chemistry, Chuo University in 1958, and obtained the Doctor degree of Engineering from Tohoku University in 1975. Since 1977, he is a professor in the Department of Applied Chemistry, Chuo University. His main research in the field of granulation techniques is concerned with fundamentals and extended application which cover three areas: fluidized bed granulation, tumbling granulation and spray drying or prilling. Additional research topic being pursued at present is a new development in the use of microcapsuled asphalt powder as an auxiliary in soil stabilization.

Kneading and Dispersing of Electrode Materials for Secondary Lithium Ion Batteries†

Keijiro Terashita, Hideya Asano and Kei Miyanami
*Department of Chemical Engineering, Osaka Prefecture University**

Abstract

Focusing on the manufacturing process of the electrode plate of lithium ion secondary batteries, this research aims to establish an evaluation method for the dispersal of positive electrode materials and to identify the kneading and dispersing methods required to form high quality film (plate).

Our research revealed that we can make quantitative evaluation of the dispersion of anode particles by measuring the film's volume resistivity rate, glossiness, film thickness and density and by organically examining these measured values. We were also able to suggest that the dispersion of the anode particle in paste form can be evaluated by measuring the particle size distribution and electric conductivity of the paste. We found that if thickener is added in stages, we can produce a plate of thin film thickness and good volume resistivity rate with high dispersion of anode particles.

1. Introduction

In recent years we have witnessed the rapid development and spread of IT equipment such as portable telephones, notebook PCs, and PDAs. For further miniaturization of such equipment or longer life, high expectations are mounting on batteries, the power source. One battery that can answer these demands is the lithium ion secondary battery.

The lithium ion secondary battery uses oxides such as lithium cobalt oxide, lithium nickel oxide, and lithium manganese oxide spinel for its positive electrode and uses carbon such as graphite for the negative electrode. The charging reaction is topochemical, with lithium ion moving between the two electrodes. Therefore, its cyclical property is good and energy density is high. Due to these strengths, the lithium ion battery is attracting attention, in the effort to make batteries smaller, lighter and greater in capacity.

The development and production of the lithium ion battery have only a recent history and therefore the manufacturing process has many latent problems. One major problem is the manufacturing process of the plate. The positive electrode is made of powdered raw material including active material and conductive agent. The fundamental problem lies in the fact that they are handled in paste form. Above all, the problem is that a method has yet to be fully established for the evaluation of the dispersion of plate material in wet form.

Focusing on the plate manufacturing process of the lithium ion secondary battery, this research was conducted for the purpose of establishing an evaluation method of the dispersion of anode material in paste form. First, we conducted mixing and kneading to make the paste, varying the mixing time and adding method of the thickener. Next, we applied the prepared paste and investigated the volume resistivity rate, glossiness and film thickness, attempting to evaluate dispersion. Then, in order to examine the evaluation of dispersion in paste form, the previous stage to film formation, we measured electric conductivity and particle size distribution. We report that as the result of our investigation, we discovered evaluation methods that are suitable for film and paste.

* 1-1, Gakuen-cho, Sakai, Osaka 599-8531, Japan
Tel: +81-722-54-9305 Fax: +81-722-54-9911

† This report was originally printed in J. of Japan Soc. of Powder and Powder Metallurgy, **47**, 97-102 (2000) in Japanese, before being translated into English by KONA Editorial Committee with the permission of the editorial committee of the Japan Society of Powder and Metallurgy.

2. Positive Electrode Materials, Equipment, and Method

2.1 Plate material, Thickener, Binder

Table 1 shows the powdered raw materials for the positive electrode materials that we used in the experiment and their mix proportion. As powdered raw materials for the lithium ion secondary battery, we used lithium cobalt oxide (active material) and carbon (conductant agent).

In order to make a good application of the plate material in paste form onto the aluminum foil, some degree of viscosity is required. Therefore, a thickener needs to be added. We used a 1 wt% water solution of carboxymethyl cellulose (CMC). In the final process of preparing the paste, in order to prevent the filmed surface of aluminum foil from bending or cracking due to folding, a binder, (polytetrafluoroethylene) was added.

Table 1 Materials and Example of Mixing Rate for Positive Electrode.

Active positive electrodes (Lithium cobaltic acid)	100%
Electrically conductive material (Carbon)	3%
Thickner (Carboxy-methyl-cellulose)	75%
Binder (Ethylene 4-fluoride resin)	23%

<Mass Fraction; $LiCoO_2$=100>

2.2 Equipment and Method

In order to evaluate the dispersion of particles for the positive electrode, the mixing and filming of the paste were conducted as follows:

Our procedure roughly broke down into four processes:

(1) Kneading and Dispersion Process: the electrode materials were dry mixed, then thickener and binder were added to make the paste: (2) Coating Process: coating was carried out in order to evaluate the mixing and dispersion of electrode materials in the paste by examining the condition of the film; (3) Heating Process: the electrode was heated in order to increase film strength; (4) Molding Process: the film was molded in order to standardize the evaluation. Below, we briefly describe each process.

(1) Kneading and Dispersion Process

As equipment, we used the planetary mixer[1] as shown in **Fig. 1**. The mixing blade, called the "hook" revolves and rotates in mixing motion to carry out the mixing and dispersing. The capacity of the mixing vessel was 8×10^{-3} m^3.

(2) Coating Process

In order to evaluate the dispersion of paste produced by means of the planetary mixer, the paste was applied onto aluminum foil using an applicator.

Fig. 2 gives a sketch diagram of the applicator used. Filming is carried out by placing the paste into the central portion of the applicator and by pulling the applicator. The aluminum foil thus becomes coated with a uniform thickness of paste. The clearance here is $\delta a = 300$ μm. Application speed was approximately 0.038 m/s.

(3) Heating Process

The heating process was carried out in order to improve the adhesion between the plate material and aluminum foil. The coated film, after air-drying for more than six hours at room temperature, was heated for two hours by changing the temperature variously inside a rack dryer.

(4) Molding Process

As the evaluation is focused on the film, we molded the heated film into samples of 50 mm × 80 mm dimension. Six samples were molded for each experimental condition.

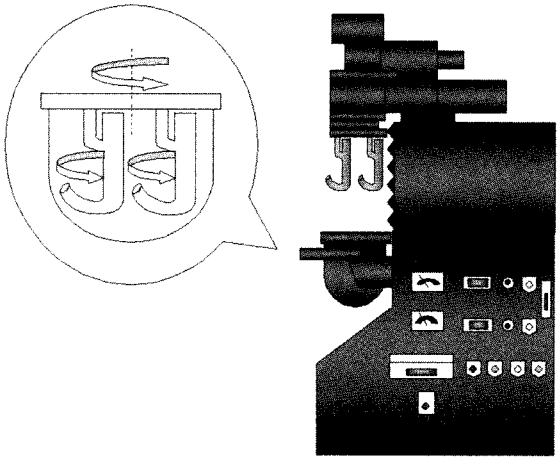

Fig. 1 Outline of Planetary Mixer

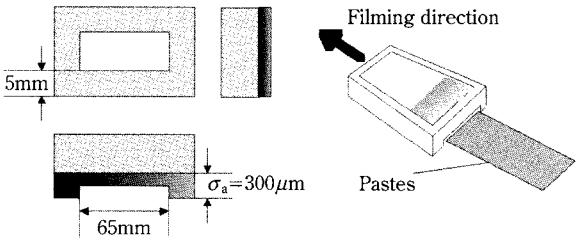

(a) Applicator (b) Film control

Fig. 2 Outline of Applicator and Film Control.

3. Evaluation Method

Diverse methods have been suggested as means of evaluating the mixing and dispersion of functionality composite material. What we need to do, however, is to devise an evaluation method that focuses on the properties of the material used and its function as a product. Here, we report on the evaluation of kneading and dispersion focusing on film, which demonstrates the properties of the battery, and the evaluation of dispersion of positive electrode particles in the paste.

3.1 Electrical Resistivity

It is extremely difficult to evaluate the dispersion of electrode particles in paste form. If the electrode particles are evenly dispersed in paste form, it is believed that they will still be evenly dispersed on the film surface after coating and drying. Therefore, we decided to evaluate the dispersion of electrode particles by measuring the electrical resistivity of the film.

In measuring electrical resistivity, we used an ordinary shop-purchased resistor. This resistor measured resistance using a 4-depth probe.

Measurement was taken of the six film samples (1 sample piece was a 50 mm × 80 mm sheet) produced by coating aluminum foil. Each sample was divided into a 3 × 3 grid and resistance was measured at a total of nine points (**Fig. 3**). This method is based on JIS K 7194. The average volume resistivity rate and the coefficient of variance were calculated in an attempt to evaluate the dispersion of electrode particles in the film.

Here, if the volume resistivity rate is low and its coefficient of variance is also small, it means that the dispersion of electrode particles is good and that the quality does not show much variation.

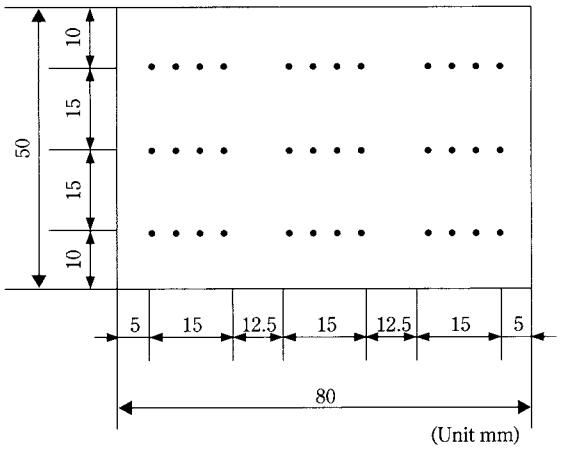

Fig. 3 Measurement Method of Resistance.

3.2 Glossiness

If the powder material is highly dispersed in the paste, it has been pointed out that the film surface after application is smooth[2]. Therefore, by measuring the glossiness of the film surface, we quantified the convexity and concavity of the surface in order to evaluate dispersion.

In measuring glossiness, a glossmeter was employed. This glossmeter allows a choice of the best angle of incidence from three options (20°, 60°, 85°). The subject of instrumentation in this research reflects little light and therefore, we selected 85° as the angle of incidence in measuring glossiness.

The measuring of glossiness was conducted at 54 points on the six samples of film piece measuring 50 mm × 80 mm as was the case in the measuring of resistivity, with each sample being divided equally into 3 × 3 grids (**Fig. 4**). The average value of glossiness was calculated in an attempt to evaluate the dispersion in the paste. If the glossiness shows a high value, it demonstrates that the electrodue particles are evenly scattered.

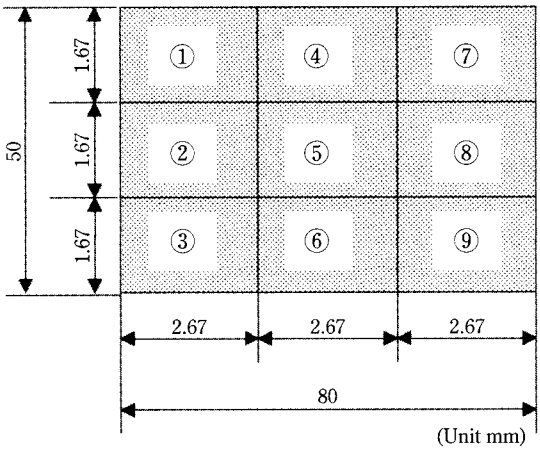

Fig. 4 Measurement Method of Glossiness Rate Gs.

3.3 Film Thickness

The film thickness is an important criterion in determining whether a film of even thickness has been produced but it is also required in converting volume resistivity rate and in calculating film density.

In measuring film thickness, a standard outside micrometer was used. For each sample, measurement was taken at 18 places from the areas shown in **Fig. 4** and their average values were used in evaluation.

3.4 Measurement of Particle Size Distribution and of Viscosity

In evaluating the dispersion of solid-liquid particulates, it is extremely important to measure the particle size in the liquid of dispersion and the viscosity of the liquid. In this research, laser diffraction scattering particle calibrator was used in order to measure the particle size of the powder particle mixed and dispersed in a high viscosity liquid. Viscosity was measured using a coaxial cylinder viscometer.

4. Results and Observations

4.1 Evaluation of Dispersion in Electrode Materials in the Film

The main factors that would influence kneading and dispersion may be the mixing time, the rotational speed of the mixer and the processing volume. In this research, we focused on the mixing time. We decided to set the mixer at 5 rps in rotation and 1.6 rps in revolution, in order to investigate the relationship between the dispersion of electrode materials and mixing time.

Meanwhile, in order to create a paste that will allow good film formation, thickener has to be added. The viscosity of the paste has been known empirically to differ between the two methods of 1) kneading and dispersing by lump addition of thickener, and 2) preparing the paste by dividing the thickener into two equal parts and adding them in two stages, from stiff paste mixing to dilution dispersion. In other words, it is conjectured that a differentiation in dispersion occurs depending on the method of thickener addition. Thus, we decided to evaluate the dispersion of electrode particles in the film by varying the method of thickener addition. Our research will report results by focusing on paste temperature at the time of film manipulation.

4.1.1 Relationship between Volume Resistivity Rate and Mixing Time

We created a paste by kneading and dispersion using electrode particles and turned the paste into film. We investigated the relationship between the volume resistivity rate ρ_v of the film plus its coefficient of variance C_v and the mixing time t. The findings are given in **Fig. 5**. The mixing ratio of lithium cobalt oxide ($LiCoO_2$) and carbon was 100:4 based on mass. From **Fig. 5**, one can see that the volume resistivity and coefficient of variance are both small when the mixing time t is roughly 1,800 sec. From this result, we can conclude that good dispersion of electrode particles is obtained with a mixing time of t = 1,800 sec or thereabouts. In other words, we discovered that we could evaluate the dispersion of electrode particles by measuring volume resistivity rate ρ_v.

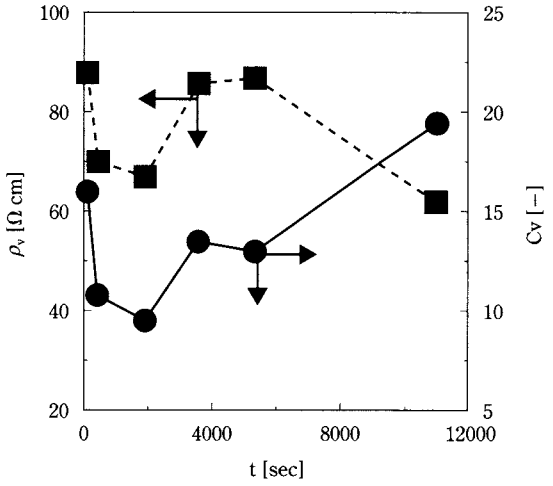

Fig. 5 Relations of Agitation time t with Volume Resistivity Rate ρ_v, and the coefficient of Variance C_v.

4.1.2 Relationship between the Method of Thickener Addition and Glossiness, Particle Size, and Film Thickness

To add the thickener, we adopted the lump addition method and the (two-stage) division addition method, and we decided to evaluate kneading and dispersion of the film made from the paste prepared in these ways.

To evaluate the film surface, we measured glossiness Gs. The findings are shown in **Fig. 6**. This figure also gives the paste particle size measured by the

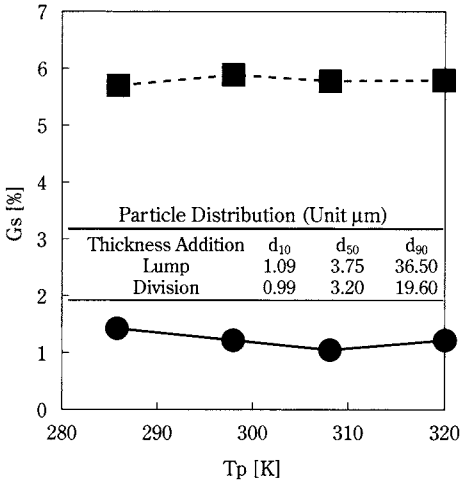

Fig. 6 Measured Value of Glossiness Gs.

laser diffraction/scattering method. **Fig. 6** clearly demonstrates that glossiness is greater when the division method is employed. In other words, if the thickener is added in two stages, we can form a film whose positive electrode particles are well dispersed. The table contained in **Fig. 6** indicates that in the division addition method, the paste particle size is small. The reason why these results are obtained is interpreted to mean that the divided addition of the thickener makes the wettability of the electrode particle and thickener better, leading to good dispersion.

From the above results, we discovered that glossiness can be used to evaluate dispersion of the positive electrode particles. Moreover, we can say that measuring particle distribution is an aid to evaluating dispersion.

Fig. 7 shows the result of our investigation into the relationship between film thickness δ and application temperature T_p, using the addition method of thickener as parameter. Film thickness in the lump addition method is determined by the temperature of application condition, with thin film being formed under low temperature conditions. By contrast, the δ of the division method is virtually constant ($\delta = 0.17 \times 10^{-3}$ m) even if the film temperature was changed. What is more, it was confirmed that δ was smaller compared to the lump addition method. This is to say, we discovered that we can design a thin plate in a condition that is not easily influenced by the filming temperature, if we use the division addition method.

In order to investigate why results such as those shown in **Fig. 7** are obtained, we measured the viscosity of the paste. **Fig. 8** shows the measurements taken. In this figure, the reason why the results obtained in the lump method are not plotted is because the values were greater than the measurement tolerance of the viscometer ($\eta = 2.0$ Pa·s or more), making instrumentation impossible. Thus, we found that the paste created using the lump addition method was of higher viscosity than the paste created using the division addition method.

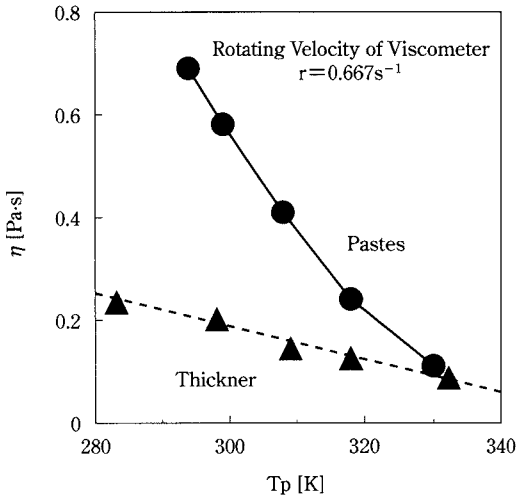

Fig. 8 Relation of Temperature T_p with Viscosity of Pastes η.

Fig. 9 shows the relationship between the volume resistivity rate ρv of the film and its coefficient of variance C_v, and the application temperature T_p. We found that both volume resistivity rate and coefficient of variance are small values when the division addition method was used. This was the same even if the temperature changed while filming. That is, in the division addition method, a film superior in electroconductivity is formed, with good reproducibility.

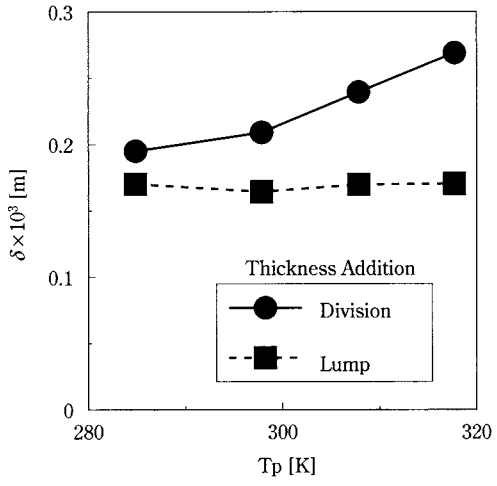

Fig. 7 Relations of Temperature T_p with Film Thickness δ.

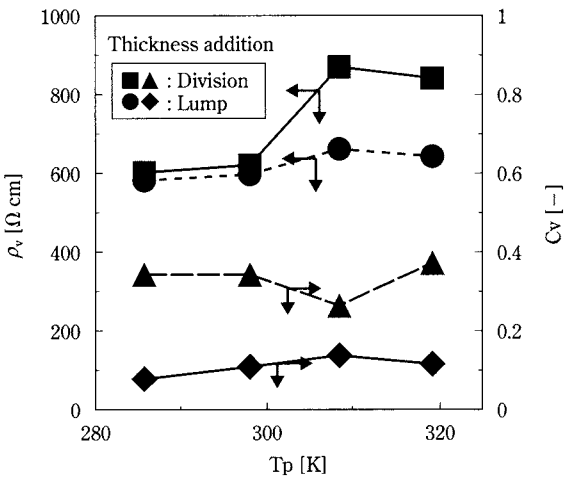

Fig. 9 Relations of Temperature T_p with Volume Resistivity Rate ρ_v and Coefficient of Variance C_v.

These results and findings indicate that by divided addition of thickener, we can produce a film (plate) for the lithium ion secondary battery, which is thin and has a high dispersion of plate particles with excellent volume resistivity rate.

4.1.3 Relationship between Volume Resistivity Rate and Glossiness and Film Density

Fig. 10 shows the relationship between volume resistivity rate of the film ρ_v and film density σ. The constituents and quantity of mix are the same in this figure. **Fig. 10** indicates the discovery that when film density is high, volume resistivity rate is low and electroconductivity is good. High film density means that the particles of the positive electrode are in close contact, creating high-density filling. We construed that if high-density filling occurs particle contact number becomes large, which becomes reflected in volume resistivity rate. In other words, good volume resistivity rate is obtained under high film density conditions. It is known that in order to form a film with high density, we can prolong the mixing time, for example.

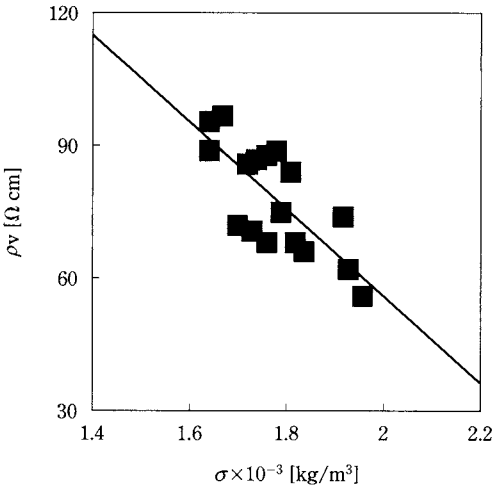

Fig. 10 Relation of Film Density σ with Volume Resistivity Rate ρ_v.

Fig. 11 shows the relationship between film density σ and glossiness Gs. We see that in a condition under which film density is high, glossiness has a high value, indicating a good dispersion of electrode particles. This result indicates that in a film where the aggregate is small and the surface is smooth, film density shows a high value.

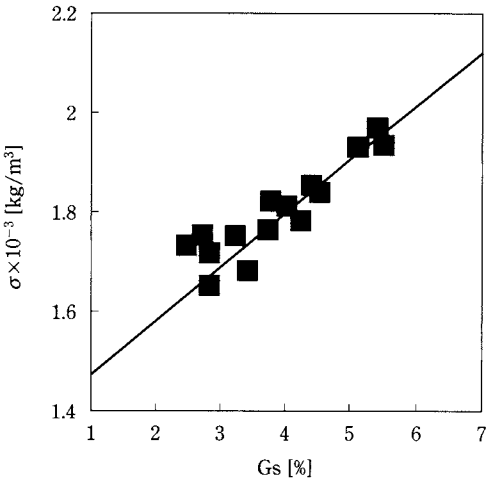

Fig. 11 Relation of Film Density σ with Glossiness Gs.

4.2 Investigation of the Evaluation Method of Dispersion in Paste

In evaluating the dispersion of positive electrode particles in the lithium ion secondary battery, one can make evaluations either by focusing on the paste form or the film form. The evaluation that is directly related to battery performance is that which focuses on the film, as described in the previous section. However, in the paste form, which is equivalent to the preliminary process in a production line, if we can already make evaluation of the state of dispersion in the film, the equivalent to the after-process, not only cost reduction through early detection of defective products can be made but also the actual production can be put on an assembly line.

As evaluation methods of dispersion of low-viscosity suspension and emulsion, viscosity distribution, sedimentation method, and zeta potential measurement are being considered. However, there is not yet any adequate evaluation method that can be applied to the kneading and dispersion of solid-liquid system of high viscosity/highly viscose state, which is the subject of this paper. This is why, in order to find an evaluation method, we decided to look at electric conductivity, in view of the electrical properties of the battery material.

To evaluate dispersion in the paste, the levels Ia of lithium cobalt oxide ($LiCoO_2$) and of carbon only were varied in the kneading and dispersion. Electric conductivity L was measured and the results are given in **Fig. 12**. To facilitate comparison and study, data on the x-axis is organized using mass ratio based on thickener. We can see from **Fig. 12** that the electric conductivity L of lithium cobalt oxide (positive

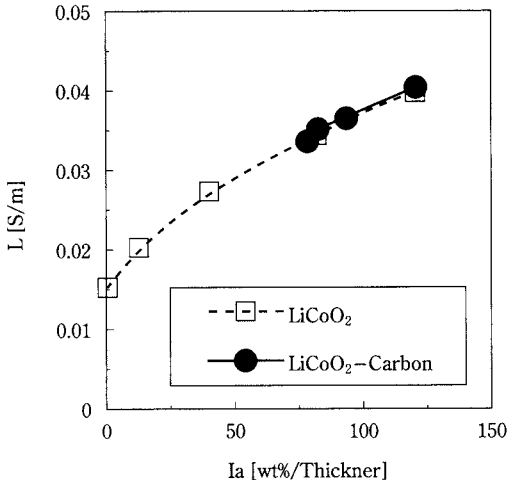

Fig. 12 Measured Value of Conductivity L.

electrode active material) on its own, and of the mixture (lithium cobalt oxide carbon), show a good match. Moreover, electric conductivity changes in proportion to the amount of plate particles (density). In short, it suggests that the dispersion of plate particles in the paste state can be evaluated using electric conductivity. Now, we conducted a flame reaction test of the supernatant liquid of the paste. Red flames resulted. From this, we can say that the electric conductivity finds lithium ion rather than carbon network, and furthermore that it is more strongly dependent on lithium cobalt oxide levels than on carbon levels.

Fig. 13 is a conceptual representation of the relationship between the electrode particle dispersion and film materials as discovered in the above findings and investigation. If the paste becomes particulates, dispersion is good, therefore, even with a thin film thickness, high density filled film can be produced.

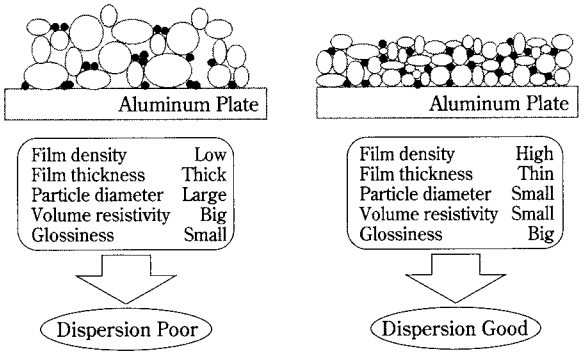

Fig. 13 Relationship Between Schematic Diagrams of Plate and Results of Measurement of Physical Properties.

Moreover, glossiness is high, meaning that a film that is not highly convex or concave is formed. A high-density filled film is good in electric conductivity.

5. Conclusion

(1) This paper has shown that dispersion of electrode particles in a lithium ion secondary battery can be quantitatively evaluated by measuring the film's volume resistivity rate, glossiness, film thickness and film density and by organically examining the instrumentation values.

(2) If thickener is added using the division addition method, we discovered that we can produce a film (plate) that is thin and good in volume resistivity rate due to highly dispersed electrode particles. Also, we pointed out that by investigating the relationship between volume resistivity rate and mixing time, the finish time of the dispersion operation can be determined.

(3) We suggested that by measuring the particle distribution and electric conductivity of the paste, the dispersion of electrode particles in the paste state could be evaluated.

References

1) Terashita, K. and K. Miyanami, "Evaluation of Microscopic Particle Mixture Condition," *J. Japan. Soc. Powder and Powder Metallurgy*, **45**, 854-858 (1998)

2) Terashita, K., K. Miyanami and K. Sakamoto, "Formation of High-grade Videotape and Dispersion of Magnetic Fine Particles," *J. Japan. Soc. Powder and Powder Metallurgy*, **40**, 855-858 (1993)

Author's short biography

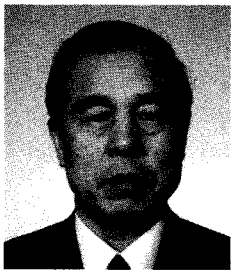

Keijirou Terashita

Keijirou Terashita received his Ph.D. in chemical engineering from Osaka Prefecture University. Currently, he is an associate professor at the department of chemical engineering, Osaka Prefecture University. He is also a visiting professor at Pharmaceutical Science, Rutgers University. Now, he is an editor of Pharm Tech Japan, boardman of Japan Society of Powder and Powder Metallurgy. His major research interest lies in mixing, kneading, granulation, coating, and computer simulation.

Kei Miyanami

Kei Miyanami graduated in Chemical Engineering from Osaka Prefecture University (OPU). After four years research on computer control of chemical plants at Hitachi, Ltd, he obtained faculty position at Chemical Engineering from OPU in 1965. He obtained Ph.D. degree in Chemical Engineering at OPU in 1971. In 1979, he became Professor of Chemical Engineering at OPU. Currently he is the Emeritus Professor. He was at the position of former editor in chief of KONA Journal of HOSOKAWA Foundation in the past, seven years. Now he is working as members of many councils and committees in local governments for environmental assessment-protection-affairs and wastes management.

Estimation of Stress Distribution Arising in a Powder Bed During Compaction by FEM considering Anisotropic Parameters†

Atsuko Shimosaka, Koji Hayashi, Yoshiyuki Shirakawa and Jusuke Hidaka
*Department of Chemical Engineering and Materials Science Faculty of Engineering Doshisha University**

Abstract

Stress analysis on the compaction of ceramic powder was performed by the finite element method (FEM) to predict the optimum conditions. For the purpose of practical application, the powder bed was treated as an elastoplastic material, and the constitutive equation was derived from Drucker-Prager's yield function expressed in terms of invariants of stress tensors and Hill's anisotropic parameters on stress in the powder bed. The powder bed has a multiform bulk density distribution, along with discontinuous deformation behavior during compression, which change the mechanical characteristics of the powder bed during compaction. It is therefore necessary to treat powder characteristics as variation associated with the progress of powder compaction.

In this paper, Young's modulus and the strain-hardening rate are expressed as functions of minor principal stress and strain. These functions can be determined by a triaxial compression test. Hill's anisotropy parameters, which are induced during the compaction process, were numerically obtained by simulating the compacting behavior of particles using the particle element method (PEM).

The problem of powder compaction was analyzed on the basis of the proposed constitutive model. The calculated results of the nonlinear stress-strain relation and stress distribution during powder compaction agreed well with the measured values. Results showed that the proposed procedure offers information that is useful in deciding the optimum conditions for powder compaction.

Keywords: PEM, FEM, elastoplasticity, anisotropy, powder compaction

Introduction

Because the microstructure of sintered products heavily influences the mechanical and electromagnetic characteristics of ceramics, obtaining ceramics with the desired characteristics necessitates precision control of the microstructure. The main processes governing microstructure formation are forming and sintering, and it is especially important that the forming process yield a product having a uniform particle structure. This is because while in the forming process the particle structure is formed by the movement of particles making up the product, in the sintering process the product's microstructure is formed by the movement of individual atoms and molecules. Hence it is quite impossible for the sintering process to correct particle structure defects that have arisen in the forming process. For the purpose of microstructure control, it is therefore necessary to obtain a product with a uniform particle structure in the forming process.

Particle structure multiformity arising in the compression forming of powders is caused by the stress characteristics peculiar to powder systems. Specifically, because friction acts on the points of contact between particles, powder deformation behavior is accompanied by intermittent shearing collapse, giving rise to a stress distribution in the powder bed that in turn causes a bulk density distribution. Thus, controlling the compact's particle structure makes it necessary to determine the relationship of operating conditions to the powder bed's stress distribution,

* 1-3, Tataramiyakodani, Kyotanabe, Kyoto 610-0321, Japan
† This report was originally printed in Kagaku Kougaku Ronbunshu, **26**, 23-29 (2000) in Japanese, before being translated into English by KONA Editorial Committee with the permission of the editorial committee of the Soc. Chemical Engineers, Japan.

which changes during the compression process, and to powder characteristics. Needless to say, it is hard to experimentally measure the stress distribution in a compact under high pressure, and therefore numerical simulations are useful for obtaining these relationships.

Simulation methods for powder phenomena are the particle element method (PEM), which treats powder as a discrete model, and the finite element method (FEM), which is a continuous model. PEM directly estimates the movements of individual particles. It can accurately express behavior of granular materials and the discontinuity of stress transmission, and has proved itself a very powerful tool for microscopic observations and estimating physical quantities in relation to powder behavior. By contrast, FEM views powder behavior macroscopically by considering powder to be a continuum, and has been used also for granular materials owing to factors including the ease by which initial conditions and boundary conditions can be treated. However, it is often the case that constitutive models are complex, or that a model's mechanical constants limit its range of applicability. At the least it is desirable that the derivation process of constitutive relationships be apparent, and that its mechanical constants can be easily measured experimentally, and are generalized. For that purpose it is important to establish a method for determining constants that are peculiar to powders and that pay sufficient attention to the stress-strain relationships of powder beds and their connection with mechanical characteristics.

For the purpose of application to practical problems, we considered a powder bed to be a compressible, elastoplastic material, and proposed a method that uses the incremental finite element method to estimate the stress distribution in the compact, which changes during the powder compression forming process. In particular we explored the determination of the anisotropic parameters of compressed powder beds using PEM, as well as the expression of the mechanical characteristics of powder beds, which change from moment to moment during the powder compression forming process, and the introduction of finite element method simulations. After confirming the validity of our estimation method, we describe how the development of stress distribution in a compression formed body is related to the powder-bed elasticity modulus and the wall friction coefficient, and show the usefulness of this estimation method in designing compression forming operations.

1. Simulation of Powder Compression Forming Behavior

1.1 Constitutive Equation for Elastoplasticity

We performed our research on a powder bed compressed in a cylindrical compression container, and assumed the bed to be much like an elastoplastic material. A major characteristic of powders, which are an assembly of individual particles, that makes them different from ordinary solid materials is that powders have very high compression rates. That is to say, from the initial compression phase the deformation behavior of powder beds in the compression process involves, in addition to elastic deformation, a plastic deformation occurring in conjunction with a change in volume, with the compression rate ultimately attaining 15 to 30%. Systems like this, in which elastic deformation and plastic deformation occur simultaneously, require the use of incremental analyses because the stress-strain relationship is nonlinear.

The powder bed in the cylindrical compression container can be treated as an axisymmetric material, for which reason the following are the basic equations for the unknown parameters in **Fig. 1**: displacement increment $\{du\}$, stress increment $\{d\sigma\}$, and strain increment $\{d\varepsilon\}$.

Stress equilibrium equations

$$\frac{d\sigma_r}{dr}+\frac{d\tau_{rz}}{dz}+\frac{\sigma_r}{r}=0 \tag{1}$$

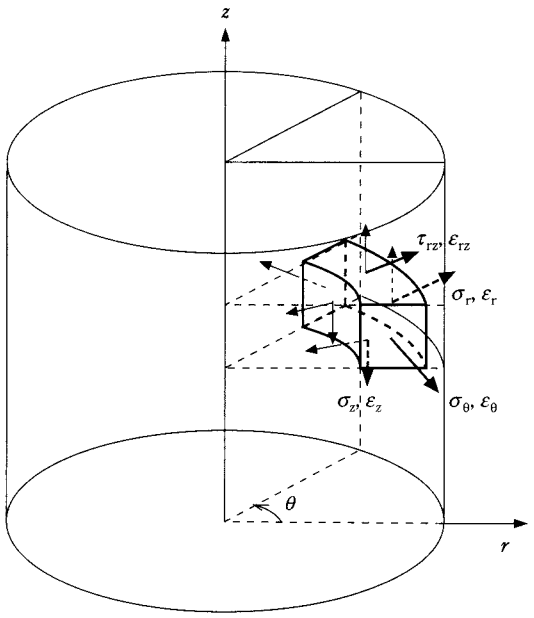

Fig. 1 Stress and Strain of Axisymmetrical Elements

$$\frac{d\sigma_z}{dz}+\frac{d\tau_{rz}}{dr}+\frac{\tau_{rz}}{r}=0 \tag{2}$$

Compatibility equation

$$\{d\varepsilon\}=[d\varepsilon_z d\varepsilon_r d\varepsilon_\theta d\varepsilon_{rz}]^T=\left\{\frac{\partial(dv)}{\partial z}\ \frac{\partial(du)}{\partial r}\ \frac{du}{r}\ \frac{\partial(du)}{\partial z}+\frac{\partial(dv)}{\partial r}\right\}^T \tag{3}$$

Constitutive equation

$$\{d\sigma\}=[D]\{d\varepsilon\} \tag{4}$$

Where:
$[D]$ is the stress-strain matrix.

The method of solving these equations according to the variational principle is the same as the method for analyzing the elastoplasticity stress of ordinary solids, but the problem is the constitutive equation that provides the constitutive relationships among substances. Deriving the constitutive equation for an elastoplast material requires a yield condition equation that determines the limit of the state of elasticity. The field of soil engineering, which concerns granular materials and rocks, analyzes elastoplasticity using the following Drucker-Prager yield condition. [1] This conditional equation is also used for powder beds because it can take compressibility and work hardening into account.

$$f=-\alpha J_1+\sqrt{J_2'}-K=0 \tag{5}$$

$$J_1=\sigma_r+\sigma_\theta+\sigma_z$$

$$J_2'=\sigma_r'\sigma_\theta'+\sigma_\theta'\sigma_z'+\sigma_z'\sigma_r'$$

$$\sigma_i'=\sigma_i-\frac{1}{3}(\sigma_r+\sigma_\theta+\sigma_z)$$

J_1 in the first expression is the first principle invariant of stress, and powder bed compressibility is taken into account by this first term. J_2' is the second principle invariant of deviatoric stress, and K is shearing elastic yield stress. While the above equation can be applied as is to isotropic materials, in a powder bed under compression, intermittent slip collapse occurs continually due to the friction acting at points of contact between particles, in turn causing the frequent realignment of particles, and thus continually changing the direction of the principal stress. It is known that for this reason particle structure change is so-called induced anisotropic change instead of isotropic. [2] To take this into account, we decided that for our yield condition equation we would use the following equation, which incorporates Hill's anisotropic parameters (F, G, H, N). [3]

$$f=-\alpha_r\sigma_r-\alpha_\theta\sigma_\theta-\alpha_z\sigma_z+\sqrt{J_2''}-K=0 \tag{6}$$

$$J_2''=(\sigma_r''^2+\sigma_r''^2+\sigma_r''^2+2\tau_{rz}'')/2$$

$$\sigma_z''=\frac{H(\sigma_z-\sigma_r)+G(\sigma_z-\sigma_\theta)}{F+G+H},\ \sigma_z''=\frac{F(\sigma_r-\sigma_\theta)+H(\sigma_r-\sigma_z)}{F+G+H},$$

$$\sigma_\theta''=\frac{G(\sigma_\theta-\sigma_z)+F(\sigma_\theta-\sigma_r)}{F+G+H},\ \tau_{rz}''=\frac{N\tau_{rz}}{F+G+H}$$

Parameters α and K are given by the following equations as functions of internal friction angle ϕ_i and shearing adhesive force c.

$$\alpha_r=\frac{\sin\phi_i}{\sqrt{9+3\sin^2\phi_i}},\ \alpha_\theta=\alpha_r\frac{\sigma_\theta''}{\sigma_r''},\ \alpha_z=\alpha_r\frac{\sigma_z''}{\sigma_r''} \tag{7}$$

$$K=\frac{3c\cos\phi_i}{\sqrt{9+3\sin^2\phi_i}} \tag{8}$$

On the basis of incremental strain theory, [1] we assumed that the strain increment $\{d\varepsilon\}$ is given as the sum of the elastic strain increment $\{d\varepsilon^e\}$ and the plastic strain increment $\{d\varepsilon^p\}$. By applying the associated flow rule, which uses the yield function as the plastic potential, the following incremental elastoplasticity constitutive relationship is obtained.

$$\{d\varepsilon\}=\{d\varepsilon^e\}+\{d\varepsilon^p\}=[D^e]^{-1}\{d\sigma\}+h\frac{\partial f}{\partial\{d\sigma\}} \tag{9}$$

$$\{d\sigma\}=[D^{ep}]\{d\varepsilon\}$$

$$=\left[[D^e]-\frac{[D^e]\left(\frac{\partial f}{\partial\{d\sigma\}}\right)\left(\frac{\partial f}{\partial\{d\sigma\}}\right)^T[D^e]}{\left(\frac{\partial f}{\partial\{d\sigma\}}\right)^T[D^e]\left(\frac{\partial f}{\partial\{d\sigma\}}\right)-\left(\frac{\partial f}{\partial\{d\varepsilon^p\}}\right)^T\left(\frac{\partial f}{\partial\{d\sigma\}}\right)}\right]\{d\varepsilon\} \tag{10}$$

Where:
$[D^e]$ is the elasticity stress-strain matrix.
With E as Young's modulus and ν as Poisson's ratio, $[D^e]$ is given by this equation.

$$[D^e]=\begin{bmatrix}d_{11}&d_{12}&d_{13}&0\\d_{21}&d_{22}&d_{23}&0\\d_{31}&d_{32}&d_{33}&0\\0&0&0&d_{44}\end{bmatrix}=\frac{E(1-\nu)}{(1+\nu)(1-2\nu)}\begin{bmatrix}1&\frac{\nu}{1-\nu}&\frac{\nu}{1-\nu}&0\\\frac{\nu}{1-\nu}&1&\frac{\nu}{1-\nu}&0\\\frac{\nu}{1-\nu}&\frac{\nu}{1-\nu}&1&0\\0&0&0&\frac{\nu}{1-\nu}\end{bmatrix} \tag{11}$$

Therefore by expanding Eq. 11 and using the strain-hardening postulate, the following elasticity stress-strain matrix $[D^{ep}]$ is obtained.

$$[D^{ep}]=[D^{e}]-[R] \tag{12}$$

$$[R]=\frac{1}{R}\begin{bmatrix} R_1^2 & & (SYM) & \\ R_1R_2 & R_2^2 & & \\ R_1R_3 & R_2R_3 & R_3^2 & \\ R_1R_4 & R_2R_4 & R_3R_4 & R_4^2 \end{bmatrix}$$

$$R=4J''_2H'-2\sqrt{J''_2}(R_1\alpha_z+R_2\alpha_r+R_3\alpha_\theta)+R_1\sigma''_z+R_2\sigma''_r+R_3\sigma''_\theta+2R_4\tau''_{rz}$$

$$R_1=-2\sqrt{J''_2}(\alpha_z d_{11}+\alpha_r d_{12}+\alpha_\theta d_{13})+\frac{E}{(1+\nu)}\sigma''_z$$

$$R_2=-2\sqrt{J''_2}(\alpha_z d_{21}+\alpha_r d_{22}+\alpha_\theta d_{23})+\frac{E}{(1+\nu)}\sigma''_r$$

$$R_3=-2\sqrt{J''_2}(\alpha_z d_{31}+\alpha_r d_{32}+\alpha_\theta d_{33})+\frac{E}{(1+\nu)}\sigma''_\theta,$$

$$R_4=-\frac{E}{(1+\nu)}\tau''_{rz}$$

Where:
H' is the strain-hardening rate.

1.2 Determining Mechanical Parameters

As observed above, the particle structure of a powder bed under compression changes moment by moment, and thus the mechanical characteristic values (E, v, H', ϕ_i, c) in the elastoplasticity stress-strain matrix also change. Accordingly, these mechanical parameters must be treated as variables that correspond to the state of compression. We therefore used a triaxial compression test to find the relationship between the compression-stress state and mechanical parameters. **Fig. 2** plots some of the triaxial compression test results obtained for an alumina sample at various minor principal stress (σ_3) values. As this example shows, the powder bed's deviatoric stress-strain relationship is generally linear, while greatly differing depending on the minor principal stress value. Soil mechanics models having the same nature use the relationships with mechanical parameters obtained from compression experiments, converted to equations in various forms. [1] Thus by seeking the apparent Young's modulus E in the constitutive equation from the initial gradient of the deviatoric stress-strain curves, it is possible to determine the relationship as in Eq. 14 with σ_3 as a variable.

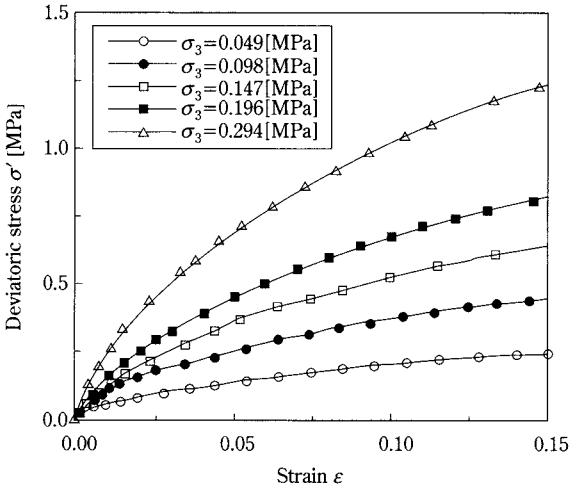

Fig. 2 Deviatoric Stress-strain Diagram (Dp=5 μm)

$$E=a\sigma_3{}^b \tag{14}$$

The strain-hardening rate H', which expresses the powder bed's work-hardening, can be expressed by the following equation with $d\sigma'$ as the deviatoric stress increment and $d\varepsilon^p$ as the plastic strain increment.

$$H'=\frac{d\sigma'}{d\varepsilon^p} \tag{15}$$

Hence, assuming that the strain-hardening rate is obtained from the gradient of the deviatoric stress-plastic strain curves, and that it is approximately proportional to minor principal stress σ_3, it is given by the following equation.

$$H'=l\sigma_3{}^m\varepsilon_p{}^n \tag{16}$$

As in this example, if the five parameters a, b, l, m and n are determined from triaxial compression test results, it is possible to find E and H' at any desired stress state. However, the functional form given as an example is that for alumina powder, and that functional form is determined by the mechanical characteristics of the substance. A powder's internal friction angle ϕ_i and adhesive force c are of course functions of bulk density, but in this research we treated them as constants because their values as obtained from triaxial compression tests within the range of our analysis were nearly constant.

1.3 Estimating Anisotropic Parameters with the Particle Element Method

Solid material anisotropic parameters H, F, G, and N are obtained by conducting tensile tests under uniaxial stress on a piece of material cut out at an arbitrary angle, and then measuring the strain increment ratio (Lankford's r value) of the test piece in the thickness and width directions. [3] However, with a powder bed under compression it is impossible to cut out a sample piece and perform a compression test, and the r value changes from moment to moment

with change in the particle structure. For this reason PEM, [4, 5, 6] which provides much detailed information on the microscopic behavior of powder beds, was used to estimate the anisotropic parameters during the compression process.

To begin with, the following equations show the plastic strain increments in the principal axis direction using the associated flow rule.

$$d\varepsilon_r^p = h\frac{\partial f}{\partial\{\sigma_r\}}df = h\left\{\frac{2\sqrt{J_2''}\alpha_r+\sigma_r''}{2\sqrt{J_2''}}\right\} \tag{18}$$

$$d\varepsilon_z^p = h\frac{\partial f}{\partial\{\sigma_z\}}df = h\left\{\frac{2\sqrt{J_2''}\alpha_z+\sigma_z''}{2\sqrt{J_2''}}\right\} \tag{19}$$

$$d\varepsilon_\theta^p = h\frac{\partial f}{\partial\{\sigma_\theta\}}df = h\left\{\frac{2\sqrt{J_2''}\alpha_\theta+\sigma_\theta''}{2\sqrt{J_2''}}\right\} \tag{20}$$

When these are reorganized for anisotropic parameters under axisymmetric conditions ($N=F+2H=G+2H$), the following equations give the stress and plasticity strain increments as parameter ratios (Lankford's r values).

$$r^0=\frac{H}{F}=\frac{A(\sigma_z-\sigma_\theta)-B(2\sigma_\theta-\sigma_r-\sigma_z)-C(\sigma_r-\sigma_\theta)}{(A-C)(\sigma_r-\sigma_z)} \tag{21}$$

$$r^{90}=\frac{H}{G}=\frac{H}{F} \tag{22}$$

$$r^{45}=\frac{2N-F-G}{2(F+G)}=\frac{H}{F} \tag{23}$$

$$A=d\varepsilon_\theta^p(d\varepsilon_z^p\alpha_r-d\varepsilon_r^p\alpha_z)-d\varepsilon_r^p(d\varepsilon_z^p\alpha_\theta-d\varepsilon_\theta^p\alpha_z)$$
$$B=d\varepsilon_z^p(d\varepsilon_z^p\alpha_r-d\varepsilon_r^p\alpha_z),\ C=d\varepsilon_z^p(d\varepsilon_z^p\alpha_\theta-d\varepsilon_\theta^p\alpha_z)$$

Although using PEM to quantitatively estimate physical quantity still involves many problems, it is likely possible to estimate the above values, which are ratios. In our simulation we therefore packed a cylindrical container with particles as shown in **Fig. 3(a)**, and established a mesoscopic observation field in the center, as in **Fig. 3(b)**. We applied compression from the top under displacement control, and for the particles in the observation field sought the average values of the contact force vectors at each moment and of displacement increments. From those values we calculated stress and strain increments, substituted the results into Eqs. 21 through 23, and solved for the anisotropic parameters during deformation. **Table 1** shows the conditions for this simulation. Although particle size is different from the actual value, we made the breadth of particle size distribution coincide with that of the alumina sample, and, by adjusting the

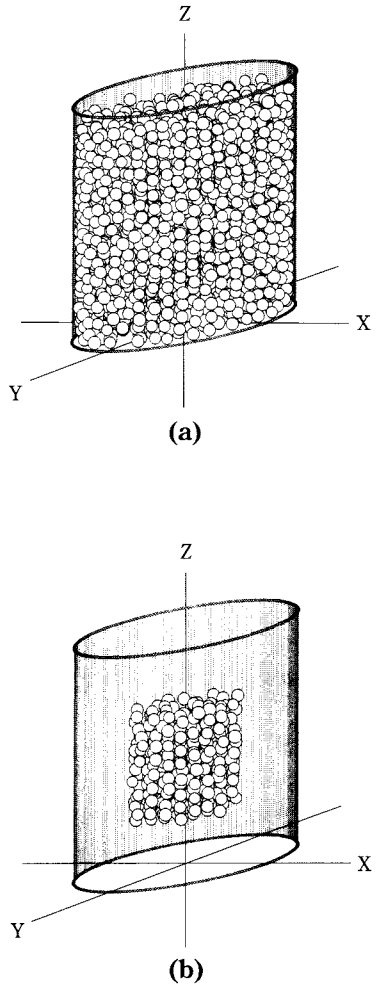

Fig. 3 Initial Position in PEM Simulation

Table 1 Calculation Conditions in the PEM Simulation

Particle density	3.99×10^3	[kg/m^3]
Young's modulus	3.8×10^{11}	[Pa]
Poisson's ratio	0.24	[−]
Coefficient of friction		
particle-particle	0.7002	[−]
particle-wall	0.4663	[−]
Coefficient of repulsion		
particle-particle	0.052	[−]
particle-wall	0.350	[−]
Cohesive force		
20 μm	0.0	[N]
5 μm	0.818	[N]
Average of particle radius	1.016×10^{-2}	[m]
Geometric standard deviation of particle size distribution		
20 μm	1.29	[−]
5 μm	1.48	[−]
Time increment	2.5×10^{-6}	[s]

values for the surface friction coefficients and adhesive force, we made the initial packing bulk densities of the experiment and simulation coincide. This means that even if particle sizes differ, as long as the bulk densities of particles and the particle size distributions of the experiment and simulation are the same, their average coordination numbers will match. [7] Thus macroscopically the configurations of particles can be regarded as having a geometrical resemblance, and one approximately obtains the compression stress and strain relationship corresponding to the alumina sample.

1.4 Compression Simulation Using FEM

As illustrated in **Fig. 4**, the powder bed in the cylindrical compression container (70 mm diameter, 70 mm height) was considered axisymmetrical materials with the central axis forming one side, and the analysis field was divided into 260 elastoplasticity elements. For the powder bed's top, bottom, and side surfaces, which come into contact with the plunger or container walls, we set the zero-thickness joint elements proposed by Goodman, [8] in order to take wall friction into account. While compressing the powder bed, we changed its top surface in 0.1-mm increments by displacement control and sought the stress in the elements at each moment. **Table 2** shows the simulation conditions for two alumina powder samples whose average particle sizes were 20 μm and 5 μm. As noted in section [1.2], the mechanical characteristic values of the elastoplastic elements were determined by triaxial compression testing and single-surface shear testing, while k_n and k_s, the rigidity coefficients of joint elements in the vertical and tangential directions, and friction coefficient ϕ_w were determined by uniaxial compression testing and single-surface shear testing performed on a very thin powder bed. We made k_s a value that is dependent on normal stress, and when shearing stress τ exceeded the threshold stress $\tau_{max}=\sigma_n \tan\phi_w+c$, it was set to $\tau=\tau_{max}$.

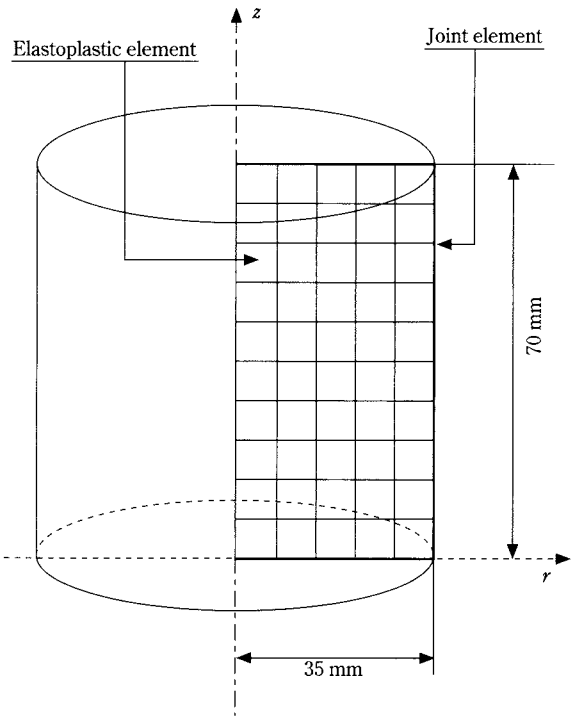

Fig. 4 Computational Region of Cylindrical Powder Bed

2. Experimental Measurement of Powder Bed Stress Distribution

We performed a compression test to confirm the validity of the stress distribution in the powder bed as given by the simulation. Fused alumina sample powder (made by Showa Denko, Dp_{50}=20 μm, 5 μm) was packed into a cylindrical compression container (70 mm diameter, 140 mm height) to a bed height of 70 mm. To measure the compression force inside the powder bed, pressure-sensitive sheets (made by Fuji Prescale, for medium-pressure use) were placed at the powder bed's top, bottom, and side surfaces, and inside the bed. Each of the total 32 sheets was a square measuring 10 mm on a side.

After performing uniaxial compression with a uniaxial compression testing apparatus (UMH-10 made by Shimadzu Corporation), we measured the color darkness of the pressure-sensitive sheets with a densitometer (FPD201 made by Fuji Prescale) and sought the stress distribution in the powder bed. The stress-strain curve was obtained from measurements of the load and compression displacement during compression.

3. Results and Discussion

3.1 Anisotropic Parameters Determined by PEM Simulation

Fig. 5 plots the anisotropic parameters for alumina of particle sizes Dp_{50}=20 μm and 5 μm. Because microscopic particle behavior engendered considerable variation in the values calculated for individual increments, we used averages of values for 500 increments. The anisotropic parameter values for the 20 μm powder fluctuated widely on both sides of the 1.0 value indicating isotropy, but 5 μm powder exhibited values below 0.5 throughout the entire compression

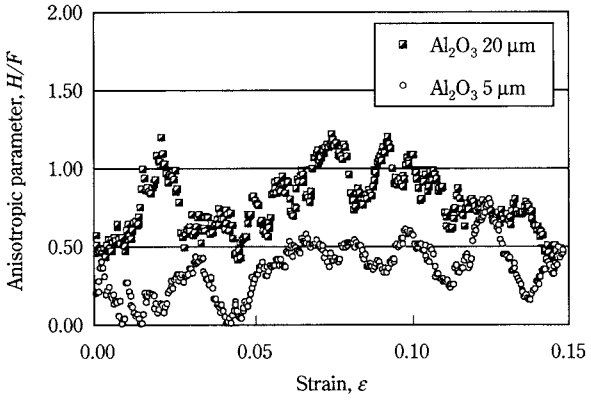

Fig. 5 Anisotropic Parameters Calculated by PEM Simulation

process, which indicates that the effect of adhesive force prevented particle realignment from occurring rapidly in the 5 μm powder. As this shows, estimate results obtained from the PEM simulation closely expressed the behavior characteristics of both powder sizes. Because the calculation of contact force used in this simulation is based on a viscoelasticity model, it cannot be used when particles under compression exhibit extensive plastic deformation and collapse, but if the model for inter-particle contact force is changed to a viscoelastoplasticity model, it will likely be a useful method for a broad range of conditions.

3.2 Uniaxial Compression Simulation Using FEM

In this section the results of the uniaxial compression process simulation, which was conducted using the anisotropic parameters from **Fig. 5** and the values from **Table 2**, are examined while comparing them with experimental results. **Fig. 6** plots the curves for stress and strain acting on the plunger, and **Fig. 7** presents the wall pressure distribution, which is shown using the ratio to σ_{cr}, or the value of horizontal stress in the center of the powder bed's top surface. With the 5 μm test powder, the large strain at the beginning of compression increased bulk density, after which stress rapidly increased. Calculated and experimental values very closely coincide for this compression behavior, for the concentration of pressure on walls, and for other phenomena. To show the effect of anisotropy in **Figs. 6** and **7**, we have used dotted lines to plot results that do not take anisotropy into account. Stress values in **Fig. 6** are the averages of stress acting on the plunger surface, which accounts for the small differences, but the 5 μm fine powder sample curve that does not account for anisotropy exhibits larger plunger stress than do experimental values in the latter phase of compression.

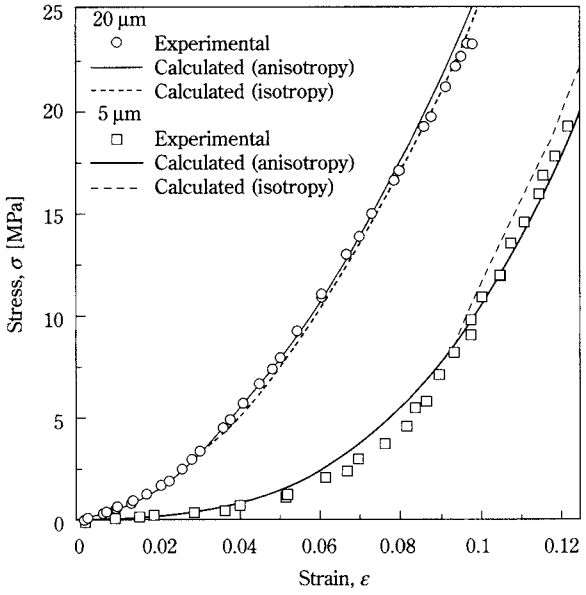

Fig. 6 Stress-strain Diagram

Table 2 Physical Properties Used in the FEM Simulation

		Alumina [20 μm]	Alumina [5 μm]	
Young's Modulus	E	$303\times\sigma_3^{0.426}$	$8.20\times\sigma_3^{0.677}$	[KPa]
Strain-hardening Rate	H'	$1020\times\sigma_3^{0.876}\times\varepsilon^{-0.45}$	$3297\times\sigma_3^{0.48}\times\varepsilon^{-0.50}$	[−]
Internal friction angle	ϕ_i	52.8	51.7	[°]
Wall friction angle	ϕ_w	12.9	13.5	[°]
Unit joint stiffness	k_n	6.00×10^{10}	5.42×10^{10}	
	k_s	$2.61\times10^6\times\sigma_n+7.55\times10^{10}$	$1.33\times10^6\times\sigma_n+4.55\times10^9$	
Cohesive force	c	17.64	19.60	[KPa]
Initial bulk density	γ_0	2019	1850	[Kg/m^3]

Meanwhile, the wall pressure in **Fig. 7**, which shows the values of the elements, indicates severe fluctuations in wall pressure distribution near the plunger's lower end. Especially because some of the wall pressure values are negative, one can see that when anisotropic parameters are not taken into account, stress values are not accurately estimated due to the considerable anisotropic effect observable by examining individual elements.

Fig. 8 is an example of using isostress lines to show the powder bed's internal stress distribution during the compression process. Numerals in the figures are ratios of σ_z to σ_{cz}, the vertical stress at the center of the powder bed's top surface. For the 20 μm powder sample in **Fig. 8(a)**, the stress concentration directly under the plunger and the tendency of the

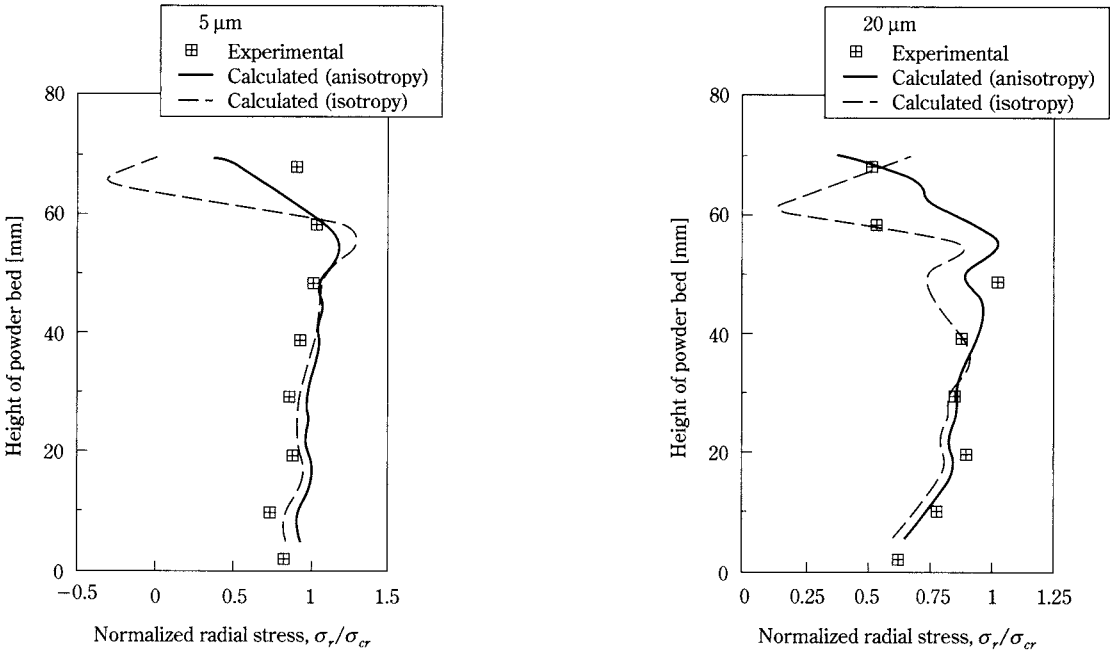

Fig. 7 Normalized Radial Stress σ_r/σ_{cz} on the Wall

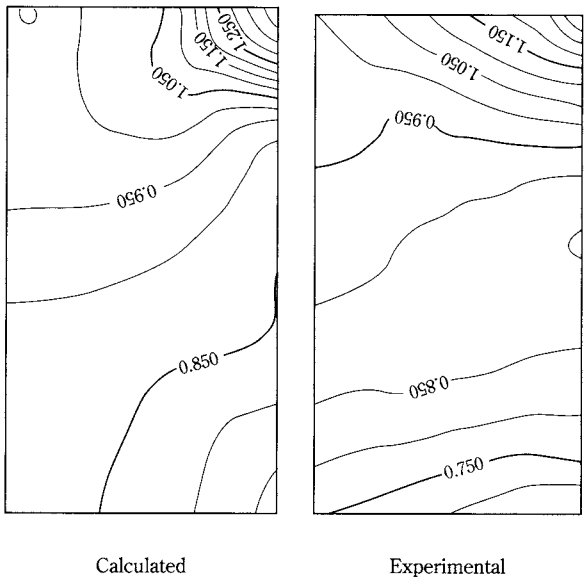

Fig. 8(a) Distribution of Normalized Normal Stress, σ_z/σ_{cz}, in Uniaxial Compression Test (Dp=20 μm, ε=0.0714)

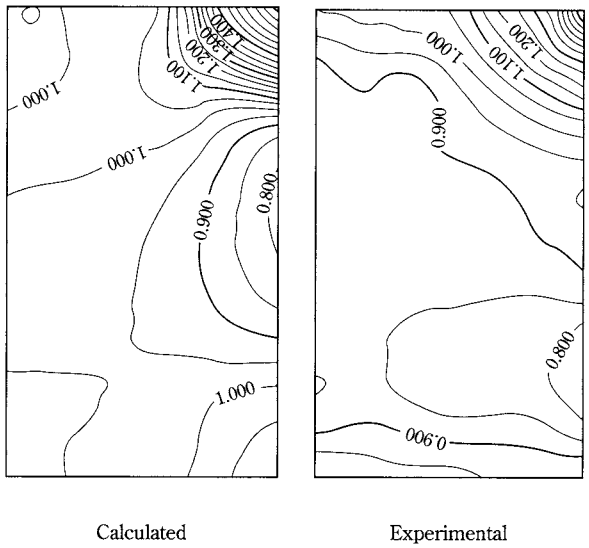

Fig. 8(b) Distribution of Normalized Normal Stress, σ_z/σ_{cz}, in Uniaxial Compression Test (Dp=5 μm, ε=0.143)

stress distribution formed in the powder bed closely coincide with the experimental results. **Fig. 8(b)**, for the fine powder sample, illustrates well the stress distribution, in which there are somewhat large stress values in the powder bed's middle region, and lower stress values in the bed's central region, which then become large again at the bottom. One can discern a few differences between the calculated and experimental values, which are likely attributable to two factors. One is the effect of the initial bulk density distribution. The distribution was uniform according to calculations, but while pains were taken to pack the experimental bed as uniformly as possible, there is never any absolute assurance that there will be no distribution, especially with fine powders such as the 5 μm sample powder. The other factor is the effect of the friction coefficient and apparent adhesive force calculated from triaxial compression testing. These values were obtained by linear approximation of the yield locus obtained from the results within the predetermined pressure range of the compressing tester, but it is known that further raising the pressure makes the yield locus into a curve. Triaxial compression testing at higher pressure is necessary in the simulation stress range, but as this would necessitate special large equipment, our research used the results from triaxial compression testing at low pressure. Nevertheless, overall results indicate that our proposed method of estimating the values for the mechanical characteristics and stress of powder beds is valid.

For that reason we then took advantage of computer simulation, which allows the performance of any desired experiment with ease, to examine the effect of powder characteristics on the stress distribution inside a compact. **Fig. 9** shows an example of the results obtained when varying only parameter b in Eq. 14, which shows the relationship between minor principal stress and Young's modulus, thereby changing the dependence of the state of stress on Young's modulus, and then calculating the development of stress distribution in a compressed powder bed. When Young's modulus was high (b=0.476), stress in the powder bed was very uniform, but when it was low (b=0.376), stress transmission in the powder bed was poor, and there was a quite low-stress region in the bed's lower portion. Near the wall just below the plunger there was a complex stress distribution and a concentration of stress. This suggests that to obtain a compact with a uniform particle structure it is desirable to use powders with a high Young's modulus, i.e., powders whose individual particles are hard and have high fluidity, and which quickly achieve realignment. **Fig. 10** plots the effects of the wall friction coefficient on stress transmission in the powder bed when the values of the bed's mechanical characteristics remained constant and only the wall friction coefficient was varied. When the alumina sample's average particle size was 20 μm and compression strain was 0.05 and 0.1, the stress transmission value was nearly constant until the wall friction coefficient reached about 0.5; at 0.5 and above, stress transmission became extremely poor, a stress distribution developed in the

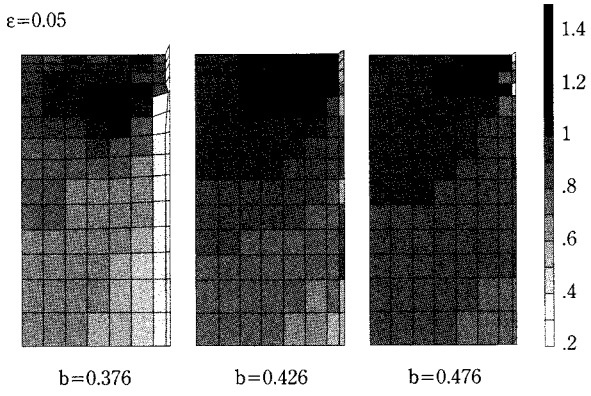

Fig. 9 Effect of Young's Modulus on the Normal Stress Distribution

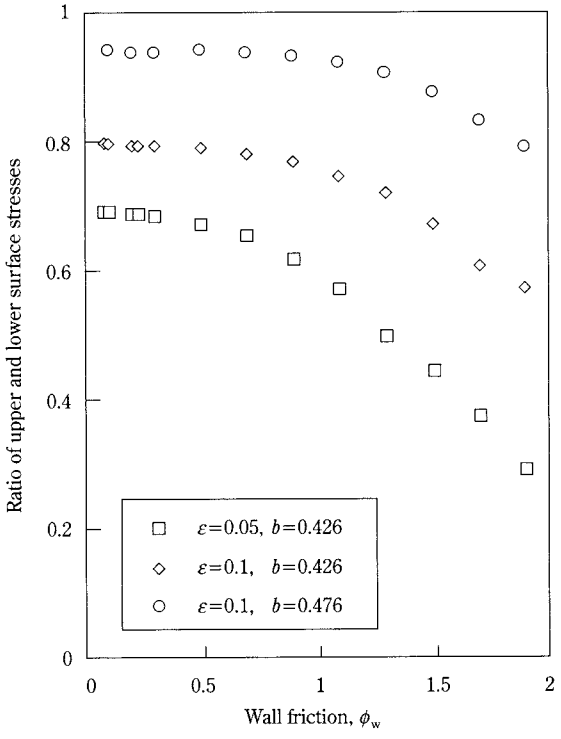

Fig. 10 Effect of Wall Friction on the Ratio of Upper to Lower Surface Stress in the Powder Bed

compact, and the particle structure became multiform. When the powder bed's Young's modulus was high (b=0.476), the stress transmission rate was high, and wall friction had little effect. As these calculation results indicate, for a powder bed having the desired mechanical characteristics it is possible to predict the wall friction coefficient conditions under which stress is sufficiently transmitted and particle structure becomes uniform. Additionally, although this paper deals with Young's modulus and the wall friction coefficient, this estimation method can similarly quantitatively examine the effects of other powder characteristics such as the internal friction coefficient and adhesive force.

Conclusion

The authors proposed a simulation method based on the incremental elastoplasticity finite element method as a way to estimate the stress distribution arising in powder that has been compression-formed. The mechanical characteristics of compressed powder beds change from moment to moment in response to the changes in particle structure and stress in powder beds during the compression process. To take the changes in mechanical characteristics into account, we used the minor principal stress function to express the mechanical characteristics obtained by triaxial compression testing, and introduced the function into a constitutive equation. We also used compression simulation based on the particle element method to find the relationship between the anisotropy induced in particle beds during compression and Hill's anisotropic parameters. The powder bed stress-strain curve and the stress distribution inside a bed obtained by the simulation coincided closely with the alumina powder compression experiment results, thereby confirming the simulation method's validity.

We then used the proposed simulation method to investigate the relationship between Young's modulus and the wall friction coefficient in a compressed powder bed. As a result we found that: the higher Young's modulus in a powder, the more uniform a particle structure the compact will have; and when the wall friction coefficient exceeds a certain critical value, a stress distribution will develop in the powder bed and the particle structure will become multiform. In other words, this method is capable of quantitatively examining the effects of the powder characteristic values that depend on differences in a powder's particle size distribution, particle shape, and other features, in relation to the stress distribution at each moment during the compression process, and the method therefore provides information useful in determining the optimum operating conditions for the compression forming of powders.

The authors would like to express their gratitude to the Doshisha University Research Center for Advanced Science and Technology (RCAST) for its assistance with part of this research.

Nomenclature

a	Parameter in Eq. 14	[−]
b	Parameter in Eq. 14	[−]
c	Internal cohesion stress	[Pa]
$[D]$	Stress-strain matrix	[Pa]
d_{ij}	Component of elastic stress-strain matrix	[Pa]
E	Young's modulus	[Pa]
F	Anisotropic parameter	[−]
f	Yield function	[Pa]
G	Anisotropic parameter	[−]
H	Anisotropic parameter	[−]
H'	Strain-hardening rate	[Pa]
h	Proportional constant in Eq. 9	[−]
J_1	First invariant of stress	[Pa]
J_2'	Second invariant of deviatoric stress	[Pa]
J_2''	Second invariant of deviatoric stress with anisotropic parameter	[Pa^2]
K	Parameter in Eq. 5	[Pa]
k	Unit joint stiffness	[Pa]
l	Parameter in Eq. 16	[−]
m	Parameter in Eq. 16	[−]
N	Anisotropic parameter	[−]
n	Parameter in Eq. 16	[−]
r	Lankford value	[−]
u	Displacement in radial direction	[m]
v	displacement in axial direction	[m]
α	Parameter in Eq. 5	[−]
γ	Bulk density	[kg/m^3]
ε	Strain	[−]
ϕ	Friction angle	[°]
ν	Poisson's ratio	[−]
σ	Normal stress	[Pa]
σ'	Deviatoric stress	[Pa]
σ''	Deviatoric stress with anisotropic parameter	[Pa]
σ_3	Minor principal stress	[Pa]
σ_m	Mean principal stress	[Pa]
τ	Shear stress	[Pa]

Subscripts

c	Center
i	Internal
n	Normal
r	Radial direction
s	Shear
w	Wall
z	Axial direction
θ	Circumference direction
0	Initial

Superscripts

e	Elastic
p	Plastic
ep	Elastoplastic
0	Angle of 0 degrees
45	Angle of 45 degrees
90	Angle of 90 degrees

Literature Cited

1) Kawamoto, T. and M. Hayashi. *JibanKogaku niokeru YuugenYosoKaiseki*, Baifukan, Tokyo, Japan (1978).
2) Oka F. and T. Nakai. "Jiban no Ihousei," *Tsuchi to Kiso*, **41**, 73-80 (1993).
3) Yamada, Y. *Sosei Nendansei*, Baifukan, Tokyo, Japan (1980).
4) Hidaka, J., A. Shimosaka and J. Kano. "Flow Mechanism of Granular Materials Discharging from Bin-Hopper System," *Kagaku Kogaku Ronbunshu*, **20**, 397-404 (1994).
5) Kano, J., A. Shimosaka and J. Hidaka. "A Consideration of the Constitutive Relationship between Flowing Particle," *J. Soc. Powder Technol.*, Japan, **33**, 95-101 (1996).
6) Shimosaka, A., S. Higashihara and J. Hidaka. "Estimation of the Sieving Rate of Powders Using Computer Simulation," *J. Soc. Powder Technol.*, Japan, **35**, 242-249 (1998).
7) Suzuki, M. and T. Oshima. "Estimation of the Co-ordination Number in a Multi-Component Mixture of Spheres," *Powder Technology*, **35**, 159-166 (1983).
8) Goodman R. E., R. L. Taylor and T. L. Breke. "A Model for the Mechanics of Jointed Rock," *J. of the Soil Mech. and Foundations Division*, Proc. ASCE, **94**, SM3, 637-659 (1968).

Author's short biography

Atsuko Shimosaka

Atsuko Shimosaka is Lecturer of Chemical Engineering and Materials Science Department at Doshisha University since 1993. Her research interests center on the mechanical analysis of granular behavior and also materials design for ceramics using computer simulations.

Koji Hayashi

Koji Hayashi received his B.S. in 1993 and M.S. in 1995 in Chemical Engineering and Materials Science Department at Doshisha University.

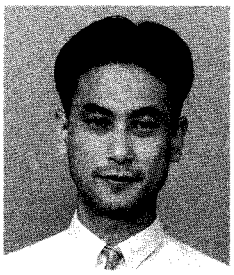

Yoshiyuki Shirakawa

Y. Shirakawa graduated in Solid State Physics from Niigata University (1988), where he also got his Ph. D. (1993). He was took a position as Post Doctor, working on structural and electronic properties of non-crystalline materials for one year, and continued on at Niigata as a research associate in Fundamental Science and Technology. Afterwards he became a research associate in Materials Science and Processing at Osaka University (1995-1998). Since 1998 he has been employed in the Chemical Engineering and Materials Science at Doshisha University, and worked on understanding of interfacial effects and development of nanoparticle composite materials.

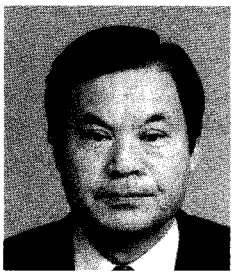

Jusuke Hidaka

Prof. Jusuke Hidaka has been at Doshisha University, Japan since 1976. His major research interests lie in mechanical analysis of powder flow using computer simulation, classification and instrumentation of powder industrial processes using acoustic emission. He is the secretary of the Society of Powder Technology, Japan.

The 35th Symposium on Powder Technology

The 35th Symposium on Powder Technology was held on Tuesday, September 11, 2001 at the Senri Life Science Center, Osaka under the sponsorship of the Hosokawa Powder Technology Foundation and with the support of Hosokawa Micron Corporation. The symposium in this year was also very successful with the attendance of more than 180 with about 30 academic people. The main subject of this year was "Expectation of Nanoparticles Materials".

The 35th Symposium on Powder Technology

Theme: "Expectation of Nanoparticles Materials"

Session 1 Chairperson: Prof. Ko Higashitani (Kyoto Univ.)

- Fabrication of Dense Paste Using Precious Metal and Application of High-Functional Coating — Dr. Toshikatsu Kobayashi (Nippon Paint Co., Ltd.)
- Continuous Synthesis of Metal Oxides Fine Particles by the Supercritical Hydrothermal Synthesis — Dr. Tadafumi Adschiri (Tohoku Univ.)

Session 2 **KONA Award commemorative lectures** Chairperson: Prof. Hiroaki Masuda (Kyoto Univ.)

- Fine Particle Technology for Development of Preparation Process of Powder Materials — Prof. Kunio Shinohara (Hokkaido Univ.)
- Production and High Performances of an Al, Mg, Fe, Zr Nonequilibrium Bulk Alloys by Warm Extrusion of High Pressure Gas Atomized Powders — Prof. Akihisa Inoue (Tohoku Univ.)

Session 3 Chairperson: Prof. Jusuke Hidaka (Doshisha Univ.)

- The Present Status and Prospects of Nano-Technology — Prof. Tomoji Kawai (Osaka Univ.)
- Nano-Technology and Permanent Magnet Materials — Dr. Akira Fukuno (TDK Corporation)
- The Formation and Properties of Nanocrystalline Composite Particles Produced by the Mechano Fusion™ Process — Dr. M. Tenhover (Hosokawa Micron Corp.)

The 9th KONA Award

The 9th KONA Award sponsored by Hosokawa Powder Technology Foundation and given to the scientists or groups who have achieved excellence in the researches related to the basic powder technology, was presented to Professor Kunio Shinohara of Hokkaido University and also to Professor Akihisa Inoue and Associate Professor Yoshihito Kawamura* of Tohoku University by Masuo Hosokawa, President of the Foundation on January 24, 2002 at the R&D Center of Hosokawa Micron Corporation in Hirakata.

Prof. Shinohara's research achievements are related to comprehensive studies on the effect of particle characteristics to the various phenomena of particles.

The research achievements in co-operation of Prof. Inoue and Associate Prof. Kawamura are related to the wide scope subjects on the amorphous alloy powders.

In these studies three Professors obtained epoch-making results.

* Since December 2000 Kumamoto University

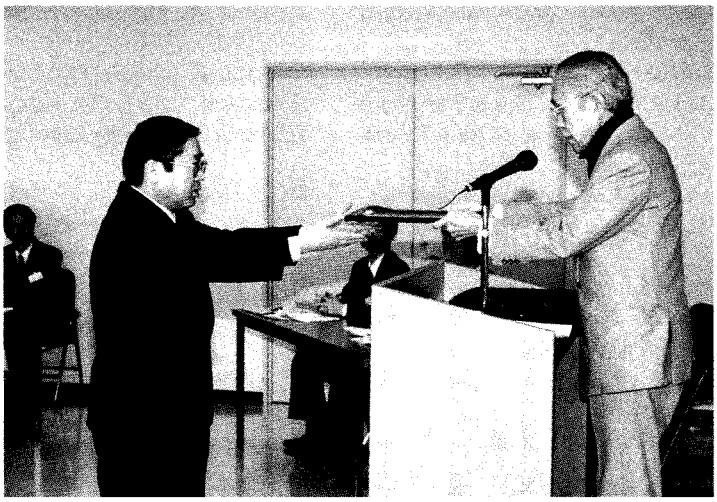

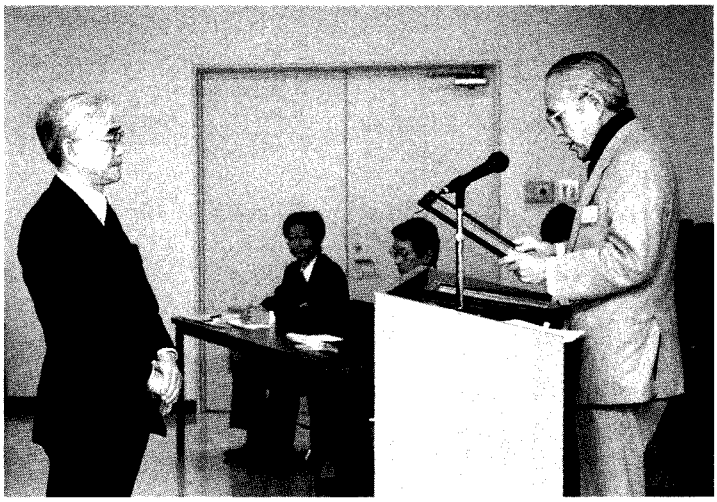

Academic publication concerning powder technology in Japan (2000)

Journal of the Society of Powder Technology, Japan Vol.37 (2000)

Kagaku Kougaku Ronbunshu Vol.26 (2000)

Solid-State Polymerization Systems (SSP) for Recycling PET

Enhance the value of your PET Flake!!

At the present time, post consumer PET bottle recycling is being conducted under the 3**R** Policy (**R**educe **R**e-use and **R**ecycle) by the Japanese government in order to realize the Circulatory Society. Hosokawa Micron has developed an economical and cost effective SSP process for recycling PET flake as a new recycle application making use of our unique SSP technology. The key word is "Lets enhance the value of PET Flake!"

What is SSP?

SSP stands for **S**olid **S**tate **P**olymerization. It is well known that post consumer PET bottles are mainly recycled into textiles (or garments), carpets and sheets. The bottle-grade PET has high quality and high performance among the various PET grades, and that presents an opportunity to utilize this high performance in recycled PET products. That leads to enhancing the value of PET flakes. SSP is a process to raise the degree of polymerization (described as I.V.) in order to reinforce the properties of PET. Through the SSP process, the recycled PET flake becomes capable of once again being converted to PET bottles, as well as producing industrial materials and construction materials which require a higher I.V. than PET bottle grade I.V..

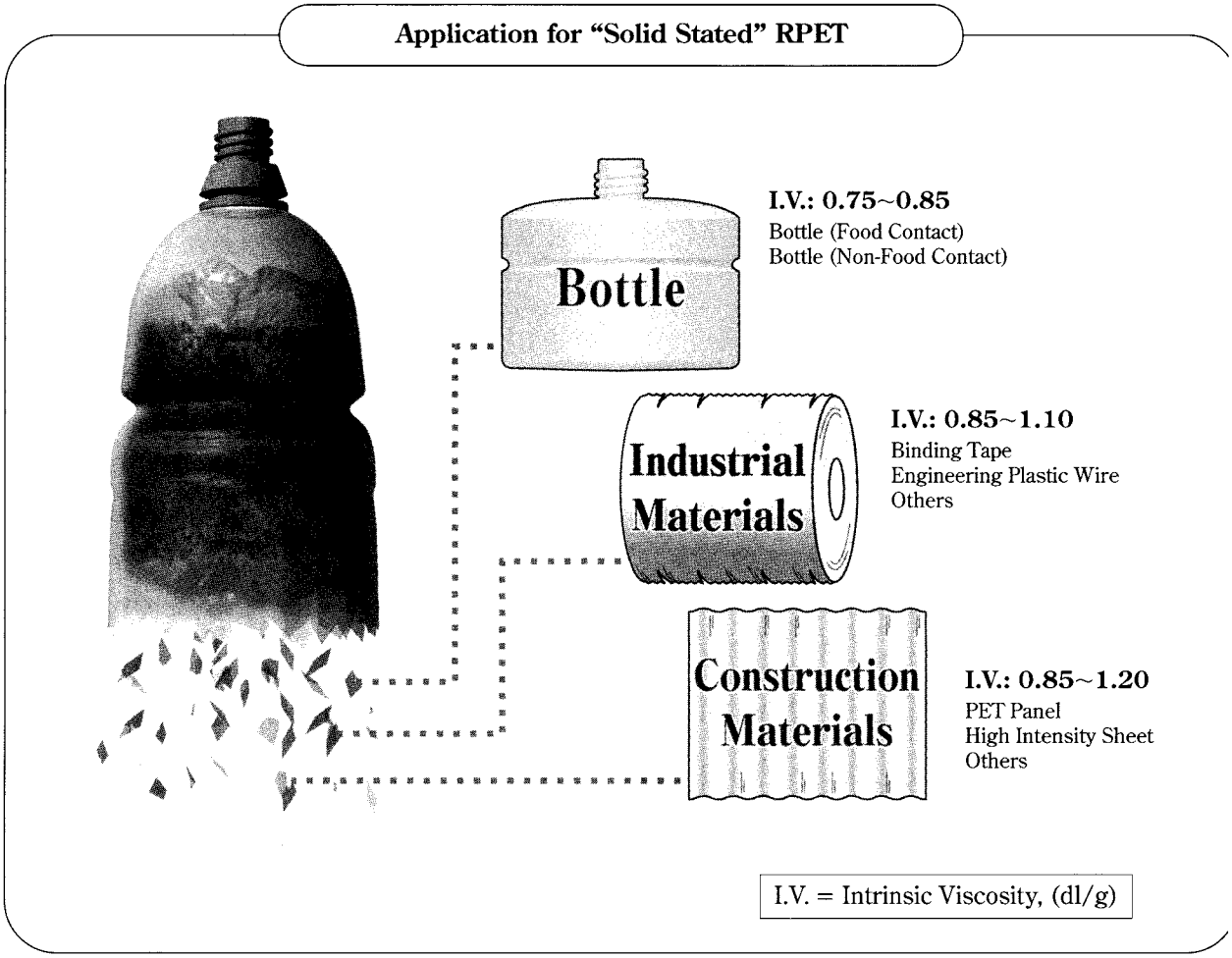

FLOW SHEET

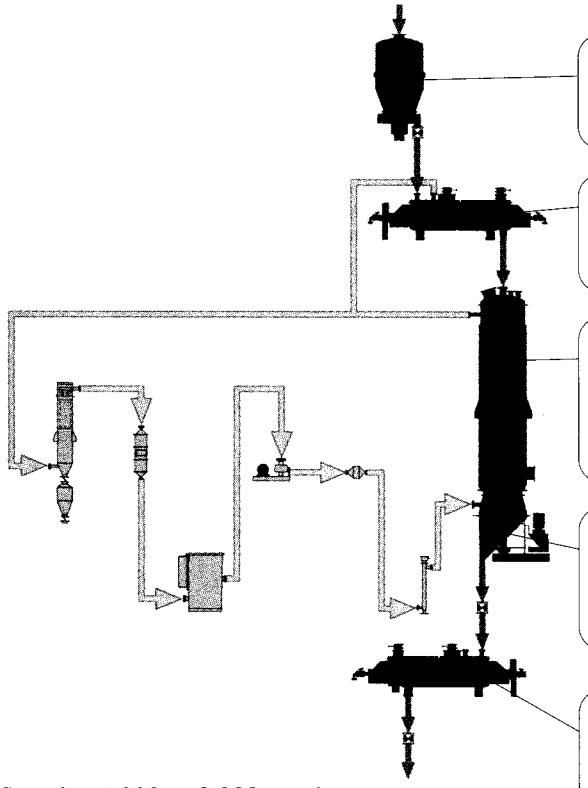

① FLAKE HOPPER
Since the PET flake has poor flow characteristics, a stable discharge is essential.

② DRYER/PREHEATER (TorusDisc)
The flake is heated up to reaction temperature while being further crystallized and dried in this stage.

③ REACTOR (HOPPER REACTOR)
The flake is retained in the reactor for a certain time period to increase its degree of polymerization (I.V.) The increase in I.V. is governed by the retention time (reaction time) and flake temperature (reaction temperature).

④ DISCHARGER (MECHANICAL DISCHARGE)
The Mechanical Discharge will ensure a steady plug flow, and will break up any caking or sintering that does occur in the reactor.

⑤ COOLER (TORUSDISC OR FLUID BED)
The Cooler stops further reaction after the required the degree of polymerization is achieved.

Capacity: 1,000 — 8,000 tons/year

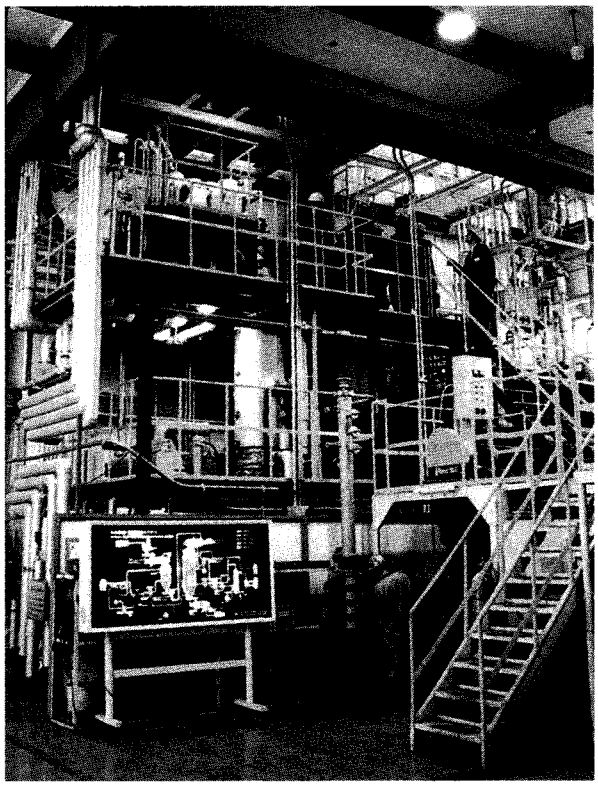

Hosokawa Micron offers you an innovative and cost effective process for PET recycling.

In Autumn 1999, Hosokawa Micron Corp. installed a state-of-the art RPET SSP pilot plant at its R&D center in Osaka, Japan. We are continually exploring new ways to advance our process capabilities, enhance our RPET quality for use in the PET recycle business. Our test facility is available to process any materials that you wish to study.

Bottle-to-Bottle

Bottle-to-Bottle process is built on Super Washing Technology and SSP Technology. The process enables the manufacture of food contact grade PET bottles from past consumer PET bottles. Hosokawa Micron has developed this process with Mitsui Chemicals Engineering Co., LTD as a strategic alliance.

*Super Washing Technology is developed by Mitsui Chemicals Engineering Co., LTD.

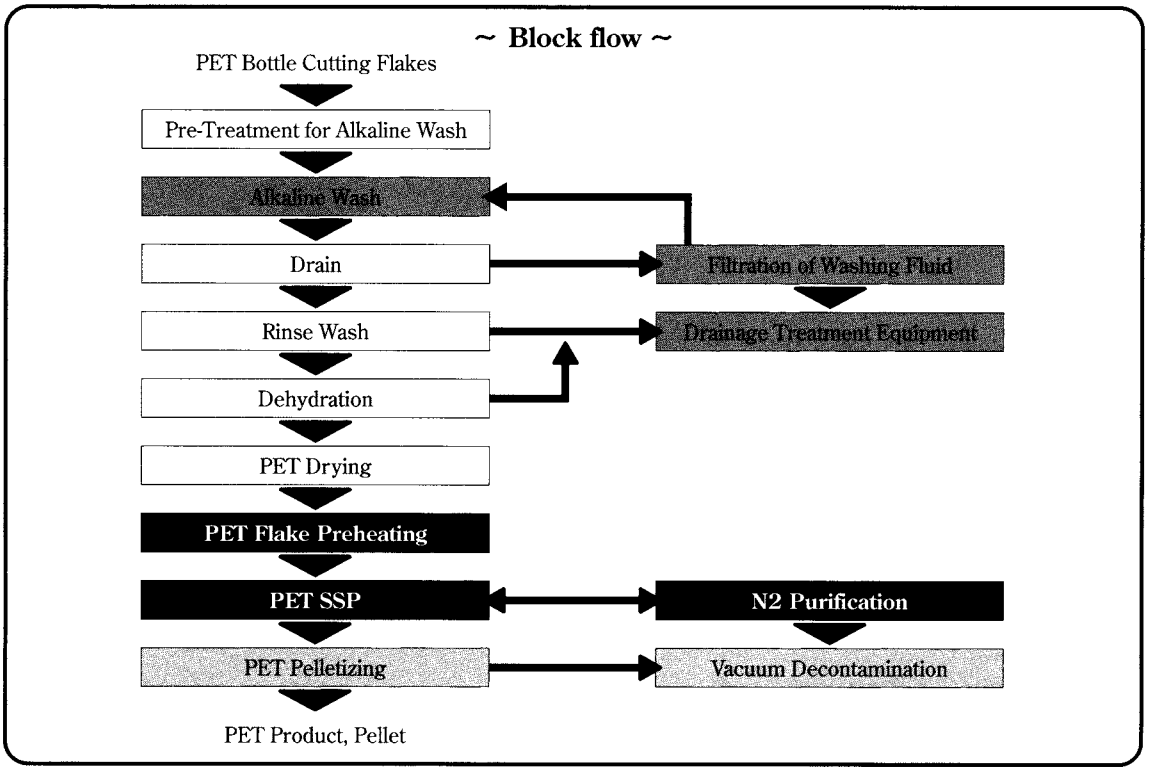

A Bottle-to-Bottle process commercial plant is very cost effective to the processor. The plant is completed with additional Super Washing and SSP systems on the processor's existing PET recycling plant. By enhancing the RPET flake, Hosokawa Micron shows it is committed to making your current recycle business more profitable.

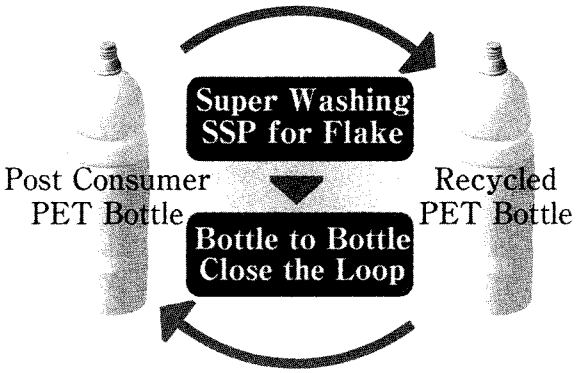

For more information contact; **HOSOKAWA MICRON CORPORATION**
Polymer Systems Company
5-14, 2-chome, Kawaramachi, Chuo-ku,
Osaka 541-0048, JAPAN
Telephone : 81-6-6233-3963
Facsimile : 81-6-6229-9313
E-mail : polymer@hmc.hosokawa.com

Introducing a Compact and Versatile Thermal Processor with a High Heat Transfer Rate and a Precise Temperature Control Over a Wide Temperature Range.

Speed-up your new resin and material research projects with the LABOT™-a joint development product from Hosokawa Micron and Matsui Mfg. Co., Ltd.

LABOT™

Torusdisc for Laboratory Use

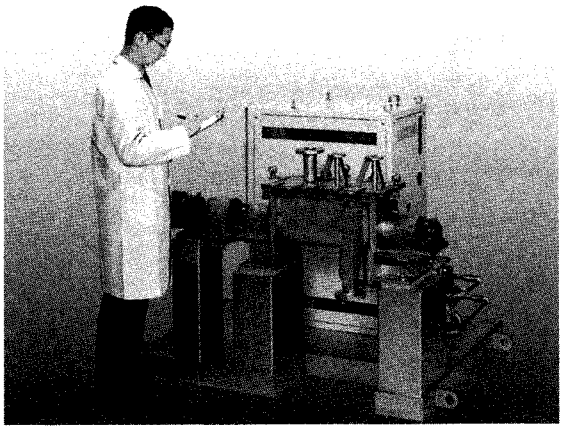

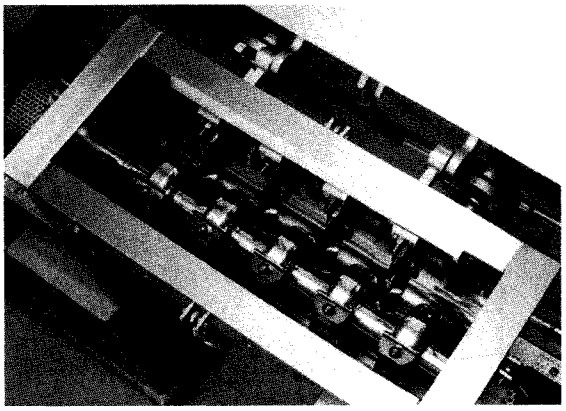

LABOT™ General

The LABOT™ indirectly heats and cools sample materials through a heat transfer media. This is a valuable tool for conducting studies on heating, drying and chemical reaction when only limited quantities of samples are available. This thermal processing unit is a newly developed TORUSDISC with an effective capacity of 5 liters. It is integrated with a compact circulating and control system for the heating media.

LABOT™ Features

1 System Integration

Since the heater and the pump for the heating media are built-in, no additional equipment or preparation is required. The unit is ready for operation by connecting it to the specified electrical energy source.

2 Wide Operating Window (120°C to 320°C)

Experimental studies for a wider range of applications are possible in this unit since the built-in heating media circulating system can operate at upto 320°C.

3 Compact System Design

No special considerations are required when installing this equipment due to its compact design. The external dimensions of the LABOT™ are 1100mm (W) X 1495mm (L) X 1183mm (H) resulting in considerable savings in expensive laboratory space.

4 Batch and Continuous Operation Capability

The LABOT™ is equipped with an adjustable weir in the discharge port. Closing the discharge port allows the unit to be operated in a batch mode. Optional feeders and an open discharge port facilitates operating this unit in the continuous mode.

5 First Step to a Commercial Plant

Reliable R & D results can be obtained with only small quantities of experimental samples with the LABOT™. This is a particularly cost effective first step for validation of a process or scale-up to a production machine.
Assistance in scale-up is available at the Hosokawa Technical Development Center at Hirakata in Osaka, Japan and at Minneapolis in Minnesota, USA.

LABOT™ Flow Chart

LABOT can feed exhaust gas in batch and continuous operations by a system as shown in the Flow Chart.

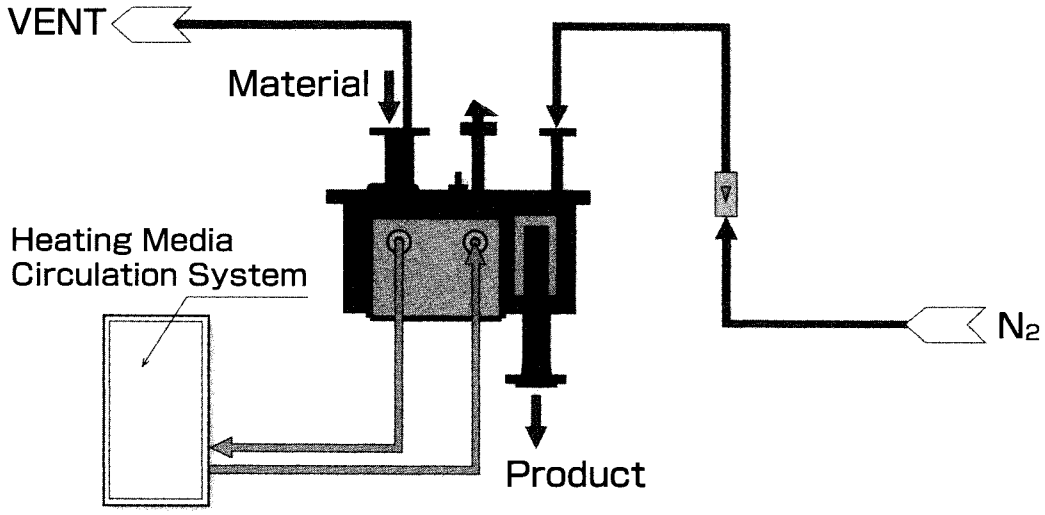

LABOT™ External Dimensions (mm)

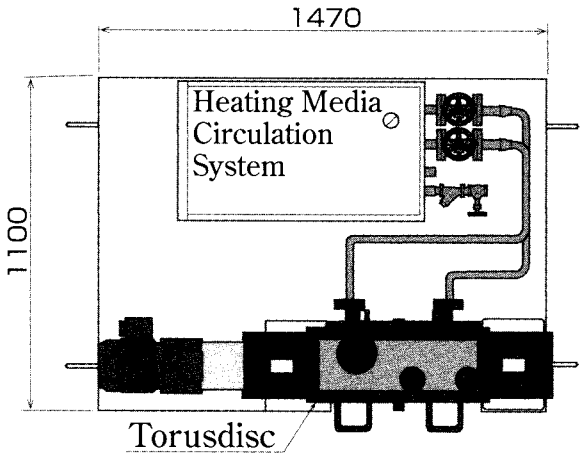

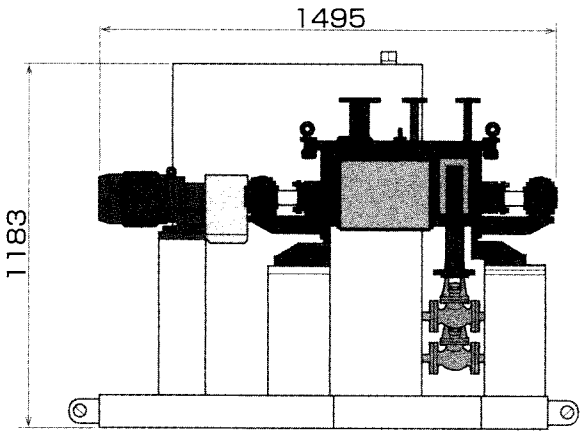

LABOT™ Specifications

Torusdisc	
Type	TDS-5-1.5
Motor	0.75kW, 4P, 1/15,
Rotor rpm	12-120rpm (inverter speed adjustable)
Heat transfer area	0.15m²
Effective capacity	5L max.
Designed pressure	0.7MPa (320°C)
Heating media circulation equipment	
Type	MC-40/30AA-HM
Recommended heating media oil	Barrel therm #400
Operating temperature range	120-320°C
Circulating pump specification	40L/min x 27m
Circulating pump capacity	1.1kW
Electric heater capacity	8kW
Cooling water	15L/min (at 0.3MPa)
Common Specification	
Power supply	220V, 60Hz
Weight	500kg

LABOT is a joint development product from Hosokawa Micron and Matsui Mfg. Co., Ltd.

HOSOKAWA MICRON

Hosokawa Micron Ltd. is a member of the Hosokawa Micron Group, responding to global needs through an emphasis on materials science and engineering. The Group is an international provider of equipment and Technology for powder and particle processing, product recovery, plastics processing and confectionery products. The Group maintains facilities for research, engineering, manufacturing, and service in each of the world's major industrial markets.

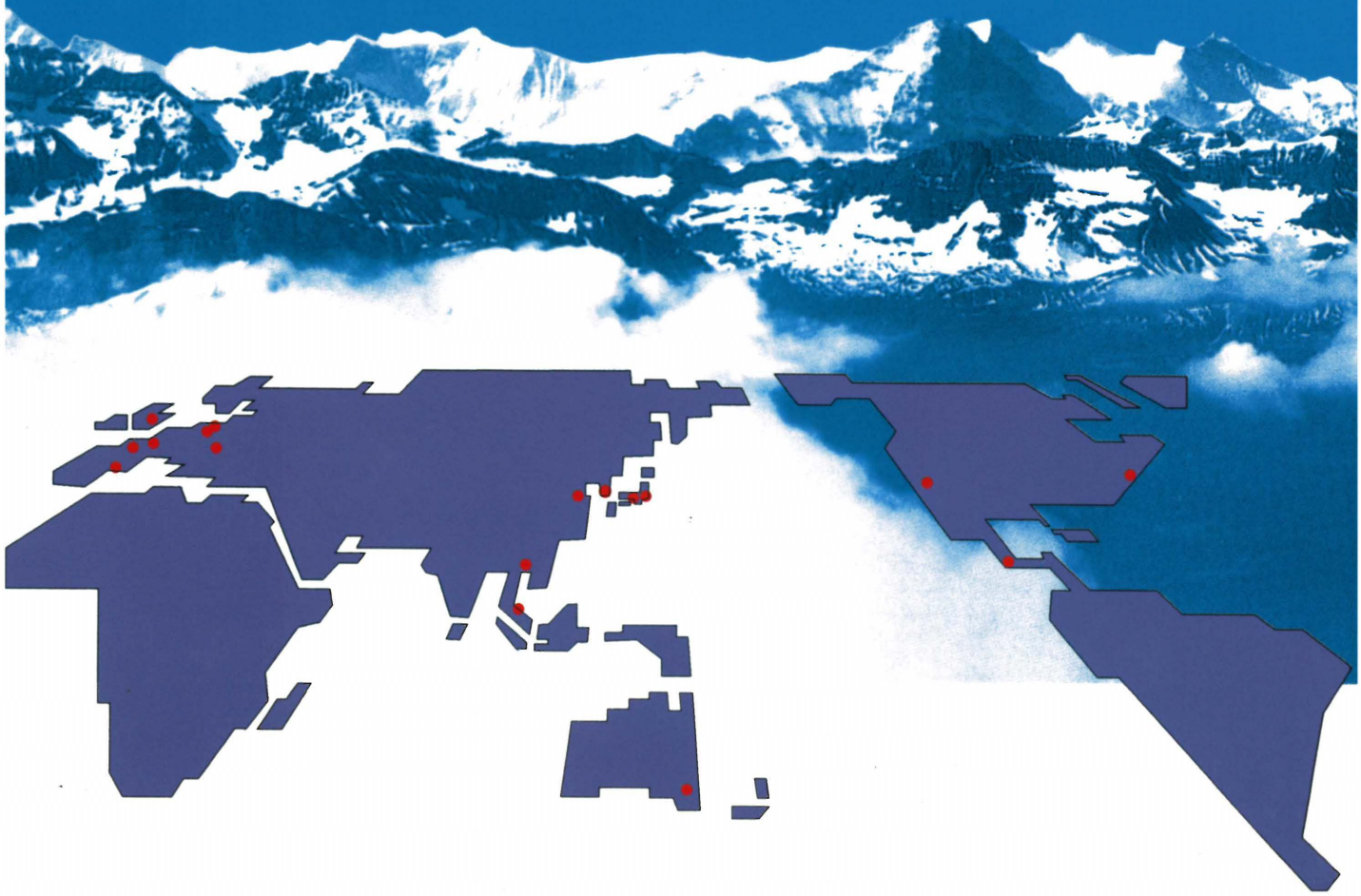

Process Technologies for Tomorrow

HOSOKAWA MICRON

Headquarter Locations;
HOSOKAWA MICRON CORPORATION
5-14, 2-chome, Kawaramachi, Chuo-ku,
Osaka 541-0048, Japan
Tel: 81-6-6233-3968
Fax: 81-6-6229-9267
http://www.hosokawamicron.com/japan